SciTech Publishing
an imprint of the IET

Novel Radar Techniques and Applications

Volume 2: Waveform Diversity and Cognitive Radar, and Target Tracking and Data Fusion

Edited by
Richard Klemm, Ulrich Nickel, Christoph Gierull, Pierfrancesco Lombardo, Hugh Griffiths, Wolfgang Koch

Novel Radar Techniques and Applications

Related titles on radar:

Advances in Bistatic Radar Willis and Griffiths
Airborne Early Warning System Concepts, 3rd Edition Long
Bistatic Radar, 2nd Edition Willis
Design of Multi-Frequency CW Radars Jankiraman
Digital Techniques for Wideband Receivers, 2nd Edition Tsui
Electronic Warfare Pocket Guide Adamy
Foliage Penetration Radar: Detection and characterisation of objects under trees Davis
Fundamentals of Ground Radar for ATC Engineers and Technicians Bouwman
Fundamentals of Systems Engineering and Defense Systems Applications Jeffrey
Introduction to Electronic Warfare Modeling and Simulation Adamy
Introduction to Electronic Defense Systems Neri
Introduction to Sensors for Ranging and Imaging Brooker
Microwave Passive Direction Finding Lipsky
Microwave Receivers with Electronic Warfare Applications Tsui
Phased-Array Radar Design: Application of radar fundamentals Jeffrey
Pocket Radar Guide: Key facts, equations, and data Curry
Principles of Modern Radar, Volume 1: Basic principles Richards, Scheer and Holm
Principles of Modern Radar, Volume 2: Advanced techniques Melvin and Scheer
Principles of Modern Radar, Volume 3: Applications Scheer and Melvin
Principles of Waveform Diversity and Design Wicks *et al.*
Principles of Space-Time Adaptive Processing, 3rd edition Klemm
Pulse Doppler Radar Alabaster
Radar Cross Section Measurements Knott
Radar Cross Section, 2nd Edition Knott *et al.*
Radar Design Principles: Signal processing and the environment, 2nd Edition Nathanson *et al.*
Radar Detection DiFranco and Ruby
Radar Essentials: A concise handbook for radar design and performance Curry
Radar Foundations for Imaging and Advanced Concepts Sullivan
Radar Principles for the Non-Specialist, 3rd Edition Toomay and Hannan
Test and Evaluation of Aircraft Avionics and Weapons Systems McShea
Understanding Radar Systems Kingsley and Quegan
Understanding Synthetic Aperture Radar Images Oliver and Quegan
Radar and Electronic Warfare Principles for the Non-specialist, 4th Edition Hannen
Inverse Synthetic Aperture Radar Imaging: Principles, algorithms and applications Chen and Martorella
Stimson's Introduction to Airborne Radar, 3rd Edition Griffiths, Baker and Adamy
Test and Evaluation of Avionics and Weapon Systems, 2nd Edition McShea
Angle-of-Arrival Estimation Using Radar Interferometry: Methods and applications Holder

Novel Radar Techniques and Applications

Volume 2: Waveform Diversity and Cognitive Radar, and Target Tracking and Data Fusion

Edited by
Richard Klemm

Volume 2 Editors

Part I: Waveform diversity and cognitive radar
Hugh Griffiths
University College London

Part II: Target tracking and data fusion
Wolfgang Koch
Fraunhofer FKIE, Germany

SciTech Publishing

Published by The Institution of Engineering and Technology, London, United Kingdom

The Institution of Engineering and Technology is registered as a Charity in England & Wales (no. 211014) and Scotland (no. SC038698).

First published 2017

The Institution of Engineering and Technology
Michael Faraday House
Six Hills Way, Stevenage
Herts SG1 2AY, United Kingdom

www.theiet.org

British Library Cataloguing in Publication Data
A catalogue record for this product is available from the British Library

ISBN 978-1-61353-226-3 (Hardback Volume 2)
ISBN 978-1-61353-228-7 (PDF Volume 2)
ISBN 978-1-61353-225-6 (Hardback Volume 1)
ISBN 978-1-61353-227-0 (PDF Volume 1)
ISBN 978-1-61353-229-4 (Hardback Volume 1 & 2)

Typeset in India by MPS Limited
Printed in the UK by CPI Group (UK) Ltd, Croydon

Contents

This page intentionally left blank

Preface to Volumes 1 and 2

The title 'Novel Radar Techniques and Applications (NRTA)' suggests that the content of these two volumes are twofold. On the one hand, the team of editors together with the authors aimed at presenting a variety of radar techniques that have not yet found their way into operational use. Techniques such as MIMO, compressive sensing, cognitive radar operation, radar management, radar networks and waveform diversity are presented in these volumes as well as tracking, data fusion, passive radar operation and new imaging techniques.

Moreover, a large number of applications demonstrate the usefulness, the potential and the limits of performance of the presented techniques. In order to reach this multifold goal, a large number of authors have been invited from universities, research laboratories and industry, so as to cover as many different aspects arising between theory, practice and operational use as possible.

These volumes are subdivided into five parts, each of them including a number of chapters. Each part is dedicated to a specific area: Vol. 1: Part I. Array Radar (interference and clutter cancellation, target parameter estimation, etc.); Part II. Imaging Radar; Part III. Passive and Multistatic Radar; Vol. 2: Part IV. Waveform Diversity; Part V. Data Fusion and Tracking. Each part has been taken care of by a co-editor, typically a renowned expert in the respective area. Each part starts with an introduction written by the associated co-editor. In their introductions, the co-editors give overviews of the current state of the art in the respective area and point out the relevance of the subsequent chapters.

These volumes would never have been completed without the enthusiastic effort of a large number of persons. First of all I have to thank the five co-editors Ulrich Nickel, Germany; Christoph Gierull, Canada; Pierfrancesco Lombardo, Italy; Hugh Griffiths, UK and Wolfgang Koch, Germany for their outstanding co-operation on this project. Based on the expertise in their respective fields, they assisted me in composing the contents of these volumes and identifying potential authors and reviewers who were selected according to their expertise in the specific fields. In this way an important feature of these volumes is the multiplicity of facets of modern radar technology and associated applications. It makes these volumes a deep source of information and inspiration for teachers, students, researchers and system designers, in summary all people involved in the development of the radar of tomorrow.

I would like to thank the authors for their excellent work over a long period of time and the reviewers whose critical comments contributed to the quality of the book. Finally the excellent cooperation with Jennifer Grace, Nikki Tarplett, and Paul Deards of IET Publishers as well as Vijay Ramalingam of MPS Ltd. is gratefully acknowledged.

Richard Klemm, Editor NRTA
08.09.2017, Bonn, Germany

This page intentionally left blank

Volume 2 Editor Biographies

Richard Klemm received his Dipl.-Ing. and Dr.-Ing. degrees in communications from the Technical University of Berlin in 1968 and 1974, respectively. Since 1968, he has been with FGAN FHR (now Fraunhofer FHR), a research institute working in the areas defence and security. From 1977 to 1980, he was with SACLANT ASW Centre, La Spezia, Italy. Richard Klemm's main fields of activity have been research into adaptive clutter and jammer suppression for radar, array processing for active and passive sonar, with emphasis on matched field processing for shallow water applications, and detection of moving targets by moving sensor platforms. Richard Klemm has published numerous articles on various aspects of radar and sonar signal processing, and a book (3rd edition) on space-time adaptive processing. He is editor of a book on 'Applications of STAP', including contributions by 45 international authors. He is a permanent reviewer of renowned journals and has provided seminars and consultancy to various organizations in different countries (European Commission, several European countries, USA, Canada, Russia, China, Turkey). Richard Klemm has been a member of the NATO AGARD AVP and RTO-SET panels and chaired various AGARD and RTO symposia. He initialized and chaired the European Conference on Synthetic Aperture Radar EUSAR in 1996 which takes place every 2 years since then. He received several awards in recognition of his scientific achievements, among them the NATO RTO von Karman medal. Richard Klemm gave seminars to different Chinese institutions (Tsinghua University Beijing; Institute of Electronics CAS, Beijing; Xi'an University, Xi'an; UESTC Chengdu; Jiaotong University, Shanghai; NRIET Nanjing). He is honorary professor of UESTC (University of Electronics Science and Technology of China) in Chengdu. His book 'Principles of Space-Time Adaptive Processing 3rd edition' was translated into Chinese by members of NRIET, Nanjing, and has been published by Higher Education Press, Beijing. In his spare time, Richard Klemm is a passionate classical pianist. Under the motto Science and Music, he likes to give piano recitals at technical conferences. He is married, has three children and seven grandchildren.

Hugh Griffiths holds the THALES/Royal Academy Chair of RF Sensors in the Department of Electronic and Electrical Engineering at University College London, England. From 2006 to 2008, he was Principal of the Defence Academy College of Management and Technology. He received the MA degree in Physics from Oxford University in 1975, then spent 3 years working in industry, before joining University College London, where he received the Ph.D. degree in 1986 and the DSc(Eng) degree in 2000 and served as Head of Department from 2001 to 2006. His research interests include radar systems and signal processing (particularly bistatic radar and synthetic aperture radar) and antenna measurement techniques. He serves as Editor-in-Chief of the *IET Radar, Sonar and Navigation* journal. He has published over 500 papers and technical articles in the fields of radar, antennas and sonar. He has received several awards and prizes, including the IEEE Picard Medal (2017), the IEEE AES Mimno Award (2015), the IET A.F. Harvey Prize (2012) and the IEEE AES Nathanson Award (1996). He has also received the Lord Brabazon Premium of the IERE and the Mountbatten and Maxwell Premium Awards of the IEE. He is a Fellow of the IET (previously IEE), Fellow of the IEEE, and in 1997, he was elected to Fellowship of the Royal Academy of Engineering. He served as President of the IEEE Aerospace and Electronic Systems Society for 2012/2013, and he is an IEEE AES Distinguished Lecturer. He has been a member of the IEEE AES Radar Systems Panel since 1989, serving as Chair from 2007 to 2009, and he chaired the Working Group which revised the IEEE Radar Definitions Standard P686 and reaffirmed the Radar Letter Band Standard. Most recently, with Chris Baker and Dave Adamy, he led the revision of the classic Stimson's *Introduction to Airborne Radar* book.

Wolfgang Koch studied Physics and Mathematics at the Aachen Technical University (RWTH Aachen), Germany, where he earned a Dr. rer. nat. degree in Theoretical Physics. For many years, he is head of the department 'Sensor Data and Information Fusion SDF' at Fraunhofer FKIE, an institute of the Fraunhofer Society, the largest institution for applied research in Europe. On various topics within the area of sensor data and information fusion, he has published a well-referenced text book on target tracking and sensor data fusion (Springer 2014, Chinese translation 2016), 16 handbook chapters and well above 200 journal and conference articles. Wolfgang Koch is a fellow of the IEEE, where he serves for the IEEE Transactions on Aerospace and Electronic Systems (T-AES) and as a Member of the Board of Governors of the Aerospace and Electronics Systems Society (AESS). He is an IEEE Distinguished Lecturer and founding chairman of the German IEEE AESS Chapter. In 2013, he served as President of the International Society of Information

Fusion (ISIF). On his areas of expertise he is active in the NATO Science and Technology Organization (STO) for many years. At Bonn University, he holds a habilitation degree on 'Applied Computer Science' and regularly delivers lecture series on Sensor Data and Information Fusion. In 2008 and 2016, he was General Co-Chair of the *IEEE ISF International Conference on Information Fusion*, in Cologne and Heidelberg, Germany, respectively.

This page intentionally left blank

List of authors

Ahmad, Fauzia	Temple University	USA
Allen, Christopher	University of Kansas	USA
Amin, Moeness	Villanova University	USA
Antoniou, Michail	University of Birmingham	UK
Aubry, Augusto	Università degli studi di Napoli Fed. II	Italy
Baker, Chris	Aveillant Ltd.	UK
Balleri, Alessio	Cranfield University	UK
Blunt, Shannon	University of Kansas	USA
Brötje, Martina	Fraunhofer FKIE	Germany
Bucciarelli, Marta	Sympas S.r.l.	Italy
Bürger, Wolfram	Fraunhofer FHR	Germany
Cerutti-Maori, Delphine	Fraunhofer FHR	Germany
Charlish, Alexander	Fraunhofer FKIE	Germany
Cherniakov, Mikhail	University of Birmingham	UK
Colone, Fabiola	DIET University of Rome 'La Sapienza'	Italy
Cristallini, Diego	Fraunhofer FHR	Germany
Damini, Anthony	DRDC Ottawa	Canada
Daniel, Liam	University of Birmingham	UK
Dawidowicz, Bartek	Warsaw University of Technology	Poland
Fargetton, Hervé	DGA Techniques Navales	France
Farina, Alfonso	Selex ES (ret.) and ELETTRONICA S.p.A	Italy
Feldmann, Michael	Fraunhofer FKIE	Germany
Fitzgerald, Dennis	Information Directorate AFRL	USA
Fornaro, Gianfranco	IREA – CNR	Italy
Fränken, Dietrich	Hensoldt Sensors GmbH	Germany
Gashinova, Marina	University of Birmingham	UK
Georgiev, Krasin	Cranfield University	UK
Gierull, Christoph	DRDC Ottawa	Canada
Govaers, Felix	Fraunhofer FKIE	Germany
Griffiths, Hugh	University College London	UK
Gromek, Damian	Warsaw University of Technology	Poland
Hack, Daniel E.	DRDC Ottawa	Canada
Hernandez, Marcel	Hernandez Technical Solutions Ltd.	UK
Himed, Braham	AFRL	USA
Hoffmann, Fabienne	Airbus Defence & Space	Germany
Hoffmann, Folker	Fraunhofer FKIE	Germany
Holderied, Marc	University of Bristol	UK
Jakabosky, John	University of Kansas	USA
Jovanoska, Snezhana	Fraunhofer FKIE	Germany
Katsilieris, Fotios	Fraunhofer FKIE	Germany
Klemm, Richard	Fraunhofer FHR ret.	Germany

(Continues)

(*Continued*)

Koch, Wolfgang	Fraunhofer FKIE	Germany
Kohlleppel, Robert	Fraunhofer FHR	Germany
Kulpa, Krzysztof	Warsaw University of Technology	Poland
Kuschel, Heiner	Fraunhofer FHR	Germany
Linderman, Richard	Office of the Secretary of Defense	USA
Lombardo, Pierfrancesco	DIET University of Rome 'La Sapienza'	Italy
De Maio, Antonio	Università degli studi di Napoli Fed. II	Italy
Maslikowski, Lukas	Warsaw University of Technology	Poland
Myakinkov, Alexander	Nishny Nowgorod Technical State University	Russia
Monti-Guarnieri, Andrea	DEI POLIMI	Italy
Nadjiasngar, Roaldje	Fraunhofer FKIE	Germany
Nickel, Ulrich	Fraunhofer FHR/FKIE	Germany
Opitz, Felix	Airbus Space & Defence	Germany
Palamà, Riccardo	University College London	UK
Pastina, Debora	DIET University of Rome 'La Sapienza'	Italy
Patton, Lee K.	Matrix Research Inc.	USA
Pauciullo, Antonio	IREA – CNR	Italy
Piezzo, Marco	Università degli studi di Napoli Fed. II	Italy
Ristic, Branko	RMIT University	Australia
Rocca, Fabio	DEI POLIMI	Italy
Rosenberg, Luke	Defence Science and Technology Group	Australia
Schroeder, Alexander	Airbus Defence & Space	Germany
Sen, Satyabrata	Oak Ridge National Laboratory	USA
Sikaneta, Ishuwa	DRDC Ottawa	Canada
Sletten, Mark	NRL	USA
Stove, Andy	Stove Specialities, Sussex	UK
Tebaldini, Stefano	DEI POLIMI	Italy
Thomä, Reiner	Technical University Ilmenau	Germany
Toporkov, Jakov	NRL	USA
Walterscheid, Ingo	Fraunhofer FHR	Germany

List of reviewers

Reviewer	Affiliation	Country
Baumgartner, Stefan	German Aerospace Center DLR	Germany
Bucciarelli, Marta	Sympas S.r.l.	Italy
Charlish, Alexander	Fraunhofer FKIE	Germany
Cristallini, Diego	Fraunhofer FHR	Germany
Damini, Anthony	DRDC Ottawa	Canada
Demissie, Bruno	Fraunhofer FKIE, Wachtberg	Germany
Erricolo, Danilo	University of Illinois at Chicago	USA
Fabrizio, Joe	DSTO	Australia
Farina, Alfonso	Selex ES (ret.) and ELETTRONICA S.p.A	Italy
Fornaro, Gianfranco	IREA – CNR	Italy
Geudtner, Dirk	European Space Agency ESA	Netherlands
Gierull, Christoph	DRDC Ottawa	Canada
Gini, Fulvio	University of Pisa	Italy
Govaers, Felix	Fraunhofer FKIE	Germany
Griffiths, Hugh	University College London	UK
Klemm, Richard	Fraunhofer FHR ret.	Germany
Koch, Wolfgang	Fraunhofer FKIE	Germany
Kohlleppel, Robert	Fraunhofer FHR	Germany
Lesturgie, Marc	ONERA	France
Livingstone, Chuck	DRDC Ottawa	Canada
Lombardo, Pierfrancesco	University of Rome La Sapienza	Italy
Mertens, Michael	Elettronica, Meckenheim	Germany
Monti-Guarnieri, Andrea	DEI POLIMI	Italy
Mihaylova, Mila	University of Sheffield	UK
Nickel, Ulrich	Fraunhofer FHR/FKIE	Germany
Pastina, Debora	DIET University of Rome 'La Sapienza'	Italy
Pauciullo, Antonio	IREA – CNR	Italy
Prati, Claudio Maria	Politecnico di Milano	Italy
Rosenberg, Luke	Defence Science and Technology Group	Australia
Savy, Laurent	ONERA DEMR	France
Schlangen,Isabel	Heriot-Watt University, Edinburgh	UK
Sikaneta, Ishuwa	DRDC Ottawa	Canada
Sletten, Mark	NRL	USA
Smith, Graeme	The Ohio State University	USA
Soldovieri, Francesco	IREA	Italy
Ulmke, Martin	Fraunhofer FKIE	Germany
Wiedmann, Michael	Airbus Defence & Space	Germany
Walterscheid, Ingo	Fraunhofer FHR	Germany
Wirth, Wulf-Dieter	Fraunhofer FKIE	Germany
Woodbridge, Karl	University College London	UK

This page intentionally left blank

Part I

Waveform diversity and cognitive radar

This page intentionally left blank

Introduction to waveform diversity and cognitive radar

Hugh Griffiths[1]

1 Introduction

This chapter serves as an introduction to Part I of Volume 2 of the book, on the subjects of Waveform Diversity and Cognitive Radar. These are relatively recent concepts, and twenty years ago the terms would hardly have been recognized. Now, though, they can both be regarded as mainstream subjects in radar research, with entire sessions at radar conferences devoted to them.

Both subjects have been enabled by enormous advances in technology and processing power. The seminal publication by Gordon Moore in 1965 [1] predicted that computing power would double every 18 months – and that has proved to be remarkably accurate. In fact, the very last word of that paper is 'radar', showing that Moore well understood the impact that this would have on the development of radar.

A two-day event held at University College London in November 2015 had as its goal to identify future directions in radar technology and techniques [2]. The event included sessions on Waveform Diversity, Bistatic Radar and Cognitive Radar. Several of the authors of the chapters in this part participated in that event, and several of the issues discussed are included in these chapters.

In addition, the topics in this part of the book have benefitted greatly from some NATO task groups and lecture series, including the SET-233 Lecture Series *Knowledge-Based Radar Signal & Data Processing*, the SET-119 Lecture Series *Waveform Diversity for Advanced Radar Systems* and the SET-216 Lecture Series *Cognition and Radar Sensing*, as well as the associated books, journal special issues and special sessions at conferences that have resulted from them.

2 Waveform diversity

Waveform Diversity has been defined in the IEEE P686 Radar Terminology Standard [3] as 'Adaptivity of the radar waveform to dynamically optimize the radar performance for the particular scenario and tasks. May also exploit adaptivity in other domains, including the antenna radiation pattern (both on transmit and receive), time domain, frequency domain, coding domain, and polarization

[1]University College London, UK

domain'. In other words, the advances in digital processing now allow us to generate precise, wide-bandwidth radar waveforms and to vary them adaptively, potentially even on a pulse-to-pulse basis [4,5]. This opens up huge possibilities and is also one of the cornerstones of cognitive radar.

It is also interesting to realize that the ambiguity function, which is the classical tool used by radar engineers to evaluate the properties of radar signals [6], says nothing about the spectral properties of the signal. It is natural, therefore to look for new tools in waveform analysis and design.

3 From adaptivity to cognition

Adaptive radar processing began to be introduced in the 1960s, as a means to automate the radar operator's control settings. Probably the first aspect of this was the development of Constant False Alarm Rate (CFAR) processing, to automatically set a detection threshold to give a fixed probability of false alarm. Various developments of the basic cell-averaging scheme were able to deal with self-masking, mutual masking and clutter edges.

Next, adaptive antenna array techniques were developed to suppress jamming and interference, first in the form of analogue sidelobe cancellers, then in the form of digital fully adaptive arrays. The 1973 publication of Brennan and Reed [7] represents a notable milestone here. These concepts were further developed to form the basis of Space-Time Adaptive Processing (STAP): two-dimensional adaptive filtering, in both angle and Doppler.

Whilst these techniques have provided a huge increase in radar performance against a wide range of target, clutter and jamming environments, they are implemented in the receiver. The next stage is to consider adaptivity in the transmitted signal as well, thereby incorporating a degree of intelligence into the radar.

Devising a satisfactory definition of cognitive radar has not proved easy. Although a significant number of papers and books have been published, there is no clear agreement on a definition of Cognitive Radar. Haykin [8] is keen to emphasize the Perception-Action Cycle (Figure 1) and that a cognitive radar possesses memory, which is updated by the information gained by the radar from the target scene. Another important criterion is stated to be that the radar should dynamically adapt its transmitted waveform in response to its perception of the target scene.

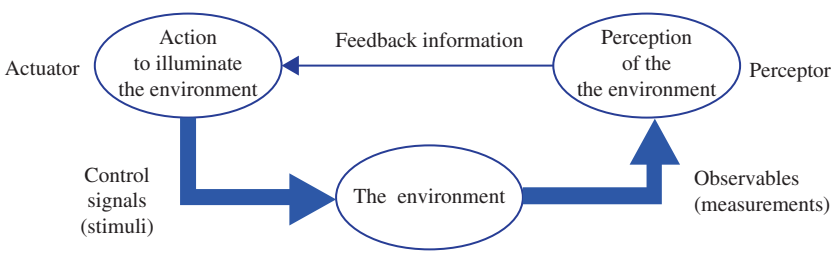

Figure 1 The perception–action cycle of cognitive radar © 2006 IEEE. Reprinted with permission from [8]

Guerci's approach [9] owes much to earlier work on knowledge-based signal processing [10–12]. Yet another factor is that a cognitive radar should demonstrate 'learning', which implies that a cognitive system presented with a dynamically changing target scene would be able to improve upon a previous encounter with the same target scene by virtue of the experience learned.

It is possible to test some of the well-established radar signal processing techniques against these criteria to see to what extent they might be regarded as cognitive. Some, such as adaptive antenna arrays and CFAR detection do not meet the criterion of adapting the transmitted waveform so cannot be considered to be cognitive. The way in which an HF Over-The-Horizon Radar (OTHR) radar dynamically selects its frequency and its waveform in response to the prevailing spectrum occupancy and ionospheric conditions might well be regarded as cognitive, as might the waveform selection of an airborne HF/VHF SAR such as CARABAS [13–15]. The CARABAS SAR operates over the band 20–90 MHz, and it is necessary to adaptively design the waveform to avoid interference with the other users within that band. Another example is the way in which a phased array radar might dynamically adjust the dwell time and update rate in tracking a particular target according to the signal-to-noise ratio and degree of manoeuvre of the target [16] (Figure 2).

Equally, we may look at the behaviour of a bat in detecting, identifying and intercepting an insect target [17]. There can be no doubt that the bat is employing cognitive processing in these operations, since it is clearly sensing the target scene and dynamically adapting its emitted signal in response to the information that it has and the information that it seeks to acquire.

To date, most of the work on cognitive radar has been theoretical or by means of simulation. There is a pressing need to undertake experimental work to demonstrate the benefits practically, and the Cognitive Radar Experimental Workspace (CREW) that is being developed at the Ohio State University represents an important step in this direction [18].

The term 'fully adaptive radar' has been used by some authors instead of cognitive radar, perhaps to emphasize the origins in classical adaptive processing (Figure 3).

4 The spectrum problem

Another significant factor in this overall subject area is the ever-increasing congestion of the RF electromagnetic spectrum [19–21]. This spectrum, extending from below 1 MHz to above 100 GHz, is a precious resource. It is used for a wide range of purposes, including communications, radio and television broadcasting, radionavigation and sensing. Radar represents a fundamentally important use of the EM spectrum, in applications which include air traffic control, geophysical monitoring of Earth resources from space, automotive safety, severe weather tracking, and surveillance for defence and security. Nearly all services have a need for greater bandwidth, which means that there will be ever-greater competition for this finite resource.

As an indication of the financial value attached to the RF spectrum, Table 1 lists the prices paid in various countries when the 3G and 4G spectrum was sold to telecommunications companies. These parts of the spectrum are of the order of a few tens of MHz – so clearly the RF spectrum has a substantial monetary value.

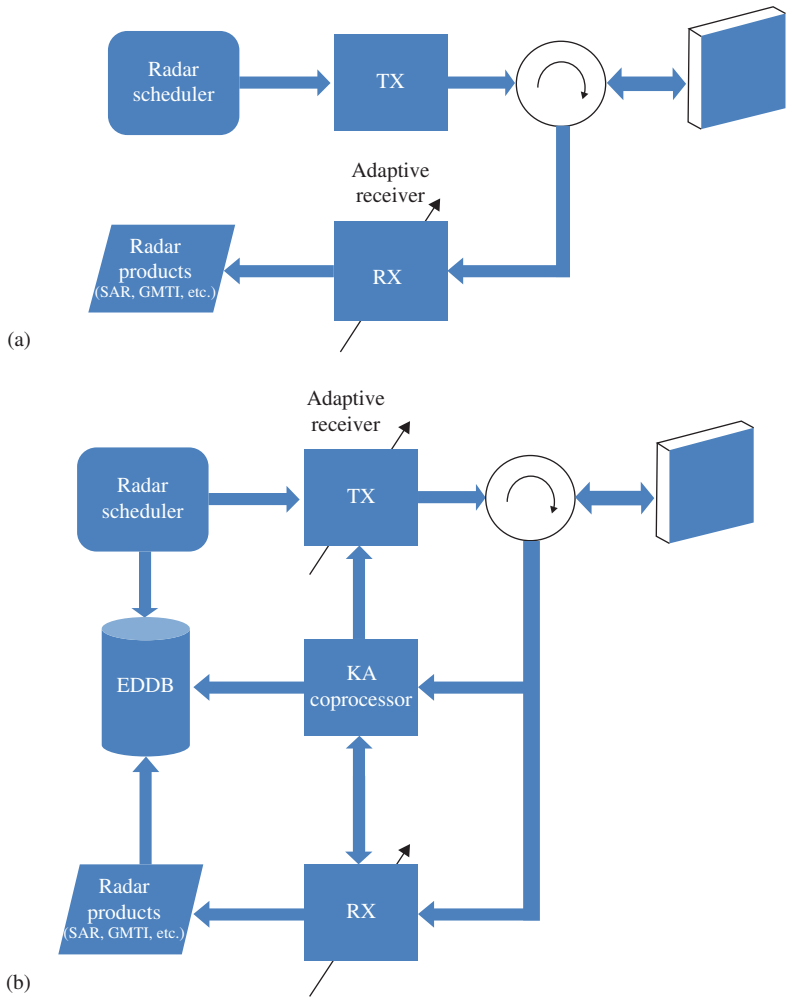

Figure 2 (a) Conventional adaptive radar; (b) cognitive radar (after Guerci © 2010 Artech House. Reprinted with permission from [9])

The issues of spectrum congestion and competition with radar from other services currently occur mainly in the frequency bands below 5 GHz (C-band). In the higher frequency bands, the use of bandwidth is still strictly regulated to prevent interference, especially to critical services such as air traffic control and aircraft landing aids. Since its inception in the 1950s, HF radar has always competed for spectrum with the primary users of HF communications and the amateur radio world. Since the late 1970s, the world's communication industries have shown greater interest in the UHF part of the spectrum, and in 1979 the World Administrative Radar Conference (WARC) took the decision to downgrade the primacy of radar in portions of the UHF band, specifically 420–430 and 440–450 MHz, to secondary status, which

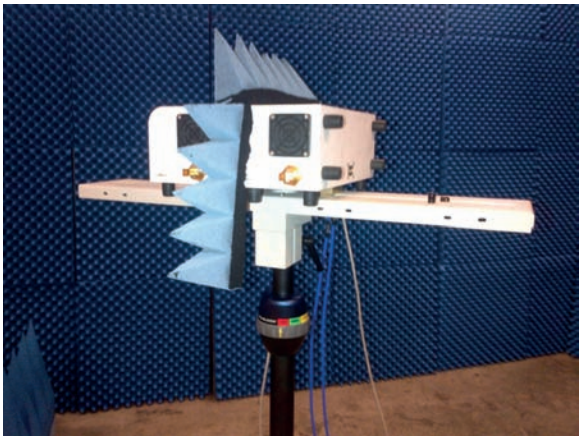

Figure 3 Transmitter/receiver of the Cognitive Radar Experimental Workspace (CREW) at The Ohio State University

Table 1 Prices paid by telecommunications companies for 3G and 4G spectrum (Figures from GSM Association – other sources vary)

3G (UK)	$38.2 bn (2000)
4G (Germany)	$4.9 bn
4G (Italy)	$7.0 bn
4G (Spain)	$1.9 bn
4G (France)	$4.9 bn
4G (USA)	$20.4 bn

means that radars can operate only as long as they do not interfere with primary users. Over the last 10 years, wireless industries have lobbied their member nations within the International Telecommunications Union (ITU) to downgrade radar in the 3.4–3.7 GHz band to secondary status as well. At present, the big competitor for the 3.4–3.7 GHz band is 4G wireless communications [WiMAX or Long Term Evolution (LTE), though all indications are that the latter will dominate].

There are several ways in which the techniques of waveform diversity and cognitive radar may address this problem.

4.1 Spectrally clean waveforms

Most waveforms, of all kinds, are spectrally quite 'dirty' – in other words they radiate significant energy outside of the intended bandwidth. Figure 4 provides an extreme example of this, showing the spectrum of an X-band magnetron over the band from 7.5 to 11.5 GHz. Although the bulk of the energy is concentrated around 9.4 GHz, there is substantial energy radiated outside of the desired band, which has

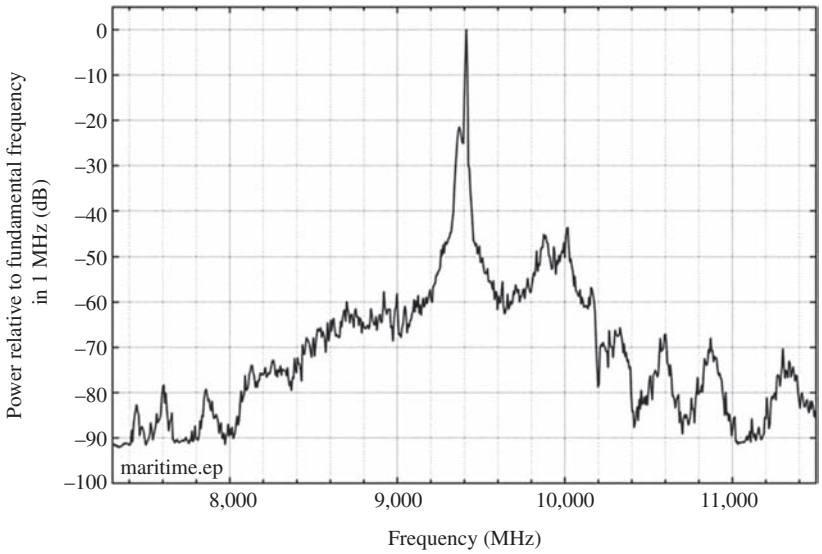

Figure 4 Spectrum of a radar using an X-band magnetron © 2015 IEEE. Reprinted with permission from [21]

the potential to interfere with other services in this band. There is clearly strong motivation to be able to generate waveforms with much better spectral purity, so that signals can be accommodated closer together without mutual interference. The techniques of digital waveform generation and of power amplifier linearization can provide substantial improvement here.

As an example of power amplifier linearization, Figure 5 shows an open-loop feedforward technique. To understand its operation, consider an input signal consisting of two tones. The main amplifier produces an amplified version of these (shown in blue), plus distortion (intermodulation) products (shown in red). Directional couplers are used to sample the input signal and the output signal, and with suitable weighting these are combined to give the distortion signal alone. This is amplified and added back into the main signal path, adjusted in amplitude and phase to cancel the distortion in the main signal path. This would require careful adjustment in setting up, and the performance would be likely to degrade as a function of time. Closed-loop architectures would give better performance in this respect, but would be more complex.

Another approach is to pre-distort the signal to take out the distortion that is introduced by the amplifier stage. This, too, can be adaptive, and lends itself well to the high-speed digital waveform generation techniques that form the basis of waveform diversity.

A third technique is to vary the load impedance into which the power amplifier works, to minimize the distortion introduced. The tool used in this design is the Smith Tube, which is the well-known Smith Chart, also plotted as a function of the duration of the transmitted pulse [22–25] (Figure 6).

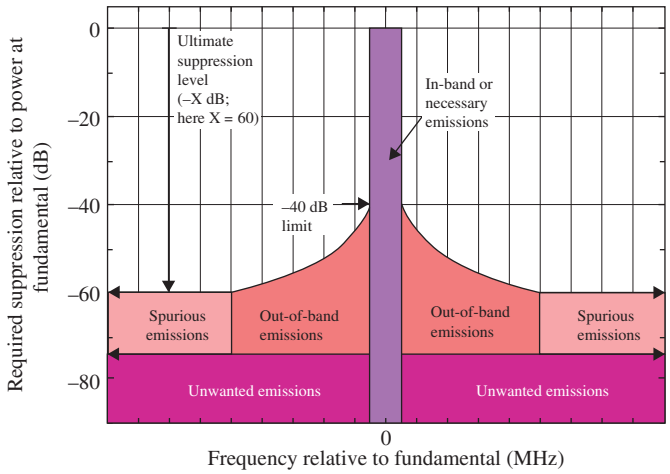

Figure 5 RSEC emission mask showing the signal domains and their permitted relative levels © 2015 IEEE. Reprinted with permission from [21]

4.2 Waveforms with dynamically variable spectral nulls

Modern military radars may require wide bandwidths to give high resolution, and may need to operate in spectrally congested environments with multiple other signals, interference and jamming which change dynamically. It may therefore be desirable to radiate signals with spectral nulls whose frequencies may be adapted according to the prevailing interference, at the same time as maintaining low range sidelobes. Jakobosky *et al*. [26] have demonstrated a Pseudo-Random Optimized FMCW (PRO-FMCW) waveform which achieves this. Figure 7 shows the measured spectrum of a waveform of this kind.

It is further proposed that such a spectrum gap could be used to hide an embedded communications signal, whose frequency could be hopped in a known pattern which would be very difficult for an adversary to discover.

4.3 Passive radar

Since passive radar makes use of transmissions that are already present (broadcast, communications, radionavigation, …) it requires no additional spectrum and no additional licensing, and has even been called ‘green radar’ [27].

If such transmissions are to be used for radar purposes, as well as for their primary purpose, there is potentially an opportunity to attempt also to optimize them as radar illuminators. This has been termed ‘commensal radar’ (literally ‘at the same table’), and the term is due to Professor Mike Inggs of the University of Cape Town, South Africa[1]. It will mean devising efficient waveform modulation and coding schemes that also give good ambiguity function performance for radar purposes [28].

Another important aspect is the coverage of such illuminators. In general, the radiation patterns of broadcast and communications transmitters are optimized so

[1] The term commensal radar has also been used by researchers in South Africa as a synonym for passive radar, especially with non-cooperative illuminators.

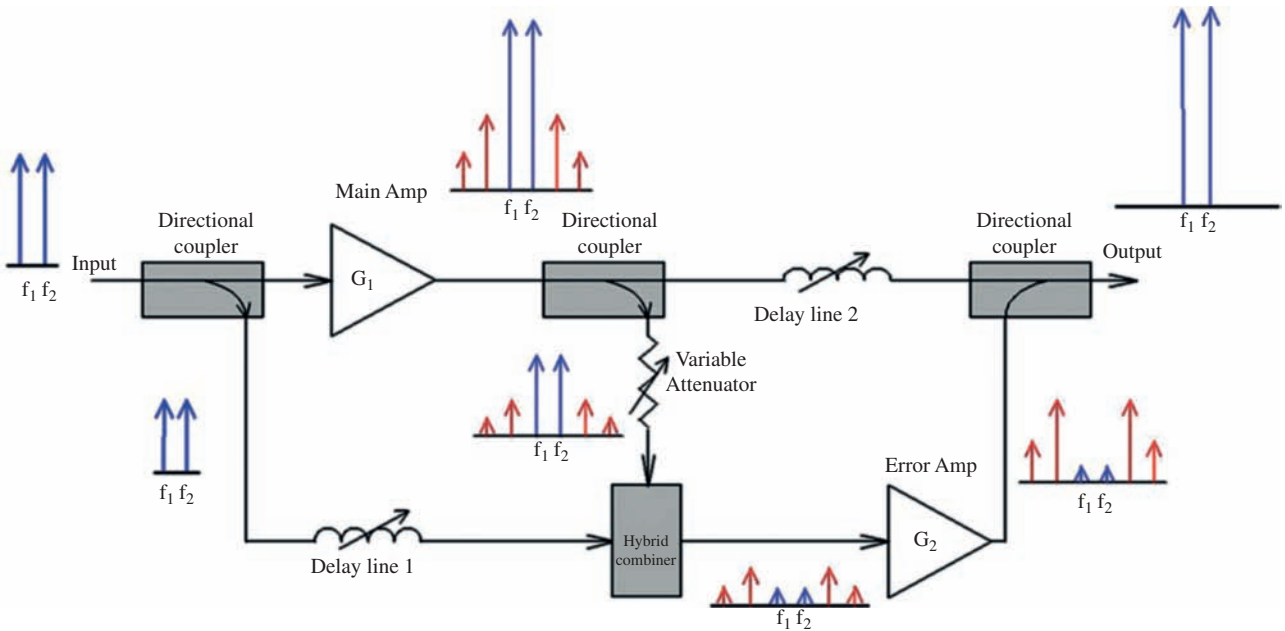

Figure 6 Open-loop feedforward power amplifier linearization technique

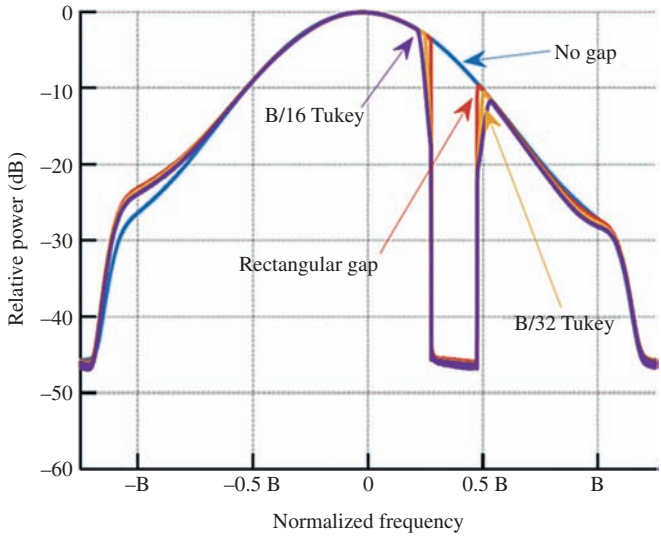

Figure 7 Measured spectrum of PRO-FMCW waveform with a static rectangular spectrum gap © 2016 IEEE. Reprinted with permission from [26]

that energy is directed only towards regions where users are located. This often means constraining the elevation-plane patterns so that energy is not wasted above the horizontal. However, if the source is to be used as an illuminator to detect and track air targets, this is precisely where the energy should be directed.

Figure 8 shows measured vertical-plane radiation patterns corresponding to two VHF FM transmitters (red and green traces) and an 8-bay DVB-T transmitter (blue trace), plotted as a function of the sine of the elevation angle. The peak sidelobe level of the VHF FM patterns are approximately −15 dB below the peak, though the nulls are as low as −30 dB. For the DVB-T pattern, the sidelobes are somewhat lower.

The effect of these patterns of passive radar detection performance can be evaluated from the radar equation for the passive radar signal-to-noise ratio:

$$\frac{S}{N} = \frac{P_t G_t G_r \lambda^2 \sigma_b G_p}{(4\pi)^3 R_T^2 R_R^2 k T_0 B F L} \tag{1}$$

in which P_t is the transmit power, G_t is the transmit antenna gain, λ is the wavelength, σ_b is the target bistatic RCS, G_p is the processing gain, R_T is the transmitter-to-target range, R_R is the target-to-receiver range, k is Boltzmann's constant, $T_0 = 290$ K, B is the receiver noise bandwidth, F is the receiver noise figure and L includes the system losses.

This can be re-arranged in the form:

$$R_{R\max} = \sqrt{\frac{P_t G_t G_r \lambda^2 \sigma_b G_p}{(4\pi)^3 R_T^2 (S/N)_{\min} k T_0 B F L}} \tag{2}$$

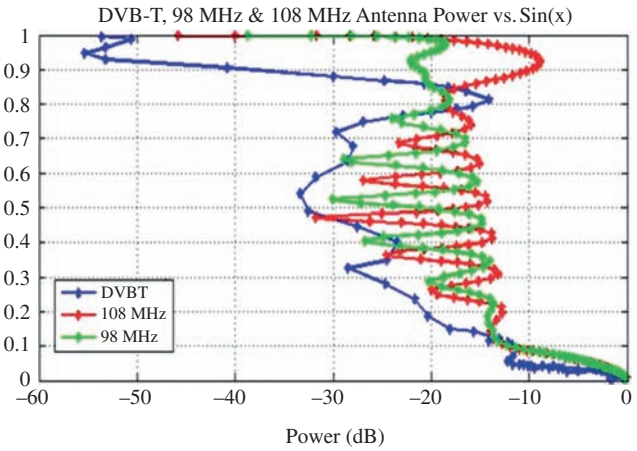

Figure 8 Measured vertical-plane radiation patterns of BBC VHF FM radio transmitter at 98 MHz, 108 MHz and 8-bay DVB-T transmitter. The vertical scale is the sine of the elevation angle at the transmitter © 2015 IEEE. Reprinted with permission from [27]

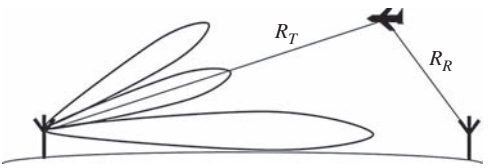

Figure 9 The effect on detection range of the elevation-plane pattern of the source can be substantial © 2015 IEEE. Reprinted with permission from [27]

which shows that for every 10 dB reduction in P_tG_t the maximum detection range R_R for a given target is reduced by a factor of 3.3 (Figure 9). Even at the peaks of the elevation-plane lobes the effect is significant, but in the nulls in between the lobes it is even more so.

4.4 Intelligent, cognitive processing

It has been remarked that actual spectrum occupancy at a given point, as a function of frequency, time, direction and polarization, … may be quite low. This can be visualized in terms of what has been called the 'Radio Frequency Transmission Hypercube' [29]. This indicates that, with suitable real-time sensing of the spectrum occupancy and control of the emitted signals, it should be possible for multiple signals to co-exist, dynamically minimizing their mutual interference by disposing their energy in the available domains. This may also include the coding domain, so that different signals may occupy the same bandwidth provided they are orthogonally coded, and recent work in MIMO radar has prompted the study of orthogonal codes of this kind.

4.5 Regulatory approaches

The other side of the coin is the regulatory framework for spectrum allocation. For radar, regulation is particularly complex due to the variety of different radar modes, their necessary power outputs (which dictates the nature of the specific transmitter) and the induced spectral emissions. Many, but not all, countries adopt the ITU emission standard. In the United States, emission standards are determined by two organizations: the National Telecommunications and Information Administration (NTIA), the governing body for all U.S. federal government spectrum use; and the U.S. Federal Communications Commission (FCC), the regulatory authority on spectrum use by non-federal entities such as the commercial broadcasting industry. The ITU has published their manual of radio regulations since the dawn of wireless in 1906. Today the regulations cover the frequency range from 9 kHz to 1000 GHz for 40 different radio services, including radar (which falls under the classification of radiodetermination or radiolocation services), in a 1000+ page publication [30]. These regulations can only be changed by agreement at the World Radiocommunication Conference.

These regulations tend to adopt a rather conservative approach. However, we argue that there is a pressing need for a more intelligent approach to regulation, in which the degree of interference of one kind of signal with another is understood in a quantitative manner, via models which are supported by experimental measurements, and the regulations framed accordingly. This represents a substantial amount of work.

5 Bistatic, multistatic and networked radar

Bistatic and multistatic radar, including passive radar, have already been covered in Part III of Volume 1 of this book, but certainly bistatic techniques provide another domain in which diversity can be exploited.

5.1 Origins and properties

Bistatic radar systems have been studied and built since the earliest days of radar. As an early example, in WW2 the Germans used the British *Chain Home* radars as illuminators for their *Klein Heidelberg* bistatic system [31,32]. Bistatic radars have some obvious attractions. The receiving systems are passive, and hence undetectable. The receiving systems are also potentially simple and cheap. Bistatic radar may also have a counter-stealth capability, since target shaping to reduce target monostatic RCS will in general not reduce the bistatic RCS. Bistatic operation is very compatible with the use of UAVs, so the transmitter (which may be heavy and require high power) may be located on a platform at stand-off range, while the receivers can be carried by multiple smaller, lighter UAVs. Furthermore, bistatic radar systems can utilize VHF and UHF broadcast and communications signals as ‘illuminators of opportunity’, at which frequencies target stealth treatment is likely to be less effective.

Bistatic systems also have some disadvantages. The geometry is more complicated than that of monostatic systems. It is necessary to provide some form of synchronization between transmitter and receiver, in respect of transmitter azimuth angle, instant of pulse transmission and (for coherent processing) transmit signal phase. Receivers which use transmitters which scan in azimuth will probably have to utilize 'pulse chasing' processing [33].

Over the years, a number of bistatic radar systems have been built and evaluated. However, rather few have progressed beyond the 'technology demonstrator' phase. Willis [34] has remarked that interest in bistatic radar has tended to vary on a period of approximately fifteen years, and that currently we are in the 'third resurgence'. Arguably now the interest is continuing unabated, since now there are applications in which bistatic operation provides a genuine advantage, and many of the obstacles that in the past meant that bistatic operation was too difficult (such as processing power and synchronization) have now largely been overcome.

5.2 Passive radar

Passive radar has already been mentioned in the previous section as one approach to address the spectrum congestion problem. Figure 10 shows the basic principle. The history goes back a long way, and some of the very earliest radar experiments were based on broadcast transmissions [35].

Passive radar has a number of significant attractions, which are listed in [27]:

- Broadcast and communications transmitters tend to be sited on high locations and hence achieve broad coverage.
- Since the system makes use of existing transmitters, the cost of a passive radar is likely to be much lower than a conventional radar.

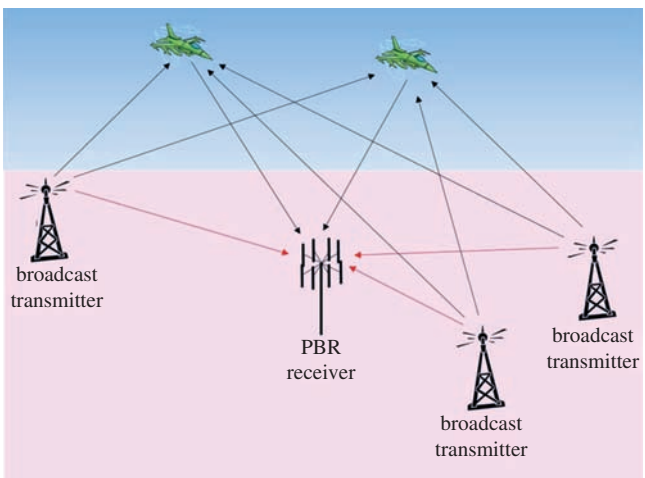

Figure 10 Passive bistatic radar – basic principle

- Similarly, there are no licensing issues.
- It allows the use of frequency bands (particularly VHF and UHF) that are not normally available for radar purposes. Such frequencies may be beneficial in detecting stealthy targets, since the wavelength is of the same order as the physical dimensions of the target, and forward scatter gives a relatively broad angular scatter.
- Since the receiver emits no signal of its own, and as long as the receive antenna is inconspicuous, the passive radar receiver may be undetectable and hence completely covert.
- It is difficult to deploy counter-measures against passive radar. Any jamming will have to be spread over a range of directions, diluting its effectiveness.
- Passive radar does not require any additional spectrum. For this reason it has been termed 'green radar'.
- There is an enormous range of transmissions that may be used. In practice, almost any emission can be used as the basis of a passive radar.

However, there are also some significant disadvantages:

- The waveforms of such transmissions are not optimized for radar purposes, so care has to be used to select the right waveforms and to process them in the optimum way.
- In many cases the transmit source is not under the control of the passive radar.
- For analogue signals, the ambiguity function (resolution in range and in Doppler) depends on the instantaneous modulation, and some kinds of modulation are better than others. Digital modulation does not suffer from these problems, so is likely to be preferred.
- The waveforms are usually continuous (i.e. a duty cycle of 100%), so significant processing has to be used to suppress the direct signal and multi-path in order to detect weak target echoes.
- In common with all bistatic radars, the resolution in range and Doppler is poor for targets on or close to the baseline between transmitter and receiver.

Passive radar systems have been built and evaluated by many workers over the past three decades. It has been a particularly suitable subject for university research, since the receiver hardware is relatively low cost. But in the last 5 years or so there has been a marked change in maturity of the subject, as several commercial companies have developed systems with greater reliability and performance (Figure 11), many of which exploit modern digital transmissions such as DVB-T. Passive radars are now being seriously considered for applications as diverse as Air Traffic Management, border or harbour surveillance and even indoor monitoring in eldercare/assisted living [27]. A recent defence business website has predicted that the military and civil aviation market for passive radar for the decade 2013–2023 is likely to be worth more than US$10 billion [36].

Further, it is reported also that China and Iran have operational passive radar systems, and that a Russian company is developing a passive radar system for drone detection [37].

Figure 11 An example of the new generation of passive radar systems, due to FHR in Germany © 2016 FHR. Reprinted with permission

6 Structure of Part I of Volume 2

The chapters within this part of the book cover a range of topics within the overall theme.

In Chapter 1 some of the practical aspects of design and generation are described. An important result is that the distinction should be drawn between a *code*, which is a sequence of phase values (bi-phase or polyphase), a *waveform*, which is the result of modulating the code onto a carrier, including the effects of the transition from one phase to the next, and the *emission*, which is the result of passing the waveform through upconversion and amplification stages, including the phase and amplitude distortion introduced by such stages.

Many modern digital communications schemes make use of Orthogonal Frequency Division Multiplex (OFDM). In order to combat multi-path propagation, the digital bitstream is multiplexed into a number of parallel channels, each with a bit length much longer than the maximum multi-path delay These parallel channels are then modulated onto a set of carriers spaced at frequencies equal to 1/(bit length), so that the carriers are orthogonal. The signals corresponding to each carrier are received, demodulated, and then combined to reconstruct the original bit stream. OFDM is used in LTE, 802.11 (WiFi), 802.16 (WiMAX) and DVB broadcasting. Its widest use is in the fourth-generation (4G) mobile systems based on LTE. Chapter 2 explores the use of OFDM waveforms as radar signals, and particularly how they may be designed and optimized adaptively.

Some of the issues associated with the spectrum problem have been mentioned earlier in this chapter. Chapter 3 takes this further by showing how waveforms may be designed using cognitive techniques, to dynamically adapt to a changing spectrum environment.

Noise radar has some significant attractions in respect of low probability of intercept, ambiguity functions which approach the 'thumbtack' ideal and the possibility of multiple quasi-orthogonal waveforms for MIMO radar. The ideas date back to the 1950s and 1960s [38], but at that time it was very difficult to perform the required cross-correlation in analogue circuitry, and digital processing was still in its infancy. Nowadays digital processing power has advanced to the point where cross-correlation of wide-bandwidth waveforms is feasible, which opens up a range of possibilities and applications, which are described in Chapter 4.

Chapter 5 focuses on the topic of management and control of radar systems based on cognitive techniques. The rapid configurability and agility of a multi-function phased array radar makes phased arrays an enabling technology for the types of cognitive algorithms described in the chapter. The work builds on a rich history of techniques that have been applied in experimental and operational radar systems over many decades, notably in Germany [16,39], the United Kingdom [40–42] and in the United States [43–45]. The chapter extends this history of radar management methods by introducing the cognitive processes of attention and anticipation. Attention is manifested by solving the resource management problem, which is formulated as a constrained multi-objective optimization problem. Anticipation is manifested by performing radar management based on predictions of how the scenario will evolve in the future. Both processes are dependent on knowledge, either estimated or learnt from encountered radar data or from external information sources.

Chapter 12 of Part III of Volume 1 has described the properties of bistatic radar clutter, and showed in particular that the amplitude statistics of bistatic clutter may be shorter-tailed (less spiky) than the equivalent monostatic clutter. This leads to the idea of 'clutter diversity', which means understanding the way in which the properties of clutter and of targets depend on the bistatic geometry, and hence being able to choose the most suitable bistatic or multistatic configuration to optimize detection and tracking, and these ideas are developed in Chapter 6.

Some mammals (notably bats and dolphins) use acoustic signals for echolocation, and there are some obvious parallels with radar. The signals used by different species of bat have been studied in some detail, and it is found that the signals are sophisticated and that they are used in an adaptive and intelligent manner, providing examples of cognitive behaviour that we might study and emulate in our cognitive radar systems. These signals and the associated processing will have been optimized over millions of years through the process of evolution (natural selection – the 'survival of the fittest') [46], but also learned by an individual bat by mimicking the behaviour of its parents and then optimized empirically. The extension of these ideas to cognitive radar systems is described in Chapter 7.

In the final chapter, many of these concepts are brought together to introduce the intelligent, adaptive radar network. Present-generation military surveillance sensor systems tend to be based on single platforms carrying conventional sensors, including monostatic radars, which are expensive and inflexible. There is therefore an imperative to think in new ways about sensor systems and to devise concepts that are more flexible, of higher performance, and at the same time more affordable. The advent of practical UAV platforms forms part of this thinking, but introduces new and significant challenges. Such a scheme has a number of attractions, including flexibility, inherent robustness and potentially lower cost. At a simplistic level, it can be appreciated that multistatic operation should increase sensitivity, since more of the energy scattered from a target is intercepted, and that it should provide more information on which to base detection, tracking and identification.

Acknowledgements

I am most grateful to the authors of all of the chapters in the part of the book, and to many people who have helped with the work described in this chapter. These include Chris Baker, Alessio Balleri, Shannon Blunt, Alex Charlish, Alfonso Farina, Francesco Fioranelli, Mike Inggs, William Miceli, Riccardo Palamà, Murali Rangaswamy, Matt Ritchie, Stefan Sandenbergh, Simon Watts and Mike Wicks. I am also grateful to the organizations who have funded the work, including THALES UK, Dstl, the Royal Academy of Engineering, the Engineering and Physical Sciences Research Council, the IET A.F. Harvey Research Prize and the Office of Naval Research (Global).

References

[1] G.E. Moore, 'Cramming more components onto integrated circuits', *Electronics*, pp. 114–117, 19 April 1965; reprinted in *IEEE Proceedings*, Vol. 86, No. 1, pp. 82–85, 1998.

[2] H.D. Griffiths and C. Stewart, 'Vectors in radar technology', *IEEE AES Magazine*, Vol. 31, No. 8, pp. 41–45, 2016.

[3] IEEE Standard Radar Definitions Std 686-2008, 2008.
[4] V. Amuso, S. Blunt, E. Mokole, R. Schneible and M.C. Wicks (eds), *Principles of Waveform Diversity and Design*, SciTech Publishing Inc., Raleigh, NC, August 2010.
[5] F. Gini, A. De Maio and L. Potter (eds), *Waveform Design and Diversity for Advanced Radar Systems*, IET, Stevenage, May 2012.
[6] P.M. Woodward, *Probability and Information Theory, with Applications to Radar*, Pergamon Press, 1953; reprinted by Artech House, 1980.
[7] L.E. Brennan and I.S. Reed, 'Theory of adaptive radar', *IEEE Transactions on Aerospace and Electronic Systems*, Vol. AES-9, No. March (2), pp. 237–252, 1973.
[8] S. Haykin, 'Cognitive radar: a way of the future', *IEEE Signal Processing Magazine*, Vol. 23, No. 1, pp. 30–40, 2006.
[9] J. Guerci, *Cognitive Radar: The Knowledge-aided Fully Adaptive Approach*, Artech House, 2010.
[10] G. Capraro, A. Farina, H.D. Griffiths and M.C. Wicks, 'Knowledge-based radar signal and data processing: a tutorial introduction', Special Issue of *IEEE Signal Processing Magazine* on Knowledge Based Systems for Adaptive Radar Detection, Tracking and Classification, Vol. 23, No. 1, pp 18–29, 2006.
[11] Special Issue of *IEEE Signal Processing Magazine* on Knowledge Based Systems for Adaptive Radar Detection, Tracking and Classification, Vol. 23, No. 1, 2006.
[12] F. Gini and M. Rangaswamy (eds), *Knowledge-Based Radar Detection, Tracking and Classification*, Wiley, 2008.
[13] H. Hellsten, L.M.H. Ulander, A. Gustavsson and B. Larsson, 'Development of VHF CARABAS II SAR', *Proceedings of SPIE*, Vol. 2747, pp. 48–60, June 1996.
[14] L.M.H. Ulander, P.-O. Frölind, A. Gustavsson, *et al*., 'Performance of the CARABAS-II VHF-band synthetic aperture radar'. *Proceedings of the IGARSS'01, International Geoscience and Remote Sensing Symposium*, Vol. 1, pp. 129–131, 2001.
[15] M.E. Davis, *Foliage Penetration Radar: Detection and Characterization of Objects Under Trees*, SciTech Inc., Raleigh, NC, 2011.
[16] G. van Keuk and S.S. Blackman, 'On phased-array radar tracking and parameter control', *IEEE Transactions on Aerospace and Electronic Systems*, Vol. 29, No. 1, pp. 186–194, 1993.
[17] C.J. Baker, G.E. Smith, A. Balleri, M.W. Holdereid and H.D. Griffiths, 'Biomimetic echolocation with application to radar and sonar sensing', *IEEE Proceedings*, Vol. 102, No. 4, pp. 447–458, 2014.
[18] G.E. Smith, Z. Cammenga, A. Mitchell, *et al*. 'Experiments with cognitive radar', *IEEE AES Magazine*, Vol. 31, No. 12, pp. 34–46, 2016.
[19] H.D. Griffiths, 'Where has all the spectrum gone?', *Proceedings of the International Radar Conference RADAR 2013*, Adelaide, Australia, 10–12 September 2013.

[20] H.D. Griffiths, 'The challenge of spectrum engineering', *EuRAD Conference 2014*, Rome, 8–10 October 2014.
[21] H.D. Griffiths, L. Cohen, S. Watts, *et al.*, 'Radar spectrum engineering and management: technical and regulatory approaches', *IEEE Proceedings*, Vol. 103, No. 1, pp. 85–102, 2015.
[22] C. Baylis, M. Moldovan, L. Wang and J. Martin, 'LiNC power amplifiers for reducing out-of-band spectral re-growth: a comparative study', *IEEE Wireless and Microwave Technology Conference*, Melbourne, FL, 12–13 Apr. 2010.
[23] C. Baylis, R.J. Marks, J. Martin, H. Miller and M. Moldovan, 'Going nonlinear', *IEEE Microwave Magazine*, Vol. 12, No. 2, pp. 55–64, April 2011.
[24] C. Baylis, L. Wang, M. Moldovan, *et al*., 'Designing transmitters for spectral conformity: power amplifier design issues and strategies', *IET Radar, Sonar & Navigation*, Vol. 5, No. 6, pp. 681–685, July 2011.
[25] C. Baylis, M. Fellows, L. Cohen and R.J. Marks II, 'Solving the spectrum crisis: intelligent, reconfigurable microwave transmitter amplifiers for cognitive radar,' *IEEE Microwave Magazine*, Vol. 15, No. 5, pp. 94–107, July 2014.
[26] J. Jakobosky, B. Ravenscroft, S.D. Blunt and A. Martone, 'Gapped spectrum shaping for tandem-hopped radar/communications and cognitive sensing', *IEEE Radar Conference 2016*, Philadelphia, PA, 2–6 May 2016.
[27] H.D. Griffiths and C.J. Baker, *An Introduction to Passive Radar*, Artech House, 2017.
[28] H.D. Griffiths, I. Darwazeh and M.R. Inggs, 'Waveform design for commensal radar', *IEEE International Conference RADAR 2015*, Arlington, VA, pp 1456–1460, 11–14 May 2015.
[29] http://sbirsource.com/sbir/awards/7205-beyond-spectrum-multiobjective-joint-optimization-for-efficient-utilization-of-the-radio-frequency-transmission-hypercube, accessed 20 March 2017.
[30] International Telecommunication Union (ITU), '2012 World Radiocommunication Conference: Agenda and references'.
[31] H.D. Griffiths and N.J. Willis, 'Klein Heidelberg – the first modern bistatic radar system', *IEEE Transactions on Aerospace and Electronic Systems*, Vol. 46, No. 4, pp. 1571–1588, October 2010.
[32] Griffiths, H.D., 'Klein Heidelberg: new information and further insight', *IET Radar, Sonar and Navigation*, Vol. 11, No. 6, pp. 903–908, June 2017.
[33] M.C. Jackson, 'The geometry of bistatic radar systems', *IEE Proceedings*, Vol. 133, Part F., No. 7, pp. 604–612, December 1986.
[34] N.J. Willis, *Bistatic Radar*, Artech House, 1991.
[35] H.D. Griffiths, 'Early history of bistatic radar', *EuRAD Conference 2016*, London, 6/7 October 2016.
[36] https://www.asdreports.com/news.asp?pr_id=1701, accessed 8 September 2016.
[37] https://sputniknews.com/russia/201611241047787964-russia-radar-system-drones/, accessed 7 March 2017.
[38] B.M. Horton, 'Noise-modulated distance measuring system', *Proceedings of the IRE*, Vol. 47, pp. 821–828, May 1959. Reprinted in *Radars*, Vol. 7, *CW and Doppler Radar* (D. K. Barton, ed.), Artech House, 1978.

[39] W-D Wirth, *Radar Techniques Using Array Antennas*, 2nd ed. Chapter 17, IET, 2013.
[40] E.R. Billam, 'MESAR-the application of modern technology to phased array radar', *IEE Tutorial Meeting on Phased Array Radar*, 1989.
[41] W.K. Stafford, 'Real time control of a multifunction electronically scanned adaptive radar (MESAR)', *IEE Colloquium on Real-Time Management of Adaptive Radar Systems*, 1990.
[42] A.R. Moore, D.M. Salter and W.K. Stafford, 'MESAR (multi-function, electronically scanned, adaptive radar)' *IEE International Radar Conference RADAR'97*, Edinburgh, pp. 55–59, 14–16 October 1997.
[43] R.A. Baugh, *Computer Control of Modern Radars*, RCS/AEGIS, 1973.
[44] W.D. Blair, G.A. Watson and S.A. Hoffman, 'Benchmark problem for beam pointing control of phased array radar against maneuvering targets', *American Control Conference*, IEEE, Vol. 2. 1994.
[45] W.D. Blair, G.A. Watson, T. Kirubarajan and Y. Bar-Shalom., 'Benchmark for radar allocation and tracking in ECM', *IEEE Transactions on Aerospace and Electronic Systems*, Vol. 34, No. 4, pp. 1097–1114, 1998.
[46] C. Darwin, *On the Origin of Species*, John Murray, Albemarle Street, London, 1859, https://en.wikisource.org/wiki/On_the_Origin_of_Species_(1859), accessed 15 March 2017.

This page intentionally left blank

Chapter 1

Radar emission spectrum engineering

Shannon D. Blunt[1], John Jakabosky[1] and Christopher Allen[1]

Abstract

The spectral containment of active radar emissions is of growing concern due to continued erosion of allocated radar spectrum and the increasing congestion driven by consumer demand for bandwidth-gluttonous wireless video applications. Strict new emission requirements are forcing the careful consideration of how to achieve radar spectral containment within the context of the ever-present pressure for enhanced sensing performance. It is thus imperative that a holistic perspective be taken that addresses the characteristics of the physical signal launched from the radar, inclusive of electromagnetics, systems engineering and signal processing attributes. This chapter introduces recent developments on the design and implementation of physical radar waveforms for spectral containment, including experimental results for various new emission schemes.

1.1 Introduction

The topic of radar waveform design has been investigated for decades [1] and includes myriad contributions including various forms of frequency modulation (FM), binary and polyphase coding, recent multiple-input–multiple-output schemes and more. However, the impact of the radar transmitter is generally not considered as part of the waveform design process. Given the impact the transmitter has on the waveform, particularly for high-power systems and in light of stricter radar emission requirements [2,3], it has become necessary to address the actual physical signal that is launched from the antenna along with all the factors that contribute to the generation of this signal.

A holistic perspective for radar emission design necessitates a mathematical representation of the intended waveform that permits physical generation. Specifically, this representation must be continuous and relatively well contained

[1]Radar Systems & Remote Sensing Lab (RSL), University of Kansas, USA

spectrally (noting that, in theory, an idealized pulse is not bandlimited). Further, it is useful if this representation provides the means with which to parameterize the waveform for optimization of the resulting physical signal according to attributes such as range sidelobes and Doppler tolerance.

It is well known that a waveform should have a constant envelope to mitigate some of the distortion induced by the transmitter power amplifier (PA) as well as to maximize 'energy on target' for subsequent detection sensitivity. However, a waveform must also be differentiable, and thus continuous, with sufficient spectral containment to minimize the spectral shaping that is imposed by the transmitter, which can compound distortion. As they inherently meet these criteria, FM waveforms such as the well-known linear FM (LFM) chirp have been widely used.

Of course, LFM is also known to possess rather high range sidelobes, which has led to the development of various non-linear FM (NLFM) waveforms that necessitate the identification of a suitable continuous phase/frequency function of time (see Section 5.2 of [1] for an overview). Many such methods are based on the principle of stationary phase [4–6], which relates the power spectral density (PSD) and the chirp rate at each frequency as a means to shape the waveform spectral content. Another class of NLFM is hyperbolic FM (HFM), otherwise known as linear period modulation [7,8], that is used in sonar and by many echo-locating mammals due to its Doppler invariance property. Further, HFM provides a relationship between peak sidelobe level (PSL) and the waveform time-bandwidth product (BT) that serves as a useful performance benchmark [8] for all constant amplitude waveforms. Other design approaches include higher order polynomials [9], use of the Zak transform [10], application of Bézier curves [11] and hybrid methods that also employ amplitude tapering on receive [12,13] (though such tapering also yields a signal-to-noise ratio, or SNR loss).

With the intent to obtain greater design freedom than could previously be achieved for NLFM, the notion of phase coding was also developed in which large-scale, parallelizable computing power can be applied to search for optimal codes having high dimensionality. This extensive litany of contributions includes Barker codes [14], P-codes [15,16], minimum peak sidelobe codes [17] and many others (see [1, Chapter 6]), with the goal of discovering ever longer codes with lower autocorrelation sidelobes (e.g., [18,19]).

Phase codes can be separated into the classes of binary codes and the more general polyphase codes, both of which have a structure involving a discrete sequence of phase values modulated onto rectangular subpulses (or chips). The theoretically instantaneous transitions between adjacent chips corresponds to infinite bandwidth, thus requiring some practical means with which to implement codes on a physical radar system. For binary codes, the most common techniques with which to convert the code into a constant envelope, continuous waveform are derivative phase shift keying (DPSK) [20] and the biphase-to-quadriphase transformation [21], which is a form of minimum shift keying (MSK). Of the two, the latter is superior from a spectral containment standpoint [20], though both are still somewhat limited in design freedom due to being constrained to a binary phase constellation.

An alternative approach proposed to limit the spectral spreading of coded waveforms is to replace the rectangular chips with windowed (and thereby truncated) sinc kernel functions [20,22]. While this approach achieves excellent spectral containment (in [20] out-of-band suppression of as much as 100 dB was achieved), the sinc kernel also produces amplitude modulation (AM) that requires linear amplification. To generate these waveforms with non-linear amplification, and thus high power efficiency, the Chiriex out-phasing configuration comprising dual non-linear amplifiers followed by a summer was used [20], which represents a form of Linear amplification with Nonlinear Components (LINC) [23,24]. It has been experimentally demonstrated that high transmit power may be achieved for this type of configuration as long as adequate cross-calibration can be maintained between the two PAs.

More recently, an implementation meeting the criteria for the generation of physical waveforms was developed that facilitates the realization of arbitrary polyphase coding as a new NLFM waveform class denoted as polyphase-coded FM (PCFM) [25,26]. This implementation is a modified form of the continuous phase modulation (CPM) scheme [27] that is commonly used for aeronautical telemetry [28,29], deep-space communications [30] and forms the basis of the Bluetooth™ wireless standard [31]. What these applications have in common are the dual requirements of power efficiency and spectral efficiency. The former is obtained by ensuring constant amplitude so that the transmitter PA can be operated in saturation, while the latter is achieved by bounding the instantaneous rate of phase change, both of which are inherently provided by the CPM structure.

By establishing the connection between phase coding and a resulting physically realizable waveform, the PCFM framework also provides the means with which to optimize the continuous waveform by searching over the high-dimensional space represented by the coding parameterization [32,33]. By direct extension, the underlying coding can likewise be optimized to account for the distortion the waveform encounters in the transmitter (via a transmitter model or actual hardware-in-the-loop) so as ultimately to optimize the physically emission [33,34]. In Section 1.2, this framework for generation and optimization of the physical emission is discussed along with a summary of various ways in which even greater design freedom can be achieved for the optimization of physical waveforms to contend with the potentially conflicting requirements of the sensing mission and spectral containment.

When addressing the physical radar emission it is observed that, with the use of spectrally efficient waveforms, the pulse rise/fall-times become the limiting factor on spectral containment due to the rather abrupt on/off nature of pulsed radars, specifically the high efficiency PAs that effectively behave like switches. As such, it becomes necessary to address the waveform and transmitter design jointly. In Section 1.3, recent work [35] is presented on the incorporation of a LINC architecture into optimization of the PCFM-based physical emission so as to design the waveform within the context of pulse shaping for spectral containment while still maintaining high power efficiency.

In Section 1.4, another recent emission implementation/optimization scheme is described that relies on the relationship between the PSD and autocorrelation of the waveform to realize pulsed [36] and continuous wave (CW) [37] modalities, respectively, that achieve both good spectral containment and low range sidelobes with little to no SNR loss. As with PCFM-based approaches, experimental measurements demonstrate the efficacy of these spectral shaping methods. This formulation also permits joint optimization of the waveform with a low-loss amplitude taper, and it is likewise shown how in-band spectral gaps (avoidance regions) can be generated without incurring the sensitivity degradation that otherwise generally arises.

1.2 Polyphase-coded FM

While considerable research has focused on polyphase code design, the physical implementation of such codes has received far less attention. Consider the mathematical representation of a continuous, baseband code consisting of a set of contiguous, constant amplitude, rectangular chips (or subpulses), each of which is modulated by an associated phase value of the code (see Figure 1.1). This idealized representation is the model used by nearly all search strategies seeking to determine an optimal sequence of code phase values (e.g., [18,19,38]). However, the abrupt phase changes between consecutive chips in the code produce extended spectral sidelobes with a $\sin(x)/x$ envelope [1, pp. 145–155]. A radar transmitter, comprised of driver amplifiers and an exciter, will not pass this extended spectral content due to inherent bandlimiting of the system. This linear distortion, combined with the non-linear characteristics of the transmitter (predominantly resulting from the PA), produces a distorted version of the idealized model of the code. Bandlimiting effects are offset by spectral regrowth arising from non-linear intermodulation products, often measured by the adjacent channel power ratio (ACPR) [3,24,39], that further complicate spectral containment. This distortion also translates into range straddling (cusping) effects for the received echoes [26,40].

In light of the description above, in [26], the nomenclature for radar waveforms is clarified since the terminology tends to be used rather loosely in the literature. A *code* is defined as the finite sequence of phase values $[\theta_0, \ldots, \theta_N]$ corresponding to the sequence of chips in Figure 1.1, noting that such a structure is not physically

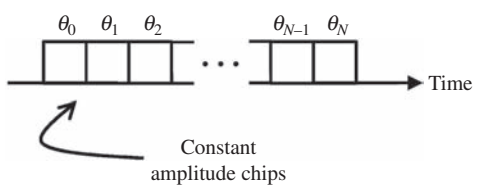

Figure 1.1 Idealistic representation of a polyphase-coded waveform (©2014 IEEE, reprinted with permission from [26])

realizable. In contrast, a *waveform* is a continuous physical signal, such as the well-known LFM chirp [1, pp. 57–61]. Finally, the *emission* is the transmitter-distorted version of the waveform that is launched into free space, including effects such as rise/fall-time ringing and distortion caused by undesired conversion of phase modulation (PM) into AM.

The purpose of the PCFM implementation is to convert an arbitrary polyphase code into a continuous FM waveform that is amenable to the bandlimiting/non-linear effects of the transmitter, the deleterious impact of which can be reduced but not eliminated. By extension, the selection of an underlying code implemented with the PCFM framework can subsume the transmitter distortion effects so as ultimately to optimize the physical radar emission launched into free space. In doing so, the spectral content may likewise be addressed for this physical emission, to the degree that the transmitter-distorted spectral response can be controlled by the underlying code. Total control over the emission necessitates joint design of the waveform and transmitter [2].

1.2.1 PCFM implementation

To provide a suitable implementation for the length $N+1$ polyphase code $[\theta_0 \quad \theta_1 \quad \cdots \quad \theta_N]^T$, a modified version of the CPM framework [27] was proposed for the radar application [26]. Figure 1.2 illustrates this scheme where a train of N consecutive impulses with time separation T_p are formed to yield a total pulse-width $T = NT_p$. The nth impulse is weighted by α_n, which is the phase change between successive chips of the polyphase code as determined by

$$\alpha_n = \Psi(\tilde{\alpha}_n) = \begin{cases} \tilde{\alpha}_n & \text{if } |\tilde{\alpha}_n| \leq \pi \\ \tilde{\alpha}_n - 2\pi \ \text{sgn}(\tilde{\alpha}_n) & \text{if } |\tilde{\alpha}_n| > \pi \end{cases} \tag{1.1}$$

where

$$\tilde{\alpha}_n = \theta_n - \theta_{n-1} \quad \text{for} \quad n = 1, \ldots, N \tag{1.2}$$

and sgn(•) is the sign operation.

The shaping filter $g(t)$ in Figure 1.2 is the same as that used for communications, with the most common examples being rectangular and raised cosine [27]. The requirements on the shaping filter are: (1) that $g(t)$ integrates to unity over the

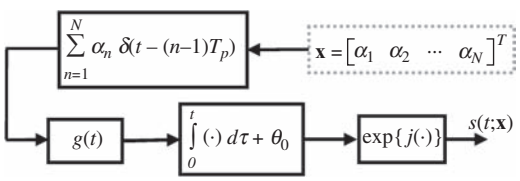

Figure 1.2 Modified CPM implementation to generate polyphase-coded FM (PCFM) radar waveforms (©2014 IEEE, reprinted with permission from [26])

real line and (2) that $g(t)$ has time support on $[0, T_p]$. The integration stage in Figure 1.2 is initialized to θ_0 and the sequence of phase changes are collected into the vector $\mathbf{x} = [\alpha_1 \quad \alpha_2 \quad \cdots \quad \alpha_N]^T$, which parameterizes the complex baseband PCFM waveform

$$s(t;\mathbf{x}) = \exp\left\{ j\left(\int_0^t g(\tau) * \left[\sum_{n=1}^{N} \alpha_n \, \delta\big(\tau - (n-1)T_p\big) \right] d\tau + \theta_0 \right) \right\} \tag{1.3}$$

Note that (1.1) and (1.2) provide for the conversion of an existing polyphase code $[\theta_0 \quad \theta_1 \quad \cdots \quad \theta_N]^T$ into the 'phase change' code $\mathbf{x}$ parameterizing the PCFM waveform. However, optimization of a PCFM waveform can be performed directly by selection of the values in $\mathbf{x}$, for $-\pi \leq \alpha_n \leq +\pi$ and with θ_0 from (1.3) an arbitrary phase offset that does not affect the goodness of the waveform. The selection of the shaping filter $g(t)$ also impacts the waveform and it could likewise be made a free parameter for optimization (though such is not considered here).

To demonstrate the physical attributes of the PCFM scheme, consider the four waveforms described in Table 1.1 that represent different implementations of a P4 code [1, Section 6.2] with $N = 64$. A discretized version of each waveform is represented with 150 samples/chip and a pulsewidth of 64 μs that is then loaded onto an arbitrary waveform generator (AWG) for measurement in a loopback configuration (the transmitter connected directly to the receiver) using an S-band testbed. The testbed includes a mixer, preamplifier, bandpass filter and a class AB solid-state GaN PA.

Figure 1.3 shows the pulse shapes for each of the four loopback measurements. The waveform denoted as 'Ideal Chip' represents the closest approximation possible to an idealized code given the sampling rate of 150 samples/chip. This waveform exhibits an amplitude null each time a chip transition occurs. Such significant deviations from constant amplitude can produce problems for a PA that is operated in saturation, including voltage-standing-wave-ratio (VSWR) fluctuations, increased phase noise and possibly even damage to components since a significant portion of the delivered power may not be radiated.

The '10% Transition' waveform partially alleviates this problem by performing a linear phase interpolation between adjacent chips, though the amplitude nulls are still clearly visible. Interestingly, the PCFM implementation using a rectangular (RECT)

Table 1.1 Waveform implementations and their characteristics

Implementation	Waveform characteristics
Ideal chip	Fastest phase transition possible given AWG limitations
10% Transition	Linearly interpolated phase transitions over 10% of each chip width
PCFM-RECT	Uses a rectangular filter for $g(t)$; approximates LFM with piecewise linear phase transitions
PCFM-RC	Uses a raised-cosine filter for $g(t)$

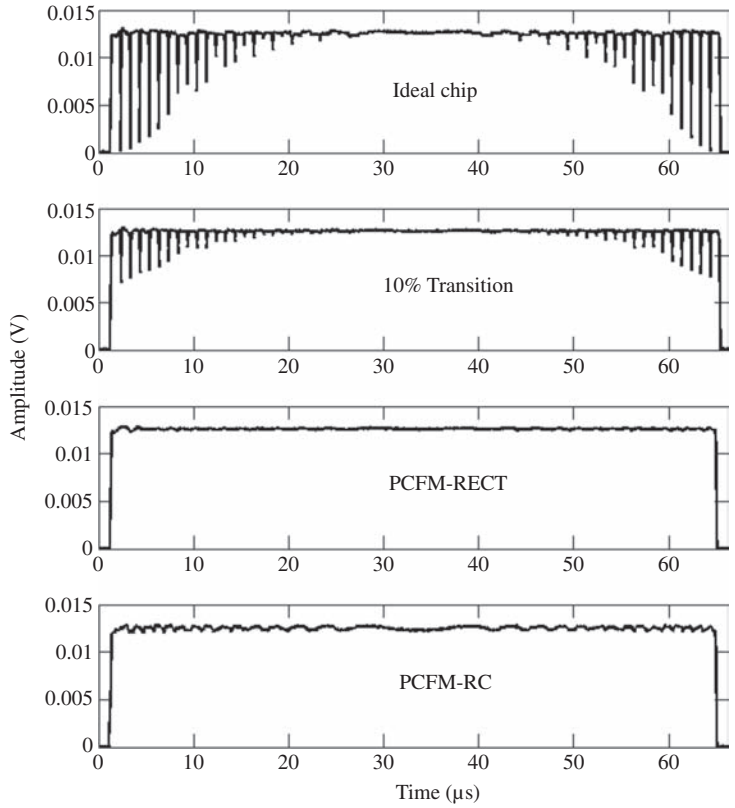

Figure 1.3 Pulse shapes for four loopback emissions after transmitter distortion [26]

filter for $g(t)$, which is a piece-wise linear phase approximation of the LFM waveform from which the P4 code is derived [1, Section 6.2], can be viewed as extending the 10% Transition case to a full 100% Transition with linear interpolation. Of course, instead of just being an ad hoc fix to the limitations of generating codes, the PCFM implementation provides a new design framework via the determination of the α_n parameters and the flexibility to select different shaping filters such as demonstrated by use of the raised-cosine (RC) filter in Figure 1.3.

Denoting *AWG waveform* as the version of each of the four waveforms that is loaded onto the AWG and *loopback emission* as the resulting version captured by the receiver of the S-band testbed, Figures 1.4–1.7 illustrate this 'before-and-after' spectral content for each of the four implementations. The distortion induced by the transmitter is most clearly evident for the Ideal Chip and 10% Transition waveforms in Figures 1.4 and 1.5, respectively. While it might appear for these cases that the transmitter is providing needed improvement in spectral containment, this distortion actually produces mismatch effects that translate into SNR losses on receive [26]. In Figures 1.4 and 1.5, the mismatch starts to appear just below −10 dB relative to the peak.

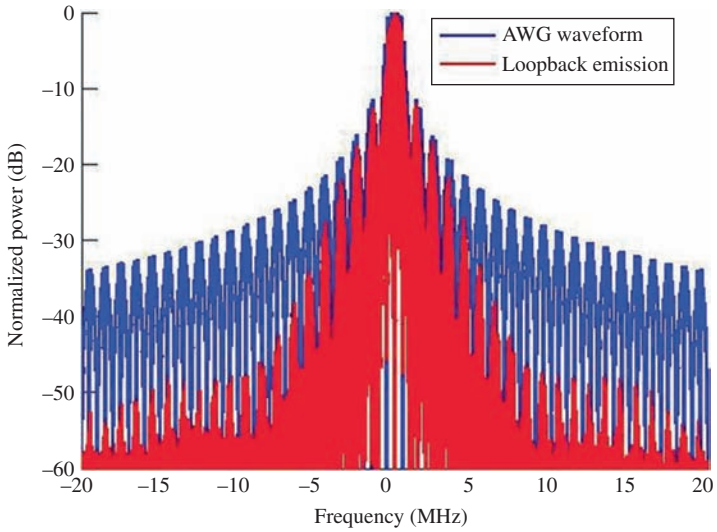

Figure 1.4 Spectral content of Ideal Chip waveform before (top) and after the transmitter (bottom) (©2014 IEEE, reprinted with permission from [26])

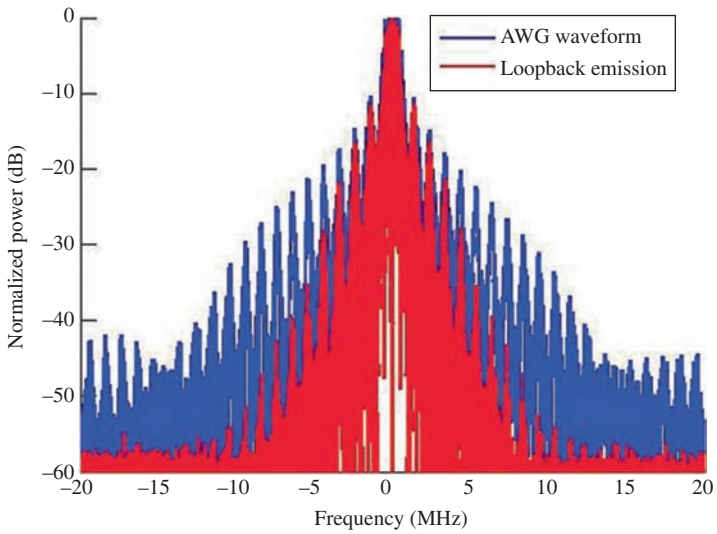

Figure 1.5 Spectral content of 10% Transition waveform before (top) and after the transmitter (bottom) (©2014 IEEE, reprinted with permission from [26])

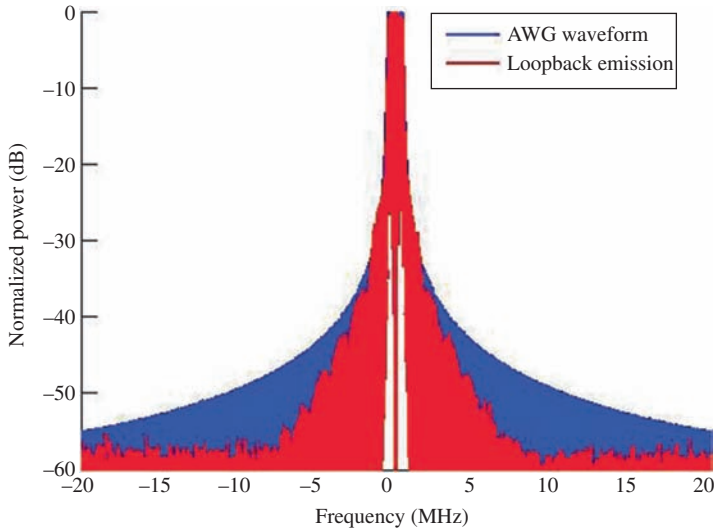

Figure 1.6 Spectral content of PCFM-RECT waveform before (top) and after the transmitter (bottom) (©2014 IEEE, reprinted with permission from [26])

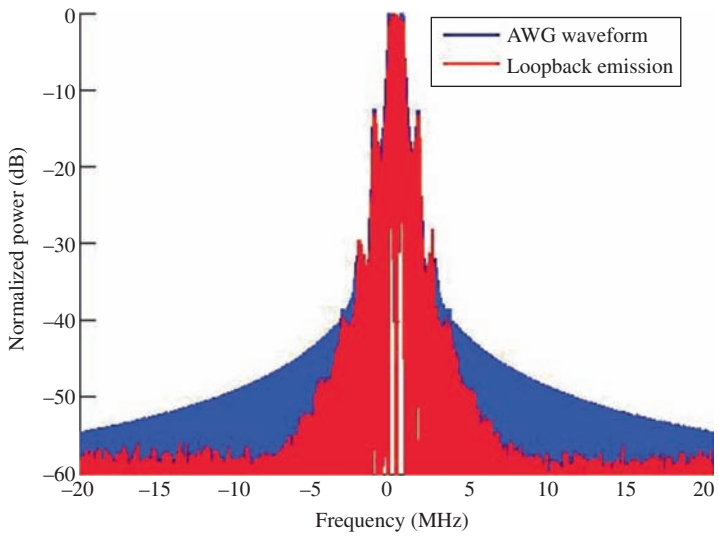

Figure 1.7 Spectral content of PCFM-RC waveform before (top) and after the transmitter (bottom) (©2014 IEEE, reprinted with permission from [26])

In contrast, the transmitter-induced mismatch for the two PCFM implementations (Figures 1.6 and 1.7) starts to appear below −30 dB relative to the peak, meaning these waveforms are much more amenable to the physical attributes of the transmitter. Also note that between the two PCFM waveforms, the one using the rectangular (RECT) shaping filter demonstrates better spectral containment, where the RC shaping filter produces a pair of close-in spectral sidelobes.

1.2.2 PCFM optimization

Inclusion of the PCFM implementation from Figure 1.2 into a comprehensive design framework permits optimization of the actual continuous waveform, and ultimately the physical free space emission inclusive of any distortion by the transmitter. Figure 1.8 provides a notional representation of this all-inclusive optimization paradigm.

The PCFM implementation defined in (1.3) and Figure 1.2 can be expressed compactly as the operator

$$s\,(t;\mathbf{x}) = T_{\mathrm{PCFM}}\{\mathbf{x}\} \tag{1.4}$$

that generates the continuous-time PCFM radar waveform associated with the phase-change code $\mathbf{x}$. The distortion induced by the transmitter may likewise be represented by the operation

$$u(t;\mathbf{x}) = T_{\mathrm{Tx}}[s(t;\mathbf{x})] = T_{\mathrm{Tx}}[T_{\mathrm{PCFM}}\{\mathbf{x}\}] \tag{1.5}$$

where the resulting signal $u(t;\mathbf{x})$ is the physical emission launched from the radar. For an idealized transmitter (no distortion) this latter operation simply yields

$$\text{idealized Tx}: \quad u(t;\mathbf{x}) = T_{\mathrm{Tx}}[s(t;\mathbf{x})] = s(t;\mathbf{x}) \tag{1.6}$$

The most common metrics for waveform (or here emission) optimization are peak sidelobe level (PSL) and integrated sidelobe level (ISL). Spectral containment to

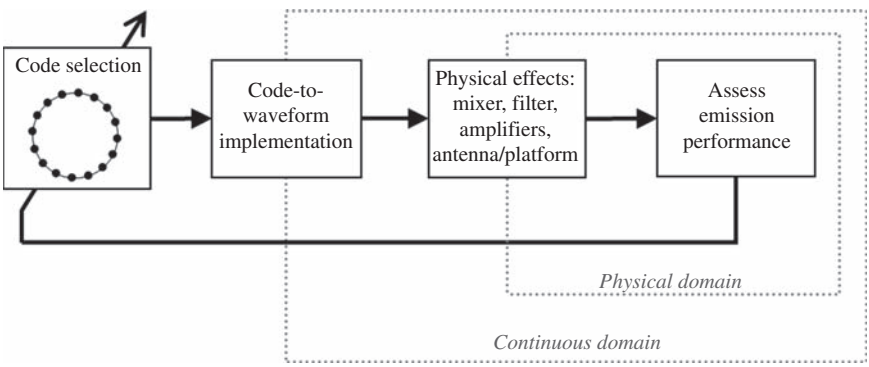

Figure 1.8 Notional representation of the optimization of physical radar emissions [33]

minimize the transmission of out-of-band spectral content and the incorporation of in-band spectral avoidance regions are emerging metrics driven by growing spectral congestion. Define $\Phi[u(t;\mathbf{x})]$ as the generic evaluation of the physical emission according to some metric.

The optimization problem then becomes one of determining the parameters in $\mathbf{x} = [\alpha_1 \quad \alpha_2 \quad \cdots \quad \alpha_N]^T$ that yield a sufficiently optimal solution, noting that the rather high dimensionality of the problem for a useful time-bandwidth product (BT) likely precludes determination of global optimality.

The goodness of a waveform (emission) is generally based on the delay-Doppler ambiguity function defined as

$$\chi(\tau,\omega) = \int_{t=-T}^{+T} e^{j\omega t}\, u(t;\mathbf{x})\, u^*(t+\tau;\mathbf{x})\, dt \tag{1.7}$$

where τ is delay, ω is Doppler and T is the pulsewidth. Clearly the $\omega = 0$ cut of this function is the waveform autocorrelation, which is worth noting, relates directly to the PSD of the waveform through a Fourier transformation.

The PSL [1] is thus usually defined for the zero-Doppler cut as

$$\Phi_{\text{PSL}}[\chi(\tau,\omega=0)] = \max_{\tau} \left| \frac{\chi(\tau,0)}{\chi(0,0)} \right| \tag{1.8}$$

for $\tau \in [\tau_m, T]$, in which the interval $[-\tau_m, \tau_m]$ corresponds to the autocorrelation mainlobe and $[-T, T]$ is the time support of $\chi(\tau,0)$ due to finite pulsewidth. The PSL metric provides a worst-case perspective on the sidelobe interference induced by a waveform/matched filter pair. Likewise, the ISL metric [1] for the zero-Doppler cut can be defined as

$$\Phi_{\text{ISL}}[\chi(\tau,\omega=0)] = \frac{\int_{\tau_m}^{T} |\chi(\tau,0)| d\tau}{\int_{0}^{\tau_m} |\chi(\tau,0)| d\tau} \tag{1.9}$$

In contrast to PSL, the ISL metric provides a measure of the aggregated sidelobe interference that could be encountered due to distributed scattering such as clutter.

Given the trend toward tighter restrictions on out-of-band radar spectral content, frequency-domain metrics are of growing importance. While it might at first seem that such a metric may be in conflict with the commonly used PSL and ISL metrics that are used to optimize for low range sidelobes, the relationship between PSD and autocorrelation reveals the fact that a PSD that decreases towards the band edges corresponds to an autocorrelation with low range sidelobes [12]. As such, it is possible to achieve both good spectral containment and low range sidelobes by employing an appropriate frequency-domain metric.

One such metric was recently defined as the frequency template error (FTE) in [33] as

$$\Phi_{\text{FTE}}[U(f;\mathbf{x})] = \left(\frac{1}{f_{\text{H}} - f_{\text{L}}} \right) \int_{f_{\text{L}}}^{f_{\text{H}}} \left| |U(f;\mathbf{x})|^p - |W(f)|^p \right|^q df \tag{1.10}$$

where f_L and f_H denote the 'low' and 'high' edges of the frequency interval of interest, $U(f;\mathbf{x})$ is the frequency response of the emission and $W(f)$ is a frequency weighting template (e.g., a Gaussian window). The values p and q permit control over the degree of emphasis placed at different frequencies. For $p = 1$ and $q = 2$, (1.10) realizes a frequency-domain mean-square error metric. Alternatively, $p > 1$ overly emphasizes in-band (higher power) frequencies while $p < 1$ overly emphasizes out-of-band (lower power) frequencies.

The notional emission design framework of Figure 1.8 is formalized in Figure 1.9 specific to the case of PCFM waveforms defined in (1.1)–(1.3). Alternatively, with small modifications one could likewise specify the design scheme for binary codes implemented with DPSK or MSK [20,21] or even orthogonal frequency division multiplexing (OFDM) [41], though the latter is not necessarily recommended for radar applications due to the significant AM exhibited by OFDM. The design problem exemplified by Figure 1.9 is of particular interest because polyphase codes provide greater freedom than binary codes and the associated PCFM implementation yields FM waveforms that are spectrally well contained and that are amenable to a high-efficiency, PA. The design problem thus becomes one of determining the sequence $\mathbf{x} = [\alpha_1 \quad \alpha_2 \quad \cdots \quad \alpha_N]^T$ that provides a subsequent physical emission to achieve a specified degree of performance according to a specified metric $\mathbf{\Phi}$.

If each phase-change parameter α_n for $n = 1, 2, \ldots, N$ can be one of L possible values from a discrete, equally spaced constellation on $[-\pi, +\pi]$, then there exist L^N different coded emissions that could possibly be generated via (1.3) for a given shaping filter $g(t)$. Clearly L and N need not be very large before the number of possibilities becomes too unwieldy to determine the global optimum via evaluation of all L^N candidate waveforms. As such, a search strategy is needed to identify locally optimum waveforms that are 'good enough'.

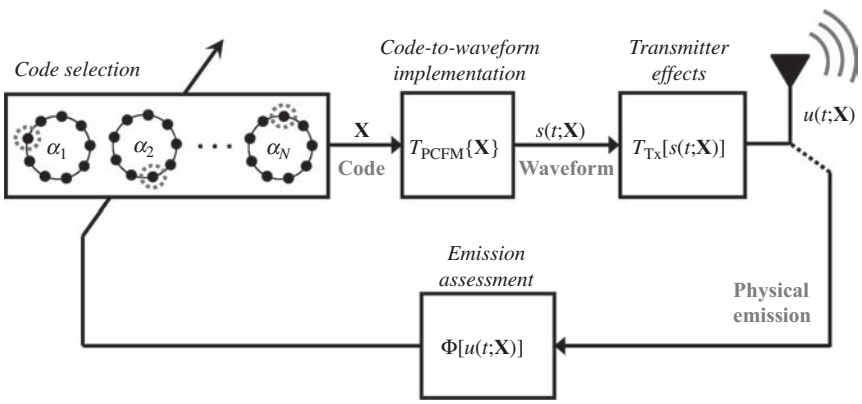

Figure 1.9 Formal representation of the optimization of physical radar emissions resulting from PCFM waveforms (©2014 IEEE, reprinted with permission from [33])

Many search strategies exist for this type of problem (e.g., Tabu search, simulated annealing, genetic algorithms, particle swarm optimization). Such strategies can generally be classified as either a single point (or local) search or as a population-based search [42]. The former rely on various heuristics to avoid local minima during the search while the latter employ a distributed sampling of the search space that is perturbed to discover new regions of the search space.

Within the context of radar waveform design, consider that the range-Doppler ambiguity function integrates to a constant for an arbitrary continuous, constant amplitude waveform [1] – meaning that sidelobes can only be moved around but not eliminated. As such, the consolidation of ambiguity into the range-Doppler ridge, as realized by chirp-like waveforms, provides an excellent initialization from which to search for optimal waveforms since the existence of the ridge effectively 'absorbs' much of the ambiguity. In other words, one can expect to obtain quite low range sidelobe levels by performing a local search on $\mathbf{x}$ in the vicinity of phase-change codes whose associated PCFM waveforms possess a chirp-like structure.

The difficulty with a local search is the prospect of 'getting stuck' in a local minimum. Well-known heuristics such as simulated annealing and Tabu search [42] were thus developed as means to escape from these local minima in the hopes of discovering the global minimum (or at least a better local one). For the problem of optimizing a physical radar waveform, a new approach was devised in [33] that relies on the complementary nature of the waveform metrics of PSL, ISL and FTE as defined in (1.8), (1.9) and (1.10), respectively. Denoted as *performance diversity*, this search strategy exploits the fact that each of these metrics differently measures the same fundamental property of 'how large are the range sidelobes relative to the mainlobe' for the zero Doppler cut (with possible simple extension to non-zero, yet small, Doppler as well). As such, an improvement in one metric tends to be an improvement in the others. An important exception, however, is that local minima are not necessarily the same across these different metrics, thus providing a way to escape some local minima by simply changing the metric being evaluated. While a local minimum shared by all three is certainly possible (though more rare), it is also likely to be a rather good local minimum, thereby likely achieving the design goal.

For example, using a phase-change code that closely approximates an LFM chirp as the initialization and assuming an idealized transmitter (i.e., no distortion), Figure 1.10 illustrates the autocorrelation obtained after optimization using the individual metrics of PSL, ISL and FTE, along with the result from using all three combined within this performance diversity paradigm. Table 1.2 quantifies the performance for each according to how the emission was optimized. Interestingly, the performance diversity approach yields the best performance for all three metrics, which stands to reason since this approach is not a multi-objective optimization in which competing goals are sought, but instead exploits the fact that these metrics are actually complementary to one another.

Relative to the LFM waveform, it is also observed in Table 1.2 and Figure 1.11 that all of the optimized waveforms involve a small degradation in range resolution. This effect is to be expected for NLFM waveforms since the more gradual spectral

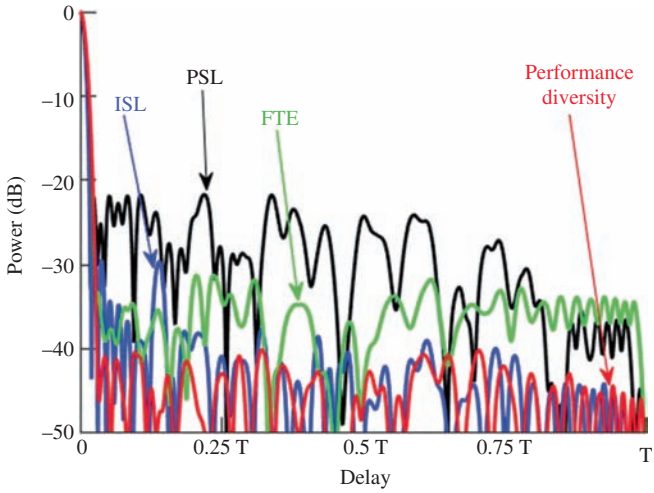

Figure 1.10 Autocorrelation of the optimized ideal emissions using the PSL, ISL and FTE metrics individually and the performance diversity paradigm (©2014 IEEE, reprinted with permission from [33])

Table 1.2 Quantified performance for optimization of emissions for an idealized transmitter (©2014 IEEE, reprinted with permission from [33])

		Optimization metrics			
	LFM waveform	**PSL only**	**ISL only**	**FTE only**	**Performance diversity**
Final PSL value (dB)	−13.5	−21.1	−27.0	−31.3	**−40.2**
Final ISL value (dB)	−9.8	−6.7	−20.0	−15.6	**−24.9**
Final FTE value (dB)	−17.0	−16.6	−22.4	−30.1	**−32.1**
Relative 3 dB resolution	1.00	**1.06**	1.11	1.26	1.28
Relative 6 dB resolution	1.00	**1.08**	1.13	1.30	1.33

roll-off (relative to LFM), which provides for the achievement of lower range sidelobes, also slightly reduces the 3 dB bandwidth. It is interesting to note that the better performing NLFM waveforms in terms of sidelobe reduction realize a slightly greater trade-off in resolution (also to be expected given the conservation of range-Doppler ambiguity). Finally, these waveforms retain the chirp-like structure and thus also retain much of their Doppler tolerance [33].

In short, it is possible to optimize an FM radar waveform by using a parameterized search in the neighbourhood of chirp-like waveforms. In so doing, the goals of spectral containment and low-range sidelobes can both be met. Now consider how the distortion induced by the radar transmitter can likewise be addressed.

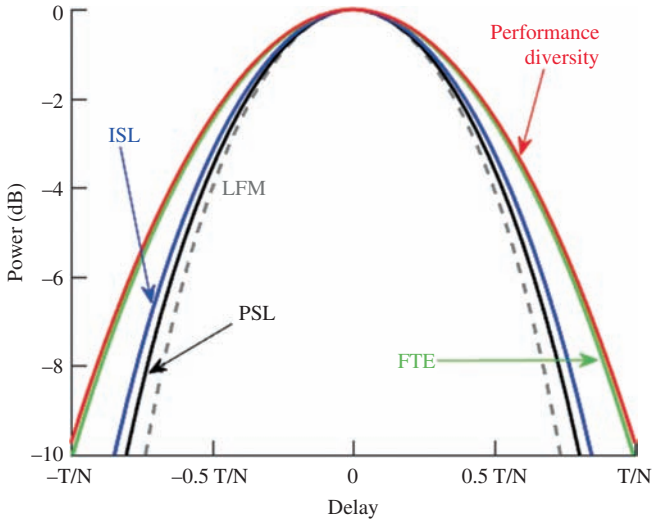

Figure 1.11 Autocorrelation of the optimized ideal emissions using the PSL, ISL and FTE metrics individually and the performance diversity paradigm (mainlobe zoom-in) (©2014 IEEE, reprinted with permission from [33])

1.2.3 Optimizing physical radar emissions

With the establishment of a framework to optimize the physical attributes of a waveform, it is possible to now consider the inclusion of transmitter distortion effects to optimize the physical emission launched from the radar. Generally speaking, there are two approaches one may take: model-in-the-loop (MiLo) optimization in which the linear/non-linear distortion is represented as a mathematical model in simulation and hardware-in-the-loop (HiLo) optimization in which the actual physical transmitter is used in the optimization process [33]. The MiLo approach has the benefit of permitting a fast search of this high-dimensional space, such as by using general purpose graphics processing units (GPGPU), though even the best model cannot exactly characterize the hardware it is intended to represent. In contrast, the HiLo approach optimizes the emission specific to the very transmitter that will use it, though the latency involved with uploading a waveform onto an AWG and subsequently capturing it for evaluation can slow down the search process considerably.

Figure 1.12 again depicts the autocorrelation of the performance diversity waveform from Figure 1.10 that was optimized under the idealistic transmitter condition (distortion free). In addition, Figure 1.12 reveals the autocorrelation of this waveform after being distorted by the solid-state amplifier model from [43]. Relative to the idealistic case, the distorted waveform results in 4.6 dB degradation in PSL and 2.8 dB degradation in ISL [33]. However, when MiLo optimization is used (Figure 1.12), 4.4 and 2.2 dB of lost PSL and ISL sensitivity is recovered, respectively.

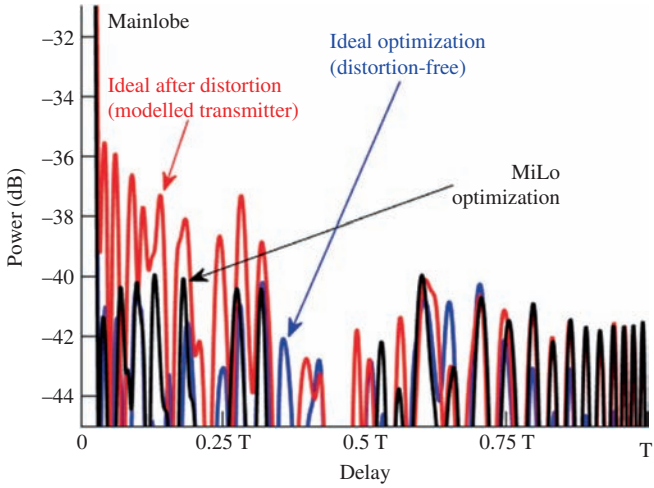

Figure 1.12 Emission autocorrelation for the ideal optimization (distortion-free) case, the modelled transmitter distortion case and transmitter Model-in-the-Loop (MiLo) optimization (©2014 IEEE, reprinted with permission from [33])

Figure 1.13 repeats the procedure of Figure 1.12, albeit for HiLo optimization involving an L-band ($f_c = 1.842$ GHz) test bed in an anechoic chamber. Here a Class A PA is used that is driven 5 dB beyond the 1 dB compression point. Each candidate waveform is converted to in-phase and quadrature-phase (I/Q) components and loaded onto an AWG. The transmit antenna is a quad-ridge horn. A separate receiver captures the emitted signal via a standard-gain horn, performs attenuation, downconversion, and digitization and then passes the captured emission back to Matlab running on a laptop for evaluation and selection of the next waveform.

As observed in Figure 1.13, the transmitter hardware degrades the waveform by 2.7 dB in terms of PSL. Subsequent HiLo optimization is able to recover 1.5 dB of this lost sensitivity. Note that this Class A amplifier is not very severe in terms of distortion. It is expected that more power-efficient amplifiers (e.g., tube-based amplifiers that may be Class C or higher) would induce greater distortion, thus providing greater impetus for HiLo optimization. However, this proof-of-concept experiment does demonstrate the potential for optimization of the physical radar emission that is launched into free space.

For these tests, the MiLo arrangement realized in excess of 500,000 waveform evaluations per second. However, when the same process was performed in a HiLo arrangement on the radar testbed the search speed dropped to 1 waveform evaluation every 1.5 s, many orders of magnitude slower than for MiLo.

Further, note that the nature of PA distortion is rather complicated, being composed of both static and dynamic characteristics (the latter arising from memory effects in the device). As such, many different general models for PA behaviour

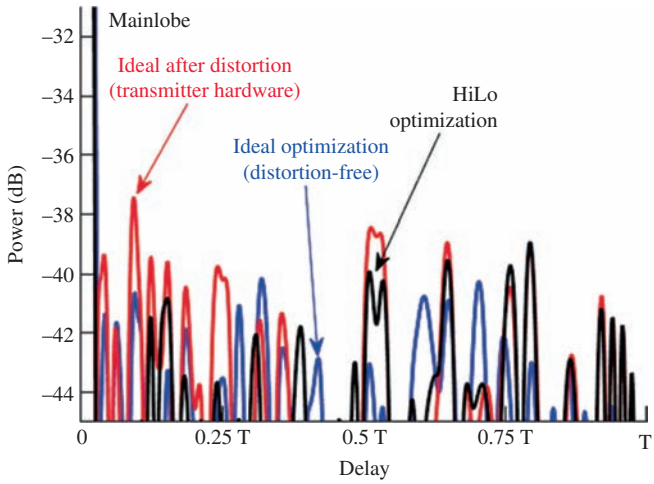

Figure 1.13 Emission autocorrelation for the ideal optimization (distortion-free) case, the physical (hardware) transmitter distortion case and transmitter Hardware-in-the-Loop (HiLo) free-space optimization (©2014 IEEE, reprinted with permission from [33])

have been proposed [44] as a means to estimate the properties of a given device to perform subsequent predistortion compensation.

Such models may thus provide the means to hybridize the MiLo and HiLo approaches such that the transmitter distortion is accurately estimated for a particular system (updated as needed) and then used to emulate the distortion for fast search of the physical emission. This notion of an 'introspective radar' represents a form of autonomic cognition that can be likened to the development of proprioception in infants, wherein a sense of the disposition of arms, legs, etc. is gained. To the degree that the interaction between the waveform and transmitter distortion has an impact on spectral regrowth, this manner of physical emission design may permit improved spectral containment. In Section 1.3, the notion of joint waveform/transmitter design is also examined.

1.2.4 Further expansion of design freedom

For the PCFM waveform structure defined by (1.1)–(1.3), BT is well approximated by N, the length of the phase-change code $\mathbf{x}$. Put another way, a PCFM waveform has N design degrees of freedom with which to realize a waveform that achieves low-range sidelobes and, to the degree to which it is affected by waveform coding, address transmitter distortion effects.

In [45], however, a modification to the PCFM structure was introduced that, while maintaining the same BT (for B specifically the 3 dB bandwidth), the design degrees of freedom can be increased significantly. This modification was denoted generally as waveform *over-coding* and consists of two attributes: (1) subtransitions

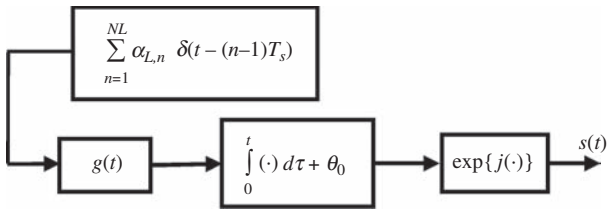

Figure 1.14 PCFM implementation using over-coding (©2014 IEEE, reprinted with permission from [45])

for phase changes to permit greater freedom in the phase trajectory and (2) over-phasing to permit the instantaneous phase-change to exceed the previous bound of $\pm\pi$. The former provides finer granularity of phase changes as a function of time while the latter provides greater utilization of the available spectral content, albeit with the additional requirement of a constraint on the overall spectral envelope to avoid expanding the specified bandwidth.

Figure 1.14 illustrates the over-coded PCFM implementation where the phase-change parameter α_n for $n = 1, 2, \ldots, N$ from Figure 1.2 has been replaced with $\alpha_{L,n}$ where $n = 1, 2, \ldots, LN$ to account for the dividing of each original phase transition into L subtransitions. Also, the previous phase-change bound defined as $-\pi \leq \alpha_n \leq +\pi$ has been replaced with $-M\pi/L \leq \alpha_{L,n} \leq +M\pi/L$, so that without a means of constraint the bandwidth could increase by a factor of M. The FTE metric from (1.10) can readily provide this constraint.

Figure 1.15 demonstrates the capability of these new degrees of freedom in terms of waveform autocorrelation for different values of L and M. The ($L = 1$, $M = 1$) case is simply the 'performance diversity' waveform from Figure 1.10. Using $L = 8$ along with either $M = 1$ or $M = 2$ enables significantly lower range sidelobes via the same form of optimization search as that described above (and the use of a GPGPU processor to handle the increased computational burden due to higher dimensionality). Specifically, the PSL value has decreased by 2.7 and 10.6 dB, respectively, for these two over-coding cases relative to the original. Likewise, ISL has decreased by 1.9 and 10.8 dB, respectively. Noting that the (not shown) case of ($L = 1$, $M = 2$) yields only 0.5 dB PSL improvement, it is clear that it is the combination of both subtransitions and over-phasing (with spectral constraint) that facilitates such significant sidelobe reduction.

It is interesting to consider the spectral content for over-coded waveforms (Figure 1.16). Relative to the original baseline case of ($L = 1$, $M = 1$), the two over-coded waveforms depicted here, ($L = 4$, $M = 2$) and ($L = 8$, $M = 2$), realize a marginal increase of spectral content in the roll-off regions. While still adhering to the spectral shape dictated by the FTE metric (again using a Gaussian window here), a 'spectral fuzz' arises due to the collection of small perturbations introduced by over-coding. Ongoing work is exploring how, within the MiLo/HiLo paradigm, over-coding may provide further control over the spectral spreading induced by transmitter distortion, particularly in the presence of memory effects [44].

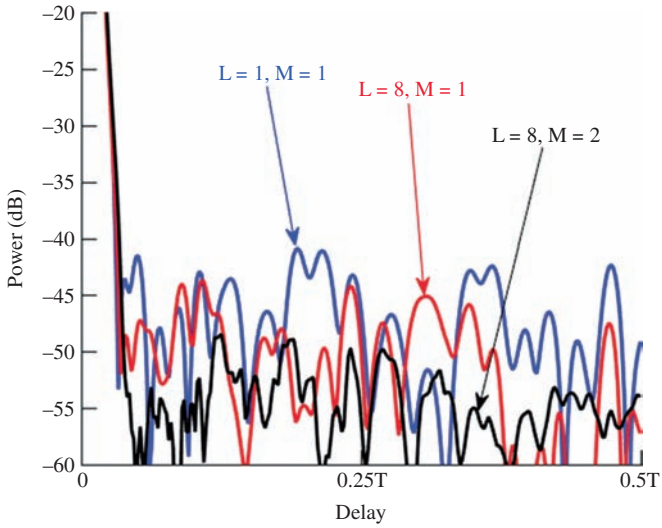

Figure 1.15 *Close-up autocorrelation comparison for over-coded optimized waveforms relative to the nonover-coded optimized waveform (BT ≅ 64) (©2014 IEEE, reprinted with permission from [45])*

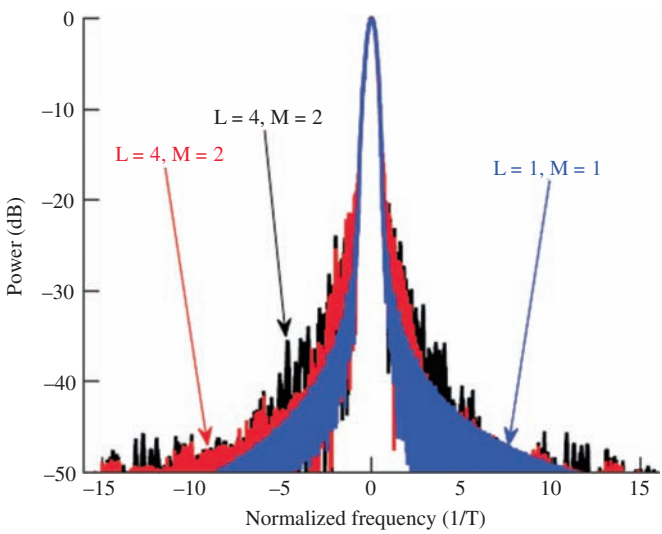

Figure 1.16 *Spectral content comparison for (L = 1, M = 1); (L = 4, M = 2); and (L = 8, M = 2) waveforms (©2014 IEEE, reprinted with permission from [45])*

Additional physically realizable degrees-of-freedom for waveform design that have recently been investigated include spatial modulation [46], polarization modulation [47] and higher order PCFM [48]. Further, optimal mismatch filtering and adaptive pulse compression receive processing have also recently been experimentally demonstrated for arbitrary FM waveforms [49].

1.3 LINC-optimized waveforms

In [2], one of the proposed challenge problems for spectrum engineering and waveform diversity is joint waveform/transmitter design. Instead of the usual component-wise perspective often taken in engineering, this holistic perspective presents the opportunity to exploit synergistic attributes of the waveform and transmitter akin to what is observed in nature (e.g., [50]), with the potential to realize new combinations and capabilities.

For instance, it is well known that the ability to modulate the amplitude of a radar waveform provides greater design freedom to achieve enhancements such as reduced range sidelobes (e.g., via tapering of LFM [1]) and better spectral containment (e.g., weighted series expansion of a binary-coded waveform [1]). However, AM effects are rather difficult to maintain through a saturated PA, necessitating the means to linearize this non-linear device [24,44]. There are many different ways to achieve this goal, including outphasing, envelope tracking, the Doherty technique, the Kahn technique, feedback linearizers, feedforward linearizers and predistortion [24], along with numerous variants. As such, one can envision the transmitter architecture as being comprised of a set of parameters that, collectively with the parameterization of the waveform such as in (1.1)–(1.3), represent a rich design space from which to consider the notion of joint optimization.

As a pertinent example, linearization techniques could be used to slow down the rapid rise-/fall-time of a radar pulse which, for a spectrally well-contained waveform (e.g., most FM waveforms), is the limiting factor for spectral containment of the overall emission (Figure 1.17). In principle, this task can be readily addressed by applying an amplitude taper onto the transmitted pulse. However, for a high-power radar in which the operation during the pulse rise/fall can be likened to the operation of a switch, such a task becomes more complicated.

To address this problem, consider the outphasing approach, otherwise known as linear amplification using non-linear components (LINC) [24]. Figure 1.18 illustrates the LINC architecture using a 180° hybrid coupler in which the sum (Σ) output terminal provides the addition of the two input signals and the difference (Δ) output terminal realizes the subtraction of one input signal from the other. Mathematically, the application of an amplitude taper onto a desired waveform $s(t)$ can be represented as [35]

$$s_1(t) = s(t) \tag{1.11}$$

$$s_2(t) = s(t)\exp\{j\phi(t)\} \tag{1.12}$$

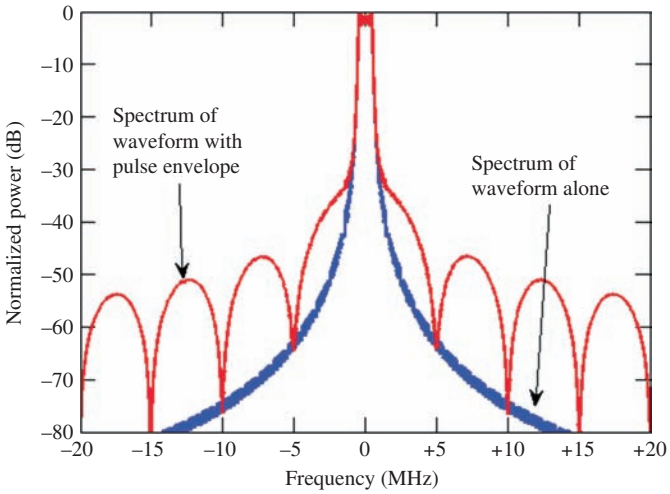

Figure 1.17 Notional spectral content of a 64 μs pulse modulated with an LFM waveform of 1 MHz bandwidth (with and without inclusion of the pulse rise/fall)

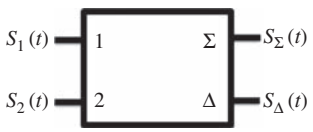

Figure 1.18 LINC transmitter implementation using a 180° hybrid coupler [35]

where

$$\phi(t) = \cos^{-1}\left(2w^2(t) - 1\right) \tag{1.13}$$

is the phase adjustment between the two input waveforms needed to generate the real-valued amplitude taper $w(t)$. The resulting output waveform on the sum (Σ) channel is thus

$$s_\Sigma(t) = s_1(t) + s_2(t) = s(t)w(t)\exp\{j\psi(t)\} \tag{1.14}$$

in which

$$\psi(t) = \tan^{-1}\left(\frac{\sqrt{1 - w^2(t)}}{w^2(t)}\right) \tag{1.15}$$

is the residual phase response that results from combining the two waveforms in this LINC configuration. The signal produced on the difference (Δ) terminal can either be directed into a matched load or may be recycled to improve overall power efficiency [51].

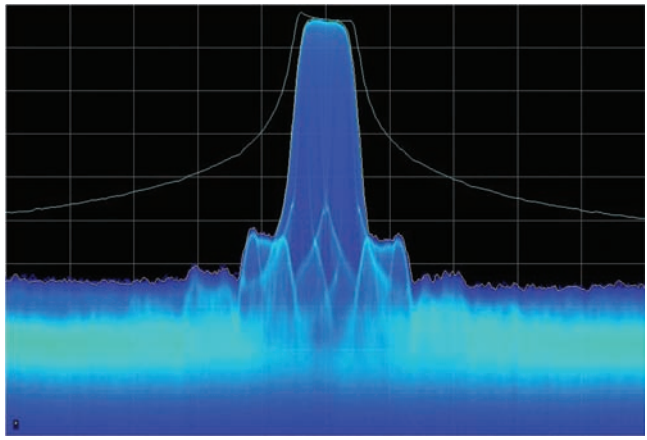

Figure 1.19 LFM spectrum with (lower trace) and without (higher trace) Tukey taper, vertical increments are 10 dB (©2014 IEEE, reprinted with permission from [35])

It is important to note that, because the weighting and associated residual phase response modify the underlying waveform $s(t)$ it is necessary to optimize the resulting emission $s_\Sigma(t)$ to account for these effects along with any other transmitter distortion. In [35] an LFM waveform with $BT = 64$ has a Tukey taper applied via this LINC method such that the pulse rise/fall effectively occur during the first and last quarter of the pulse. The hardware setup is the same as for the results in Figure 1.13 from the previous section, aside from the addition of the 180° coupler and a second AWG. Per Figure 1.19 that was captured with a real-time spectrum analyzer (RSA), the taper provides about 15 dB of additional spectral containment in the out-of-band region. Of course, the Tukey taper is convenient to use because its amplitude rolls off to zero at the edges, but this taper is actually not well-suited for LFM, with the tapered waveform yielding a PSL of only −16.4 dB.

It was shown in [35] that performing HiLo optimization for this hardware configuration, initialized with the tapered LFM waveform, can reduce the PSL to −42.8 dB, an improvement of 26.4 dB. Figure 1.20 depicts the associated RSA captured spectrum when HiLo optimization is performed, both with and without the Tukey taper. It is thus observed that a significant reduction in PSL can be achieved while still preserving the roughly 15 dB improvement in out-of-band suppression.

Using the associated matched filter, this particular taper resulted in an SNR loss of 3.2 dB, which clearly is not feasible for many sensing applications. Further, to realize the substantial tapering at the rise/fall edges of this 64 μs pulse, where better than −30 dB suppression was achieved, picosecond level timing calibration was needed to ensure sufficient synchronization between the two AWG-generated pulsed waveforms. Without this degree of timing calibration the HiLo optimization could not converge due to drift (as determined in preliminary experimentation using lower fidelity AWGs). However, this proof of concept does demonstrate the potential for

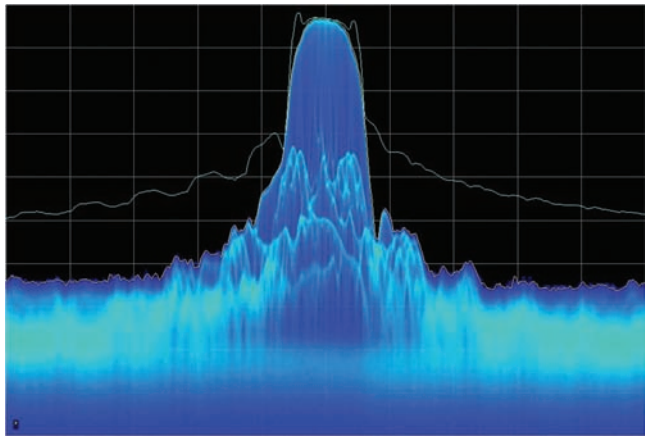

Figure 1.20 Hardware-optimized spectrum with (lower trace) and without (higher trace) Tukey taper, vertical increments are 10 dB (©2014 IEEE, reprinted with permission from [35])

enhanced control over radar emissions, as a means to realize better spectral containment and to start realizing the practical potential of waveform diversity.

1.4 Spectrally shaped optimization

This final section of the chapter considers a different form of waveform design that specifically addresses spectral content. This approach relies on an iterative spectral shaping procedure that is essentially a form of alternating projection [52]. In one manifestation of this approach a pulsed waveform is designed jointly with a low-loss amplitude taper to achieve ultra-low range sidelobes. In another, a non-repeating FMCW waveform is realized as an instantiation of FM noise radar. Both cases demonstrate good spectral containment and good sensing performance based on experimental measurements.

1.4.1 Ultra-low sidelobe emissions

In [36], a method was developed to enable joint optimization of an FM waveform and a low-loss amplitude taper. As discussed for the FTE metric in (1.10), a Gaussian PSD translates into a Gaussian autocorrelation, meaning low range sidelobes in practice. The previous waveform optimization based on the PCFM structure inherently constrained the optimization to one of adjusting the FM aspects of the waveform while the pulse shape was fixed (either as a constant or, like in Section 1.3, to adhere to a predefined amplitude taper). Here, both FM and AM attributes are jointly optimized, with the additional degrees of freedom provided by joint inclusion of AM yielding tremendous improvement in sidelobe suppression while maintaining good spectral containment.

Given an initial waveform $p_0(t)$, a desired PSD $|G(f)|^2$, and a desired amplitude taper $w(t)$ to serve as a soft constraint to minimize SNR loss, the first stage of the optimization process [36] involves the iterative application of

$$r_{i+1}(t) = \mathcal{F}^{-1}\{|G(f)|\exp(j\angle\mathcal{F}\{p_i(t)\})\} \tag{1.16}$$

and

$$p_{i+1}(t) = w(t)\exp(j\angle r_{i+1}(t)), \tag{1.17}$$

where $\mathcal{F}$ is the Fourier transform, $\mathcal{F}^{-1}$ is the inverse Fourier transform and $\angle(\cdot)$ extracts the phase of the argument. These steps are repeated I times to generate the first stage output waveform $p_I(t)$ that possesses both FM and AM attributes.

Setting $q_0(t) = p_I(t)$ as the initialization for the second stage, the iterative application of

$$q_{k+1}(t) = x(t)\mathcal{F}^{-1}\{|G(f)|\exp(j\angle\mathcal{F}\{q_k(t)\})\} \tag{1.18}$$

is then performed K times to produce the final waveform $q_K(t)$, with $x(t)$ a rectangular window having the same length as the pulsewidth T which serves to limit the temporal extent of $q_{k+1}(t)$. Both stages can be efficiently implemented using FFT and IFFT processing on a GPGPU.

As an example, a joint waveform/taper optimization is performed for $BT = 128$, where bandwidth $B = 80$ MHz and pulsewidth $T = 1.6\,\mu$s. The PSD $|G(f)|^2$ is a Gaussian shape and the initial taper $w(t)$ is a Tukey taper with amplitude roll-off occurring during the first and last 50 ns. The waveform/taper is optimized for $I = K = 5{,}000$ iterations in each of the two stages. The initial waveform $p_0(t)$ is the $(L = 8, M = 2)$ over-coded waveform from Section 1.4 having $BT = 64$ that has been interpolated up to $BT = 128$ using polynomial fitting. Note that this initial waveform from [45] is still rather chirp-like, albeit with the time-frequency dithering that arises when optimizing physical FM waveforms.

Figure 1.21 depicts the resulting amplitude envelope after joint waveform/taper optimization in which the associated SNR loss is only 0.26 dB. The trade-off for this small SNR loss can be observed in Figure 1.22 in which the autocorrelation is shown for the intermediate stage as well as the final stage, with and without inclusion of the taper. While the intermediate stage achieves a PSL of -59.9 dB, the joint waveform/taper optimization attains a PSL of -108.1 dB, far exceeding what would often be needed for many sensing applications. Interestingly, if the taper is removed the PSL degrades by more than 60 dB. Further, Figure 1.23 shows that removal of the amplitude taper likewise results in significant degradation in terms of spectral containment, thus emphasizing the important linkage between waveform performance for sensing and the spectral containment of the radar emission.

Finally, Figure 1.24 illustrates the matched filter response for a loopback measurement when this jointly optimized emission is implemented on the radar testbed used in the previous sections. This response includes the effect of a Least-Squares based compensation of linear artifacts that were generated by the spectrum analyzer and LINC architecture. The loopback measurement without using LINC yields a PSL

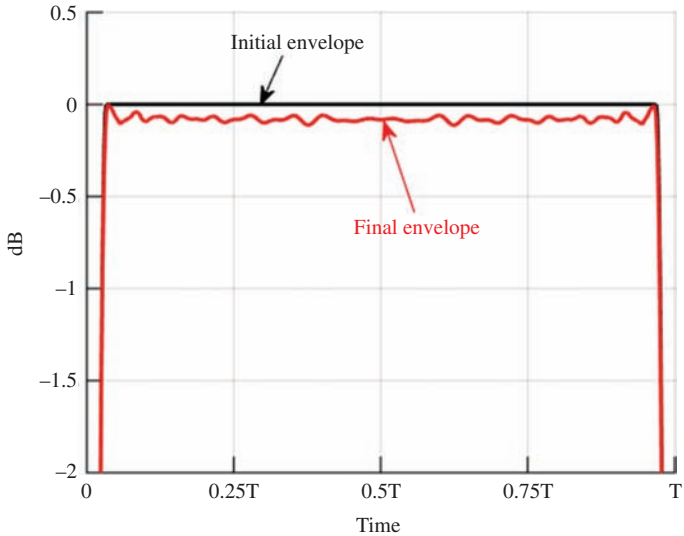

Figure 1.21 *Pulse amplitude envelope after optimized joint waveform/taper optimization with BT = 128 (©2015 IEEE, reprinted with permission from [36])*

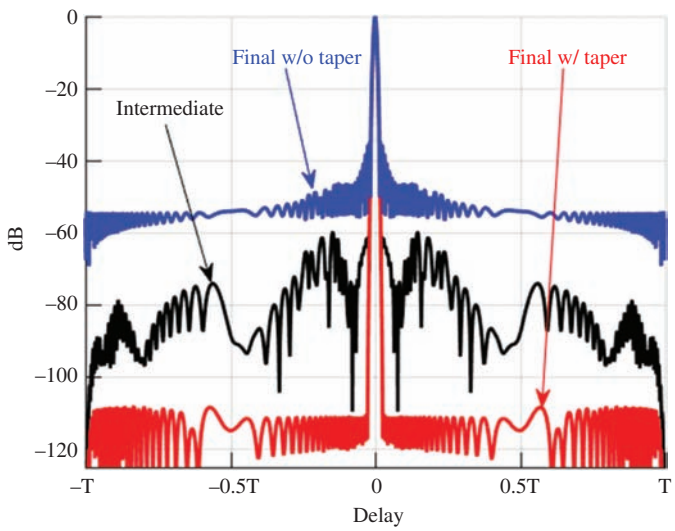

Figure 1.22 *Waveform autocorrelation of intermediate design stage, and with and without jointly optimized amplitude taper (©2015 IEEE, reprinted with permission from [36])*

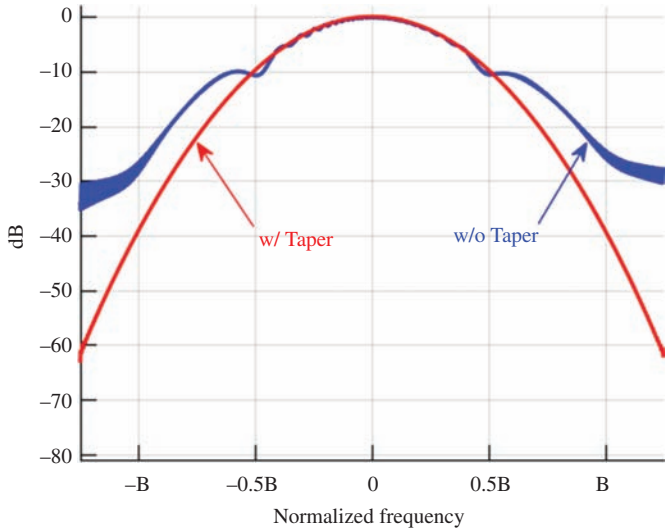

Figure 1.23 Spectral content of waveform with and without jointly optimized amplitude taper. The case that includes the taper closely matches the desired Gaussian PSD (©2015 IEEE, reprinted with permission from [36])

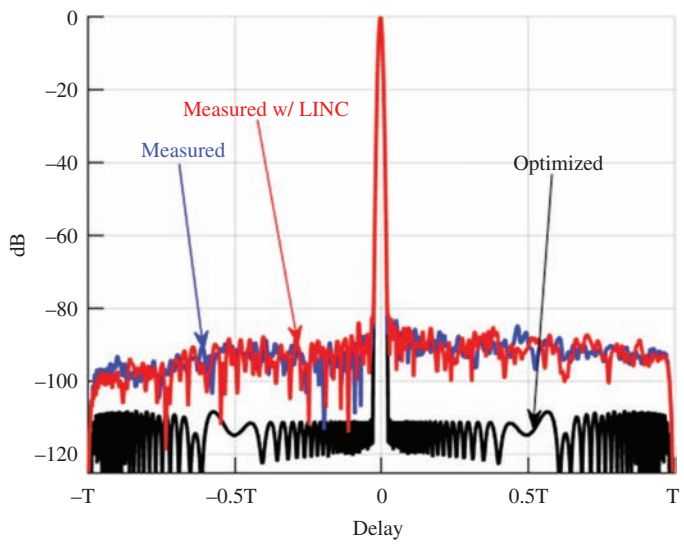

Figure 1.24 Matched filter response using an experimental loopback measurement (©2015 IEEE, reprinted with permission from [36])

of −83.2 dB while the use of LINC realizes a PSL of −81.8 dB, thus demonstrating the potential to implement these AM effects at high power. The difference between these measured results and simulated performance is most likely due to the 10-bit resolution of the AWG. The measured waveform also maintains the same spectral containment as demonstrated in Figure 1.23. In [36] it is shown how this ultra-low sidelobe emission provides dynamic range greater than 70 dB for free-space measurements.

1.4.2 Non-recurrent nonlinear FMCW emissions

The spectrally shaped design approach from the previous section addressed joint waveform/taper optimization to obtain a particular ultra-low sidelobe radar emission that is repeated during a coherent processing interval (CPI). Here we consider a similar design approach but focus instead on the development of a non-repeating structure for which sidelobes do not coherently combine [37]. As such, the following can be viewed as a form of FM noise radar [53] that is designed on a segment-wise basis.

Denoted as pseudo-random optimized (PRO) FMCW, this formulation relies on the same strategy as (1.16) and (1.17), with two important differences. First, because a constant amplitude is desired to simplify transmitter requirements and mitigate SNR loss, $w(t)$ in (1.16) is now a rectangular window of length T, which corresponds to the length of each waveform segment. Second, each segment is initialized with a new randomly generated FM waveform (generally not chirp-like) that, via iterative application of (1.16) and (1.17), is imbued with the desired spectrum shape (Gaussian is still used). The mth optimized waveform segment is then phase rotated as

$$s_m(t) = \exp\left(j\phi_{\text{end},m-1}\right)p_{K,m}(t) \tag{1.19}$$

where $\phi_{\text{end},m-1}$ is the ending phase value for the $(m-1)$th segment, to avoid phase discontinuities. As such, each segment is optimized to provide low autocorrelation range sidelobes, yet does not repeat, thereby avoiding range ambiguities via low crosscorrelation with other segments. The varying structure also prevents sidelobes from combining coherently when performing subsequent Doppler processing across the segments on receive.

As an example, consider a bandwidth of $B = 80$ MHz and a total length of 200 ms comprised of 10^4 segments of 20 μs each. Thus, each segment has $BT = 1{,}600$ and the total processing gain is 1.6×10^7, or 72 dB. Each segment was optimized for $K = 500$ iterations, with the initialization a random sequence of 1,600 phase values drawn from a uniform distribution on $[-\pi, \pi]$ and subsequently implemented using the PCFM framework of [26].

Figure 1.25 depicts the RMS average autocorrelation responses for the initialization and optimized measurements across the 10^4 segments. On average, the PSL per segment is improved by 10 dB by using the spectral shaping approach. In contrast, the RMS average crosscorrelation between adjacent segments increases by 1.5 dB (see Figure 1.26) for the optimized measurement relative to the initialization. This result is to be expected since the optimization imposes greater

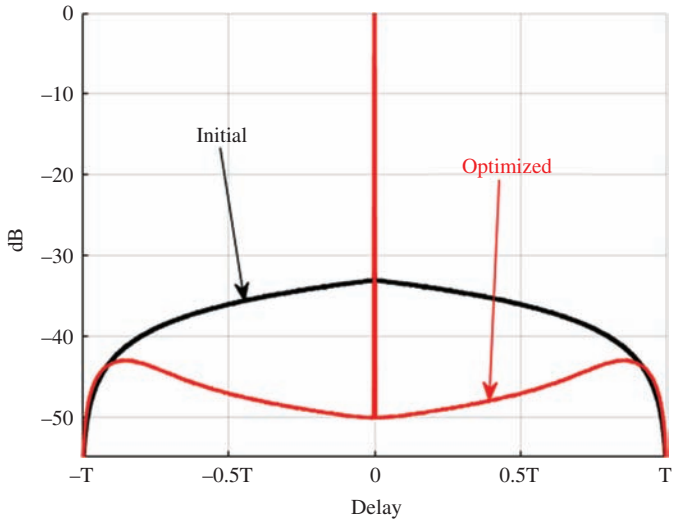

Figure 1.25 RMS average autocorrelation responses for initialization and measurement of optimized (©2015 IEEE, reprinted with permission from [37])

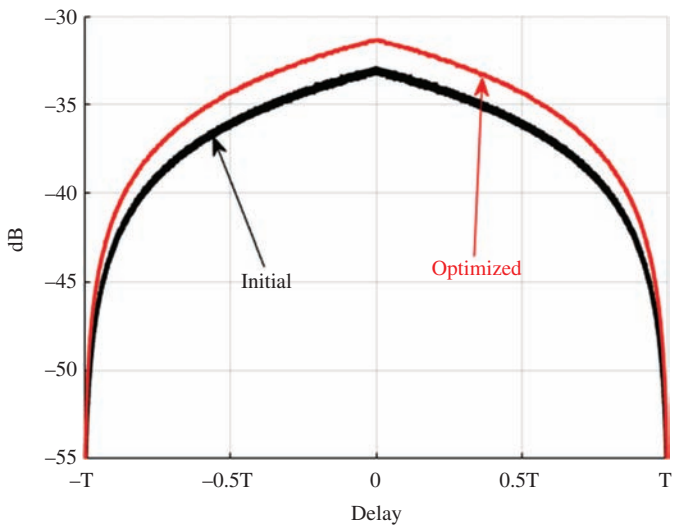

Figure 1.26 RMS average crosscorrelation response for adjacent segments using initialization and measurement of optimized (©2015 IEEE, reprinted with permission from [37])

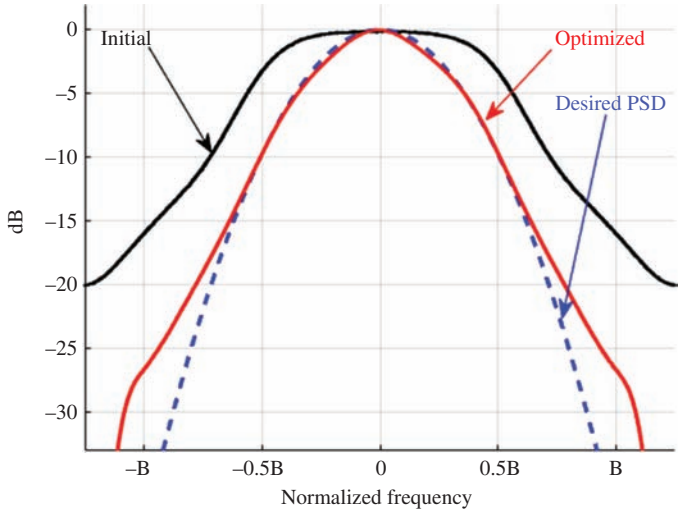

Figure 1.27 Spectral content for initialization, desired PSD and measurement of optimized (©2015 IEEE, reprinted with permission from [37])

spectral containment and thus naturally introduces somewhat greater similarity between different optimized segments (Figure 1.27).

In Figure 1.27, the desired PSD is again a Gaussian spectrum. The alternating projection optimization procedure is found to attain this desired PSD fairly well given the initial random FM waveform segments (that possess a greater bandwidth due to being unconstrained). Note that at the edges (just beyond $\pm$B) the measured optimized spectral response is truncated by the 160 MHz analysis bandwidth of the spectrum analyzer.

When Doppler processing is performed over the set of 10^4 segments, the range sidelobes do not combine coherently since the PRO-FMCW waveform does not repeat. Figure 1.28 illustrates the resulting zero-Doppler integrated autocorrelation response where it is observed that nearly 40 dB improvement is achieved relative to the RMS average autocorrelation. A similar improvement is observed is Figure 1.29 for the zero-Doppler integrated crosscorrelation response between adjacent segments. In [37], it is shown how this emission scheme provides the means to detect moving targets more than 75 dB below the dominant scattering in free-space measurements.

1.4.3 Hopped spectral gaps

Given the relationship between the PSD of a waveform and the sidelobe level in the associated autocorrelation, one can draw the logical conclusion that the introduction of spectral gaps into the PSD will generally result in an increased sidelobe level for an otherwise optimized waveform (e.g., [54–56]). In [57],

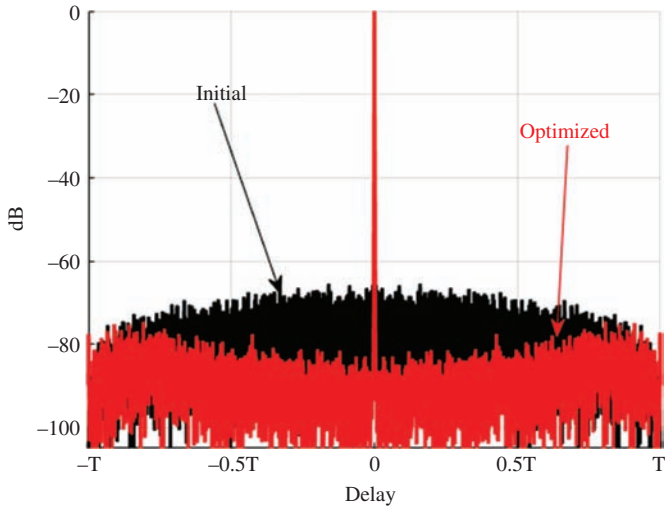

Figure 1.28 Integrated autocorrelation response of PRO-FMCW emissions (©2015 IEEE, reprinted with permission from [37])

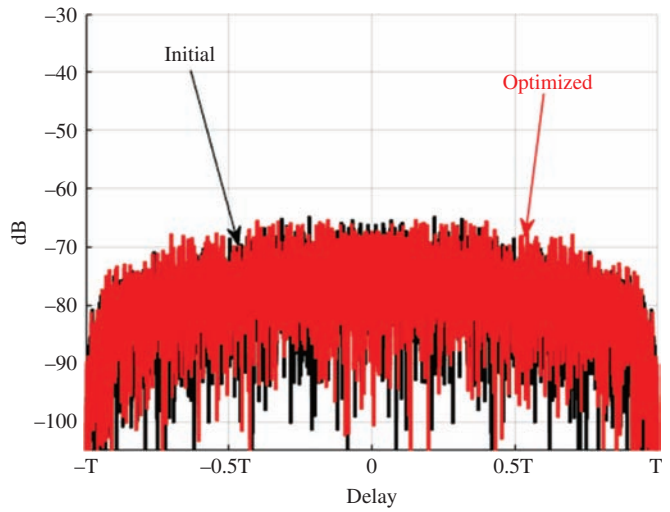

Figure 1.29 Integrated crosscorrelation response of PRO-FMCW segments (©2015 IEEE, reprinted with permission from [37])

the PRO-FMCW waveform [37] described above is modified to provide for gaps in the emitted spectrum to avoid other spectrum users or potentially to enable embedding of another RF function such as communications or navigation.

Figure 1.30 illustrates the mean PSD realized for cases involving 1 and 2 spectrum gaps that are stationary over the total waveform length of 200 ms

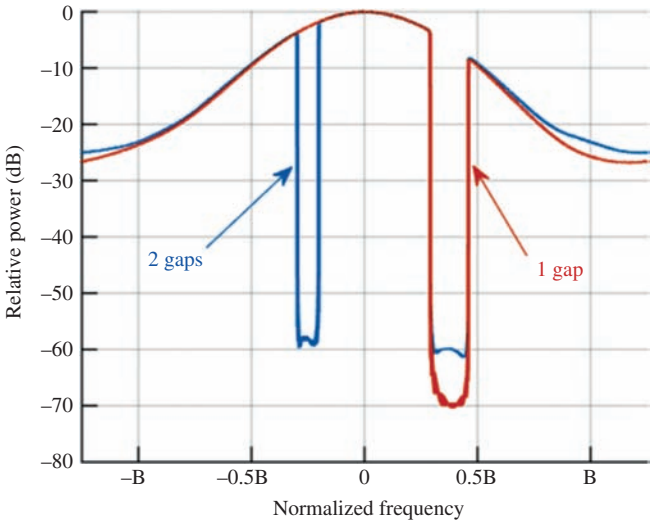

Figure 1.30 Mean PSD for 1 spectral gap and 2 spectral gap cases (©2015 IEEE, reprinted with permission from [57])

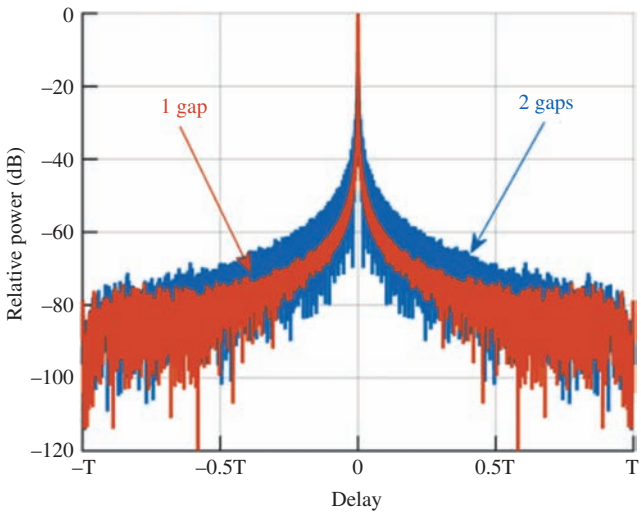

Figure 1.31 Doppler integrated autocorrelation responses for 1 gap and 2 gap cases (©2015 IEEE, reprinted with permission from [57])

(same bandwidth $B = 80$ MHz and 10^4 segments as used in the previous section). The simulation results in Figure 1.31 clearly show how the associated range sidelobe responses (zero-Doppler integrated over the 10^4 segments) have degraded relative to the previous measured result from Figure 1.28 due to the introduction of these stationary spectral gaps.

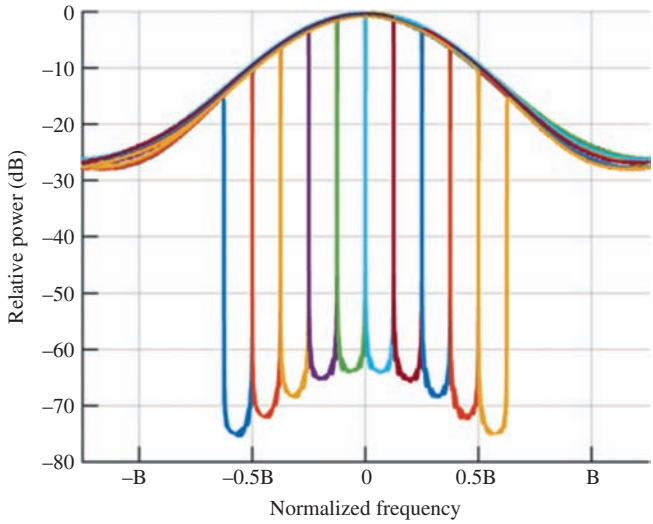

Figure 1.32 Mean PSDs for each of 10 sequentially hopped spectral gaps (©2015 IEEE, reprinted with permission from [57])

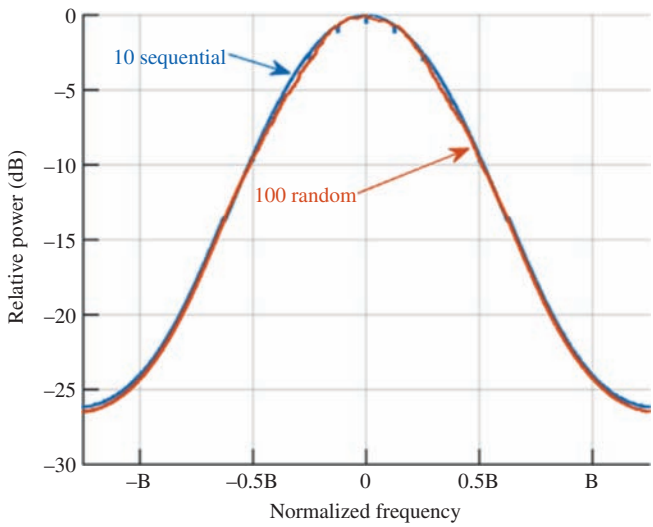

Figure 1.33 Overall mean PSD for sequential and random hopped spectral gaps (©2015 IEEE, reprinted with permission from [57])

However, if the spectral gaps are hopped during the CPI, their deleterious impact on the PSD is significantly reduced. Figure 1.32 shows the mean PSD for each of 10 different spectral gaps that occur sequentially during the 200 ms interval. Overall, this hopping produces the PSD in Figure 1.33 in which the impact of any

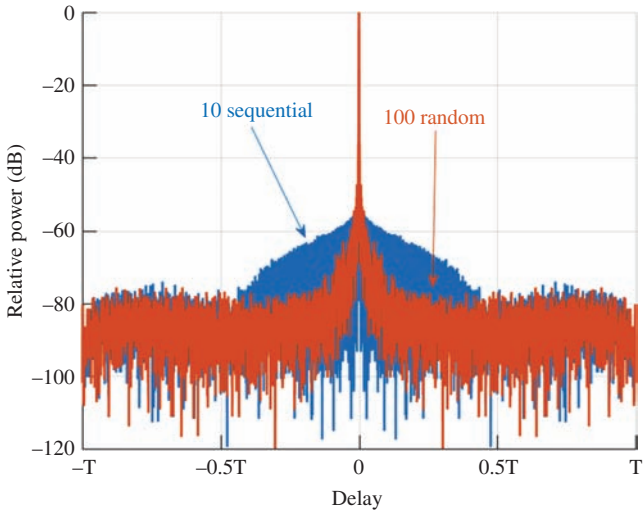

Figure 1.34 Doppler integrated autocorrelation responses for sequential and random hopping gaps (©2015 IEEE, reprinted with permission from [57])

single spectral gaps has been virtually eliminated, thus producing the improved Doppler integrated autocorrelation in Figure 1.34.

Further, when 100 spectral gaps are randomly hopped over the same time interval, the smoother overall PSD in Figure 1.33 is achieved which realizes the associated Doppler integrated autocorrelation in Figure 1.34 that is approaching the same performance as when no gaps are present at all. Ongoing work is investigating how to implement these hopped spectral gaps when transmitter distortion induces spectral regrowth effects.

1.5 Conclusions

Within the context of waveform diversity, radar spectrum engineering can be posed as a spectral containment (or spectral shaping) optimization problem. To be meaningful, however, this framework must account for the transmitter induced distortion that may be mathematically modelled or measured using actual hardware so that the ultimate physical emission yields the desired sensing performance while also maintaining the required spectral containment/avoidance. Ongoing work is exploring different approaches to optimize physical emissions and to develop a formulation for the joint optimization of the waveform and transmitter.

References

[1] N. Levanon and E. Mozeson, *Radar Signals*, John Wiley & Sons, Inc., Hoboken, NJ, 2004.

[2] H.D. Griffiths, S. Blunt, L. Cohen, and L. Savy, 'Challenge problems in spectrum engineering and waveform diversity,' *IEEE Radar Conf.*, Ottawa, Canada, 29 Apr. 3 to May 2013.

[3] H.D. Griffiths, L. Cohen, S. Watts, E. Mokole, C. Baker, M. Wicks, and S. Blunt, 'Radar spectrum engineering and management: technical and regulatory issues,' *Proc. IEEE*, vol. 103, no. 1, pp. 85–102, 2015.

[4] E. Fowle, 'The design of FM pulse compression signals,' *IEEE Trans. Inf. Theory*, vol. 10, no. 1, pp. 61–67, 1964.

[5] C.E. Cook, 'A class of nonlinear FM pulse compression signals,' *Proc. IEEE*, vol. 52, no. 11, pp. 1369–1371, 1964.

[6] R. De Buda, 'Stationary phase approximations of FM spectra,' *IEEE Trans. Inf. Theory*, vol. 12, no. July (3), pp. 305–311, 1966.

[7] T. Collins and P. Atkins, 'Nonlinear frequency modulation chirps for active sonar,' *IEE Proc. Radar, Sonar Navigation*, vol. 146, no. Dec. (6), pp. 312–316, 1999.

[8] J.J. Kroszczynski, 'Pulse compression by means of linear-period modulation,' *Proc. IEEE*, vol. 57, no. 7, pp. 1260–1266, 1969.

[9] A.W. Doerry, 'Generating nonlinear FM chirp waveforms for radar,' Sandia Report, SAND2006-5856, Sept. 2006.

[10] I. Gladkova, 'Design of frequency modulated waveforms via the Zak transform,' *IEEE Trans. Aerosp. Electr. Syst.*, vol. 40, no. 1, pp. 355–359, 2004.

[11] J.M. Kurdzo, B.L. Cheong, R.D. Palmer, and G. Zhang, 'Optimized NLFM pulse compression waveforms for high-sensitivity radar observations,' *SEE Intl. Radar Conf.*, Lille, France, 13–17 Oct. 2014.

[12] J.A. Johnston and A.C. Fairhead, 'Waveform design and Doppler sensitivity analysis for nonlinear FM chirp pulses,' *IEE Proc. F—Commun. Radar Signal Proc.*, vol. 133, no. Apr. (2), pp. 163–175, 1986.

[13] E. De Witte and H.D. Griffiths, 'Improved ultra-low range sidelobe pulse compression waveform design,' *Electron. Lett.*, vol. 40, no. Oct. (22), pp. 1448–1450, 2004.

[14] R.H. Barker, 'Group synchronization of binary digital systems,' *Communication Theory*, Academic Press, London, pp. 273–287, 1953.

[15] B.L. Lewis and F.F. Kretschmer, 'A new class of polyphase pulse compression codes and techniques,' *IEEE Trans. Aerosp. Electr. Syst.*, vol. AES-17, no. May (3), pp. 364–372, 1981.

[16] B.L. Lewis and F.F. Kretschmer, 'Linear frequency modulation derived polyphase pulse compression codes,' *IEEE Trans. Aerosp. Electr. Syst.*, vol. AES-18, no. Sept. (5), pp. 637–641, 1982.

[17] G. Coxson and J. Russo, 'Efficient exhaustive search for optimal-peak-sidelobe binary codes,' *IEEE Trans. Aerosp. Electr. Syst.*, vol. 41, no. 1, pp. 302–308, 2005.

[18] J.D. Jenshak and J.M. Stiles, 'A fast method for designing optimal transmit codes for radar,' *IEEE Radar Conf.*, Rome, Italy, May 2008.
[19] C.J. Nunn and G.E. Coxson, 'Polyphase pulse compression codes with optimal peak and integrated sidelobes,' *IEEE Trans. Aerosp. Electr. Syst.,* vol. 45, no. Apr. (2), pp. 775–781, 2009.
[20] H. Faust, B. Connolly, T.M. Firestone, R.C. Chen, B.H. Cantrell, and E.L. Mokole, 'A spectrally clean transmitting system for solid state phased-array radars,' *IEEE Radar Conf.*, Philadelphia, PA, pp. 140–144, Apr. 2004.
[21] J.W. Taylor and H.J. Blinchikoff, 'Quadriphase code – a radar pulse compression signal with unique characteristics,' *IEEE Trans. Aerosp. Electr. Syst.,* vol. 24, no. Mar. (2), pp. 156–170, 1988.
[22] R. Chen and B. Cantrell, 'Highly bandlimited radar signals,' *IEEE Radar Conf.*, Long Beach, CA, pp. 220–226, Apr. 2002.
[23] H. Chiriex, 'High power outphasing modulation,' *Proc. IRE*, pp. 1370–1392, Nov. 1935.
[24] F.H. Raab, P. Asbeck, S. Cripps, *et al.*, 'Power amplifiers and transmitters for RF and microwave,' *IEEE Trans. Microwave Theory Tech.*, vol. 50, no. 3, pp. 814–826, 2002.
[25] S. Blunt, M. Cook, E. Perrins, and J. de Graaf, 'CPM-based radar waveforms for efficiently bandlimiting a transmitted spectrum,' *IEEE Radar Conf.*, Pasadena, CA, May 2009.
[26] S.D. Blunt, M. Cook, J. Jakabosky, J. de Graaf, and E. Perrins, 'Polyphase-coded FM (PCFM) waveforms, part I: implementation,' *IEEE Trans. Aerosp. Electr. Syst.*, vol. 50, no. July (3), pp. 2218–2229, 2014.
[27] J.B. Anderson, T. Aulin, and C.-E. Sundberg, *Digital Phase Modulation*, Plenum Press, New York, NY, 1986.
[28] IRIG Standard 106-00: Telemetry Standards, Range Commanders Council Telemetry Group, Range Commanders Council, White Sands Missile Range, New Mexico.
[29] E. Perrins and M. Rice, 'Reduced complexity detectors for multi-h CPM in aeronautical telemetry,' *IEEE Trans. Aerosp. Electr. Syst.*, vol. 43, no. 1, pp. 286–300, 2007.
[30] *Bandwidth-Efficient Modulations: Summary of Definitions, Implementation, and Performance*, Report Concerning Space Data System Standards, Informational Report CCSDS 413.0-G-2.
[31] Specifications of the Bluetooth System, *Bluetooth Special Interest Group, ver*. 1.2, Nov. 2003.
[32] J. Jakabosky, P. Anglin, M.R. Cook, S.D. Blunt, and J. Stiles, 'Non-linear FM waveform design using marginal Fisher's information within the CPM framework,' *IEEE Radar Conf.*, pp. 513–518, Kansas City, MO, May 2011.
[33] S.D. Blunt, J. Jakabosky, M. Cook, J. Stiles, S. Seguin, and E.L. Mokole, 'Polyphase-coded FM (PCFM) waveforms, part II: optimization,' *IEEE Trans. Aerosp. Electr. Syst.*, vol. 50, no. July (3), pp. 2230–2241, 2014.

[34] J. Jakabosky, S.D. Blunt, M.R. Cook, J. Stiles, and S.A. Seguin, 'Transmitter-in-the-loop optimization of physical radar emissions,' *IEEE Radar Conf.*, pp. 874–879, Atlanta, GA, May 2012.

[35] L. Ryan, J. Jakabosky, S.D. Blunt, C. Allen, L. Cohen, 'Optimizing polyphase-coded FM waveforms within a LINC transmit architecture,' *IEEE Radar Conf.*, Cincinnati, OH, pp. 835–839, 19–23 May 2014.

[36] J. Jakabosky, S.D. Blunt, and T. Higgins, 'Ultra-low sidelobe waveform design via spectral shaping and LINC transmit architecture,' *IEEE Intl. Radar Conf.*, Arlington, VA, 11–15 May 2015.

[37] J. Jakabosky, S.D. Blunt, and B. Himed, 'Waveform design and receive processing for nonrecurrent nonlinear FMCW radar,' *IEEE Intl. Radar Conf.*, Arlington, VA, 11–15 May 2015.

[38] W. Roberts, H. He, J. Li, and P. Stoica, 'Probing waveform synthesis and receiver filter design,' *IEEE Signal Proc. Mag.*, vol. 27, no. July (4), pp. 99–112, 2010.

[39] C. Baylis, L. Wang, M. Moldovan, *et al*., 'Designing transmitters for spectral conformity: power amplifier design issues and strategies,' *IET Radar, Sonar Navigation*, vol. 5, no. 6, pp. 681–685, 2011.

[40] A.M. Klein and M.T. Fujita, 'Detection performance of hard-limited phase-coded signals,' *IEEE Trans. Aerosp. Electr. Syst.*, vol. AES-15, no. Nov. (6), pp. 795–802, 1979.

[41] J. Jakabosky, L. Ryan, and S.D. Blunt, 'Transmitter-in-the-loop optimization of distorted OFDM radar emissions,' *IEEE Radar Conference*, Ottawa, Canada, 29 Apr.–3 May, 2013.

[42] C. Blum and A. Roli, 'Metaheuristics in combinatorial optimization: overview and conception comparison,' *ACM Comp. Surv.*, vol. 35, no. Sept. (3), pp. 268–308, 2003.

[43] E. Costa, M. Midrio, S. Pupolin, 'Impact of amplifier nonlinearities on OFDM transmission system performance,' *IEEE Commun. Lett.*, vol. 3, no. 2, pp. 37–39, 1999.

[44] F.M. Ghannouchi and O. Hammi, 'Behavioral modeling and predistortion,' *IEEE Microw. Mag.*, vol. 10, no. Dec. (7), pp. 52–64, 2009.

[45] J. Jakabosky, S.D. Blunt, B. Himed, 'Optimization of 'over-coded' radar waveforms,' *IEEE Radar Conf.*, Cincinnati, OH, pp.1460–1465, 19–23 May 2014.

[46] S.D. Blunt, P. McCormick, T. Higgins, and M. Rangaswamy, 'Physical emission of spatially-modulated radar,' *IET Radar Sonar Navigation*, vol. 8, no. 12, pp. 1234–1246, 2014.

[47] P. McCormick, J. Jakabosky, S.D. Blunt, C. Allen, and B. Himed, 'Joint polarization/waveform design and adaptive receive processing,' *IEEE Intl. Radar Conf.*, Arlington, VA, 11–15 May 2015.

[48] P.S. Tan, J. Jakabosky, J.M. Stiles, and S.D. Blunt, 'On higher-order representations of polyphase-coded FM radar waveforms,' *IEEE Intl. Radar Conf.*, Arlington, VA, 11–15 May 2015.

[49] D. Henke, P. McCormick, S.D. Blunt, and T. Higgins, 'Practical aspects of optimal mismatch filtering and adaptive pulse compression for FM waveforms,' *IEEE Intl. Radar Conf*., Arlington, VA, 11–15 May 2015.

[50] W.W.L. Au and S.W. Martin, 'Why dolphin biosonar performs so well in spite of mediocre 'equipment',' *IET Radar Sonar Navigation*, vol. 6, no. 6, pp. 566–575, 2012.

[51] X. Zhang, L.E. Larson, P.M. Asbeck, and R.A. Langridge, 'Analysis of power recycling techniques for RF and microwave outphasing power amplifiers,' *IEEE Trans. Circuits & Systems II: Analog and Digital Signal Processing*, vol. 49, no. 5, pp. 312–320, May 2002.

[52] H.H. Bauschke and J.M. Borwein, 'On projection algorithms for solving convex feasibility problems,' *SIAM Rev.*, vol. 38, no. Sept. (3), pp. 367–426, 1996.

[53] S.R.J. Axelsson, 'Noise radar using random phase and frequency modulation,' *IEEE Trans. Geosci. Remote Sens.*, vol. 42, no. 11, pp. 2370–2384, 2004.

[54] M.R. Cook, T. Higgins, and A.K. Shackelford, 'Thinned spectrum radar waveforms,' *Intl. Waveform Divers. Des. Conf.*, pp. 238–243, Niagara Falls, Canada, 8–13 Aug. 2010.

[55] K. Gerlach, M.R. Frey, M.J. Steiner, and A. Shackelford, 'Spectral nulling on transmit via nonlinear FM radar waveforms,' *IEEE Trans. Aerosp. Electr. Syst.,* vol. 47, no. Apr. (2), pp. 1507–1515, 2011.

[56] L.K. Patton, C.A. Bryant, and B. Himed, 'Radar-centric design of waveforms with disjoint spectral support,' IEEE Radar Conf., Atlanta, GA, pp. 269–274, 7–11 May 2012.

[57] J. Jakabosky, S.D. Blunt, and A. Martone, 'Incorporating hopped spectral gaps into nonrecurrent nonlinear FMCW radar emission,' *IEEE Intl. Workshop on Computational Advances in Multi-Sensor Adaptive Processing*, Cancun, Mexico, 13–16 Dec. 2015.

This page intentionally left blank

Chapter 2

Adaptive OFDM waveform design for spatio-temporal-sparsity exploited STAP radar

Satyabrata Sen[1]

Abstract

In this chapter, we describe a sparsity-based space–time adaptive processing (STAP) algorithm to detect a slowly moving target using an orthogonal frequency division multiplexing (OFDM) radar. The motivation of employing an OFDM signal is that it improves the target-detectability from the interfering signals by increasing the frequency diversity of the system. However, due to the addition of one extra dimension in terms of frequency, the adaptive degrees-of-freedom in an OFDM-STAP also increases. Therefore, to avoid the construction a fully adaptive OFDM-STAP, we develop a sparsity-based STAP algorithm. We observe that the interference spectrum is inherently sparse in the spatio-temporal domain, as the clutter responses occupy only a diagonal ridge on the spatio-temporal plane and the jammer signals interfere only from a few spatial directions. Hence, we exploit that sparsity to develop an efficient STAP technique that utilizes considerably lesser number of secondary data compared to the other existing STAP techniques, and produces nearly optimum STAP performance. In addition to designing the STAP filter, we optimally design the transmit OFDM signals by maximizing the output signal-to-interference-plus-noise ratio (SINR) in order to improve the STAP performance. The computation of output SINR depends on the estimated value of the interference covariance matrix, which we obtain by applying the sparse recovery algorithm. Therefore, we analytically assess the effects of the synthesized OFDM coefficients on the sparse recovery of the interference covariance matrix by computing the coherence measure of the sparse measurement matrix. Our numerical examples demonstrate the achieved STAP-performance due to sparsity-based technique and adaptive waveform design.

[1]Center for Engineering Science Advanced Research, Computational Sciences and Engineering Division, Oak Ridge National Laboratory, USA

2.1 Introduction

The problem of detecting slowly moving targets using airborne radars, particularly in the presence of background clutter and hostile electronic countermeasures or jamming, has led to the development of the space–time adaptive processing (STAP) algorithms in the radar community. Since the publication of a seminal paper by Brennan and Reed [1], the STAP techniques have been extensively researched and well documented in the literature over the last few decades [2–6]; interested readers may refer to [7–9] and references therein for a comprehensive survey of different STAP methodologies.

Conventionally, STAP involves the design of a two-dimensional spatio-temporal filter in order to cancel out the interference effects from the measurements of the primary range gate [also commonly known as the cell-under-test (CUT)] that contains a target. Assuming that the secondary range gates adjacent to the CUT are target free and have the same statistical characteristics of the interference returns as in the CUT [2], they are used to estimate the interference covariance matrix required for the computation of the STAP filter weights. The estimation accuracy of the interference covariance matrix, and consequently the effectiveness of the STAP filter, depends on a number of homogeneous secondary measurements used (given by the Reed-Mallett-Brennan (RMB) rule) [10]. Unfortunately, in a fully adaptive STAP, the number of required secondary measurements is so large that they do not satisfy the essential homogeneity property due to the intrinsic non-stationarity of the interference statistics.

To overcome such practical limitations of a fully adaptive STAP, several partially adaptive STAP algorithms are proposed. Popular among them are various rank-reduction techniques that assume the dominant interferences to be confined within a low-dimensional subspace. In general, these methods transform the STAP filtering process from its original high-dimensional space to a lower dimensional subspace, for example, by applying eigen-decomposition on the interference covariance matrix [11–13]. The data-dependent rank-reduction algorithms, such as the principal components [14,15], relative importance of eigenbeam [6, Ch. 5], cross-spectral metric [16], parametric adaptive matched filter [17,18] and multistage Wiener filter [19], are shown in [20] to provide improved STAP performance at the expense of higher computational cost when compared with the data-independent methods, such as the joint-domain localization [9,21].

While the radar community continued the development of various partially adaptive STAP methods (and also recently knowledge-aided or knowledge-based STAP techniques [22–27]), the research efforts have been primarily biased toward the improvement of receiver signal processing algorithms, which can intelligently utilize the secondary measurements to estimate the interference covariance matrix required for the computation of the STAP filter weights. However, the measurements collected at the receiver are mere representations of the interactions of the transmitted signal with the operational scenarios. Therefore, if the transmit signal is kept fixed (non-adaptive), then depending on the variabilities in the environmental

conditions, the STAP performance may heavily deteriorate. This is why we propose to operate the transmitter and receiver of a STAP radar in a closed-loop fashion via an adaptive waveform design module.

With the recent technological advancements in the fields of flexible waveform generators and high-speed signal processing hardware, it is now possible to generate and transmit sophisticated radar waveforms that are dynamically adapted to the sensing environments on a periodic basis (potentially on a pulse-by-pulse basis) [28–32]. This dynamic transmit-signal adaptation becomes possible due to the proper utilizations of relevant information fed back by the receiver regarding the target and interference characteristics. Consequently, the radar systems can potentially achieve a significant performance gain by appropriately reciprocating to any changes in the target and interference responses, particularly in the defence applications involving fast-changing scenarios.

Now, to obtain the full benefits of the adaptive waveform design techniques, it is necessary for us to employ such a waveform whose parameters can be easily modified in accordance to the system objectives. To fulfil this goal, in this work, we use an orthogonal frequency division multiplexing (OFDM) radar signal [33–36] to detect a target using a STAP technique; see also [37,38]. The motivation of employing an OFDM signal is that it offers a very efficient way to optimally tailor its spectrum as each of the designed OFDM coefficients determines the transmit energy at a particular subchannel. Therefore, depending on the frequency variabilities of the target and interference responses, we adaptively synthesize the OFDM spectral parameters in order to improve the system performance. In addition, the OFDM signalling technique increases the frequency diversity of the system by providing additional information about the target, as different scattering centres resonate at different frequencies [39,40], and thus improves the target-detectability from the interfering signals.

However, due to the addition of one extra dimension in terms of frequency, the use of an OFDM signal for the STAP applications also causes one disadvantage by increasing the adaptive degrees of freedom from MN to LMN, where M denotes the number of antenna-array elements, N is the pulse repetition periods and L is the number of OFDM subcarriers. Thereby, the construction of a fully adaptive OFDM-STAP becomes practically impossible because of the requirement of a larger number of homogeneous secondary data and the computational burden of a bigger matrix inversion [1,10]. To circumvent these challenges, we propose a sparsity-based STAP algorithm. We observe that the target and interference spectra are inherently sparse in the spatio-temporal domain, as the clutter responses occupy only a diagonal ridge on the spatio-temporal plane and the jammer signals interfere only from a few spatial directions. Hence, we exploit that sparsity to develop an efficient OFDM-STAP technique requires considerably lesser number of secondary data compared to the other existing STAP techniques and produces a near-optimum STAP performance. Similar spatio-temporal sparsity-exploited STAP techniques, but without the OFDM signalling scheme, are lately proposed in [41–54]. It is also to be noted here that an OFDM-STAP filter operates on the received data as a

whole, in contrast to the subband STAP approach which partitions the data among different subchannels by assuming frequency independence [55,56].

We first develop a sparsity-based STAP technique by formulating a realistic sparse-measurement model for OFDM radar that accounts for measurements over multiple frequencies. Though both the spatial and temporal frequencies are continuously varying parameters, the superiority of sparse signal processing can still be availed by *just discretizing* the spatio-temporal plane into a finite number of spatio-temporal frequency grids [57]. Then, the sparse nature of the target and interference spectra on this spatio-temporal grid structure is exploited by the standard sparse-recovery techniques to produce an estimate of the clutter covariance matrix. In particular, to design the STAP filter, we use the secondary range gate data and estimate the interference-only covariance matrix in two steps: (i) apply the LASSO estimator [58] as a sparse-recovery technique to obtain the clutter response from the secondary measurements and (ii) premultiply the sparsely recovered clutter responses with the known sparse-measurement matrix to compute the clutter covariance matrix. One additional benefit of this approach is that the estimated clutter support provides the necessary information to form a masking matrix [44], which is used in the sparse-recovery of target response from the primary gate measurements, and thus, we can avoid the explicit estimation and inversion of the interference covariance matrix.

In addition to designing the STAP filter, we propose to optimally design the transmit OFDM signals by maximizing the output signal-to-interference-plus-noise ratio (SINR) in order to improve the STAP performance. However, in practical scenarios, the computation of output SINR depends on the estimated value of the interference covariance matrix, which we obtain by applying the sparse recovery algorithm. Obtaining good estimates of the interference covariance matrix heavily influence the achievable improvement of output SINR via adaptive waveform design. Therefore, we investigate the effects of different choices of the transmit signal parameters on the accuracy of sparse recovery technique by computing the coherence measure [59–61] of the sparse-measurement matrix. Subsequently, we provide a closed-form expression of the optimal OFDM coefficients by reasonably considering that the estimation accuracy of the interference covariance matrix insignificantly depends on the signal parameters.

We present several numerical examples to demonstrate the OFDM-STAP performance obtained by employing spatio-temporal sparsity framework, and the achieved performance gain due to adaptive OFDM waveform design. We analyze the performance in terms of the SINR-loss measure and the receiver operating characteristics (ROCs) and make comparative characterizations with respect to the ideal STAP technique which has the full knowledge about the target and interference characteristics. Our analyses include both the idealistic and non-idealistic [including the presence of temporal decorrelation effects caused by the intrinsic clutter motion (ICM) [6, Ch. 4, 62]] STAP scenarios with a Doppler-unambiguous clutter characteristic. The scattering coefficients of the target are also varied to construct two scenarios having different target-energy distributions across different subchannels. We show that the spatio-temporal sparsity-based OFDM-STAP

approach yields near-optimum performances by utilizing a substantially small number of secondary measurements. For example, in the ideal scenario, only two to five secondary data are found to be enough to produce a near-optimum performance. In the presence of temporal decorrelation, although we get a wider mainbeam clutter notch, the near-optimum SINR-loss performance is still attained by using only two to five secondary measurements. A significant amount of improvement in performance due to the use of adaptive OFDM waveform is demonstrated by computing the ROCs for two different target responses. For example, in the presence and absence of temporal decorrelation effects, we respectively observe approximately 3 and 6 dB of improvement in detection performance.

The rest of the chapter is organized as follows. In Section 2.2, we first develop a parametric sparse-measurement model for OFDM-STAP radar. Then, in Section 2.3, we describe a sparse recovery technique to estimate the interference covariance matrix and to design the STAP filter weights. An adaptive OFDM waveform design algorithm is proposed in Section 2.4. We discuss the numerical results in Section 2.5. Conclusions and possible future work are given in Section 2.6.

2.1.1 Notations

We present here some notational conventions that are used throughout this chapter. We use math italic (a) for scalars, lowercase bold ($\boldsymbol{a}$) for vectors and uppercase bold ($\boldsymbol{A}$) for matrices. For a matrix $\boldsymbol{A} \in \mathbb{C}^{k\times m}$, $\boldsymbol{A}^T$, $\boldsymbol{A}^H$ and $\mathrm{tr}\{\boldsymbol{A}\}$ denote the transpose, conjugate transpose and trace of $\boldsymbol{A}$, respectively. $\boldsymbol{I}_k$ represents an identity matrix of dimension k. $\mathrm{blkdiag}(\cdots)$ forms a block-diagonal matrix with nonzero submatrices only on the main diagonal. $\mathrm{Re}\{\cdot\}$ is the real part and $|\cdot|$ is the magnitude of a complex quantity. Among different types of vector norms, we consider the ℓ_1 and ℓ_2 norms, expressed as $\|\cdot\|_1$ and $\|\cdot\|_2$, respectively. In addition, $\langle , \rangle$, $\otimes$ and $\odot$ are the inner product, Kronecker product and point-wise Hadamard product operators, respectively. For a random variable a, $E(a)$ and $\mathrm{var}(a)$, respectively, denote the mean and variance of a.

2.2 Sparse-measurement model

Figure 2.1 presents a schematic representation of the problem scenario. We consider a radar system residing on an airborne platform [5, Ch. 2], and having an M-element uniformly spaced linear array (ULA) antenna with interelement spacing d. Without loss of generality, we assume that the array elements are identical and have omnidirectional radiation patterns. The axis of the ULA is oriented along the direction of the platform movement (this is commonly known as the sidelooking array configuration). The platform is flying at a fixed height H and with a constant velocity $\boldsymbol{v}_R$ along the y-direction. The chosen coordinate system is also depicted in Figure 2.1. We define the x-direction as the zero azimuth (i.e., $\psi = 0^\circ$) and the xy-plane as the zero elevation (i.e., $\psi = 0^\circ$). Therefore, a unit vector $\boldsymbol{k}$ pointing toward a patch on the ground at the (ψ, θ) direction can be expressed as

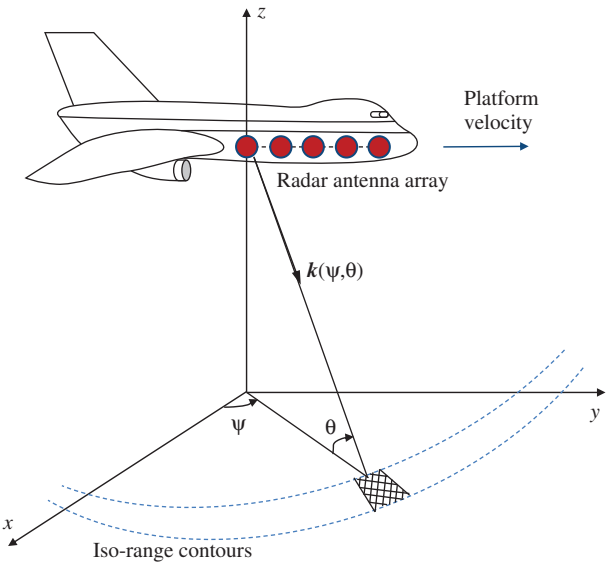

Figure 2.1 A schematic representation of the problem scenario

$\boldsymbol{k}(\psi,\theta) = \cos\psi\cos\theta\hat{\boldsymbol{x}} + \sin\psi\cos\theta\hat{\boldsymbol{y}} + \sin\theta\hat{\boldsymbol{z}}$, where $\hat{\boldsymbol{x}}$, $\hat{\boldsymbol{y}}$ and $\hat{\boldsymbol{z}}$ are the unit vectors of the Cartesian coordinate system.

In the following, we first describe the OFDM signal model and then develop a sparse-measurement model for a target located at a specific range gate and direction. We also discuss in detail the effects of the interfering signals (clutter and thermal noise) on the received signal.

2.2.1 OFDM signal model

We consider a wideband OFDM signalling system with L active subcarriers, a bandwidth of B Hz, and a pulse duration of T_p seconds. Let $\boldsymbol{a} = [a_0, a_1, \ldots, a_{L-1}]^T$ represent the complex weights transmitted over the L subcarriers and satisfy $\sum_{l=0}^{L-1} |a_l|^2 = 1$. Then, the complex envelope of the transmitted signal can be represented as follows:

$$s(t) = \sum_{l=0}^{L-1} a_l e^{j2\pi l\Delta f t}, \quad \text{for } 0 \le t \le T_p \tag{2.1}$$

where the subcarrier spacing is $\Delta f = B/(L+1) = 1/T_p$. Denoting f_c to be the carrier frequency, a coherent burst of N transmitted OFDM pulses [in a particular coherent processing interval (CPI)] is given by

$$\tilde{s}(t) = 2\,\mathrm{Re}\left\{\sum_{n=0}^{N-1} s(t-nT)\, e^{j2\pi f_c t}\right\} \tag{2.2}$$

where T is the pulse repetition interval (PRI). We point out here that, during the adaptive waveform design, we choose the spectral parameters of the OFDM waveform, a_l, in order to improve the STAP performance.

2.2.2 Sparse measurement model

We develop the OFDM-STAP measurement model similar to that in [2]. The only difference is that we use OFDM signalling technique, which gives rise to slightly different STAP models across different subchannels depending on the corresponding subcarrier frequencies. We consider that the target is at a far-field distance r_0 and along a direction (ψ_T, θ_T) and is moving with velocity $\boldsymbol{v}_T$. The distance r_0 corresponds to a specific range gate, denoted by a round-trip delay $\tau = 2r_0/c$, where c is the speed of propagation. We further assume that the target has multiple scattering centres that resonate variably at different transmitted frequencies.

Then, the complex envelope of the received signal at the output of the lth subchannel is expressed as follows:

$$\boldsymbol{y}(l) = \zeta_{T_l} a_l \boldsymbol{\phi}(\alpha_l, \nu_l) + \boldsymbol{e}(l) \tag{2.3}$$

where ζ_{T_l} is the target-scattering coefficient at the lth subchannel;

$$\boldsymbol{\phi}(\alpha_l, \nu_l) = \boldsymbol{f}_D(\nu_l) \otimes \boldsymbol{f}_S(\alpha_l) \tag{2.4}$$

is an $MN \times 1$ space–time steering vector at the lth subchannel with

$$\boldsymbol{f}_D(\nu_l) = \left[1, e^{j2\pi\nu_l}, \ldots, e^{j2\pi(N-1)\nu_l}\right]^T \tag{2.5}$$

$$\boldsymbol{f}_S(\alpha_l) = e^{-j2\pi f_l \tau_0} \cdot \left[1, e^{j2\pi\alpha_l}, \ldots, e^{j2\pi(M-1)\alpha_l}\right]^T \tag{2.6}$$

representing the Doppler and spatial steering vectors, respectively; and $\boldsymbol{e}(l)$ represents the interference along the lth subchannel. Here, the normalized spatial and Doppler frequencies are, respectively, defined as follows:

$$\alpha_l = f_l(1+\beta)\Delta\tau \quad \text{and} \quad \nu_l = f_l \beta T \tag{2.7}$$

where $f_l = f_c + l\Delta f$ is the lth subcarrier frequency; $(1+\beta)$ accounts for the stretching or compressing in time of the reflected signal due to the relative motion between the radar and target; $\beta = 2\langle(\boldsymbol{v}_R - \boldsymbol{v}_T), \boldsymbol{k}\rangle/c$ is the relative Doppler shift; and $\tau = \langle d\hat{y}, \boldsymbol{k}\rangle/c$ is the interelement time delay. However, note that, in most of the practical scenarios, $|\beta| \ll 1$, and therefore $1 + \beta \approx 1$.

Now, suppose instead of a specific pair of (α_l, ν_l), we consider all the possible combinations of $(\alpha_{l,i}, \nu_{l,j})$ for $i = 1, 2, \ldots, G_\alpha$ and $j = 1, 2, \ldots, G_\nu$. In other words, we discretize the spatio-temporal domain into $G = G_\alpha G_\nu$ grid points (see Figure 2.2), where G_α and G_ν are the number of grids along the spatial and temporal axes, respectively. Then, a non-zero content from any such grid point would

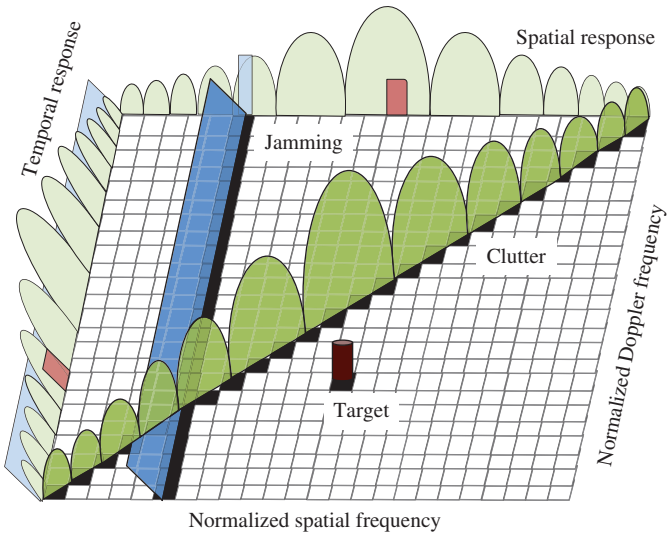

Figure 2.2 Spatio-temporal sparsity of the target and interference spectra

suggest the presence of a scatterer at that particular spatial and temporal frequencies. Hence, we can rewrite the measurement model as follows:

$$\boldsymbol{y}(l) = a_l \boldsymbol{\Phi}_l \boldsymbol{x}_{T,l} + \boldsymbol{e}(l) \tag{2.8}$$

where

- $\boldsymbol{\Phi}_l = [\boldsymbol{\phi}_l(1,1)\ \ \boldsymbol{\phi}_l(1,2)\ \ \cdots\ \ \boldsymbol{\phi}_l(G_\alpha, G_\nu)]$ is an $MN \times G$ matrix containing all the possible combinations of spatial and Doppler steering vectors (for notational simplicity, we write $\boldsymbol{\phi}(\alpha_{l,i}, \nu_{l,j})$ as $\boldsymbol{\phi}_l(i,j)$); and
- $\boldsymbol{x}_{T,l}$ is a $G \times 1$ sparse vector having only one non-zero entry corresponding to the target response at the true spatial and Doppler frequencies, i.e.,

$$x_{T,l}(i,j) = \begin{cases} \zeta_{T,l}, & \text{if } \alpha_{l,i} = \alpha_l \text{ and } \nu_{l,j} = \nu_l \\ 0, & \text{otherwise} \end{cases}$$

Then, stacking all $\boldsymbol{y}(l)$s, we get the sparse-measurement model as

$$\boldsymbol{y} = \boldsymbol{\Psi} \boldsymbol{x}_T + \boldsymbol{e} \tag{2.9}$$

where

- $\boldsymbol{y} = [\boldsymbol{y}(0)^T, \ldots, \boldsymbol{y}(L-1)^T]^T$;
- $\boldsymbol{\Psi} = \text{blkdiag}\,(a_0\boldsymbol{\Phi}_0, \ldots, a_{L-1}\boldsymbol{\Phi}_{L-1})$ is an $LMN \times LG$ sparse spatio-temporal measurement matrix;

- $\boldsymbol{x}_T = [\boldsymbol{x}_{T,0}^T, \ldots, \boldsymbol{x}_{T,L-1}^T]^T$ is an $LG \times 1$ sparse vector having only L non-zero entries that are equal to the actual target-scattering coefficients $[\zeta_{T,0}, \ldots, \zeta_{T,L-1}]^T$; and
- $\boldsymbol{e} = [\boldsymbol{e}(0)^T, \ldots, \boldsymbol{e}(L-1)^T]^T$ is the interference vector.

The interference vector $\boldsymbol{e}$ contains not only the thermal noise at the sensors but also the clutter returns. For an airborne radar, the main contribution to the clutter originates due to the ground reflections from all the azimuth directions. Though the ground has zero velocity, the ground-clutter is spread in both the angle and Doppler frequency due to the platform velocity $\boldsymbol{v}_R$. We represent the clutter returns (from a particular range gate) as a coherent summation of a large number (N_c) of clutter patches evenly distributed in azimuth angles $\psi_k, k = 1, 2, \ldots, N_c$. Then, ignoring the effects of any ambiguous range gates and noticing that the target and clutter returns are affected in a similar way by the radar transmission, we construct a sparse representation of the interference model as follows:

$$\boldsymbol{e} = \sum_{k=1}^{N_c} \boldsymbol{\Psi} \boldsymbol{x}_{C,k} + \boldsymbol{n} = \boldsymbol{\Psi} \boldsymbol{x}_C + \boldsymbol{n} \tag{2.10}$$

where

- $\boldsymbol{x}_{C,k}$ is an $LG \times 1$ sparse vector having L non-zero entries that correspond to the clutter returns from a specific azimuth angle ψ_k;
- $\boldsymbol{x}_C$ is another $LG \times 1$ sparse vector with sparsity level LN_c, and it represents the overall clutter response; and
- $\boldsymbol{n}$ is the additive thermal noise component.

The construction of this type of interference model makes it explicit here that we are dealing with the signal-dependent clutter model (i.e., transmit signal parameter $\boldsymbol{a}$ affects the interference vector $\boldsymbol{e}$ through the matrix $\boldsymbol{\Psi}$), which is a more realistic representation than to assume uncorrelated clutter returns with the transmitted signal.

2.2.3 Statistical assumptions

To complete the description of our measurement model, we assume that the target is a small manmade object for which $\boldsymbol{x}_T$ is deterministic and unknown. On the other hand, the clutter returns from a particular patch at (ψ_k, θ) can be considered to be originated from a large collection of incoherent point scatterers, and hence applying the central limit theorem, we model the clutter returns as a circularly symmetric, zero-mean complex Gaussian process with unknown covariance matrix $\boldsymbol{R}_{C,k}$. Conventionally, the clutter returns from different patches are assumed to be uncorrelated to each other. Hence, overall, the clutter covariance matrix is expressed as $\boldsymbol{R}_C = \sum_{k=1}^{N_c} \boldsymbol{R}_{C,k}$. Next, we consider that the thermal noise components among different subchannels are uncorrelated; they are also both spatially and temporally uncorrelated. So, the noise component $\boldsymbol{n}$ is represented as another

circularly symmetric, zero-mean complex Gaussian process with covariance matrix $\sigma_n^2 \boldsymbol{I}_{LMN}$. Hence, overall, the OFDM-STAP measurements are distributed as follows:

$$\boldsymbol{y} \sim \mathbb{C}\mathcal{N}(\boldsymbol{y}_T, \boldsymbol{R}_I) \tag{2.11}$$

where $\boldsymbol{y}_T = \boldsymbol{\Psi}\boldsymbol{x}_T$ and $\boldsymbol{R}_I = \sum_{k=1}^{N_c} \boldsymbol{R}_{C,k} + \sigma_n^2 \boldsymbol{I}_{LMN}$.

2.3 STAP filter design

In STAP, the received data are first processed with a linear filter having weights $\boldsymbol{w}$ to yield a scalar output:

$$z = \boldsymbol{w}^H \boldsymbol{y} \tag{2.12}$$

The primary objective of designing the STAP-filter weights $\boldsymbol{w}$ is to maximize the SINR at the filter output:

$$\text{SINR} = \frac{|E(z)|^2}{\text{var}(z)} = \frac{|\boldsymbol{w}^H \boldsymbol{y}_T|^2}{\boldsymbol{w}^H \boldsymbol{R}_I \boldsymbol{w}} \leq \boldsymbol{y}_T^H \boldsymbol{R}_I^{-1} \boldsymbol{y}_T \tag{2.13}$$

Next, z is fed to a detector that chooses one of the two possible hypotheses: the null hypothesis (target-free hypothesis) or the alternate hypothesis (target-present hypothesis), which are mathematically expressed as follows:

$$\begin{cases} \mathcal{H}_0\text{:} & \begin{cases} \boldsymbol{y}_p = \boldsymbol{e}_p \\ \boldsymbol{y}_s = \boldsymbol{e}_s,\ s = 1, 2, \ldots, N_s \end{cases} \\ \mathcal{H}_1\text{:} & \begin{cases} \boldsymbol{y}_p = \boldsymbol{y}_T + \boldsymbol{e}_p \\ \boldsymbol{y}_s = \boldsymbol{e}_s,\ s = 1, 2, \ldots, N_s \end{cases} \end{cases} \tag{2.14}$$

where subscript 'p' suggests the primary range gate measurements, subscript 's' denotes the secondary measurements, and N_s is the number of secondary range gates considered. Based on the statistical assumptions of the previous section, we know that the optimum detector compares $|z|$ with a predefined threshold [1]. The threshold is determined to achieve a specified probability of false alarm (P_{FA}) of the decision problem. Now, for a fixed value of P_{FA}, the probability of detection (P_D) of such a detector is given by [1]

$$P_D = Q\left(\sqrt{\text{SINR}}, \sqrt{-2 \ln P_{FA}}\right) \tag{2.15}$$

where $Q(\cdot, \cdot)$ is the Marcum Q-function of order 1.

Following [1,10], we know that the maximum SINR and consequently maximum value of P_D are attained when the optimal STAP-filter weight is

$$\boldsymbol{w}_{\text{opt}} \propto \boldsymbol{R}_I^{-1} \boldsymbol{y}_T \tag{2.16}$$

In practical scenarios, since the knowledge of $\boldsymbol{R}_I$ is unknown, we have to estimate it using the measurements of the secondary range gates. To efficiently estimate $\boldsymbol{R}_I$, we first employ the sparse-recovery technique to obtain the estimates of $\boldsymbol{x}_C$ and then premultiply it with the known sparse-measurement matrix $\boldsymbol{\Psi}$. We explicitly denote the secondary measurements as $\boldsymbol{y}_s = \boldsymbol{\Psi}\boldsymbol{x}_{C,s} + \boldsymbol{n}_s$, for $s = 1, 2, \ldots N_s$.

We employ a LASSO estimator [58] on these secondary measurements to obtain

$$\widehat{\boldsymbol{x}}_{C,s} = \arg\min_{\boldsymbol{x}_{C,s}} \|\boldsymbol{y}_s - \boldsymbol{\Psi}\boldsymbol{x}_{C,s}\|_2^2 + \varepsilon_C \|\boldsymbol{x}_{C,s}\|_1 \tag{2.17}$$

with $\varepsilon_C = \sigma_n^2\sqrt{c_C \ln(LG)}$ and c_C being a tuning parameter. Then, we estimate the clutter covariance matrix as follows:

$$\widehat{\boldsymbol{R}}_C = \frac{1}{N_s}\sum_{s=1}^{N_s}\left[\sum_{g\in\widehat{\mathscr{C}_s}} \left|\hat{x}_{C,s,g}\right|^2 \boldsymbol{\Psi}_g \boldsymbol{\Psi}_g^H\right] \tag{2.18}$$

where $\widehat{\mathscr{C}_s}$ is the non-zero support-set of the estimated clutter response from the sth secondary data; and $\boldsymbol{\Psi}_g$ denotes the gth column of $\boldsymbol{\Psi}$. Hence, the estimate of the overall interference covariance matrix is given by $\widehat{\boldsymbol{R}}_I = \widehat{\boldsymbol{R}}_C + \eta\boldsymbol{I}_{LMN}$, where $\eta = 10\sigma_n^2$ is chosen as 10 times the white noise level, similar to the approach of [63].

2.4 Optimal waveform design

From the discussion of the previous section, we notice that we can improve the STAP performance by maximizing the optimal SINR. Therefore, we formulate an optimization problem to design the OFDM spectral coefficients $\boldsymbol{a}$ as

$$\boldsymbol{a}_{\text{opt}} = \arg\max_{\boldsymbol{a}\in\mathbb{C}^L} \boldsymbol{y}_T^H \boldsymbol{R}_I^{-1} \boldsymbol{y}_T, \quad \text{subject to} \quad \boldsymbol{a}^H\boldsymbol{a} = 1 \tag{2.19}$$

Rewriting the expression of $\boldsymbol{y}_T$ as $\boldsymbol{y}_T = \widetilde{\boldsymbol{\Psi}}\boldsymbol{X}_T\boldsymbol{a}$, where $\widetilde{\boldsymbol{\Psi}} = \text{blkdiag}(\boldsymbol{\Phi}_0, \boldsymbol{\Phi}_1, \ldots, \boldsymbol{\Phi}_{L-1})$ and $\boldsymbol{X}_T = \text{blkdiag}(\boldsymbol{x}_{T,0}, \ldots, \boldsymbol{x}_{T,L-1})$, we have the optimization problem as

$$\boldsymbol{a}_{\text{opt}} = \arg\max_{\boldsymbol{a}\in\mathbb{C}^L} \boldsymbol{a}^H [\boldsymbol{X}_T^H \widetilde{\boldsymbol{\Psi}}^H \boldsymbol{R}_I^{-1} \widetilde{\boldsymbol{\Psi}} \boldsymbol{X}_T]\boldsymbol{a}, \quad \text{subject to} \quad \boldsymbol{a}^H\boldsymbol{a} = 1 \tag{2.20}$$

Now, from Section 2.2, we notice that the interference covariance matrix $\boldsymbol{R}_I$ is also a function of $\boldsymbol{a}$ as we modelled the clutter return as a signal-dependent quantity. Therefore, considering the true $\boldsymbol{R}_I$, we cannot obtain a simple closed-form expression of $\boldsymbol{a}_{\text{opt}}$.

However, in practice, we estimate $\boldsymbol{R}_I$ from the secondary range-gate measurements, and consequently, we aim to actually solve an optimization problem as follows:

$$\boldsymbol{a}_{\text{opt}} = \arg\max_{\boldsymbol{a}\in\mathbb{C}^L} \boldsymbol{a}^H \left[\boldsymbol{X}_T^H \widetilde{\boldsymbol{\Psi}}^H \widehat{\boldsymbol{R}}_I^{-1} \widetilde{\boldsymbol{\Psi}} \boldsymbol{X}_T\right]\boldsymbol{a}, \quad \text{subject to} \quad \boldsymbol{a}^H\boldsymbol{a} = 1 \tag{2.21}$$

Now, since we calculate $\widehat{\boldsymbol{R}_I}$ using a sparse recovery procedure, it is important to investigate how different choices of the transmit signal parameters $\boldsymbol{a}$ affect such an estimation procedure.

We characterize the accuracy of sparse recovery algorithm by computing the coherence of sparse-measurement matrix as [59–61]

$$\mu = \max_{g,g\neq g'} |\widetilde{\boldsymbol{\Psi}_g}^H \widetilde{\boldsymbol{\Psi}_{g'}}| \tag{2.22}$$

and we want this metric to have as small a value as possible. Here, $\widetilde{\boldsymbol{\Psi}_g}$ denotes the gth column of $\boldsymbol{\Psi}$ which is normalized to have unit magnitude. Noticing the block-diagonal construction of $\boldsymbol{\Psi}$, we have

$$\mu = \max_{l} \max_{g,g\neq g'} \frac{|a_l|^2 \left|\boldsymbol{\phi}_{l,g}^H \boldsymbol{\phi}_{l,g'}\right|}{MN|a_l|^2} \tag{2.23}$$

Denoting the grid points g and g', respectively, with (i,j) and (i',j'), we get

$$\boldsymbol{\phi}_{l,g}^H \boldsymbol{\phi}_{l,g'} = e^{j(M-1)\pi\alpha_{l,\Delta}} e^{j(N-1)\pi\nu_{l,\Delta}} \frac{\sin(M\pi\alpha_{l,\Delta})}{\sin(\pi\alpha_{l,\Delta})} \frac{\sin(N\pi\nu_{l,\Delta})}{\sin(\pi\nu_{l,\Delta})} \tag{2.24}$$

where $\alpha_{l,\Delta} = \alpha_{l,i} - \alpha_{l,i'}$, $\nu_{l,\Delta} = \nu_{l,j} - \nu_{l,j'}$. Therefore, the absolute value

$$\left|\boldsymbol{\phi}_{l,g}^H \boldsymbol{\phi}_{l,g'}\right| = \frac{\sin(M\pi\alpha_{l,\Delta})}{\sin(\pi\alpha_{l,\Delta})} \frac{\sin(N\pi\nu_{l,\Delta})}{\sin(\pi\nu_{l,\Delta})} \tag{2.25}$$

is maximized when the distinct grid points are chosen adjacent to each other, i.e., $i = i' \pm 1$ or $j = j' \pm 1$, and then

$$\max_{(i,j),(i',j'):i\neq i',j\neq j'} |\boldsymbol{\phi}_{l,(i,j)}^H \boldsymbol{\phi}_{l,(i',j')}| \approx MN \tag{2.26}$$

Consequently, we have

$$\mu = \max_{l} \max_{g,g\neq g'} \frac{|\boldsymbol{\phi}_{l,g}^H \boldsymbol{\phi}_{l,g'}|}{(MN)} \approx 1 \tag{2.27}$$

Therefore, we can reasonably assume that the estimation accuracy of $\boldsymbol{R}_I$ does not significantly depend on $\boldsymbol{a}$.

Hence, ignoring any explicit dependence of the estimation of $\boldsymbol{R}_I$ on $\boldsymbol{a}$ in the optimization problem

$$\boldsymbol{a}_{\text{opt}} = \arg\max_{\boldsymbol{a}\in\mathbb{C}^L} \; \boldsymbol{a}^H \left[\boldsymbol{X}_T^H \widetilde{\boldsymbol{\Psi}}^H \widehat{\boldsymbol{R}}_I^{-1} \widetilde{\boldsymbol{\Psi}} \boldsymbol{X}_T\right] \boldsymbol{a}, \quad \text{subject to} \quad \boldsymbol{a}^H \boldsymbol{a} = 1 \tag{2.28}$$

we recognize that the optimization problem is in the form of an eigenvalue-eigenvector formulation and its solution $\boldsymbol{a}_{\text{opt}}$ is the eigenvector corresponding to the largest eigenvalue of $[\boldsymbol{X}_T^H \widetilde{\boldsymbol{\Psi}}^H \widehat{\boldsymbol{R}}_I^{-1} \widetilde{\boldsymbol{\Psi}} \boldsymbol{X}_T]$.

2.5 Numerical results

In this section, we present the results of several numerical examples to illustrate the OFDM-STAP performance obtained by utilizing the spatio-temporal sparsity approach, and the achieved performance gain due to adaptive OFDM waveform design. First, we provide a description of the simulation setup and then discuss different numerical results.

Radar parameters—We considered a radar moving with a speed of $|\boldsymbol{v}_R| = 100$ m/s along the y-direction (see Figure 2.1). It used a linear array with $M = 10$ sensor elements having interelement spacing $d = \lambda_c/2 = 0.33$ m, and a CPI having $N = 8$ temporal pulses to collect the spatio-temporal measurements. The transmitted waveform was an $L = 4$ subcarrier OFDM signal with the following parameters: carrier frequency $f_c = 450$ MHz, bandwidth $B = 5$ MHz, subcarrier spacing $\Delta f = B/(L+1) = 1$ MHz, pulse width $T_p = 1/\Delta f = 1$ μs and PRI $T = 1.67$ ms. This ensured an unity Doppler foldover factor (i.e., $\chi = 2|\boldsymbol{v}_R|T/d = 1$) for the clutter ridge on the spatio-temporal plane.

Interference parameters—We modelled the thermal noise covariance matrix as $\sigma_n^2 \boldsymbol{I}_{LMN}$ with $\sigma_n^2 = 1$. The clutter responses were assumed to be equally spaced in azimuth angles with $N_c = 72$ over the entire range gate. We simulated the clutter responses of each kth patch from an independent complex Gaussian distribution $\mathbb{C}\mathcal{N}\left(\boldsymbol{0}, \boldsymbol{R}_{C,k}\right)$ and scaled $\boldsymbol{R}_{C,k}$ to satisfy the required clutter-to-noise ratio (CNR), defined as

$$\text{CNR} = \frac{\sum_{k=1}^{N_c} \text{tr}\left(\boldsymbol{R}_{C,k}\right)}{LMN\sigma_n^2} \tag{2.29}$$

For all the results presented in this section, we kept the CNR fixed at 40 dB.

In addition, to represent the non-idealistic real-world STAP scenario, we considered the effects of temporal decorrelation (or ICM) on our sparsity-based OFDM-STAP method. Various natural environmental variations, such as wind blowing over foliage, motion of ocean waves, induce pulse-to-pulse fluctuations in clutter reflectivity, which is commonly referred to as ICM [6, Chapter 4, 62]. In general, the temporal-only decorrelation can be modelled with a modified clutter covariance matrix as

$$\widetilde{\boldsymbol{R}_C} = \boldsymbol{R}_C \odot \text{blkdiag}\left(\boldsymbol{T}_{D,0} \otimes \boldsymbol{1}_M, \ldots, \boldsymbol{T}_{D,L-1} \otimes \boldsymbol{1}_M\right) \tag{2.30}$$

where $\boldsymbol{T}_{D,l}$ is an $N \times N$ temporal correlation matrix at the lth subcarrier and $\boldsymbol{1}_M$ is an $M \times M$ matrix having all the entries to be one. In this work, we constructed the temporal decorrelation for a water scenario with $\boldsymbol{T}_{D,l} = \text{toeplitz}(\rho_{D,l}(0), \rho_{D,l}(1), \ldots, \rho_{D,l}(N-1))$, where the temporal autocorrelation of the fluctuations had a Gaussian shape [2]:

$$\rho_{D,l}(n) = \exp\left\{\frac{-8\pi^2\sigma_v^2 T^2 n^2 f_l^2}{c^2}\right\} \tag{2.31}$$

with σ_v^2 representing the variance of the clutter spectral spread. In the simulations, we used $\sigma_v^2 = 0.5$.

Target parameters—The target was simulated at an azimuth direction of $\psi_T = 0°$, and it was moving with a speed of $|\boldsymbol{v}_T| = 20$ m/s. The scattering coefficients of the target, $\zeta_T = [\zeta_{T,0}, \ldots, \zeta_{T,L-1}]^T$, were varied to construct two scenarios having different target-energy distributions across different subchannels, i.e., Scenario I with $\boldsymbol{\zeta}_T^{(\mathrm{I})} = [1, 2, 3, 1]^T$ and Scenario II with $\boldsymbol{\zeta}_T^{(\mathrm{II})} = [1, 5, 1, 0.5]^T$. To create various signal-to-noise ratio conditions, these target scattering vectors were further scaled to satisfy

$$\mathrm{SNR} = \frac{\|\boldsymbol{\zeta}_T\|_2^2}{L\sigma_n^2} \tag{2.32}$$

Simulation parameters—The spatio-temporal sparsity-based STAP problem was solved following the LASSO formulation after constructing the dictionary matrix with $G_\alpha = G_v = 144$ grid points by equally partitioning the azimuth angle ψ with an interval of 2.5°. The LASSO estimator was implemented using CVX [64]. It was first operated separately on each secondary data $s = 1, 2, \ldots, N_s$, and then the recovered clutter responses were used to construct $\widehat{\boldsymbol{R}}_C$. Finally, an estimate of the interference covariance matrix was obtained as $\widehat{\boldsymbol{R}}_I = \widehat{\boldsymbol{R}}_C + \eta \boldsymbol{I}_{LMN}$ with $\eta = 10\sigma_n^2$.

Performance metrics—To analyze the performance of the sparse-STAP technique, we examined its characteristics with respect to the ROCs and SINR-loss measure. The evaluation of ROCs was essential as the STAP algorithms are mainly used in the detection problems. To compute the ROC curves, we used the relationship between P_{FA} and P_D as $P_D = Q\left(\sqrt{\mathrm{SINR}}, \sqrt{-2\ln P_{FA}}\right)$ [1].

The SINR-loss performance metric characterizes the STAP performance relative to what could be obtained in the absence of interference (clutter). In our case, if only thermal noise is present, i.e., $\boldsymbol{R}_I = \boldsymbol{I}_{LMN}$, then the noise-only SINR value is equal to LMN. When clutter was present and we estimated the interference covariance matrix as $\widehat{\boldsymbol{R}}_I$, the output SINR was computed as a function of target Doppler as

$$\mathrm{SINR}(\nu) = \frac{\left|\breve{\boldsymbol{\phi}}_T(\nu)^H \widehat{\boldsymbol{R}}_I^{-1} \breve{\boldsymbol{\phi}}_T(\nu)\right|^2}{\breve{\boldsymbol{\phi}}_T(\nu)^H \widehat{\boldsymbol{R}}_I^{-1} \boldsymbol{R}_I \widehat{\boldsymbol{R}}_I^{-1} \breve{\boldsymbol{\phi}}_T(\nu)} \tag{2.33}$$

where $\breve{\boldsymbol{\phi}}_T(\nu) = [(\boldsymbol{f}_D(\nu_0) \otimes \boldsymbol{f}_S(\alpha_{0,T}))^T, \ldots, (\boldsymbol{f}_D(\nu_{L-1}) \otimes \boldsymbol{f}_S(\alpha_{L-1,T}))^T]^T$ represented a steering vector with fixed target angle and varying target Doppler. Then, the SINR-loss measure at the output of the proposed STAP filter was calculated as $\mathrm{SINRloss}(\nu) = \mathrm{SINR}(\nu)/LMN$.

2.5.1 Sparsity-based STAP performance

Figure 2.3 depicts the spatio-temporal spectrum of the estimated clutter response by applying the proposed sparse recovery algorithm on a single secondary range gate measurement (i.e., $N_s = 1$). In the ideal scenario (without any temporal decorrelation), we could clearly observe the diagonal clutter ridge of the estimated spectrum along with extremely few non-zero off-diagonal elements. In the presence of temporal decorrelation, we still saw a prominent diagonal ridge characteristic, but with

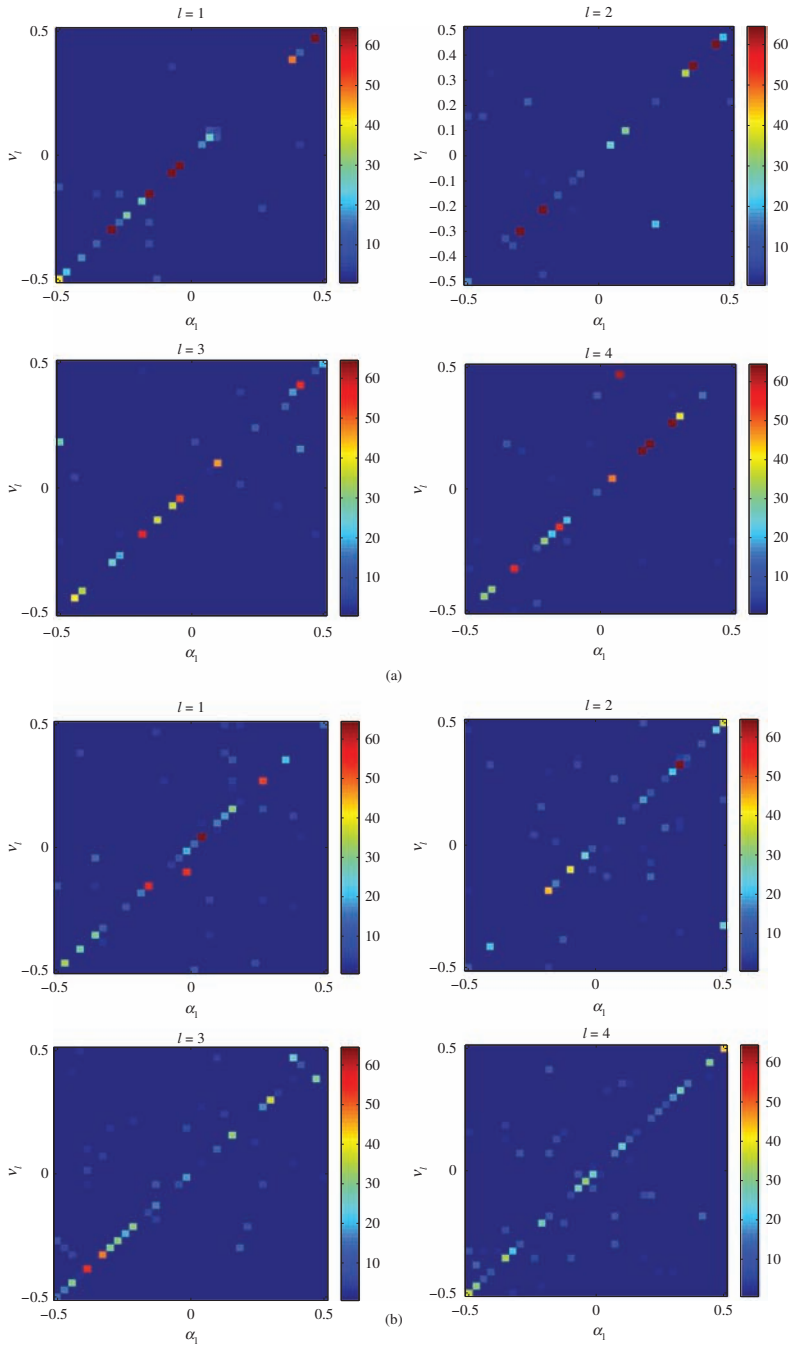

Figure 2.3 Estimated clutter spectra (at L = 4 subcarriers) of the sparsity-based STAP method in the (a) ideal scenario (no decorrelation) and (b) presence of temporal decorrelation [the colorbar is in linear scale]

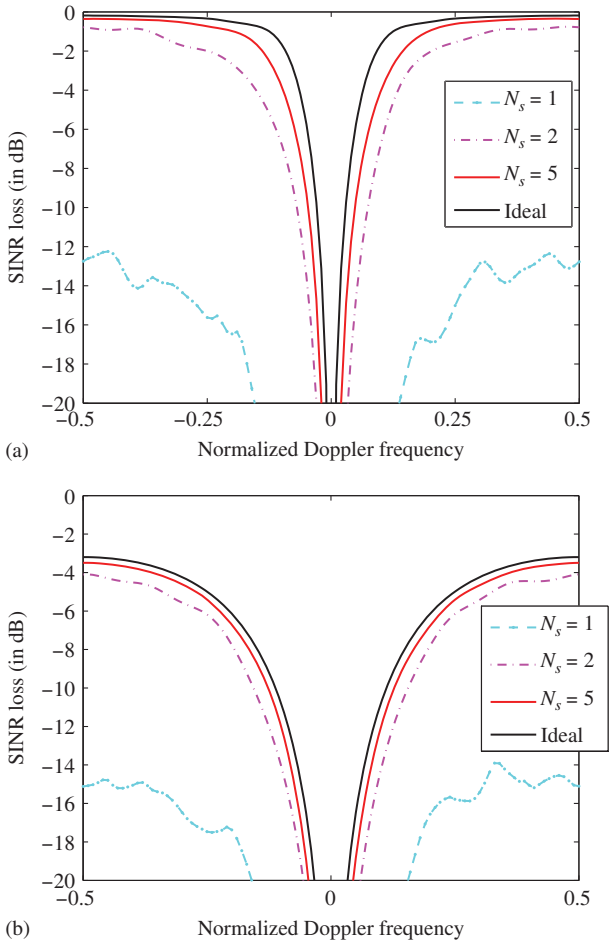

Figure 2.4 SINR-loss performance of the sparsity-based STAP method with fixed (non-adaptive) OFDM signalling in the (a) ideal scenario (no decorrelation) and (b) presence of temporal decorrelation

a slight increase in the number and strength of the off-diagonal elements. We want to mention here that, because of the inherent randomness of the clutter returns, the estimated spectra would look different when obtained from a different set of secondary measurements.

The SINR-loss performance of the sparsity-based STAP technique is demonstrated in Figure 2.4. In this setup, we employed a conventional (non-adaptive) OFDM signal with equal magnitude spectral coefficients (i.e., $a_l = 1/\sqrt{L} \forall l$). In the ideal scenario of Figure 2.4(a), it is clearly evident that we achieved within -3 dB of optimum SINR-loss by using only $N_s = 2$ secondary measurements (to estimate the interference covariance matrix). Furthermore, use of about $N_s = 5$ secondary data resulted into a near-optimum performance. In the presence of

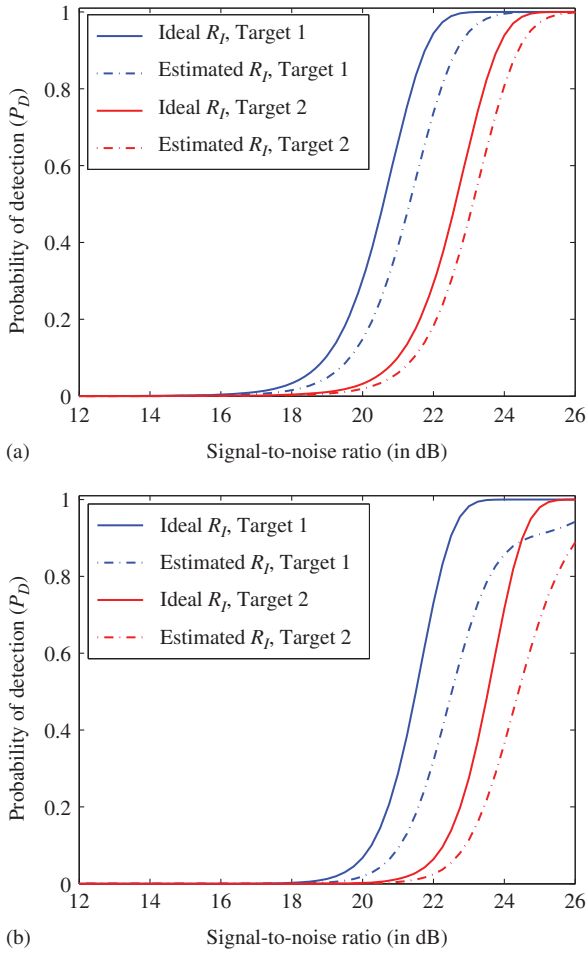

Figure 2.5 Receiver operating characteristics of the sparsity-based STAP method with fixed (non-adaptive) OFDM signalling in the (a) ideal scenario (no decorrelation) and (b) presence of temporal decorrelation

temporal correlation of Figure 2.4(b), the optimum SINR-loss performance showed a much wider mainbeam clutter notch and a smaller maximum value when compared with the ideal scenario without any decorrelation. As before, we could still attain the near-optimum SINR-loss performance by utilizing only $N_s = 2-5$ secondary data. Therefore, irrespective of whether any temporal decorrelation was present or not, our sparsity-based STAP approach employed considerably lesser number of secondary data to produce a near-optimum SINR-loss performance.

The ROC curves in Figure 2.5 show the detection performances of the sparsity-based STAP approach for two targets $\boldsymbol{\zeta}_T^{(\mathrm{I})}$ and $\boldsymbol{\zeta}_T^{(\mathrm{II})}$, both in the absence and in the presence of temporal decorrelation effect. The resulting ROCs, obtained by utilizing the interference covariance matrix estimated via sparsity-based STAP

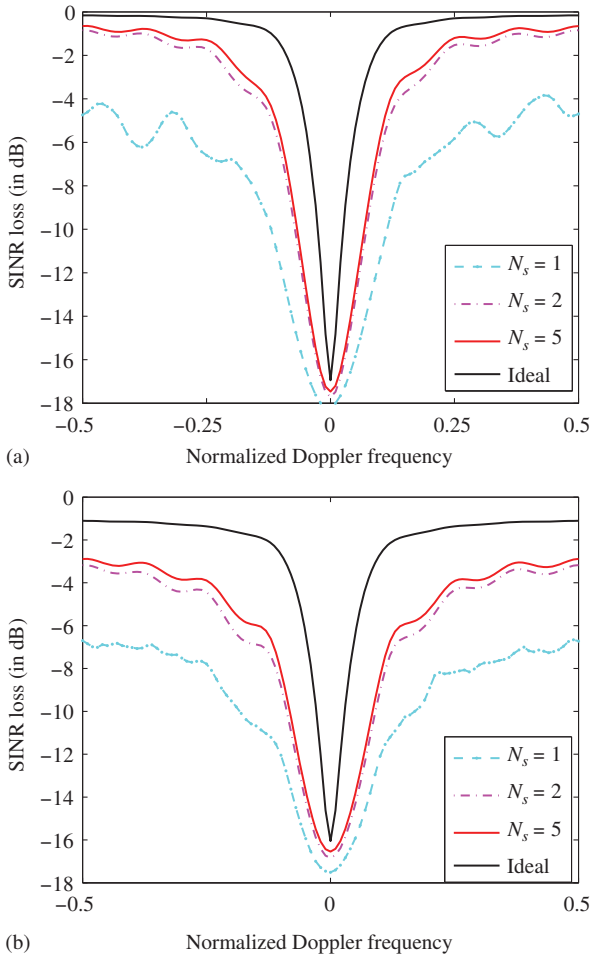

Figure 2.6 SINR-loss performance of the sparsity-based STAP method with adaptive OFDM signalling in the (a) ideal scenario (no decorrelation) and (b) presence of temporal decorrelation

approach, were compared with their counterparts that assume the complete knowledge of the interference covariance matrix. ROCs of the sparsity-based STAP method were approximately within 1.2 dB of the optimum performance limit for both the target scenarios.

2.5.2 Performance improvement due to adaptive waveform design

Figures 2.6 and 2.7, respectively, demonstrate the SINR-loss and ROC performances when we used the adaptively designed OFDM coefficients $\boldsymbol{a}_{\text{opt}}$. The SINR-loss performances of Figure 2.6 show that, both in the absence or presence of the

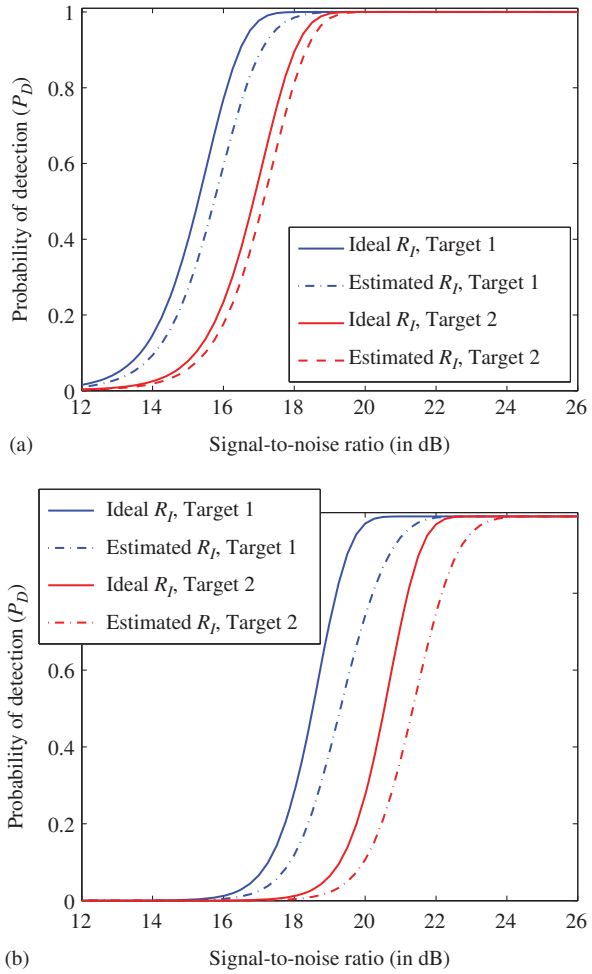

Figure 2.7 Receiver operating characteristics of the sparsity-based STAP method with adaptive OFDM signalling in the (a) ideal scenario (no decorrelation) and (b) presence of temporal decorrelation

temporal decorrelation, the change in the transmit signal parameters did not affect the SINR-loss performance in a significant way. In Figure 2.6(a), we observe that the SINR-loss of the sparsity-based STAP approach remained within -1 dB of the optimum performance by using only $N_s = 5$ secondary measurements, whereas when temporal decorrelation was present, we achieved within -2 dB of the optimum performance by utilizing the same number of secondary data.

The improvement in detection performance due to the adaptive waveform design is clearly noticeable when we compare the ROC plots in Figure 2.7 with their equivalents in Figure 2.5. For example, in the ideal scenario with no

decorrelation effect, we observed almost 5.5 dB improvement in detection performance for $\boldsymbol{\zeta}_T^{(\mathrm{I})}$ and approximately 6 dB for $\boldsymbol{\zeta}_T^{(\mathrm{II})}$ when $P_D = 0.5$. On the other hand, when temporal decorrelation was present, the detection performance was improved by approximately 3 dB for both the targets at $P_D = 0.5$.

2.6 Conclusions

In this paper, we exploited the spatio-temporal sparsity of the interference spectra to develop a sparse-STAP algorithm for an OFDM radar. The use of OFDM signal not only improved target-detectability by increasing the frequency diversity of the system but also allowed us to efficiently design the transmit signals by maximizing the output SINR in order to further enhance the STAP performance. In addition, since the computation of SINR depends on the estimated value of the interference covariance matrix, which we calculated by using a sparse recovery algorithm, we analytically investigated effects of different choices of the designed OFDM parameters on the accuracy of sparse recovery technique by computing the coherence measure of the sparse-measurement matrix. This led us to formulate a closed-form solution of the optimal waveform design problem in terms of the OFDM spectral coefficients. We demonstrated with numerical examples the achieved near-optimum STAP performance by utilizing substantially small number of secondary data, and the improvement in detection performance due to adaptive OFDM waveform design.

In future, we will extend our model to incorporate more realistic physical effects, such as the antenna array misalignment and channel mismatch. This will help us to understand how robust our algorithm is with respect to different practical considerations. At the same time, a comprehensive analysis will also be carried out to analyze the effects of a mismatched grid-position on proposed sparse-STAP algorithm. In addition, we will validate the performance of our proposed technique with real data.

Acknowledgements

This research was partially supported by the US Missile Defense Agency (MDA) at the Oak Ridge National Laboratory, managed by UT-Battelle, LLC, for the US Department of Energy, under contract DE-AC05-00OR22725. The US government retains and the publisher, by accepting the article for publication, acknowledges that the US government retains a non-exclusive, paid-up, irrevocable, worldwide licence to publish or reproduce the published form of this manuscript or allow others to do so, for US government purposes. The Department of Energy will provide public access to these results of federally sponsored research in accordance with the DOE Public Access Plan (http://energy.gov/downloads/doe-public-access-plan).

References

[1] L. E. Brennan and I. S. Reed, 'Theory of adaptive radar,' *IEEE Trans. Aerosp. Electron. Syst.*, vol. AES-9, no. Mar. (2), pp. 237–252, 1973.

[2] J. Ward, 'Space–time adaptive processing for airborne radar,' Lincoln Laboratory, Massachusetts Institute of Technology, Lexington, MA, Tech. Rep. 1015, Dec. 1994.

[3] V. Cavo, 'MCARM/STAP data analysis,' Air Force Research Laboratory, Rome, NY, Tech. Rep. AFRL-SN-RS-TR-1999-48, Vol I, May 1999.

[4] B. Himed, 'MCARM/STAP data analysis,' Air Force Research Laboratory, Rome, NY, Tech. Rep. AFRL-SN-RS-TR-1999-48, Vol II, May 1999.

[5] R. Klemm, *Principles of Space–Time Adaptive Processing*. London, United Kingdom: IET, 2002.

[6] J. R. Guerci, *Space–Time Adaptive Processing for Radar*. Norwood, MA: Artech House, 2003.

[7] J. R. Guerci, J. S. Goldstein, and I. S. Reed, 'Optimal and adaptive reduced-rank STAP,' *IEEE Trans. Aerosp. Electron. Syst.*, vol. 36, no. Apr. (2), pp. 647–663, 2000.

[8] W. L. Melvin, 'A STAP overview,' *IEEE Aerosp. Electron. Syst. Mag.*, vol. 19, no. 1, pp. 19–35, 2004.

[9] M. C. Wicks, M. Rangaswamy, R. Adve, and T. B. Hale, 'Space–time adaptive processing: A knowledge-based perspective for airborne radar,' *IEEE Signal Process. Mag.*, vol. 23, no. 1, pp. 51–65, 2006.

[10] I. S. Reed, J. D. Mallett, and L. E. Brennan, 'Rapid convergence rate in adaptive arrays,' *IEEE Trans. Aerosp. Electron. Syst.*, vol. AES-10, no. Nov. (6), pp. 853–863, 1974.

[11] D. W. Tufts, I. Kirsteins, and R. Kumaresan, 'Data-adaptive detection of a weak signal,' *IEEE Trans. Aerosp. Electron. Syst.*, vol. AES-19, no. Mar. (2), pp. 313–316, 1983.

[12] A. M. Haimovich and Y. Bar-Ness, 'An eigenanalysis interference canceler,' *IEEE Trans. Signal Process.*, vol. 39, no. 1, pp. 76–84, 1991.

[13] A. Haimovich, 'The eigencanceler: Adaptive radar by eigenanalysis methods,' *IEEE Trans. Aerosp. Electron. Syst.,* vol. 32, no. Apr. (2), pp. 532–542, 1996.

[14] R. Kumaresan and D. W. Tufts, 'Data-adaptive principal component signal processing,' in *Proc. 19th IEEE Conf. Decision and Control Including Symp. on Adaptive Processes*, Albuquerque, NM, Dec. 10–12, 1980, pp. 949–954.

[15] L. Chang and C.-C. Yeh, 'Performance of DMI and eigenspace-based beamformers,' *IEEE Trans. Antennas Propag.*, vol. 40, no. 11, pp. 1336–1347, 1992.

[16] J. S. Goldstein and I. S. Reed, 'Reduced-rank adaptive filtering,' *IEEE Trans. Signal Process.*, vol. 45, no. 2, pp. 492–496, 1997.

[17] J. R. Roman, M. Rangaswamy, D. W. Davis, Q. Zhang, B. Himed, and J. H. Michels, 'Parametric adaptive matched filter for airborne radar

applications,' *IEEE Trans. Aerosp. Electron. Syst.*, vol. 36, no. Apr. (2), pp. 677–692, 2000.

[18] C. Jiang, H. Li, and M. Rangaswamy, 'Conjugate gradient parametric adaptive matched filter,' in *Proc. IEEE Radar Conf.*, Washington, DC, May 10–14, 2010, pp. 740–745.

[19] J. S. Goldstein, I. S. Reed, and L. L. Scharf, 'A multistage representation of the Wiener filter based on orthogonal projections,' *IEEE Trans. Inf. Theory*, vol. 44, no. Nov. (7), pp. 2943–2959, 1998.

[20] C. D. Peckham, A. M. Haimovich, T. F. Ayoub, J. S. Goldstein, and I. S. Reed, 'Reduced-rank STAP performance analysis,' *IEEE Trans. Aerosp. Electron. Syst.*, vol. 36, no. Apr. (2), pp. 664–676, 2000.

[21] R. Fa and R. C. de Lamare, 'Reduced-rank STAP algorithms using joint iterative optimization of filters,' *IEEE Trans. Aerosp. Electron. Syst.*, vol. 47, no. Jul. (3), pp. 1668–1684, 2011.

[22] K. Gerlach and M. Picciolo, 'Airborne/spacebased radar STAP using a structured covariance matrix,' *IEEE Trans. Aerosp. Electron. Syst.*, vol. 39, no. 1, pp. 269–281, 2003.

[23] J. S. Bergin, C. M. Teixeira, P. M. Techau, and J. R. Guerci, 'Improved clutter mitigation performance using knowledge-aided space–time adaptive processing,' *IEEE Trans. Aerosp. Electron. Syst.*, vol. 42, no. Jul. (3), pp. 997–1009, 2006.

[24] W. L. Melvin and G. A. Showman, 'An approach to knowledge-aided covariance estimation,' *IEEE Trans. Aerosp. Electron. Syst.,* vol. 42, no. Jul. (3), pp. 1021–1042, 2006.

[25] O. Besson, S. Bidon, and J.-Y. Tourneret, 'Covariance matrix estimation with heterogeneous samples,' *IEEE Trans. Signal Process.*, vol. 56, no. 3, pp. 909–920, 2008.

[26] P. Stoica, J. Li, X. Zhu, and J. R. Guerci, 'On using a priori knowledge in space–time adaptive processing,' *IEEE Trans. Signal Process.*, vol. 56, no. 6, pp. 2598–2602, 2008.

[27] X. Zhu, J. Li, and P. Stoica, 'Knowledge-aided space–time adaptive processing,' *IEEE Trans. Aerosp. Electron. Syst.*, vol. 47, no. Apr. (2), pp. 1325–1336, 2011.

[28] M. C. Wicks, 'A brief history of waveform diversity,' in *Proc. IEEE Radar Conf.*, Pasadena, CA, May 4–8, 2009, pp. 1–6.

[29] A. Nehorai, F. Gini, M. S. Greco, A. P. Suppappola, and M. Rangaswamy, 'Introduction to the issue on adaptive waveform design for agile sensing and communication,' *IEEE J. Sel. Top. Signal Process.*, vol. 1, no. Jun. (1), pp. 2–5, 2007.

[30] R. Calderbank, S. Howard, and B. Moran, 'Waveform diversity in radar signal processing,' *IEEE Signal Process. Mag.*, vol. 26, no. 1, pp. 32–41, 2009.

[31] M. C. Wicks, E. Mokole, S. Blunt, R. Schneible, and V. Amuso, Eds., *Principles of Waveform Diversity and Design.* Raleigh, NC: SciTech Pub., Aug. 2010.

[32] F. Gini, A. De Maio, and L. K. Patton, *Waveform Design and Diversity for Advanced Radar Systems*. London, UK: Inst of Engineering & Technology, Jun. 2011.

[33] D. Garmatyuk, 'Ultrawideband imaging radar based on OFDM: System simulation analysis,' in *Proc. SPIE*, vol. 6210, no. 1, Orlando, FL, May 2006, paper 621007.

[34] G. Franken, H. Nikookar, and P. van Genderen, 'Doppler tolerance of OFDM-coded radar signals,' in *Proc. 3rd European Radar Conf. (EuRAD)*, Manchester, UK, Sep. 13–15, 2006, pp. 108–111.

[35] S. Sen and A. Nehorai, 'OFDM MIMO radar with mutual-information waveform design for low-grazing angle tracking,' *IEEE Trans. Signal Process.*, vol. 58, no. 6, pp. 3152–3162, 2010.

[36] S. Sen and A. Nehorai, 'Adaptive OFDM radar for target detection in multipath scenarios,' *IEEE Trans. Signal Process.*, vol. 59, no. 1, pp. 78–90, 2011.

[37] S. Sen, 'OFDM radar space–time adaptive processing by exploiting spatio-temporal sparsity,' *IEEE Trans. Signal Process.*, vol. 61, no. 1, pp. 118–130, 2013.

[38] S. Sen, 'PAPR-constrained Pareto-optimal waveform design for OFDM-STAP radar,' *IEEE Trans. Geosci. Remote Sens.*, vol. 52, no. 6, pp. 3658–3669, 2014.

[39] E. F. Knott, 'Radar cross section,' in *Radar Handbook*, 2nd ed., M. I. Skolnik, Ed. Boston, MA: McGraw-Hill, Inc., Jan. 1990, ch. 11.

[40] F. Weinmann, 'Frequency dependent RCS of a generic airborne target,' in *URSI Int. Symp. Electromagnetic Theory (EMTS)*, Berlin, Germany, Aug. 16–19, 2010, pp. 977–980.

[41] S. Maria and J.-J. Fuchs, 'Application of the global matched filter to STAP data an efficient algorithmic approach,' in *Proc. 31st Int. Conf. on Acoustics, Speech, and Signal Processing (ICASSP)*, Toulouse, France, May 14–19, 2006, pp. 1013–1016.

[42] H. Zhang, G. Li, and H. Meng, 'A class of novel STAP algorithms using sparse recovery technique,' Apr. 2009. [Online]. Available: http://arxiv.org/abs/0904.1313.

[43] K. Sun, H. Zhang, G. Li, H. Meng, and X. Wang, 'A novel STAP algorithm using sparse recovery technique,' in *Proc. IEEE Int. Geoscience and Remote Sensing Symp. (IGARSS)*, vol. 5, Cape Town, South Africa, Jul. 12–17, 2009, pp. 336–339.

[44] I. W. Selesnick, S. U. Pillai, K. Y. Li, and B. Himed, 'Angle-Doppler processing using sparse regularization,' in *Proc. 35th Int. Conf. on Acoustics, Speech, and Signal Processing (ICASSP)*, Dallas, TX, Mar. 14–19, 2010, pp. 2750–2753.

[45] J. T. Parker and L. C. Potter, 'A Bayesian perspective on sparse regularization for STAP post-processing,' in *Proc. IEEE Radar Conf.*, Washington, DC, May 10–14, 2010, pp. 1471–1475.

[46] K. Sun, H. Zhang, G. Li, H. Meng, and X. Wang, 'Airborne radar STAP using sparse recovery of clutter spectrum,' Aug. 2010. [Online]. Available: http://arxiv.org/abs/1008.4185.

[47] K. Sun, H. Meng, Y. Wang, and X. Wang, 'Direct data domain STAP using sparse representation of clutter spectrum,' *Signal Process.*, vol. 91, no. 9, pp. 2222–2236, 2011.
[48] S. Sen and C. Glover, 'Frequency adaptability and waveform design for OFDM radar space–time adaptive processing,' in *Proc. IEEE Radar Conf.*, Atlanta, GA, May 7–11, 2012, pp. 230–235.
[49] Z. Yang, Z. Liu, X. Li, and L. Nie, 'Performance analysis of STAP algorithms based on fast sparse recovery techniques,' *Prog. Electromagnet. Res. B*, vol. 41, pp. 251–268, 2012.
[50] Z. Yang, X. Li, and H. Wang, 'Space–time adaptive processing based on weighted regularized sparse recovery,' *Prog. Electromagnet. Res. B*, vol. 42, pp. 245–262, 2012.
[51] S. Sen, 'OFDM radar space–time adaptive processing by exploiting spatio-temporal sparsity,' *IEEE Trans. Signal Process.*, vol. 61, no. 1, pp. 118–130, 2013.
[52] Z. Yang, X. Li, H. Wang, and W. Jiang, 'On clutter sparsity analysis in space–time adaptive processing airborne radar,' *IEEE Geosci. Remote Sens. Lett.*, vol. 10, no. Sep. (5), pp. 1214–1218, 2013.
[53] Z. Yang, X. Li, H. Wang, and L. Nie, 'Sparsity-based space–time adaptive processing using complex-valued Homotopy technique for airborne radar,' *IET Signal Process*., vol. 8, no. Jul., pp. 552–564, 2014.
[54] S. Sen, 'Low-rank matrix decomposition and spatio-temporal sparse recovery for STAP radar,' *IEEE J. Sel. Top. Signal Process.*, vol. 9, no. 8, pp. 1510–1523, Dec. 2015.
[55] A. Steinhardt and N. Pulsone, 'Subband STAP processing, the fifth generation,' in *Proc. IEEE Sensor Array and Multichannel Signal Processing Workshop (SAM)*, Cambridge, MA, Mar. 16–17, 2000, pp. 1–6.
[56] A. Hoffman and S. M. Kogon, 'Subband STAP in wideband radar systems,' in *Proc. IEEE Sensor Array and Multichannel Signal Processing Workshop (SAM)*, Cambridge, MA, Mar. 16–17, 2000, pp. 256–260.
[57] G. Tang, B. N. Bhaskar, and B. Recht, 'Sparse recovery over continuous dictionaries – Just discretize,' in *Proc. 38th Int. Conf. on Acoustics, Speech, and Signal Processing (ICASSP)*, Pacific Grove, CA, Nov. 3–6, 2013, pp. 1043–1047.
[58] R. Tibshirani, 'Regression shrinkage and selection via the lasso,'*J. R. Stat. Soc.. Ser. B (Methodol.)*, vol. 58, no. 1, pp. 267–288, 1996.
[59] D. L. Donoho and X. Huo, 'Uncertainty principles and ideal atomic decompositions,' *IEEE Trans. Inf. Theory*, vol. 47, no. Nov. (7), pp. 2845–2862, 2001.
[60] M. Elad and A. M. Bruckstein, 'A generalized uncertainty principle and sparse representation in pairs of bases,' *IEEE Trans. Inf. Theory*, vol. 48, no. 9, pp. 2558–2567, 2002.
[61] J. Tropp, 'Greed is good: Algorithmic results for sparse approximation,' *IEEE Trans. Inf. Theory*, vol. 50, no. 10, pp. 2231–2242, 2004.

[62] J. R. Guerci and J. S. Bergin, 'Principal components, covariance matrix tapers, and the subspace leakage problem,' *IEEE Trans. Aerosp. Electron. Syst.*, vol. 38, no. 1, pp. 152–162, 2002.

[63] B. D. Carlson, 'Covariance matrix estimation errors and diagonal loading in adaptive arrays,' *IEEE Trans. Aerosp. Electron. Syst.,* vol. 24, no. Jul. (4), pp. 397–401, 1988.

[64] M. Grant and S. Boyd, 'CVX: Matlab software for disciplined convex programming, version 2.1,' Mar. 2014. http://cvxr.com/cvx.

This page intentionally left blank

Chapter 3

Cognitive waveform design for spectral coexistence

A. Aubry, A. De Maio*, A. Farina[†,‡] and M. Piezzo**

Abstract

Radar signal design in a spectrally dense environment is a very challenging and topical problem due to the increasing demand of both defence surveillance/remote sensing capabilities and civilian wireless services. This chapter describes an optimization theory-based radar waveform design to deal with the spectrum congestion problem. Cognition provided by a radio environmental map paves the way for an intelligent dynamic spectrum allocation. It pushes for dynamic spectral constraints on the radar waveform which is thus the result of a constrained optimization process aimed at improving some radar performance (such as detection, classification and tracking capabilities) while ensuring spectral compatibility with the surrounding radio frequency licensed systems. Finally, some spectrally crowded illustrative scenarios are analyzed to show the effectiveness of the considered optimization theory-based approach.

3.1 Introduction

The radio frequency (RF) electromagnetic spectrum is a limited natural resource necessary for an ever-growing number of services and systems. It is used in several applications, such as mobile communications, radio and television broadcasting, as well as remote sensing. Together with oil and water, nowadays, the RF spectrum represents one of the most important, significant, crucial and critical commodities due to the huge impact of radio services on the society. Both high-quality/high-rate wireless services (4G and 5G) and accurate and reliable remote-sensing capabilities (air traffic control, geophysical monitoring of Earth and defence and security applications) call for increased amounts of bandwidth [1,2]. Besides basic

[*]Università degli studi di Napoli "Federico II", Dipartimento di Ingegneria Elettrica e delle Tecnologie dell'Informazione, Italy
[†]ELETTRONICA S.p.A., Italy
[‡]Selex ES (retired), Italy

electromagnetic considerations, such as good foliage penetration [3], low path loss attenuation and reduced size of the devices push some systems to coexist in the same frequency band [4] (for instance very high frequency and ultra high frequency). As a result, the RF spectrum congestion problem has been attracting the interest of many scientists and engineers during the last few years and is currently becoming one among the hot topics in both regulation and research field [5,6].

RF spectrum assignment and regulation is coordinated worldwide through the International Telecommunications Union (ITU) and it is reviewed every three to four years at the World Radiocommunication Conference (WRC) [6,7]. Specifically, the scope of the WRC is to review and, if necessary, revise the radio regulations that form the international treaty ruling the use of the RF spectrum, as well as geostationary-satellite and non-geostationary-satellite orbits. Revisions are performed on the basis of an agenda determined by the ITU Council, which accounts for recommendations made by previous WRCs. Significantly, the trend of the actual regulations is to relax the original conservative, static and possibly inefficient strategy in which "nothing should ever interfere with anything else" allowing some levels of "acceptable interference" among coexisting systems. This is because experimental evidences have revealed the substantial underutilization of the instantaneous spectrum at a given spatial location, as a function of direction, frequency, time and polarization, which should be reduced as much as possible, via a more flexible, dynamic and intelligent spectrum usage [6,8]. Of course, this process will require a quantitative and rigorous study of what can be accepted as tolerable level of disturbance so as to suitably formulate the regulations.

Starting from the above considerations, during the last year's several approaches have been proposed in both radar and communication research field to deal with the spectrum congestion problem and allow a more efficient spectrum use. In this context, passive bistatic radar (PBR) represents a reasonable strategy to handle this critical issue [6,9] for low/medium range applications. In fact, this sensing system, also known as "Green Radar", is able to detect, track and classify objects of interest without additional RF emissions but exploiting non-cooperative high-power illuminators of opportunity, i.e., radio FM, GSM, Universal Mobile Telecommunications System, GPS, Digital Video Broadcasting, other radar, satellite transmission, etc., as sources [10–12]. In this context, the main research activity concerns the design of advanced receiver structures able to process the direct path signal (from the selected emitter) and the received echoes from the surveillance area [13–16]. Evidently, this technology avoids the need of transmit licences and, as a by-product, offers a high level of covertness to the monitoring system, which may be advantageous for defence applications. Nevertheless, this approach may suffer significant performance degradation, in terms of detection and tracking capabilities, with respect to conventional monostatic radars as the employed waveforms are not devised to fulfil radar requirements and also exhibit time-varying features due to their information content sensitivity [6,17,18].

A possible means to overcome the above PBR shortcomings is represented by the so-called commensal radar (literally "from the same table") [19,20]. The key idea behind this approach is to synthesize the waveforms associated with broadcast, communications, or navigation services so that they not only satisfy their primary

goals but also share some features making them appealing as radar sources [21]. In this respect, in [21], it is highlighted that there are several parameters of the long term evolution (LTE) modulation and signal format that can be optimized.

A dual perspective to PBR and commensal radar approaches is represented by radar-embedded communication strategies [22,23]. Therein, covert communications are established embedding the information in the environmental reverberation induced by the radar probing waveforms [24,25]. Otherwise stated, the communications' signals are devised so that the information signal looks like a clutter return. By doing so, such communication link does not require additional spectrum resources and indirectly provides spectrum coexistence. Nevertheless, the achievable data rate is usually low.

Last but absolutely not least, an important solution to the spectrum congestion problem is provided by the waveform design and diversity (WDD) paradigm, pioneered by Dr. Wicks [26–29]. It refers to the radar waveform adaptation aimed at dynamically optimizing the radar performance for the particular scenario and tasks. This amazing and powerful feature is enabled by the new computing architectures, high-speed and off-the-shelf processors, arbitrary digital waveform generators, solid-state transmitters, active phased arrays, etc. and represents a viable tool to improve spectrum-usage efficiency. Relying on real-time spectrum occupancy awareness, it is possible to dynamically [30–32] select the probing waveforms in response to changing conditions so as to enhance radar performance while controlling its impact on the other surrounding RF systems. Specifically, WDD can enable an intelligent and agile spectrum management. Significantly, the underlying optimization process can also benefit from multiple degrees of freedom, including spatial, temporal and polarization's domains, to further improve the achievable performance.

The research in this field has been quite fertile. A plethora of papers have addressed the problem of designing radar waveforms with a smart frequency allocation [33], so as to control the interference brought on overlaid wireless networks (communication and navigation systems), while enhancing radar performance requirements in terms of range-Doppler resolution, low range and Doppler sidelobes, detection and tracking capabilities. In [34], a waveform design technique is introduced to confer some desired spectral nulls to the radar signal. The idea is to perturb a stepped frequency modulated pulse forcing an additional fast time polyphase code. The approach is extended in [35] to the case of continuous phase waveforms that place nulls at specific frequencies. The effectiveness of both the aforementioned methods is considered in [36], via an experimental analysis. An alternate projection algorithm for the construction of chirp-like constant-modulus signals with a single spectral null is proposed in [37], whereas in [38], its extension, addressing the production of multiple notches, is established. Some iterative algorithms are introduced in [39] for the joint design of the transmit signal and the receive filter achieving frequency stop-band suppression and range sidelobes minimization. A genetic algorithm to design sparse waveforms for high-frequency surface wave radar systems is investigated in [40]. In [41], a fast coding technique based on alternate projections and successive fast Fourier transforms is developed to obtain sparse waveforms with a controlled peak sidelobe level (PSL). In [42] and

[43], sparse frequency constant modulus radar signals with a low integrated sidelobe level (ISL) are built optimizing a suitable combination between the ISL metric and a penalty function accounting for the waveform frequency allocation. In [44], a spectrum-centric signal design is developed based on the minimization of the transmitted energy on a set of disjoint stop-band frequencies under a unimodularity constraint and autocorrelation function (ACF) masking. In [45], a friendly spectral shaped radar waveform design is considered to allow the coexistence of the radar with one or more communication systems. Finally, in [46], the design of sparse frequency waveform with low ISL values is addressed.

In this chapter, following the WDD paradigm, we provide a unifying and systematic approach that summarizes some recent results on waveform optimization with spectral compatibility requirements [47–49]. Specifically, we present an optimization theory-based waveform design framework that attempts to enhance the target detection probability while controlling both the amount of interfering energy produced in the licensed bands and some desirable features of the transmitted waveform. It is supposed that the radar system has the ability to predict the behaviour of surrounding licensed RF systems, for instance using a radio environmental map (REM) [50], containing geographical features, available wireless services and their spectral regulations and locations and activities of the transmitters. This is the key to an efficient adaptation as the aforementioned information allows an intelligent spectrum utilization in a spectrally crowded environment. More in details, the described approach considers as figure of merit the signal to interference plus noise ratio (SINR) and jointly optimizes the radar code and the receive filter constraining the amount of interference energy on crowded/reserved frequency bands. Both signal-dependent and signal-independent interference scenarios are addressed. To manage some relevant features of the probing signal, other than an energy constraint, a similarity constraint is enforced on the transmit sequence, so as to control significant characteristics of the waveform, such as range-Doppler resolution, variations in the signal modulus, and PSL.

Significantly, the similarity and the spectral compatibility constraints are generally competing requirements that may lead to an unfeasible design problem. Hence, the feasibility of the resulting waveform design is analyzed by means of the interference/similarity (I/S) achievable region, namely the set of the admissible interference and similarity levels. Then, solution techniques leading to optimized waveform both in the presence of signal-independent and signal-dependent interference are presented. Finally, some interesting case studies are reported highlighting the trade-off among the achievable SINR, spectral shape, and ACF features of the synthesized signals. The results illustrate the effectiveness of the considered waveform design framework and show that high SINR values and enhanced interference suppression capabilities can be traded off with a partial degradation in terms of autocorrelation properties, in both signal-dependent and signal-independent interference scenario.

The remainder of the chapter is organized as follows. In Section 3.2, the model for the radar transmitted signal, the description of coexisting wireless systems, and the formulation of the waveform design problem are reported. In Section 3.3, the

joint design of the transmit code and receive filter in the presence of signal-independent disturbance is addressed, and the performance of the described algorithm analyzed. In Section 3.4, the signal-dependent interference environment is considered, and the effectiveness of the described procedure assessed. Finally, Section 3.5 is devoted to conclusions and proposals for possible future research tracks.

3.2 System model and problem formulation

Let $c(t)$ be the baseband equivalent of the transmitted radar pulse modelled as the superposition of N linearly modulated unitary energy sub-pulses complying with some specific regularity conditions [47]. The code element associated with the ith sub-pulse is denoted $c(i)$ and the vector $\boldsymbol{c} = [c(1), \ldots, c(N)]^T \in \mathbb{C}^N$ represents the fast-time radar code. The waveform at the receiver end is down-converted to baseband, undergoes a sub-pulse matched filtering operation, and then is sampled [47].

As a result, the N-dimensional column vector $\boldsymbol{v} = [v(1), \ldots, v(N)]^T \in \mathbb{C}^N$ of the fast time observations from the range-azimuth cell under test can be expressed as

$$\boldsymbol{v} = \alpha_T \boldsymbol{c} + \boldsymbol{n} \tag{3.1}$$

with α_T a complex parameter accounting for channel propagation and backscattering effects from the target within the range-azimuth bin of interest and $\boldsymbol{n}$ the N-dimensional column vector containing the filtered disturbance signal samples. Specifically, the vector $\boldsymbol{n}$ accounts for both signal-independent and signal-dependent interference and it is modelled as a complex, zero-mean, circularly symmetric Gaussian random vector with positive definite covariance matrix $\mathbb{E}[\boldsymbol{n}\boldsymbol{n}^\dagger] = \boldsymbol{M}(\boldsymbol{c})$, possibly depending on $\boldsymbol{c}$. In Sections 3.3 and 3.4, further details about these interference models as well as their practical relevance are provided.

Concerning the licensed systems coexisting with the radar of interest, it is supposed that each of them is operating over a frequency band $\Omega_k = [f_1^k, f_2^k]$, $k = 1, \ldots, K$, where f_1^k and f_2^k denote the lower and upper normalized frequencies for the kth system, respectively. To ensure spectral compatibility with the surrounding licensed telecommunication services, the radar has to properly shape its transmitted waveform to manage the amount of interfering energy produced on the shared frequency bands. Indeed, from an analytical point of view, the energy transmitted in the kth band can be essentially computed as

$$\int_{f_1^k}^{f_2^k} S_c(f)df = \boldsymbol{c}^\dagger \boldsymbol{R}_I^k \boldsymbol{c} \tag{3.2}$$

where

$$S_c(f) = \left| \sum_{i=1}^{N} \boldsymbol{c}(i) e^{-j2\pi f(i-1)} \right|^2 \tag{3.3}$$

is the energy spectral density (ESD) of the fast-time code $\boldsymbol{c}$ and

$$\boldsymbol{R}_I^k(m,l) = \begin{cases} f_2^k - f_1^k & m = l \\ \dfrac{e^{j2\pi f_2^k(m-l)} - e^{j2\pi f_1^k(m-l)}}{j2\pi(m-l)} & m \neq l \end{cases} \qquad (m,l) \in \{1,\ldots,N\}^2 \tag{3.4}$$

Thus, denoting by E_I, the amount of allowed interference, to overlay the radar with K coexisting telecommunication networks, the transmitted waveform has to fulfil the constraint

$$\boldsymbol{c}^\dagger \boldsymbol{R}_I \boldsymbol{c} \leq E_I \tag{3.5}$$

where

$$\boldsymbol{R}_I = \sum_{k=1}^{K} w_k \boldsymbol{R}_I^k \tag{3.6}$$

Significantly, different weights and importance can be given to the coexisting wireless networks, for instance based on their distance from the radar, their relative angular positions with respect to the actual radar boresight, and their tactical importance (i.e., navigation systems, military communications, public services, etc.), by suitably choosing the coefficients $w_k \geq 0, k = 1,\ldots,K$.

3.2.1 Code design optimization problem

In this subsection, a waveform design approach that attempts to enhance the target detection probability while controlling both the amount of interfering energy produced in the licensed bands and some desirable features of the transmitted waveform is introduced. To this end, recall that in a Gaussian interference environments, the detection probability is maximized by jointly designing the radar code $\boldsymbol{c}$ and the receive filter $\boldsymbol{w} \in \mathbb{C}^N$ so as to optimize the SINR, defined as

$$\mathrm{SINR}(\boldsymbol{c},\boldsymbol{w}) = \frac{|\alpha_T|^2 |\boldsymbol{w}^\dagger \boldsymbol{c}|^2}{\boldsymbol{w}^\dagger \boldsymbol{M}(\boldsymbol{c}) \boldsymbol{w}} \tag{3.7}$$

To control some relevant features of the probing signal, other than an energy constraint, a similarity constraint is enforced on the transmit sequence, $\|\boldsymbol{c} - \boldsymbol{c}_0\|^2 \leq \varepsilon$, where the parameter $0 \leq \varepsilon \leq 2$ rules the size of the trust hypervolume and $\boldsymbol{c}_0$ is a suitable reference code. There are several reasons that motivate the use of this constraint. In a nutshell, an unconstrained optimization can lead to signals with significant modulus variations, poor range resolution, high PSL and more generally with an undesired ambiguity function response. These drawbacks can be partially circumvented forcing the solution to be similar to a known code $\boldsymbol{c}_0$ ($\|\boldsymbol{c}_0\|^2 = 1$), which shares some nice properties such as constant modulus and a reasonable PSL.

Summarizing, leveraging on the aforementioned guidelines, the waveform design problem of interest can be formulated as the following non-convex optimization problem

$$\mathrm{P}\begin{cases} \max\limits_{\boldsymbol{c},\boldsymbol{w}} & \mathrm{SINR}(\boldsymbol{c},\boldsymbol{w}) \\ \text{s.t.} & \|\boldsymbol{c}\|^2 = 1 \\ & \boldsymbol{c}^{\dagger}\boldsymbol{R}_I\boldsymbol{c} \le E_I \\ & \|\boldsymbol{c}-\boldsymbol{c}_0\|^2 \le \varepsilon \end{cases} \tag{3.8}$$

3.2.2 Cognitive spectrum awareness

To quantify and control the amount of interference induced on coexisting telecommunication networks, the radar needs to know the number K of coexisting licensed systems, their bandwidth (referred to as stop-band in the following and defined by the lower and upper normalized frequencies f_1^k and f_2^k), and the penalty weights w_k's to assign to each competing system [see Equation (3.6)]. It is thus of paramount importance for the sensing radar to have an accurate, reliable and comprehensive radio environment awareness. REM [50] represents the key to gain the aforementioned spectrum cognizance that is at the base of an intelligent and agile spectrum management. First introduced by the Virginia Tech team [51] as the main foundation for a novel approach to CR networking, REM can be considered as an *abstraction* of real-world radio scenarios and can be considered as an integrated database digitizing and indexing the available e.m. information.

Figure 3.1 illustrates some REM multidomain knowledge sources represented by geographical features, available services and spectral regulations, locations and activities of telecommunication networks and previous sensing acquisitions (radio experiences and measurements) [52,53]. Indeed, the idea behind REM is to store and process a variety of data, so as to make possible the inference of a multitude of environmental characteristics, such as locations of transmitters, prevailing propagation conditions and estimates of spectrum usage over time and space. Thus, REM offers a suitable vehicle of Cognitive Radio (CR) system support, which can be exploited by cognitive engines for most cognitive functionalities, such as situation awareness, learning, reasoning, planning and decision support.

To populate and update the REM, both *a priori* knowledge as well as spectral sensing techniques (like feature-based signal detectors) can be used [53]. Furthermore, as depicted in Figure 3.1, a dedicated sensor network could be also employed to improve the quality of the scenario monitoring. Obviously, the better the characterization and modelling of the radio environment, the more the system can benefit by *a priori* information and past experiences and adapt to the operational environment. Summarizing, exploiting the REM, the radar can become aware of the surrounding e.m. environment; hence, it can intelligently use the available data/information/knowledge sources to make an agile transmission suitably diversifying the probing waveform [29]. In addition, a prediction of the overlaid networks

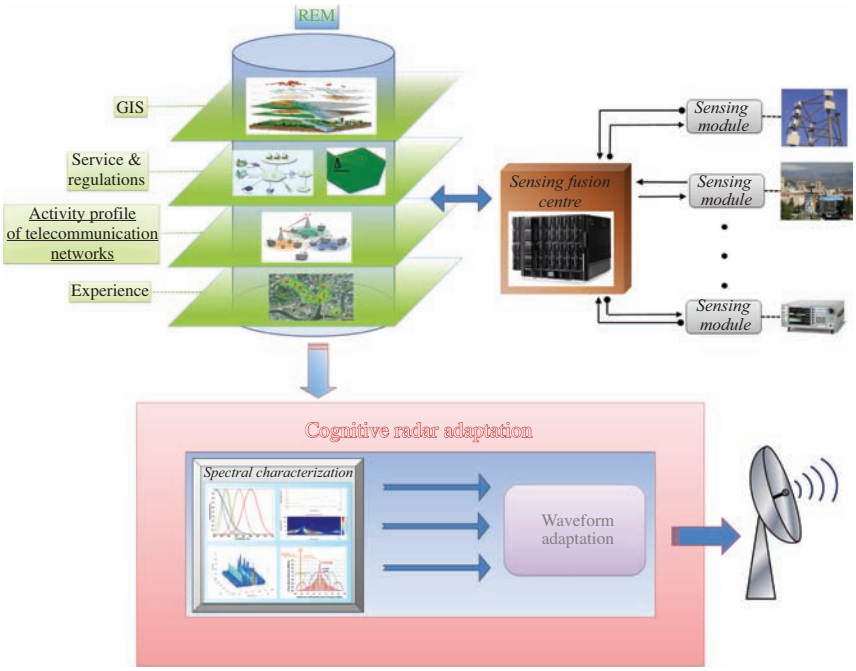

Figure 3.1 A pictorial representation of the REM and its usage in a cognitive radar

coverage can be obtained and used together with the radar antenna pointing direction, to select a suitable weight w_k for each stop-band.

3.2.3 Feasibility issues

The similarity and the spectral compatibility constraints are generally competing requirements that may lead to an unfeasible design problem. For instance, assuming $\varepsilon = 0$ Problem P is infeasible whenever $\boldsymbol{c}_0{}^{\dagger}\boldsymbol{R}_I\boldsymbol{c}_0 > E_I$. This motivates the study of the I/S achievable region for any fixed similarity code $\boldsymbol{c}_0$, namely, the set of the admissible interference and similarity levels. It is defined as

$$\mathscr{F} = \{(E_I, \varepsilon) : E_I \geq \lambda_{\min}(\boldsymbol{R}_I), 0 \leq \varepsilon \leq 2, \text{ problem P is feasible}\} \tag{3.9}$$

and represents the set of pairs (E_I, ε) defining a feasible Problem P. As shown in [47], $\mathscr{F}$ shares some important features, reported below for completeness:

- Each point on the boundary of $\mathscr{F}$ can be computed in a polynomial time;
- $\mathscr{F}$ is a convex set. From a practical point of view, this allows to control its accuracy description. In fact, the convex hull of the I/S levels (E_{Ii}, ε_i) $i = 1, \ldots, N_a$, associated to an arbitrary set of N_a admissible radar codes, is contained in the I/S region;

- Each point on the boundary of $\mathscr{F}$ (with $E_I > \lambda(R_I)$) is uniquely associated to a radar code (under some mild technical conditions). Hence, it is possible to associate to the boundary of the feasible region some important radar performance metrics, such as ISL, PSL and, obviously, the produced interference power.

A graphical example of I/S achievable region is given in Figure 3.2. Therein, it is assumed that the overlaid licensed radiating systems, spectrally coexisting with the radar of interest, are working over the following normalized (according to the sampling frequency $f_s = 810$ kHz) frequency bands [54]:

$$\begin{aligned}
&\Omega_1 = [0.0000, 0.0617], \quad \Omega_2 = [0.0988, 0.2469], \quad \Omega_3 = [0.2593, 0.2840], \\
&\Omega_4 = [0.3086, 0.3827], \quad \Omega_5 = [0.4074, 0.4938], \quad \Omega_6 = [0.5185, 0.5556], \\
&\Omega_7 = [0.9383, 1.0000]
\end{aligned} \tag{3.10}$$

As reference waveform $\boldsymbol{c}_0$, a unitary norm complex linear frequency modulated (LFM) pulse with a duration of 200 μs and a chirp rate $K_s = (750 \times 10^3)/(200 \times 10^{-6})$ Hz/s is considered; moreover, $w_k = 1$ for $k = 1, \ldots, 7$. Further details about the considered simulation setup can be found in Section 3.3.

Before concluding this section, it is worth pointing out that the radar designer can choose the pair (E_I, ε), referred to in the sequel as operative point, to reasonably trade off spectral coexistence, desirable radar waveform characteristics and achievable SINR of the system. For instance, with respect to Figure 3.2, considering (E_I, ε) equal to the point A, the frequency coexistence of the radar with

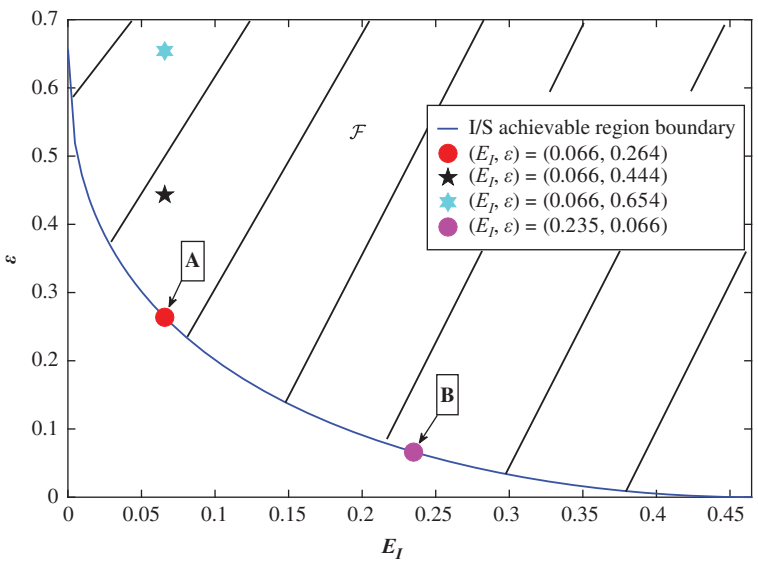

Figure 3.2 I/S achievable region for chirp similarity code and $K = 7$ overlaid licensed wireless systems

the overlaid telecommunication networks is emphasized, with respect to choosing (E_I, ε) equal to the point B. In the last case, other radar features, such as low PSL and/or ISL, are privileged.

The interested reader may refer to Appendix 3.6.1 for all the analytical details concerning the study of the I/S achievable region.

3.3 Signal-independent interference scenario

In this section, the joint design of the transmit code and receive filter is addressed assuming that signal-independent disturbance impairs the useful target return. This is a useful and meaningful model to describe radar scenarios where the main sources to the overall disturbance are represented by white internal thermal noise, hot clutter, interfering signals due to unlicensed and possibly hostile jammers, as well as licensed overlaid telecommunication networks sharing the same frequencies as the radar of interest.

In Appendix 3.6.2, the non-convex optimization Problem P is studied for $\boldsymbol{M}(\boldsymbol{c}) = \bar{\boldsymbol{M}}$, showing that an optimal pair $(\boldsymbol{c}^*, \boldsymbol{w}^*)$ can be devised with a polynomial time procedure [47]. Specifically, exploiting the closed form expression of the optimal filter for fixed transmit signal, Problem P can be recast as a quadratically constrained quadratic programming problem that is, in general, difficult to solve [55]. Hence, some hidden convexities of the resulting problem can be exploited to get the transmit signal and receive filter maximizing the SINR with a polynomial complexity. From a technical point of view, P is equivalent to a Semidefinite Programming (SDP) convex problem whose optimal solution $\boldsymbol{C}^*$ allows the design of $\boldsymbol{c}^*$ and $\boldsymbol{w}^*$ resorting to a specific rank-one decomposition procedure [55]. Figure 3.3 summarizes the main steps involved in the optimal design. Therein, it is highlighted that the Capon filter associated with the resulting optimal code and the perceived interference environment provides the optimal receiver.

The performance of the waveform design technique described in Appendix 3.6.2, i.e., Algorithm 1, is now shown in terms of achievable SINR value, spectral

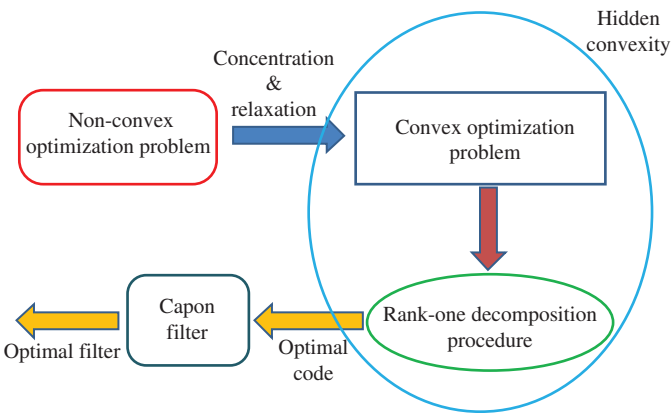

Figure 3.3 Block scheme of the optimization procedure leading to the optimal transmit code receive filter pair

shape and autocorrelation features. Hereafter, a radar whose baseband equivalent transmitted signal has a two-sided bandwidth of 810 kHz and a Nyquist sampling frequency are considered. In addition, the interference is composed of unlicensed narrowband continuous jammers, white interference and licensed coexisting telecommunication networks spectrally overlaid to the radar of interest. Specifically, the disturbance covariance matrix is modelled as:

$$\bar{\boldsymbol{M}} = \sigma_0 \boldsymbol{I} + \sum_{k=1}^{K} \frac{\sigma_{I,k}}{\Delta f_k} \boldsymbol{R}_I^k + \sum_{k=1}^{K_J} \sigma_{J,k} \boldsymbol{R}_{J,k} \tag{3.11}$$

where $\sigma_0 = 0$ dB is the thermal noise level; $K = 7$ is the number of licensed radiating systems; $\sigma_{I,k}$ accounts for the energy of the kth coexisting telecommunication network operating on the normalized frequency band $[f_2^k, f_1^k]$ ($\sigma_{I,k} = 10$ dB, $k = 1, \ldots, K$); $\Delta f_k = f_2^k - f_1^k$ is the bandwidth associated with the kth licensed system, for $k = 1, \ldots, K$; $K_J = 2$ is the number of active and unlicensed narrowband jammers; $\sigma_{J,k}$, $k = 1, \ldots, K_J$, accounts for the energy of the kth active jammer ($\sigma_{J,1\,\mathrm{dB}} = 50$ dB, $\sigma_{J,2\,\mathrm{dB}} = 40$ dB); $\boldsymbol{R}_{J,k}$, $k = 1, \ldots, K_J$, is the normalized disturbance covariance matrix of the kth active unlicensed jammer, defined as $\boldsymbol{R}_{J,k} = \boldsymbol{r}_{J,k} \boldsymbol{r}_{J,k}^{\dagger}$, with $r_{J,k}(n) = e^{j2\pi f_{J,k} n / f_s}$, where $f_{J,k}$ denotes the Doppler shift of the kth jammer ($f_{J,1}/f_s = 0.7$ and $f_{J,2}/f_s = 0.75$).

Concerning the overlaid licensed radiating systems, the baseband equivalent radar stop-bands given in (3.10) are considered. Furthermore, all the licensed/foreseen overlaid systems are assumed with the same relevance, namely, $w_k = 1$ for $k = 1, \ldots, 7$. Based on the assumed stop-bands (3.10) and weights w_k's, the interference energy constraint on the transmitted radar waveform can be now enforced. Notice that, the matrix $\boldsymbol{R}_I$ does not depend on the frequencies of the unlicensed jammers and is the only function of the spectral bands (3.10) and weights associated to the licensed networks. Finally, the LFM pulse in Section 3.2.3 is used as reference waveform $\boldsymbol{c}_0$; it results in $N = 162$ samples due to the considered sampling frequency. The I/S achievable region for the considered scenario is represented in Figure 3.2.

For comparison purpose also, the transmit sequence $\tilde{\boldsymbol{c}}_0$ and the receive filter $\tilde{\boldsymbol{g}}_0$ devised according to the procedure in [39] are considered. Specifically, with reference to the *soft-power constraint* transmit waveform design technique [39], the code $\boldsymbol{c}_0$ is used as starting sequence, and $\delta = 0.9$, $\lambda_T = 10^{-5}$ and $\boldsymbol{R}^{(2)} = \boldsymbol{R}_I$. Moreover, $\beta = 0.05$, $\lambda_T = 10^{-5}$, $\Delta n = 10$ and $\boldsymbol{R}^{(2)} = \boldsymbol{M}$ are used for the receive filter design. The interested reader may refer to [39] for additional details about Lindenfeld's algorithms, the aforementioned parameters and their setting [39].

In Figure 3.4, the ESD, the squared modulus of the ACF, and the normalized SINR of the waveforms devised for three operative points (red dot, black star and cyan hexagram in Figure 3.2) are reported. Specifically, the points $(\bar{E}_I, \varepsilon_i)$, $i = 1, 2, 3$, with $\bar{E}_I = 0.066$, $\varepsilon_1 = 0.264$, $\varepsilon_2 = 0.444$, $\varepsilon_3 = 0.654$ are considered, where $(\bar{E}_I, \varepsilon_1)$ corresponds to the point **A** in Figure 3.2, and the results are compared with those achievable by the signal/receiver pair $(\tilde{\boldsymbol{c}}_0, \tilde{\boldsymbol{g}}_0)$. In Figure 3.4(a), the ESD of the synthesized signals versus the normalized frequency, together with that of the reference code is shown. The stop-bands in which the licensed systems are located are shaded in light grey. The curves highlight the capability of Algorithm 1 to suitably control the amount of energy produced over the shared frequency bands.

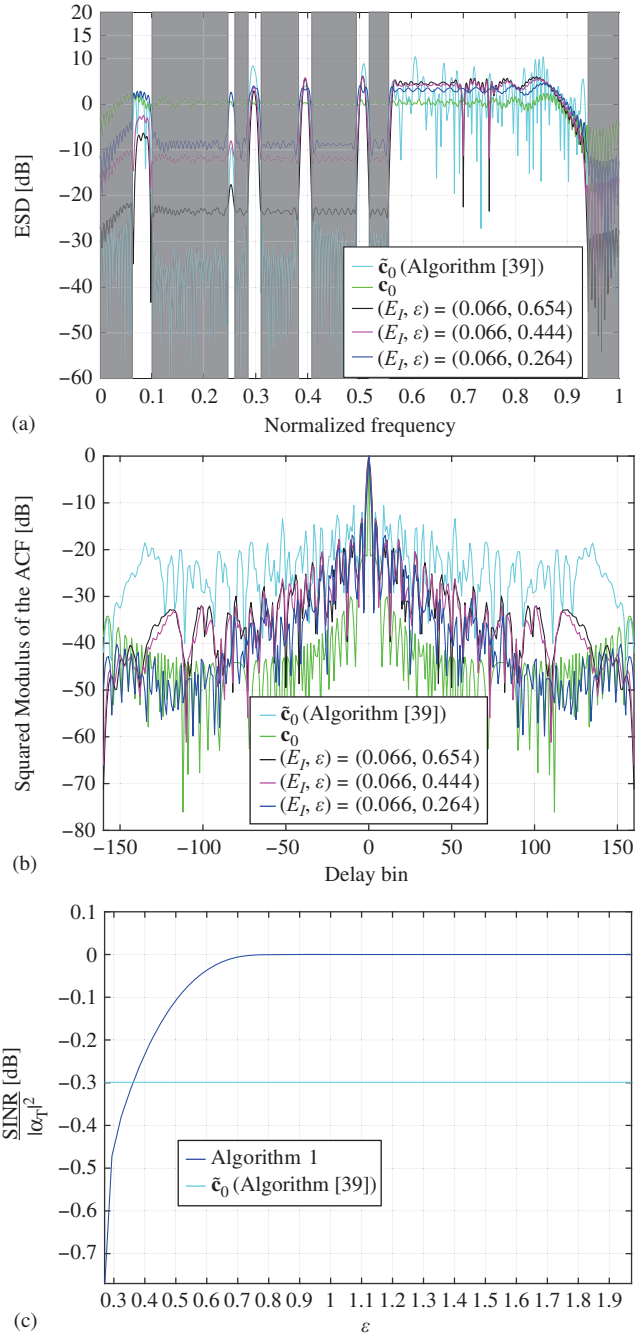

Figure 3.4 *(a) ESD; (b) Squared modulus of the ACF. Green curve: reference code $\mathbf{c}_0$; blue curve: Algorithm 1, $E_I = 0.066$, $\varepsilon = 0.264$; magenta curve: Algorithm 1, $E_I = 0.066$, $\varepsilon = 0.444$; black curve: Algorithm 1, $E_I = 0.066$, $\varepsilon = 0.654$; cyan curve: Algorithm [39]; (c) blue curve: Algorithm 1, Normalized SINR vs ε, $E_I = 0.066$; cyan curve: $\tilde{\mathbf{c}}_0$, Algorithm [39]*

In fact, for each ε, the energy transmitted in the stop-bands is lower than the allowed level, thus ensuring the coexistence with the other transmitting systems.

Significantly, for the considered simulation setup, the transmit signal $\tilde{\boldsymbol{c}}_0$ is capable of ensuring an even greater suppression of the interference at the stop-bands than the devised codes. Nevertheless, this behaviour is quite expected as the signal design technique of [39] only focuses on the coexistence problem. Otherwise stated, the figure of merit is represented by the interference reduction, and no additional constraints are forced neither on the shape of the sought waveform (whose autoambiguity properties are unpredictable) nor on the SINR at the receiver side. On the contrary, the aim of Algorithm 1 is to maximize the attainable SINR, providing at the same time a control over the total amount of interference produced at certain frequencies as well as on the resulting signal shape.

In addition, it can be observed that increasing the similarity parameter ε, smarter and smarter distributions of the useful energy are achieved. Indeed, a progressive reduction of the radar emission in correspondence of the shared frequencies as well as an enhancement of the unlicensed jammer rejection capabilities is highlighted. As a result, higher and higher SINR values can be achieved. This is actually shown in Figure 3.4(c), where the SINR normalized to $|\alpha_T|^2$ is plotted versus ε, assuming $E_I = 0.066$. As expected, a proper choice of the design parameters enables good interference rejection properties as well as high SINR values. It is worth pointing out that, starting from $\varepsilon = 0.72$, with reference to Algorithm 1, the maximum normalized SINR of the system is achieved.

In Figure 3.4(b), a performance analysis in terms of autocorrelation properties of the designed waveforms is provided. Better SINR values, spectral compatibility, and interference rejection are traded-off for worse and worse range resolutions and/or ISLs/PSLs. It can also be observed that the waveform devised through [39] exhibits worse range-sidelobe profiles than those associated with Algorithm 1, reflecting the fact that the algorithm in [39] does not directly control the auto-ambiguity properties of the sought waveform. Nevertheless, the smoother behaviour of the signals synthesized according to Algorithm 1 agrees with the design criterion P. In fact, the optimization problem itself involves a compromise between the desire of lowering the transmitted energy in the stop-bands as well as in correspondence of the jammer central frequencies, and the need of keeping under control the ambiguity features of the sought signals.

3.4 Signal-dependent interference scenario

In this section, a radar operating in a highly reverberating environment is considered and the design Problem P is solved in the presence of signal-dependent interference. This self-induced interference is due to reflections of the signal transmitted by the radar from objects without tactical importance (clutter) located in the surveillance area and, if not properly accounted for at the design stage, can seriously impair the radar performance. Specifically, the overall interference covariance matrix is modelled as

$$\boldsymbol{M}(\boldsymbol{c}) = \sum_{k=-N+1, k\neq 0}^{N-1} \beta_k \boldsymbol{J}_k \boldsymbol{c}\boldsymbol{c}^{\dagger} \boldsymbol{J}_k^T + \bar{\boldsymbol{M}} \tag{3.12}$$

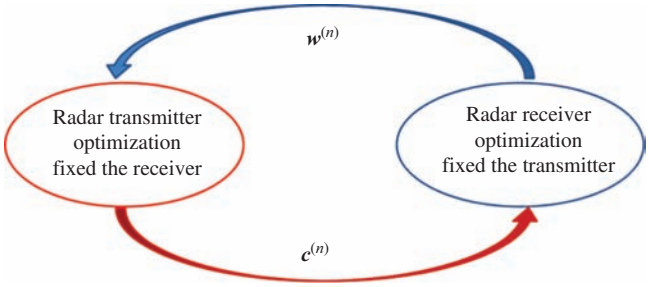

Figure 3.5 Block scheme of the considered transmit-receive optimization procedure in the presence of signal-dependent interference

where $\boldsymbol{J}_k$, $k = \pm 1, \ldots, \pm(N-1)$, denotes the shift matrices[1] [49], $\{\beta_k\}_{k \neq 0}$ represents the mean scatterer powers of the adjacent range cells and $\bar{\boldsymbol{M}}$ is the signal-independent contribution as in Section 3.3. Notice that the prediction of the actual scattering scenario can be accomplished by means of the cognitive framework, i.e., exploiting a dynamic environmental database including a geographical information system, previous scans, meteorological data, some theoretical (or possibly empirical) e.m. reflectivity and spectral clutter models [56,57].

In Appendix 3.6.3, it is shown that in the presence of signal-dependent interference, Problem P boils down to a non-convex quadratically constrained fractional quartic problem that is, in general, very hard to solve [58,59]. Hence, an alternating optimization procedure for the transmit signal and the receive filter design that monotonically improves the SINR is devised. Each iteration of the algorithm, whose convergence is analytically proved, requires the solution of both a convex and a hidden convex optimization problem. In detail, exploiting the Charnes–Cooper [60] transformation and a specific rank-one matrix decomposition procedure, it is shown that the optimal code for a fixed filter can be obtained based on the optimal solution to a specific SDP problem. The resulting computational complexity of the devised algorithm is linear with the number of iterations and polynomial with receive filter length. Figure 3.5 depicts the block diagram of the optimization procedure adopted to handle Problem P when the radar system operates in signal-dependent interference.

Let us now assess the performance of the waveform design technique described in Appendix 3.6.3, i.e., Algorithm 3. The same simulation setup as in Section 3.3 is considered, but with $K = 2$ licensed radiating systems ($\Omega_1 = [0.05, 0.08]$ and $\Omega_2 = [0.4, 0.435]$), a duration of 148 μs for the reference chirp waveform (resulting in $N = 120$ samples) and $\sigma_{J,1} = 25$ dB, $\sigma_{J,2} = 30$ dB. Besides, as to the signal-dependent interference, a uniform clutter environment with $\beta_k = 8$ dB, $k = \pm 1, \ldots, \pm(N-1)$ is assumed and a signal-to-noise power ratio $|\alpha_T|^2/|\sigma_0| = 10$ dB is supposed.

In Figure 3.6(a), the SINR behaviour versus the number of iterations is provided, for the operative points $(\bar{E}_I, \varepsilon_i)$, $i = 1, 2, 3$, with $\bar{E}_I = 0.0017$, $\varepsilon_1 = 0.1$, $\varepsilon_2 = 0.15$ and[2] $\varepsilon_3 = 0.3$. As expected, increasing ε, the optimized SINR value improves as the

[1] $\boldsymbol{J}_k(i,m) = 1$ if $i - m = k$ and $\boldsymbol{J}_k(i,m) = 0$ otherwise, $(l,m) \in \{1, \ldots, N\}^2$, $k = \pm 1, \ldots, \pm(N-1)$.
[2] As starting sequence $\boldsymbol{c}^{(0)}$ to the iterative procedure, the one corresponding to the boundary point $\bar{E}_I = 0.0017$, $\varepsilon_0 = 0.089$ is considered.

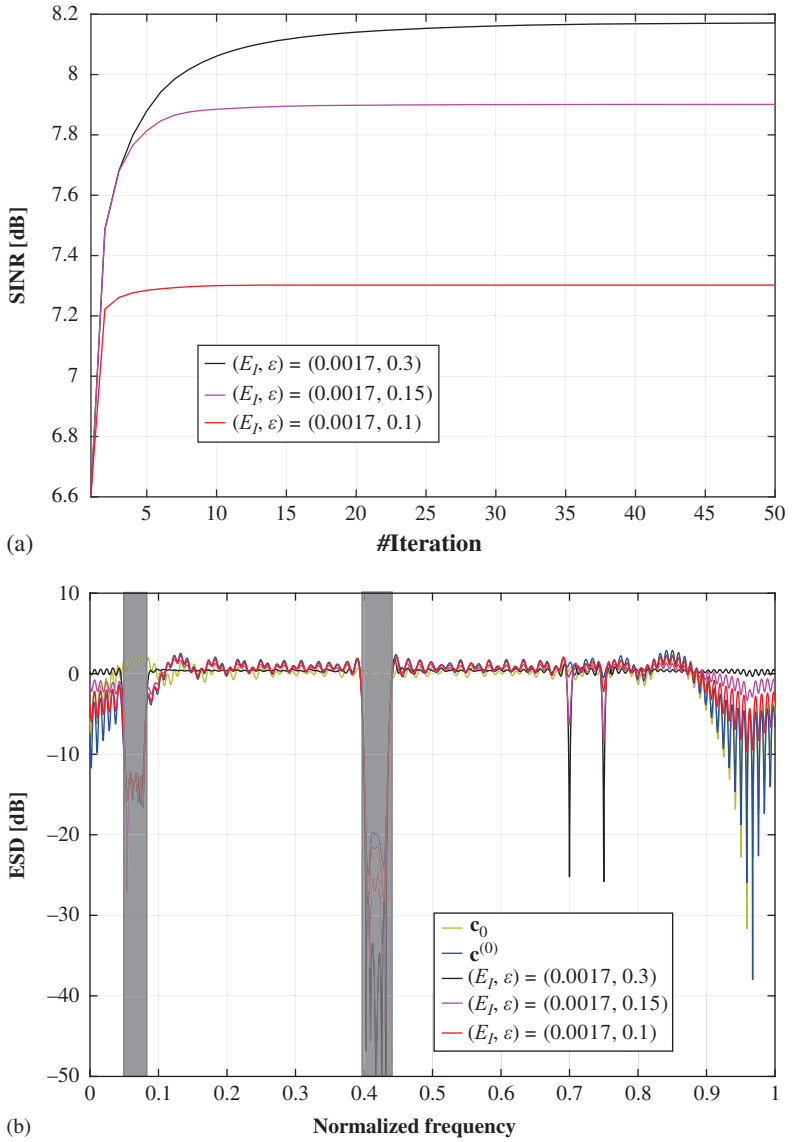

Figure 3.6 (a) SINR; (b) ESD (stop-bands shaded in light grey); brown curve: reference code $\mathbf{c}_0$; blue curve: starting sequence $\mathbf{c}^{(0)}$; red curve: Algorithm 3, $E_I = 0.0017$, $\varepsilon = 0.1$; magenta curve: Algorithm 3, $E_I = 0.0017$, $\varepsilon = 0.15$; black curve: Algorithm 3, $E_I = 0.0017$, $\varepsilon = 0.3$

feasible set of the optimization problem becomes larger and larger (with performance gains up to approximately 1.6 dB). In Figure 3.6(b), with reference to the same operative points of Figure 3.6(a), the ESD of the synthesized signals versus the normalized frequency is reported, together with that of the reference code $\boldsymbol{c}_0$. The stop-bands in which the licensed systems are located are shaded in light grey.

Table 3.1 ISL and PSL of the CCFs for the transmit waveform $\boldsymbol{c}^{(n)}$ and the receive filter $\boldsymbol{w}^{(n)}$, for iteration number $n = 1, 10, 30, 50$ and $(\bar{E}_I, \varepsilon_3) = (0.0017, 0.3)$

n	1	10	30	50
ISL [dB]	−7.91	−10.84	−11.24	−11.28
PSL [dB]	−19.03	−21.53	−22.02	−22.05

The curves show that Algorithm 3 is capable to suitably control the amount of energy produced over the shared frequency bands. In addition, increasing the similarity parameter ε, namely increasing the available degrees of freedom, smarter and smarter distributions of the useful energy are achieved. In fact, as in Figure 3.4(a), both a lower and lower radar radiated energy in correspondence of the shared frequencies and improved jammer rejection capabilities are experienced.

Finally, in Table 3.1, the ISL and the PSL for the cross-correlation functions (CCFs) of the radar codes and receive filters, corresponding to the operative point $(\bar{E}_I, \varepsilon_3) = (0.017, 0.3)$, for different values of the iteration number ($n = 1, 10, 30, 50$) are provided. The values in the table reflect the capability of the considered joint transmit-receive optimization procedure to iteratively achieve better and better signal-dependent disturbance suppression levels.

3.5 Conclusions

The challenging spectrum congestion problem has been addressed through an optimization theory-based radar waveform design approach. Cognition provided by a REM represents the key to an intelligent, dynamic and optimized spectrum allocation. In fact, REM information induces dynamic spectral constraints on the radar waveform that is thus the result of a constrained optimization process aimed at enhancing some radar performance measures, such as detection capabilities and ambiguity function properties, while keeping the mutual interference on frequency overlaid licensed systems to acceptable level. The concept of I/S achievable region has been introduced to control the feasibility of the formulated waveform design optimization problem. Moreover, polynomial computational complexity algorithms leading to optimized radar waveforms, both in the presence of signal-independent and signal-dependent interference, have been presented.

The reported case studies have highlighted the effectiveness of the described procedures to allow a dynamic spectrum-usage optimization. Indeed, the devised waveforms are able to ensure both spectral coexistence with the overlaid RF systems and reasonable detection performance at the possible expense of other radar signal features (as for instance, low sidelobe levels).

The spectrum congestion problem is far from being completely solved due to the ever increasing demand of bandwidth and the presence of technological limitations. In this respect, some open issues involved in the WDD paradigm concern

the control of the transmitted energy on each specific stop-band to fulfil spectral mask regulations, the development of robust frameworks to contrast transmitter impurities, as well as the fully exploitation of the available multiple dimensions, i.e., spatial, temporal and polarizations, to further enhance systems capabilities. Further research activity is necessary toward the synthesis of new advanced adaptive receivers in PBR with improved interference suppression capabilities, the development of commensal radar strategies with enhanced control of the LTE modulations parameters, and the design of radar-embedded communications able to exploit multiple domains to increase data rates.

3.6 Appendix

3.6.1 Feasibility of P

In this appendix, the properties of the set $\mathscr{F}$ are determined. To this end, let us introduce the following optimization problem:

$$(\mathrm{QP})_{E_I}\begin{cases}\min\limits_{\boldsymbol{c}} & \|\boldsymbol{c}-\boldsymbol{c}_0\|^2\\ \text{s.t.} & \boldsymbol{c}^\dagger\boldsymbol{R}_I\boldsymbol{c}\le E_I\\ & \|\boldsymbol{c}\|^2=1\end{cases}\tag{3.13}$$

whose solution and optimal value depend on the variable E_I. It is evident that $(\mathrm{QP})_{E_I}$ is solvable[3] if and only if $\lambda_{\min}(\boldsymbol{R}_I)\le E_I$, as the feasible set of problem $(\mathrm{QP})_{E_I}$ is a compact set and the objective function is a continuous function. Moreover, for any fixed E_I, the pair $(E_I,\varepsilon)\in\mathscr{F}$ if and only if $\varepsilon\ge v((\mathrm{QP})_{E_I})$; notice that for $E_I\ge \boldsymbol{c}_0{}^\dagger\boldsymbol{R}_I\boldsymbol{c}_0$, $v((\mathrm{QP})_{E_I})=0$, thus the focus is mainly on $\lambda_{\min}(\boldsymbol{R}_I)\le E_I\le \boldsymbol{c}_0{}^\dagger\boldsymbol{R}_I\boldsymbol{c}_0$. As a consequence, defining the function

$$\varepsilon(E_I): E_I\in\left[\lambda_{\min}(\boldsymbol{R}_I),\boldsymbol{c}_0{}^\dagger\boldsymbol{R}_I\boldsymbol{c}_0\right]\to v((\mathrm{QP})_{E_I})\in[0,2]\tag{3.14}$$

it holds true that

$$\mathscr{F}=\mathscr{F}_1\cup\mathscr{F}_2\tag{3.15}$$

with

$$\mathscr{F}_1=\left\{(E_I,\varepsilon):\lambda_{\min}(\boldsymbol{R}_I)\le E_I\le \boldsymbol{c}_0{}^\dagger\boldsymbol{R}_I\boldsymbol{c}_0,\varepsilon(E_I)\le\varepsilon\le 2\right\}\tag{3.16}$$

and

$$\mathscr{F}_2=\left\{(E_I,\varepsilon):E_I\ge \boldsymbol{c}_0{}^\dagger\boldsymbol{R}_I\boldsymbol{c}_0,0\le\varepsilon\le 2\right\}\tag{3.17}$$

Remarkably, the key portion of the I/S achievable region is provided by $\mathscr{F}_1$. Based on (3.15), characterizing the I/S achievable region $\mathscr{F}$ is tantamount to

[3]By "solvable", it is meant that the problem is feasible and bounded, and the optimal value is attained, see [61, p. 13].

determine the properties of the function $\varepsilon(E_I)$ given in (3.14). To this end, it can be proved that

Proposition 3.6.1. *For any E_I, $\varepsilon(E_I)$ can be evaluated solving the following SDP problem*

$$(\overline{\text{QP}})_{E_I}\begin{cases}\max\limits_{\boldsymbol{C}} & \text{tr}(\boldsymbol{C}\boldsymbol{C}_0)\\ \text{s.t.} & \text{tr}(\boldsymbol{C}) = 1\\ & \text{tr}(\boldsymbol{C}\boldsymbol{R}_I) \le E_I\\ & \boldsymbol{C} \succcurlyeq \boldsymbol{0}\end{cases} \tag{3.18}$$

namely $\varepsilon(E_I) = 2 - 2\sqrt{(v((\overline{\text{QP}})_{E_I})}$.

Proof. See Section 3.6.1.1. □

The above proposition implies that $\varepsilon(E_I)$ can be evaluated in polynomial time. Moreover, the function $\varepsilon(E_I)$ shares the following properties.

Proposition 3.6.2. *The function $\varepsilon(E_I)$ is a strictly decreasing and convex function.*

Proof. See Section 3.6.1.2. □

Notice that, through Proposition 3.6.2, it can be claimed that the I/S achievable region $\mathscr{F}$ is a convex set, and that the function $\varepsilon(E_I)$ is invertible, with its inverse function $E_I(\varepsilon)$ defined as the optimal solution to the optimization problem

$$(\text{QP})_{\varepsilon}\begin{cases}\min\limits_{\boldsymbol{c}} & \boldsymbol{c}^{\dagger}\boldsymbol{R}_I\boldsymbol{c}\\ \text{s.t.} & \|\boldsymbol{c}-\boldsymbol{c}_0\|^2 \le \varepsilon\\ & \|\boldsymbol{c}\|^2 = 1\end{cases} \tag{3.19}$$

In addition, as the I/S achievable region is a convex set, from a practical point of view, its accuracy description can be controlled. In fact, the convex hull of the I/S levels (E_{Ii}, ε_i) $i = 1, \ldots, N_a$, associated to an arbitrary set of N_a admissible radar codes, is contained in the I/S region.

The following important property, regarding the I/S achievable region, characterizes the radar codes belonging to the boundary of the I/S achievable region. Precisely, it can be proved that

Proposition 3.6.3. *Let $\boldsymbol{U}\,\text{diag}(\boldsymbol{\lambda})\boldsymbol{U}^{\dagger} = \boldsymbol{R}_I$ be the eigenvalue decomposition of $\boldsymbol{R}_I$, with $\boldsymbol{U}$ a unitary matrix and $\lambda(1) \ge \lambda(2) \ge \ldots \ge \lambda(N) > 0$ (where the eigenvalues are not all equal), and let $\boldsymbol{x}_0 = \boldsymbol{U}^{\dagger}\boldsymbol{c}_0$ the transformed reference code. Assuming $x_0(N) \ne 0$ and $\lambda(N) < \boldsymbol{c}_0^{\dagger}\boldsymbol{R}_I\boldsymbol{c}_0$, the optimal solution to (3.19) is unique for any $0 \le \varepsilon < \varepsilon(\lambda(N))$, namely each point on the boundary of the I/S achievable region, is uniquely associated to a radar code.*

Proof. See Section 3.6.1.3. □

Based on Proposition 3.6.3, some important radar performance metrics, such as ISL, PSL and, obviously, the produced interference power can be associated to the boundary of the feasible region. Whenever these metrics are computed, the designer can look at the boundary of the feasibility region and determine the operating point

sharing the desired radar features. Hence, the designer can select a proper pair (ε, E_I) and optimize the SINR by moving in a neighbourhood of the selected operating point.

3.6.1.1 Proof of Proposition 3.6.1

As $\|\boldsymbol{c}-\boldsymbol{c}_0\|^2 = 2 - 2\mathrm{Re}(\boldsymbol{c}^\dagger \boldsymbol{c}_0)$, problem $(\mathrm{QP})_{E_I}$ is equivalent to problem

$$(\mathrm{QP})'_{E_I}\begin{cases}\max\limits_{\boldsymbol{c}} & |\boldsymbol{c}^\dagger \boldsymbol{c}_0|^2 \\ \text{s.t.} & \boldsymbol{c}^\dagger \boldsymbol{R}_I \boldsymbol{c} \le E_I \\ & \|\boldsymbol{c}\|^2 = 1\end{cases} \tag{3.20}$$

Indeed, any optimal solution to $(\mathrm{QP})_{E_I}$ is an optimal solution to $(\mathrm{QP})'_{E_I}$ and vice versa, given an optimal solution $\boldsymbol{c}'$ to $(\mathrm{QP})'_{E_I}$, $\boldsymbol{c}' e^{j\arg(\boldsymbol{c}'^\dagger \boldsymbol{c}_0)}$ is an optimal solution to $(\mathrm{QP})_{E_I}$. Furthermore, $v((\mathrm{QP})_{E_I}) = 2 - 2\sqrt{v((\mathrm{QP})'_{E_I})}$. Let us now observe that problem $(\overline{\mathrm{QP}})_{E_I}$ is the SDP relaxation of problem $(\mathrm{QP})'_{E_I}$. Moreover, the feasible set of problem $(\overline{\mathrm{QP}})_{E_I}$ is a compact set; thus, it admits an optimal solution, say $\bar{\boldsymbol{C}}$. As a consequence, resorting to the rank-one matrix decomposition theorem [55, Theorem 2.3], reported as *Lemma 3.6.4* in Appendix 3.6.2, with $\boldsymbol{X} = \bar{\boldsymbol{C}}$, $\boldsymbol{A}_1 = \boldsymbol{C}_0$, $\boldsymbol{A}_2 = \boldsymbol{I}$, $\boldsymbol{A}_3 = \boldsymbol{I}$ and $\boldsymbol{A}_4 = \boldsymbol{R}_I$, it can be claimed that the relaxation is tight, namely $v((\overline{\mathrm{QP}})_{E_I}) = v((\mathrm{QP})'_{E_I})$ and conclude that $v((\mathrm{QP})_{E_I}) = 2 - 2\sqrt{v((\overline{\mathrm{QP}})_{E_I})}$.

3.6.1.2 Proof of Proposition 3.6.2

First of all, let us focus on the convexity of the function $\varepsilon(E_I)$. Consider two points $E_I^{'}$ and $E_I^{''}$ and denote by $\boldsymbol{C}'$ and $\boldsymbol{C}''$ the optimal solutions to problems $(\overline{\mathrm{QP}})_{E_I^{'}}$ and $(\overline{\mathrm{QP}})_{E_I^{''}}$, respectively. As $\forall \lambda \in [0,1]$, $\lambda \boldsymbol{C}' + (1-\lambda)\boldsymbol{C}''$ is a feasible solution to problem $(\overline{\mathrm{QP}})_{\lambda E_I^{'} + (1-\lambda)E_I^{''}}$, exploiting Proposition 3.6.1, it follows that

$$\begin{aligned}\varepsilon\left(\lambda E_I^{'} + (1-\lambda)E_I^{''}\right) &= 2 - 2\sqrt{v\left(\left(\overline{\mathrm{QP}}\right)_{\lambda E_I^{'} + (1-\lambda)E_I^{''}}\right)} \\ &\le 2 - 2\sqrt{\lambda\left(v\left(\left(\overline{\mathrm{QP}}\right)_{E_I^{'}}\right)\right) + (1-\lambda)\left(v\left(\left(\overline{\mathrm{QP}}\right)_{E_I^{'}}\right)\right)} \\ &\le \lambda\varepsilon(E_I^{'}) + (1-\lambda)\varepsilon(E_I^{''})\end{aligned} \tag{3.21}$$

Let us now analyze the monotonicity of $\varepsilon(E_I)$. Let $E_I^{'} < E_I^{''} \le \boldsymbol{c}_0{}^\dagger \boldsymbol{R}_I \boldsymbol{c}_0$ be two values of the allowed interference energy, and let $\boldsymbol{C}'$ be an optimal solution to $(\overline{\mathrm{QP}})_{E_I^{'}}$. As $E_I^{'} < E_I^{''}$, $\boldsymbol{C}'$ is a strictly feasible solution of $(\overline{\mathrm{QP}})_{E_I^{''}}$. Let us define the matrix

$$\boldsymbol{C}^{''} = (1-\alpha)\boldsymbol{C}^{'} + \alpha \boldsymbol{C}_0 \tag{3.22}$$

with $0 < \alpha \le 1$. For $\alpha > 0$ small enough, $\boldsymbol{C}^{''}$ is a feasible point of $(\overline{\mathrm{QP}})_{E_I^{''}}$, as

$$\mathrm{tr}(\boldsymbol{C}^{''}) = 1 \tag{3.23}$$

$$\mathrm{tr}(\boldsymbol{C}^{''}\boldsymbol{R}_I) = (1-\alpha)\mathrm{tr}(\boldsymbol{C}'\boldsymbol{R}_I) + \alpha\mathrm{tr}(\boldsymbol{C}_0\boldsymbol{R}_I) \le E_I^{''} \tag{3.24}$$

Furthermore, for all $\alpha > 0$

$$\begin{aligned}\mathrm{tr}(\boldsymbol{C}''\boldsymbol{C}_0) &= (1-\alpha)\mathrm{tr}(\boldsymbol{C}'\boldsymbol{C}_0) + \alpha\mathrm{tr}(\boldsymbol{C}_0\boldsymbol{C}_0) \\ &= \mathrm{tr}(\boldsymbol{C}'\boldsymbol{C}_0) + \alpha(1-\mathrm{tr}(\boldsymbol{C}'\boldsymbol{C}_0)) \\ &> \mathrm{tr}(\boldsymbol{C}'\boldsymbol{C}_0) \end{aligned} \tag{3.25}$$

where (3.25) follows from the fact that

$$\alpha(1-\mathrm{tr}(\boldsymbol{C}'\boldsymbol{C}_0)) > 0 \tag{3.26}$$

as $\alpha > 0$ and $|\mathrm{tr}(\boldsymbol{C}'\boldsymbol{C}_0)| < \sqrt{\mathrm{tr}(\boldsymbol{C}'\boldsymbol{C}')}\sqrt{\mathrm{tr}(\boldsymbol{C}_0\boldsymbol{C}_0)} \leq \mathrm{tr}(\boldsymbol{C}')\mathrm{tr}(\boldsymbol{C}_0) = 1$.

3.6.1.3 Proof of Proposition 3.6.3

Notice that problem $(\mathrm{QP})_\varepsilon$ is equivalent to

$$(\mathrm{QP})_{\delta_\varepsilon} \begin{cases} \min\limits_{\boldsymbol{x}} & \boldsymbol{x}^\dagger \mathbf{diag}(\boldsymbol{\lambda})\boldsymbol{x} \\ \text{s.t.} & \mathrm{Re}(\boldsymbol{x}^\dagger\boldsymbol{x}_0) \geq \sqrt{\delta_\varepsilon} \\ & \|\boldsymbol{x}\|^2 = 1 \end{cases} \tag{3.27}$$

where $\delta_\varepsilon = (1-\varepsilon/2)^2$, namely, given an optimal solution $\boldsymbol{c}^*$ to $(\mathrm{QP})_\varepsilon$ $\tilde{\boldsymbol{x}} = \boldsymbol{U}^\dagger\boldsymbol{c}^*$ is an optimal solution to $(\mathrm{QP})_{\delta_\varepsilon}$; vice versa, given an optimal solution $\boldsymbol{x}^*$ to $(\mathrm{QP})_{\delta_\varepsilon}$ $\tilde{\boldsymbol{c}} = \boldsymbol{U}\boldsymbol{x}^*$ is an optimal solution to $(\mathrm{QP})_\varepsilon$. Hence, let us focus on $(\mathrm{QP})_{\delta_\varepsilon}$ and $\delta_\varepsilon < 1$ as for $\delta_\varepsilon = 1$, the only optimal solution is $\boldsymbol{x}_0$.

As shown in Proposition 3.6.2, the function $\varepsilon(E_I)$ is a strictly decreasing function; hence, it can be assumed that the optimal solutions to $(\mathrm{QP})_{\delta_\varepsilon}$ are different from $\gamma\boldsymbol{x}_0, \gamma \in \mathbb{C}$. As a consequence, any optimal solution to problem $(\mathrm{QP})_{\delta_\varepsilon}$ is a regular vector.[4] Thus, the first-order optimality conditions imply that for any optimal solution $\boldsymbol{x}^*$ there exist Lagrangian multipliers $\tilde{\mu} \geq 0$ and $\tilde{\nu}$ such that:

- $\boldsymbol{x}^*$ is a stationary point for the Lagrangian function evaluated at $\tilde{\mu}$ and $\tilde{\nu}$, namely, it is a stationary point for

$$f_1(\boldsymbol{x}, \tilde{\mu}, \tilde{\nu}) = \boldsymbol{x}^\dagger \mathbf{diag}(\boldsymbol{\lambda})\boldsymbol{x} + \tilde{\nu}\left(\|\boldsymbol{x}\|^2 - 1\right) + \tilde{\mu}\left(2\sqrt{\delta_\varepsilon} - \boldsymbol{x}^\dagger\boldsymbol{x}_0 - \boldsymbol{x}_0^\dagger\boldsymbol{x}\right) \tag{3.28}$$

- $$\left(2\sqrt{\delta_\varepsilon} - \boldsymbol{x}^{*\dagger}\boldsymbol{x}_0 - \boldsymbol{x}_0^\dagger\boldsymbol{x}^*\right) \leq 0 \tag{3.29}$$

- $$\tilde{\mu}\left(2\sqrt{\delta_\varepsilon} - \boldsymbol{x}^{*\dagger}\boldsymbol{x}_0 - \boldsymbol{x}_0^\dagger\boldsymbol{x}^*\right) = 0 \tag{3.30}$$

- $\|\boldsymbol{x}^*\|^2 = 1$

Let us now observe that all the optimal solutions to $(\mathrm{QP})_{\delta_\varepsilon}$ satisfy $(2\sqrt{\delta_\varepsilon} - \boldsymbol{x}^{*\dagger}\boldsymbol{x}_0 - \boldsymbol{x}_0^\dagger\boldsymbol{x}^*) = 0$. To show this, let us assume that there exists an optimal solution $\boldsymbol{x}_1$ such that $(2\sqrt{\delta_\varepsilon} - \boldsymbol{x}_1{}^\dagger\boldsymbol{x}_0 - \boldsymbol{x}_0^\dagger\boldsymbol{x}_1) < 0$; this means that $\boldsymbol{U}\boldsymbol{x}_1$ is

[4]Given an optimization problem, a feasible point is regular if the gradients of the active constraints are linearly independent [62].

also an optimal solution to $(\mathrm{QP})_{\varepsilon'}$, with $\varepsilon' = \|\boldsymbol{x}_1 - \boldsymbol{x}_0\|^2 < \varepsilon$. This is clearly a contradiction as, from Proposition 3.6.2, $v((\mathrm{QP})_{\varepsilon'}) > v((\mathrm{QP})_{\varepsilon})$.

Differentiating (3.28) with respect to $\boldsymbol{x}$, the first-order necessary optimality condition is obtained

$$(\mathbf{diag}(\boldsymbol{\lambda}) + \tilde{\nu}\boldsymbol{I})\boldsymbol{x} = \tilde{\mu}\boldsymbol{x}_0 \tag{3.31}$$

In addition, based on [63], any optimal solution to (3.27) has to comply with the constraint

$$(\mathbf{diag}(\boldsymbol{\lambda}) + \tilde{\nu}\boldsymbol{I}) \succcurlyeq \mathbf{0} \tag{3.32}$$

namely its Lagrangian multiplier has to satisfy $\tilde{\nu} \geq -\lambda(N)$. Now, let us observe that the condition $\tilde{\nu} = -\lambda(N)$ is impossible. In fact, $\tilde{\mu} \neq 0$, otherwise $\mathbf{c}$ is an eigenvector of $\mathbf{R}_I$ corresponding to $\lambda(N)$. Hence $0 = x_0(N)$, which is clearly a contradiction. Hence, the focus is on $\tilde{\nu} > -\lambda(N)$, which also implies that $(\mathbf{diag}(\boldsymbol{\lambda}) + \tilde{\nu}\boldsymbol{I})$ is not singular.

Based on the first-order optimality condition (3.32), it follows that the optimal solutions share the form:

$$\boldsymbol{x}_{\tilde{\mu},\tilde{\nu}} = \tilde{\mu}(\mathbf{diag}(\boldsymbol{\lambda}) + \tilde{\nu}\boldsymbol{I})^{-1}\boldsymbol{x}_0 \tag{3.33}$$

Now, as for any optimal solution $\boldsymbol{x}^*$, $(2\sqrt{\delta_\varepsilon} - \boldsymbol{x}^{*\dagger}\boldsymbol{x}_0 - \boldsymbol{x}_0^{\dagger}\boldsymbol{x}^*) = 0$, from (3.33) it follows that

$$\boldsymbol{x}_{\tilde{\nu}} = \frac{\sqrt{\delta_\varepsilon}}{\boldsymbol{x}_0^{\dagger}(\mathbf{diag}(\boldsymbol{\lambda}) + \tilde{\nu}\boldsymbol{I})^{-1}\boldsymbol{x}_0}(\mathbf{diag}(\boldsymbol{\lambda}) + \tilde{\nu}\boldsymbol{I})^{-1}\boldsymbol{x}_0 \tag{3.34}$$

with $\tilde{\mu} = \dfrac{\sqrt{\delta_\varepsilon}}{\boldsymbol{x}_0^{\dagger}(\mathbf{diag}(\boldsymbol{\lambda}) + \tilde{\nu}\boldsymbol{I})^{-1}\boldsymbol{x}_0} > 0$. As a consequence, any optimal solution is such that

$$\|\boldsymbol{x}_{\tilde{\nu}}\|^2 = \frac{\delta_\varepsilon}{\left[\boldsymbol{x}_0^{\dagger}(\mathbf{diag}(\boldsymbol{\lambda}) + \tilde{\nu}\boldsymbol{I})^{-1}\boldsymbol{x}_0\right]^2}\|(\mathbf{diag}(\boldsymbol{\lambda}) + \tilde{\nu}\boldsymbol{I})^{-1}\boldsymbol{x}_0\|^2 = 1 \tag{3.35}$$

namely the solutions $\tilde{\nu} > -\lambda(N)$ to the following equation [64] have to be found

$$\frac{\boldsymbol{x}_0^{\dagger}(\mathbf{diag}(\boldsymbol{\lambda}) + \tilde{\nu}\boldsymbol{I})^{-2}\boldsymbol{x}_0}{\left[\boldsymbol{x}_0^{\dagger}(\mathbf{diag}(\boldsymbol{\lambda}) + \tilde{\nu}\boldsymbol{I})^{-1}\boldsymbol{x}_0\right]^2} = \frac{1}{\delta_\varepsilon} \tag{3.36}$$

Notice that Equation (3.36) can be obtained equating to zero the first-order derivative of the following function:

$$g(\tilde{\nu}) = -\tilde{\nu} + \frac{\delta_\varepsilon}{\boldsymbol{x}_0^{\dagger}(\mathbf{diag}(\boldsymbol{\lambda}) + \tilde{\nu}\boldsymbol{I})^{-1}\boldsymbol{x}_0} = -\tilde{\nu} + \frac{\delta_\varepsilon}{\sum\limits_{i=1}^{N}\frac{|\boldsymbol{x}_0(i)|^2}{\lambda(i)+\tilde{\nu}}} \tag{3.37}$$

In particular, the left hand side (LHS) of (3.36) is proportional to the first-order derivative of (3.37) but for constant term.

As (3.37) is a strictly concave function for $\tilde{\nu} > -\lambda(N)$, the LHS of (3.36) is a strictly decreasing function. Hence, there exists a unique solution $\tilde{\nu}$ to (3.36).

Notice that the LHS of (3.36) converges to one as $\tilde{\nu} \to \infty$ and to $\frac{1}{\sum_{i=N-M+1}^{N} |\boldsymbol{x}_0(i)|^2}$ as $\tilde{\nu} \to -\lambda(N)$ (M is the dimension of the eigenspace associated to the smallest eigenvalue $\lambda(N)$). As the assumption $\varepsilon < \varepsilon(\lambda(N))$ implies that all the eigenvectors associated to the smallest eigenvalue of $\boldsymbol{R}_I$ are not feasible for $(\mathrm{QP})_\varepsilon$, then $\sum_{i=N-M+1}^{N} |\boldsymbol{x}_0(i)|^2 < \delta_\varepsilon$: otherwise, the eigenvector $\frac{1}{\sqrt{\sum_{i=N-M+1}^{N} |\boldsymbol{x}_0(i)|^2}}$ $[0, 0, \ldots, 0, x_0(N-M+1), \ldots, x_0(N)]$ would be feasible. Hence, there exists a unique optimal solution to $(\mathrm{QP})_\varepsilon$.

3.6.2 *Waveform design algorithm for signal-independent scenario*

In this section, it is formally shown how an optimal solution to the non-convex optimization problem P can be computed in polynomial time as the radar operates in the presence of signal-independent interference. First of all, let us observe that after the filter concentration, the design problem boils down in

$$\mathrm{P}_1 \begin{cases} \max\limits_{\boldsymbol{c}} & \boldsymbol{c}^\dagger \boldsymbol{R} \boldsymbol{c} \\ \text{s.t.} & \|\boldsymbol{c}\|^2 = 1 \\ & \boldsymbol{c}^\dagger \boldsymbol{R}_I \boldsymbol{c} \le E_I \\ & Re\left(\boldsymbol{c}^\dagger \boldsymbol{c}_0\right) \ge 1 - \varepsilon/2 \end{cases} \tag{3.38}$$

where $\boldsymbol{R} = \bar{\boldsymbol{M}}^{-1}$. Now, an optimal solution to P_1 can be obtained from an optimal solution to the following enlarged quadratic problem (EQP)

$$\mathrm{P}_2 \begin{cases} \max_{\boldsymbol{c}} & \boldsymbol{c}^\dagger \boldsymbol{R} \boldsymbol{c} \\ \text{s.t.} & \|\boldsymbol{c}\|^2 = 1 \\ & \boldsymbol{c}^\dagger \boldsymbol{R}_I \boldsymbol{c} \le E_I \\ & Re^2\left(\boldsymbol{c}^\dagger \boldsymbol{c}_0\right) + Im^2\left(\boldsymbol{c}^\dagger \boldsymbol{c}_0\right) = \boldsymbol{c}^\dagger \boldsymbol{c}_0 \boldsymbol{c}_0{}^\dagger \boldsymbol{c} \ge \delta_\varepsilon \end{cases} \tag{3.39}$$

In fact, as the feasible region of P_2 is larger than that of P_1, every optimal solution of P_2, which is feasible for P_1, is also an optimal solution for P_1 [65]. Thus, assume that $\bar{\boldsymbol{c}}$ is an optimal solution to P_2 and let $\phi = \arg(\bar{\boldsymbol{c}}^\dagger \boldsymbol{c}_0)$. It is easily seen that $\bar{\boldsymbol{c}} e^{j\phi}$ is still an optimal solution to P_2. Now, observing that $(\bar{\boldsymbol{c}} e^{j\phi})^\dagger \boldsymbol{c}_0 = |\bar{\boldsymbol{c}}^\dagger \boldsymbol{c}_0|$, $\bar{\boldsymbol{c}} e^{j\phi}$ is a feasible solution to P_1. In other words, $\bar{\boldsymbol{c}} e^{j\arg(\bar{\boldsymbol{c}}^\dagger \boldsymbol{c}_0)}$ is optimal for both P_1 and P_2.

Now, an optimal solution to P_2 has to be found and, to this end, the following equivalent matrix formulation is exploited

$$\mathrm{P}_2 \begin{cases} \max\limits_{\boldsymbol{C}} & \mathrm{tr}(\boldsymbol{C}\boldsymbol{R}) \\ \text{s.t.} & \mathrm{tr}(\boldsymbol{C}) = 1 \\ & \mathrm{tr}(\boldsymbol{C}\boldsymbol{R}_I) \le E_I \\ & \mathrm{tr}(\boldsymbol{C}\boldsymbol{C}_0) \ge \delta_\varepsilon \\ & \boldsymbol{C} = \boldsymbol{c}\boldsymbol{c}^\dagger \end{cases} \tag{3.40}$$

where $\boldsymbol{C}_0 = \boldsymbol{c}_0\boldsymbol{c}_0^\dagger$. All the non-convexity of problem P_3 is now confined in the rank-one constraint $\boldsymbol{C} = \boldsymbol{c}\boldsymbol{c}^\dagger$.

Problem (3.40) can be relaxed into a convex SDP optimization problem, neglecting the rank-one constraint [66]. By doing so, an EQP relaxed (EQPR) is obtained

$$\mathrm{P}_3 \begin{cases} \max\limits_{\boldsymbol{C}} & \mathrm{tr}(\boldsymbol{C}\boldsymbol{R}) \\ \text{s.t.} & \mathrm{tr}(\boldsymbol{C}) = 1 \\ & \mathrm{tr}(\boldsymbol{C}\boldsymbol{R}_I) \leq E_I \\ & \mathrm{tr}(\boldsymbol{C}\boldsymbol{C}_0) \geq \delta_\varepsilon \\ & \boldsymbol{C} \succcurlyeq \boldsymbol{0} \end{cases} \tag{3.41}$$

Let us now observe that problem P_3 is solvable; in fact, the feasible set

$$\begin{cases} \mathrm{tr}(\boldsymbol{C}) = 1 \\ \mathrm{tr}(\boldsymbol{C}\boldsymbol{R}_I) \leq E_I \\ \mathrm{tr}(\boldsymbol{C}\boldsymbol{C}_0) \geq \delta_\varepsilon \\ \boldsymbol{C} \succcurlyeq \boldsymbol{0} \end{cases} \tag{3.42}$$

is a compact set (closed and bounded) and the objective function of P_3 is continuous; furthermore, as shown in Section 3.6.2.1, assuming that problem P is strictly feasible, problem P_3 is strictly feasible. This property can be of paramount importance from a numerical point of view, as it guarantees that at any optimal point the complementary conditions are satisfied [61] and interior point methods [65] can be used.

To prove the hidden convexity of problem P_2, namely that the relaxation of P_2 into P_3 is tight, a rank-one optimal solution $\bar{\boldsymbol{c}}\bar{\boldsymbol{c}}^\dagger$ to P_3 is constructed starting from an arbitrary rank optimal solution $\bar{\boldsymbol{C}}$ to problem P_2. To this end, the rank-one matrix decomposition theorem [55, Theorem 2.3], which is cited as the following lemma, is used.

Lemma 3.6.4. *Let $\boldsymbol{X}$ be a non-zero $N \times N$ ($N \geq 3$) complex Hermitian positive semidefinite matrix and $\{\boldsymbol{A}_1, \boldsymbol{A}_2, \boldsymbol{A}_3, \boldsymbol{A}_4\}$ be Hermitian matrices, and suppose that $(\mathrm{tr}(\boldsymbol{Y}\boldsymbol{A}_1), \mathrm{tr}(\boldsymbol{Y}\boldsymbol{A}_2), \mathrm{tr}(\boldsymbol{Y}\boldsymbol{A}_3), \mathrm{tr}(\boldsymbol{Y}\boldsymbol{A}_4)) \neq (0,0,0,0)$ for any non-zero complex Hermitian positive semidefinite matrix $\boldsymbol{Y}$ of size $N \times N$. Then,*

- *if* $\mathrm{rank}(\boldsymbol{X}) \geq 3$, *one can find, in polynomial time, a rank-one matrix $\boldsymbol{x}\boldsymbol{x}^\dagger$ such that $\boldsymbol{x}$ (synthetically denoted as $\boldsymbol{x} = \mathscr{D}_1(\boldsymbol{X}, \boldsymbol{A}_1, \boldsymbol{A}_2, \boldsymbol{A}_3, \boldsymbol{A}_4)$) is in* $\mathrm{range}(\boldsymbol{X})$, *and*

$$\boldsymbol{x}^\dagger \boldsymbol{A}_i \boldsymbol{x} = \mathrm{tr}(\boldsymbol{X}\boldsymbol{A}_i), \quad i = 1,2,3,4 \tag{3.43}$$

- *if* $\mathrm{rank}(\boldsymbol{X}) = 2$, *for any $\boldsymbol{z}$ not in the range space of $\boldsymbol{X}$, one can find a rank-one matrix $\boldsymbol{x}\boldsymbol{x}^\dagger$ such that $\boldsymbol{x}$ [synthetically denoted as $\boldsymbol{x} = \mathscr{D}_2(\boldsymbol{X}, \boldsymbol{A}_1, \boldsymbol{A}_2, \boldsymbol{A}_3, \boldsymbol{A}_4)$] is in the linear subspace spanned by $\{\boldsymbol{z}\} \cup \mathrm{range}(\boldsymbol{X})$, and*

$$\boldsymbol{x}^\dagger \boldsymbol{A}_i \boldsymbol{x} = \mathrm{tr}(\boldsymbol{X}\boldsymbol{A}_i), \quad i = 1,2,3,4 \tag{3.44}$$

Let us check the applicability of Lemma 3.6.4 to both $\bar{\boldsymbol{C}}$ and the matrix parameters of P_3. Indeed, the condition $N \geq 3$ is mild and practical (the number of transmitted pulses is usually greater than or equal to 3). Now, in order to verify

$$(\mathrm{tr}(\boldsymbol{YR}), \mathrm{tr}(\boldsymbol{YI}), \mathrm{tr}(\boldsymbol{YR}_I), \mathrm{tr}(\boldsymbol{YC}_0)) \neq (0,0,0,0), \text{ for any non-zero } \boldsymbol{Y} \succcurlyeq \boldsymbol{0} \tag{3.45}$$

it suffices to prove that there is $(a_1, a_2, a_3, a_4) \in \mathbb{R}^4$ such that

$$a_1\boldsymbol{R} + a_2\boldsymbol{I} + a_3\boldsymbol{R}_I + a_4\boldsymbol{C}_0 \succ \boldsymbol{0} \tag{3.46}$$

But this is evident for the matrix parameters[5] of P_3. As a consequence, after constructing a rank-one optimal solution $\bar{\boldsymbol{c}}\bar{\boldsymbol{c}}^\dagger$ to P_3, an optimal solution to P is given by $\boldsymbol{c}^* = \bar{\boldsymbol{c}}e^{j\arg(\bar{\boldsymbol{c}}^\dagger \boldsymbol{c}_0)}$. Algorithm 1 summarizes the procedure leading to an optimal solution to P in the presence of signal-independent interference.

The computational complexity connected with the implementation of the algorithm is polynomial as both the SDP problem and the decomposition of Lemma 3.6.4 can be performed in polynomial time. In fact, the amount of operations, involved in solving the SDP problem, is $O(N^{4.5}\log\frac{1}{\xi})$ [61, p. 250] and the rank-one decomposition requires $O(N^3)$ operations.

Algorithm 1: Algorithm for Cognitive Radar Code Optimization in the Presence of Signal-Independent Interference

Input: $\boldsymbol{c}_0, \boldsymbol{R}, \boldsymbol{R}_I, E_I, \delta_\varepsilon$.
output: An optimal solution $\boldsymbol{c}^*$ to P.

1: solve SDP P_3 finding an optimal solution $\boldsymbol{C}^*$ and the optimal value v^*;
2: **if** $\mathrm{rank}(\boldsymbol{C}^*) = 1$, **then**
3: set $\bar{\boldsymbol{c}} = \sqrt{\lambda_{\max}(\boldsymbol{C}^*)}\boldsymbol{v}$, with $\boldsymbol{v}$ being an eigenvector associated to the maximum eigenvalue of $\boldsymbol{C}^*$;
4: **else**
5: apply the rank-one decomposition theorem [55, Theorem 2.3] to the set of matrices $(\boldsymbol{R}, \boldsymbol{I}, \boldsymbol{R}_I, \boldsymbol{C}^*)$ and get $\bar{\boldsymbol{c}}$;
6: **end**
7: output $\boldsymbol{c}^* = \bar{\boldsymbol{c}}e^{j\arg(\bar{\boldsymbol{c}}^\dagger \boldsymbol{c}_0)}$.

3.6.2.1 Feasibility of P_3

Problem P_3 is strictly feasible due to the strict feasibility of P. In fact, let us assume that $\boldsymbol{c}_s$ is a strictly feasible solution of P, i.e., $\boldsymbol{c}_s^\dagger\boldsymbol{c}_s = 1$, $\boldsymbol{c}_s^\dagger\boldsymbol{R}_I\boldsymbol{c}_s < E_I$ and $|\boldsymbol{c}_s^\dagger\boldsymbol{c}_0|^2 \geq (\mathrm{Re}(\boldsymbol{c}_s^\dagger\boldsymbol{c}_0))^2 > \delta_\varepsilon$. Then there are $\boldsymbol{u}_1, \boldsymbol{u}_2, \ldots, \boldsymbol{u}_{N-1}$ such that

[5]In fact, taking $a_1 = a_3 = a_4 = 0$ and $a_2 = 1$, then $a_1\boldsymbol{R} + a_2\boldsymbol{I} + a_3\boldsymbol{R}_I + a_4\boldsymbol{C}_0 = \boldsymbol{I} \succ \boldsymbol{0}$.

$\boldsymbol{U} = [\boldsymbol{c}_s, \boldsymbol{u}_1, \boldsymbol{u}_2, \ldots, \boldsymbol{u}_{N-1}]$ is a unitary matrix [67], and for any $0 < \eta < 1$ the matrix

$$\boldsymbol{C}_s = (1-\eta)\boldsymbol{U}\boldsymbol{e}_1\boldsymbol{e}_1^{\dagger}\boldsymbol{U}^{\dagger} + \frac{\eta}{N-1}\boldsymbol{U}\left(\boldsymbol{I} - \boldsymbol{e}_1\boldsymbol{e}_1^{\dagger}\right)\boldsymbol{U}^{\dagger} \succ \boldsymbol{0} \tag{3.47}$$

with $\boldsymbol{e}_1 = [1, 0, \ldots, 0]^T$ is a strictly feasible solution of the SDP problem EQPR. In fact,

$$\mathrm{tr}(\boldsymbol{C}_s) = 1 \tag{3.48}$$

$$\mathrm{tr}(\boldsymbol{C}_s\boldsymbol{R}_I) = (1-\eta)\boldsymbol{c}_s^{\dagger}\boldsymbol{R}_I\boldsymbol{c}_s + \frac{\eta}{N-1}\sum_{n=1}^{N-1}\boldsymbol{u}_n^{\dagger}\boldsymbol{R}_I\boldsymbol{u}_n \tag{3.49}$$

$$\mathrm{tr}(\boldsymbol{C}_s\boldsymbol{C}_0) = (1-\eta)\boldsymbol{c}_s^{\dagger}\boldsymbol{C}_0\boldsymbol{c}_s + \frac{\eta}{N-1}\sum_{n=1}^{N-1}\boldsymbol{u}_n^{\dagger}\boldsymbol{C}_0\boldsymbol{u}_n \tag{3.50}$$

which highlight that if η is suitable chosen, then $\boldsymbol{C}_s$ is a strictly feasible solution, i.e., $\mathrm{tr}(\boldsymbol{C}_s) = 1,\ \mathrm{tr}(\boldsymbol{C}_s\boldsymbol{R}_1) > E_I$ and $\mathrm{tr}(\boldsymbol{C}_s\boldsymbol{C}_0) > \delta_{\varepsilon}$.

3.6.3 Waveform design algorithm for signal-dependent scenario

In this section, it is described the polynomial time procedure employed to obtain an optimized solution to the non-convex optimization problem P in the presence of signal-dependent interference. In this case, the design problem is given by

$$\bar{\mathrm{P}}_1 \begin{cases} \max\limits_{\boldsymbol{c},\boldsymbol{w}} & \dfrac{|\alpha_T|^2\left|\boldsymbol{w}^{\dagger}\boldsymbol{c}\right|^2}{\boldsymbol{w}^{\dagger}\boldsymbol{M}(\boldsymbol{c})\boldsymbol{w}} \\ \text{s.t.} & \|\boldsymbol{c}\|^2 = 1 \\ & \boldsymbol{c}^{\dagger}\boldsymbol{R}_I\boldsymbol{c} \le E_I \\ & \|\boldsymbol{c} - \boldsymbol{c}_0\|^2 \le \varepsilon \end{cases} \tag{3.51}$$

Notice that problem $\bar{\mathrm{P}}_1$ is a non-convex optimization problem, as the objective function is a non-convex function and the constraint $\|\boldsymbol{c}\|^2 = 1$ defines a non-convex set. Therefore, following the guidelines in [57], the goal is to derive optimized solutions to $\bar{\mathrm{P}}_1$ via a alternating maximization procedure. The idea is to iteratively improve the SINR, controlling, at the same time, the total amount of energy injected in the licensed bandwidth, as well as radar waveform features. Specifically, given $\boldsymbol{w}^{(n-1)}$, an admissible radar code $\boldsymbol{c}^{(n)}$ at step n improving the SINR corresponding to the receive filter $\boldsymbol{w}^{(n-1)}$ and the transmitted signal $\boldsymbol{c}^{(n-1)}$ is searched. Whenever $\boldsymbol{c}^{(n)}$ is found, the filter $\boldsymbol{w}^{(n)}$ that improves the SINR corresponding to the radar code $\boldsymbol{c}^{(n)}$ and the receive filter $\boldsymbol{w}^{(n-1)}$ is searched, and so on. Otherwise stated, $\boldsymbol{w}^{(n)}$ is used as starting point at step $n+1$. To trigger the procedure, the optimal receive filter $\boldsymbol{w}^{(0)}$, for an admissible code $\boldsymbol{c}^{(0)}$, is considered. Notice that the proposed optimization procedure requires a condition to stop the iterations; to this end, an iteration gain constraint can be forced, namely $|\mathrm{SINR}^{(n)} - \mathrm{SINR}^{(n-1)}| \le \zeta$, where $\zeta \ge 0$ is the desired precision.

From an analytical point of view, $\boldsymbol{w}^{(n)}$ can be computed solving the optimization problem

$$\mathrm{P}_{\boldsymbol{w}}^{(n)} \begin{cases} \max\limits_{\boldsymbol{w}} & \dfrac{|\alpha_T|^2 \left|\boldsymbol{w}^\dagger \boldsymbol{c}^{(n)}\right|^2}{\boldsymbol{w}^\dagger \boldsymbol{M}(\boldsymbol{c}^{(n)})\boldsymbol{w}} \end{cases} \tag{3.52}$$

whose optimal solution, for any fixed $\boldsymbol{c}^{(n)}$, is given by

$$\boldsymbol{w}^{(n)} = \frac{\boldsymbol{M}(\boldsymbol{c}^{(n)})^{-1}\boldsymbol{c}^{(n)}}{\boldsymbol{c}^{(n)\dagger}\boldsymbol{M}(\boldsymbol{c}^{(n)})^{-1}\boldsymbol{c}^{(n)}} \tag{3.53}$$

On the other hand, $\boldsymbol{c}^{(n)}$ is an optimal solution to the following non-convex optimization problem

$$P_{\boldsymbol{c}}^{(n)} \begin{cases} \max\limits_{\boldsymbol{c}} & \dfrac{|\alpha_T|^2 |\boldsymbol{w}^{(n-1)\dagger}\boldsymbol{c}|^2}{\boldsymbol{w}^{(n-1)\dagger}\boldsymbol{M}(\boldsymbol{c})\boldsymbol{w}^{(n-1)}} \\ \text{s.t.} & \|\boldsymbol{c}\|^2 = 1 \\ & \boldsymbol{c}^\dagger \boldsymbol{R}_I \boldsymbol{c} \le E_I \\ & \|\boldsymbol{c} - \boldsymbol{c}_0\|^2 \le \varepsilon \end{cases} \tag{3.54}$$

It is possible to show that problem $\mathrm{P}_{\boldsymbol{c}}^{(n)}$ is a hidden-convex optimization problem. Precisely, its optimal solution can be computed in polynomial time (resorting to the rank-one matrix decomposition theorem [55, Theorem 2.3]), starting from an optimal solution to the SDP problem

$$\bar{\mathrm{P}}_2 \begin{cases} \max\limits_{\boldsymbol{C},t} & \mathrm{tr}(\boldsymbol{Q}\boldsymbol{C}) \\ \text{s.t.} & \mathrm{tr}\big(\boldsymbol{M}_1(\boldsymbol{w}^{(n)})\boldsymbol{C}\big) = 1 \\ & \mathrm{tr}(\boldsymbol{C}) = t \\ & \mathrm{tr}(\boldsymbol{R}_I\boldsymbol{C}) \le tE_I \\ & \mathrm{tr}(\boldsymbol{C}_0\boldsymbol{S}) \ge t\delta_\varepsilon \\ & \boldsymbol{C} \succcurlyeq \boldsymbol{0} \\ & t \ge 0 \end{cases} \tag{3.55}$$

with t an auxiliary variable, $\boldsymbol{C}_0 = \boldsymbol{c}_0\boldsymbol{c}_0^\dagger$, $\boldsymbol{C} \in \mathbb{H}^N$, $\boldsymbol{Q} = \boldsymbol{w}^{(n-1)}\boldsymbol{w}^{(n-1)\dagger}$, $\boldsymbol{M}_1(\boldsymbol{w}^{(n)}) = \sum_{k=-N+1,k\neq 0}^{N-1} \beta_k \boldsymbol{J}_k^T \boldsymbol{w}^{(n-1)} \boldsymbol{w}^{(n-1)\dagger} \boldsymbol{J}_k + \boldsymbol{w}^{(n-1)\dagger}\bar{\boldsymbol{M}}\boldsymbol{w}^{(n-1)}\boldsymbol{I}$ and $\delta_\varepsilon = (1-\varepsilon/2)^2$. Algorithms 2 describes the procedure leading to an optimal solution $\mathrm{P}_{\boldsymbol{c}}^{(n)}$.

Algorithm 2: Algorithm for Radar Code Optimization

Input: $\boldsymbol{M}_1(\boldsymbol{w}^{(n)}), \boldsymbol{Q}, \boldsymbol{R}_I, \boldsymbol{c}_0, \delta_\varepsilon, E_I$.
Output: An optimal solution $\boldsymbol{c}^{(n)}$ to $P_{\boldsymbol{c}}^{(n)}$.

1: solve SDP $\bar{\mathrm{P}}_2$ finding an optimal solution $(\boldsymbol{C}^*, t^*)$ and the optimal value v^*;
2: let $\boldsymbol{C}^* := \boldsymbol{C}^*/t^*$;

3: **if** $\text{rank}(\boldsymbol{C}^*) = 1$ **then**
4: perform an eigen-decomposition $\boldsymbol{C}^* = \boldsymbol{c}^*(\boldsymbol{c}^*)^\dagger$ and get $\boldsymbol{c}^*$
5: **else**
6: apply the rank-one decomposition theorem [55, Theorem 2.3] to the set of matrices $(\boldsymbol{C}^*, \boldsymbol{Q} - v^*\boldsymbol{M}_1(\boldsymbol{w}^{(n)}), \boldsymbol{c}_0\boldsymbol{c}_0^\dagger, \boldsymbol{I}, \boldsymbol{R}_I)$ and get $\boldsymbol{c}^*$;
7: **end**
8: output $\boldsymbol{c}^{(n)} := \boldsymbol{c}^* e^{j\arg(\boldsymbol{c}^{*\dagger}\boldsymbol{c}_0)}$ and terminate.

Finally, Algorithm 3 summarizes the devised alternating optimization procedure. To trigger the recursion, an initial radar code $\boldsymbol{c}^{(0)}$ from which obtaining the optimal filter $\boldsymbol{w}^{(0)}$ is required; a natural choice is $\boldsymbol{c}^{(0)} = \boldsymbol{c}_0$.

Algorithm 3: Algorithm for Transmit-Receive System Design in the Presence of Signal-Dependent Interference

Input: $\{\beta_k\}$, $\bar{\boldsymbol{M}}$, $\boldsymbol{R}_I$, E_I, ε, $\boldsymbol{c}_0$.
Output: A solution $(\boldsymbol{c}^*, \boldsymbol{w}^*)$ to P.
1: set $n = 0$, $\boldsymbol{c}^{(n)} = \boldsymbol{c}_0$,

$$\boldsymbol{w}^{(n)} = \frac{\boldsymbol{M}(\boldsymbol{c}^{(n)})^{-1}\boldsymbol{c}^{(n)}}{\boldsymbol{c}^{(n)\dagger}\boldsymbol{M}(\boldsymbol{c}^{(n)})^{-1}\boldsymbol{c}^{(n)}},$$

and the value of the SINR for the pair $(\boldsymbol{c}^{(n)}, \boldsymbol{w}^{(n)})$;
2: **do**
3: $n = n + 1$;
4: construct the matrix $\boldsymbol{M}_1(\boldsymbol{w}^{(n)})$;
5: solve problem $\text{P}_{\boldsymbol{c}}^{(n)}$ finding an optimal radar code $\boldsymbol{c}^{(n)}$, through the use of Algorithm 2;
6: construct the matrix $\boldsymbol{M}(\boldsymbol{c}^{(n)})$;
7: solve problem $\text{P}_{\boldsymbol{w}}^{(n)}$ finding an optimal receive filter

$$\boldsymbol{w}^{(n)} = \frac{\boldsymbol{M}(\boldsymbol{c}^{(n)})^{-1}\boldsymbol{c}^{(n)}}{\boldsymbol{c}^{(n)\dagger}\boldsymbol{M}(\boldsymbol{c}^{(n)})^{-1}\boldsymbol{c}^{(n)}},$$

and the value of the SINR for the pair $\left(\boldsymbol{c}^{(n)}, \boldsymbol{w}^{(n)}\right)$;
8: let $\text{SINR}^{(n)} = \text{SINR}$;
9: **until** $|\text{SINR}^{(n)} - \text{SINR}^{(n-1)}| \leq \zeta$
10: output $\boldsymbol{c}^* = \boldsymbol{c}^{(n)}$ and $\boldsymbol{w}^* = \boldsymbol{w}^{(n)}$.

As to the computational complexity of Algorithm 3, it is linear with respect to the number of iterations $\bar{N}$, whereas in each iteration, it includes the computation of the inverse of $\boldsymbol{\Sigma}_{\boldsymbol{c}}\left(\boldsymbol{c}^{(n)}\right) + \boldsymbol{R}_{\text{ind}}$ and the complexity effort of Algorithm 2. The former is in the order of $\mathcal{O}(N^3)$. The latter is connected with the complexity of SDP solution, i.e., $\mathcal{O}(N^{4.5})$.

References

[1] M. Wicks, "Spectrum Crowding and Cognitive Radar", *International Workshop on Cognitive Information Processing (CIP)*, pp. 452–457, Elba Island, Italy, 14–16 June 2010.

[2] L. S. Wang, J. P. McGeehan, C. Williams, and A. Doufexi, "Application of Cooperative Sensing in Radar – Communications Coexistence", *IET Communications*, Vol. 2, No. July (6), pp. 856–868, 2008.

[3] J. D. Taylor, Ultra-Wideband Radar Technology, CRC Press LLC, 2000.

[4] J. Salzman, D. Akamine, and R. Lefevre, "Optimal Waveforms and Processing for Sparse Frequency UWB Operation", *IEEE Radar Conference*, pp. 105–110, Atlanta (GA), USA, 1–3 May 2001.

[5] H. D. Griffiths, "The Challenge of Spectrum Engineering", *European Radar Conference (EuRAD)*, pp. 1–4, Rome, Italy, 8–10 October 2014.

[6] H. D. Griffiths, L. Cohen, S. Watts, *et al*., "Radar Spectrum Engineering and Management: Technical and Regulatory Issues", *Proceedings of the IEEE*, Vol. 103, No. 1, pp. 85–102, 2015.

[7] https://www.itu.int/en/Pages/default.aspx.

[8] H. D. Griffiths, S. Blunt, L. Cohen, and L. Savy, "Challenge Problems in Spectrum Engineering and Waveform Diversity", *IEEE Radar Conference*, pp. 1–5, Ottawa (ON), Canada, April 29–May 3 2013.

[9] A. Farina, "Green Radar State of Art: Theory, Practice and Way Ahead", *Plenary Talk ICASSP*, Florence, Italy, 8 May 2014. http://www.icassp2014.org/final200614/er2/0005/index.html.

[10] H. D. Griffiths and N. R. W. Long, "Television-Based Bistatic Radar", *IEE Proceedings F (Communications, Radar and Signal Processing)*, Vol. 133, No. December (7), pp. 649–657, 1986.

[11] N. J. Willis and H. D. Griffiths, *Advances in Bistatic Radar*, Raleigh, NC, USA: Scitech Publishing, 2007.

[12] M. Cherniakov, *Bistatic Radars: Emerging Technology*, New York, NY, USA: John Wiley & Sons, 2008.

[13] K. S. Kulpa and Z. Czekala, "Masking Effect and Its Removal in PCL Radar", *IEE Proceedings of Radar*, *Sonar & Navigation*, Vol. 152, No. June (3), pp. 174–178, 2005.

[14] F. Colone, D. W. O'Hagan, P. Lombardo, and C. J. Baker, "A Multistage Processing Algorithm for Disturbance Removal and Target Detection in Passive Bistatic Radar", *IEEE Transactions on Aerospace and Electronic Systems*, Vol. 45, No. April (2), pp. 698–722, 2009.

[15] F. Colone, R. Cardinali, and P. Lombardo, "Cancellation of Clutter and Multipath in Passive Radar Using a Sequential Approach", *IEEE Radar Conference*, pp. 393–399, Verona (NY), USA, 24–27 April 2006.

[16] R. Cardinali, F. Colone, P. Lombardo, O. Crognale, and A. Cosmi, "Multipath Cancellation on Reference Antenna for Passive Radar which Exploits FM Transmission", *IET International Radar Conference*, Edinburgh, UK, 15–18 October 2007.

[17] H. D. Griffiths and C. J. Baker, "Passive Bistatic Radar and Waveform Diversity", in *Waveform Design and Diversity for Advanced Radar Systems,* F. Gini, A. De Maio, *and* L. Patton, Eds. Stevenage, UK: IET, 2012.

[18] H. D. Griffiths and C.J. Baker, "Passive Coherent Radar Systems – Part I: Performance Prediction", *IEE Proceedings on Radar, Sonar & Navigation*, Vol. 152, No. June (3), pp. 153–159, 2005.

[19] M. Inggs and C. Tong, "Commensal Radar using Separated Reference and Surveillance Channel Configuration", *Electronics Letters*, Vol. 48, No. August (18), pp. 1158–1160, 2012.

[20] M. Inggs, A. van der Byl, and C. Tong, "Commensal Radar: Range-Doppler Processing using a Recursive DFT", *IEEE International Radar Conference*, pp. 292–297, Adelaide (SA), 9–12 September 2013.

[21] H. D. Griffiths, I. Darwazeh, and M. Inggs, "Waveform Design for Commensal Radar", *IEEE Radar Conference*, pp. 1456–1460, Arlington (VA), USA, 10–15 May 2015.

[22] B. H. Cantrell, J. O. Coleman, and G. V. Trunk, "Radar Communications", Naval Research Lab Report, Tech. *Rep*. 8515, 1981.

[23] S. D. Blunt, P. Yatham, and J. Stiles, "Intrapulse Radar-Embedded Communications", *IEEE Transactions on Aerospace and Electronic Systems*, Vol. 46, No. July (3), pp. 1185–1200, 2010.

[24] S. D. Blunt, J. G. Metcalf, C. R. Biggs, and E. Perrins, "Performance Characteristics and Metrics for Intra-Pulse Radar-Embedded Communication", *IEEE Journal on Selected Areas in Communications*, Vol. 29, No. December (10), pp. 2057–2066, 2011.

[25] D. Ciuonzo, A. De Maio, G. Foglia, and M. Piezzo, "Intrapulse Radar-Embedded Communications via Multi-objective Optimization", *IEEE Transactions on Aerospace and Electronic Systems*, Vol. 51, No. 4, pp. 2960–2974, 2015.

[26] G. T. Capraro, C. T. Capraro, M. C. Wicks, and R. A. Liuzzi, "Artificial Intelligence and Waveform Diversity," *IEEE International Conference on Integration of Knowledge Intensive Multi-Agent Systems*, pp. 270–274, 30 September–4 October 2003.

[27] M. C. Wicks and P. Antonik, "Waveform Diversity in Intelligent Sensor Systems," *The Institution of Engineering and Technology Forum on Waveform Diversity and Design in Communications, Radar and Sonar*, pp. 1–6, London, 2006.

[28] M. Wicks, E. Mokole, S. Blunt, R. Schneible, and V. Amuso, *Principles of Waveform Diversity and Design*, Raleigh, NC: SciTech Publishing, 2011.

[29] F. Gini, A. De Maio, and L. Patton, Waveform Design and Diversity for Advanced Radar Systems, *The Institution of Engineering and Technology (IET)*, June 2012.

[30] J. R. Guerci, *Cognitive Radar, The Knowledge-Aided Fully Adaptive Approach*, Artech House, 2010.

[31] S. Haykin, "Cognitive Radar: A Way of the Future", *IEEE Signal Processing Magazine*, Vol. 23, No. 1, pp. 30–40, 2006.

[32] S. Haykin, "Cognitive Dynamic Systems: Radar, Control, and Radio [Point of View]", *Proceedings of the IEEE*, Vol. 100, No. 7, pp. 2095–2103, 2012.
[33] C. Nunn and L. R. Moyer, "Spectrally-Compliant Waveforms for Wideband Radar", *IEEE Aerospace and Electronics Systems Magazine*, Vol. 27, No. 8, pp. 11–15, 2012.
[34] K. Gerlach, "Thinned Spectrum Ultrawideband Waveforms Using Stepped-Frequency Polyphase Codes", *IEEE Transactions on Aerospace and Electronic Systems*, Vol. 34, No. October (4), pp. 1356–1361, 1998.
[35] K. Gerlach, M. R. Frey, M. J. Steiner, and A. Shackelford, "Spectral Nulling on Transmit via Nonlinear FM Radar Waveforms", *IEEE Transactions on Aerospace and Electronic Systems*, Vol. 47, No. April (2), pp. 1507–1515, 2011.
[36] M. R. Cook, T. Higgins, and A. K. Shackelford, "Thinned Spectrum Radar Waveforms", *International Waveform Diversity and Design Conference (WDD)*, pp. 238–243, Niagara Falls, Canada, 8–13 August 2010.
[37] I. W. Selesnick, S. U. Pillai and R. Zheng, "An Iterative Algorithm for the Construction of Notched Chirp Signals", *IEEE Radar Conference*, pp. 200–203, Washington (DC), USA, 10–14 May 2010.
[38] I. W. Selesnick and S. U Pillai, "Chirp-Like Transmit Waveforms with Multiple Frequency-Notches", *IEEE Radar Conference*, pp. 1106–1110, Kansas City (MO), USA, 23–27 May 2011.
[39] M. J. Lindenfeld, "Sparse Frequency Transmit and Receive Waveform Design", *IEEE Transactions on Aerospace and Electronic Systems*, Vol. 40, No. 3, pp. 851–861, July 2004.
[40] W. X. Liu, Y. L. Lu, and M. Lesturgie, "Optimal Sparse Waveform Design for HFSWR System", *International Waveform Diversity and Design Conference (WDD)*, pp. 127–130, Pisa, Italy, 4–8 June 2007.
[41] R. Kassab, M. Lesturgie, and J. Fiorina, "Alternate Projections Technique for Radar Waveform Design", *IEEE International Radar Conference – Surveillance for a Safer World*, pp. 1–4, Bordeaux, France, 12–16 October 2009.
[42] H. He, P. Stoica, and J. Li, "Waveform Design with Stopband and Correlation Constraints for Cognitive Radar", *International Workshop on Cognitive Information Processing (CIP)*, pp. 344–349, Elba Island, Italy, 14–16 June 2010.
[43] G. Wang and Y. Lu, "Designing Single/Multiple Sparse Frequency Waveforms with Sidelobe Constraint", *IET Radar, Sonar & Navigation*, Vol. 5, No. 1, pp. 32–38, 2011.
[44] L. Patton, C. A. Bryant, and B. Himed, "Radar-Centric Design of Waveforms with Disjoint Spectral Support", *IEEE Radar Conference*, pp. 1106–1110, Atlanta (GA), USA, 269–274 May 2012.
[45] R. A. Romero and K. D. Shepherd, "Friendly Spectrally Shaped Radar Waveform With Legacy Communication Systems for Shared Access and Spectrum Management", *IEEE Access*, Vol. 3, pp. 1541–1554, 2015.

[46] W. Guohua, M. Chaoyun, S. Jinping, L. Yilong, "Sparse Frequency Waveform Analysis and Design Based on Ambiguity Function Theory", *IET Radar, Sonar & Navigation*, Vol. 10, no. 4, pp. 707–717, Mar. 2016.

[47] A. Aubry, A. De Maio, M. Piezzo, and A. Farina, "Radar Waveform Design in a Spectrally Crowded Environment via Nonconvex Quadratic Optimization", *IEEE Transactions on Aerospace and Electronic Systems*, Vol. 50, No. April (2), pp. 1138–1152, 2014.

[48] A. Aubry, A. De Maio, Y. Huang, M. Piezzo, and A. Farina, "A New Radar Waveform Design Algorithm with Improved Feasibility for Spectral Coexistence", *IEEE Transactions on Aerospace and Electronic Systems*, Vol. 51, No. April (2), pp.1029–1038, 2015.

[49] A. Aubry, A. De Maio, M. Piezzo, M.N. Naghsh, M. Soltanalian, and P. Stoica, "Cognitive Radar Waveform Design for Spectral Coexistence in Signal-Dependent Interference", *IEEE Radar Conference*, pp. 474–478, Cincinnati (OH), USA, 19–23 May 2014.

[50] Y. Zhao, J. Gaeddert, K. K. Bae, and J. H. Reed, "Radio Environment Map-Enabled Situation-Aware Cognitive Radio Learning Algorithms", *Software Defined Radio (SDR) Technical Conference*, Orlando (FL), USA, November 2006.

[51] Y. Zhao, J. H. Reed, M. Shiwen, K. K. Bae, "Overhead Analysis for Radio Environment Map-enabled Cognitive Radio Networks", *IEEE Workshop on Networking Technologies for Software Defined Radio Networks*, Reston (VA), USA, pp. 18–25, September 2006.

[52] Y. Zhao, L. Morales, J. Gaeddert, K. K. Bae, J.-S. Um, and J. H. Reed, "Applying Radio Environment Maps to Cognitive Wireless Regional Area Networks", *IEEE International Symposium on New Frontiers in Dynamic Spectrum Access Networks*, pp. 115–118, Dublin, Ireland, April 2007.

[53] T. Yucek and H. Arslan, "A Survey of Spectrum Sensing Algorithms for Cognitive Radio Applications", *IEEE Communications Surveys & Tutorials*, Vol. 11, No.1, pp. 116–130, 2009.

[54] H. Leong and B. Sawe, "Channel Availability for East Coast High Frequency Surface Wave Radar Systems", No. DREO TR 2001-104, Defence Research Establishment Ottawa (Ontario), *Technical Report*, November 2001.

[55] W. Ai, Y. Huang, and S. Zhang, "New Results on Hermitian Matrix Rank-One Decomposition", *Mathematical Programming*, Series A, Vol. 128, No. June (1–2), pp. 253–283, 2011.

[56] C. T. Capraro, J. T. Capraro, A. De Maio, A. Farina, and M. Wicks, "Demonstration of Knowledge Aided Space-Time Adaptive Processing using Measured Airborne Data", *IEE Proceedings on Radar, Sonar & Navigation*, Vol. 153, No. December (6), pp. 487–494, 2006.

[57] A. Aubry, A. De Maio, A. Farina, and M. Wicks, "Knowledge-Aided (Potentially Cognitive) Transmit Signal and Receive Filter Design in Signal-Dependent Clutter", *IEEE Transactions on Aerospace and Electronic Systems*, Vol. 49, No. 1, pp. 93–117, 2013.

[58] A. I. Barros, J. B. G. Frenk, S. Schaible, and S. Zhang, "A New Algorithm for Generalized Fractional Programs", *Math. Program.*, Vol. 72, pp. 147–175, 1996.

[59] Z. Q. Luo and S. Z. Zhang, "A Semidefinite Relaxation Scheme for Multivariate Quartic Polynomial Optimization with Quadratic Constraints", *Technical Report, Department of SEEM, Chinese University of Hong Kong*, Hong Kong, 2009.

[60] A. Charnes and W. W. Cooper, "Programming with Linear Fractional Functionals", *Naval Research Logistics Quarterly*, Vol. 9, pp. 181–186, 1962.

[61] A. Ben-Tal and A. Nemirovski, *Lectures on Modern Convex Optimization: Analysis, Algorithms, and Engineering Applications*, MPS-SIAM Series on Optimization, 2001.

[62] D. P. Bertsekas, *Nonlinear Programming, 2nd ed*., Belmont, MA: Athena Scientific, 1999.

[63] A. Wenbao and S. Zhang, "Strong Duality for the CDT Subproblem: A Necessary and Sufficient Condition", *SIAM Journal on Optimization*, Vol. 19, No. 4, pp. 1735–1756, 2009.

[64] J. Li, P. Stoica, and Z. Wang, "Doubly Constrained Robust Capon Beamformer," *IEEE Transactions on Signal Processing*, Vol. 52, No. 9, pp. 2407–2423, 2004.

[65] S. Boyd and L. Vandenberghe, *Convex Optimization*, New York, NY: Cambridge University Press, 2003.

[66] A. d'Aspermont and S. Boyd, *Relaxations and Randomized Methods for Nonconvex QCQPs*, Stanford Univ., Stanford, CA, 2003, EE392o Class Notes.

[67] R. A. Horn and C. R. Johnson, *Matrix Analysis*, New York, NY: Cambridge University Press, 1985.

Chapter 4

Noise Radar Technology

Krzysztof S. Kulpa[1] *and Lukasz Maslikowski*[1]

Abstract

The well-known classical pulse radar has several disadvantages. The high transmitted peak power can be easily detected and warn an enemy, and the ambiguities in both range and Doppler measurements lead to problems with unambiguous localization and tracking. For a long time researchers have tended to overcome these problems and find waveforms that will free the radar from the aforementioned issues. The design of the frequency modulated continuous wave radar with linear frequency modulation was an important step; the mean power is equal to the peak power and it is much harder to detect such radar, but range and Doppler ambiguities remain due to periodicity in the waveform repetition. The next step was the introduction of the noise radar concept. At first glance it is hard to believe that a noise signal, without any clear internal structure and well-defined instantaneous frequency, can be used for radar purposes. But thanks to the development of digital correlators which are able to compute the ambiguity function in real time, it is now possible to unambiguously estimate the range and radial velocity of the target using noise illumination. But of course one must pay a price: noise radar is limited not only by ambiguities in range and Doppler, but also in dynamic range. The strong return signal from nearby targets, or clutter, can entirely mask a weak and distant target's echoes. The second drawback is that signal processing is much more complex than in classical radars and thus the radar signal processing unit for a noise radar must have much higher computational power, which is achievable only by using modern computers equipped with graphical processing (GPU) units.

The potential applications for noise radar can be vast; it is possible to use it for surveillance, traffic monitoring, and early warning and imaging (SAR, ISAR) purposes as the time on target is usually very long (hundreds of milliseconds to seconds).

4.1 Introduction

The classical radar emits short pulses towards a target and receives the echoes. The radar's antenna, used both for transmitting and receiving, forms a narrow beam to

[1]Warsaw University of Technology, Institute of Electronic, Systems (ISE), Poland

concentrate the energy on the target. As this same antenna is used for transmission and reception, the emitted pulse should be short enough to allow switching between these two functions of the antenna. In cases where an un-modulated pulse is emitted, the range resolution of the radar is inversely proportional to the pulse duration, so very short pulses should be used. To achieve 15 m range resolution, a pulse length of 100 ns should be used. The detection range depends on the energy transmitted towards the target, so the peak power of these short pulses must be very high (up to several MW). This leads to several difficulties in designing modern radars, especially with solid state transmitters. Nowadays, by using semiconductor components, it is much easier to generate relatively long low power pulses or a continuous wave rather than powerful short pulses. This fact has led radar engineers to begin looking for new concepts in the exploitation of low power signal sources for short and medium range sensing.

The trend in the direction of lowering the peak transmitting power has led to the continuous wave radar concept. The idea is not new – single tone continuous wave radars have been used for more than a decade by police to enforce speed limits. Classical police radar guns emit sine waves and use a homodyne receiver to detect a vehicle's echo which has shifted in frequency due to the Doppler effect and then measure the Doppler frequency of the echo. The disadvantage of this approach is the lack of range resolution, so in the case of several targets, it is very difficult to assign the velocity to an individual vehicle.

The problem of range resolution has been solved by using the linear frequency modulation of the transmitted continuous signal (FMCW – frequency modulated continuous wave radar) [1,2]. In such a radar, the received echo is mixed with the transmitted signal in a homodyne receiver, and the beat frequency signal is then analysed. Since the echo delay is proportional to the range to the target, the beat frequency is also proportional to the range. The fast Fourier transform then converts this frequency to the range to the target. The big problem with this type of radar is in the coupling between range and velocity. As the Doppler effect also changes the beat frequency of the echo, it is not possible to determine in a single sweep of an FMCW radar which part of the frequency is caused by the range to the target and which by the target velocity. For a single target, such a problem can be solved using two measurements, such as up and down chirp (with increasing and decreasing frequencies) for example, but in the case of several targets, the problem may be ambiguous. Also, due to the periodicity of the transmitted signal, range and Doppler measurements are ambiguous in an FMCW radar in a very similar manner to that of pulse radars.

Another problem with continuous wave (CW) radars lies in the feasibility of conducting simultaneous transmission and reception. To have a long detection range, it is necessary to emit strong signals, at levels from mW to kW (0 to +60 dBm). The echo signals are usually comparable with the thermal noise level floor (−113 dBm for 1 MHz bandwidth) so the required dynamic range between transmission and reception is 100–160 dB. With technology in its present state, such a high dynamic range cannot be achieved using a single antenna system, and it is a technological challenge to achieve it using separate transmit and receive antennas. Thus, in modern medium range CW radars, two separate antennas are used, and only very short distance CW radars (such as police guns) are equipped with a single Rx/Tx antenna.

The linear chirp is the most natural waveform for a CW radar, and such waveforms are also used in nature. Bats and dolphins navigate and hunt using echolocation and chirp signals. But as mentioned above, the sawtooth modulation is periodic, which leads to ambiguities either in range or range velocity measurement.

For many years, radar engineers have been looking for different waveforms which will give them more freedom to design a radar able to produce the required performance. An effective waveform is one with a 'thumbtack' ambiguity function (single sharp peak accompanied with low sidelobes) and no range or Doppler ambiguities (no additional peaks in the ambiguity function) as presented in Figure 4.1(a).

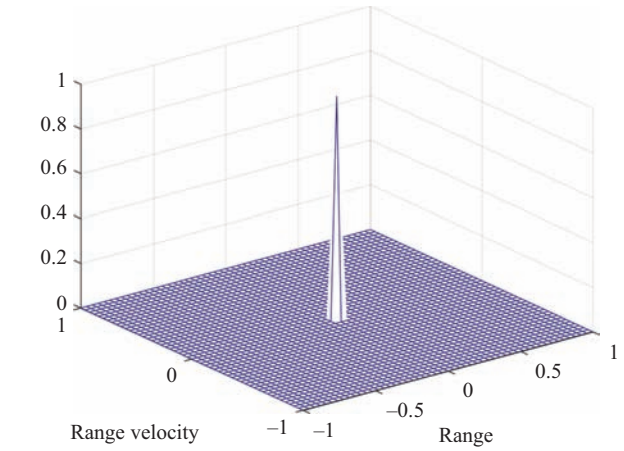

(a)

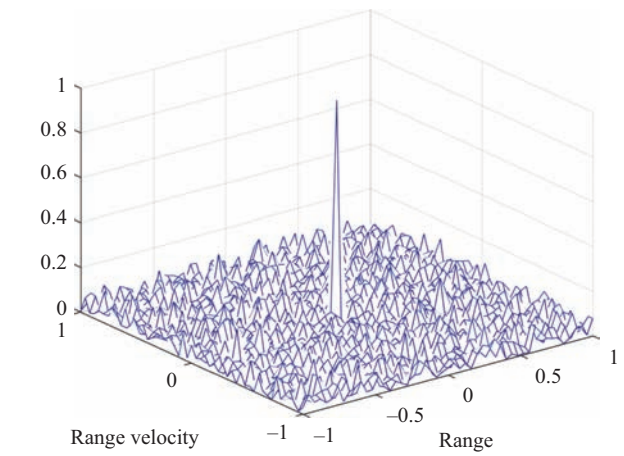

(b)

Figure 4.1 The desired shape of radar waveform ambiguity function; (a) ideal without range and Doppler sidelobes (noise floor), (b) practical – with sidelobes in range and Doppler

To be able to exploit the transmitters fully a constant amplitude signal is preferred. As a result, candidates for perfect radar waveforms have been searched for in the class of phase-coded signals (with constant amplitude). A number of such waveforms have been developed in the past. One of the first signals of this type is the binary-phase Barker code [3]. The amplitude of the main peak of the correlation function of the Barker code is equal to the length of the code, while the peak sidelobe level is unity. There are Barker codes in existence up to (and including) a length of 13, so the best possible mainlobe-to-sidelobe ratio is 22.2 dB. More freedom is given by polyphase codes. An intensive search of polyphase unimodular Barker codes led to codes to a length of 19 in 1989 [4] and to a length of 65 in 2007 [5]. Other polyphase codes such as Frank codes [6], and P-codes [7], among others, have also been developed.

All of the above-mentioned codes have some disadvantages. One of the most important is that the code is pre-defined and usually fixed, so it is easy to detect the radar and for adversaries to produce false target echoes.

An alternative to pre-defined fixed codes (waveforms) are random waveforms. They can be generated completely randomly using analogue devices such as a resistor with a chain of amplifiers or noisy Zener diodes or can be generated digitally using pseudo-random sequence generators. The waveforms can be generated on-line in real time or generated off-line and stored in the radar waveform memory. Radars using random or pseudo-random waveforms can be named **noise radars**. Such radars can be used in a relatively wide range of applications [8–16]. It is possible to construct surveillance [17], tracking, guidance, collision warning, SAR [18–27] ISAR [28], ground penetrating [29–31] and through-the-wall radars using noise signals.

Noise radars have several advantages over the classical pulse, pulse-Doppler and FMCW radars. A continuous noise waveform does not have range and Doppler ambiguity, and the peak power is equal to the mean power and is much lower than in pulse radars of the same detection range. It also has good electromagnetic compatibility with other devices sharing the same frequency band. The low peak power and lack of modulation of the noise waveform also ensures a very good electronic counter-countermeasure capability: the probability of the interception of this kind of radar is very low, and even if the emission is detected, it is very difficult to assign such a signal to a radar waveform class and identify it as the threat. Furthermore, it is either very hard (in the case of pseudo-random sequences) or impossible (for true random signals) to predict the future waveform, which is key for active counter-measuring or spoofing such radars.

As usual, the benefits come at a certain price. In the case of noise radars, the price that must be paid is the complexity of signal-processing algorithms and the high-processing noise floor – equivalent to time and Doppler sidelobes known in deterministic waveforms. As a result, the near-far problem, very well known in radio communication, has to be mitigated in noise radars.

The first fundamental paper on noise radars was published by Horton in 1959 [32], presenting the concept of a range measuring radar-based system. The idea of noise radars was further investigated in the 1960s and 1970s [33,34] and at that time the idea of non-ambiguous velocity measurement was introduced.

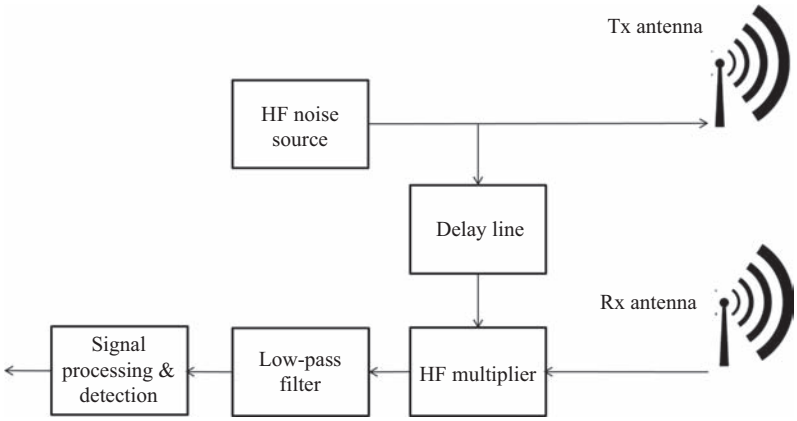

Figure 4.2 Block diagram of the noise radar based on the delay line

Unfortunately, using analogue circuits made it extremely difficult to build noise radars with real-time capabilities, as it was necessary to compute the correlation function in order to obtain the range profile of the radar data and the fast Fourier transform (FFT) so as to find the Doppler shifts corresponding to range velocities. In 1961, Grant and Cooper [35] proposed the use of the analogue delay line as a way to compensate for the time delay of the echo signal and the use of an analogue multiplier and low-pass filter to calculate the correlation at the selected delay. The block diagram of their radar is shown in Figure 4.2.

In the presented solution, only stationary or slow targets (with a Doppler frequency lower than the bandwidth of a low-pass filter) could be detected at a distance determined by the selected delay line. To build a fully functional analogue radar working in real time, it is necessary to use a set of delay lines to obtain measurements at several range gates and use a bank of bandpass filters (the analogue version of FFT) to obtain velocity measurements, as depicted in Figure 4.3.

Such an approach is feasible, but its complexity and price is very high, so the idea was not exploited in practice.

Another possible approach was to use pulses with noise modulation, as proposed by Krehbiel and Brook in 1979 [36]. The radar was used for cloud and rain detection, but only amplitude data was used. In practice, there were no differences between sine-wave pulse radars and that particular noise radar in their principles, as in both cases a square law amplitude detector was used and no phase information was retrieved.

The situation changed significantly in the 1990s, when rapid progress in digital technology took place [37,38] in accordance with Moore's law, whereby the number of electronic components in integrated circuits and computational power doubles approximately every 18 months. The speed of analogue to digital converters has reached the level of 5 Gs/s (10^9 Gigasamples per second), and powerful field programmable logic circuitry (FPGAs), together with multi-core graphics

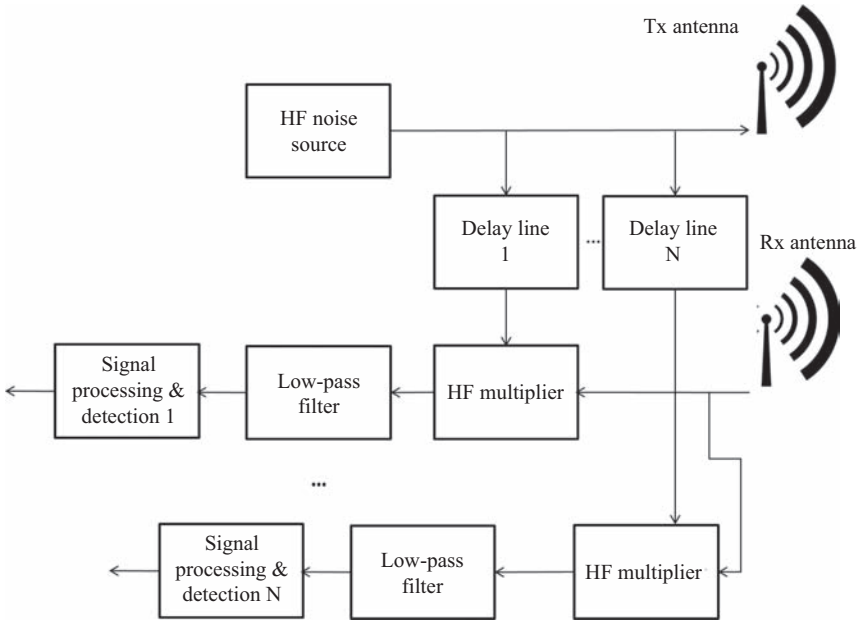

Figure 4.3 Block diagram of the noise radar based on sets of delay lines

processing unit (GPU) processors now have a processing power of several TFlops/s (10^{12} floating point operation per second). In addition, communication links can send data at a speed of 10 Gb/s per channel, and thanks to global navigation satellite systems (GPS, GLONASS, GALILEO, BeiDou, COMPASS), it is easy to synchronize in time and frequency the remote devices by building wide area multiple-input–multiple-output (MIMO) systems.

All of these digital technologies can now provide a cost- and performance-effective platform to build modern noise radars.

4.1.1 Signal processing in noise radars

A monostatic noise radar illuminates the target with a noise waveform and listens to the echo, as depicted in Figure 4.4. It uses a separate antenna for the transmission of an illuminating signal (Tx antenna) and a separate antenna for the reception of the target echoes.

Suppose that the radar transmits the noise signal $x_t(t)$. Typically, this is a band-limited signal of carrier frequency F_c and effective bandwidth B. The emitted signal is scattered from a point-like target at distance R_0 at time T_0. The target can be either a stationary target or a moving target with a position history (range to target) $r(t)$. The signal received by the receive antenna can be expressed as

$$x_R(t) = x_T\left(t - \frac{2r(t-\tau_r)}{c}\right) + \xi_R(t) \tag{4.1}$$

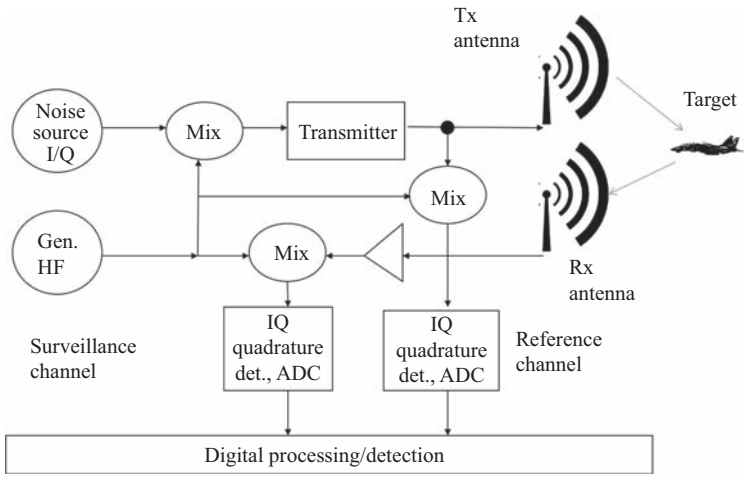

Figure 4.4 Monostatic noise radar structure

where $\xi_R(t)$ is the receiver noise and $\tau_r$is the time delay between the signal reflection from the target and the signal reception. In the simplified case, it can be assumed that $\tau_r$is equal to 0, and for most targets, such a simplification is valid. For stationary or slow moving targets, it can be assumed that $\tau_r = r(t)/c$ and thus (4.1) can be expressed as

$$x_R(t) = x_T\left(t - \frac{2r(t - r(t)/c)}{c}\right) + \xi_R(t) \tag{4.2}$$

Let the assumption be made that the received signal was collected in the time interval (T_0, T_0+ t_i) where t_i is the observation or integration time. To detect the presence of the echo, a correlation receiver that computes the correlation coefficient between the transmitted and received signals can be used

$$y_r(r(t)) = \int_{t=T_0}^{T_0+t_i} x_R(t)x_T^*\left(t - \frac{2r(t-\tau_r)}{c}\right)dt \tag{4.3}$$

and compared with the pre-defined threshold, or by using the classical constant false alarm rate detectors described in [39].

Equation (4.3) is the fundamental equation for all noise radars (or more generally, for all radars, independent of the applied waveform). It should be noted that for different targets, it is necessary to re-calculate (4.3). If the target position and motion is unknown, it is necessary to make calculations for all possible positions and motion models.

Depending on the waveform, target motion model and transmitted signal model, a different simplification of (4.3) can be applied.

4.1.1.1 Stationary target model

Consider the simplest case – a stationary target model. In this case, $r(t) = R_0$ and (4.3) hold in the form

$$y_r(R_0) = \int_{t=T_0}^{T_{0+}t_i} x_R(t) x_T^*\left(t - \frac{2R_0}{c}\right) dt \tag{4.4}$$

which can be expressed as a correlation function between a transmitted and received signal

$$y_r(\tau) = \int_{t=T_0}^{T_{0+}t_i} x_R(t) x_T^*(t-\tau) dt \tag{4.5}$$

where $\tau = 2R_0/c$. Equation (4.5) represents the function of the unknown variable τ which should be calculated for all values in the interval $(0, 2R_{\mathrm{MAX}}/c)$, where R_{MAX} is the maximum detectable range assumed for the radar. The direct calculation of (4.5) is not computationally effective, so more often it is calculated using FFT procedures such as

$$y_r(\tau) = \mathrm{FFT}^{-1}(\mathrm{FFT}(x_R(t))\mathrm{FFT}^*(x_T(t))) \tag{4.6}$$

Stationary targets are usually not of great interest for radar engineers, so more advanced models are considered. Usually, models are based on the Taylor series expansion of the motion model

$$r(t) = r_0 + v_0 t + a_0 \frac{t^2}{2} + \cdots \tag{4.7}$$

All detection schemas for noise radars are derived from (4.3) using an appropriate order motion model and appropriate signal model.

4.1.1.2 Constant radial velocity model

The most popular detection scheme is based on the linear, constant velocity motion model $r(t) = r_0 + v_0 t$ and a band limited signal model in the form of low-pass noise upconverted to a carrier frequency F_c.

$$x_T(t) = x_B(t)\exp(j2\pi F_c t) \tag{4.8}$$

where $x_B(t)$ is low-pass (frequency limited) complex value noise, as depicted in Figure 4.5.

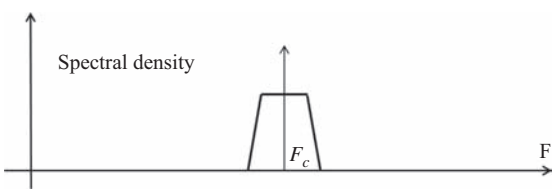

Figure 4.5 Transmitted signal spectrum

Neglecting the τ_r term in (4.3) one can obtain the equation

$$y(r,v) = \int_{t=T_0}^{T_{o+}t_i} x_R(t)\exp(j2\pi F_c t)x_B^*\left(t - \frac{2r+2vt}{c}\right)\exp\left(-j2\pi\left(-\frac{2vF_c}{c}\right)t\right)dt \quad (4.9)$$

This equation can be further simplified by neglecting the stretch effects caused by target motion.

$$y(r,v) = \int_{t=T_0}^{T_{o+}t_i} x_{\mathrm{RB}}(t)x_B^*\left(t - \frac{2r}{c}\right)\exp\left(-j2\pi\left(-\frac{2vF_c}{c}\right)t\right)dt \quad (4.10)$$

where $x_{\mathrm{RB}}(t) = x_R(t)\exp(j2\pi F_c t)$ is the received signal shifted to the baseband.

Again it is possible to change the variable from motion notation (range and velocity) to signal notation (delay and frequency) and obtain

$$y(\tau,f) = \int_{t=T_0}^{T_{o+}t_i} x_{\mathrm{RB}}(t)x_B^*(t-\tau)\exp(-j2\pi ft)dt \quad (4.11)$$

where $\tau = 2r/c$ and $f = 2vF_c/c$.

In addition, to limit the velocity sidelobes, a time windowing function $w(t)$ such as a Hamming, Hanning or Blackman window is usually applied

$$y(\tau,f) = \int_{t=T_0}^{T_{o+}t_i} w(t)x_{\mathrm{RB}}(t)x_B^*(t-\tau)\exp(-j2\pi ft)dt \quad (4.12)$$

This is a fundamental equation for noise radar signal processing. It is very similar to an ambiguity function [40–42] and again can be calculated using different computational schemas, directly from (4.11) for example, as $y(\tau,v) = fft\left\{w(t)x_{\mathrm{RB}}(t)x_B^*(t-\tau)\right\}$ or applying more advanced computational algorithms.

Equation (4.11) has to be calculated for all possible delays and frequency shifts in the ranges $\tau \in (0, 2R_{\mathrm{MAX}}/c)$ and $f \in (-2V_{\mathrm{MAX}}/\lambda, 2V_{\mathrm{MAX}}/\lambda)$ where V_{MAX} is the maximum velocity of the target.

An example of target echoes in a noise radar using rectangular and Hamming windows is presented in Figure 4.6.

The question is, what are the limits of application for the simplified target motion model? The stationary target model (4.5) can be applied if the phase shift due to the Doppler component is small, usually smaller than π. Thus, the integration time is limited to the value

$$t_i < \frac{c}{4V_{\mathrm{MAX}}F_c} \quad (4.13)$$

These limits can be also expressed in terms of the wavelength λ of the transmitted signal instead of the carrier frequency.

$$t_i < \frac{\lambda}{4V_{\mathrm{MAX}c}} \quad (4.14)$$

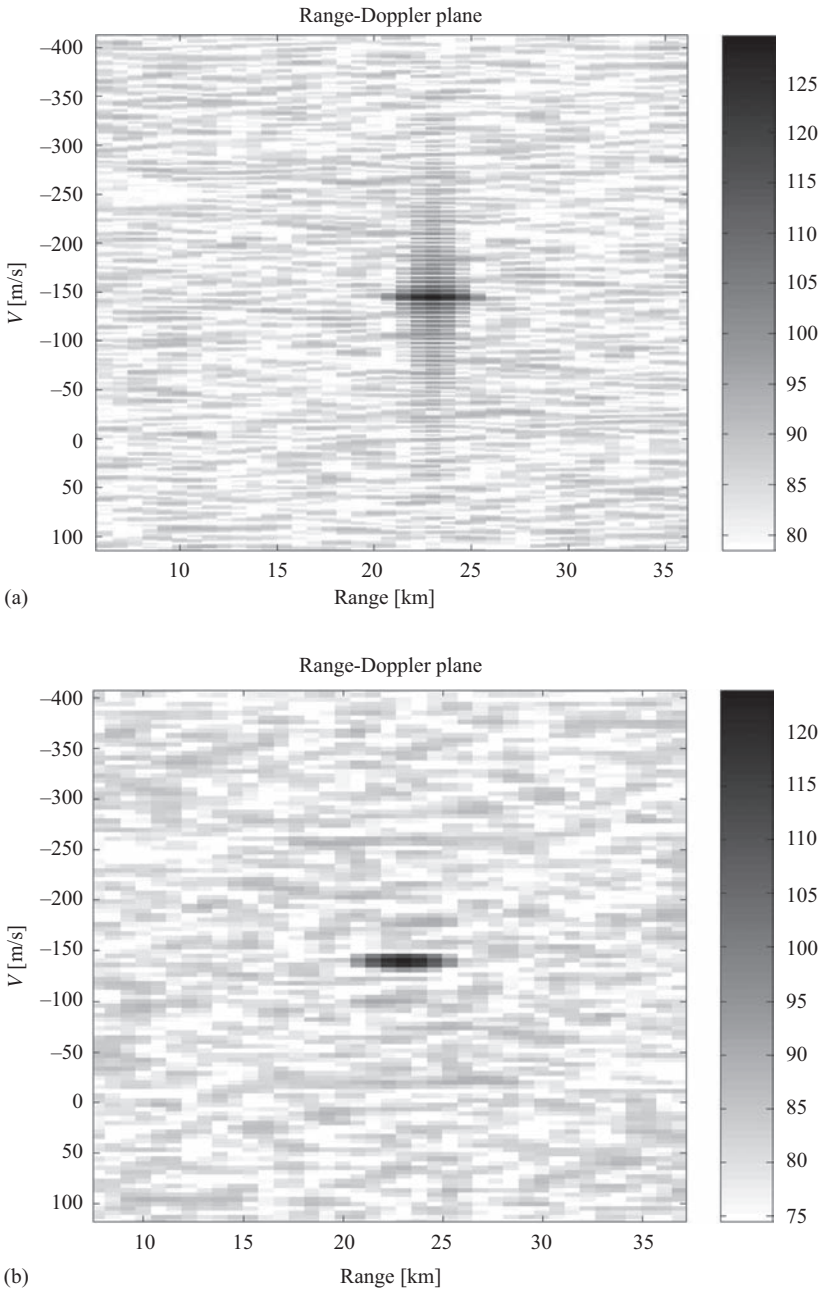

Figure 4.6 An example of the range-Doppler correlation function of noise radar return – rectangular time window (a) and Hamming window (b)

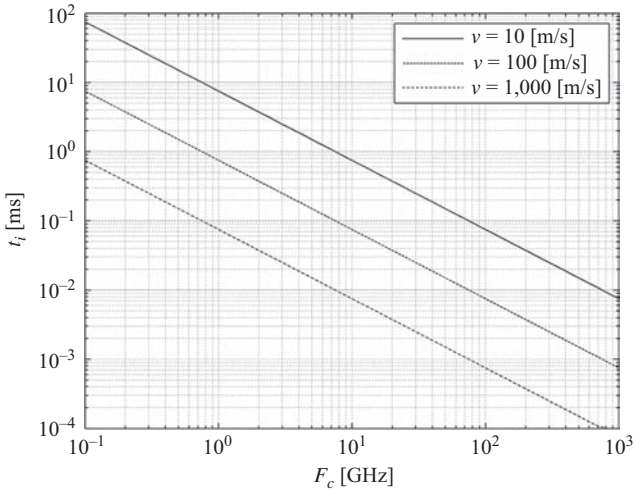

Figure 4.7 Maximum integration time for a noise radar using stationary target model (4.5)

The constraint (4.14) has a very clear physical interpretation: the target displacement during observation time should be smaller than a quarter of the wavelength. The results are plotted in Figure 4.7. For an L-band noise radar ($\lambda = 20$ cm) observing aircraft targets with a maximum target velocity of 1000 m/s (Mach 3), the maximum integration time is equal to 50 μs and for humans with a maximum velocity of 10 m/s the maximum integration time is limited to 5 ms.

Constraint (4.14) is not applicable for radars working at baseband. Such radars do not have a carrier frequency and the direct application of constraint (4.14) will allow infinite integration time. In such cases, the limitation originates from range walk phenomena. The range resolution of the noise radar, defined as the width of the correlation peak (4.4), can be expressed as

$$\Delta R = \frac{c}{2B} \tag{4.15}$$

The range resolution versus signal bandwidth is plotted in Figure 4.8.

As the target has to remain in the correlation gate during the observation time, the second constraint is in the form

$$t_i < \frac{\Delta R}{V_{\mathrm{MAX}}} = \frac{c}{2BV_{\mathrm{MAX}}} \tag{4.16}$$

The integration time limitation caused by the range walk is presented in Figure 4.9.

For supersonic targets and medium resolution radar ($B = 10$ MHz), the maximum integration time is limited to a few ms (15 ms).

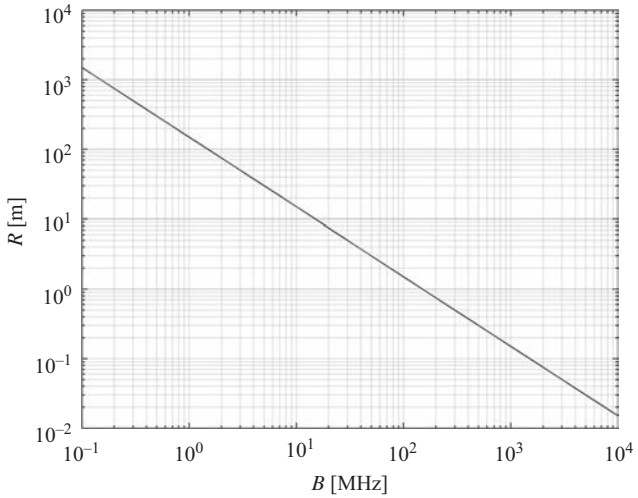

Figure 4.8 Radar range resolution versus signal bandwidth

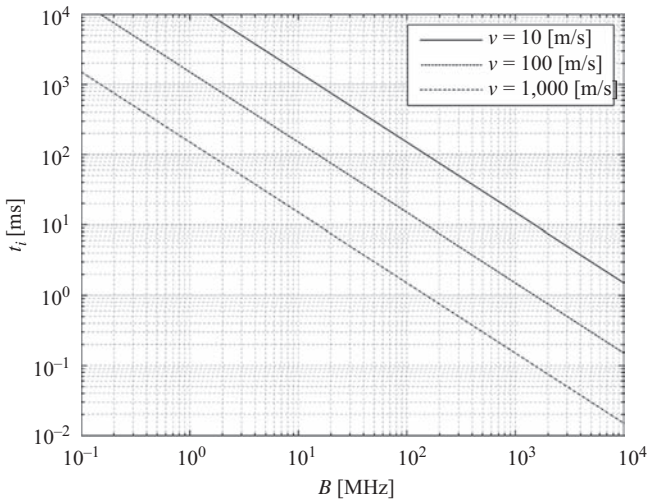

Figure 4.9 Maximum integration time versus bandwidth – limited by range walk phenomena (4.16)

Constraint (4.16) can also be re-written in the slightly modified form

$$Bt_i < \frac{c}{2V_{\mathrm{MAX}}} \tag{4.17}$$

The term Bt_i is the integration gain of the processing (the signal-to-noise ratio after processing to signal-to-noise ratio before processing). This ratio is then limited by

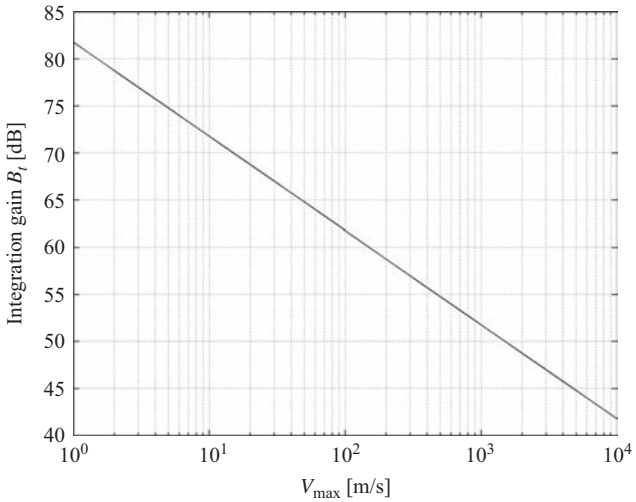

Figure 4.10 Maximum processing gain versus maximum target velocity – limited by range walk phenomena (4.17)

range walk phenomena to the value predicted by constraint (4.17), which is depicted in Figure 4.10.

The application of a simple stationary target model significantly limits the integration time in a noise radar. The application of a constant velocity model leads to the significant extension of possible integration time. Now, constraints come from two phenomena. As using a constant velocity model, noise radar estimates two parameters – range and range velocity – both the range and velocity walk limit the integration time.

The target detection is performed in this case using (4.12). For a selected velocity, this equation is identical to (4.5), so the range resolution for the constant velocity model is the same as for the stationary target model as described by (4.15). As a result, the integration time is limited by constraint (4.16).

The target range velocity is calculated using Doppler frequency estimation. For constant delay formula (4.12) is equivalent to FFT, with frequency resolution $\Delta f_d = 1/t_i$. As $\Delta f_d = 2\Delta v/\lambda$, the velocity resolution defined as the width of the peak of the ambiguity function (4.10) in the velocity dimension is equal to

$$\Delta v = \frac{\lambda}{2t_i} = \frac{c}{2t_i F_c} \tag{4.18}$$

The velocity resolution versus integration time for different carrier frequencies is plotted in Figure 4.11.

The target velocity should remain within the velocity cell during the integration time. If a more advanced target model was assumed – a constant acceleration model for example – then the velocity changes linearly with time $v(t) = v_o + a_0 t$.

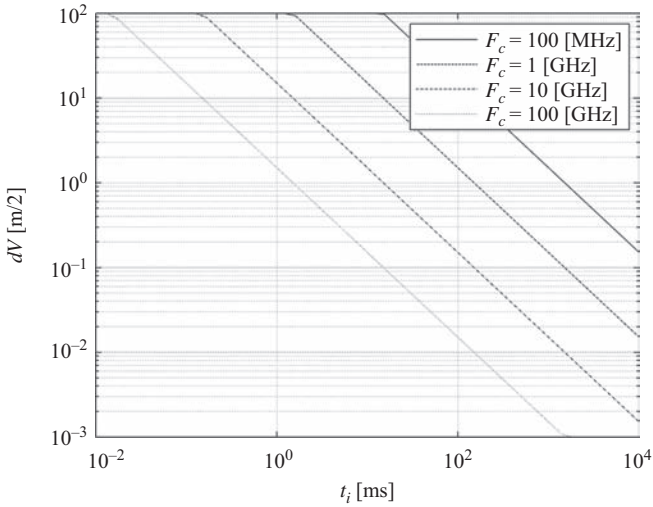

Figure 4.11 Velocity resolution versus integration time for different carrier frequencies

If the target velocity is to remain in the velocity cell, then a constraint appears for the integration time in the form

$$t_i < \frac{\Delta v}{a_{\mathrm{MAX}}} = \sqrt{\frac{\lambda}{2a_{\mathrm{MAX}}}} = \sqrt{\frac{c}{2a_{\mathrm{MAX}}F_c}} \tag{4.19}$$

The integration time constraints due to velocity migration for different accelerations versus carrier frequencies are plotted in Figure 4.12.

It is worth mentioning that (4.9) is simplified as the term τ_r in (4.3) was omitted. Additionally, in (4.10), a simplification is made by skipping the time stretch component so $x_B^*(t-(2r/c))$ is used instead of $x_B^*(t-((2r+2vt)/c))$. The skipped term $2vt/c$ is responsible for signal stretch, while

$$x_B^*\left(t-\frac{2r+2vt}{c}\right) = x_B^*\left(t\left(1-\frac{2vt}{c}\right)-\frac{2r}{c}\right) \tag{4.20}$$

The reference signal has to be scaled in time (stretch) by the factor $(1-(2vt/c))$ depending on the actual target radial velocity. Linear stretch processing is not a new idea in radar signal processing. It was introduced in the FMCW radar in [43]. The applications of stretch processing were also presented in [44–47].

In noise radars, stretch processing can be implemented in many different ways. Among others, the three most popular algorithms that are used are as follows: linear interpolation between samples, cubic spline interpolation and re-sampling based on the pairing of chirp transform and inverse FFT. The results obtained by using the algorithms mentioned above are similar to each other.

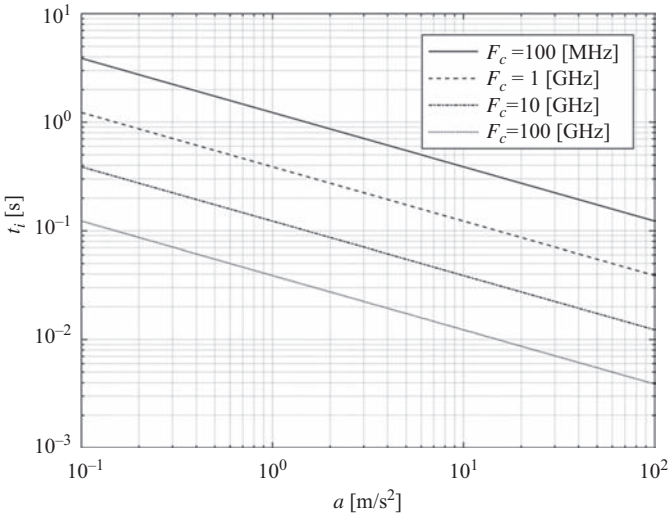

Figure 4.12 Integration time constraints due to velocity migration for different accelerations versus carrier frequencies

It should be pointed out that stretch processing has to be performed independently for each velocity resolution cell. Such an approach, however, requires very high computational power. In most cases, it is sufficient to stretch the reference signal not for each Doppler resolution cell but for the group of velocity cells occupying the velocity strip of width $c/2Bt_i$. Thus, in order to calculate the whole range-Doppler correlation plane, it is necessary to perform $N = 4Bt_i v_{\max}/c$ stretching operations and calculate the range-Doppler correlation in each narrow velocity interval. The details of stretch processing and its impact on the processing gain losses, processing complexity and implementation can be found in [45].

The application of stretch processing allows for extension of integration time, while the range migration due to the constant velocity component is mitigated. For such processing schema limitation (4.16) is not valid, and the integration time is limited by target acceleration. In such cases, the integration time is limited by acceleration introduced velocity walk – see constraint (4.19) – and also by acceleration introduced range walk. Assuming constant target acceleration, the range walk caused by the acceleration is equal to $at^2/2$, so the integration time is limited to

$$t_i < \sqrt{\frac{2\Delta R}{a_{\mathrm{MAX}}}} = \sqrt{\frac{c}{a_{\mathrm{MAX}} B}} \tag{4.21}$$

The time limits introduced by acceleration range walks are presented in Figure 4.13. It is worth noticing that the constraint (4.21) is less restrictive than (4.19), while bandwidth is usually smaller than carrier frequency.

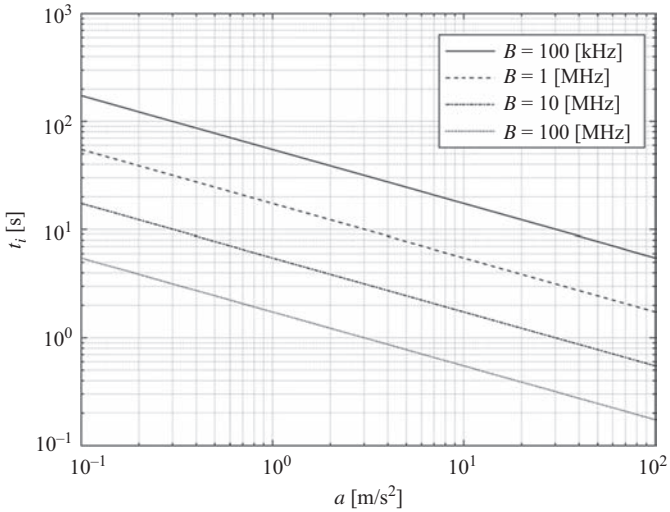

Figure 4.13 Integration time constraints due to range migration for different accelerations versus bandwidth

The omitted term τ_r in (4.3) for the constant velocity model is equal to

$$\tau_r = \frac{r_0}{c - v_0} \tag{4.22}$$

As a result the full echo model takes the form

$$x_R(t) = x_T\left(t - \frac{2r_0 + 2v_0t - 2r_0v_0/(c - v_0)}{c}\right) + \xi_R(t) \tag{4.23}$$

After straightforward simplification, one can obtain a more convenient expression in the form

$$x_R(t) = x_T\left(t\left(1 - \frac{2v_0}{c}\right) - \frac{2r_0}{c}\left(1 - \frac{v_0}{(c - v_0)}\right)\right) + \xi_R(t) \tag{4.24}$$

As a result, not only time is scaled by the factor $1 - (2v_0/c)$ but also the range is scaled by the factor $1 - (v_0/(c - v_0))$.

4.1.1.3 Constant acceleration model

For longer integration time, it is necessary to apply high order motion models. In this section, a constant acceleration model will be applied in the form $r(t) = r_0 + v_0t + a_0(t^2/2)$.

The received signal (neglecting the τ_r term) is now in the form

$$x_R(t) = x_T\left(t - \frac{(2r_0 + v_0t + a_0t^2)/2}{c}\right) + \xi_R(t) \tag{4.25}$$

and the processing formula now has the form

$$y(r,v,a)=\int_{T_0}^{T_{0+}t_i} x_R(t)\cdot x_B^*\left(t-\frac{2r+2vt+at^2}{c}\right)\cdot\exp\left(\frac{-j2\pi(2vt+at^2)F}{c}\right)dt \tag{4.26}$$

It is noticeable that in the case of constant acceleration, the output of the correlation receiver is three dimensional. The correlation function (4.26) can be calculated directly from the equation above or calculated independently for each acceleration.

Acceleration of the target can also be estimated after estimation of the target range and Doppler shift. In such cases, for the co-ordinates of the maximum of the cross-ambiguity function (4.12) the single-dimensional acceleration transform [48] is calculated for the estimated target range and velocity:

$$y_a(a)=\int_{-t_i/2}^{t_i/2} x_R(t)\cdot x_T^*(t-2\frac{r_0}{c})\cdot\exp\left(\frac{-j2\pi(2v_0t+at^2)F}{c}\right)dt \tag{4.27}$$

The estimated acceleration is a co-ordinate of the maximum of (4.27).

An alternative solution is to apply the set of acceleration filters to the range-Doppler correlation defined by (4.12). Equation (4.26) can be re-written as

$$y(r,v,a)=\int_{T_0}^{T_{0+}t_i} x_R(t)\cdot x_B^*\left(t-\frac{2r+2vt+at^2}{c}\right)\cdot\exp\frac{-j4\pi vtF}{c}\exp\left(\frac{-j2\pi at^2F}{c}\right)dt \tag{4.28}$$

and the term $\exp(-j2\pi at^2F/c)$ can be treated as the time window. Thus, (4.28) in the case where envelope time stretch can be omitted (at least in the acceleration part), the equation can be written as a convolution of the range-Doppler correlation with the spectrum of the chirp signal related to a given acceleration.

$$y(r,v,a)=y(r,v)\otimes fft\left\{\exp\left(\frac{-j2\pi at^2F}{c}\right)\right\} \tag{4.29}$$

The idea of acceleration estimation in a radar is not new, and several publications are available in the open literature, such as [49]. The accuracy of the acceleration estimation depends on the wavelength and the observation time. The acceleration resolution is equal to

$$\Delta a=\frac{2\lambda}{t_i^2}=\frac{2c}{F_ct_i^2} \tag{4.30}$$

The acceleration resolution versus integration time for different carrier frequencies is presented in Figure 4.14.

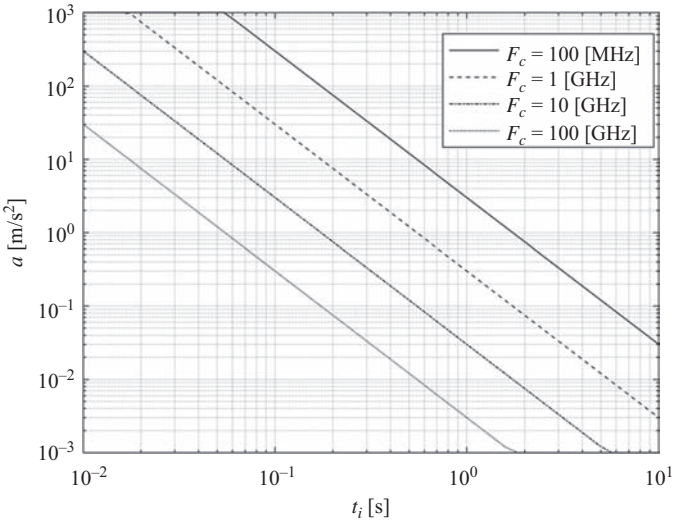

Figure 4.14 Acceleration resolution versus integration time for different carrier frequencies

In classical pulse radars, the illumination time is of the order of a few ms. It depends on the antenna beamwidth and re-visit time. For example, for an antenna with a beamwidth of 1.8^0 and rotation (re-visit) period of 2 s (30 RPM), the illumination time is 4 ms, and for a period of 10 s (6 RPM) is 20 ms. As can be seen from (4.30), acceleration measurement is almost impossible. In FMCW radars, the illumination time is usually much longer, of the order of tens or hundreds of milliseconds, making acceleration measurement possible, as was presented in [1,2,50]. In a noise radar working with fixed beams, the illumination time can be virtually infinite, and the integration time is limited only by the selected integration time. Applying a constant acceleration model, one can increase the integration time over the limits presented in (19) and estimate radial acceleration using (4.29). The details of acceleration estimation in noise radars are presented in [48,51,52].

4.2 Clutter and direct signal cancellation

The detection scheme based on the matched filtering concept [39,53], described by (4.10) for the constant velocity case or (4.26) for the constant acceleration case, is optimal only in single object cases. In the case where there are more targets visible in the antenna beam, the signals originating from one target can be treated as additional noise when the filter is tuned to the second one. The sidelobes originating from the strong targets can then mask the weak target echo, as shown in Figure 4.15. If only a weak target echo is present, the noise floor is low and the target echo is visible. In the case of presence of both weak and strong target echo, only the strong target peak is visible, and the weak one is masked by processing sidelobes.

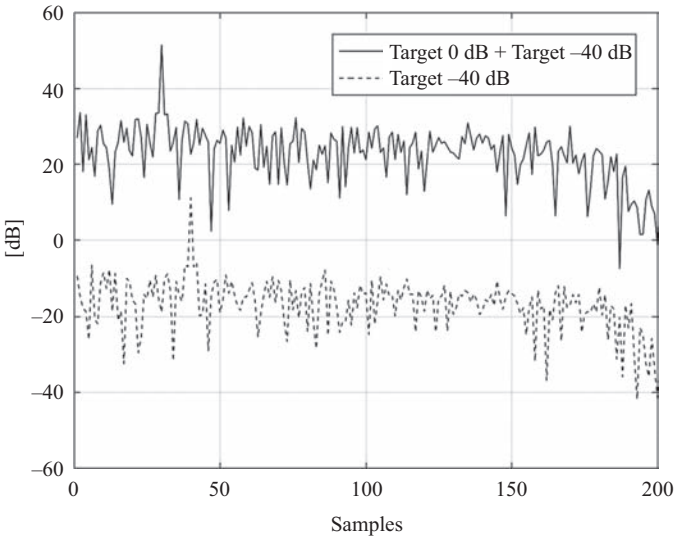

Figure 4.15 Masking effect in noise radar

In the case of a single target, the detection range is limited in noise (and other) radars by receiver thermal noise. In the multi-target cases, the detection range can be limited by ground clutter or strong echoes, while the direct signal, strong echo returns, ground clutter echoes and distant targets' weak echoes are received simultaneously. Such an effect is not present in pulse radars, as all of these components are separated in time, and range gain control can solve the dynamic problem of noise radar.

4.2.1 Noise radar range equation

The echo power received by the noise radar receiver is equal to

$$P_R = \frac{P_T G_T}{16\pi^2 R^4 L} S_o S_R \tag{4.31}$$

where P_T denotes the effective transmitted power, G_T is the transmit antenna gain, S_o is the target radar cross-section, S_R is the received antenna effective surface, R is the range to the target and L denotes all the losses in the radar system, including transmission losses, propagation losses and receiving losses. This expression can be also presented in the form:

$$P_R = \frac{P_T G_T G_R \lambda^2}{(4\pi)^3 R^4 L} S_o \tag{4.32}$$

where G_R is the receiving antenna gain, and $\lambda = cF$ is the wavelength of the transmitted signal.

In the single target cases, the target echo power has to be detected in the presence of receiver thermal noise

$$P_N = kT_R B \tag{4.33}$$

where T_R is the effective system noise temperature (dependent on the temperature of the receiver, the receiver's noise figure, antenna noise and outer space noise), B – the receiver bandwidth, and k is Boltzmann's constant (1.380×10^{-23} [J K^{-1}]). The radar detection criterion can then be written as

$$\frac{P_T G_T G_R \lambda^2}{(4\pi)^3 R^4 L} S_o > kT_R B D_o \tag{4.34}$$

where D_o is the detection threshold, usually having the value of 10–16 dB, depending on the assumed probability of a false alarm in the Neyman–Pearson detector. The maximum detection range can be predicted by the equation

$$R_{\max} = \sqrt[4]{\frac{P_T G_T G_R \lambda^2 S_o}{(4\pi)^3 L k T_R B D_o}} \tag{4.35}$$

For a noise radar, after the matched filtering, the effective receiver bandwidth is reduced to the value $1/t_i$ which is usually much lower than the original radar bandwidth B. In a typical case, the radar bandwidth is in the range of 1 MHz to 1 GHz, while the effective receiver bandwidth obtained by coherent integration is in the range of 0.1–1000 Hz. The effect of reducing receiver bandwidth in integration processing is called integration gain, which is equal to the time-bandwidth product Bt_i. Applying the effective bandwidth to (4.35), one can obtain the final noise radar range equation as

$$R_{\max} = \sqrt[4]{\frac{E_T G_T G_R \lambda^2 S_o}{(4\pi)^3 L k T_R D_o}} \tag{4.36}$$

where $E_T = P_T t_i$ is the total energy sent towards the target during the integration time.

In a multiple target scenario, when the filter is tuned to a distant target, the total noise power is now equal to

$$P_N = kT_R B + P_{RN} \tag{4.37}$$

where P_{RN} is the sum of all received echo powers except for the one to which the filter is tuned. Each echo power is described by (31). If $P_{RN} \gg kT_R B$, then (4.34) for a two-target case, taking in consideration the integration gain, takes the form

$$\frac{P_T G_T G_R \lambda^2}{(4\pi)^3 R^4 L} S_o > \frac{P_T G_T G_R \lambda^2}{B t_i (4\pi)^3 R_N^4 L} S_N D_o \tag{4.38}$$

where R_N is the range to the strongest near target (or clutter), and S_N is the radar cross-section of this target.

As a result, the radar detection range is shortened to the value of

$$R_{\max} = R_N \sqrt[4]{\frac{S_o B t_i}{S_N D_o}} \tag{4.39}$$

Assuming that both the targets are of similar size, the integration gain is at the level of 50 dB, and the detection threshold is at the level of 10 dB, the noise radar detection range is limited to 10 R_N. The situation can be much worse when a near target or ground clutter radar cross-section is significantly higher than that of the target.

Another limitation relates to the total dynamic range of the noise radar receiver. The power received by the radar is proportional to the integration gain, equating to $1/R^4$. If the radar has to observe two identical targets, one at a distance of 10 m and one at a distance of 10 km, the difference between the near and far echo power is 120 dB. Adding 10 dB of threshold, the required dynamic of the radar receiver is equal to 130 dB. This dynamic range requirement is defined after integration processing, but assuming 50 dB of integration gain, l80 dB of dynamic range in the analogue part, and an analogue-to-digital converter (ADC) is still required, which is a high number.

4.2.2 Ground clutter cancellation

In the presence of direct signal interferences and multiple targets, more sophisticated detection schema has to be used. The optimal solution to the masking problem is to solve the non-linear equation set for each sampling instance t_j, presented by

$$X_R(t_j) = \xi(t_j) + \sum_i A_i X_T\left(t_j - 2\frac{r_i}{c}\right) e^{-4\pi(F_t v_{ti}/c)t_j} \tag{4.40}$$

where A_i, r_i, v_i are complex amplitudes, ranges and range velocities of all observed targets, including ground clutter returns, for which $v_i = 0$. The mean-square solution gives the unknown vectors [A_i], [r_i] and [v_i]. This approach, although optimal, is computationally very inefficient and cannot be performed in real time. It requires the solving of a non-linear equation set. In real time, it is possible to apply a sub-optimal approach. The received signal consists of three signal groups: receiver thermal noise, ground clutter echoes and moving target echoes.

Under the assumption that the echo power originating from moving targets is much smaller than the echo power originating from ground clutter, it is possible to find the ground clutter parameters by solving the simplified equation set

$$X_R(t_j) = \xi_e(t_j) + \sum_i A_i X_T\left(t_j - 2\frac{r_i}{c}\right) \tag{4.41}$$

which is related only to ground clutter. The equation set is still non-linear and difficult to solve. Further simplification is based on the assumption that the clutter is placed on an equal-spaced distance grid related to the sampling period $r_i = iT_s/2c$.

Under such assumptions, the equation set (4.41) becomes linear versus the unknown clutter amplitude vector [A_i].

$$X_R(t_j) = \xi_e(t_j) + \sum_i A_i X_T\left(t_{(j-i)}\right) \tag{4.42}$$

The estimated clutter echo amplitudes [$\hat{A}_i$] can be further used for ground clutter attenuation. The attenuation is performed by the subtraction of the modelled clutter echoes' signals from the received signal, according to

$$X_R^{rem}(t_j) = X_R(t_j) - \sum_i \hat{A}_i X_T\left(t_{(j-i)}\right) \tag{4.43}$$

and the cleaned signal can be used for moving target detection using (4.12) or (4.20).

The direct solution of (4.42) is still computationally inefficient, so several more computationally effective methods have been devised using an adaptive filter concepts, e.g. the block lattice filter orthogonalization of the signal base set $\{X_T(t_{(j-i)})\}$ and iterative block ground clutter removal.

Figure 4.16 shows an example of a noise radar observing moving targets on the road [9]. It also receives strong ground clutter originating from trees. In Figure 4.17, the cross-section of the zero Doppler beam of the ambiguity function before and after the application of clutter cancellation is presented. It is easily seen that the residual fluctuations at the level of $Bt = 60$ dB below the strongest return completely masks the weak targets. After clutter cancellation, the strongest components are attenuated by 70 dB, and the noise floor is decreased by more than 40 dB. The cross-ambiguity function of the received signal is shown in Figure 4.18. The direct signal interferences and ground clutter are visible out to a range of 150 m. All moving targets are masked by ground clutter.

Figure 4.16 Experimental noise radar used for the detection of road traffic. Two antennas of the radar, mounted on a trailer next to the road, is visible on the right-hand side

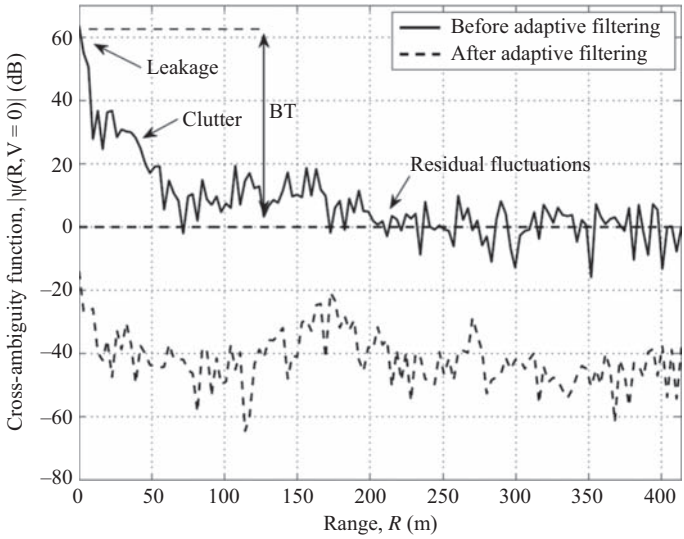

Figure 4.17 Signal at the output of correlation processing before and after the application of the clutter cancellation algorithm

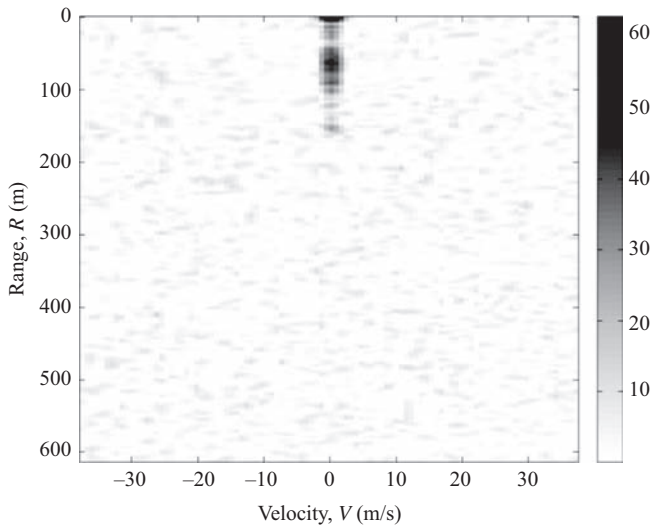

Figure 4.18 Cross-ambiguity function of the received signal (without ground clutter cancellation) – only ground clutter visible. Grey scale in dB

In Figure 4.19, the cross-ambiguity function of the received signal after clutter cancellation is presented. Clutter was cancelled up to the range of 560 m. Radar detections at the level of −30 to −10 dB are visible, together with the track of the co-operating target. The target echoes levels are 70 to 90 dB below the strongest

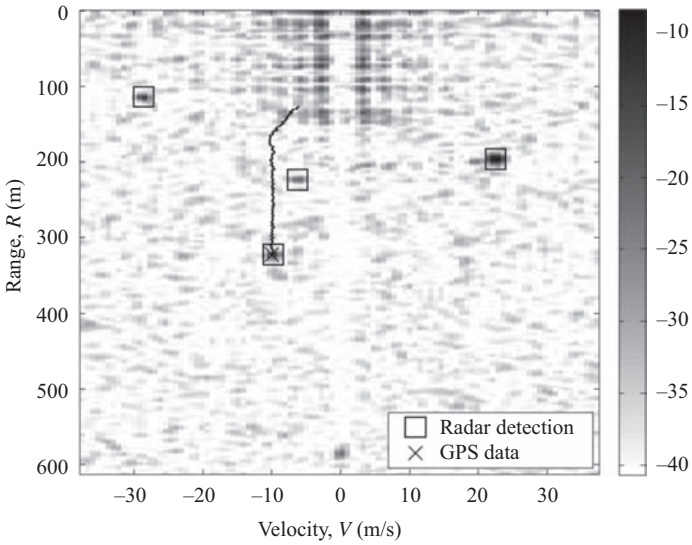

Figure 4.19 The cross-ambiguity function of the received signal after ground clutter cancellation – moving targets visible, ground clutter attenuated by 70 dB. Grey scale in dB

received signal component. The ground clutter at the distance of 600 m is also visible, together with the Doppler spread clutter at a distance of up to 150 m, caused by trees and canopy motion. The Doppler spread components can also be attenuated, which is described in detail in [54].

4.3 MIMO noise radars

In the last few years, the concept of MIMO radar [55,56] has gained considerable popularity among radar researchers. The most distinctive feature of such a radar is the transmission of multiple waveforms from different locations and their reception at different receivers that can separate captured signals in terms of their origin. This definition of spatial waveform diversity is true both for statistical MIMO radar with widely spread nodes [57], known for many years as multistatic radar [58], as well as for co-located MIMO radar which enables coherent beamforming [59,60]. The most common technique to allow signal separation is transmission division in time or frequency domain. Another solution is to maintain waveform orthogonality with respect to the inner product over the integration period.

The latter approach is perfectly suited for noise radar, whose waveforms, by definition, are orthogonal to a degree defined by their time-bandwidth product, if different realizations of random process are used. In such cases, all nodes can transmit simultaneously in the same band, which allows for a fully continuous waveform operation mode.

The following section will focus on co-located MIMO, which means that the radiators of the antenna array are close enough to each other so that they can observe the object at the same aspect and, thus, the same phase of its scattering coefficient. As a result, coherent beamforming is possible. Another assumption is that the radar works in continuous wave mode. It is not a crucial requirement but it allows the achievement of good integration gain and to avoid distinctive pulse modulation.

The definition of MIMO above says nothing about the potential advantages of this mode over its classical electronically scanned phased-array counterpart which would justify the computational burden of the correlation between received waveforms and all transmit templates, instead of one. To derive them, reasonable criteria for comparison must be set. The following assumptions will be made: there are K transmit and L receive antennas, each antenna radiates the same power, and there is a time of N samples for single integration. Another assumption is that at least K transmit beams must be produced to satisfactorily cover the whole azimuth sector.

4.3.1 Signal model

For any array radar, the narrow-band signal reflected from a point scatterer and received by an lth antenna can be described after quadrature de-modulation as

$$y_l(t;\phi_0) = \alpha_0 e^{-j\omega_d t} \sum_{k=1}^{K} x_k(t-\tau_0) \cdot e^{-j\omega_c[\tau_k(\phi_0)+\tau_l(\phi_0)]} + w_l(t) \tag{4.44}$$

where α_0 is the complex amplitude of target reflectivity, x_k is the waveform transmitted by the kth antenna, τ_0 is the main time delay, τ_k and τ_l are the relative delays between a target placed at angle ϕ_0 and the subsequent antennas, ω_c is the carrier angular frequency, ω_d is the Doppler frequency shift and $w_l(t)$ is additive noise or interference.

This can be simplified by the use of vector notation so that the set of received signals can be described by

$$\mathbf{y}(t;\phi_0) = \alpha_0 e^{-j\omega_d t}\mathbf{b}(\phi_0)\mathbf{a}^{\mathrm{T}}(\phi_0)\mathbf{x}(t-\tau_0) + \mathbf{w}(t) \tag{4.45}$$

where

$$\mathbf{a} = \left[e^{-j\omega_c\tau_{R\times 1}(\phi)}, \ldots, \mathrm{e}^{-j\omega_c\tau_{R\times K}(\phi)}\right]^T \tag{4.46}$$

and

$$\mathbf{b} = \left[e^{-j\omega_c\tau_{T\times 1}(\phi)}, \ldots, \mathrm{e}^{-j\omega_c\tau_{T\times L}(\phi)}\right]^T \tag{4.47}$$

are the steering vectors of the transmit and receive array.

The distinction between a classical phased array and MIMO lies within the form of $\mathbf{x}(t)$. In the first case, this is the same noise realization $x_0(t)$ phase shifted at following transmitters according to the weighting vector $\mathbf{a}^*(\phi_T)$. The weights are

derived from the steering vector corresponding to the wanted illumination angle ϕ_T. In the case of MIMO, each entry in $\mathbf{x}(t)$ is an independent noise realization.

The noise radar processing is based on the correlation of the received signal with a template. In the case of MIMO, that can be synthetically written as follows (for simplification, further considerations are limited to a single cell of the cross-ambiguity function):

$$\mathbf{Z}(\phi_0) = \int_0^{T_0} \mathbf{y}(t)\mathbf{x}^H(t)dt = \alpha_0 \mathbf{b}(\phi_0)\mathbf{a}^T(\phi_0)\mathbf{R_{xx}} + \mathbf{V} \tag{4.48}$$

$\mathbf{Z}$ is the measurement matrix for a target placed at angle ϕ_0. The $\mathbf{R_{xx}}$ is the matrix of the spatial correlation of the transmitted signal, while $\mathbf{V}$ is post-integration noise.

When more than one target appears in the examined cell, it is a sum of scaled steering vectors' products obtained for subsequent target angles that is multiplied by the $\mathbf{R_{xx}}$ correlation matrix instead of one. When a classical phased array is considered, only the correlation with $x_0^H(t)$ is needed in practice but the result must be multiplied by a transmit steering vector to keep the generality of notation.

In the case of MIMO radar, the $\mathbf{R_{xx}}$ is diagonal with respect to residuals at the level of the time-bandwidth product below the diagonal.

For a classical phased array, the matrix has a form of $\mathbf{a}^*(\phi_T)\mathbf{a}^\mathbf{T}(\phi_T)$ and is singular. The form of the matrix is crucial to the antenna-pattern comparison.

4.3.2 Beamforming and antenna pattern

To perform beamforming, an appropriate criterion regarding its output must be formulated. The most commonly used one is to minimize the output noise with constrained amplitude of the template signal $\mathbf{s}(\phi)$ at the output:

$$\min_{\mathbf{h}} \mathbf{h}^{\mathrm{H}}(\phi)\mathbf{R}\mathbf{h}(\phi) \tag{4.49}$$

with constraint $\mathbf{h}^{\mathrm{H}}(\phi)\mathbf{s}(\phi) = 1$. The solution to such an optimization problem is given by

$$\mathbf{h}(\phi) = \frac{\mathbf{R}^{-1}\mathbf{s}(\phi)}{\sqrt{\mathbf{s}^{\mathbf{H}}(\phi)\mathbf{R}^{-1}\mathbf{s}(\phi)}} \tag{4.50}$$

When the MIMO radar is considered, the closed form expression for the output signal-to-noise power ratio can be derived as a ratio of output signal power to the power of noise propagating through the filter. In this case, the spatial correlation matrix of noise $\mathbf{R}$ will be replaced with the extended auto-correlation $\mathbf{R_{vv}}$ of the vectorized post-correlation noise $\mathbf{v}$. The measurement signal will also be in the vectorized form $\mathbf{z}$.

$$\widehat{\mathbf{P}}_{\mathbf{S/N}}(\phi) = \frac{\left|\mathbf{h}^{\mathrm{H}}(\phi)\mathbf{z}\right|^2}{\mathbf{h}^{\mathrm{H}}(\phi)\mathbf{R_{vv}}\mathbf{h}(\phi)} \tag{4.51}$$

By substituting **h** with (4.50), assuming Kronecker's structure of channel, and exploiting the properties of the Kronecker product, (4.51) can be re-formulated as [59]:

$$\widehat{\mathbf{P}}_{\mathbf{S/N}}(\phi) = \frac{\left|\mathbf{b}^{\mathrm{H}}(\phi)\mathbf{R}_{\mathbf{ww}}^{-\mathbf{1}}\mathbf{Z}\mathbf{a}^{*}(\phi_{\mathrm{T}})\right|^{\mathbf{2}}}{\mathbf{a}^{\mathrm{H}}(\phi_{\mathrm{T}})\mathbf{R}_{\mathbf{xx}}^{*}\mathbf{a}(\phi_{\mathrm{T}})\mathbf{b}^{\mathrm{H}}(\phi)\mathbf{R}_{\mathbf{ww}}^{-\mathbf{1}}\mathbf{b}(\phi)} \tag{4.52}$$

where $\mathbf{R_{ww}}$ is the spatial correlation matrix of noise and interferences. In this form, if **Z** is replaced with a point response template $\mathbf{S}(\phi_0)$, it is simple to derive theoretical array radiation patterns and quantify the impact of transmitted signal auto-correlation on the radar performance:

$$\mathrm{G}(\phi,\phi_{\mathrm{T}},\phi_0)=G_{\mathrm{Tx}}(\phi_0)\frac{\left|\mathbf{a}^{\mathrm{H}}(\phi_0)\mathbf{R}_{\mathbf{xx}}^{*}\mathbf{a}(\phi_{\mathrm{T}})\right|^{\mathbf{2}}}{\mathbf{a}^{\mathrm{H}}(\phi_{\mathrm{T}})\mathbf{R}_{\mathbf{xx}}^{*}\mathbf{a}(\phi_{\mathrm{T}})}G_{\mathrm{Rx}}(\phi_0)\frac{\left|\mathbf{b}^{\mathrm{H}}(\phi_0)\mathbf{R}_{\mathbf{ww}}^{-\mathbf{1}}\mathbf{b}(\phi)\right|^{\mathbf{2}}}{\mathbf{b}^{\mathrm{H}}(\phi)\mathbf{R}_{\mathbf{ww}}^{-\mathbf{1}}\mathbf{b}(\phi)} \tag{4.53}$$

When the matrix $\mathbf{R_{xx}}$ is replaced with a diagonal one, which is characteristic for the MIMO mode, the transmit part of the expression will take the form of $|\mathbf{a}^{\mathrm{H}}(\phi_0)\mathbf{a}(\phi_{\mathrm{T}})|^{\mathbf{2}}/\mathbf{K}$, while in the phased array mode with a strictly correlated set of transmitted signals it is $|\mathbf{a}^{\mathrm{H}}(\phi_0)\mathbf{a}(\phi_{\mathrm{T}})|^{\mathbf{2}}/\mathbf{1}$. This means that in MIMO mode, the achievable signal-to-noise ratio (SNR) is K times smaller due to beamforming properties than in its phased array counterpart. This can be explained quite straightforwardly, since in classical radar, the amplitude of a transmitted signal grows K times due to coherent summation, while in MIMO only medium power grows that much. Therefore, under the same conditions, the shape of the angular response for a single scatterer is exactly the same in MIMO and conventional phase radar, with K-fold gain in favour of the classical solution. An exemplary angular radiation pattern of a 10-by-10 array of omni-directional radiators and a reflecting point placed at the azimuth angle of 0º is presented in Figure 4.20.

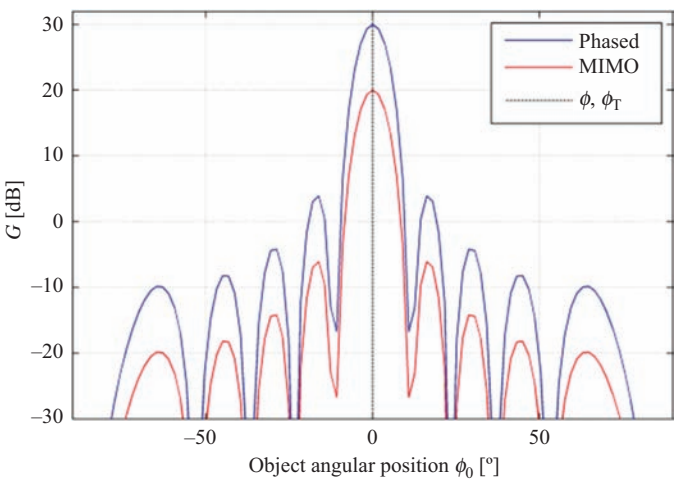

Figure 4.20 Radiation-pattern comparison

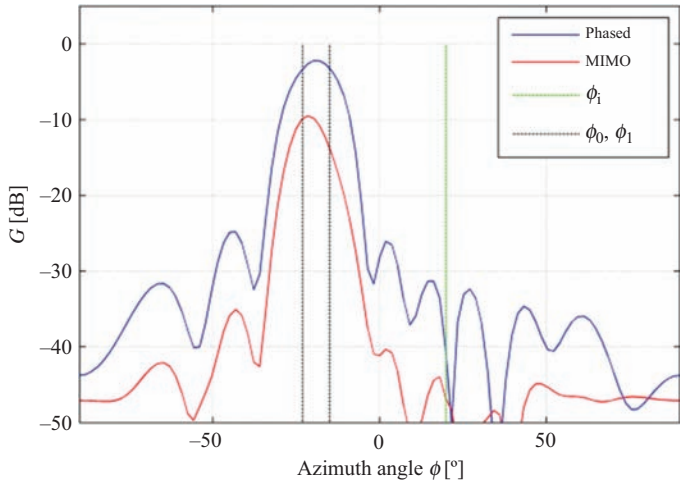

Figure 4.21 Simulated result of Capon beamformer response

4.3.3 Adaptive beamforming

Depending on the knowledge of the spatial interference distribution, different beamforming results may be obtained with (4.53). When the interferences are non-directional and come from receiver noise, the $\mathbf{R}_{ww}$ matrix is diagonal, and it is the conventional beamformer that should be used. When there are directional interferences and matrix $\mathbf{R}_{ww}$ is known, then they can be cancelled. The spatial correlation matrix of the interferences may be known, for example, when they are stationary and receive-only observation was done. When such a procedure is not possible, one may use the $\mathbf{R}_{yy}$ matrix instead of $\mathbf{R}_{ww}$. Such a solution is known as a Capon beamformer or minimum variance distortionless response; however, some authors use different naming conventions. In this case, apart from the interferences, the echo signature is also present in the matrix. Due to the constraint in (4.6), the beamformer does not cancel the useful echo. An example of its use is presented in Figure 4.21 where two objects and interference were placed on a simulated scene with SNR equal to −30 dB. The interference was cancelled in both cases but the phased array suffers slight gain degradation in comparison to MIMO. What is worth mentioning is that if the SNR before integration was around 0 dB or higher, the beamformer would allow the separation of two objects with super-resolution for MIMO and spoil the performance for the phased array.

4.3.4 Virtual Nyquist array

In the MIMO radar bibliography, there is a widely spread concept of virtual aperture resulting from the spatial convolution of transmit and receive radiators [59,61]. Such convolution has an interesting property when one of the arrays – transmit or receive – is full, which means $\lambda/2$ spacing preventing the occurrence of prevents

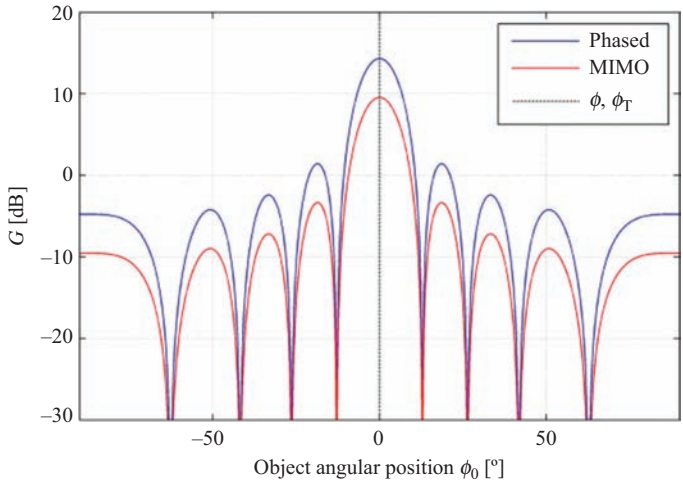

Figure 4.22 Radiation-pattern comparison for virtual Nyquist arrays

aliasing and grating lobes, and the second is sparse in a specific way; namely, the spaces between the radiators are one $\lambda/2$ slot smaller than the size of the full array. The resultant convolution produces a uniform dense array of the size KL. Such an aperture provides much better angular resolution than two dense arrays with the same number of elements with no grating lobes.

The point is that it is not a feature of the MIMO mode but of the array geometry itself [62]. A classical phased array would behave in exactly the same way. If proper spacing is maintained, nulls of the full array cancel the grating lobes of the sparse one. If the transmit array of classical radar is sparse, apart from the main beam, the energy will be transmitted in unwanted directions according to the grating lobes, but any return from those angles will be nullified by the receive pattern. When the receive array is sparse, there will be grating lobes in the receive pattern but no energy radiated in those directions by the full transmit array. As an illustration, the gain patterns obtained for a 3-by-3 array according to (4.10) are presented in Figure 4.22. The shape is the same and the overall level is K times higher for classical radar, accordingly to the explanation from previous sections. What is worth mentioning is that such an array configuration works well only for a diagonal interference matrix, since the cancellation of grating lobes consumes all degrees of freedom that could be used for adaptive beamforming.

4.3.5 Benefit of MIMO

The MIMO radar gains considerably when not a single angle but an angular sector observation is performed. The pattern presented in Figure 4.23 is valid for a scenario where a conventional array illuminates a single angle for a given time, equal to the acquisition of N samples. If it was to cover K angles within the same time, it would have to divide the integration time by K, thus reducing the integration gain

Figure 4.23 MIMO noise radar demonstrator

from the correlation processing. What is gained from transmit beamforming in comparison to the MIMO is to be lost due to time division between observation angles. The production of multiple beams on receive is in this case redundant, since other directions are not illuminated. The MIMO radar constantly illuminates the whole scene, and a high number of transmit–receive synthetic beams can be produced. Therefore, if a sector observation scenario is considered, the achievable SNR is the same, provided the sector observation time is not excessively long, and target movement does not cause coherency loss.

With equal SNR, there are some undeniable gains from MIMO in the discussed scenario. The first is the extension of integration time, simultaneous for all beams, that results in improved velocity resolution which can be crucial in some applications. The other is the decrease in peak-radiated power and the lack of envelope modulation due to transmit beam sweeping. In the case of CW operation mode, where reflections form strong, close scatterers which can saturate the receiver, an increase in radiated power does not necessarily lead to improved SNR, since the reflected power grows as well. In MIMO, the lack of such spatial power accumulation allows the use of a more sensitive receiver without the risk of constant saturation.

There is an interesting analogy between FMCW radar versus CW noise radar and a conventional array versus a MIMO array. The first pair differs in the time–frequency distribution of radiated power. In FMCW, the power is focused on one point of the spectrum at a time, with the point of focus sweeping through the whole band, while in noise radar it is randomly distributed for the whole integration period. Similarly, in a classical phased array, the focused beam sweeps through the spatial domain, while in CW noise MIMO there is a constant spatially spread

transmission. To conclude, CW noise MIMO radar is the most energy-spread radar system one can imagine. This feature makes it less prone to being detected and less likely to produce disturbances to other devices sensitive to peak power level.

4.3.6 Experimental results

In order to prove some features of noise MIMO radar, a demonstrator based on a commercial off-the-shelf (COTS) hardware platform and offline processing was developed. It used an arbitrary waveform generator as a transmitter and a vector signal analyser as a receiver, with 50 MHz of instantaneous bandwidth. There were three phase-coherent transmit channels, three receive channels and one reference waveform input allowing digital synchronization between the transmitter and receiver. WiFi sector antennas for 2.4 GHz were used, with a simple front end including amplifiers and a bandpass filter. Each antenna had a width of a single patch radiator along the array axis equal to 6 cm, which allowed for nearly $\lambda/2$ spacing. Phase calibration was carried out either using an active corner reflector with Doppler modulation capability, or allowing only relative angular measurements of the target. Calibration on a stationary corner reflector turned out to be inaccurate due to the influence of the ground echo from the same range cell. The radar demonstrator on the test site is presented in Figure 4.23.

The first task of the radar was to perform imaging of the whole scene within a single integration of 100 ms. The result is presented in Figure 4.24. The empty car park is marked with a dashed line, the active calibrator placed on a car with a triangle and the passive corner reflector with a circle. The positions of buildings are shown with solid rectangles. The seemingly poor quality of the image is fully justified by the system parameters – range resolution and number of array elements. What is important is that to produce the equivalent with a classical array, one would have to sweep through all the angles with a transmit beam. For the given time slot for the whole scene, the achievable SNR would have been the same.

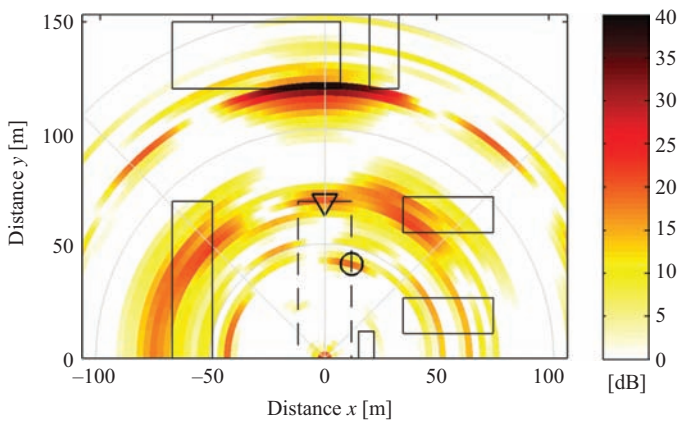

Figure 4.24 Image of stationary objects obtained in MIMO mode

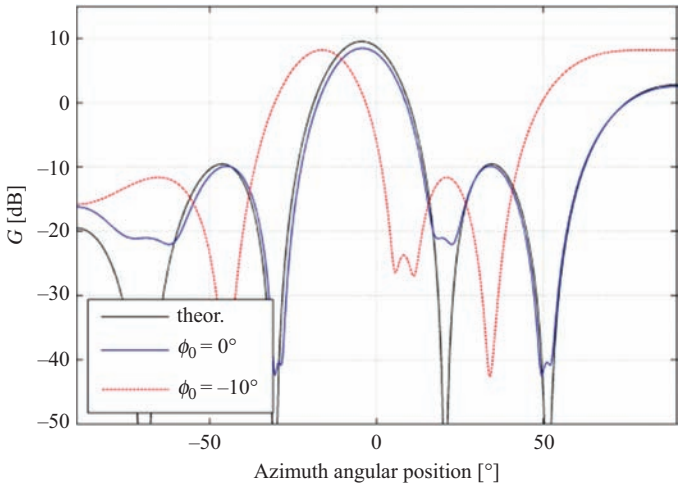

Figure 4.25 Azimuth response of point-like moving object – theoretic and measured

Another result was obtained for a moving target – a man with an active signal repeater running radially towards the radar – in two turns at two different angles. In this case, the range-Doppler cell containing the target was extracted, and for each time snapshot range beamforming was done. The echoes from the dominant stationary scatterers were cancelled using a set of lattice filters. An angular response of the man for two runs at different azimuth angles is presented against the theoretic array response pattern. Since the point-like target was well isolated from the other ones, the measured pattern nearly overlays the theoretical one in Figure 4.25; the form of one of the patterns extracted was exactly the same as the recording of the scene image. In this case, the radar looked in all directions simultaneously, which allowed multi-angle observation with long integration time and good velocity resolution. With a classical array counterpart and the same time assigned for the whole-scene observation, the velocity resolution would be three times lower, which in the case of a relatively slow target would cause its overlap by velocity sidelobes of strong stationary targets.

4.3.7 Conclusions

When the task of the radar is to cover a given angular sector in surveillance or search mode, continuous wave noise radar in MIMO mode brings several advantages over its phased array counterpart:

- If there are K transmit beams, and a fixed time to scan the whole sector, the MIMO and phased array achieve the same SNR. The phased array gains on transmit power concentration whereas MIMO makes it up with longer target illumination and effective integration.

- Longer integration gives better velocity resolution for the whole sector at the same time.
- If the radar is to detect some ephemeral phenomenon at an unknown angle, simultaneous multi-directional observation MIMO mode prevents the radar from missing it.
- In MIMO continuous wave radar, due to multi-directional simultaneous illumination, the transmitted peak power and thereby peak power of strong echoes is statistically K times smaller for the Gaussian waveform, which improves usage of the vertical range of the radar receiver, resulting in greater obtainable range.
- Lower peak power and lack of modulation caused by the angular beam sweep in MIMO mode may be crucial to the LPI properties of the radar.
- Capon beamformers works better for MIMO but only for high input SNR, barely possible in radar. Otherwise, the spatial resolution is exactly the same in MIMO as it is in a phased array, unless the influence of transmit beamforming is neglected for the phased array.
- The ability to form an extended virtual array improving spatial resolution is not a feature of MIMO but of array geometry itself and can be obtained in a phased array as well.
- In MIMO, the calibration of the transmit array may be done offline, whereas in a phased array it must be assured before transmission.

MIMO needs more independent transmit channels, the data throughput of reference signals is K times larger, and instead of K or L correlations, KL must be calculated. Moreover, tracking of a single distant object with no masking interference from close objects is done better with a conventional phased array. Before implementing a MIMO noise radar to a particular application, one must consider whether the need for the exploitation of the advantages above is justified.

References

[1] A. Wojtkiewicz, M. Nałęcz, K. Kulpa and W. Klembowski, 'Use of polynomial phase modeling to FMCW radar. Part C: Estimation of target acceleration in FMCW radars', in *NATO Research and Technology Agency, Sensors & Electronics Technology Symposium on Passive and LPI (Low Probability of Intercept) Radio Frequency Sensors*, Warsaw, Poland, 23–25 April 2001, paper #40C.

[2] R. Zhang, Y. Huang, J. Yang and J. Xiong, 'LFMCW radar multi-target acceleration and velocity estimation method', in *2004 Seventh International Conference on Signal Processing*, vol. 3, 2004, pp. 1989–1992.

[3] R. H. Barker, 'Group synchronizing of binary digital systems', in *Communications Theory*, Butterworth, London, pp. 273–287, 1953.

[4] P. Borwein and R. Ferguson, 'Polyphase sequences with low autocorrelation', *IEEE Transactions on Information Theory*, vol. 51, no. 4, pp. 1564–1567, April 2005.

[5] P. Borwein and R. Ferguson, 'Barker sequences', in *CMSMITACS Joint Conference*, Winnipeg, Manitoba, 31 May–3 June 2007.
[6] R. Frank, 'Polyphase codes with good nonperiodic correlation properties', *IEEE Transactions on Information Theory*, vol. 9, no. 1, pp. 43–45, January 1963.
[7] B. L. Lewis and F. F. Kretschmer, 'A new class of polyphase pulse compression codes and techniques', *IEEE Transactions on Aerospace and Electronic Systems*, vol. AES-17, no. 3, pp. 364–372, May 1981.
[8] L. Guosui, G. Hong and S. Weimin, 'Development of random signal radars', *IEEE Transactions on Aerospace and Electronic Systems*, vol. 35, no. 3, pp. 770–777, July 1999.
[9] M. Malanowski and K. Kulpa, 'Detection of moving targets with continuous-wave noise radar: Theory and measurements', *IEEE Transactions on Geoscience and Remote Sensing*, vol. 50, no. 9, pp. 3502–3509, September 2012.
[10] M. Malanowski and P. Roszkowski, 'Bistatic noise radar using locally generated reference signal', in *2011 12th International Radar Symposium (IRS)*, Leipzig, 2011, pp. 544–549.
[11] V. I. Kalinin and V. V. Chapursky, 'Wideband noise radar for detection of slow moving objects', in *2004 14th International Crimean Conference 'Microwave and Telecommunication Technology' (IEEE Cat. No. 04EX843)*, 2004, pp. 695–696.
[12] T. Thayaparan, M. Dakovic and L. Stankovic, 'Mutual interference and low probability of interception capabilities of noise radar', *IET Radar, Sonar & Navigation*, vol. 2, no. 4, pp. 294–305, August 2008.
[13] D. D. Garmatyuk and R. M. Narayanan, 'Ultrawideband noise synthetic aperture radar: Theory and experiment', in *IEEE Antennas and Propagation Society International Symposium. 1999 Digest. Held in conjunction with: USNC/URSI National Radio Science Meeting (Cat. No. 99CH37010)*, Orlando, FL, USA, vol. 3, 1999, pp. 1764–1767.
[14] Y. Duan, Z. Yu and Y. Zhang, 'Research progress of noise radar technologies', *2011 3rd International Asia-Pacific Conference on Synthetic Aperture Radar (APSAR)*, Seoul, 2011, pp. 1–4.
[15] D. Tarchi, K. Lukin, J. Fortuny-Guasch, A. Mogyla, P. Vyplavin and A. Sieber, 'SAR imaging with noise radar', *IEEE Transactions on Aerospace and Electronic Systems*, vol. 46, no. 3, pp. 1214–1225, July 2010.
[16] X. Gu, Y. Zhang and X. Zhang, 'Stepped frequency random noise UWB radar signal', *2011 3rd International Asia-Pacific Conference on Synthetic Aperture Radar (APSAR)*, Seoul, 2011, pp. 1–4.
[17] K. S. Kulpa, Z. Czekala and M. Smolarczyk, 'Long-integration-time noise surveillance radar', in *First International Workshop on the Noise Radar Technology NRTW-2002*, 18–20 September 2002, pp. 238–243.
[18] Ł. Maślikowski and K. Kulpa, 'Bistatic quasi-passive noise SAR experiment', in *11th International Radar Symposium*, Vilnius, Lithuania, 2010, pp. 1–3.

[19] Ł. Maślikowski, C. Contartese, M. Malanowski and K. Kulpa, 'Preliminary results of ground-based noise SAR experiments', *Eighth European Conference on Synthetic Aperture Radar*, Aachen, Germany, 2010, pp. 1–4.

[20] L. Maslikowski, M. Malanowski and K. Kulpa, 'Stepped frequency ground-based noise SAR demonstrator', in *2011 Third International Asia-Pacific Conference on Synthetic Aperture Radar (APSAR)*, Seoul, 2011, pp. 1–2.

[21] X. Xu and R. M. Narayanan, 'FOPEN SAR imaging using UWB step--frequency and random noise waveforms', *IEEE Transactions on Aerospace and Electronic Systems*, vol. 37, no. 4, pp. 1287–1300, October 2001.

[22] K. Lukin, P. Vyplavin and N. Kolchigin, 'Noise waveform SAR imaging in antenna near zone', in *2006 International Radar Symposium*, Krakow, Poland, 2006, pp. 1–4.

[23] D. Tarchi, D. Leva, K. A. Lukin, A. A. Mogyla, G. Nesti and A. J. Sieber, 'Short range imaging applications of noise radar technology', in *Proceedings of EUSAR 2000*, Munich, Germany, 23–24, May 2000, pp. 361–364.

[24] D. S. Garmatyuk and R. M. Narayanan, 'SAR imaging using a coherent ultra wideband random noise radar', in *Radar Processing, Technology, and Applications IV* (William J. Miceli, ed.), *Proceedings of SPIE*, Denver, CO, vol. 3810, July 1999, pp. 223–230.

[25] K. A. Lukin, 'Ground based noise-waveform-SAR for monitoring of Chernobyl sarcophagus', in *Proceedings of IRS 2005*, Berlin, 6–8 September 2005, pp. 655–659, German Institute of Navigation (DGON e.V.).

[26] D. S. Garmatyuk and R. M. Narayanan, 'SAR imaging using fully random bandlimited signals', in *IEEE Antennas and Propagation Society International Symposium. Transmitting Waves of Progress to the Next Millennium. 2000 Digest. Held in conjunction with: USNC/URSI National Radio Science Meeting*, Salt Lake City, UT, USA, vol. 4, 2000, pp. 1948–1951.

[27] A. A. Mogila, K. A. Lukin, N. P. Kovalenko and R. P. Kovalenko, 'Ka-band noise SAR simulation', in *The Fourth International Kharkov Symposium on Physics and Engineering of Millimeter and Sub-Millimeter Waves, 2001*, vol. 1, 4–9 June 2001, pp. 441–443.

[28] D. C. Bell and R. M. Narayanan, 'ISAR turntable experiments using a coherent ultrawide band random noise radar', in *IEEE Antennas and Propagation Society International. Symposium*. 1999, Orlando, FL, July 1999, pp. 1768–1771.

[29] Y. Xu, R. M. Narayanan, X.-J. Xu and J. O. Curtis, 'Polarimetric processing of coherent random noise radar data for buried object detection', *IEEE Transactions on Geoscience and Remote Sensing*, vol. 39, no. 3, pp. 467–478, March 2001.

[30] B. A. Reeves and W. B. Müller, 'Traffic-speed 3-D noise modulated ground penetrating radar (NM-GPR)', in *2012 14th International Conference on Ground Penetrating Radar (GPR)*, Shanghai, 2012, pp. 165–171.

[31] W. B. Müller and B. A. Reeves, 'Comparing traffic speed deflectometer and noise-modulated ground penetrating radar data for rapid road pavement

investigations', in *2012 14th International Conference on Ground Penetrating Radar (GPR)*, Shanghai, 2012, pp. 502–509.

[32] B. M. Horton, 'Noise-modulated distance measuring system', *Proceedings of the IRE*, V0147, pp. 821–828, May 1959. Reprinted in *Radars*, vol. 7, *CW and Doppler Radar* (D. K. Barton, ed.), Artech House, Norwood, MA, 1978.

[33] G. R. Cooper and C. D. McGillem, 'Random signal radar', School of Electrical Engineering, Purdue University, Final Report, TREE67-11, June 1967.

[34] S. E. Craig, W. Fishbein and O. E. Rittenbach, 'Continuous-wave radar with high range resolution and unambiguous velocity determination', in *IRE Transactions on Military Electronics*, vol. MIL-6, no. 2, pp. 153–161, April 1962.

[35] M. P. Grant, G. R. Cooper and A. K. Kamal, 'A class of noise radar systems', *Proceedings of the IEEE*, vol. 51, no. 7, pp. 1060–1061, July 1963.

[36] P. R. Krehbiel and M. Brook, 'A broad-band noise technique for fast-scanning radar observations of clouds and clutter targets', *IEEE Transactions on Geoscience Electronics*, vol. 17, no. 4, pp. 196–204, October 1979.

[37] J. Tsui, *Digital Techniques for Wideband Receivers*, Artech House Radar Library, Artech House, Norwood, MA, 2001, ISBN-10/ISBN-13: 1580532993/9781580532990.

[38] P. E. Pace, *Advanced Techniques for Digital Receivers*, Artech House, Norwood, MA, 30 June 2000, ISBN-13: 978-1580530538.

[39] M. I. Skolnik, *Radar Handbook*, 3rd ed., McGraw-Hill, New York, 2008, ISBN: 978-0-07-148547-0.

[40] M. J. D. Rendas and J. M. F. Moura, 'Ambiguity in radar and sonar', *IEEE Transactions on Signal Processing*, vol. 46, no. 2, pp. 294–305, February 1998.

[41] H. D. Griffiths, C. J. Baker, H. Ghaleb, R. Ramakrishnan and E. Willman, 'Measurement and analysis of ambiguity functions of off-air signals for passive coherent location', in *Electronics Letters*, vol. 39, no. 13, pp. 1005–1007, June 2003.

[42] L. Auslander and R. Tolimieri, 'Characterizing the radar ambiguity functions', *IEEE Transactions on Information Theory*, vol. 30, no. 6, pp. 832–836, November 1984.

[43] Z. Yang, J. Ni and G. Liu, 'Delay compensation of stretching signal in OTHR', in *Sixth International Conference on Signal Processing, 2002*, 2002, vol. 2 pp. 1461–1464.

[44] M. Schikorr, 'High range resolution with digital stretch processing', *2008 IEEE Radar Conference*, Rome, 2008, pp. 1–6.

[45] K. S. Kulpa and J. Misiurewicz, 'Stretch processing for long integration time passive covert radar', in *2006 CIE International Conference on Radar*, Shanghai, 2006, pp. 1–4.

[46] W. J. Caputi, 'Stretch: A time-transformation technique', *IEEE Transactions on Aerospace and Electronic Systems,* vol. AES-7, no. 2, pp. 269–278, March 1971.

[47] W. Jun, Z. Shouhong and B. Zheng, 'On motion compensation for weak radar reflected signal detection', in *Sixth International Conference on Signal Processing, 2002*, vol. 2, 2002, pp. 1445–1448.

[48] K. Kulpa, 'Target acceleration estimation for continuous wave noise radar', in *International Radar Symposium 2005*, 6–8 September 2005, Berlin, Germany, pp. 177–183, German Institute of Navigation (DGON e.V.).

[49] T. J. Abatzoglou and G. O. Gheen, 'Range, radial velocity, and acceleration MLE using radar LFM pulse train', *IEEE Transactions on Aerospace and Electronic Systems*, vol. 34, no. 4, pp. 1070–1083, October 1998.

[50] H. Xiao, W. D. Hu and W. X. Yu, 'Parameter estimation of accelerating target based on direct phase differentiation method in LFMCW radar', in *2008 International Conference on Information and Automation*, Changsha, 2008, pp. 1142–1147.

[51] K. Kulpa, *Signal Processing in Noise Waveform Radar*, Artech House, Norwood, MA, 2013, ISBN 978-1-60807-661-1.

[52] M. Malanowski, K. Kulpa and J. Misiurewicz, 'Acceleration estimation for passive coherent location radar', *2008 IEEE Radar Conference*, Rome, 2008, pp. 1–5.

[53] Robert N. McDonough and A. D. Whalen, *Detection of Signals in Noise*, 2nd ed., Academic Press, New York, 1995, ISBN: 0127448527.

[54] K. Kulpa, 'Simple sea clutter canceller for noise radar', in *2006 International Radar Symposium*, Krakow, Poland, 2006, pp. 1–4.

[55] E. Fishler, A. Haimovich, R. Blum, D. Chizhik, L. Cimini and R. Valenzuela, 'MIMO radar: An idea whose time has come', in *Proceedings of the 2004 IEEE Radar Conference (IEEE Cat. No. 04CH37509)*, 2004, pp. 71–78.

[56] F. C. Robey, S. Coutts, D. Weikle, J. C. McHarg and K. Cuomo, 'MIMO radar theory and experimental results', in *Conference Record of the Thirty-Eighth Asilomar Conference on Signals, Systems and Computers, 2004*, vol. 1, 2004, pp. 300–304.

[57] E. Fishler, A. Haimovich, R. Blum, R. Cimini, D. Chizhik and R. Valenzuela, 'Performance of MIMO radar systems: Advantages of angular diversity', in *Conference Record of the Thirty-Eighth Asilomar Conference on Signals, Systems and Computers*, vol. 1, 2004, pp. 305–309.

[58] H. Griffiths, 'Multistatic, MIMO and networked radar: The future of radar sensors?', *The Seventh European Radar Conference*, Paris, 2010, pp. 81–84.

[59] M. S. Davis, G. A. Showman and A. D. Lanterman, 'Coherent MIMO radar: The phased array and orthogonal waveforms', *IEEE Aerospace and Electronic Systems Magazine*, vol. 29, no. 8, pp. 76–91, August 2014.

[60] J. Tabrikian, 'Performance bounds and techniques for target localization using MIMO radar', in J. Li and P. Stoica (eds.). *MIMO Radar Signal Processing*, Wiley, Hoboken, NJ, 2009, pp. 153–192.

[61] J. Li and P. Stoica, 'MIMO radar: diversity means superiority', in J. Li and P. Stoica (eds.). *MIMO Radar Signal Processing*, Wiley, Hoboken, NJ, 2009. pp. 1–64

[62] E. Brookner, 'MIMO radar demystified and where it makes sense to use', in *2014 International Radar Conference*, Lille, 2014, pp. 1–6.

This page intentionally left blank

Chapter 5

Cognitive radar management

Alexander Charlish[1] and Folker Hoffmann[1]

Abstract

Cognitive radar is a radar system that acquires knowledge and understanding of its operating environment through online estimation, reasoning and learning or from databases comprising context information. Cognitive radar then exploits this acquired knowledge and understanding to enhance information extraction, data processing and radar management. In order to make progress to this goal, the topic of cognitive radar attempts to shift the cognitive processes previously performed by an operator into automated processes in the radar system. Families of cognitive processes are well defined in cognitive psychology [1], such as the perceptual processes, memory processes, languages processes and thinking processes. In this chapter, we discuss radar management techniques that enable the manifestation of one or more cognitive processes, with a particular view towards electronically steered phased array and multifunction radar systems. In particular, this chapter focuses on two cognitive processes: *attention* and *anticipation*. Attention can be manifested by effective resources management, whereby a quality of service-based task management layer connects radar control parameters to mission objectives. Anticipation can be generated using stochastic control that is non-myopic, allowing the radar system to act with a consideration of how the radar system, scenario and environment will evolve in the future.

5.1 Cognitive radar architecture

An architecture can be adopted for a cognitive radar system where information abstraction levels bridge the gap between the operator and the reception and transmission of radar signals. Abstraction levels for information processing have been widely discussed, most notably through the Joint Directors of Laboratories (JDL) model [2] and its revised versions [3,4]. By extending these ideas, the information abstraction levels of signal, measurement, object, situation and mission can be identified as relevant for a radar system. These information abstraction

[1]Fraunhofer FKIE, Germany

levels have an inherent structure in that the data volume reduces for each higher level. For example, multiple signals contribute to a measurement and multiple measurements contribute to a track on an object. The lower levels execute feedback cycles with much shorter time horizons, whereas the higher levels execute feedback cycles over much longer time horizons.

A cognitive radar architecture is illustrated in Figure 5.1, which is based on the general architecture by Smits *et al*. [5] and Kester [6]. In the architecture, each of the previous identified abstraction levels is comprised of an assessment module for data processing and a management module for control. This stresses the duality between assessment and management processes [7] and extends the original JDL model, where sensor management was considered in a stand-alone level called 'process refinement'. The processes of assessment and management at each level

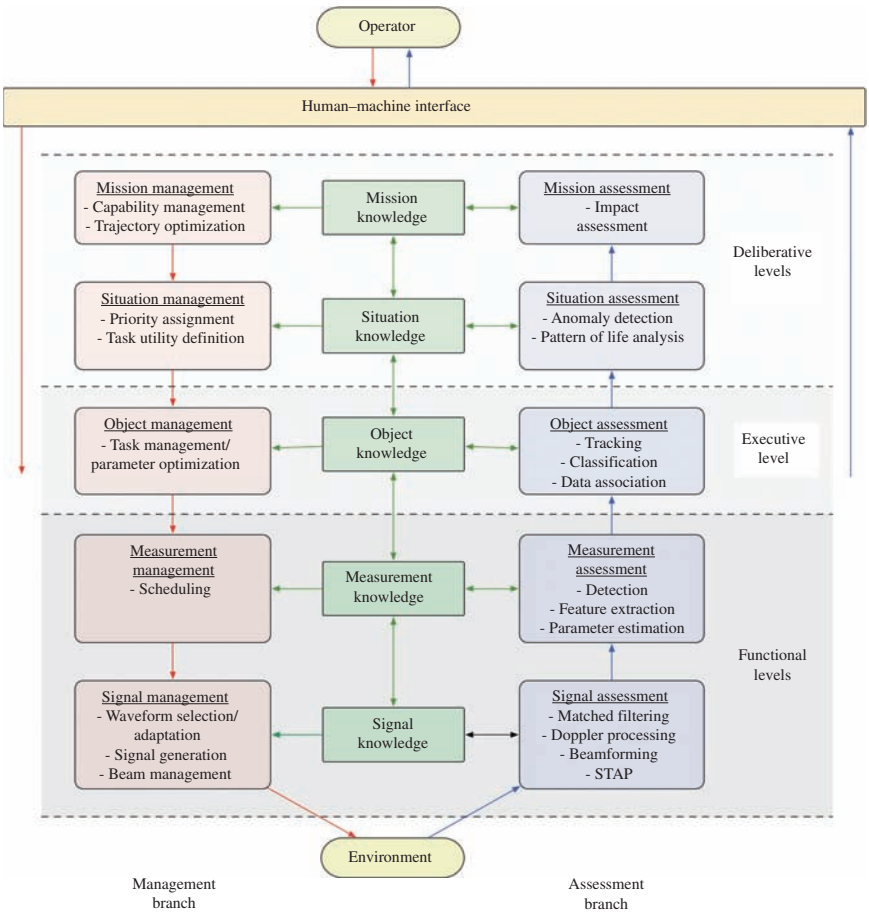

Figure 5.1 Hierarchy for assessment and management

exploit knowledge, which can be fixed knowledge from a database or acquired online. This architecture bears similarity to the general levels described in Haykin's cognitive architecture [8, Ch. 2].

Knowledge-based adaptive methods for assessment at varying abstraction layers are well developed through decades of radar research. For example, at the signal level, Space Time Adaptive Processing techniques [9] apply two-dimensional filtering based on learnt statistics of the interference environment to maximize the signal-to-interference ratio. At the measurement level, learnt statistics of the current clutter environment aid robust detection in complex environments [10]. At the task level, multi-hypothesis tracking [11, Ch. 6, 16] builds hypotheses to explain the measurement data, interacting multiple model filtering [12] estimates the current target manoeuvre state and context information can be exploited for improved tracking performance [13].

In comparison to the assessment branch, the management branch is relatively underdeveloped. This is unsurprising, as the management branch is dependent on the information from the assessment branch in order to apply radar management. However, many radar management techniques exist, such as methods for waveform adaptation, scheduling, task parameter optimization and priority assignment as covered in Volume 1, Chapter 3. This chapter focuses on techniques for the radar management branch that enable the manifestation of the cognitive processes of attention and anticipation.

5.2 Effective QoS-based resources management

Radar resources management (RRM) addresses the two key problems of deciding how to allocate finite radar resource between numerous radar tasks, as well as deciding how to optimize the selection of control parameters for each individual radar task. Examples of radar tasks are tracking a target or searching a region. Conventional RRM approaches optimize individual radar task control parameter selection using rules and heuristics, which are tuned by the system designer. This is done with an implicit assumption that a set of successful tasks leads to a successful mission. In contrast, effective resources management aims to manage the radar resource with respect to the mission objectives. This represents a shift of a cognitive process from the operator to the radar system, as the attention of the radar is focussed on mission objectives. This section describes how quality of service techniques can be applied to achieve effective resources management.

5.2.1 QoS resource allocation problem

Resource management involves allocating resource between competing radar tasks as well as selecting control parameters for each task. In this subsection, the problem of resource allocation is considered alone. This problem formulation is then extended in the following subsection to include control parameter selection, such as selecting task revisit interval times and waveforms.

5.2.1.1 Problem formulation

In the resource allocation problem, a set of K independent tasks $T = \{T_1, T_2, \ldots, T_K\}$ must share the finite resource available. In order to share the finite resource, a resource allocation $r = \{r_1, r_2, \ldots, r_K\}$ must be found, where r_k denotes the resource allocated to task T_k. For a radar problem, this resource can be a temporal loading that represents the amount of the radar time-energy budget that is allocated to the task. Let R_k denote the resource allocation space for task T_k as the real numbers in the interval $[0, 1]$, and let R denote the K-dimensional resource allocation space for all tasks.

A resource function $g : R \mapsto [-1, 0]$ can be defined based on the summations of the resources allocated to each task:

$$g(r) = \left(\sum_{k=1}^{K} r_k \right) - \hat{r} \tag{5.1}$$

where $\hat{r} \in [0, 1]$ is the maximum resource available. The resource function should satisfy the constraint:

$$g(r) \leq 0 \tag{5.2}$$

so that the resource allocated to all of the tasks does not exceed the resource available for the tasks.

Each task utilizes the allocated resource to provide a quality of service level. The expected quality level over the considered time horizon is denoted $q_k \in \mathrm{Q}_k$ for task T_k. Each task can use a different quality measure, which is relevant to the task being performed. This formulation is easy to extend if a task has multiple quality dimensions, for example by taking a weighted sum [14].

The task quality of service is affected by environmental parameters that are not under control. Examples of the environmental parameters for a radar tracking task are the target range, target bearing or parameters of the target manoeuvre model. The set of environmental parameters for task T_k are denoted $e_k \in \mathrm{E}_k$. In practice, these environmental parameters are not known and must be estimated from the received measurements.

The quality of service of a resource allocation for task T_k can be calculated through a task quality function:

$$q_k : R_k \times E_k \mapsto Q_k \tag{5.3}$$

which is a mapping from the environmental parameters and the resource allocated to the task into quality space.

To formulate an objective function for the resource allocation problem, a mapping between K task specific qualities to a scalar valued mission effectiveness is sought. This mapping is based on the mission specific task requirements that are specified by the situation management module. A task requirement is comprised of a task utility function, which describes the satisfaction associated with an achieved

task quality, and a task weighting, which describes the mission relevance of the task relative to other tasks. The utility of task T_k can be calculated through the task utility function:

$$u_k : Q_k \mapsto U \tag{5.4}$$

where U is the task utility space defined on the real numbers in the interval $[0, 1]$. Models for the quality and utility functions are discussed in Section 5.2.4. The importance weighting of task T_k is denoted ω_k and:

$$\sum_{k=1}^{K} \omega_k = 1 \tag{5.5}$$

The mission effectiveness can be found as a weighted sum across the individual task utilities:

$$u(r) = \sum_{k=1}^{K} \omega_k \cdot u_k(q_k(r_k, e_k)) \tag{5.6}$$

This mission effectiveness represents the ability of the radar system to meet the mission specific task quality requirements. This quality of service-based resource allocation problem can be formulated as a constrained optimization problem:

$$\underset{r}{\textbf{maximize:}} \quad u(r) = \sum_{k=1}^{K} \omega_k \cdot u_k(q_k(r_k, e_k)) \tag{5.7}$$

$$\textbf{subject to:} \quad g(r) \leq 0 \tag{5.8}$$

$$\textbf{where:} \quad g(r) = \left(\sum_{k=1}^{K} r_k \right) - \hat{r} \tag{5.9}$$

therefore the objective is to maximize the summation of importance weighted task utilities, given the constraint on the resource available.

The resource allocation problem is dynamic, in that the number of tasks, the environmental parameters for each task and the maximum resource available can vary over time. Therefore, it is necessary to iteratively solve this constrained optimization problem for all time instances, by applying receding horizon control as illustrated in Figure 5.2. When applying receding horizon control, a resource allocation plan is sought at the start of the allocation frame that is based on a non-myopic quality model that extends over multiple frames in the future. Although the plan is valid over multiple frames, it is executed only for a single frame before the plan is recomputed. The plan that is generated for a frame is passed to a scheduler, which schedules antenna jobs. As the resource allocation represents a continuous plan, many tasks may have been allocated resource but only a subset would be scheduled in a single frame. The time indexing of each resource allocation frame is omitted in this work for brevity.

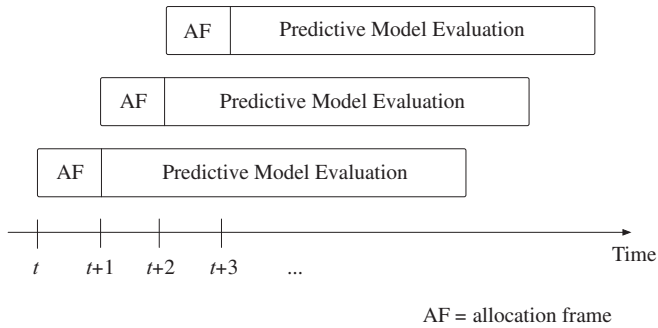

Figure 5.2 Receding horizon control structure. A resource allocation plan is constructed based on non-myopic models that extend over multiple allocation frames

5.2.1.2 Optimality conditions

If it is assumed that the task utility function $u_k(q_k(r_k, e_k))$ is a continuous convex function of the task resource r_k, then the problem objective function is also convex. This assumption is well justified due to the principle of diminishing returns, that is increasing the resource allocation to a task results in decreasing utility increments. This principle of diminishing returns is illustrated in Figure 5.3.

As the objective and constraint functions in (5.7) and (5.8) are convex, then the Karush–Kuhn–Tucker (KKT) conditions [15, Sec. 5.5.3] are sufficient conditions for the optimal resource allocation $r^* = \left\{r_1^*, r_2^*, \ldots, r_K^*\right\}$. The KKT conditions for this problem are as follows:

Feasibility:	$g(r^*) \leq 0$
Dual Feasibility:	$\mu \geq 0$
Complementary Slackness:	$\mu g(r^*) = 0$
Stationarity:	$-\nabla u(r^*) + \mu \nabla g(r^*) = 0$

where μ is the KKT multiplier. The feasibility and dual feasibility conditions imply that the optimal solution must be feasible for both the primal and dual problems [15, Sec. 5.5.3]. The stationarity condition has an interesting interpretation, as the tasks are assumed to be independent, $u(r)$ in (5.7) is a sum of independent components and so:

$$\frac{\partial u(r^*)}{\partial r_k^*} = \frac{du_k(q_k(r_k^*, e_k))}{dr_k^*} \tag{5.10}$$

Therefore, the stationary condition can be rewritten as:

$$\omega_k \frac{du_k\left(q_k\left(r_k^*, e_k\right)\right)}{dr_k^*} = \mu \quad \forall k \in \{0, 1, \ldots, K\}$$

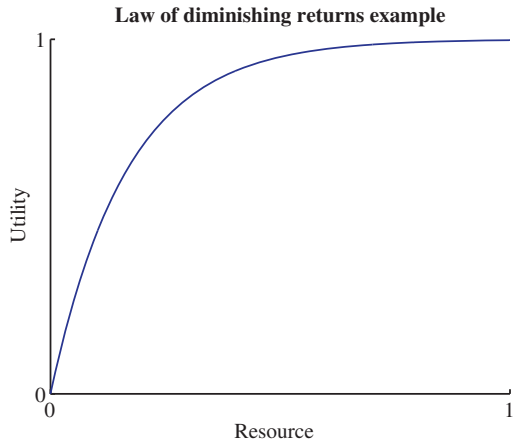

Figure 5.3 Principle of diminishing returns. As the resource allocated to a task increases, the increment in returned utility decreases

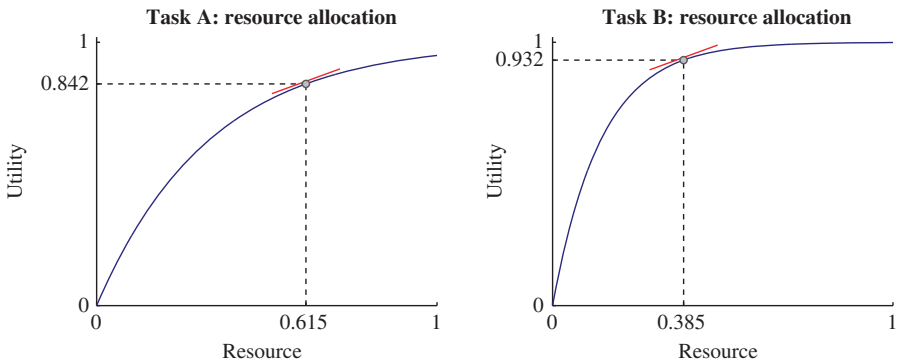

Figure 5.4 Example optimal resource allocation for two tasks where the gradient in resource utility space is equal. Any adjustment to the resource allocation results in a utility loss for a task that is greater than the utility increase for the other task

which implies that the optimum solution is located at a point where the gradients in resource utility space are equal for all tasks. The complementary slackness condition is satisfied either when no resource is left ($g(r^*) = 0$), or when the further allocation of resource no longer results in an increase in utility and so the gradients in resource utility space are zero ($\mu = 0$).

An example, optimum resource allocation for two tasks is illustrated in Figure 5.4, where the gradients in resource utility space are equal. The optimality of this resource allocation is very intuitive. If the resource allocated to task A were increased, then the resource allocated to task B must decrease. However, the loss in utility from task B would be greater than the gain in utility for task A.

5.2.2 QoS resource management problem

In the previous section, the problem of allocating finite resource to tasks was considered. However, for radar resource management, it is also possible to select control parameters which determine how the allocated resource is used. Consequently, this subsection describes how to extend the resource allocation problem into a resource management problem where control parameters are also selected.

5.2.2.1 Problem formulation

The resource allocation problem is coupled to the problem of selecting control parameters for each task, such that the resource allocated is optimally utilized. Examples of the control parameters are the task dwell duration, the task revisit interval time or the transmitted waveform for a track update or search beam position. The control parameters for task T_k are denoted υ_k. Again, receding horizon control is applied and therefore these control parameter selections represent the current resource management plan for a time horizon extending into the future, as illustrated in Figure 5.2.

To solve the QoS resource management problem, it is required to select parameters for all the tasks, to give the set of selections $\upsilon = \{\upsilon_1, \upsilon_2, \ldots, \upsilon_K\}$. As each control parameter for each task uses a certain amount of resource, a resource allocation is also generated. The parameter selection υ_k is itself a set of parameters with a number of dimensions which depends on the task, i.e. $\upsilon_k = \left\{\upsilon_k^1, \upsilon_k^2, \ldots, \upsilon_k^{M_k}\right\}$ where M_k is the number of control parameter dimensions for task T_k. Let $\upsilon_k \in \Upsilon_k$ denote the control parameter space for task T_k and $\upsilon \in \Upsilon$ denote the control parameter space for all tasks.

As with the resource allocation problem, a task quality function is required, which in this case maps task control parameters and environmental parameters into quality space:

$$\hat{q}_k : \Upsilon_k \times E_k \mapsto Q_k \tag{5.11}$$

In the resource management problem, a task resource function is also required, which maps the task control parameters and environmental parameters into resource space:

$$\hat{g}_k : \Upsilon_k \times E_k \mapsto R_k \tag{5.12}$$

Based on these functions and the utility function given in (5.4), the resource, quality and utility of control parameter selections can be evaluated. The evaluation of control parameters can then be visualized in resource utility space, as illustrated in Figure 5.5. Each line in Figure 5.5 represents the variation in a single control parameter dimension, while the other dimension is kept static.

Based on the resource and quality functions, and the utility function from the resource allocation problem (Equation (5.4)), a constrained optimization problem

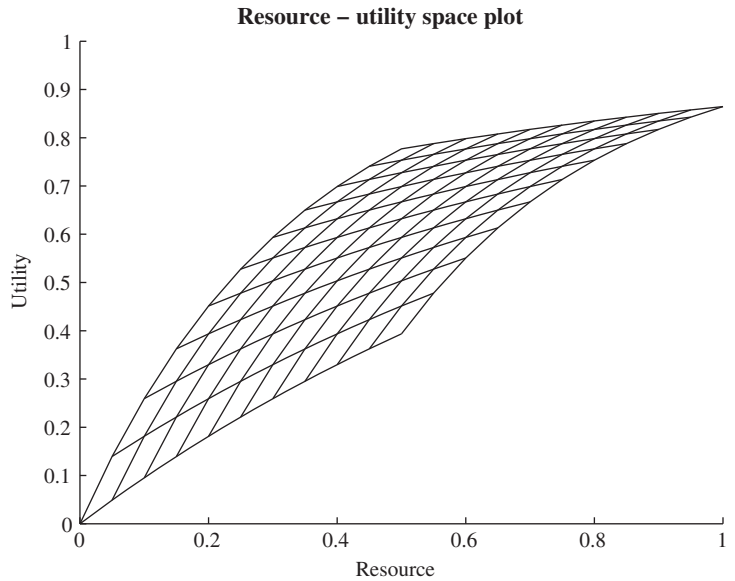

Figure 5.5 Visualization of control parameters in resource utility space. Each line illustrates the variation in one control parameter dimension while the other control parameter dimension is kept static

can be formulated for the resource management problem:

$$\underset{\upsilon}{\textbf{maximize:}} \quad \hat{u}(\upsilon) = \sum_{k=1}^{K} \omega_k \cdot u_k(\hat{q}_k(\upsilon_k, e_k)) \tag{5.13}$$

$$\textbf{subject to:} \quad \hat{g}(\upsilon) \leq 0 \tag{5.14}$$

$$\textbf{where:} \quad \hat{g}(\upsilon) = \left(\sum_{k=1}^{K} \hat{g}_k(\upsilon_k, e_k) \right) - \hat{r} \tag{5.15}$$

5.2.2.2 Optimality conditions

Conditions for the optimal solution of the resource management problem can be derived by introducing a change of variable, to give an equivalent problem to the resource allocation problem in (5.7). Alternatively, the KKT conditions can be applied directly to the problem in (5.13).

Change of variable

The control parameter selection problem can be related to the resource allocation problem in (5.7) by introducing a change of variable. Consider a one-to-one function ϕ defined on just a subset of all of the possible control parameter selections $\hat{\Upsilon} \subset \Upsilon$:

$$\phi : \hat{\Upsilon} \mapsto R \tag{5.16}$$

A subset of control parameters must be taken in order for the function ϕ to be one-to-one. A control parameter selection from the subset $\hat{\Upsilon}$ is denoted as $\hat{v} = \{\hat{v}_1, \hat{v}_2, \ldots, \hat{v}_K\} \in \hat{\Upsilon}$.

As the tasks are assumed to be independent, the function ϕ can be broken down into a one-to-one function for each of the tasks:

$$\phi(\hat{v}) = \sum_{k=1}^{K} \phi_k(\hat{v}_k) \tag{5.17}$$

where $\phi_k : \hat{\Upsilon}_k \mapsto R_k$ is a mapping from the control parameters for task T_k into resource space.

Then, the problem of finding the optimal parameter selections $\hat{v}_t^*$ from the subset of control parameters can also be formulated as a constrained optimization problem that is equivalent to the problem formulation for the resource allocation problem given in (5.7):

$$\underset{\hat{v}}{\textbf{maximize:}} \qquad u(\phi(\hat{v})) = \sum_{k=1}^{K} \omega_k \cdot u_k(q_k(\phi_k(\hat{v}_k), e_k)) \tag{5.18}$$

$$\textbf{subject to:} \qquad g(\phi(\hat{v})) \leq 0 \tag{5.19}$$

$$\text{where :} \qquad g(\phi(\hat{v})) = \left(\sum_{k=1}^{K} \phi_k(\hat{v}_k) \right) - \hat{r} \tag{5.20}$$

This constrained optimization problem is equivalent to the problem for resource allocation in (5.7); however, r has been substituted with $\phi(\hat{v})$. As these problems are equivalent, exactly the same optimality conditions apply to this problem. Therefore, the optimal parameter selection from $\hat{v}$ must be primal and dual feasible, there must be no resource left or no further benefit of further resource allocation and the gradient in resource utility space at the parameter selections for all tasks must be equal.

Although this optimization problem is equivalent to the resource allocation problem (Equation (5.7)), it is not equivalent to the resource management problem (Equation (5.13)) as it selects control parameters from the reduced subset of control parameter selections $\hat{\Upsilon}$ and not the complete set of possible control parameter selections Υ. However, reducing the problem to the set of parameter selections $\hat{\Upsilon}$ can be a very useful step as long as the optimal parameter selections from Υ are contained in $\hat{\Upsilon}$. A logical choice for the function ϕ is the mapping of the control parameters that lie on the Pareto frontier in Figure 5.5 into resource, as this subset ensures that utility is maximized for all resource. However, the subset $\hat{\Upsilon}$ must be chosen such that the objective function remains convex. Consequently, the concave majorant is typically taken, which is discussed further in Section 5.2.3.

Application of KKT conditions

Instead of applying a change of variable, the KKT conditions can be directly applied to (5.13), if it is assumed that the objective function $\hat{u}(v)$ is a concave

differentiable function and the resource function $\hat{g}(v)$ is a convex differentiable function, then the following KKT conditions can then be derived:

$$-\nabla\hat{u}(v^*) + \mu\nabla\hat{g}(v^*) = 0 \tag{5.21}$$

$$\hat{g}(v^*) \leq 0 \tag{5.22}$$

$$\mu \geq 0 \tag{5.23}$$

$$\mu\hat{g}(v^*) = 0 \tag{5.24}$$

where μ is a KKT multiplier.

As shown in [16], the stationarity condition can be rearranged as follows:

$$\mu = \frac{\partial_l \omega_k \cdot u_k(\hat{q}_k(v_k^*, e_k))}{\partial_l \hat{g}_k(v_k^*, e_k)} \quad \begin{matrix} \forall k \in \{1, 2, \ldots, K\} \\ \forall l \in \{1, 2, \ldots, M_k\} \end{matrix} \tag{5.25}$$

where ∂_l denotes the partial derivative with respect to v_k^{l*}, which occurs as v_k^* is itself a vector given by $v_k^* = (v_k^{1*}, v_k^{2*}, \ldots, v_k^{L*})$.

This set of conditions implies that the stationarity condition is satisfied when the gradients of resource over utility in all dimensions and for all tasks are equal to a common value, which is the KKT multiplier μ. The optimal solution is found when the stationarity condition is satisfied (Equation (5.21) and Equation (5.25)) and the solution is primal feasible (Equation (5.22)) and dual feasible (Equation (5.23)) and either all the resource has been allocated or there would be no utility increase from further resource allocation (Equation (5.24)).

Applying the KKT conditions directly yields the optimality conditions; however, it must be assumed that the utility and resource functions are concave functions of the control parameters. Introducing a change of variable demonstrates that the utility and resource functions do not need to be concave functions of the control parameters, as long as a subset can be found that is concave in resource utility space.

5.2.3 Quality of service algorithms

If the resource, quality and utility functions are closed-form expressions, then the KKT conditions can be solved analytically. However, it is often the case that these models do not have a closed-form, and instead require numerical evaluation. In the previous subsection, it was assumed that the resource, quality and utility functions are defined on a continuous space. However, the control parameters may in fact be discrete, or it may be desirable to discretize the control parameters due to the need to perform the numerical evaluations. Figure 5.6 illustrates a quality function (Figure 5.6(a)) as well as a discretized resource utility space (Figure 5.6(b)) generated from discretized control parameters. It can be seen that even though the quality function is a non-convex function of the control parameters, a concave majorant can still be generated in resource utility space. However, as the concave majorant does not cover the complete Pareto front, a suboptimal solution could

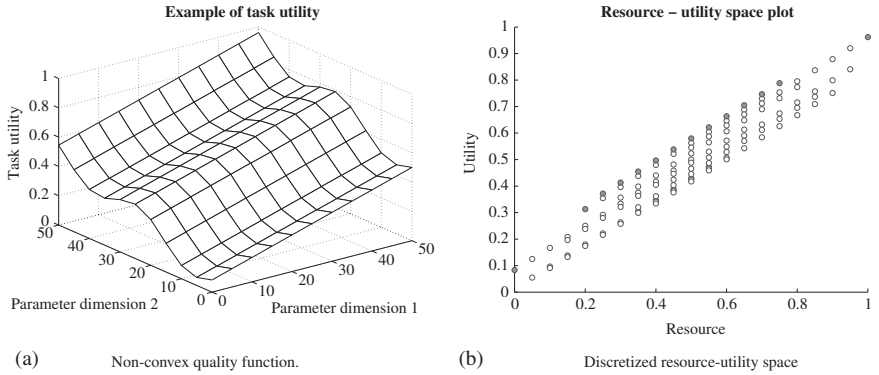

Figure 5.6 Example of discrete control parameter selections in resource utility space for a non-convex utility function on the control parameters. Grey markers indicate the control parameters that lie on the concave majorant. (a) Non-convex quality function, (b) discretized resource-utility space

be found. Careful design of the performance model and adequate sampling of the discrete control parameters can ensure that the deviation from the optimal is small.

Once control parameters are selected by the resource management algorithm, these selected control parameters are used to schedule radar dwells for each task. Therefore, it is assumed that a scheduler at the measurement level below has access to the control parameters at every resource management frame. Schedulers are discussed in detail in Volume 1, Chapter 3. The scheduler may not be able to perfectly resolve radar dwell conflicts and therefore the actual behaviour may deviate from the desired control parameters. However, as the quality of service management ensures that the resource allocated is matched to the resource available, the scheduler is never overloaded and therefore the deviation should be small. It is also assumed that the mission level above provides the utility function and importance weighting for each task, with respect to the current mission.

This section describes two algorithms for solving the resource management problem: the quality of service resource allocation method (Q-RAM) and the continuous double auction parameter selection (CDAPS) algorithm.

5.2.3.1 Quality of service resource allocation method Q-RAM

Q-RAM is a numerical method for satisfying the KKT conditions for discrete parameter selections. The algorithm starts with no resource allocated to any task, and then allocates resource increments to tasks in order of the highest marginal utility. Consequently, when the resource runs out, the marginal utilities will be as close to equal as possible, thus satisfying the KKT conditions.

Q-RAM [17] generates a solution through the following steps:

1. Evaluate the resource and utility values for all possible control parameter selections for all tasks.

2. Apply a convex hull operation [18] to extract the parameter selections that lie on the concave majorant [19] for each task.
3. Calculate the marginal utility between the parameter selections on the concave majorant for each task. The marginal utility is the difference in utility over the difference in resource.
4. Order parameter selections on the concave majorants for all tasks in a single list with descending order with respect to marginal utility.
5. Iteratively allocate resource to the parameter selection with the highest marginal utility until no resource remains.
6. Resource allocation frame is complete.

The algorithm achieves a near-optimal solution, as the optimal parameter selections may not lie on the concave majorant as identified by the suboptimal stopping conditions in [20]. Such a suboptimal stopping condition can be recognized in the example presented in Figure 5.6(b). If the optimal parameter selection for the task lies on the Pareto frontier in the resource ranges between 0 and 0.2 or 0.8 and 1.0, then it will not be on the concave majorant and hence a suboptimal solution will result. However, large deviations from the optimum can be avoided when a reasonable number of control parameters are used and the performance model is known to be concave in resource utility space.

The original algorithm proposed Graham's scan as the convex hull extraction procedure, which requires all parameter selections to be evaluated. However, assuming monotonic resource and utility functions in the parameter dimensions, then traversal methods can be applied [21,22] which do not require all parameter selections to be evaluated. This can greatly reduce the number of parameter selections that are evaluated, which is especially valuable if the performance model has non-trivial computational complexity.

5.2.3.2 Continuous double auction parameter selection

The CDAPS algorithm [23–25] is an alternative algorithm for solving the constrained optimization problem in (5.13). CDAPS utilizes a continuous double auction (CDA) mechanism [26] which settles on a market equilibrium that satisfies the KKT conditions.

In the CDAPS algorithm, each radar task is represented by a task agent, who competes with other task agents for the finite radar resource. The competition is facilitated through a CDA market. Consequently, each agent can hold an amount of resource r_k at any time which may be used for its task and the total resource held by all agents may not exceed the resource available. Each agent announces offers to trade comprising of bids to buy more resource or asks to sell resource. Bids are then matched to asks such that the resource trade results in a net increase in utility.

Each agent calculates its bids and asks based on the utility and resource evaluation of control parameters adjacent to the currently active control parameter. As illustrated in Figure 5.7, the announced bid price p_b^k for agent T_k is the possible increase in utility over the increase in resource:

$$p_b^k = \frac{\Delta u_b}{\Delta r_b} \tag{5.26}$$

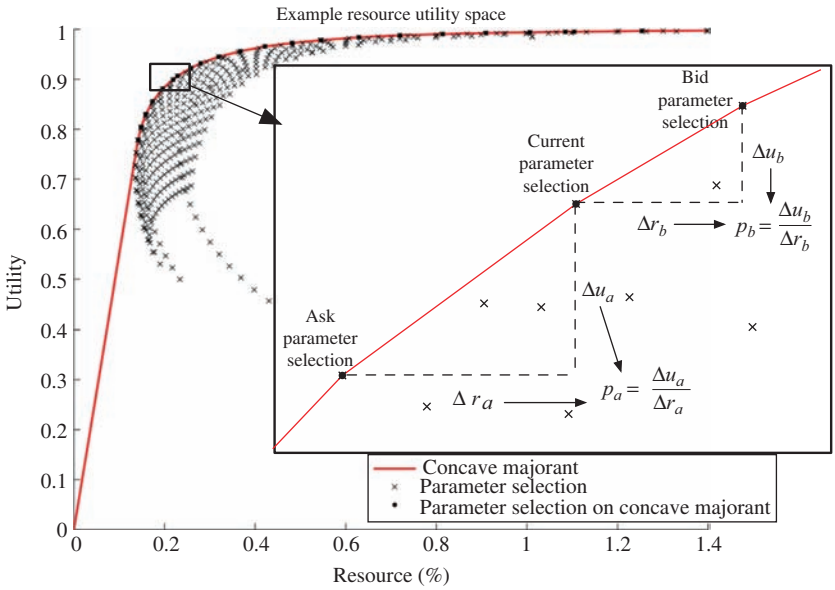

Figure 5.7 Bid and ask evaluation process in continuous double auction parameter selection algorithm. © 2015 IEEE. Reprinted, with permission, from [16]

and the announced ask price p_a^k is the possible decrease in utility over the decrease in resource:

$$p_a^k = \frac{\Delta u_a}{\Delta r_a} \tag{5.27}$$

As each trade results in a utility increase, the market settles on an equilibrium that maximizes utility. As shown in [16], this equilibrium satisfies the KKT conditions.

The key benefit of CDAPS in comparison to Q-RAM is that the solution from the previous time step can be adapted to the current time step, without a complete recomputation of the resource allocation. Consequently, the number of parameter selections that are evaluated per second is significantly reduced [16]. This is useful when the performance model used to calculate the resource, quality and utility has a non-trivial computational cost.

5.2.4 Performance models

Quality of service management relies on performance models that relate the control parameters to the quality that can be achieved. A performance model can be a forwards model, which calculates the quality a task can achieve given a set of control parameters. Alternatively, a model can be a backwards model, which calculates the control parameters that are required to achieve a specified quality.

Forwards models are generally easier to define and consequently the problem formulation and algorithms in the previous subsections assumed forwards models. However, using a backwards model can result in a simpler implementation, as it is not necessary to search over a large number of control parameters for suitable quality values. Practically, a high fidelity model may be used as a basis for curve fitting or a look-up table in order to reduce online computation.

A forwards model predictively evaluates the expected resource (Equation (5.12)) and quality (Equation (5.11)) for a candidate parameter selection, over a future time horizon but based on the current state of the task. A performance model for active tracking was given in an application of Q-RAM to radar tracking [21]. This subsection describes alternative performance models that can be used for the search and tracking functions.

5.2.4.1 Active tracking performance models

Active tracking is the process of maintaining tracks on targets using measurements from a series of dwells which are dedicated to each target. Control parameters for waveform and revisit interval selection must be performed such that the quality requirement of the tracking task is met. In addition, the selection of control parameters must consider the beam positioning loss that results from the mismatch between the target's true and estimated position. This beam positioning loss increases as the track estimation error increases and therefore limits the revisit time between track updates.

Van Keuk and Blackman model

Van Keuk and Blackman [27] describe models that can be used for active tracking. The Van Keuk and Blackman strategy is described in detail in Volume 1, Chapter 3. In the model, the task control parameters are the track revisit interval and the received signal-to-noise ratio (SNR), which implies the coherent dwell length. The quality of the task is the track sharpness, which is the track angular estimation error in units of the radar 3 dB beamwidth. Van Keuk and Blackman give a backwards model that enables the track revisit interval t_r control parameter to be selected:

$$t_r = 0.4\left(\frac{r_t\sigma\sqrt{\Theta}}{\Sigma}\right)^{0.4}\frac{u_v^{2.4}}{1+\left((1/2)u_v^2\right)} \tag{5.28}$$

where σ is the measurement error standard deviation, r_t is the target range and Θ and Σ are the Singer model parameters. u_v is the variance reduction ratio, which is the ratio of the track to measurement angular error [28]. It is also recommended to select the coherent dwell length to give a received 16–19 dB SNR, based on the estimated target radar cross-section.

The equations from the Van Keuk and Blackman model can also be used as a forwards model [16], so that the steady state expected track sharpness can be calculated based on a specified track revisit interval and the coherent dwell length. However, the Van Keuk and Blackman model is constrained to the use of a Singer target motion model.

Posterior Cramér-Rao lower bound

Alternatively, a forwards model for target tracking can be produced by predicting the posterior Cramér-Rao lower bound (PCRLB) over the future time horizon, based on the filter predicted covariance at the current time. In this case, the control parameters can be the revisit interval, dwell time and waveform and the track quality can be derived from the predicted track, for example the track position error standard deviation. Such an approach is described in [29] for a radar network; however, the process is also the same for a single radar.

Predicting the PCRLB involves more computation than the Van Keuk and Blackman model; however, it is independent of the tracker, and can be used for any target model, and any task quality that can be derived from the filter predicted error covariance.

5.2.4.2 Search performance models

A search volume can be served by a number of beam positions as described in Volume 1, Chapter 3. It is then possible to control the time between revisits as well as the transmitted waveform and hence dwell time in each beam position. The tradeoff between the revisit interval and the dwell time is discussed in Volume 1, Chapter 3. As the objective of search is to detect previous undetected targets, control parameters should be selected to detect targets as early as possible. Therefore, a suitable performance criterion is the cumulative detection range.

Cumulative detection range

The cumulative probability of detection is the probability that a target is detected at least once from a certain number of dwells on a target [30]. The cumulative detection range is the range at which the cumulative detection probability over multiple dwells on a target exceeds a specified probability, e.g. 0.9. In order to calculate the cumulative detection probability or range, the target trajectory and radar cross-section should be known. As this is not known, an expected or worst case can be taken, such as assuming an inbound trajectory with radial velocity v_r. An example of the cumulative detection probability over successive dwells is illustrated in Figure 5.8.

The cumulative probability of detection after n dwells for a target appearing at range r_{pu} is then:

$$P_C(r_t|r_{\text{pu}}) = 1 - \prod_{i=1}^{n} 1 - P_D(r_{\text{pu}} - v_r \cdot ri \cdot i - \Delta) \tag{5.29}$$

where Δ is a uniform distributed random variable, between 0 and $v_r \cdot ri$, which is the distance the target travels between the target's appearance and the first scheduled dwell. $P_D(t)$ is the probability of detection at range r_t.

A simple method to calculate the 90% cumulative detection range from (5.29) is to successively increase n until the cumulative probability of detection is greater than 90% and then averaging over the possible arrival time Δ between the scans [23].

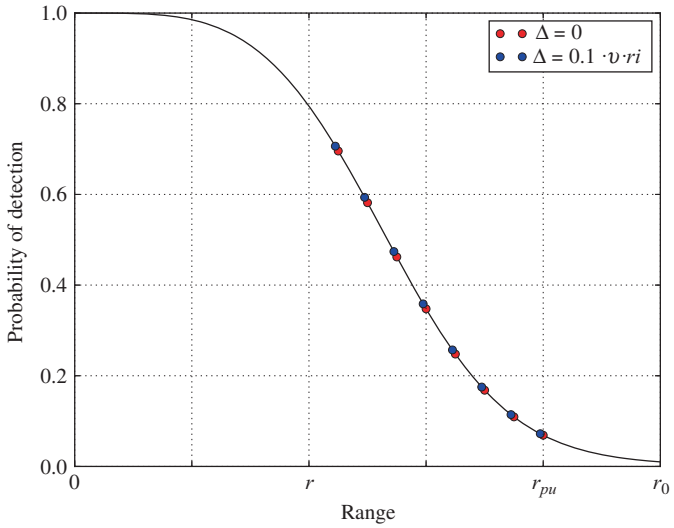

Figure 5.8 A target appearing at range r_{pu} is regularly covered by dwells, while it comes nearer to the radar. Each dwell has a certain probability of detection. The cumulative probability of detection is the probability that at least one of the dwells detects the target. Because the target can arrive at any time between two successive dwells, the exact ranges when the beams are scheduled can vary

Inclusion of pop-up range

Radar search can also be optimized based on known information about the current operating environment. For example, targets may pop-up at specific ranges instead of following inbound trajectories from great range. This could be due to for example targets breaking the horizon, airports, shadowing from terrain or the beam position intersecting the ground plane for an airborne platform [31].

5.2.5 QoS radar management example

This section presents an example of rule-based management compared with QoS-based radar management with differing mission requirements.

Simulation description

In the simulated scenario, an airborne radar detects and tracks multiple inbound targets, as illustrated in Figure 5.9. The platform is equipped with a forward facing electronically steered phased array antenna that has a maximal field of view of $\pm 60^\circ$ in azimuth and a beam width of 2°. A medium pulse repetition frequency (MPRF) mode with linear frequency modulated pulses is simulated, with eight PRFs taken from [32, Sec. 5.3]. A maximum duty factor of 10% is used, which dictates the uncompressed pulse width for each PRF. The compressed pulse width, and hence also the pulse compression ratio, is chosen to give a range resolution of

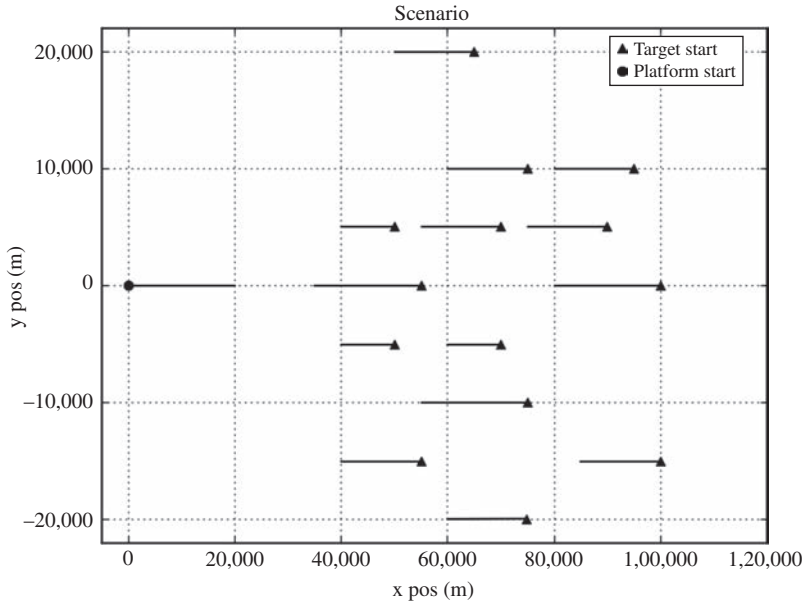

Figure 5.9 Scenario

64 m. Tracks are initialized using an alert-confirm process [11, Ch. 14] and an interacting multiple models tracker is used for target tracking [12].

QoS radar management is applied using the Q-RAM algorithm as described in Section 5.2.3.1. For this scenario, every beam position in the search lattice and each track corresponds to a single radar task. The possible control parameters for each task are evaluated using the performance models described in Section 5.2.4.2 for each search beam position and Section 5.2.4.1 for each track. For tracking tasks the quality is taken as the track sharpness [27] and for search the quality is the 90% cumulative detection range. For both tracking and search, the utility function is defined linearly between mission specific worst and best acceptable values. Two mission profiles are defined, one for engagement with a focus on tracking and the other for surveillance with a focus on searching. The configurations of these mission profiles are shown in Tables 5.1 and 5.2.

In the following results, the QoS approach is compared with a rule-based approach, where the rules dictate the task control parameters that are selected. The rule-based approach applies adaptive tracking [27,33,34] with a threshold on the track sharpness of 0.12. It also selects the number of pulses in each MPRF burst to achieve an expected SNR of 22 dB, based on the estimated RCS of the target. Each search beam position is revisited as quickly as possible, with a revisit interval time varying between 3 and 6 s. The number of pulses in each search beam position is varied to compensate for the loss of effective aperture when scanning off the radar boresight.

Table 5.1 Q-RAM configuration with a focus on tracking

Profile	Weighting	Quality	Worst	Best
Engagement	80%	Track sharpness	0.1	0.01
Surveillance	20%	Cumulative detection range	40 km	100 km

Table 5.2 Q-RAM configuration with a focus on searching

	Weighting	Quality	Worst	Best
Engagement	10%	Track sharpness	0.15	0.06
Surveillance	90%	Cumulative detection range	40 km	100 km

Results

Figure 5.10(a) plots the track sharpness of the target tracks averaged over 100 Monte Carlo runs. It can be seen that after initializing the tracks at a sharpness of 0.04, Q-RAM with the engagement mission profile improves the track sharpness whereas Q-RAM with the surveillance mission profile and the rule-based approach allocate few resources to tracking, which results in a degraded track sharpness. Consequently, the engagement profile focusses on tracking and achieves the sharpest tracks which equates to a low-angular estimation error. The differences in the track sharpness are also reflected in the average posterior root mean square error (RMSE), (Figure 5.10(b)) which is the average of the RMSE after each track update.

The performance of the search function is illustrated by the track completeness plot in Figure 5.10(c). The track completeness is the fraction of the tracked targets to the total number of targets in the surveillance region. It can be seen that Q-RAM with the surveillance profile achieves the greatest track completeness as the search detects targets and initializes tracks faster. An interesting effect can be seen at the beginning of the simulation, where the completeness of both Q-RAM configurations is almost equal. This is because at the beginning of the simulation there are not many detected targets and so Q-RAM with an engagement profile receives most of its utility due to the search and therefore also focusses on search. It is only later, when a higher number of targets are initialized, that the search performance is reduced in favour of the tracking performance.

In Figure 5.10, it can be seen that Q-RAM with a surveillance profile has similar track sharpness as the rule-based method but achieves a much better track completeness. This improvement in performance is due to Q-RAM optimizing the selection of the task control parameters. It can also be seen that the two different Q-RAM profiles enable the compromise between tracking and search to be managed. This compromise is based on the quality levels that are required to satisfy the mission. Although it was not known before the simulation what performance the rule-based method would achieve, Q-RAM always achieves a performance within the specified quality limits.

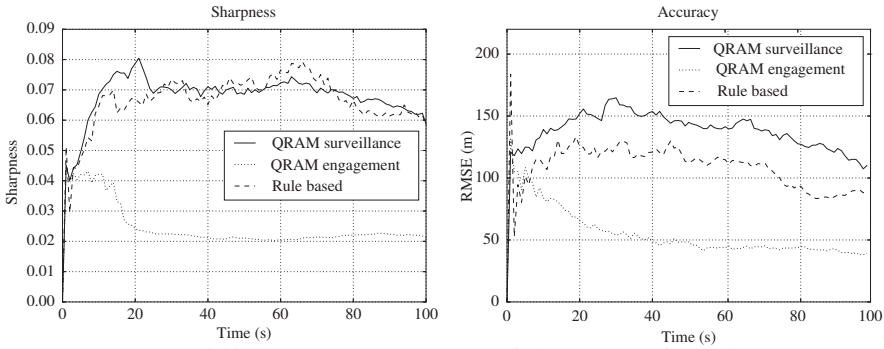

(a) Average Track Sharpness (b) Average Posterior RMSE

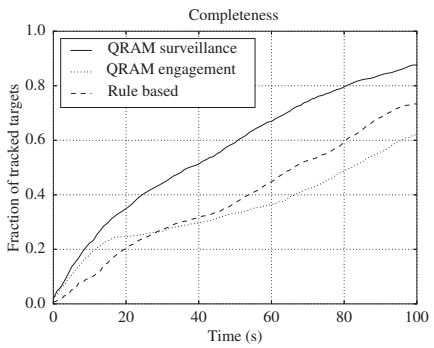

(c) Track Completeness

Figure 5.10 Performance assessment for rule based and QoS methods. (a) Average track sharpness, (b) average posterior RMSE, (c) track completeness

5.3 Stochastic control

The previous section described how effective resources management can enable the cognitive process of attention. This section addresses the cognitive process of anticipation. Anticipation in cognitive radar can be generated using a partially observable Markov decision process (POMDP). A POMDP is a framework for sequential decision making on the selection of actions that trigger stochastic transitions in a system state that is only partially observable through noisy measurements. In radar applications, the state is the sensed environment and the actions controlled by the POMDP can be measurement times for radar tasks and the corresponding waveforms. As the system state is not fully observable, the controller constructs a belief state, which is a probability distribution on the state-space. This belief state can be thought of as a perception of the memory of all previous measurements. Actions, to schedule measurements and waveforms, are taken based on the belief state, but also based on the expected evolution of the system state over a time horizon in the future. By taking actions that consider the future system evolution, the radar is able to act with anticipation.

5.3.1 Partially observable Markov decision process

A POMDP is a sequential decision-making process where actions are sought at each decision instance, which maximize rewards that are accumulated over a time horizon in the future. A POMDP consists of the following components:

State Space – The state space X describes the range of possible states of the system, where a state at time step k is denoted x_k. For radar tracking, the state can be the true positions of the target and the radar platform. For search, the state can be the location of undetected targets.

Action Space – The action space A describes the range of possible actions that can be taken, where an action at time step k is denoted a_k. The action can be the scheduling of a measurement at a certain time with a corresponding waveform.

State Transition Probability – The state transition probability function $p(x_{k+1}|x_k, a_k)$ gives the probability of transitioning to state x_{k+1} from state x_k when taking action a_k.

Observation Space – The observation space Z describes the range of possible measurements that can be observed, where a measurement at time k is denoted z_k.

Observation Likelihood Function – The observation or measurement likelihood function describes the probability $p(z_k|x_k)$ of observing measurement z_k given that the system is in state x_k.

Reward Function – The reward function $r(x_k, a_k)$ gives the reward received when action a_k is taken when the system is in state x_k. This reward must reflect the radar's sensing objective.

Given a reward is received for the pairing of the true system state and an action, the objective of the POMDP is to maximize the cumulated reward V_H starting from the time step k_0 up to the end of the time horizon H:

$$V_H = E\left[\sum_{k=k_0}^{k_0+H} r(x_k, a_k)\right] \tag{5.30}$$

At each decision stage, the controller is required to select an action a_k, as the first step in the action trajectory that maximizes (5.30). The selection of an action at decision step k is based on the set of actions that have been performed and the measurements that have been observed prior to time step k, which is denoted as the data set $d_k = \{z_0, a_0, \ldots, z_{k-1}, a_{k-1}, z_k\}$.

As the true state of the system is unobservable, the controller forms a belief b of the unobservable system state, which is represented by a probability distribution on the state space X. The belief state b_k is conditioned on the prior data:

$$b_k = p(x_k|d_k) \tag{5.31}$$

The optimal policy function is then sought, which maps the belief on the system state that the controller currently holds, into the best action to take:

$$\pi^* : b_k \mapsto A \tag{5.32}$$

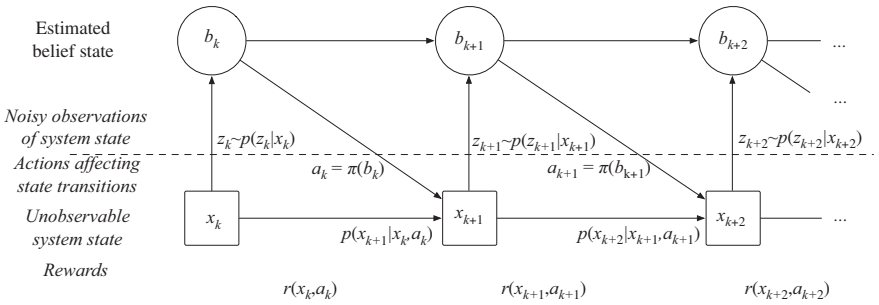

Figure 5.11 Illustration of a partially observable Markov decision process. A system state x, which is partially observed through noisy measurements z, is controlled by actions a that trigger Markovian transitions. Rewards are accumulated over the decision stages depending on the system state and the action taken. © 2015 IEEE. Reprinted, with permission, from [35]

A POMDP is illustrated in Figure 5.11. As shown in the figure, the true state of the system is only partially observable through noisy observations/measurements. Consequently, the controller maintains a belief state b which is used to select the action a which maximizes the expected reward over multiple future decision stages up to the specified time horizon H.

In order to make decisions about the best action to perform, it is necessary to evaluate the expected value of a belief state, which is based on the expected reward of possible future system states. As the controller has an uncertain belief on the true system state, let $R(b_k, a_k)$ be the expected reward with respect to belief-state b_k. Then, the expected value of belief b_t is as follows:

$$V_H(b_t) = E\left[\sum_{k=t}^{t+H} R(b_k, a_k)|b_t\right] \tag{5.33}$$

The optimal value $V_H^*(b_t)$ of a belief state b_t is the expected value when the actions a_k are selected due to the optimal policy π^*, i.e. in a way that maximized above expectation. Using Bellman's equation, $V_H^*(b_t)$ can be decomposed into the expected reward $R(b_t, a)$ of taking action a from belief state b_t and the optimal value of the subsequent belief state b_{t+1} that would be reached after the action:

$$V_H^*(b_t) = \max_a \left(R(b_t, a) + E\left[V_{H-1}^*(b_{t+1})|b_t, a\right]\right) \tag{5.34}$$

Based on this, the optimal policy can be defined as the selection of the action that maximizes the value of being in the belief state b_t:

$$\pi^*(b_t) = \arg\max_a \left(R(b_t, a) + E\left[V_{H-1}^*(b_{t+1})|b_t, a\right]\right) \tag{5.35}$$

Within this equation, the commonly termed Q-value can be defined as follows:

$$Q_H(b_t, a) = R(b_t, a) + E\left[V^*_{H-1}(b_{t+1})|b_t, a\right] \tag{5.36}$$

Using the definition of the Q-value, the optimal policy from (5.35) can then be rewritten as finding the action that maximizes the Q-value:

$$\pi^*_t(b_t) = \arg\max_a Q_H(b_t, a) \tag{5.37}$$

To find the optimal action to take at time step t, it is necessary to evaluate the Q-value for all possible candidate actions. The Q-value is comprised of two terms, the instantaneous reward and the possible future reward. Unfortunately, this Q-value is almost impossible to calculate exactly, which necessitates the use of approximate methods.

POMDP cognitive processes

The POMDP formulation incorporates the following cognitive processes:

Memory and Perception – The concept of memory and perception is central to the POMDP, as the belief state b_k represents the interpretation of the partially observable system state. This perception is clearly based on memory, as b_k is conditioned on the entire action-measurement history $d_k = \{z_0, a_0, \ldots, z_{k-1}, a_{k-1}, z_k\}$.

Decision Making – Decision making to select actions is the core task of a POMDP. The best action is sought based on the memory of previous actions and measurements, and the perception of the partially observable system state.

Anticipation – By evaluating the expected rewards over a future time horizon, a POMDP selects actions based on how the system state is anticipated to evolve in the future.

The following two cases demonstrate the differentiation between adaptation and anticipation:

- *Case 1 – Time horizon $H = 1$:* (5.30) simplifies to the reward $r(x_k, a_k)$ and therefore the optimal action is based only on the belief b_k of the system state at the current time k. Action selection based only on the current belief state can be thought of as *adaptive*.
- *Case 2 – Time horizon $H \gg 1$:* (5.30) is comprised of a trajectory of future actions and states; therefore, the POMDP reasons about the rewards it anticipates to receive in the future. This anticipation of future rewards can be considered a *cognitive* process.

The effect of the time horizon in a POMDP is widely discussed in the sensor management literature as myopic (considering only the present) or non-myopic (considering also the future) management.

5.3.2 Approximate solutions

Unfortunately, an optimal solution to a POMDP is intractable for all problems except those involving a small number of finite system states [36]. Therefore, a lot of research has been dedicated to generating approximate solutions to POMDPs.

5.3.2.1 Algorithm types

Solution methods for POMDPs can be separated into offline and online algorithms. Offline algorithms precompute policies for possible belief states before deployment, whereas online algorithms compute policies online based on the current belief of the system state.

Offline algorithms

An offline algorithm precomputes policies before deployment. Therefore, an action is specified for each belief state that could be encountered. These algorithms rely on the fact that the optimal value function over the belief state is piecewise linear convex [37], and therefore representable with a finite set of vectors, so called α-vectors.

An important breakthrough for offline algorithms came with the introduction of point-based-value iteration [38]. These algorithms exploit the fact that only a small set of α-vectors is needed to compute a sufficiently good approximation of the optimal value function. Therefore, a small subset of belief points is selected and value iteration is performed over these points. A survey of point-based POMDP solvers can be found in [39].

Most of the existing research in offline algorithms is based on discrete systems. As radar systems observe a continuous state space from continuous measurements, these methods require an additional discretization step. Existing algorithms for continuous states and measurements [40–43] are computationally intensive and currently do not scale well for sensor management problems.

Online algorithms

In contrast to offline algorithms, online algorithms compute policies during deployment. Consequently, it is only necessary to explore belief states that are reachable from the current system belief state. The belief states which follow the current belief state build a tree, where the nodes of the tree are the possible future beliefs, connected by the possible observations and actions. This tree of possible future beliefs is illustrated in Figure 5.12. Online algorithms search this tree to effectively approximate the Q-value in (5.36).

If the measurements were discrete and finite, the tree could theoretically be exhaustively searched. However for radar, like in most sensor management applications, measurements are considered as continuous and therefore an exhaustive search is impossible. Instead, measurements can be stochastically sampled, deterministically sampled or only the most likely measurement can be considered. Regardless, the tree is typically too big to allow a complete search and therefore an approximation is required. Frequently used approximations are as follows:

Pruning: If it is possible to compute upper and lower bounds for the future reward of a belief state, several branches of the belief tree can be completely ignored, if they cannot contain the optimal future decisions.

Rollout: The rollout method [44] assumes that the controller behaves in the future according to a so-called *base policy*, which is a heuristic policy for generating an action from a belief state. Therefore, not every future action

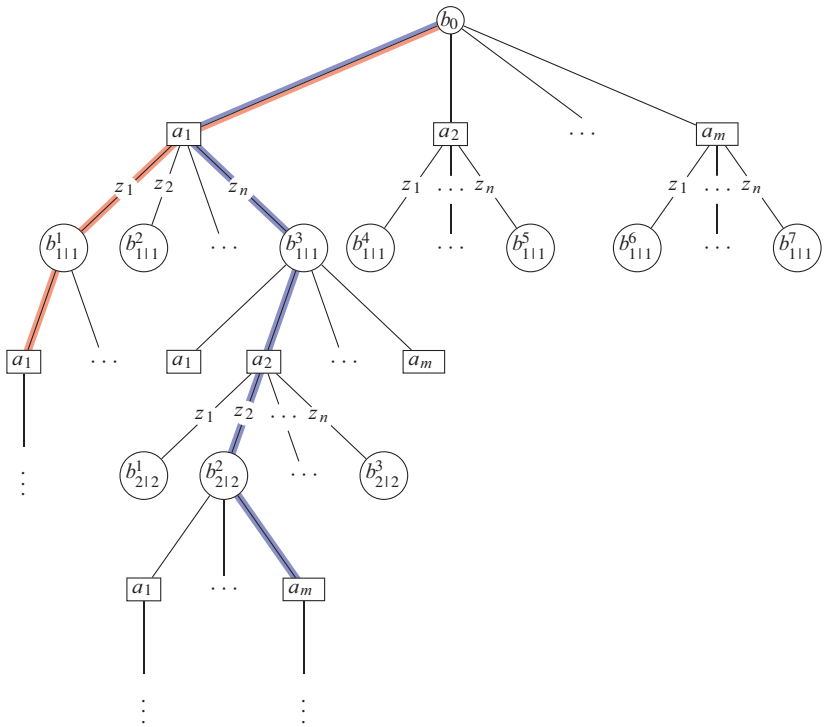

Figure 5.12 The possible future belief states of the system form a tree. The future beliefs are influenced by the actions of the system and the measurements. The diagram also shows two executions of a rollout policy, which evaluate the action a_1. Although both executions follow the same base policy, they explore different sections of the belief space, as the different measurements are sampled during the rollout

has to be evaluated, but instead only those actions that are generated from the base policy. The rollout method is described in detail in Section 5.3.2.2.

Noise Reduction: There are two potentially noisy components in the POMDP: The state transition and the measurement of the state. An often used assumption is that the target transition deterministically, i.e. there is no noise in the state transition. The measurement can be similarly approximated by a single, nominal measurement [45]. An alternative is to select a specific set of measurements that optimally approximate the measurement probability [46].

Model Simplification: While the description of the original problem might require a complex model, the optimization can be done on a simplification of the model. For example, a particle filter might be too computationally intensive for repeated evaluation, while using a Kalman filter as approximation might give sufficiently good approximation. Similarly, if the reward is the error of the estimate, this could be replaced by the Fisher Information.

Numerical Optimization: If the action space is continuous and the remaining parts of the model are sufficiently well-behaved, often techniques from numerical optimization (e.g. Gradient Descent) can be used. In this case, the future actions over the horizon are considered as a multi-dimensional vector and the vector that maximizes the expected reward (or an approximation) is sought.

A detailed overview about online POMDP solutions can be found in [47]. Approximate POMDP solutions in sensor management are covered in [48].

5.3.2.2 Policy rollout

According to (5.36), the Q-value consists of two values: The immediate reward and the expected reward in the future. Rollout replaces the expected future value that would be achieved if the optimal policy were followed, with the expected value when a base policy is followed. The base policy is a hand crafted policy which describes a sensible heuristic to generate actions based on an encountered belief state. The rollout procedure traverses the belief tree, while selecting the actions according to the base policy. This process of rollout is motivated by the fact that it is not necessary to calculate the values of each candidate action exactly, it is just sufficient to know the relative rankings of the candidate actions, for the best action to be taken.

Given a base policy

$$\pi_B : b \rightarrow a \tag{5.38}$$

the Q-value is replaced by:

$$Q_H^{\pi_B}(b_t, a) = R(b_t, a) + E\left[V_{H-1}^{\pi_B}(b_{t+1})|b_t, a\right] \tag{5.39}$$

where $V_{H-1}^{\pi_B}(b_{t+1})$ is the value of belief b_{t+1} if the system follows the base policy π_B. As the optimal value $V_{H-1}^{*}(b_{t+1})$ is defined as the value achieved, if the controller follows an optimal policy, $V_{H-1}^{\pi_B}$is a lower bound on the optimal value. This value can be computed for example via Monte Carlo simulation of future belief states.

Figure 5.12 shows the realization of two rollouts for evaluation of the action a_1, with the same base policy. Computation can be reduced by simplifying the rollout step, for example, by using the expected measurement instead of multiple Monte Carlo runs with sampled measurements. In this case, care must be taken that the simplified rollout still accurately reflects the trade-offs between the different actions.

Parallel rollout

A direct extension to the rollout algorithm, is *parallel rollout*, which considers multiple base policies [49]. It is based on the fact that $V_{H-1}^{\pi_B}(b_{t+1})$ is a lower bound to the optimal value. Therefore, given a set of base policies Π, the value:

$$V_{H-1}^{\Pi} = \max_{\pi \in \Pi} E\left[V_{H-1}^{\pi}(b_{t+1})|b_t, a\right] \tag{5.40}$$

is a tighter bound on the optimal value than the simple rollout.

5.3.3 Anticipative target tracking

POMDPs have been applied in sensor management for active sensing [50–54]. These techniques are applicable for active sensing in general and not just for radar applications, however, a radar model is frequently adopted. A Markov decision-process (MDP) approach has been applied to radar problems by Wintenby [55,56], whereby the partial observability is modelled by a number of discrete states in an MDP. POMDP approaches have also been applied for alternative sensor management problems, such as path planning for a unmanned aerial vehicle with a radar [50,57,58] and waveform scheduling [59–61].

In this section, an example of stochastic control applied to a target tracking problem is described [35]. The objective is for the controller to select the time interval between radar measurements for a target track, such that a desired estimation error is achieved and track loss is prevented with the minimum resource usage. An electronically steered array antenna is assumed, such that measurements are made by steering the beam to the estimated target position. As a scenario may dictate that measurements provide different amounts of information, the anticipated future development of the situation must be taken into account. This is done with a rollout-based approach.

5.3.3.1 Scenario description

The scenario consists of an airborne radar platform and a Swerling 1 target with nearly constant velocity motion at 200 m/s, as illustrated in Figure 5.13. In the

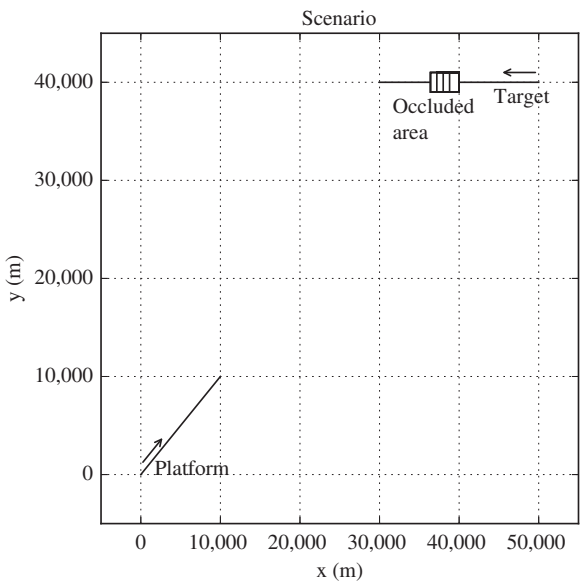

Figure 5.13 The simulated scenario where the airborne radar platform tracks the target. The target is non-observable for a period of time. © 2015 IEEE. Reprinted, with permission, from [35]

scenario, the target is unobservable during a certain period of time. This non-observability could be due to a number of reasons, such as a blockage to the line of sight, a jammer or the unavailability of a multifunction radar when a different non-interruptible function is executed. It is assumed that the borders of the unobservable region are known.

5.3.3.2 POMDP formulation

The problem can be formalized as a POMDP, based on the definition given in Section 5.3.1.

System state

The system state is a stacked vector comprised of the target and platform kinematics $\mathbf{x} = (\mathbf{x}^p, \mathbf{x}^t) \in X \subset \mathbb{R}^{12}$ where $\mathbf{x}^p = (x^p, \dot{x}^p, y^p, \dot{y}^p, z^p, \dot{z}^p)^T \in \mathbb{R}^6$ is the position and velocity of the platform and $\mathbf{x}^t = (x^t, \dot{x}^t, y^t, \dot{y}^t, z^t, \dot{z}^t)^T \in \mathbb{R}^6$ the position and velocity of the target and T is the transpose operator.

A belief on the system state is estimated by the controller using a Kalman filter and Interacting Multiple Model filtering. Consequently, the belief state b_k at time k is represented by a Gaussian $b_k = \mathcal{N}(\mathbf{x}_k^t; \mathbf{x}_{k|k}^t, \mathbf{P}_{k|k})$. The posterior filter state estimate is denoted $\mathbf{x}_{k|k}^t$ and the covariance matrix $\mathbf{P}_{k|k}$ is the filter calculated MSE in the estimate:

$$\mathbf{P}_{k|k} = E\left[\left(\mathbf{x}_k - \mathbf{x}_{k|k}\right)\left(\mathbf{x}_k - \mathbf{x}_{k|k}\right)^T | Z^k\right] \tag{5.41}$$

where Z^k is the set of measurements received up to and including time k. Probabilistic data association is applied to accommodate for the possible lack of measurements and the presence of false measurements.

Actions

In this example, an action is the selection of the time interval until the next measurement of the target is performed. The action space is a discrete set of possible time intervals:

$$A = \{a = t_r | t_r \in [0.5 : 0.5 : 5.0]\} \tag{5.42}$$

This action space could be extended to include waveform selection, such as the number of transmit pulses or the intra-pulse modulation.

State transition probability

During the selected time interval, the target is assumed to follow a linear movement with Gaussian noise whereas the platform follows a linear deterministic trajectory. Therefore, the state transition equations are as follows:

$$\mathbf{x}_k^t = \mathbf{F}_{k|k-1}(t_r)\mathbf{x}_{k-1}^t + \mathbf{w}_{k|k-1}(t_r) \tag{5.43}$$

$$\mathbf{x}_k^p = \mathbf{F}_{k|k-1}(t_r)\mathbf{x}_{k-1}^p \tag{5.44}$$

where $\mathbf{F}_{k|k-1}$ is the transition matrix, and $\mathbf{w}_{k|k-1}$ is a zero-mean white-noise Gaussian distributed variable, with covariance matrix $\mathbf{Q}_{k|k-1}$. As the selected

action determines, the time of the next measurement influences the system state transition matrix, although the target moves irrespective of the selected action.

Observations

The radar produces measurements of range r, bearing θ and elevation ϕ, corrupted by Gaussian noise. These are converted into Cartesian coordinates [62] to give the measurement vector $\mathbf{z}_k = (\tilde{x}^t, \tilde{y}^t, \tilde{z}^t)^T$.

Observation likelihood function

The radar measurements are assumed to be corrupted by Gaussian noise with range, azimuth and elevation standard deviations of σ_r, σ_θ and σ_ϕ, respectively. These measurement errors are SNR dependent [63, Ch. 8], with a higher SNR leading to a lower standard deviation. The measurement noise in spherical coordinates is then converted into Cartesian coordinates to give the measurement noise covariance $\mathbf{R}_k$ [62]. Therefore, the observation function is as follows:

$$\mathbf{z}_k = \mathbf{H}_k \mathbf{x}_k^t + \mathbf{v}_k \tag{5.45}$$

where $\mathbf{H}_k$ is the observation matrix and $\mathbf{v}_k$ is a zero-mean white-noise Gaussian distributed variable with covariance matrix $\mathbf{R}_k$. The conversion from spherical into Cartesian coordinates is geometry dependent and therefore the Cartesian covariance $\mathbf{R}$ is dependent on the system state $\mathbf{x}_k$.

The observation likelihood function is then:

$$p(\mathbf{z}_k|\mathbf{x}_k) = \mathcal{N}(\mathbf{z}_k; \mathbf{H}_k\mathbf{x}_k, \mathbf{R}_k(\mathbf{x}_k)) \tag{5.46}$$

Reward

In this example, it is desired to minimize the tracking error and track loss while also minimizing the resource usage. These conflicting objectives require a trade-off to be found. Consequently, the reward is taken as the tracking utility generated divided by the resource usage. The utility function captures the tracking performance and is defined on the predicted covariance when using action t_r, $u : \mathbf{P}_{k+1|k}(t_r) \mapsto U \in [0, 1]$:

$$u(\mathbf{P}_{k+1|k}(t_r)) = \begin{cases} 0.0 & \text{if} \quad \sigma\big(\mathbf{P}_{k+1|k}(t_r)\big) \geq 1 \\ 1.0 & \text{if} \quad \sigma\big(\mathbf{P}_{k+1|k}(t_r)\big) \leq 0.2 \\ \left(\dfrac{1 - \sigma\big(\mathbf{P}_{k+1|k}(t_r)\big)}{0.8}\right)^{\eta} & \text{otherwise} \end{cases} \tag{5.47}$$

where η is a sensitivity parameter and $\sigma(\mathbf{P}_{k+1|k}(t_r))$ calculates the track sharpness as defined in Section 5.2.4.1.

The reward of the belief state b_k is then a function of the utility and the resource:

$$R(b_k, a_k) = \frac{u(\mathbf{P}_{k+1|k}) \cdot t_r}{r_l} \tag{5.48}$$

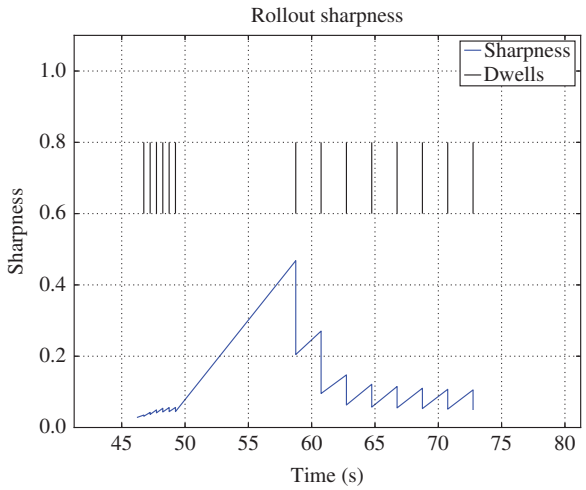

Figure 5.14 Example of a single rollout branch, which represents a hypothesis on the future system evolution. The candidate action is a revisit interval of 0.5 s, which is applied for 5 s before adopting 2 s for the remainder of the time horizon. During the occlusion no measurements are assumed. ©2015 IEEE. Reprinted, with permission, from [35]

where r_l is the resource loading, which is the fraction of radar time used by this task:

$$r_l = \frac{\tau_c}{t_r} \tag{5.49}$$

with measurement duration τ_c, which is assumed constant for all actions.

5.3.3.3 Rollout

To solve the POMDP, the method of policy rollout is applied, as described in Section 5.3.2.2. The base policy used in this work is to use the same revisit interval as the candidate action for a 5 s period in the future, and then to use a 2 s revisit interval for the rest of the time horizon, which extends over a total of 25 s. The heuristic is chosen on the intuition that the same revisit interval is necessary for a short duration before converging to a regular revisit interval. An example of a rollout execution can be seen in Figure 5.14 for a 0.5 s revisit interval candidate action.

During rollout, expected measurements are generated based on the hypothesis of the system state generated in the rollout branch, and the state dependent measurement covariance described in Section 5.3.3.2. The SNR for the expected measurement is scaled by a beam positioning loss factor that is a function of the track sharpness [11,27]. This accounts for the inability to correctly direct the radar beam at the target when the track uncertainty is large. The reduced SNR is used to calculate the probability of detection, which is incorporated into the Kalman filter update [64].

5.3.3.4 Simulated results

In the following results, the POMDP with policy rollout described in the previous section is compared against standard adaptive tracking [11,27,34], where the track

sharpness parameter is set at 0.2. The sensitivity parameter in (5.47) is taken as $\eta = 4$.

Figure 5.15 plots the number of measurements per second that are executed by adaptive tracking and the POMDP for a 2 km occlusion. It can be seen that both methods use a high number of measurements at the start of the simulation to initialize the track. It can also be seen that the POMDP anticipates the occlusion by scheduling an increased number of measurements just before the target enters the occluded region. Consequently, the POMDP is able to maintain the tracks during the occlusion and continue tracking once the target is again observable. In contrast, adaptive tracking does not anticipate the occlusion and therefore tracks are lost during the occlusion, which must then undergo a resource expensive track re-acquisition when the target is again observable.

The track sharpness for adaptive tracking and the POMDP method are shown in Figure 5.16. As the POMDP method anticipates the occlusion, it sharpens the track before it enters the unobservable region. In contrast, adaptive tracking does not anticipate the occlusion, leading to a much larger track sharpness during the occlusion. The larger track sharpness for adaptive tracking results in track drops and subsequent resource expensive track reacquisitions.

In Figure 5.17, the probability of a track loss is shown, evaluated over 100 Monte Carlo runs. It can be seen that the probability of a track loss is significantly reduced by the rollout-based method, because it anticipates the occlusion and

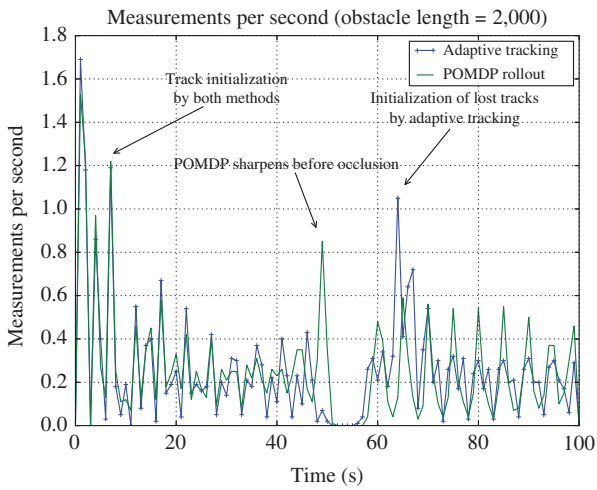

Figure 5.15 Number of measurements per second for the POMDP with policy rollout in comparison to adaptive tracking over 100 Monte Carlo runs. The POMDP anticipates the occluded region which leads to a spike in the number of measurements before the occlusion. The adaptive tracking method loses tracks during the occlusion leading to track initializations when the target is again visible. ©2015 IEEE. Reprinted, with permission, from [35]

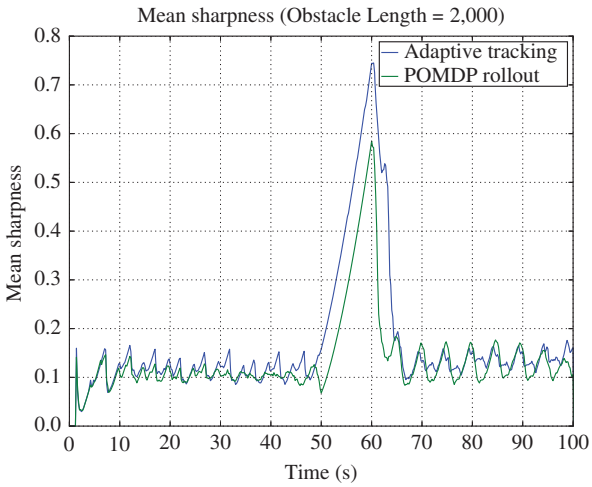

Figure 5.16 The mean sharpness of both methods, averaged over 100 Monte Carlo runs. A lower track sharpness corresponds to more accurate tracking. It can be seen that the sharpness during the occluded time is lower for the rollout-based method, which leads to lower number of track losses. © 2015 IEEE. Reprinted, with permission, from [35]

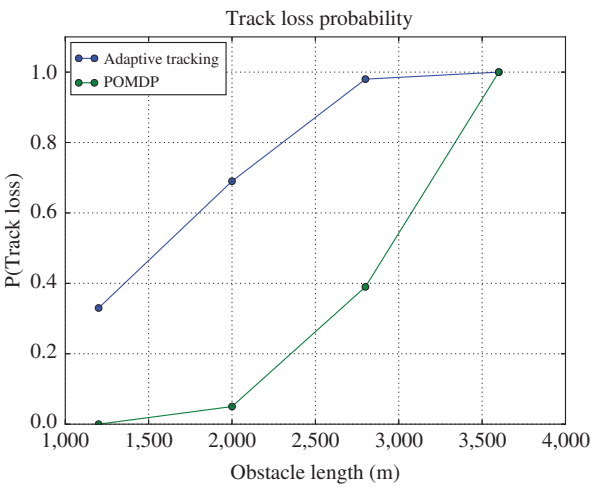

Figure 5.17 The probability of a track loss, based on 100 Monte Carlo runs. It can be seen that the rollout-based method has a significantly lower probability of track loss. This is because the rollout anticipates the occlusion, and therefore sharpens the track before the occluded period, leading to a lower number of track losses. © 2015 IEEE. Reprinted, with permission, from [35]

therefore schedules a number of additional measurements shortly before the target is occluded.

5.4 Summary

A cognitive radar acquires and exploits knowledge and understanding of its environment to enhance data processing and radar management. This can be seen as transitioning cognitive capabilities from the human operator into automated processes in a radar system. In this chapter, it was shown how the cognitive process of attention can be manifested by effective resources management, whereby a quality of service-based task management layer connects radar control parameters to mission objectives. In a simulation example, it was shown that rule-based methods result in a task quality that varies unpredictably depending on the environment and scenario, whereas effective radar resource management controls the task qualities such that mission requirements are satisfied. This chapter also described how the cognitive process of anticipation can be generated using non-myopic stochastic control, allowing the radar system to act with a consideration of how the radar system, scenario and environment will evolve in the future. In an anticipative target tracking control example, it was shown how a parallel rollout approximation to a POMDP can significantly reduce track loss by anticipating an imminent occlusion.

Abbreviations

CDA continuous double auction
CDAPS continuous double auction parameter selection
IMM interacting multiple models
JDL joint directors of laboratories
KKT Karush–Kuhn–Tucker
MDP Markov decision process
MPRF medium pulse repetition frequency
PCRLB posterior Cramér-Rao lower bound
POMDP partially observable Markov decision process
PRF pulse repetition frequency
QoS quality of service
Q-RAM quality of service resource allocation method
RCS radar cross section
RMSE root mean square error
RRM radar resource management
SNR signal-to-noise ratio
STAP apace time adaptive processing

References

[1] Braisby N., Gellatly A. (eds.). *Cognitive Psychology*. Oxford: Oxford University Press, 2nd ed., 2012.

[2] White F.E. 'A model for data fusion'. *1st National Symposium on Sensor Fusion*, 1988, pp. 149–158.

[3] Steinberg A.N., Bowman C.L., White F.E. 'Revisions to the JDL data fusion model'. *AeroSense'99*, 1999, pp. 430–441.

[4] Llinas J., Bowman C., Rogova G., Steinberg A., Waltz E., White F. 'Revisiting the JDL data fusion model II'. *7th International Conference on Information Fusion*, 2004.

[5] Smits F., Huizing A., van Rossum W., Hiemstra P. 'A cognitive radar network: Architecture and application to multiplatform radar management'. *European Radar Conference*, 2008, pp. 312–315.

[6] Kester L. 'Method for designing networking adaptive interactive hybrid systems'. *Interactive Collaborative Information Systems*, 2010, 281:401–421.

[7] Steinberg A.N., Bowman C.L., White F.E. 'Rethinking the JDL data fusion model'. *National Symposium on Sensor & Data Fusion*, 2004, pp. 79–97.

[8] Haykin S. *Cognitive Dynamic Systems: Perception-action Cycle*, *Radar and Radio*. Cambridge: Cambridge University Press, 2012.

[9] Klemm R. *Principles of Space-Time Adaptive Processing*. Croydon, UK: Institution of Engineering and Technology, 2006.

[10] Ward K.D., Tough R.J.A., Watts S. *Sea Clutter: Scattering, the K Distribution And Radar Performance*. Croydon, UK: Institution of Engineering and Technology, 2006.

[11] Blackman S., Popoli R. *Design and Analysis of Modern Tracking Systems*. Norwood, MA: Artech House, 1999.

[12] Blom H.A.P., Bar-Shalom Y. 'The interacting multiple model algorithm for systems with Markovian switching coefficients'. *IEEE Transactions on Automatic Control*, 1988, 33(8):780–783.

[13] Ulmke M., Koch W. 'Road-map assisted ground moving target tracking'. *IEEE Transactions on Aerospace and Electronic Systems*, 2006, 42 (4):1264–1274.

[14] Lee C., Lehoczky J., Siewiorek D., Rajkumar R., Hansen J. 'A scalable solution to the multi-resource QoS problem'. *20th IEEE Real-Time Systems Symposium*, 1999, pp. 315–326.

[15] Boyd S., Vandenberghe L. *Convex Optimization*. Cambridge, UK: Cambridge University Press, 2004.

[16] Charlish A.B., Woodbridge K., Griffiths H.D. 'Phased array radar resource management using continuous double auction'. *IEEE Transactions on Aerospace and Electronic Systems*, 2015. 51(3):2212–2224.

[17] Rajkumar R., Lee C., Lehoczky J., Siewiorek D. 'A resource allocation model for QoS management'. *18th Real-Time Systems Symposium*, San Francisco, CA, 1997, pp. 298–307.

[18] Graham R.L. 'An efficient algorithm for determining the convex hull of a finite planar set'. *Information Processing Letters*, 1972, 1:132–133.
[19] Rajkumar R., Lee C., Lehoczky J., Siewiorek D. 'Practical solutions for QoS-based resource allocation problems'. *19th IEEE Real-Time Systems Symposium*. Madrid, Spain, 1998, pp. 296–306.
[20] Irci A., Saranli A., Baykal B. 'Study on Q-RAM and feasible directions based methods for resource management in phased array radar systems'. *IEEE Transactions on Aerospace and Electronic Systems*, 2010, 46(4):1848–1864.
[21] Hansen J.P., Ghosh S., Rajkumar R., Lehoczky J. 'Resource management of highly configurable tasks'. *18th International Parallel and Distributed Processing Symposium*. Santa Fe, NM, 2004.
[22] Hansen J., Rajkumar R., Lehoczky J., Ghosh S. 'Resource management for radar tracking'. *IEEE Radar Conference*, 2006, pp. 140–147.
[23] Charlish A.B., Woodbridge K., Griffiths H. 'Agent based multifunction radar surveillance control'. *IEEE Radar Conference (RadarConf)*, 2011, pp. 824–829.
[24] Charlish A.B. *Autonomous agents for multi-function radar resource management*. Ph.D. thesis, University College London, 2011.
[25] Charlish A.B., Woodbridge K., Griffiths H. 'Multi-target tracking control using continuous double auction parameter selection'. *15th International Conference on Information Fusion*, 2012, pp. 1269–1276.
[26] Friedman D., Rust J. *The Double Auction Market: Institutions, Theories and Evidence*. Cambridge, MA: Perseus Publishing, 1993.
[27] van Keuk G., Blackman S.S. 'On phased-array radar tracking and parameter control'. *IEEE Transactions on Aerospace and Electronic Systems*, 1993, 29(1):186–194.
[28] Blackman S. *Multiple-Target Tracking with Radar Applications*. Norwood, MA: Artech House, 1986.
[29] Nadjiasngar R., Charlish A.B. 'A performance model for target tracking with a radar network'. *IEEE Radar Conference*. Johannesburg, 2015, pp. 1–6.
[30] Mallett J.D., Brennan L.E. 'Cumulative probability of detection for targets approaching a uniformly scanning search radar'. *Proceedings of the IEEE*, 1963, 51(4):596–601.
[31] Hoffmann F., Charlish A.B. 'A resource allocation model for the radar search function'. *International Radar Conference*, 2014, pp. 1–6.
[32] Skolnik M.I. (ed.). *Radar Handbook*. New York, NY: McGraw-Hill, 3rd ed, 2008.
[33] Kirubarajan T., Bar-Shalom Y., Blair W.D., Watson G.A. 'IMMPDAF for radar management and tracking benchmark with ECM'. *IEEE Transactions on Aerospace and Electronic Systems*, 1998, 34(4):1115–1134.
[34] Koch W. 'Adaptive parameter control for phased-array tracking'. *SPIE Signal and Data Processing of Small Targets*, 1999, pp. 444–455.
[35] Charlish A.B., Hoffmann F. 'Anticipation in cognitive radar using stochastic control'. *IEEE International Radar Conference*. Washington, DC, 2015, pp. 1692–1697.

[36] Papadimitriou C.H., Tsitsiklis J.N. 'The complexity of Markov decision processes'. *Mathematics of Operations Research*, 1987, 12(3):441–450.
[37] Smallwood R.D., Sondik E.J. 'The optimal control of partially observable Markov decision processes over a finite horizon'. *Operations Research*, 1973, 21(5):1071–1088.
[38] Pineau J., Gordon G., Thrun S. 'Point-based value iteration: An anytime algorithm for POMDPs'. *Proceedings of the Sixteenth International Joint Conference on Artificial Intelligence (IJCAI)*. Acapulco, Mexico, 2003, pp. 1025–1032.
[39] Shani G., Pineau J., Kaplow R. 'A survey of point-based POMDP solvers'. *Autonomous Agents and Multi-Agent Systems*, 2012, 27(1):1–51.
[40] Porta J.M., Vlassis N., Spaan M.T.J., Poupart P. 'Point-based value iteration for continuous POMDPs'. *Journal of Machine Learning Research*, 2006, 7(Nov):2329–2367.
[41] Thrun S. 'Monte Carlo POMDPs'. *Advances in Neural Information Processing Systems 12*. Cambridge, MA: MIT Press, 2000, pp. 1064–1070.
[42] Bai H., Hsu D., Lee W.S., Ngo V.A. 'Monte Carlo value iteration for continuous-state POMDPs'. In D. Hsu, V. Isler, J.C. Latombe, M.C. Lin (eds.), *Algorithmic Foundations of Robotics IX*, vol. 68 of *Springer Tracts in Advanced Robotics*, pp. 1–16. Berlin: Springer, 2011.
[43] Bai H., Hsu D., Lee W.S. 'Integrated perception and planning in the continuous space: A POMDP approach'. *The International Journal of Robotics Research*, 2014, 33(9):1288–1302.
[44] Bertsekas D.P., Castañon D.A. 'Rollout algorithms for stochastic scheduling problems'. *Journal of Heuristics*, 1999, 5(1):89–108.
[45] Miller S.A., Harris Z.A., Chong E.K. 'A POMDP framework for coordinated guidance of autonomous UAVs for multitarget tracking'. *EURASIP Journal on Advances in Signal Processing*, 2009, 2009(1):724597.
[46] Weissel F., Schreiter T., Huber M., Hanebeck U. 'Stochastic model predictive control of time-variant nonlinear systems with imperfect state information'. *IEEE International Conference on Multisensor Fusion and Integration for Intelligent Systems*. Seoul, Korea, 2008, pp. 40–46.
[47] Ross S., Pineau J., Paquet S., Chaib-draa B. 'Online planning algorithms for POMDPs'. *Journal of Artificial Intelligence Research*, 2008, 32:663–704.
[48] Chong E.K.P., Kreucher C.M., Hero A.O. 'POMDP approximation using simulation and heuristics'. In *Foundations and Applications of Sensor Management*, pp. 95–119. New York, NY: Springer, 2008.
[49] Chang H.S., Givan R., Chong E.K.P. 'Parallel rollout for online solution of partially observable Markov decision processes'. *Discrete Event Dynamic Systems: Theory and Applications*, 2004, 14(3):309–341.
[50] Chong E., Kreucher C., Hero A.O. 'Partially observable Markov decision process approximations for adaptive sensing'. *Discrete Event Dynamic Systems*, 2009, 19:377–422.

[51] Chong E.K.P. 'POMDP approximations using simulation and heuristics'. In *Foundations and Applications of Sensor Management*, pp. 95–119. New York, NY: Springer, 2008.
[52] Castanon D.A., Carlin L. 'Stochastic control theory for sensor management'. In *Foundations and Applications of Sensor Management*, pp. 7–32. New York, NY: Springer, 2008.
[53] Kreucher C., Hero A.O., Kastella K. 'A comparison of task driven and information driven sensor management for target tracking'. *44th IEEE Conference on Decision and Control*, 2005, pp. 4004–4009.
[54] Kreucher C., Hero A.O., Kastella K., Chang D. 'Efficient methods of non-myopic sensor management for multitarget tracking'. *43rd IEEE Conference on Decision and Control*, vol. 1. Bahamas, 2004, pp. 722–727.
[55] Wintenby J. *Resource allocation in airborne surveillance radar.* Ph.D. thesis, Chalmers University of Technology, 2003.
[56] Wintenby J., Krishnamurthy V. 'Hierarchical resource management in adaptive airborne surveillance radars'. *IEEE Transactions on Aerospace and Electronic Systems*, 2006, 42(2):401–420.
[57] Li Y., Krakow L., Chong E., Groom K. 'Approximate stochastic dynamic programming for sensor scheduling to track multiple targets'. *Digital Signal Processing*, 2009, 19(6):978–989.
[58] Ragi S., Chong E. 'UAV path planning in a dynamic environment via partially observable Markov decision process'. *IEEE Transactions on Aerospace and Electronic Systems*, 2013, 49(4):2397–2412.
[59] La Scala B.F., Moran W., Evans R.J. 'Optimal adaptive waveform selection for target detection'. *International Radar Conference*, 2003, pp. 492–496.
[60] La Scala B.F., Moran W. 'Optimal target tracking with restless bandits'. *SPIE Signal Processing, Sensor Fusion, and Target Recognition XV*, 2006, 16(5):479–487.
[61] La Scala B.F., Rezaeian M., Moran W. 'Optimal adaptive waveform selection for target tracking'. *8th International Conference on Information Fusion*, vol. 1. Philadelphia, PA, 2005, pp. 1–6.
[62] Fletcher F.K., Kershaw D.J. 'Performance analysis of unbiased and classical measurement conversion techniques'. *IEEE Transactions on Aerospace and Electronic Systems*, 2002, 38(4):1441–1444.
[63] Barton D.K. *Radar Systems Analysis and Modelling*. Norwood, MA: Artech House, rev. 1st. ed., 2004.
[64] Fortmann T., Bar-Shalom Y., Scheffe M., Gelfand S. 'Detection thresholds for tracking in clutter – A connection between estimation and signal processing'. *IEEE Transactions on Automatic Control*, 1985, 30(3):221–229.

This page intentionally left blank

Chapter 6

Clutter diversity

Hugh Griffiths[1] *and Riccardo Palamà*[1]

Abstract

Measurements of the properties of bistatic radar clutter have shown that amplitude statistics of bistatic clutter depend on the bistatic geometry, such that the distribution of the bistatic clutter may be shorter-tailed (less 'spiky') than the equivalent monostatic clutter. At the same time, the bistatic signature of targets may be significantly different from their monostatic signatures. Clutter Diversity may be defined as: 'understanding and quantifying these effects, and finding out how best to exploit them', and offers a new degree of freedom in the design of radar systems. This chapter reviews the properties of clutter and of targets as a function of bistatic geometry, and explores the effects of detection performance.

6.1 Introduction

Multistatic radar systems offer multiple degrees of freedom that can be exploited in order to improve the radar performance in detecting, classifying and tracking targets, as well as in reconstructing the image of a radar scene. The multiple receiver–transmitter pairs yield the capability of either selecting a subset of the best channels or combining all of them. In general, the increasing complexity of radar scenes has led to an increasing need for adaptive and cognitive radar systems, with the capability of reacting to dynamic scenarios. On the other hand, measuring performance – required during the design and acceptance testing stages – for more and more advanced complex radar systems is a challenge, as the results are highly scenario dependent. In order to ensure effective operation of radars and optimize performance, practical measurements should be supported by computer modelling and simulation, thus target and clutter models should be studied and continuously trained, under a wide variety of environmental conditions [1].

Chapter 12 of Volume 1 on bistatic clutter has shown that the properties of clutter in a bistatic/multistatic radar depend on the bistatic geometry, and that some geometries are more favourable than others in terms of target-detection performance.

[1]University College London, UK

The differences between monostatic and bistatic clutter were evaluated in terms of the mean clutter reflectivity and clutter statistics [2–4]. A definition of *Clutter Diversity* is therefore: 'understanding and quantifying these effects, and finding out how best to exploit them'. This should take account not only the geometry-dependent properties of the clutter but also those of the targets.

In order to take advantage of a system with multiple transmitters and multiple receivers, there is the need to understand how clutter and target signatures vary: understanding these effects is critical to being able to exploit their diversity and to make the system robust against a dynamically varying radar scene.

Clutter from land, sea and other sources has been studied since the earliest days of radar, as clutter can heavily impact the performance of a radar system due to its high clutter signal level (in particular for land clutter) and non-stationarity (in particular for sea clutter). Essential parameters that have been used to characterize the clutter are mean radar cross section (RCS) per unit area, amplitude statistics, Doppler spectrum and temporal and spatial correlation. Sea clutter is probably the most difficult type of clutter to cope with, due to the fact that, in maritime environments, a radar target may have small RCS and slow speed, completely embedding its return within the clutter region. Bistatic clutter is even more variable than monostatic clutter, as more parameters and degrees of freedom are involved. Recent work has shown that bistatic clutter distribution is, for some geometries, shorter tailed than monostatic clutter, which may improve the radar performance in regulating false alarm. In Figure 6.1, the probability density function in the upper diagram has a longer tail than the lower one, resulting in two different values of the detection threshold, V_T, to set in order to achieve a fixed probability of false alarm (P_{FA}). In general, the longer the tail of a distribution, the higher the detection threshold, thus the target signal should have a higher power to achieve detection at a satisfactory probability of detection P_D – achievable through shorter range and/or higher target RCS.

Shifting our attention to radar targets, the total RCS of an object results from the electromagnetic backscattering from the multiple scatterers located on the object. Key factors to quantify the contribution of each scatterer to the global RCS are its shape, its dimension relative to the wavelength and its orientation relative to the radar geometry. In the case of bistatic and multistatic radars, the target RCS is heavily influenced by the radar geometry, i.e. by the aspect angles of the target with respect to the transmitter and receiver boresights, and by the bistatic angle.

The forward-scatter geometry can be considered as a particular case of bistatic geometry, where transmitter, receiver and targets lie on the same line. According to Babinet's principle [5], the target RCS is determined by its geometrical silhouette area, which makes forward-scatter radars suitable to detect radar targets with low monostatic RCS, such as stealth targets.

The remainder of this chapter is organized as follows: Section 6.2 illustrates the impact of bistatic geometries on target RCS and Doppler signature, by first discussing the properties of simple objects, then evaluating the diversity in target signatures for maritime targets and aircraft – with a particular focus on drones – then the final subsection deals with the forward-scatter region. Section 6.3 addresses the impact of

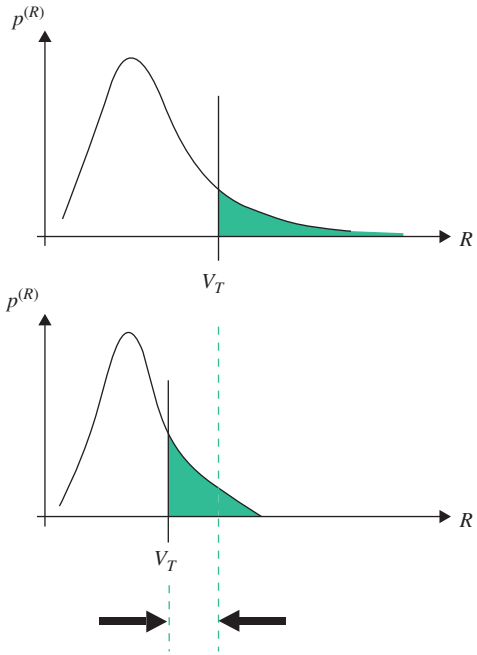

Figure 6.1 Examples of long-tailed (top) and short-tailed (bottom) probability density functions, showing the detection threshold V_T for the same probability of false alarm P_{FA}

clutter diversity on the radar performance in regulating false alarms and correctly detecting a target, showing results obtained by applying both single-channel- and multi-channel-detection algorithms on simulated and real data multistatic radar data. Section 6.4 summarizes the results and points the way forward.

6.2 Diversity in target signatures

6.2.1 Introduction

A general overview of the impact of system geometry on multistatic target scattering is given by the studies on electromagnetic modelling of bistatic scattering from simple objects, such as the sphere, cylinder and dihedral corner reflector.

The scattering from a spherical object is a function of the ratio of its radius to the radar wavelength. The net scattered signal results from the vector sum of the contribution from the front face of the sphere and a creeping wave contribution that travels around the circumference of the sphere. There are three different regimes of the sphere scattering, i.e. the Rayleigh region, the resonance region and the optical region, as shown in Figure 6.2. In particular, in the optical region, where the radius of the sphere is much larger than the radar wavelength, the sphere RCS is equal to the silhouette area of the sphere and is independent from the direction of the

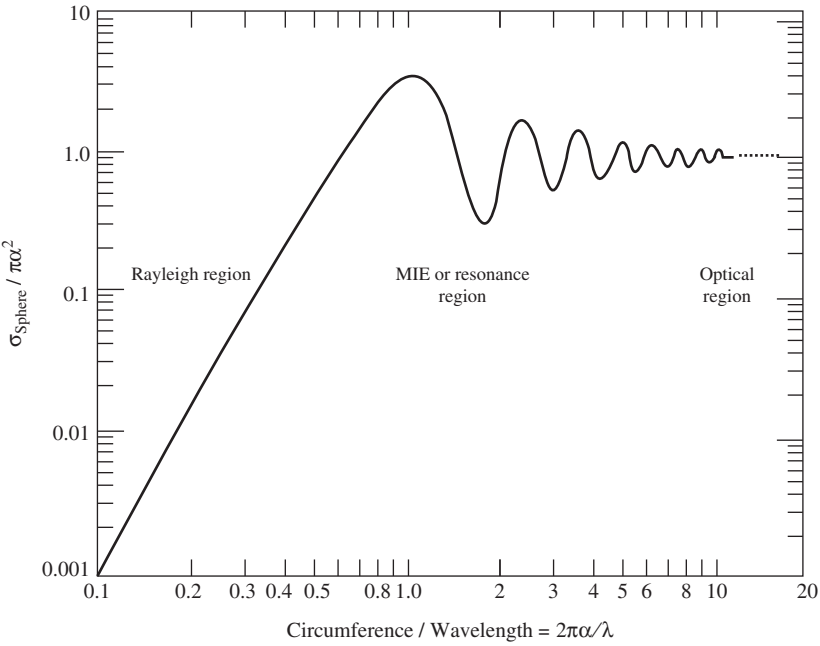

Figure 6.2 Radar scattering from a sphere as a function of the circumference-to-wavelength ratio

incident wave. The spherical symmetry of the sphere, independent of bistatic angle, makes it a widely used object for polarimetric calibration for multistatic radars [6].

A cylindrical scattering object offers a higher RCS than a sphere of equivalent diameter and, if rotated, also high cross-polar components. The RCS of a cylinder is given by $\sigma = 2\pi L^2 r/\lambda$, where L is the height of the object, r is the radius of its circular section and λ is the radar wavelength. However, the accuracy of the predicted RCS is heavily influenced by the precision of the alignment of the object. Another object with interesting bistatic scattering properties is the dihedral corner reflector, which consists of two facets positioned next to the other, with a fixed angle.

A study of the bistatic scattering of simple objects is relevant not only for antenna calibration purposes but also because the electromagnetic scattering from complex objects, such as boats, ships and aircraft, is often considered as the superposition of multiple scatterers, whose properties are equivalent to those of simple objects.

Practical targets will be more complex, consisting of several scattering centres. The relationship between the monostatic and bistatic RCS of such targets was considered by Crispin, Goodrich and Siegel in the 1950s [7] and by Kell [8] in the 1960s. The latter attributed the differences between monostatic and bistatic RCS, as a function of bistatic angle β, to

- Changes in relative phase between the individual scattering centre contributions,
- Changes in radiation from individual scattering centres,
- Changes in existence of centres – appearance of new scattering centres or disappearance of hose previously present.

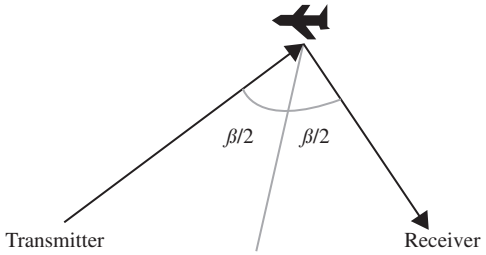

Figure 6.3 The bistatic equivalence theorem [7]

This led to the 'bistatic equivalence theorem', which states that the bistatic RCS of a target is equal to the monostatic RCS measured at the bisector of the bistatic angle, reduced in frequency by the factor $\cos(\beta/2)$ (Figure 6.3). This will be true as long as the targets are sufficiently smooth, that there is no shadowing of one part of the target by another and that the scatterers persist in angle. In practice, these conditions will not strictly be met, especially for complex targets and at large values of β, so the theorem should be used with caution, but it provides a good rule of thumb.

6.2.2 Multistatic scattering from maritime targets

This subsection addresses the phenomenology of multistatic scattering from maritime targets, illustrating the results of measurement campaigns realized and published by a number of different authors. In the open literature, there are relatively few publications illustrating measurements of the radar scattering from civilian and – to an even smaller extent – military targets. One of the first experimental studies comparing the bistatic RCS of maritime targets with their monostatic RCS, for different values of the bistatic angle (X-band) is the work published by Ewell and Zehner [8]. The measurements were realized on four different ship targets (called *Kansas*, *Hellenic Challenger*, *Philippean Rizal* and *Delaware Sun*) using an X-band radar system near grazing incidence, at horizontal and vertical polarization. The monostatic–bistatic baseline was 1.9 nautical miles (i.e. approximately 3.5 km) and the bistatic angle, β, was varied between 0.7 and 54 deg. In [8], the results are shown (as in Figure 6.4) as plots of the ratio of the bistatic to monostatic RCS as a function of the bistatic angle, whose exact values are also reported within a table. In most of the analysed cases, bistatic RCS values are smaller than monostatic RCS ones, and the difference increases with increasing bistatic angle. The only exception of this trend is the RCS values of the *Kansas* (VV data) at bistatic angles lower than 10 deg, for which the bistatic RCS is slightly greater than the monostatic one, with a maximum difference of 3.2 dB. The values of the *Hellenic Challenger* RCS (HH data) were measured for bistatic angles included between 10 and 25 deg, showing a monostatic RCS higher than the bistatic one with a 3–5-dB difference. In the case of the *Philippean Rizal* (HH data), the minimum value of the bistatic-to-monostatic RCS ratio is about -8 dB, for a bistatic angle of 23 deg, whereas the maximum values is about -4 dB, for $\beta = 7.4$ deg. The values of the *Delaware Sun* RCS (VV data) reveal the highest difference between monostatic and bistatic data, with a

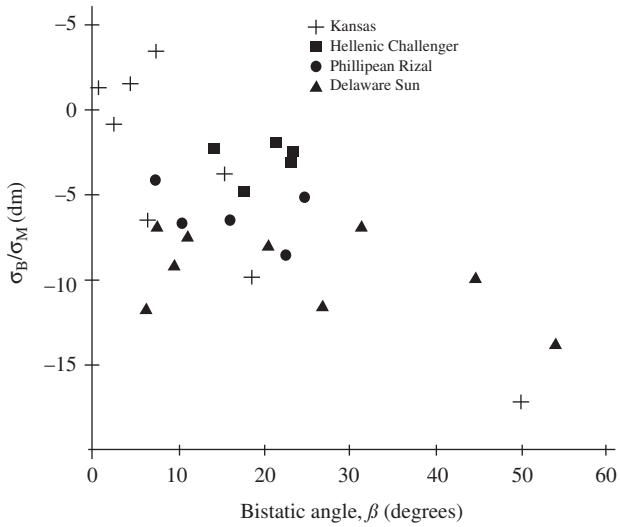

Figure 6.4 A plot of the ratio of the median bistatic RCS to the monostatic RCS as a function of bistatic angle, β for four small ship targets © 1980 IEEE. Reprinted with permission from [8]

maximum and minimum differences equal to about −7 dB ($\beta = 7.4$ deg) and −14 dB ($\beta = 7.4$ deg), respectively.

This RCS pattern, where maxima are located in the monostatic and quasi-monostatic regions, is due to the superstructure of the ships, containing dihedral and trihedral-type features. These give strong monostatic scattering, but weaker scattering as β increases.

In addition to the simple RCS analysis, further information about the target scattering is given by its micro-Doppler signature, which is due to the sea motion and the target wakes. The general expression for the bistatic Doppler frequency f_D is given by

$$f_D = \frac{2v}{\lambda} \cos\,\delta \cos\left(\frac{\beta}{2}\right) \tag{6.1}$$

where λ is the radar wavelength, v is the target speed, δ is the direction of the target velocity relative to the bistatic bisector and β is the bistatic angle. However, the target velocity is not time-invariant but shows fluctuations depending on the target micro-motions, due to the pitch and roll of a maritime target, which are even more accentuated in the case of small boats. These micro-motions generate time-varying Doppler fluctuations, which are usually referred to as the micro-Doppler signature [9]. A useful tool for micro-Doppler analysis is the short-time Fourier transform, which computes the Fourier transform over consecutive temporal sequences of data, thus producing a map of the amplitude as a function of both time and Doppler (i.e. a time-Doppler map). The information contained in such maps can be exploited for target detection and classification purposes.

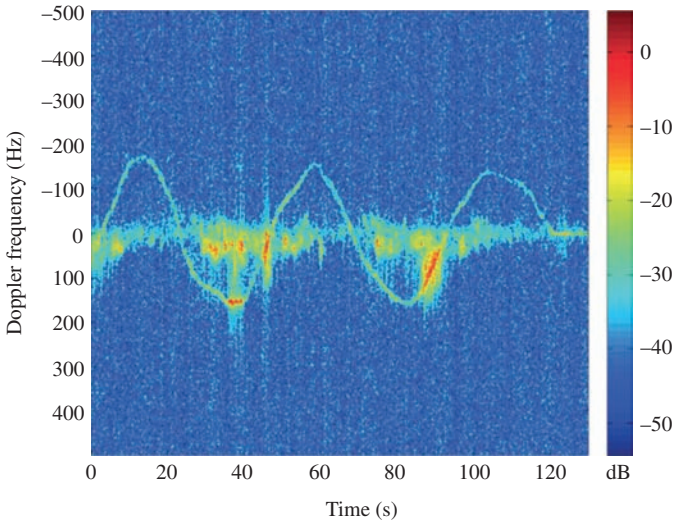

Figure 6.5 Monostatic Doppler signature of a RHIB © 2013 IEEE. Reprinted with permission from [10]

A preliminary analysis of the multistatic micro-Doppler signature of a rigid hull inflatable boat (RHIB) is shown in [10], concerning bistatic and monostatic data collected by the UCL NetRAD system during a measurement campaign realized in October 2010 and April 2011 in Simon's Town, South Africa, both in low sea state conditions. An example of time-frequency representation of this kind is shown in Figure 6.5, for the monostatic data collected on 14 October 2010. It can be noted that the target Doppler has a sinusoidal behaviour as a function of time, which is due to the circular trajectory of the target. In addition, the effect of the wakes is noticeable, consisting of target-dependent broadening of the Doppler spectrum, evident at around 40 and 85 s in Figure 6.5. In many cases, the wake may actually be the dominant feature of the overall signature. These data sets were collected at small bistatic angles (around 4 deg), thus minor differences are noticeable between the bistatic and monostatic data. On the other hand, data sets collected at larger bistatic angles (about 90 deg) highlight greater deviations between monostatic and bistatic data.

A further analysis is shown in [11], where the multistatic back scattering and forward scattering from a RHIB are analysed for different target trajectories. Data sets were collected during a measurement campaign using the UCL NetRAD system, in February 2015 at Langstone Harbour, United Kingdom.

Figure 6.6 shows the time-Doppler maps of the signal scattered from a RHIB for one monostatic (node 3) and two bistatic (nodes 1 and 2) geometries. The Doppler shift is higher for monostatic data with respect to both the bistatic data.

The duration of the micro-Doppler signature of the boat seems to be longer for the monostatic data than for the bistatic. In the monostatic data, it is noticeable from the beginning of the recording to about 19 s, whereas in the bistatic data,

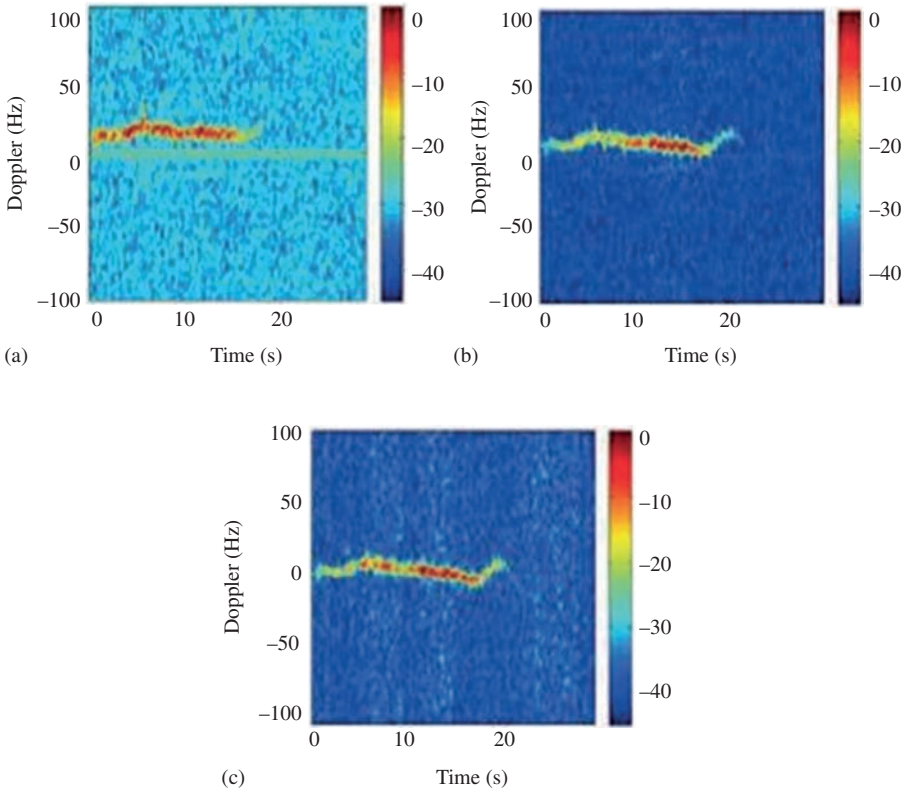

Figure 6.6 Time-Doppler plots of the first joint experiment as recorded at NetRAD node 3 (a), node 1 (b) and node 2 (c) © 2015 IEEE. Reprinted with permission from [11]

it appears smoothed between 5 and 18 s, with a peak between 13 and 15 s (this behaviour is similar for both the bistatic nodes). The shorter visibility time experienced by the bistatic channels is due to the fact that the target is perfectly visible at the bistatic nodes only when it is located within the intersection area between the transmitter and receiver antenna patterns.

The main Doppler is approximately 17.5 Hz for the monostatic data, equivalent to 1.1 m/s target speed along the monostatic line of sight, whereas it fluctuates around the zero-Doppler in both the bistatic channels.

An experiment with a different target trajectory, i.e. a target moving away from the monostatic node along its line of sight, showed a target spectrum centred on a negative Doppler frequency, for all the nodes, with similar values of the visibility time.

6.2.3 Multistatic scattering from aircraft and drones

Diversity in aircraft scattering was considered in [12], studying the behaviour of the bistatic RCS relative to the monostatic RCS of a large civilian jet aircraft at a frequency of 250 MHz, as a function of the aspect and bistatic angles. Similarly to

the case of maritime targets – addressed in the previous subsection – the bistatic RCS is generally lower than the monostatic, and their difference increases with increasing bistatic angle – for values between 0 and 60 degrees, with a minimum around 60 degrees. The maximum bistatic RCS is achieved at an aspect angle of 90 degrees and tends to decrease if the value of the aspect angle gets farther from the maximum point.

A conventional aircraft will consist of several scatterers, i.e. edges, surface discontinuities and corners (dihedrals and trihedrals), which usually maximize the back scattering along the monostatic line of sight. In recent decades, stealth techniques have been developed in order to reduce the target signature and hence its detection range. Possible stealth techniques consist of covering the target surface in radio-absorbing material, using RF-transparent composite material, reducing the presence of the aforementioned scatterers and shaping the target to reflect radiation in directions other than the monostatic. As a consequence, the behaviour of the bistatic –to– monostatic RCS ratio of stealthy targets is – in many cases – opposite to that of conventional targets, showing a bistatic RCS higher than the monostatic, with increasing bistatic angle. Hence, bistatic radars are often considered a successful countermeasure to stealth targets, together with forward-scatter radars that are the subject of the next subsection.

In addition to conventional aircraft, growing interest has been shown by the radar community towards drones and micro-drones, whose extremely low RCS makes them difficult to detect using traditional radar techniques.

On the other hand, the micro-Doppler signature of drones – in particular those using rotating blades, such as quadcopters – may provide useful information to extract through proper signal-processing techniques. The diversity in the micro-Doppler signatures resulting from the use of multiple transmitters and receivers is again a further degree of freedom to exploit.

Measurements of the micro-Doppler signatures of a drone – with and without a payload – were realized by using the UCL NetRAD in a multistatic configuration [13]. Figure 6.7 shows the time-Doppler plots of the signals back scattered by the drone – with and without payload – for both monostatic and bistatic geometries. The effect of the rotation of the blades consists of a series of horizontal lines, which are more straight and associated to higher Doppler frequencies in the case there is a payload on the drone. This phenomenon is probably due to the higher rotational velocity needed to sustain the drone with the additional weight due to the payload. Differences between the monostatic and bistatic micro-Doppler signatures can be observed on the no-payload data, whereas the monostatic data seem to have a wider Doppler bandwidth with respect to bistatic.

In [13], target signatures at monostatic and bistatic nodes are used to classify the different target classes: classification accuracy is shown to increase if multistatic data are combined together, in comparison with using only monostatic data.

6.2.4 Forward scatter

Forward scatter is often considered as the third bistatic RCS region [14], consisting of a bistatic configuration with bistatic angle equal or close to 180 degrees. The

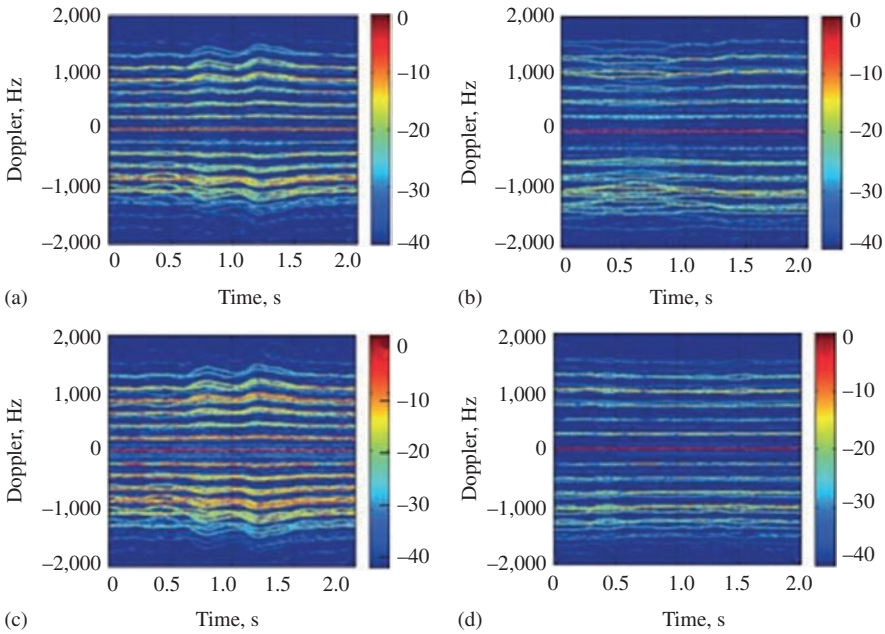

Figure 6.7 Micro-Doppler signatures of hovering drone: (a) monostatic no payload, (b) monostatic 500 g payload, (c) bistatic no payload and (d) bistatic 500 g payload © 2015 IET. Reprinted with permission from [13]

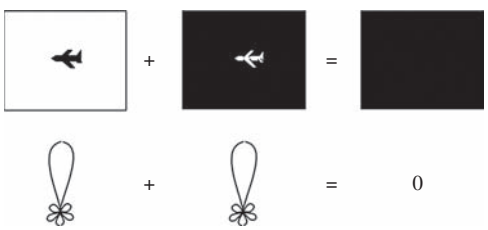

Figure 6.8 Babinet's principle applied to determine the forward-scatter radar signature of a target

enhancement in RCS can be understood by making reference to Babinet's principle from physical optics [5]. Suppose that an infinite screen is placed between the transmitter and receiver, so that the signal received is zero. Now suppose that a target-shaped hole is cut in the screen, between the transmitter and receiver. Babinet's principle states that the signal that would be diffracted through the target-shaped hole must be equal and opposite to the signal diffracted around the target, since the two contributions must add to zero (Figure 6.8).

Calculation of the signal diffracted through an aperture of a given size and shape is a standard problem in electromagnetics, and for simple shapes the results are well known. For example, for a rectangular aperture of sides a and b, the pattern

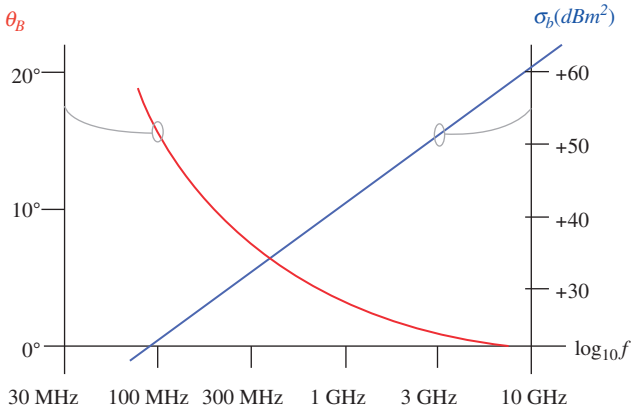

Figure 6.9 Forward-scatter RCS σ_{FS} and angular width of scatter θ_B for an idealized small aircraft target with $A = 10\ m^2$ and $d = 10\ m$

in each plane has a sinc shape with main lobes whose angular widths are λ/a and λ/b, and the peak scattered signal corresponds to a forward-scatter RCS of

$$\sigma_{\mathrm{FS}} = \frac{4\pi A^2}{\lambda^2} \tag{6.2}$$

where A is the area of the aperture ($A = ab$ in the case of a rectangular aperture).

Figure 6.9 shows the predicted forward-scatter RCS of an idealized aircraft whose silhouette area and linear dimension (height or width) are 10 m^2 and 10 m, respectively. It can be noted that, by increasing frequency, the angular width of the forward-scatter radiation pattern – θ_B – decreases and the object RCS increases. A trade-off between the minimum target RCS and the maximum forward-scatter width should be achieved, as decreasing the parameter θ_B will require more directive receive antennas and precise alignment of the target along the baseline. Therefore, a common choice consists of using low frequencies for forward-scatter operation. On the other hand, a target that lies exactly on the transmitter–receiver baseline will give no range information and no Doppler information, and even for a target slightly off-baseline, the range and Doppler resolution will be poor. Hence, whilst a forward-scatter radar will be good for target detection, location and tracking will be more difficult.

In [15], the authors address the modelling of the forward-scatter Doppler phase signature with a particular focus on configurations where the target crosses the baseline, i.e. for pure forward scatter. It should be noted that for forward-scatter geometries, the trajectory of a maritime target is assumed as uniform and linear, as the visibility time is of the order of seconds. The maximum of the forward-scatter signal is achieved when the target is exactly on the baseline, giving a $\pi/2$ phase deviation with respect to the direct path signal. In general, the Doppler frequency of forward-scatter signals is of the order of few Hz at most.

Measurements of the forward-scatter signature of a RHIB were realized simultaneously with the multistatic ones described in the previous subsection, by

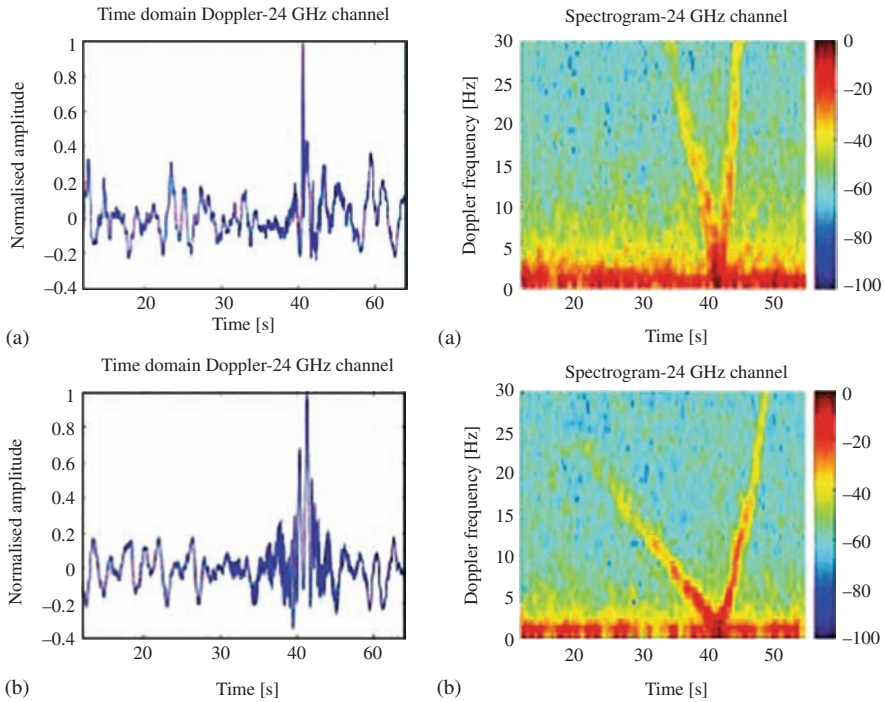

Figure 6.10 Forward-scatter target data at for 24 GHz (a) and 7.5 GHz (b): time-domain Doppler and spectrograms © 2015 IEEE. Reprinted with permission from [11]

using two carrier frequencies, at 7.5 and 24 GHz. Figure 6.10 shows the behaviours of the signal amplitude and of the Doppler frequency as a function of time, for both the frequency channels, in the case that the target is crossing the baseline at its midpoint. It could be noted that different Doppler chirp rates are associated to the two frequency channels, as well as different visibility times that depend on the transmitter and receiver antenna beamwidths, as well as the forward-scatter beamwidth of the object (in turn influenced by the carrier frequency). The measured visibility time is approximately 30 and 10 s for the 7.5 and 24 GHz channels, respectively. As previously mentioned, higher frequencies imply smaller forward-scatter beamwidths, which reduces the visibility time of a target crossing the baseline.

6.2.5 Summary

For many types of conventional targets (such as boats, ships and aircraft), the bistatic RCS is smaller than the monostatic. But for stealthy targets, and particularly in forward scatter, the bistatic RCS may be substantially greater than monostatic. On the other hand, forward-scatter radars work if the target of interest lies on the baseline and low carrier frequencies are preferred in order to increase the visibility time. In addition, the impact of clutter on forward-scatter radar performance should still be

studied, as it is likely to be a critical limitation for this technology. This is due the very large dimension of one clutter cell area in forward-scatter geometry, with one of the dimensions approximately equal to the baseline.

Micro-Doppler signature analysis can also benefit from the spatial diversity introduced by multistatic systems, which result in improved classification performance of radar targets with relevant micro-Doppler signatures. This has been demonstrated also in the case that targets are drones with rotating blades, carrying a payload.

6.3 Radar target detection

This section addresses the impact of clutter diversity on the performance of a radar system in detecting a target, based on the signals received by the nodes of a bistatic or multistatic radar. As illustrated in chapter 12 of Volume 1, the statistical and spectral properties of clutter depend on the system geometry, thus a crucial feature of multistatic systems consists of either choosing the best transmitter–receiver pair or combining all of them, in order to maximize the detection performance.

6.3.1 Introduction

A preliminary analysis of the impact of clutter diversity on detection performance is addressed by authors in [3], evaluating the difference in detection performance between the monostatic and bistatic nodes. The probability of false alarm (P_{FA}) was computed by integrating the values of the empirical probability density function of the clutter samples, $p_c(x)$, as a function of a detection threshold V_{T}, i.e. $P_{\mathrm{FA}} = \int_{V_T}^{\infty} p_c(x)dx$, then the value of V_{T} was set in order to achieve a P_{FA} of 10^{-4}. The signal associated to a point target was injected to compute the probability of detection (P_{D}), in order to evaluate the behaviour of P_{D} as a function of the signal-to-clutter ratio (SCR). Denoted as $p_{C+T}(x)$, the probability density function of the clutter-plus-target samples, the P_{D} values, were computed as $P_{\mathrm{D}} = \int_{V_T}^{\infty} p_{C+T}(x)dx$. The clutter data were collected by the monostatic and bistatic nodes of the NetRAD system in conditions of both low and high sea state. Results associated with low sea state and vertically polarized antennas show that, in order to achieve a P_{D} of 0.8, the bistatic SCR is 15 dB, whereas the monostatic SCR is 17 dB. Hence, the SCR gain is 2 dB, whereas, accounting for the lower clutter power associated with the bistatic channel, the gain in the required target RCS is approximately 12 dB. In the case of cross-polarized data, the SCR gain of the bistatic channel with respect to the monostatic is approximately 3 dB, whereas in the horizontally polarized data, the gain is 5 dB.

A different trend is revealed by the results obtained from high sea state data – shown in Figure 6.11. In the case of horizontally polarized data, a P_{D} of 0.8 is achieved for values of the monostatic and bistatic SCR of 17 and 21 dB, respectively, yielding an SCR gain of 4 dB of the monostatic channel over the bistatic one. Given that the bistatic -to-monostatic clutter power ratio is 4 dB, the two channels require the same value of the target RCS. In the high sea state data at vertical polarization, the SCR gain of the bistatic channel over the monostatic one is approximately 1 dB, confirming the trend noticed by the results obtained on the horizontally polarized data.

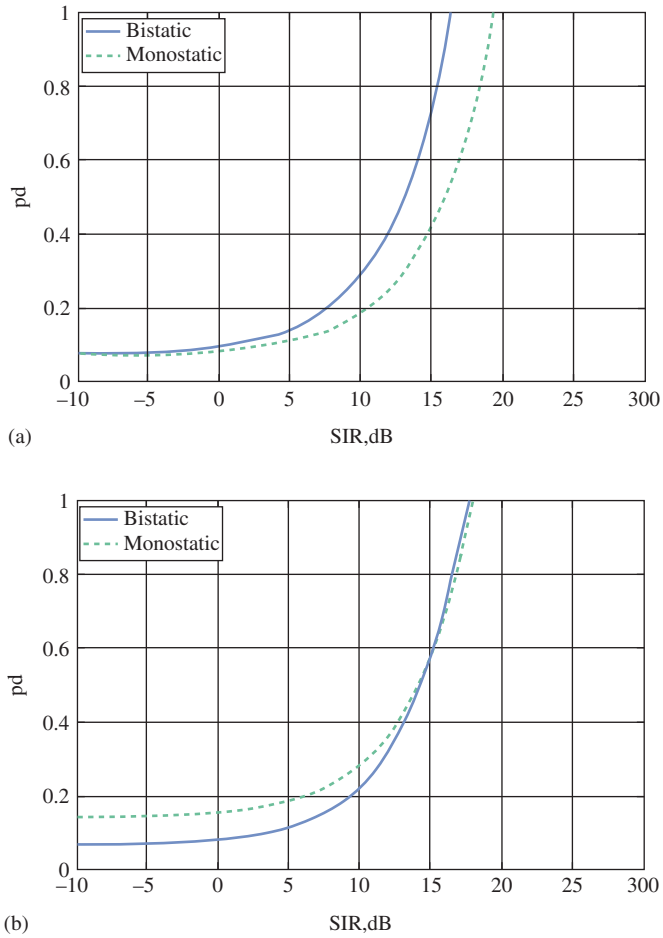

Figure 6.11 Preliminary analysis of the probability of detection as a function of SCR for bistatic and monostatic channels at horizontal (a) and vertical (b) polarization. High sea state © 2014 IEEE. Reprinted with permission from [3]

6.3.2 Multistatic detection algorithms

Radar detection techniques for multistatic radars can be distinguished between centralized and distributed ones. In a centralized detection scheme, each receiver node computes a local statistic, then all the local statistics are transmitted to a central processor, which in turn computes a global statistic [16] to compare with a threshold. An alternative detection rule is the decentralized one [17], according to that each node performs a hard decision then transmits the resulting binary symbols to a central processor, which executes the final decision. A drawback of centralized detection techniques is that they require wide (ideally infinite) bandwidth of

the communication network link between the system nodes and the fusion centre. A consequence of a finite communication bandwidth is that the local statistics – transmitted by each node to the fusion centre – are distorted, thus decreasing the detection performance. Solutions to the communication bandwidth bottleneck have been addressed by several works: in [18], the authors derive a distributed detection rule under capacity constraint, based on the concept of dependent randomization.

One of the first works dealing with the design of centralized detection for multistatic radar [16] proposes both optimum- and suboptimum-detection algorithms in the case of white Gaussian noise. In [19], the authors discuss again optimum and suboptimum multistatic radar detection techniques in the cases where clutter and jamming are Gaussian and correlated in both time and space. More recently, the radar community has devoted great interest towards the concept of multiple-input–multiple-output radars, with co-located or widely separated antennas. In [20], the authors discuss the impact of target spatial diversity in radars with a number of different configurations, such as multiple-input–multiple-output (MIMO), phased-array, multiple-input–single-output (MISO), by deriving an optimal detection rule under Gaussian disturbance and evaluating its performance. An operational definition of diversity order (DO) for radar networks is proposed in [21], where the authors adapt the concept of degrees-of-freedom in a multi-antenna wireless communication systems to multi-antenna radars. The DO has been defined as the slope of the probability of detection versus SCR curve at $P_{\mathrm{D}} = 0.5$, for a fixed P_{FA}, i.e.

$$\mathrm{DO} = \left.\frac{\partial P_{\mathrm{D}}}{\partial \mathrm{SCR}}\right|_{P_{\mathrm{D}}=0.5} \tag{6.3}$$

This is a measure of the 'steepness' of the P_{D}-vs-SCR curve, showing the performance of the radar system in switching from a low P_{D} to a high P_{D}, for a particular multistatic detection algorithm. The authors in [19] analyse the DO for different radar configurations, consisting of K sensors each with N antennas. If the sensors are collocated, DO is equal to NK (i.e. the upper performance limit), whereas if the sensors are not collocated, the DO is equal to $N\sqrt{K}$ if optimal techniques are used, for both centralized and distributed schemes. In the case that an 'or' rule is employed, the DO is given by $N\log K$. In synthesis, increasing the number of sensors yields an increase of the DO, whose behaviour (linear, logarithmic or square-root-based) depends on the configuration and on the detection rule. It should be noted that these results were obtained by considering Gaussian-distributed clutter.

In the case of non-Gaussian clutter, multistatic extension of the normalized adaptive matched filter, introduced with the name of MIMO Generalized Likelihood Ratio – Linear Quadratic by authors in [22]. The performance analysis shown in [23] addresses the impact of clutter diversity in both simulated and real clutter data. Simulations are realized by generating clutter samples according to the K-plus-noise distribution, with 10 dB clutter-to-noise-ratio (CNR) and 15 dB SCR, and different values of the shape parameters (ν_1, ν_2), both included between 0.04 and 1.2. The threshold values are set in order to obtain a $P_{\mathrm{FA}} = 10^{-5}$, and different covariance estimation methods are employed, i.e. the normalized sample

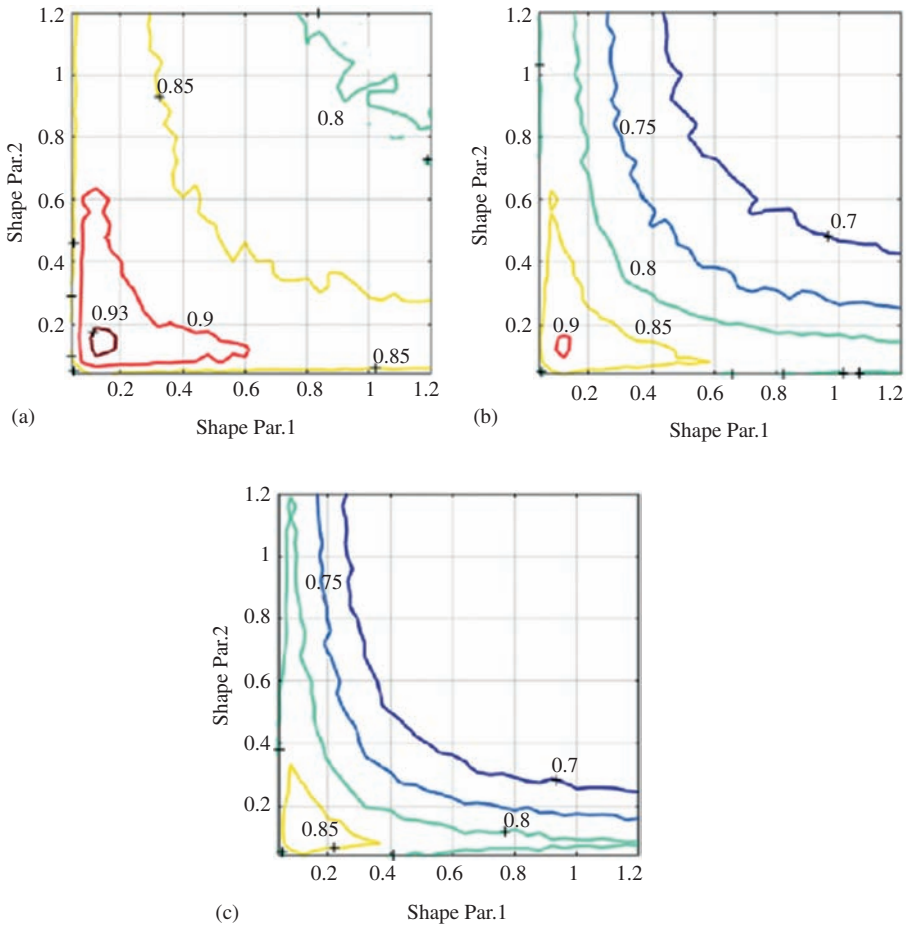

Figure 6.12 Contour plots of the probability of detection versus the shape parameter pairs, the first and second channel, in the cases of known (a) covariance matrix, NSCM (b) and FP (c) estimates, SCR = 15 dB, CNR = 10 dB, $P_{FA} = 10^{-5}$ © 2016 IEEE. Reprinted with permission from [23]

covariance matrix (NSCM) and fixed point (FP) estimator. Figure 6.12 shows 3D contour plots of the P_D values versus (ν_1, ν_2).

A peak occurs for both the shape parameters equal to about 0.15, whereas, for both the shape parameters greater than 0.1, the contour plots are similar to hyperbolas, meaning that high P_D values are obtained for low values of the shape parameters.

Furthermore, the gradient – through which the values of P_D decrease with increasing either one or both the shape parameters – is less steep in the case of known covariance matrix with respect to the cases of unknown estimated covariance matrix. In addition, the NSCM covariance estimator shows better performance than the FP one and a less steep gradient. The contour plots highlight that identical values of P_D are achieved by the multistatic detector for different

combinations of the shape parameters associated with the two jointly processed channels, which means that the clutter conditions experienced by each of the two channels jointly influence the global detection performance.

Real data results are obtained by using sea clutter data collected by the NetRAD system. The single channel detector is applied separately to the monostatic and bistatic data, and the multistatic detector is applied by combining them. Detection performance is evaluated by setting a threshold to achieve a P_{FA} of 10^{-2}. Figure 6.13 shows the resulting P_D values as a function of the SCR, comparing real and simulated data results. In the case of horizontally polarized real data, for a P_D of 0.8, an SCR of about 3 and 7.5 dB is required by the bistatic and monostatic channel, respectively, yielding a 4.5 dB gain of the bistatic channel over the monostatic one. For the vertically polarized real data, the corresponding SCR values are 6 and 9 dB, thus the bistatic-to-monostatic gain is 3 dB. It can be noted also that using a multistatic-detection technique yields a gain of about 2 dB (horizontal polarization) and 1 dB (vertical polarization) over the single-channel detector applied on the bistatic data.

The comparison between real and simulated data results reveals a large deviation in the detection performance of the multi-channel detector. The statistical correlation between the real bistatic and monostatic data, simultaneously collected by the NetRAD nodes, may play an important role in the evaluated behaviour. This paves the way to further analyses of the degrees of freedom introduced by clutter diversity of the final performance of radar systems.

6.4 Conclusion

This chapter has explored how a knowledge of the dependence of the signatures of clutter and of targets on bistatic geometry may be exploited in a bistatic or multistatic radar to give improved detection performance. This has been named 'clutter diversity'.

Some general observations can be made. The mean reflectivity of clutter is greatest for specular geometries and at low grazing angles. It has been found that, for many types of clutter the amplitude statistics of bistatic clutter are such that the clutter pdf is shorter-tailed (less spiky) than for the equivalent monostatic clutter. In some cases (i.e. urban or forested regions), this may be attributed to dihedral corner-reflector scatterers, but for sea clutter, the mechanism is not yet fully understood.

For conventional maritime of airborne targets the bistatic RCS is usually lower than the monostatic RCS, and the difference increases with bistatic angle β. For stealthy targets, and particularly in forward scatter, the opposite behaviour is observed.

In order to exploit these effects, a much fuller understanding of the bistatic signatures of targets and clutter will be needed, and this will need careful measurement and modelling that may be expected to take several years of work. But the exploitation of these effects in intelligent, adaptive radar networks – which is the subject of the next chapter – promises great rewards.

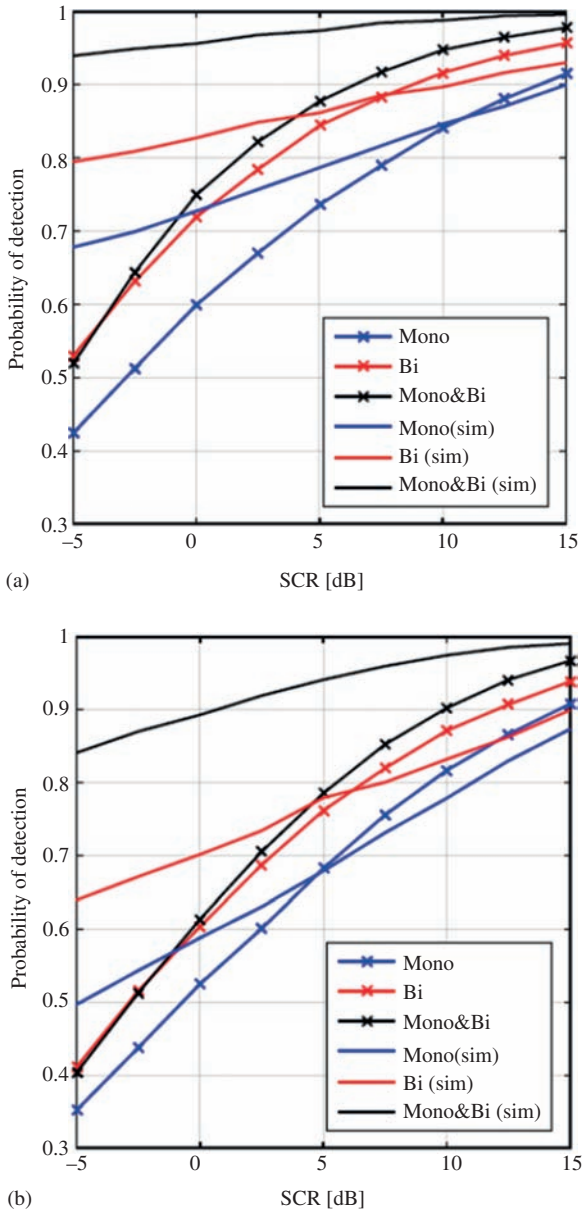

Figure 6.13 Values of the probability of detection versus SCR, for the monostatic -only, bistatic-only and monostatic –bistatic (combined) channels, HH (a) and VV (b) data, $\beta = 30$ deg, $P_{FA} = 10^{-2}$ © 2016 IEEE. Reprinted with permission from [23]

Acknowledgements

We are most grateful to the many people who have helped with the work described in this chapter. These include Waddah Al-Ashwal, Chris Baker, Mike Cherniakov, Francesco Fioranelli, Marina Gashinova, Sabrina Greco, Mike Inggs, Matt Ritchie and Mike Wicks. We are also grateful to the organizations that have funded the work, including THALES UK, the Royal Academy of Engineering, the Engineering and Physical Sciences Research Council, the IET A.F. Harvey Research Prize and the Office of Naval Research (Global).

References

[1] S. Watts, H.D. Griffiths, J.R. Holloway, *et al*., 'The specification and measurement of radar performance', *IEE International Radar Conference RADAR 2002*, Edinburgh; IEE Conf. Publ. No. 490, pp. 542–546, 15–17 October 2002.

[2] W.A. Al-Ashwal, K. Woodbridge and H.D. Griffiths, 'Analysis of bistatic sea clutter – Part I: Average reflectivity', *IEEE Transactions on Aerospace and Electronic Systems*, vol. 50, no. 2, pp. 1293–1303, April 2014.

[3] W.A. Al-Ashwal, K. Woodbridge and H.D. Griffiths, 'Analysis of bistatic sea clutter – Part II: Amplitude statistics', *IEEE Transactions on Aerospace and Electronic Systems*, vol. 50, no. 2, pp. 1293–1303, April 2014.

[4] R. Palamà, M. S. Greco, P. Stinco and F. Gini, 'Statistical analysis of bistatic and monostatic sea clutter', *IEEE Transactions on Aerospace and Electronic Systems*, vol. 51, no. 4, pp. 3036–3054, October 2015.

[5] M. Born and E. Wolf, *Principles of Optics*, Pergamon Press, Oxford, UK, 1980.

[6] J.W. Crispin, R.F. Goodrich and K.M. Siegel, 'A theoretical method for the calculation of the radar cross-sections of aircraft and missiles', University of Michigan, report 2591-1-1-M, AF 19(604)-1949, AFCRC-TN-59-774, 1959.

[7] R.E. Kell, 'On the derivation of bistatic RCS from monostatic measurements', *Proceedings of the IEEE*, vol. 53, pp. 983–988, 1965.

[8] G. Ewell and S. Zehner, 'Bistatic radar cross section of ship targets', *IEEE Journal of Oceanic Engineering*, vol. 5, no. 4, pp. 211–215, October 1980.

[9] V.C. Chen, F. Li, S.S. Ho and H. Wechsler, 'Micro-Doppler effect in radar: Phenomenon, model, and simulation study', *IEEE Transactions on Aerospace and Electronic Systems*, vol. 42, no.1, pp. 2–21, 2006.

[10] W.A. Al-Ashwal and H.D. Griffiths, 'Preliminary analysis of monostatic and bistatic Doppler signature of small maritime target', *2013 International Conference on Radar*, Adelaide, SA, pp. 494–499, 9–12 September 2013.

[11] M. Ritchie, F. Fioranelli, K. Woodbridge, *et al*., 'Simultaneous data collection of small maritime targets using multistatic and forward scatter radar', *2015 IEEE Radar Conference,* Johannesburg, pp. 203–208, 27–30 October 2015.

[12] K.M. Siegel *et al*., 'RCS calculation of simple shapes – Bistatic', Chapter 5 in *Methods of Radar-Cross-Section Analysis*, Academic Press, New York, 1968.

[13] F. Fioranelli, M. Ritchie, H.D. Griffiths and H. Borrion, 'Classification of loaded/unloaded micro-drones using multistatic radar', *Electronics Letters*, vol. 51, no. 22, pp. 1813–1815, October 2015.
[14] Willis N.J., *Bistatic Radar*, Scitech Publishing, Raleigh NC, 2005 (and references therein).
[15] M. Gashinova, L. Daniel, V. Sizov, E. Hoare and M. Cherniakov, 'Phenomenology of Doppler forward scatter radar for surface targets observation', *IET Radar, Sonar & Navigation*, vol. 7, no. 4, pp. 422–432, 2013.
[16] E. Conte, E. D'Addio, A. Farina and M. Longo, 'Multistatic radar detection: Synthesis and comparison of optimum and suboptimum receivers', *IEE Proceedings-Communications, Radar and Signal Processing*, vol. 130, no. 6, pp. 484–494, October 1983.
[17] M. Barkat and P.K. Varshney, 'Decentralized CFAR signal detection', *IEEE Transactions on Aerospace and Electronic Systems*, vol. 25, no. March (2), pp. 141–149, 1989.
[18] F. Gini, F. Lombardini and L. Verrazzani, 'Decentralised detection strategies under communication constraints', *IEE Proceedings of the Radar, Sonar and Navigation*, vol. 145, no. 4, pp. 199–208, August 1998.
[19] E. D'Addio and A. Farina, 'Overview of detection theory in multistatic radar', *IEE Proceedings – Communications, Radar and Signal Processing*, vol. 133, no. 7, pp. 613–623, December 1986.
[20] E. Fishler, A. Haimovich, R.S. Blum, L.J. Cimini, D. Chizhik and R.A. Valenzuela, 'Spatial diversity in radars: Models and detection performance', *IEEE Transactions on Signal Processing*, vol. 54, no. 3, pp. 823–838, 2006.
[21] R. Daher and R. Adve, 'A notion of diversity order in distributed radar networks', *IEEE Transactions on Aerospace and Electronic Systems*, vol. 46, no. 2, pp. 818–831, April 2010.
[22] C.Y. Chong, F. Pascal, J. Ovarlez and M. Lesturgie, 'MIMO radar detection in non-Gaussian and heterogeneous clutter', *IEEE Journal of Selected Topics in Signal Processing*, vol. 4, no. 1, pp. 115–126, February 2010.
[23] R. Palamà, M. Greco and F. Gini, 'Multistatic adaptive CFAR detection in non-Gaussian clutter', *EURASIP Journal on Advances in Signal Processing*, pp. 1–17, 2016.

Chapter 7

Biologically inspired processing of target echoes

Alessio Balleri[1], Krasin Georgiev[1], Andy Stove[2], Hugh Griffiths[3], Chris Baker[4] and Marc Holderied[5]

Abstract

Echolocating bats have evolved an impressive ability to detect and discriminate targets in highly challenging environments. It is believed that over 50 million years of evolution have contributed to optimize their echolocation system so that high-level performance could be achieved within their operating environment. The way bats interrogate the surroundings present differences, as well as similarities, with respect to typical signal processing techniques used in synthetic sensors. In identifying and investigating these differences, useful lessons can be made available to engineers that can potentially be used to improve radar and sonar systems.

In this chapter, we review some of the strategies that bats are believed to employ to detect and classify moving and static targets and present a comparison with the radar and sonar counterparts. We introduce a baseband receiver based on an existing model of the bat auditory system and apply it to baseband synthetic ultrasound signals to investigate target detection and resolution performance.

7.1 Introduction

In the natural world, echolocating mammals use waveform diversity as an inherent component of their normal behaviour. The constantly changing time and frequency structure, and location and direction of their transmitted signals represent a proactive approach to interrogation of the surrounding environment. In addition, a multiplicity of processing streams collectively extracts information from received echoes to build up an accurate picture that is supplemented by long-term experiential memory. In this way, bats, whales and dolphins are able to perceive and

[1]Centre for Electronic Warfare, Information and Cyber, Cranfield University, Defence Academy of the United Kingdom, UK
[2]Stove Specialities, Sussex, UK
[3]University College London, UK
[4]Aveillant Ltd, UK
[5]School of Biological Sciences, University of Bristol, UK

understand their environment. Further, bats, for example, are able to do this, such that they can navigate, feed, socialize and otherwise conduct their lives.

Echolocating mammals such as bats, whales and dolphins have been using echolocation for over 50 million years and have presumably been using waveform diversity for nearly as long. In contrast, synthetic systems such as sonar and radar have been in existence for not much more than 100 years. Echolocating mammals vary parameters including the pulse repetition frequency, and power and frequency content of their transmitted waveforms. Modern technology means that it is now possible to replicate easily such diversity in radar and sonar systems. With modern digital technology, high-precision, wide-bandwidth waveforms can be generated and varied even on a pulse-to-pulse basis. If we understand how bats exploit echolocation for autonomous navigation, collision avoidance and recognition, perhaps we can build this understanding into our synthetic systems, and potentially, this can provide a step function change in radar and sonar performance.

In the past few years, the radar and sonar communities have shown particular interest in understanding the remarkable success of the bat in detecting and classifying stationary and moving 'targets'.

7.1.1 Detection and identification of stationary targets – flowers

Nectar-feeding bats, for example, play an important role in the process of pollination of plants, which, with their flowers, represent a very interesting class of organisms for the study of target classification. First, flowers are motionless and silent so that bats cannot rely on Doppler information or passive location based on target sounds, and second, their habitat is often a densely cluttered environment. Finding and approaching a flower is a gradual process that involves all the bats senses. Although bats can only use vision at dusk, they can rely on their sense of smell and on echolocation to search for flowers in darkness. Nectar-feeding bats have a highly developed sense of smell and they are attracted by the scent of sulphur compounds which are produced by many plants pollinated by bats [1]. Although the sense of smell certainly plays an important role, and in particular for long-range attraction, latest research results support the theory that nectar-feeding bats largely rely on echolocation to plan their approach flight and to detect and select the flowers in the proximity of the plant. Indeed, it has been shown that bats are capable of detecting and selecting objects by echolocation only. The flowers of the bat-pollinated vine *Mucuna holtonii* release the greatest amount of nectar reward only on the first visit by the bat. By landing into the flower corolla, the bat ignites an explosion of the flower's vexillum which functions as a trigger for the pollen and nectar release. Behavioural experiments have shown that bats can successfully select unvisited flowers within an inflorescence in darkness, and this is a task that can only be done by echolocation. The scent of the flower, in fact, remains unchanged before and after the explosion. It has further been shown that by modifying the acoustic echo properties of these flowers, via insertion of a small pad of cotton in the cavity of the vexillum (i.e. without altering the scent and visual aspect of the flower), there is a resulting drop in the rate of successful classification [2,3].

7.1.2 Detection and identification of moving targets – insects

Bats that emit constant frequency signals can detect and classify fluttering insects from the amplitude and frequency modulations of the echoes that result from the movement of the wing of the insect [4,5]. These modulations, called acoustical glints, provide information about wing-beat rate and flight angle and are very specific to each species of insect. Glints turn out to be useful not only for the detection of the prey but also for its identification. Amplitude modulations are the result of the fact that echo strength is strongest when the insect wings are perpendicular to the sound source and gets weaker as the insect wing moves away from the perpendicular position. The precise timing of the glint depends on the angular orientation of the insect [6]. The amplitude modulations give information about the target elevation and are related to the timing of the glint production [7]. The wing movement towards and away from the receiver induces Doppler shifts in the echoes, providing information of wing-beat movement that are important signatures for species identification, since insect wing-beat frequency scales with body size [8]. As the way in which a given insect species moves its wings is highly specific, the structure of glints varies across different species and even insects with the same wing-beat frequency may provide different spectral signature in the echo [9]. Figure 7.1 shows the spectrogram of four echoes from four different insects:

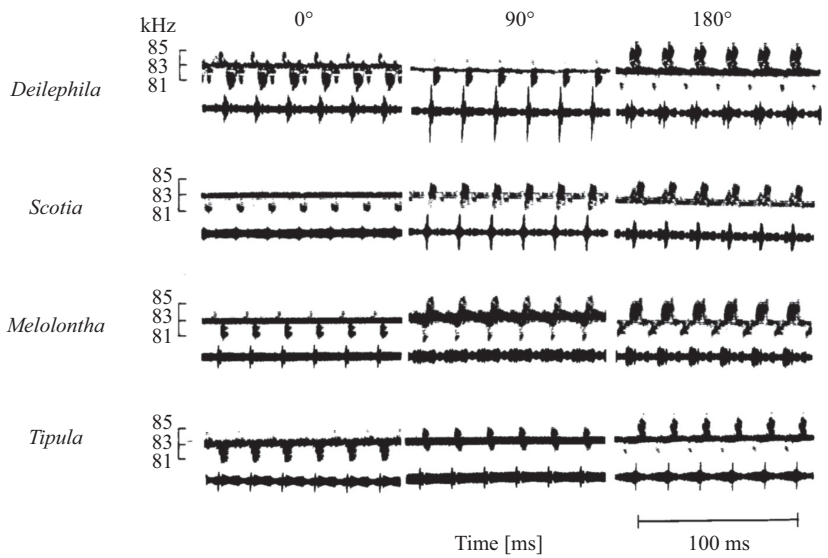

Figure 7.1 Short-time Fourier transforms and time-domain signals of the echoes from four insect species all fluttering at 50 Hz but with different spectral patterns in echoes from their wing beats. For each insect, the upper trace represents the spectrogram of the echo and the lower trace the time oscillation. © 1994 Springer. Reprinted, with permission, from [9]

Deilephila elpenor, *Scotia exclamationes*, *Melolontha melolontha* and *Tipula oleracea*. These were flying with the same wing-beat rate and were illuminated from 0, 90 and 180 degrees with respect to the sound source.

The figure shows that spectrograms for each species present different characteristics, although the flutter frequency is the same. It also shows that, for the same insect, the properties of the spectrogram are also dependent on the angle from which the sound source emanates, confirming that spectral cues provide information on angular position [7,10].

7.1.3 Comparison between radar, sonar and biological systems

Indeed, there are a number of similarities with the radar and sonar cases. For example, the types of waveforms deployed by bats are modulated in a fashion similar to linear and hyperbolic chirps commonly used by radar and sonar systems [11]. Also, radar and sonar systems typically use a range resolution which will separate the target into the order of 30 'cells', and the ratio between the flower size and the range resolution achieved by bats is similar to this ratio, which appears to give best performance using radar or sonar sensors. This provides still further cause for optimism that methods employed by natural systems can be usefully exploited in synthetic counterparts.

The mechanisms we believe a bat employs to process target-echo signals present apparent differences with respect to standard radar and signal processing. Bats exploit spatial and temporal adaptations in the process of target detection and recognition and adaptive waveform diversity [11], cognitive guidance and control [11,12] and memory [12,13] are characteristics that are studied in the context of cognitive sensing. However, work by radar and sonar engineers on target detection and classification inspired by what is known about how bats perform this task has generally still assumed that the receiver includes a matched filter, e.g. see [11,14].

The Spectrogram Correlation And Transformation (SCAT) receiver is an existing model of the bat auditory system that takes into account the physiology and underlying neural organization in bats which emit chirped signals.

In this chapter, we present a baseband receiver equivalent to the SCAT so to allow SCAT-like signal processing to be applied to radar signals characterized by a much larger carrier frequency than their sonar counterpart. We present a theoretical analysis and highlight potential advantages and limitations of the 'bat signal processing' for the purpose of target detection, localization and resolution. The equivalence is demonstrated by comparing the output of the original SCAT to that of our proposed baseband version using both simulated and experimental target echoes. The results show that the baseband receiver provides comparable frequency interference patterns to those produced by the SCAT for two closely located scatterers.

7.2 The need for a receiver model

The need of developing an accurate model of the bat receiving chain has arisen as a result of previous behavioural experiments showing that bats are able to achieve

performance far better of what would be expected when standard radar and sonar signal processing is applied to bat-like waveforms. For example, in [15,16], Simmons showed that the big brown bat (*Eptesicus fuscus*) can perceive the arrival-time of virtual echoes with an accuracy of 10–15 ns in quiet ambient laboratory conditions and an accuracy of 40 ns for a signal-to-noise ratio of 36 dB. He also showed that a typical two-point resolution falls between 2 and 10 μs with a 85-kHz bandwidth. Schmidt showed that the bat *Megaderma lyra* is able to discriminate between two phantom target echoes delayed of about 1 μs [17] with a bandwidth up to 100 kHz, suggesting the bat capability to achieve higher range resolution than is possible with conventional radar processing of the signals at the output of the matched filter (above 10 μs or 1.7 mm at a speed of sound equal to 340 m/s). Discrimination of surface structures was demonstrated in [18], where some individuals of *Glossophaga soricina* were trained to distinguish between a smooth and a coarse surface with a structure depth bigger than 0.38 mm. The emitted waveform recorded in the experiment was an FM down-chirp characterized by three harmonics between 95 and 55, 150 and 86 and 190 and 140 kHz, respectively. It is worth noting that this is one of the few experiments deploying real targets that demonstrate the fine-resolution capabilities of the bat.

Different aspects of the way bats process echoes from targets and the surrounding environment have been studied in the literature [19–21]. Although it is not plausible that these models can exactly replicate all the bat neural processing, because they only account for range information and have only been applied to the case of a single receiver with no directional sensitivity, they can offer a good starting point to understand the origins of the remarkable bat capabilities. Most of the models available in the literature assume that the emitted call and the received echoes are FM signals. The cochlea is modelled as a filter bank that generates an auditory spectrogram and this is followed by a temporal processing block that models the delay tuned neurons in the brain. The temporal block is used for ranging the targets. A spectral processing block follows, that can resolve the mutual interference between targets which are close together [19,21]. Bat precision in echo resolution is presumed by some authors to require a fully coherent receiver so these authors try to preserve the phase of the sound wave in their models to implement coherent signal processing [19,20,22]. Others argue that a coherent receiver is physiologically implausible [21]. The effect of bandpassed signal smoothing on coherence is explored in [23].

Although the aim of the bat auditory system models is to reproduce the acoustic images as we believe, from a variety of behavioural experiments, that the bats perceive them, there is no explanation on what exactly brings the performance improvement so it could be exploited in a technological system.

7.3 Description of the spectrogram correlation and transformation model

The SCAT receiver is a model of the auditory system that was proposed by Saillant *et al.* in [19] for the bat *Eptesicus fuscus*. It accounts for the underlying neural organization in bats which use FM signals, namely FM bats, by special emphasis on the

physiological correlation of the model. The main modules of the SCAT are the cochlear block, the temporal block (spectrogram correlation) and the spectral block (spectrogram transformation). A detailed analytical modelling of the temporal block was presented by Peremans and Hallam [22]. The closed-form equations approximating the spectral block are derived by Park and Allen [24]. In these analyses of the SCAT, the outputs of the bandpass filters when excited by a chirp were approximated with cosines shaped by Gaussian envelopes. The bat auditory system processes both the emitted call and the received echo through an auditory periphery and then through some higher level brain structures. The auditory periphery includes the outer, the middle and the inner ear and provides a time-frequency representation of the input signal. The frequency content is sampled in a non-linear scale (hyperbolic or logarithmic). The consequent brain processing provides an estimate of the time delay between the call and the echo and provides cues about the structure of each echo.

A short summary of the SCAT model building blocks based on [19] follows together with some notes on other alternative models available in the literature.

7.3.1 Cochlear block

The cochlear block is modelled with a bank of 81 Butterworth bandpass filters of order 10 and each having a bandwidth $B = 4$ kHz. Each filter is followed by a signal rectifier and a 3 kHz bandwidth low-pass filter (Figure 7.2) in order to extract the envelope of the signal. The central frequencies f_c of the bandpass filters span the bandwidth between 20 and 100 kHz and are arranged in a hyperbolic scale as $f_c = 1/T_c$, where the central period T_c changes linearly from 10 μs to 50 μs with increments of 0.5 μs. It will be appreciated that in this model the overlap between the

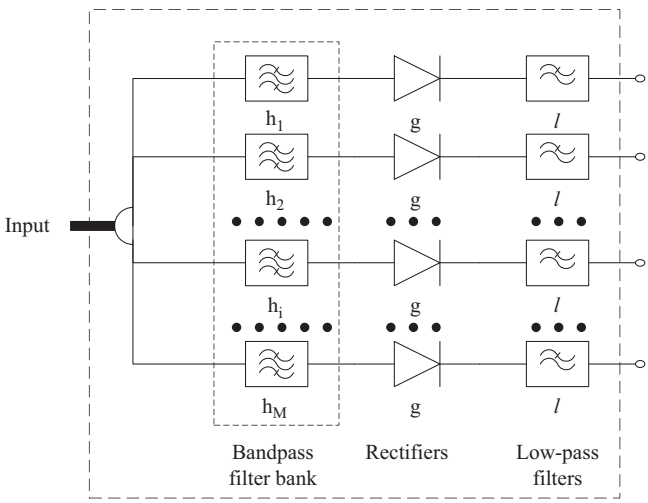

Figure 7.2 Cochlear block of SCAT receiver. Filter bank of $M = 81$ bandpass filters h_i with central frequencies from 20 to 100 kHz. Rectifier g and Butterworth low-pass filter l follow after each bandpass filter

responses of adjacent filters varies across the bank. Two levels of smoothing of the envelope have been proposed with the SCAT, namely a high smoothing and a low smoothing. The high smoothing consists of a full wave rectifier followed by a second-order low-pass filter, whilst the low smoothing consists of a half wave rectifier followed by a first order low-pass filter. In both cases, the low-pass filter is an Infinite Impulse Response (IIR) Butterworth with a bandwidth of 3 kHz. It will be shown later that the choice of model for the low-pass filtering has a negligible effect on the behaviour of the processor. The output of the cochlear block is called the *auditory spectrogram* or *cochleogram*. A representative block diagram is shown in Figure 7.2.

In the literature, some modified versions of the original SCAT have been proposed which differ on how the initial splitting of the signal into frequency channels is carried out. For example, the bank of constant bandwidth Butterworth filters is replaced by gammatone filters [21] with frequency-dependent bandwidth after [25] or Gaussian chirplets with carrier frequencies compatible with the emission sweep rate [20]. Some models use additional non-linear transformations, e.g. raising the amplitude of the detected signal to a power of 0.4 to account for the non-linear interactions in the organ of corti [21].

7.3.2 Temporal block

The purpose of the temporal block is to estimate the time delay between the call and the echo based on the output of the cochlear block. It consists of a set of tapped delay lines that implement a cross-correlation function between the call and the echo. These are triggered by the call signal.

The temporal block processes the output of the cochlear block and converts it into neural spikes. The neural coding can either be considered as part of the cochlear block or not. The spike decay period is 4 μs [19]. A spike rise results in an increase of the threshold and inhibits the same neuron from producing another spike. The spike activation threshold decays to its initial value over a period of 1 ms.

The temporal block carries out a 'de-chirping' of the signal by adding appropriate delays to each frequency channel. Figure 7.3 shows an example of the output from the temporal block when two groups of scatterers are present. Delays are calculated using the emitted signal as a trigger. Simultaneous activity in multiple channels is detected by a set of coincidence detection neurons and is a sign of the target presence. Target detection is implemented by summing the output over all channels and the target is declared with a peak-detection algorithm.

7.3.3 Spectral block

The spectral block is responsible for extracting the fine structure of the target. It is used to detect and measure the delay between highly overlapping echoes, which cannot be resolved by the temporal block. The spectral block exploits the interference pattern between overlapping echoes, which results in the suppression or amplification of the power of the output of some of the filters of the cochlear block. It integrates the output signal of each frequency channel for a specific time interval (about 350 μs [19]). The interference arises as follows: if we ignore the windowing due to the finite length of the chirp, the transmitted signal can be considered to be $e^{j\alpha t^2}$. In the simplest case, the

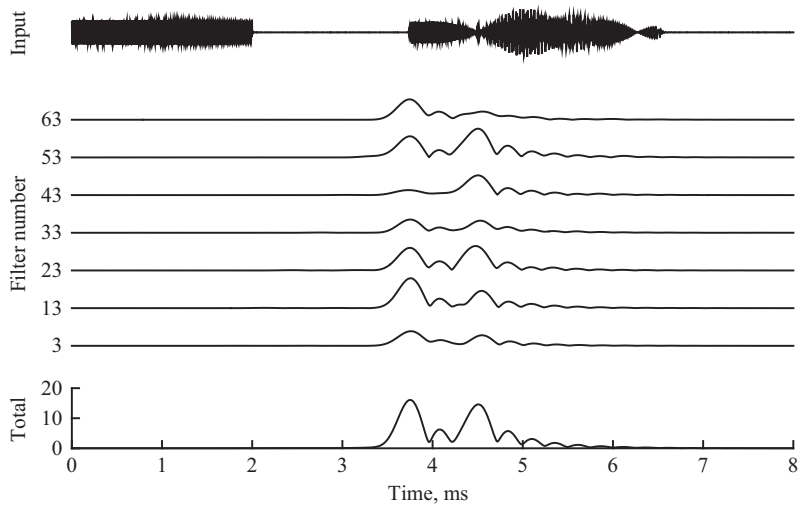

Figure 7.3 Example of a dechirped output of the temporal block in the presence of two groups of scatterers

signal $x(t)$ reflected from two equal-sized targets with a separation $\delta\tau$ in time and at a mean time delay τ can be considered to be $e^{j\alpha(t-\tau-\delta\tau/2)^2} + e^{j\alpha(t-\tau+\delta\tau/2)^2}$ and hence

$$\begin{aligned} x(t) &= e^{j\alpha(t^2-2t\tau+\tau^2+\delta\tau^2/4)}\left(e^{j\alpha\delta\tau(t-\tau)} + e^{-j\alpha\delta\tau(t-\tau)}\right) \\ &= 2e^{j\alpha(t^2-2t\tau+\tau^2+\delta\tau^2/4)}\cos(\alpha\delta\tau(t-\tau)) \end{aligned} \tag{7.1}$$

The first term is the conventional return, which when homodyned with the transmitted signal gives a beat frequency proportional to range ($e^{j\alpha t\tau}$), rotated by a fixed phase term, and the second term is the modulating frequency. It gives rise to a sinusoidal amplitude modulation of the return. When the targets are of equal strength the modulation has a depth of 100%. It can readily be seen that when the target sizes are different the modulation is still present, but the depth will be reduced. Likewise, if more than two targets are present the modulation is no longer a single sinusoid, but is still made of a relatively small number of sinusoids.

De-chirp delays are also compensated so that only the signals coming from the same target are integrated. The output of the integration represents the frequency spectrum of the signal. A modified inverse cosine transform is then used to convert the frequency spectrum back into the time domain. Some studies concentrate on the time domain re-construction of the target image ([19,20,22]), but others emphasize the spectral based perception of the target [18,21]. A 'pattern-matching' interpretation of the transformation of spectral interference patterns into fine delays is proposed in [24].

7.4 Baseband equivalent of the spectrogram transformation

In this chapter, we propose a baseband receiver equivalent to the SCAT [19]. It is denoted as the BSCT (Baseband Spectrogram Correlation and Transformation). The equivalence of the BSCT to the SCAT will be demonstrated by comparing the

model output of the original and baseband model using both simulated signals and laboratory measurements.

This model is developed to allow the processing of target echoes with a receiver based on the bat auditory system for radar signals that are centred on very high carrier frequencies. The BSCT significantly simplifies the analytical treatment of such receivers and hence can be used for further investigations. This will be the foundation for further studies with the ultimate goal to understand how bat signal processing differs from matched filtering and investigate its advantages and disadvantages for the task of target detection and identification.

The scope of the model as presented here is limited to the spectral part of the SCAT model. For a group of closely positioned targets the temporal block gives information about the time-delay (or range) for the group as a whole, and the spectral block describes the intra-group behaviour either as an interference spectrum or as fine delays (that is relative distances). The spectral block is important because it potentially provides the processing algorithm to allow the fine range resolution needed for target discrimination [19].

The results are compared by calculating the differences between both model outputs for different experimental settings.

The baseband equivalent of the spectrogram transformation proposed in this chapter deals with a complex analytical form of the input signal. A block diagram of the BSCT is shown in Figure 7.4.

Let us have a filter bank composed of M filters with centre frequencies f_i, $i = 0 \ldots M-1$, and bandwidth B_i and all having the same shape. In the version of the model for which the experiments were performed we assumed, following the basic SCAT model as described in Section 7.3.3, that all filters are with the same bandwidth B and that the impulse response $h_i(t)$ of any filter i in the filter bank can be produced from the same baseband (low-pass) filter with impulse response $h(t)$ by a spectral shift

$$h_i(t) = h(t)e^{j2\pi f_i t} \tag{7.2}$$

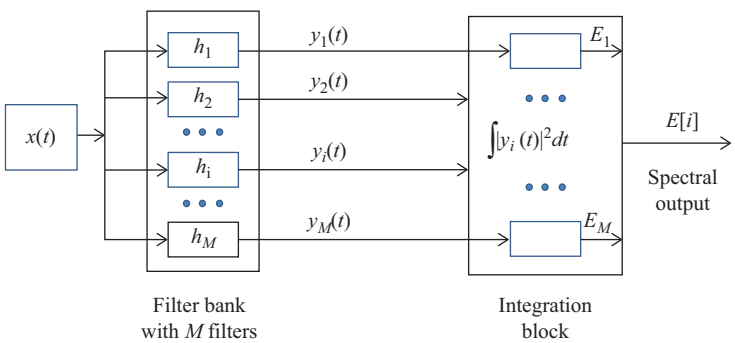

Figure 7.4 BSCT spectral processing diagram. Model input $x(t)$ is analytical signal. It is passed through a filter bank of M complex bandpass filters h_i. The absolute value of each filter output y_i is squared and integrated over time to get the energy $E[i]$ of the corresponding frequency

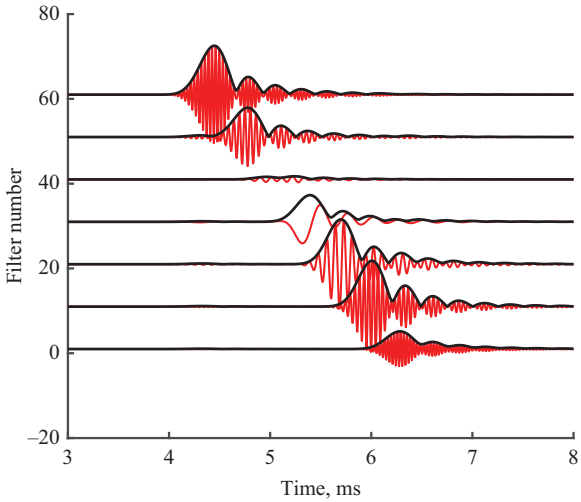

Figure 7.5 Bandpass filter bank output, in-phase (real) component and envelope

Note that the assumption that the filters all have the same bandwidth is much more obvious for the radar case than for sonar or acoustic signals. In the radar case, the signal bandwidth is small compared to the carrier frequency so, when referred to the transmitted signal, the difference between a constant-Q and a constant bandwidth filter will be small.

The response at the output of the ith filter to the signal $x(t)$ is the convolution of the filter impulse response and the signal

$$y_i(t) = x(t)^* h_i(t) \tag{7.3}$$

After each bandpass filter the cochlear block contains a rectifier and a low-pass filter (Figure 7.2). We replace these with ideal amplitude extractors. Therefore, the envelope of the bandpass filtered signal is produced by taking the amplitude of the signal (Figure 7.5). This alternative to the signal rectification and low-pass filtering completely discards the phase information. The envelopes are then converted to an auditory spectrogram by squaring (Figure 7.6).

In the spectral block the total energy of the output of each filter is computed by integration (Figure 7.4). Since the aim of the experiment is to investigate the separation of the spectral signature of multiple groups of scatterers, we may note that the returned signals are effectively coincident in time (we consider temporal separations of less than 100 μs with pulse lengths of 2 ms) so the integration may be performed over a fixed interval around the location of the group of returns under consideration (Figure 7.6). This way the spectrum is calculated for each group. Different groups of returns which are more widely separated in time can readily be resolved by the temporal block.

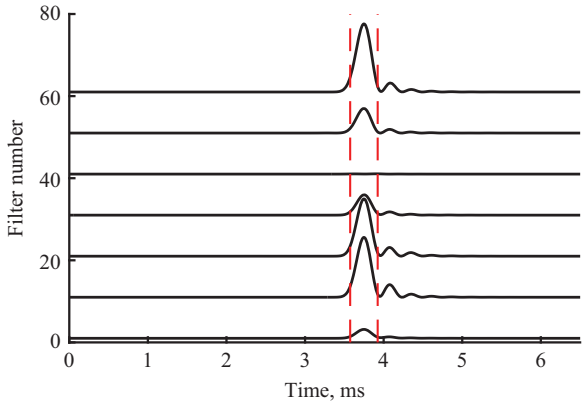

Figure 7.6 Example of de-chirped squared envelopes for seven filters and integration interval (red dashed lines) over which the total energy for each filter is calculated

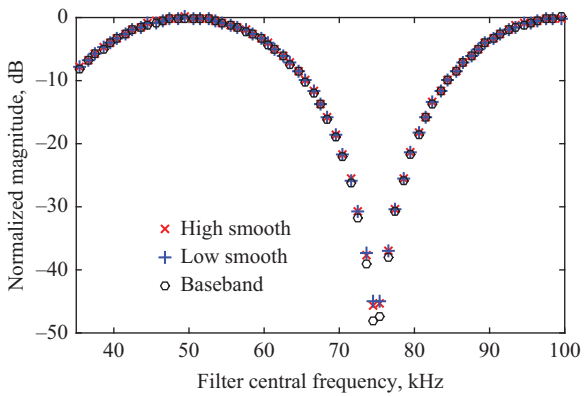

Figure 7.7 Spectral output of BSCT (baseband) and SCAT (high and low smoothing), simulated two targets with separation 3.4 mm (delay 20 μs)

The case of a single group of scatterers the spectral block can thus be simplified by ignoring the output of the temporal block and integrating the whole filter output. The spectral output of the BSCT can then be written as

$$E[i] = \int_{-\infty}^{\infty} |y_i(t)|^2 dt \tag{7.4}$$

Finally, the spectral output (Figure 7.7) can be inverse transformed into the time domain (space) so both temporal and spectral output can be presented on the delay (range) axis.

7.5 Experimental setup to compare BSCT and SCAT

Computer simulations and real experiments have both been performed using a set of targets with the same parameters in both cases. Both the simulated and the measured data have been processed using both the original SCAT algorithm and our BSCT. The comparison between the two algorithms using simulated data can be expected to be successful since the behaviour of the algorithms can be predicted in advance, but this is a useful baseline for the comparison of how the two algorithms behave with real data with its practical imperfections.

7.5.1 Data collection and digitization

The transmission (or 'bat call', $x_C(t)$) was a linear chirp from 100 kHz down to 35 kHz with duration of 2 ms. The same call signal is used for both the simulations and for the experiments. All signals were sampled at 1 MHz rate. In total, 10,000 samples were saved per measurement, which corresponds to a signal duration of 10 ms. Digital to analogue and analogue to digital conversion were carried out with a TiePie Handyscope HS5-540 dual channel oscilloscope with function generator.

7.5.2 Targets and echo

Two close-spaced point targets were created by producing two time delayed versions of the emitted calls. The relative position of the targets was varied by using different values for the delay τ (5, 10, 15, 20, 25, 50, 100) μs, corresponding to separations of (0.85, 1.7, 2.55, 3.4, 4.25, 8.5, 17) mm. With this arrangement, the impulse response of the targets is

$$x_T(t) = \delta(t) + \delta(t - \tau) \tag{7.5}$$

where $\delta(t)$ is the Dirac delta function.

The received signal (or 'echo'), $x_E(t)$ is the reflection of the call signal from the target. For the simulations it was generated by time shifting the call by $t_1 = 3,740\ \mu s$ and convolving with the target as

$$x_E(t) = x_C(t - t_1)^* x_T(t) \tag{7.6}$$

The real measurements were recorded with an ultrasound microphone (type CM16, Avisoft Bioacoustics, Berlin, Germany). A phantom target was created using an ultrasound loudspeaker (type S55/6, Ultra Sound Advice, London, UK). Reflection from two scatterers was reproduced by emitting not just the call $x_C(t)$ but the call convolved with the target $x_C(t)^* x_T(t)$. The delay between the call and the first target t_1 was achieved by putting the speaker at distance 1.272 m from the microphone.

Both simulations and measurements reproduce reflections from the same targets – two ideal point targets with the specified separations. The measurements however include the effect of air attenuation, noise and transmitter/receiver imperfections.

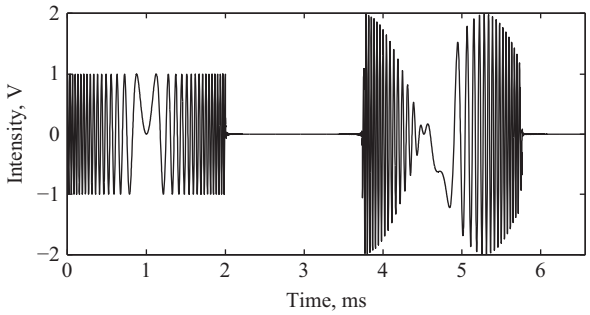

Figure 7.8 Baseband model input, real component. The signal frequency is shifted to baseband. Emitted call has duration 2 μs and spans linearly from −32.5 to +32.5 kHz. Received echo comes from two scatterers with delay 20 μs and equal amplitude

7.5.3 Data processing

All experimental measurements were pre-processed by removing the mean value from the data. The inputs to the BSCT were first convolved with a Hilbert filter to create complex values from the real data values and then converted to baseband by multiplying with the carrier. Figure 7.8 shows the real component of the resulting baseband signal. Both SCAT and BSCT were implemented in Matlab (release 2015a, MathWorks, Natick Mass., USA). A linear frequency spacing of the filters in the bandpass filter bank is used to allow processing of a linear chirp. The filter bank contains 65 bandpass filters with linear frequency spacing from −32 to 32 kHz for BSCT and from 35.5 to 99.5 kHz for SCAT (1 kHz increments). All other parameters follow the ones previously described in section 7.3 after [19]. Two versions of the SCAT differing in the level of smoothing are considered, namely, the SCAT-L for low smoothing and the SCAT-H for high smoothing.

Finally the output of the spectral block for each model is calculated by passing the call and echo signals through the model and normalizing by dividing by the maximum value of each output.

7.6 Results

The spectral output of the proposed BSCT is compared with the output of both versions of the original SCAT (with low and high smoothing) for different delays between the glints in the target. The difference is measured by using the root mean square (RMS) error:

$$\text{error} = \sqrt{\frac{1}{M}\sum_{i=1}^{M}\left(E_{\text{SCAT}}[f_i] - E_{\text{BSCT}}[f_i]\right)^2} \tag{7.7}$$

where E_{SCAT} and E_{BSCT} are the normalized outputs of the models compared and $M = 65$ is the number of filters.

The results of the comparison, expressed as the RMS error in % of the maximal value, are presented for all datasets in Table 7.1. Results show the error is less than 1% for delays below 50 μs and less than 5% up to 100 μs. Figure 7.7 displays the full outputs of BSCT and SCAT expressed as a function of the frequency for the case of two simulated targets delayed by 20 μs. We can see that the level of smoothing in the original SCAT does not influence the spectral output. The same is valid for the baseband model which gives practically the same results.

In the real measurements, the influence of both the air and the non-perfect microphone and speaker characteristics modify the target response. The outputs of the BSCT for the simulated and phantom targets are compared in Table 7.2 and shown in Figure 7.9. The real experiments introduce significant deformation of the target spectrum relative to the simulations. Indeed, the difference can be above 10%. This shows that although the real data behaves in a way which is not identical to the simulated data – as would be expected, the two algorithms are stable to the imperfections in the data and both still behave in a similar manner.

Looking more closely at the interference patterns for different relative positions between the scatterers (Figure 7.10) we can see that the general shape and, in particular, the locations of the zeroes, are preserved between the experiments and the simulations. These features are likely to be significant for any scheme for resolving the close-spaced targets and this result indicates that the new algorithm, like the SCAT algorithm, retains the information which will later be needed to resolve the targets.

Table 7.1 Difference between proposed BSCT and original SCAT with high (SCAT-H) and low (SCAT-L) smoothing, expressed as RMS, %

Delay	**Simulations, %**		**Experiments, %**	
μs	**SCAT-H**	**SCAT-L**	**SCAT-H**	**SCAT-L**
5	0.20	0.19	0.78	0.81
10	0.54	0.68	0.39	0.42
15	0.34	0.34	0.38	0.39
20	0.67	0.52	0.60	0.59
25	0.41	0.39	0.57	0.55
50	0.94	0.98	0.85	0.90
100	4.4	4.6	2.1	2.1

Table 7.2 Root mean squared difference between simulations and experiments processed with BSCT

Delay	**μs**	**5**	**10**	**15**	**20**	**25**	**50**	**100**
Error	%	12.3	13.9	16.4	15.1	15.0	20.8	17.4

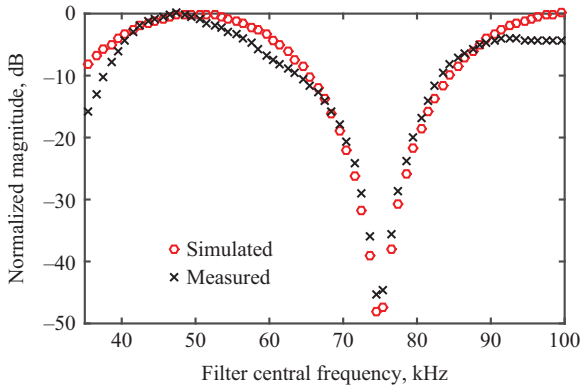

Figure 7.9 Spectral output of BSCT model, simulated vs measured two targets separated by 3.4 mm (delay 20 μs)

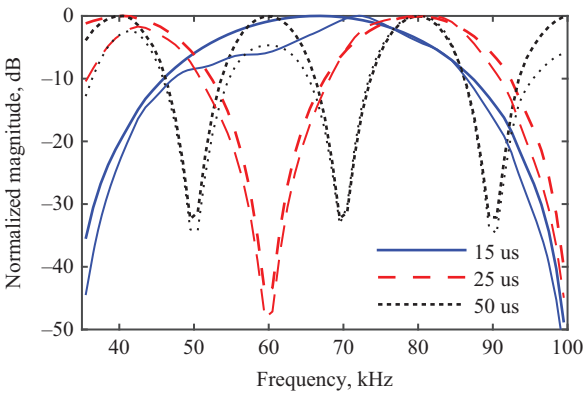

Figure 7.10 Spectral output of BSCT model for two targets for delays 15 μs, 25 μs and 50 μs. Simulated (thick lines) and measured (thin lines) input signals

7.7 Conclusion

In this chapter, we have presented a baseband receiver equivalent to the SCAT to allow SCAT-like signal processing to be applied to radar signals that are characterized by a much larger carrier frequency than their sonar counterpart. The scope of the investigated was limited to the spectral part of the model because that is the component of the SCAT that can potentially provide the fine range resolution needed for target detection and discrimination. Results have shown that the

proposed baseband spectrogram transformation model gives an output that is compatible with that of the original SCAT receiver. This implies that

- processing of target echoes with a receiver based on the bat auditory system can be applied to signals that are centred on very high carrier frequencies, such as radar signals.
- the output of the spectral block does not depend on the phase information of the carrier signal and is a form of non-coherent signal processing; the spectral block will be more robust to loss of signal coherence than the matched filter.
- advanced signal analysis techniques based on complex signal representation could be used for further understanding of the model.

References

[1] O. von Helversen, L. Winker, and H. Bestmann, 'Sulphur-containing 'perfumes' attract flower-visiting bats,' *Journal of Comparative Physiology A*, vol. 186, pp. 143–153, 2000.

[2] D. von Helversen and O. von Helversen, 'Acoustic guide in bat-pollinated flower,' *Nature*, vol. 398, pp. 759–760, 1999.

[3] D. von Helversen, 'Object classification by echolocation in nectar feeding bats: size-independent generalization of shape,' *Journal of Comparative Physiology. A, Neuroethology, Sensory, Neural, and Behavioral Physiology*, vol. 190, no. 7, pp. 515–21, 2004.

[4] J. Ostwald, 'Tonotopical organization and pure tone response characteristics of single units in the auditory cortex of the Greater Horseshoe Bat,' *Journal of Comparative Physiology A: Neuroethology, Sensory, Neural, and Behavioral Physiology*, vol. 155, pp. 821–834, 1984.

[5] G. von der Emde and H.-U. Schnitzler, 'Fluttering target detection in hipposiderid bats,' *Journal of Comparative Physiology A: Neuroethology, Sensory, Neural, and Behavioral Physiology*, vol. 159, pp. 765–772, 1986.

[6] H.-U. Schnitzler, D. Menne, R. Kober, and K. Heblich, 'The acoustical image of fluttering insects in echolocating bats,' *Neuroethology and Behavioral Physiology*, pp. 235–250, 1983.

[7] R. Kober and H.-U. Schnitzler, 'Information in sonar echoes of fluttering insects available for echolocating bats,' *The Journal of the Acoustical Society of America*, vol. 87, no. 2, pp. 882–896, 1990.

[8] O. Sotavalta, 'The flight tone (wing stroke frequency) of insects,' *Acta Entomologica Fennica*, vol. 4, pp. 5–117, 1947.

[9] G. von der Emde and H.-U. Schnitzler, 'Classification of insects by echolocating greater horseshoe bats,' *Journal of Comparative Physiology A: Neuroethology, Sensory, Neural, and Behavioral Physiology*, vol. 167, pp. 423–430, 1990.

[10] H.-U. Schnitzler, 'Echoes of fluttering insects: Information for echolocating bats,' Cambridge University Press, pp. 226–243, 1987.

[11] C. J. Baker, H. D. Griffiths, and A. Balleri, 'Biologically inspired waveform diversity,' in *Waveform Design and Diversity for Advanced Radar Systems*, ser. Radar, Sonar, Navigation and Avionics, F. Gini, A. De Maio, and L. Patton, Eds. Institution of Engineering and Technology, 2012, vol. 22, ch. 6, pp. 149–172.

[12] C. J. Baker, G. E. Smith, A. Balleri, M. Holderied, and H. D. Griffiths, 'Biomimetic echolocation with application to radar and sonar sensing,' *Proceedings of the IEEE*, vol. 102, no. 4, pp. 447–458, 2014.

[13] J. R. Barchi, J. M. Knowles, and J. A. Simmons, 'Spatial memory and stereotypy of flight paths by big brown bats in cluttered surroundings,' *Journal of Experimental Biology*, vol. 216, no. 6, pp. 1053–1063, 2013.

[14] A. Balleri, H. D. Griffiths, C. J. Baker, K. Woodbridge, and M. W. Holderied, 'Analysis of acoustic echoes from a bat-pollinated plant species: Insight into strategies for radar and sonar target classification,' *IET Radar, Sonar and Navigation*, vol. 6, no. 6, pp. 536–544, 2012.

[15] J. A. Simmons, M. Ferragamo, C. F. Moss, S. B. Stevenson, and R. A. Altes, 'Discrimination of jittered sonar echoes by the echolocating bat, *Eptesicus fuscus*: The shape of target images in echolocation,' *Journal of Comparative Physiology A*, vol. 167, no. 5, pp. 589–616, 11 1990.

[16] J. A. Simmons, P. A. Saillant, J. M. Wotton, T. Haresign, M. J. Ferragamo, and C. F. Moss, 'Composition of biosonar images for target recognition by echolocating bats,' *Neural Networks*, vol. 8, no. 7-8, pp. 1239–1261, 1995.

[17] S. Schmidt, 'Perception of structured phantom targets in the echolocating bat, *Megaderma lyra*,' *The Journal of the Acoustical Society of America*, vol. 91, no. 4, pp. 2203–2223, 1992.

[18] R. Simon, M. Knörnschild, M. Tschapka, A. Schneider, N. Passauer, E. K. V. Kalko, and O. von Helversen, 'Biosonar resolving power: echo-acoustic perception of surface structures in the submillimeter range,' *Frontiers in physiology*, vol. 5, p. 64, 1 2014.

[19] P. A. Saillant, J. A. Simmons, S. P. Dear, and T. A. McMullen, 'A computational model of echo processing and acoustic imaging in frequency-modulated echolocating bats: The spectrogram correlation and transformation receiver,' *The Journal of the Acoustical Society of America*, vol. 94, no. 5, pp. 2691–2712, 11 1993.

[20] I. Matsuo, K. Kunugiyama, and M. Yano, 'An echolocation model for range discrimination of multiple closely spaced objects: transformation of spectrogram into the reflected intensity distribution,' *The Journal of the Acoustical Society of America*, vol. 115, no. 2, pp. 920–928, 2 2004.

[21] L. Wiegrebe, 'An autocorrelation model of bat sonar,' *Biological cybernetics*, vol. 98, no. 6, pp. 587–595, 2008.

[22] H. Peremans and J. Hallam, 'The spectrogram correlation and transformation receiver, revisited,' *The Journal of the Acoustical Society of America*, vol. 104, no. 2, pp. 1101–1110, 8 1998.

[23] M. I. Sanderson, N. Neretti, N. Intrator, and J. A. Simmons, 'Evaluation of an auditory model for echo delay accuracy in wideband biosonar,' *The*

Journal of the Acoustical Society of America, vol. 114, no. 3, pp. 1648–59, 9 2003.

[24] M. Park and R. Allen, 'Pattern-matching analysis of fine echo delays by the spectrogram correlation and transformation receiver,' *The Journal of the Acoustical Society of America*, vol. 128, no. 3, pp. 1490–1500, 2010.

[25] R. D. Patterson, M. H. Allerhand, and C. Giguère, 'Time-domain modeling of peripheral auditory processing: a modular architecture and a software platform,' *The Journal of the Acoustical Society of America*, vol. 98, no. 4, pp. 1890–4, 10 1995.

Chapter 8

The concept of the intelligent radar network

Hugh Griffiths[1]

Abstract

Future radar systems are likely to be distributed, intelligent, multistatic and spectrally efficient, taking into account many of the concepts developed in this section of the book, and offering greater flexibility, greater robustness and lower cost than conventional single-platform monostatic approaches. This chapter describes the 'intelligent radar network' and some of the developments that will be necessary for its realization. In particular, the resource management of a radar network, the means of communication between the nodes of the network, and geolocation and synchronization between the nodes of the network all represent significant challenges.

8.1 Introduction

Historically, the co-location of a single transmitter and receiver in the conventional form of monostatic radar has been the basis of almost all radar systems. The relative simplicity of the monostatic geometry, coupled with high sensitivity, has stood the test of time extremely well. However, in many cases we are beginning to reach a point of diminishing returns when attempting to improve target detection and location, whilst reliable classification, especially of ground targets, has remained elusive. Removing the monostatic constraint uncovers a large number of design degrees of freedom. For example, the passive receiver part of the bistatic system can be located nearer to the target or area of interest, thus inherently improving sensitivity. By exploiting more than one transmitter, as might be the case for passive radar that exploits the many illuminators that can be used opportunistically, a more complete form of spatial diversity can be exploited in the form of an 'ad-hoc' network with the potential to improve performance still further.

However, formation and optimal exploitation of such networks requires improved signal processing consistent with the concepts that are known to be fundamental to intelligence and cognition. For example, if the receiver in a passive network system is made mobile, such as in an airborne configuration, spatial

[1]University College London, UK

diversity becomes a function of time. By means of a thorough understanding of target and clutter signatures the geometry may be controlled, and through intelligent choice the most favourable configurations can be adopted. This ensures constancy of lines of sight as well as favourable target and clutter backscattering geometries.

We can take this concept of applied intelligence much further by applying processing architectures that take their cue from mammalian cognition. Although highly complex and currently a long way from being fully understood, we can 'borrow' architectures that used sensed data to form a 'perception' of the target scene that is sufficiently accurate to enable the radar itself to make decisions and initiate 'actions'. Indeed, it is the 'perception–action cycle' together with the use of memory and other stored information that is at the core of cognition. We can implement architectures to support the perception–action cycle through adaptive feedback between the receiver and the transmitter and radar platform. For example, in an active network this might adapt the transmitted waveforms to maintain target-tracking performance, or in an airborne passive system might automatically and autonomously steer the platform to more favourable locations.

In this chapter, we review the features, benefits and challenges of creating radar networks. We subsequently speculate on aspects of bio-inspired cognitive processing concepts and architectures that potentially offer both performance improvement and even wholly new applications. Having said that, we must caution that research into intelligent adaptive networked radar systems is at the earliest of stages. Indeed, much remains to be accomplished before such systems offer such high levels of improvement that they may be genuinely find take-up within the commercial world.

8.2 Towards networks and diversity

8.2.1 Bistatic and multistatic radar

Bistatic radar has a history dating back to the earliest days of radar [1]. Some of the claimed advantages of bistatic radar include:

- Bistatic radar has potential advantages in detection of targets which are shaped to scatter energy in directions away from the monostatic;
- the receiver is covert and therefore safer in many situations;
- countermeasures are difficult to deploy against bistatic radar;
- increasing use of systems based on unmanned air vehicles (UAVs) makes bistatic systems attractive;
- many of the synchronization and geolocation problems that were previously very difficult are now readily soluble using global positioning system (GPS); and
- the extra degrees of freedom may make it easier to extract information from bistatic clutter for remote sensing applications.

More recently, a set of trials using the UCL NetRAD multistatic radar have indicated that bistatic sea clutter may be less 'spiky' than the equivalent simultaneously measured monostatic clutter, and hence that there should be an advantage to the bistatic configuration in detecting small targets against a sea clutter background [2]. These results have been described in more detail in Chapter 12 of Part III of Volume 1.

The magnitude of this advantage depends on the exact geometry, but may be 6 dB or even more. This has led to the term 'clutter diversity': since the properties of clutter in a bistatic/multistatic radar depend on the bistatic geometry, and since some geometries are more favourable than others. Clutter diversity is attempting to understand and quantify these effects in order to find out how best to exploit them, and have been described in more detail in Chapter 6 of Part I of Volume 2.

At the same time, ideas have begun to emerge for the 'adaptive intelligent radar network' [3–5]. These have partly been driven by a realization that present-generation military surveillance sensor systems tend to be based on single platforms carrying conventional sensors, including monostatic radars. Such systems are expensive and inflexible, and there is therefore an imperative to think in new ways about sensor systems and to devise concepts that are more flexible, of higher performance, and yet more affordable. The advent of practical UAV platforms forms part of this thinking, but introduces new and significant challenges.

The radars of the future (Figure 8.1) will therefore be distributed, intelligent, multistatic and spectrally efficient. There are many challenges, in respect of understanding and exploiting bistatic operation, exploiting clutter diversity, geolocation and synchronization and communication between nodes, and intelligent control of the network.

Such a scheme has a number of attractions:

- It is inherently flexible. The number and the locations of the individual platforms can be optimized to the particular tasks and varied dynamically.
- The network has the same advantage of 'graceful degradation' of a phased-array radar, in which the failure of one element of the array does not cause catastrophic failure but only degrades the overall performance slightly. In the case of the sensor network, not only may the loss of one node of the network be tolerated, but also the network may be re-configured accordingly in response.

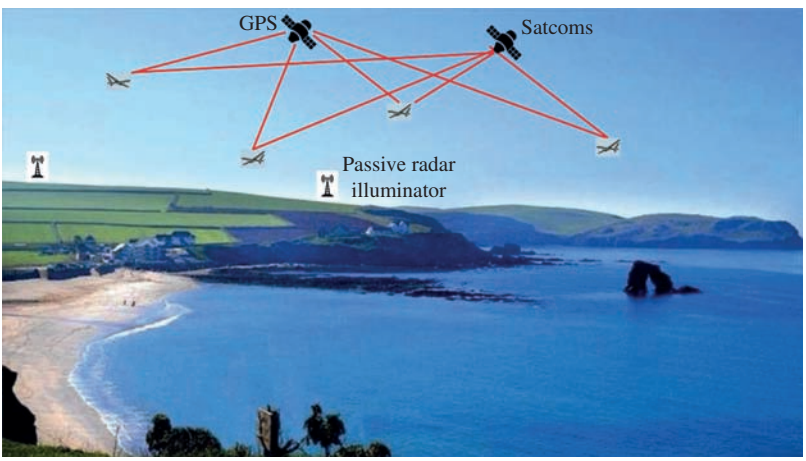

Figure 8.1 An intelligent adaptive radar network. In this example, there are four nodes and communication and control of the network is via satcom links. The network also exploits passive radar illuminators

- The platforms and the sensors carried by them need not be homogeneous. Different types of platform and sensors can be used within the network according to the requirement.
- The sensors may also exploit 'illuminators of opportunity', allowing passive radar modes of operation and the possibility that some nodes might be totally passive.
- The locations of the platforms can give multiple perspective views of targets ('spatial diversity') to aid in target classification and identification.

Radar sensors can be used multi-statically, giving potential advantages in detecting stealthy targets, including the enhancement of target signatures that occurs in forward scatter (whilst recognizing that this gives poor range and Doppler resolution). Some platforms might be receive-only and hence potentially covert, and might operate closer to the target scene.

Seen in this way, the network has some similarities to a phased-array radar – except that here the target is actually *inside* the network. In an analogous way to a multi-function phased array radar, the waveforms, beam pointing directions and hence dwell times and update rates for a particular target can be varied dynamically according to the behaviour of the targets within the scene.

8.2.2 Sensors as robots

A particularly visionary publication in this subject was provided by Wicks, in a keynote presentation at the 2003 International Radar Conference in Adelaide, Australia, entitled 'Sensors as Robots' [6]:

> A … scout troop is charged with cleaning the town park. Initially, each boy is assigned a specific task and timeline. However, soon into the exercise, and as a result of some minor and perhaps major situational changes, the original individual marching orders are modified, or perhaps even ignored, on the fly. In any event, however, each member of the troop does his part to accomplish the goal of cleaning the park. In the end, the mission is successfully completed. Independent entities (the Scouts) have operated in an autonomous manner using cognitive reasoning in responding to real-time changes in the environment, to accomplish a preassigned mission. The individual Scouts, by sensing the behavior and activities of their colleagues in response to the changing environment, and by communicating the necessary data and information, achieved a collective response that resulted in a 'successful' operation. This 'system' worked as a result of the autonomous and intelligent interaction between the individual 'sub-systems'.

This analogy is compelling. The individuals act autonomously, but perceive the target scene and the progression of the operation, and can communicate with each other. They may modify their intended tasks on the basis of this information.

Translating these ideas to an intelligent, adaptive radar represents a bold vision, but there are many issues to be resolved before such a system could genuinely be realized. Three particular issues are (i) the control and management of such networks, (ii) geolocation and synchronization and (iii) communication between platforms. These are developed in the following sections (Figure 8.2).

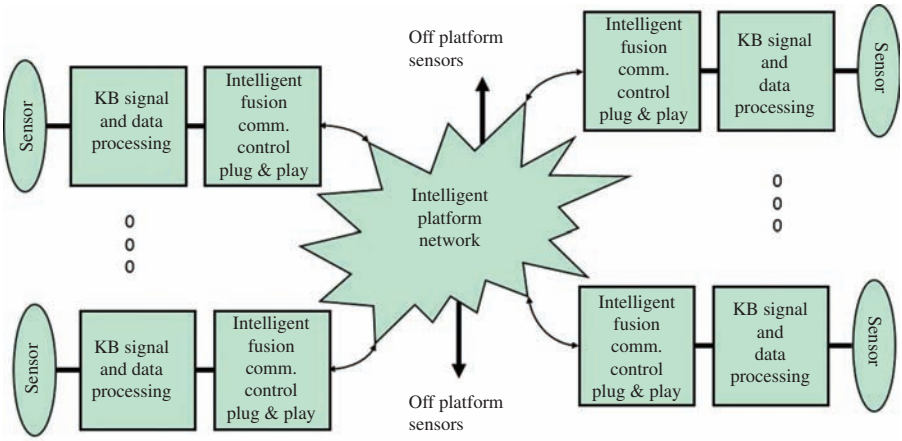

Figure 8.2 An intelligent sensor system. ©2003 IEEE. Adapted from [6]

8.3 Resource management

The control of a network of this kind represents a major challenge, especially if the nodes are on moving platforms. At one extreme the management of the network might be centralized; at the other extreme the individual nodes might act essentially autonomously. There is scope for including cognitive techniques which allow the system to adaptively exploit prior information and to 'learn' about the environment and target scene to optimize performance. This may build upon the ideas described in Chapter 5 of Part 1 of Volume II.

8.3.1 Examples of networked radar

To illustrate this, Figure 8.3 shows a set of six examples of networked radar, of progressively greater sophistication, and assessed using a 'traffic light' colour scheme.

Case 1 consists of N conventional monostatic radars in fixed locations. Each radar performs its own detection and tracking processing, and the tracks from the radars are combined to form a 'master' track, in a de-centralized manner. This does not require coherence to be maintained between the radars, and since only track information is exchanged, the communication bandwidth is modest. This is judged to be straightforward.

The track fusion could be done in a number of ways:

1. *Track selection:* Generate a track with each radar and choose one of the tracks as the system track.
2. *Average track:* Generate a track with each radar and weight according to the Kalman filters' covariance matrices, then the individual tracks are used to form a system track.

	Case 1	Case 2	Case 3	Case 4	Case 5	Case 6
Location	Fixed	Fixed	Fixed	Fixed	Fixed and moving platforms	Nodes on moving platforms
Data level	Tracks	Tracks	Detections	Detections	Raw	Raw
Coherency	Incoherent	Incoherent	Incoherent	Coherent	Coherent	Coherent
Operation mode	*N* Tx,*N* Rx monostatics	1 Tx,*N* Rx multistatic	1 Tx,*N* Rx multistatic	*M* Tx,1 Rx multistatic	*M* Tx,1 Rx multistatic	*M* Tx,N Rx multistatic
Distribution	De-centralized	De-centralized	Semi de-centralized	Centralized	Centralized	Centralized
Assessment	Straight-forward	Multiple bistatics	Challenging	Complex	Very complex	Extremely complex

Figure 8.3 Increasing levels of sophistication of networked radar

3. *Augmented track:* Generate a track with each radar, choose one of the tracks as the system track and use selected detections from the others to update the system track.
4. *Detection to track:* Use all the radar detections to update the system track. Tracks may or may not be initiated by using all detections from all the radar system.

Case 2 is similar to case 1, but now instead of *N* individual monostatic radars the system now consists of one transmitter and *N* receivers, so effectively *N* bistatic radars. The tracks are combined in one of the ways listed above in case 1, and again it is judged to be straightforward.

Case 3 is similar to case 2, but now the detections from each receiver are combined rather than the tracks, giving a semi-de-centralized system. This would require greater communication bandwidth than cases 1 and 2, and is judged to be challenging.

Case 4 differs from case 3 in two respects. First, the system consists of *M* transmitters and one receiver, and second the entire system is now coherent, requiring a common stable phase reference. The processing is now centralized and judged to be complex.

Case 5 now includes the possibility that some of the platforms may be moving, and it is the raw data from each receiver that is combined. Both of these introduce substantial additional complication. For moving platforms, it is now necessary to have a knowledge of the instantaneous platform location, and to dynamically maintain the phase reference for coherent operation, and transmission of the raw data would require much greater communication bandwidth. This is judged to be very complex.

Case 6 now consists of M transmitters and N receivers, forming a dynamically adaptive multistatic network. This represents the 'Holy Grail' and is judged to be extremely complex.

The resource management of a radar network of this kind has some strong similarities to the resource management of a monostatic multi-function radar, in which the various tasks to be undertaken by such a radar (surveillance, tracking of individual targets, weapon control, ...) are prioritized and the overall radar resource deployed in some optimal manner so that the highest priority tasks are performed first and the others subsequently within the various constraints. Various approaches to this problem have been proposed and evaluated, including fuzzy logic, neural networks and autonomous agents [7–15].

Cognitive approaches have some clear attractions, and these have been described in detail in Chapter 5 of Part 1 of Volume II of this book. The extension to a network will involve not only the transmit and receive beam pointing, dwell times, update times and waveforms, but also the platform locations.

Haykin [16] draws the distinction between:

- *Distributed cognition*, where the individual radar components as well as the central base station are all cognitive and
- *Centralized cognition*, where cognition (including sensor fusion) is confined to the central base station; in effect, the central base station acts as the *brain* of the entire network.

The scout troop analogy mentioned earlier illustrates this distinction nicely. This distinction has important implications for the nature and bandwidth of the communication between the nodes of the network, which is considered in the next section.

8.3.2 Biologically inspired approaches to resource management

A potential construct in the form a 'Distributed Active Control' (DAC) architecture has been developed by the bio-inspired computational science community and has met with some success (e.g. [17]). This provides both a useful starting point for designing a cognitive processing architecture for radar systems as well as providing access to a much broader portfolio of research being carried out in the computing community. A simple block diagram of the DAC architecture is shown in Figure 8.4.

In essence, DAC is both a parallel and simultaneously serial architecture (sometimes referred to as layers and columns) operating on data to produce information from which perception and decision-making can occur. This is in marked contrast to the linear processing architectures under-pinning almost all current radar systems. In fact, DAC has been subjected to some experimental verification in both neurological and robotic domains and found to hold up well [17]. It is an attractive start point as it appears well suited to providing an environment in which many forms of adaptive signal processing can be hosted and allowed to interact. The DAC approach has close parallels with mammalian cognition and should be readily scalable between sensor types dependent on the sophistication of the required processing.

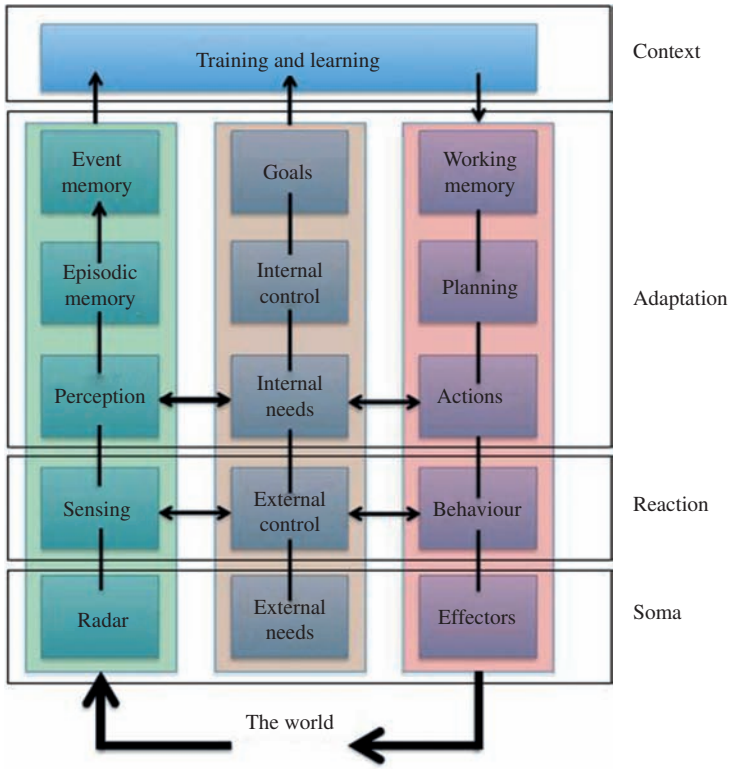

Figure 8.4 Distributed Adaptive Control (DAC) architecture for cognitive radar sensing. © 2013 IEEE. Reprinted with permission from [5]

8.4 Communications between platforms

8.4.1 Fixed and mobile nodes

If the nodes of a network are fixed, then in principle the communications can be achieved by landline (cable or optical fibre) links, allowing reliable high-bandwidth communications, but in the case of nodes on moving platforms this becomes much more difficult. The degree of difficulty is a strong function of the data bandwidth, and also of the range between platforms. Such communications are likely to require significant power and antenna gain, which implies directionality and beam steering. In addition, the links would be potentially vulnerable to interception, or to jamming, or spoofing.

Candidate techniques include satcom links, or free-space RF, or optical links. The latter offer potentially very high data rate (>1 Gb/s), but would be subject to the effects of weather. The link budgets of sitcom and free-space RF links can be established using the standard link equations, in terms of the required range, transmit power, transmit and receive antenna gains and bandwidth. The use of

narrow, high-gain beams would reduce the transmit power requirements and the vulnerability to interception and jamming, but would require intelligent beam steering to direct the transmit and receive beams in the right directions at the right times.

8.4.2 Synchronized rendezvous

An interesting example of this kind of network, although in a rather different context, is provided by a network of autonomous underwater vehicles (AUVs). In this case, the sensors are imaging sonars, or possibly optical cameras, and the application considered is mine countermeasures (MCM), which is the detection and disposal of mines on the seabed (Figure 8.5).

In this way, a number of AUV platforms might carry out a search operation of a given area of seabed and record the locations of initial detections. These detections would then be re-visited and re-investigated to confirm the detection (or not) and if positive, to assess the type of mine. Finally, if appropriate, confirmed targets would be neutralized.

A significant difference from the above-water radar network considered in the bulk of this chapter is the difficulty of communications between platforms. The propagation of RF signals underwater is severely limited, and although blue-green lasers might be considered, they would require sophisticated beam steering, and the propagation in shallow water (which is the primary area of interest for MCM) is somewhat variable. In practice, therefore, communication is likely to be acoustic. However, the attenuation of acoustic signals through seawater increases rapidly with frequency (at a frequency of 500 kHz the attenuation is of order 100 dB/km).

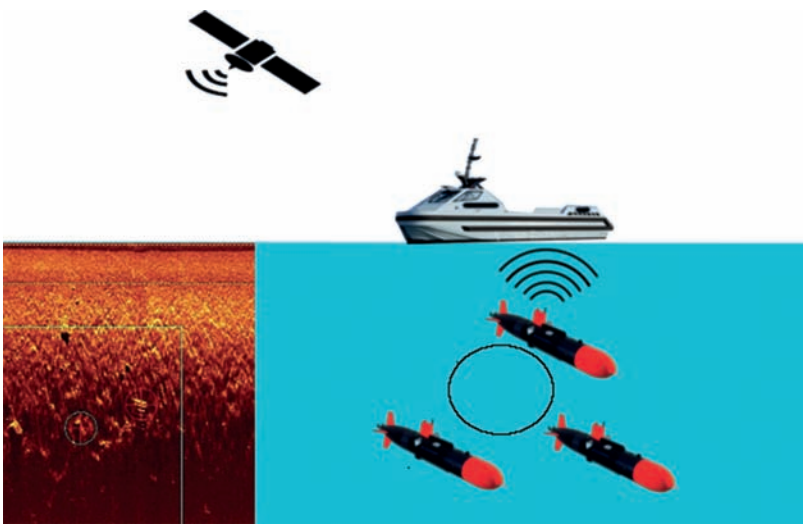

Figure 8.5 An underwater intelligent adaptive network. In this case, a surface vessel is used to oversee the operation

In addition, variations in temperature and salinity mean that there may be multiple transmission paths. All of these effects mean that the range, and also the bandwidth of communications, is severely constrained.

The proposed solution to this is the 'synchronous rendezvous' technique [18,19], in which the individual platforms undertake the first part of the mission in some prescribed manner, each for example carrying out a fixed 'lawnmower' search pattern. At the conclusion of the first phase, the platforms then rendezvous at a pre-arranged location, exchange information and plan the next phase of the mission. This might also involve communication with a surface vessel. Following this rendezvous, the next stage would be undertaken, followed by further stages of rendezvous, communication and mission. The rendezvous might also be used to re-synchronize timing and navigation information on the individual platforms.

Figure 8.6 shows a dynamic simulation of this approach, using the MOOS-IvP package, which is a set of open-source C++ modules to investigate autonomy on robotic platforms, in particular autonomous marine vehicles [20]. In this simulation, there are three AUVs undertaking an MCM mission. Figure 8.7 compares the resource loss for a baseline case against that with the Rendezvous Point (RP) method. In the case of RP, the resource loss is the time spent by the vehicles to travel to the meetings points. In the case of the baseline case, the loss comes from the lack of adaptation of the system – sometimes there are too few contacts and the identification vehicle that is tasked to re-acquire contacts for extra data is idle, and sometimes, there are too many targets and by the end of the mission there are some that are not identified. In Figure 8.7, the *x* axis is simulation number – there

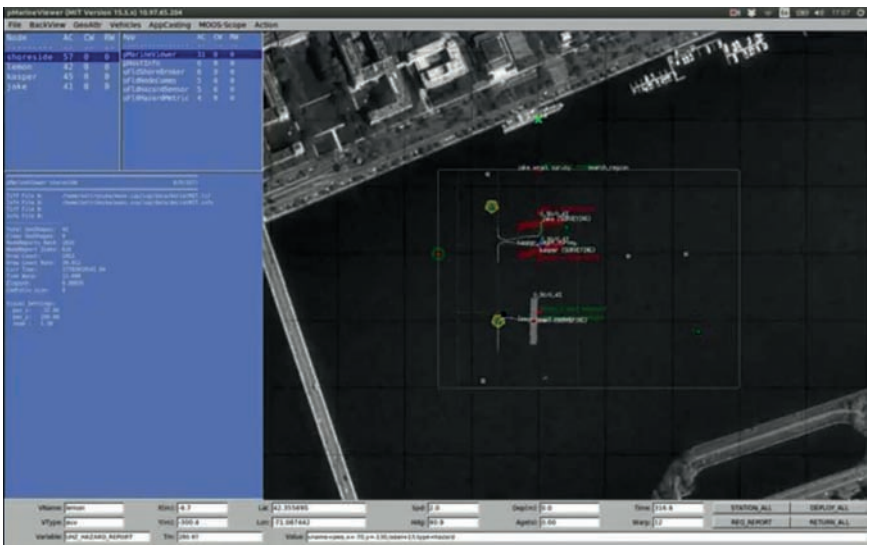

Figure 8.6 Dynamic simulation of the synchronized rendezvous technique using MOOS-IvP. Here, three AUVs are undertaking the first phase of an MCM mission, and are about to rendezvous

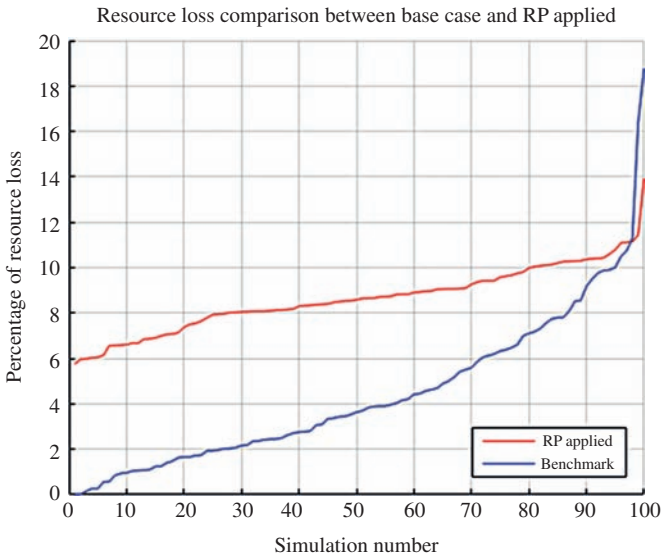

Figure 8.7 Comparison between the resource loss of the benchmark case (blue) and RP technique (red)

are 100 runs of the simulation and each produces a point on the graph. The *y* axis is the percentage of the loss. The results are sorted in ascending order.

Extension of the Synchronized Rendezvous principle to an airborne radar network has some evident attractions. The advantage would be potentially a large reduction in the required transmit power for communications and hence a lower power burden, higher bandwidth and substantially reduced vulnerability to interception and jamming. The disadvantage would be the degree to which the overall mission would have to be disrupted to accommodate the rendezvous. These ideas are at an early stage but are certainly worthy of deeper investigation.

8.5 Geolocation and synchronization

Establishment of precise timing and phase references across a multi-sensor radar network presents a very difficult challenge, particularly when the platforms are mobile or when GPS is denied, either due to shadowing of the platform location or to deliberate countermeasures. (Strictly, GNSS is the overall term for satellite navigation and includes the original US NAVSTAR GPS and the Russian *GLObal'naya NAvigatsionnaya Sputnikovaya Sistema*. Further, the European GALILEO system, the Chinese BeiDou and the Indian NAVIC systems are to set become fully operational by 2020. Here, the term GPS will be used, it being understood that this includes the other systems as well.)

The overall problem is known as Position, Navigation and Timing (PNT), and the fact that DARPA and the UK Ministry of Defence (and no doubt several others) have

substantial research programmes on this shows that it is regarded as a key set of capabilities. The DARPA programme [21], subtitled 'Beyond GPS: 5 Next-Generation Technologies for Positioning, Navigation & Timing' is sub-divided into:

- Adaptable Navigation Systems;
- Microtechnology for PNT;
- Quantum-Assisted Sensing and Readout;
- Programme in Ultrafast Laser Science and Engineering;
- Spatial, Temporal and Orientation Information in Contested Environments programme.

There are few currently known methods in which the necessary phase references can be derived and distributed appropriately. One such architecture involves the utilization of the timing signals communicated by a GPS satellite and decomposing the information in order to develop a coherent phase reference. This is an attractive solution as these timing signals are extremely accurate (reported to be at the sub-nanosecond level if both L1 and L2 frequencies are used [22]), since they are fundamentally derived from atomic clocks on board each satellite. This has been the widely accepted method of dealing with this issue, as wide coverage is provided by the different national systems already mentioned.

In order to provide the degree of coherence necessary for the systems to the right-hand side of Figure 8.3, we can say that the phase drift must be less than that which would cause a target to be ambiguously wrapped into adjacent range bins throughout the time of operation.

A solution to this issue within a spatially diverse network is to provide highly stable GPS disciplined oscillators (GPSDOs) at each node. These systems combine the reliability of crystal oscillators with the precision of a periodic GPS synchronization process. In the following section, the development of an experimental multistatic radar network will be discussed, together with a system which addresses the issue of coherence within a radar network, by means of a physical realization of a GPSDO.

8.5.1 NetRAD

The original NetRAD system [23–26] was conceived as a low-cost flexible S-band networked radar to undertake bistatic and multistatic radar experiments at relatively short ranges (of the order of a few hundred metres). In its original incarnation, the nodes were connected by Ethernet cables of length 200 m and had a maximum transmit power at each node of 200 mW (+23 dBm). For short-range experiments (Figure 8.8) the constraint of cable length did not pose any particular problems, but in experiments involving wider or more complex geometries, this presented significant issues.

This led to the development from 2007 onwards, by collaborators at the University of Cape Town (UCT), South Africa, of GPSDOs for the NetRAD radar [27–29]. At the same time, a High-Power Amplifier (HPA) was added to one of the NetRAD nodes, increasing the peak transmit power to 500 W (+57 dBm).

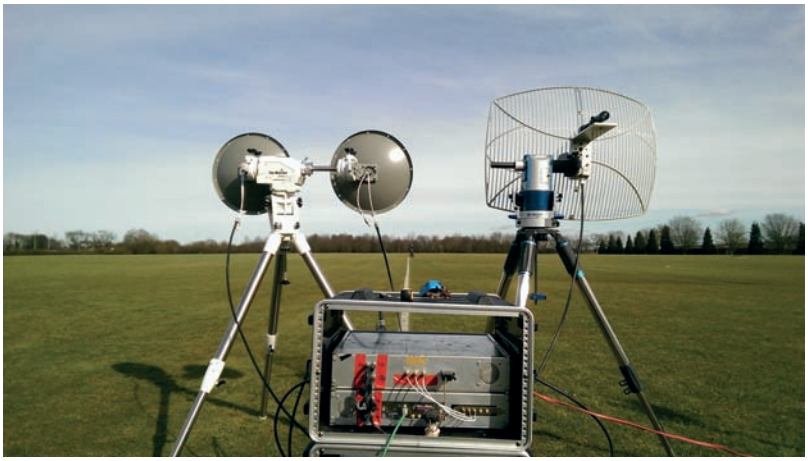

Figure 8.8 One node of the NetRAD radar in its earliest configuration, with the nodes connected via Ethernet cables

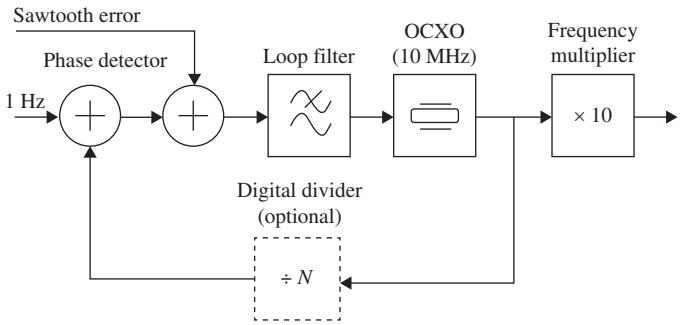

Figure 8.9 Functional block diagram of the GPSDO unit [27]

This was the configuration of the radar used for the bistatic clutter trials in 2011, described in Chapter 12 of Part III of Volume 1.

The GPSDOs are described as 'all-in-view', in the sense that each GPS receiver sees the same set of GPS satellites. Each node employs a Motorola M12+T GPS receiver with an antenna that gives visibility of up to 12 GPS satellites simultaneously (Figure 8.9). These provide a 1 Hz reference at each node. Hambly and Clark [30] reported measurements of the stability of examples of the same M12+T receivers, showing that they provide relative time stability of 4.2 ns rms over a 21.5 km baseline on a timescale of several days, which is more than adequate for the NetRAD application.

The GPSDOs themselves are designed to be low cost, based on a 10 MHz single-oven-controlled crystal oscillator (OCXO) clock reference, and built around an active control system which tracks a 1 Hz PPS (pulse-per-second) signal received from GPS. The measured phase discrepancy, between the 1 Hz and

10-MHz signals, is sawtooth corrected and fed to the second-order infinite impulse response loop filter. Averaging at this point may be useful for very stable Rubidium or Caesium oscillators, updating at intervals of the order of a hundreds of seconds. The filter output is then used to compensate for the measured error by fine steering of the OCXO, inherently synchronizing the phase of the PPS signal with that of the oscillator. Finally, the 10 MHz output is multiplied to 100 MHz by analogue frequency multipliers and conditioned, to provide compatibility with the NetRAD radar [29].

The requirement for stability within this GPSDO system is extremely stringent, since every nanosecond of jitter correspondingly produces about 15 cm monostatic range jitter and 30 cm bistatic jitter. The operating bandwidth of the radar signal is 50 MHz, yielding a range resolution of 3 m, so the worst case tolerable timing jitter is 20 (monostatic) and 10 ns (bistatic).

The measured maximum time interval error of the UCT GPSDOs is better than 7 ns with an Allan Deviation below 3.5×10^{-13} [29].

8.5.2 Atomic clock oscillators

Significant advances in recent years in the miniaturization and commercialization of atomic clocks have enabled these devices to be obtained as commercial off-the-shelf units. They provide higher precision than free running crystal-based oscillators as they exploit the hyperfine transitions of electrons in an excited alkali metal vapour cloud, achieved by optically pumping the vapour cell and monitoring the emitted photons through a highly sensitive photodiode. The reference clock is then phase locked to an appropriate low frequency temperature-controlled crystal oscillator, enabling the synthesis of an extremely precise reference frequency.

Atomic elements typically used to produce the appropriate frequency determination are Rubidium-87 and Caesium-110. Such atomic oscillators provide phase noise figures of the order of -103 dBc/Hz @1 Hz offset [31] and are, therefore, the prime choice for timing references and synchronization on satellites.

8.5.3 GPS-denied environments

For military operations, the availability of GPS signals cannot be guaranteed, since an adversary may jam or otherwise prevent GPS reception. This would significantly disrupt the operation of a coherent radar network (Figure 8.3).

There is however a partial solution to this issue, subject to the condition of phase discrepancies acceptable by the radar over an extended length of time. A frequency holdover system may be implemented, whereby measurements of frequency settings are recorded periodically over time. In the absence of GPS connectivity, the next appropriate frequency value is predicted based on the previous frequency samples. The limitation to this technique is that it involves the approximation of non-linear behaviour and is influenced by unpredictable factors, which could affect the developed model of frequency deviation.

Another solution proposed by Fisher and Raquet [32] involves the deployment of ‘pseudolites’, which are air platforms equipped with high power transmitters which broadcast time reference signals in much the same way as GPS.

The advantages of such are that the systems should be immune to jamming intended for GPS communications, as they may operate at different frequencies. In addition, the high transmit power may allow the signal to 'burn through' any low-level jamming techniques within the local space.

8.5.4 White rabbit timing protocol

The White Rabbit (WR) protocol was developed by researchers at the CERN European nuclear research facility [33] as an Open-Source, Open-Hardware approach to meet the stringent timing requirements for coherent synchronization at the Large Hadron Collider experiment site. It is based on the IEEE Precision Time Protocol (IEEE 1558-2008), and provides 1 ps timing accuracy via a 1 Gigabit Ethernet optical fibre data network. Inggs, Sandenbergh and Lewis at UCT, South Africa, have investigated how this might be extended to synchronization of a radar network, using RF or free-space optical links. In the specific case of NeXtRAD (the X-band/L-band successor to NetRAD), they propose to discipline the GPSDO from a WR PPS instead of the normal satellite PPS [34,35] (Figures 8.10 and 8.11).

Figure 8.10 NetRAD GPS and wireless link antennas. For this particular experiment the nodes had been placed at different heights to give vertical-plane bistatic operation, so the wireless link antenna points slightly downwards

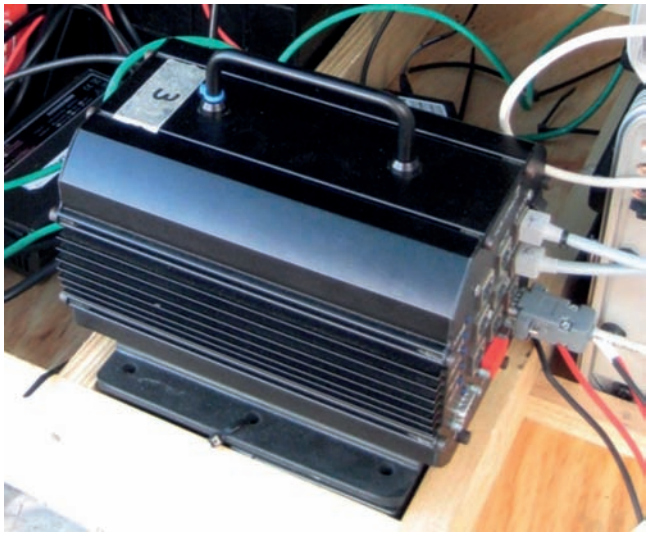

Figure 8.11 The GPSDO unit developed at the University of Cape Town (UCT) provides a measured maximum time interval error (MTIE) of better than 7 ns [29]

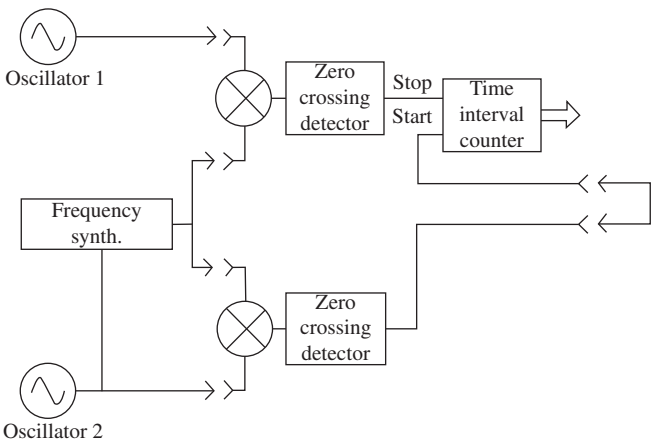

Figure 8.12 Dual Mixer Time Difference (DMTD) measurement technique [37]

They have built and evaluated a system based on a two-node WR network kit supplied by Seven Solutions [36]. The test measurement uses the Dual Mixer Time Difference technique [37], in which the two oscillators are downconverted using a common local oscillator (Figure 8.12). The outputs of the two mixers each produce a beat frequency, of the order of 1–100 Hz, and are compared using zero-crossing detectors. This method provides a very sensitive way of measuring the time difference between the zero crossings.

Results are presented in [35] which show that a WR Disciplined Oscillator of this kind has better performance than GPS synchronization, giving a measured short-term Modified Allan Deviation of 1.61×10^{-11} at 1 s. This must be regarded as very promising.

8.5.5 Multistatic mobile platforms

An expansion of these ideas to airborne platforms presents a substantial complication, in that the motion of the aircraft must also be compensated for, taking into account the time of arrival of such synchronization signals and propagation delays relative to the radar transmitter. As new radar systems are continually placing more pressure on timing requirements, it is extremely challenging to achieve coherence in a configuration like that considered even with modern day technology; the number of factors involved and the complexity is substantial. However, the development of alternative precision timing schemes, such as the WR architecture, is a fertile area of research with applications to much more than just radar networks.

8.6 Summary

This chapter has described the concept of the intelligent, adaptive radar network. Such a network is inherently more flexible, robust and potentially lower cost than conventional single-platform monostatic radars. We can predict that the radars of the future will therefore be distributed, intelligent, multistatic and spectrally efficient.

However, there are many open challenges, in respect of understanding and exploiting bistatic operation, exploiting clutter diversity, geolocation and synchronization and communication between nodes, and intelligent control of the network.

Acknowledgements

I am most grateful to the many people who have helped with the work described in this chapter and who have provided advice and criticism, especially Chris Baker, Brice Beaudouin, Alfonso Farina, Mike Inggs, William Miceli, Riccardo Palamà, Jarez Patel, Matt Ritchie, Stephan Sandenbergh, Xavier Savalle, Mike Wicks and Veronika Yordonova.

I am also grateful to the organizations who have funded the work, including THALES UK, Atlas Elektronik UK, the Royal Academy of Engineering, the Engineering and Physical Sciences Research Council, the IET A.F. Harvey Research Prize, FFI (Norway) and the Office of Naval Research (Global).

References

[1] H.D. Griffiths, 'Early history of bistatic radar', *EuRAD Conference* 2016, London, 6/7 October 2016.

[2] W.A. Al-Ashwal, C.J. Baker, A. Balleri, *et al*., 'Statistical analysis of simultaneous monostatic and bistatic sea clutter at low grazing angles', *Electronics Letters*, vol. 47, no. 10, pp. 621–622, May 2011.

[3] C.J. Baker and A. Hume, 'Netted radar sensing', *IEEE AES Magazine*, vol. 18, no. 2, pp. 3–6, 2003.
[4] H.D. Griffiths, 'Multistatic, MIMO and networked radar: the future of radar sensors?', *EuRAD Conference* 2010, Paris, 30 September 2010.
[5] H.D. Griffiths and C.J. Baker, 'Towards the intelligent adaptive radar network', *IEEE Radar Conference 2013*, Ottawa, 30 April–2 May 2013.
[6] M.C. Wicks, 'Radar the next generation – sensors as robots', *International Radar Conference RADAR 2003*, Adelaide, Australia, pp. 8–14, 3–5 September 2003.
[7] A. Izquierdo-Fuente and J.R. Casar-Corredera, 'Optimal radar pulse scheduling using a neural network', *Proceedings of IEEE International Conference on Neural Networks*, Orlando, FL, vol. 7, pp. 4558–4591, 1994.
[8] D. Strömberg and P. Grahn, 'Scheduling of tasks in phased array radar', *Proceedings of IEEE International Symposium on Phased Array Systems and Technology*, Boston, MA, pp. 318–321, 1996.
[9] A.J. Orman, C.N. Potts, A.K. Shahani and A.R. Moore, 'Scheduling for a multifunction array radar system', *European Journal of Operational Research*, no. 90, pp. 13–25, 1996.
[10] J.M. Butler, 'Multi-function radar tracking and control', PhD thesis, UCL University of London, 1998.
[11] S.L.C. Miranda, C.J. Baker, K. Woodbridge and H.D. Griffiths, 'Fuzzy logic approach for prioritisation of radar tasks and sectors of surveillance in multifunction radar', *IET Radar, Sonar and Navigation*, vol. 1, no. April (2), pp. 131–141, 2007.
[12] S.L.C. Miranda, C.J. Baker, K. Woodbridge and H.D. Griffiths, 'Comparison of scheduling algorithms for multifunction radar', *IET Radar, Sonar and Navigation*, vol. 1, no. 6, pp. 414–424, December 2007.
[13] A. Charlish, K. Woodbridge and H.D. Griffiths, 'Information theoretic measures for MFR tracking control', *IEEE International Conference RADAR 2010*, Washington, DC, pp. 987–992, May 2010.
[14] A. Charlish, 'Autonomous agents for multi-function radar resource management', PhD thesis, University College London, September 2011.
[15] A. Charlish, K. Woodbridge and H.D. Griffiths, 'Phased array radar resource management using continuous double auction', *IEEE Transactions on Aerospace and Electronic Systems*, vol. 51, no. 3, pp. 2212–2224, July 2015.
[16] S. Haykin, 'Cognitive radar networks', *Fourth IEEE Workshop on Sensor Array and Multichannel Processing*, Waltham, MA, 12–14 July 2006.
[17] P.F.M.J. Verschure, 'Distributed adaptive control: a theory of the mind, brain, body nexus', *Journal of Biologically Inspired Cognitive Architectures*, vol. 1, pp. 55–72, 2012.
[18] V. Yordanova and H.D. Griffiths, 'Synchronous rendezvous technique for multi-vehicle mine countermeasure operations', *IEEE OCEANS 2015 Conference*, Washington, DC, 19–22 October 2015.
[19] V. Yordanova and H.D. Griffiths, 'Rendezvous point technique for multi-vehicle mine countermeasure operations in communication-constrained environments', *Marine Technology Society Journal*, vol. 50, no. 2, pp. 5–16, 2016.

[20] www.moos-ivp.org, accessed 22 March 2017.
[21] Beyond GPS: 5 Next-Generation Technologies for Positioning, Navigation & Timing (PNT), http://www.darpa.mil/news-events/2014-07-24, accessed 21 March 2017.
[22] M.A Lombardi, 'The use of GPS disciplined oscillators as primary frequency standards for calibration and metrology laboratories', [Online]. Available: http://tf.nist.gov/general/pdf/2297.pdf, accessed 16 March 2017.
[23] T.E. Derham, K. Woodbridge, H.D. Griffiths and C.J. Baker, 'The design and development of an experimental netted radar system', *International Radar Conference RADAR 2003*, Adelaide, Australia, pp. 293–298, 3–5 September 2003.
[24] T.E. Derham, 'The design and calibration of a coherent multistatic radar system', PhD thesis, University College London, 2005.
[25] T.E. Derham, S.R. Doughty, K. Woodbridge and C.J. Baker, 'Design and evaluation of a low-cost multistatic netted radar system', *IET Radar, Sonar & Navigation*, vol. 1, no. 5, pp. 362–368, 2007.
[26] S.R. Doughty, 'Development and performance evaluation of a multistatic radar system', PhD thesis, University College London, 2008.
[27] J.S. Sandenbergh and M.R. Inggs, 'A common view GPSDO to synchronize netted radar', *IET International Radar Conference RADAR 2007*, Edinburgh, 15–18 October 2007.
[28] M.R. Inggs, H.D. Griffiths, K. Woodbridge, W.A. Al-Ashwal, J.S. Sandenbergh and G.E. Inggs, 'Experimental coherent networked radar using GPS-disciplined reference oscillators', *Cognitive Systems with Interactive Sensors*, Crawley, 22 November 2010.
[29] J.S. Sanderbergh and M.R. Inggs, 'Synchronizing network radar using all-in-view GPS-disciplined oscillators', *IEEE Radar Conference* 2017, Seattle, WA, 9–12 May 2017.
[30] R.M. Hambly and T.A. Clark, 'Critical evaluation of the Motorola M12+ GPS timing receiver vs. the master clock at the United States Naval Observatory, Washington, DC', *Proceedings of the 34th Annual Precise Time and Time Interval (PTTI) Meeting*, pp. 109–116, 2002.
[31] Spectratime, 'LNRClok-1500 rubidium atomic clock', [Online]. Available: http://www.spectratime.com/products/isync/gps-rb/LNRClok-1500-GPS/, accessed 16 March 2017.
[32] K.A. Fisher and J.F. Raquet, 'Precision position navigation and timing without the global positioning system', *Air and Space Power Journal*, vol. 5, no. 2, pp. 24–33, 2011.
[33] M. Lipínski, T. Włostowski, J. Serrano and P. Alvarez, 'White Rabbit: a PTP application for robust sub-nanosecond synchronization', *IEEE International Symposium on Precision Clock Synchronization for Measurement Control and Communication (ISPCS)*, 12–16 September 2011.
[34] M.R. Inggs, J.S. Sandenbergh and S.A.C. Lewis, 'Investigation of White Rabbit for synchronization and timing of netted radar', *IEEE International Conference RADAR 2015*, Arlington, VA, pp. 214–217, 11–14 May 2015.

[35] S. Lewis, J.S. Sandenbergh and M.R. Inggs, 'Evaluating an off-the-shelf White Rabbit system to synchronise network radar via optic fibre', *IEEE Radar Conference 2017*, Seattle, WA, 9–12 May 2017.
[36] Seven Solutions [Online]. Available: http://sevensols.com
[37] S. Stein, D. Glaze, J. Levine, *et al.*, 'Performance of an automated high accuracy phase measurement system', *36th Annual Symposium on Frequency Control*, pp. 314–320, June 1982.

Part II

Target tracking and data fusion

This page intentionally left blank

Introductory remarks on tracking- and fusion-driven radar systems technology

*Wolfgang Koch**

To fulfil their duties even in demanding environments as well as for being able to protect themselves and others in an increasing number of applications, decision makers acting on all levels of hierarchies need to be aware of complex and dynamically changing overall situations. This comprises military missions as well as remote sensing use cases and emerging topics such as autonomous driving, inserting unmanned aircraft systems safely into the airspace, even automated industrial manufacturing and many others areas where radar sensor are or will be playing a key role. Situational awareness is not only the key to efficiently reaching certain goals of action, however, but to reach them also in an acceptable and responsible way.

Radar, and radiofrequency sensors in a more general sense, have been in the past, are currently, and will be in the foreseeable future the backbone sensing option for producing reliable and comprehensive situation pictures, the prerequisites of achieving situational awareness.

Although radar is an established and mature sensor technology that is reliably used in countless applications and available at all scales and for specialized purposes, we are facing five overall technological trends that are profoundly transforming radar and radiofrequency-sensing systems already for some time. They will be increasingly important by the advent of even more powerful processing units, broadband communication links, data-base systems, high-precision, robust navigation systems and mobile platform technologies in general, on the one hand, and sophisticated mathematical algorithms on the other. We thus expect that the future development will evolve according to the following five theses, which might be questionable in themselves, of course, as all attempts of technology predictions.

1. The system design principles of future radar systems are changing towards a predominant role of software in comparison to classical hardware components.
2. radar and radiofrequency sensors will be embedded in overall systems of complementary and heterogeneous sensors on multiple mobile sensor platforms.

*Fraunhofer FKIE, Germany

3. Multi-functionality in radar sensor design is and will be a predominant factor, i.e. the shared use of sensing hardware to achieve specialized goals.
4. Emphasis will increasingly be placed on system security aspects. Besides robustness to electronic countermeasures, this also comprises navigation and cyber warfare.
5. Future radar systems will be inherently adaptive to specific scenario and mission requirements and will massively exploit external knowledge bases.

In summary, future radar and radiofrequency systems will provide not only kinematic measurements and classification spectra at high update rates with much improved qualities in terms of accuracy, reliability, resolution, robustness, etc., but will also offer new types of classification attributes, mission-relevant environmental information and complimentary information provided by other sensors via sensor data fusion. Moreover, these rich informational sources for producing real-time situation pictures will be collected by an optimized use of all available sensing, communications and platform-related resources.

Figure 1 shows a schematic overview of a generic radar and radiofrequency system that may possibly consist of multiple individual sensor sub-systems or multifunctional sensor components on multiple platforms. The data and information between human decision makers and the mission-related entities in their respective environment basically flows in two directions. First, there is a flow while

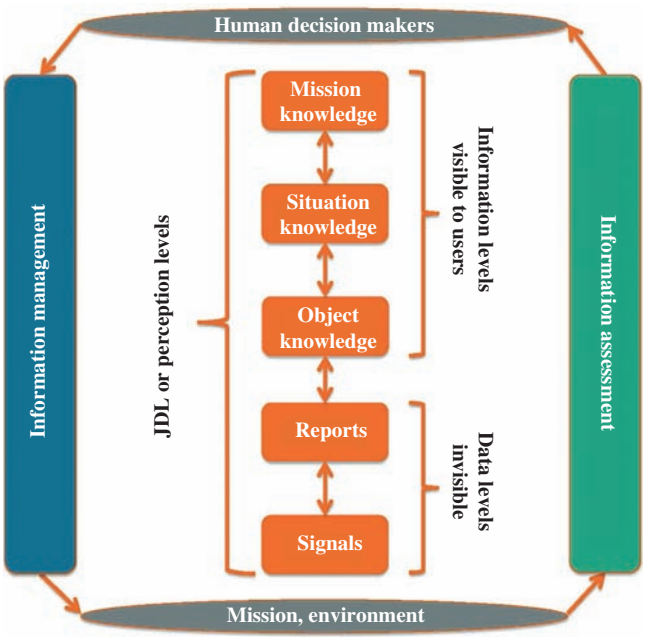

Figure 1 Schematic overview of a generic radar or radio frequency system with its basic flows of information and various perception levels

assessing data and information that is harvesting increasingly higher levels of information with a more and more advanced informational content. It begins with elementary sensor signals. The signal, data and information processing techniques are typically rooting in mathematical statistics and combinatorial optimization for solving the various data and information association problems involved [1].

A second flow of information, data and signals that is needed for resources management and actively controlling the information acquisition processes begins with the overarching, high-level mission goals and finally aims at choosing, for example at the right time, the right waveform to be transmitted into the right direction in order to optimize object detection, tracking and classification functionalities. Quite expectedly, the information management flow is dominated by advanced methods from statistical decision theory and mathematical game theory.[1]

This two-fold flow of information, assessment and management is driven and maintained by mathematical learning and reasoning algorithms. They may be collected into three more general groups. In the first group, the focus is on adaptively learning the features characterizing the sensing environment in order to adapt or to optimize the sensing system appropriately to a dynamically changing sensing environment. Second, algorithms are to be considered that sequentially provide the elements for producing situation pictures, i.e. algorithms that are answering the 'situation picture building question': 'What belongs where when in which way to what?' A third group of algorithms is required to predict the effect probably achieved by a potential data acquisition decision. These provide the basis of any type of radar resources management techniques.

As indicated in Figure 1, five different levels can be distinguished in the realm of algorithms that are related to the so called *JDL levels* of information fusion in the terms of the sensor data and information fusion community [2] or by the *perception levels* according a more psychologically inspired approach, which is often referred to as *cognitive sensing* [3]. The two levels primarily dealing with radar signals and reports, i.e. the measurements, are addressed as 'data levels' and are typically invisible to the user in a given application. The three remaining levels are representing information related to an individual objects, to several objects of interest and their mutual interrelation, i.e. situational elements, and, finally, to the mission, i.e. to a particular situation where human decision makers with their specific goals play an active role, for example when multifunctional sensors, mobile sensor platforms, or effectors and actuators need to be controlled.

On each perception level, the aspects of assessment, learning and reasoning, as well as management are intimately interrelated to each other and essentially form nested or multiple layer OODA loops: Observe, Orient, Decide, Act. In a different wording, this overall principle has always been present in classical radar systems design on the two data levels and is the model for the three information levels, object, situation and mission, in the more comprehensive picture as well.

[1]See the chapters by Alexander Charlish in this handbook, for example.

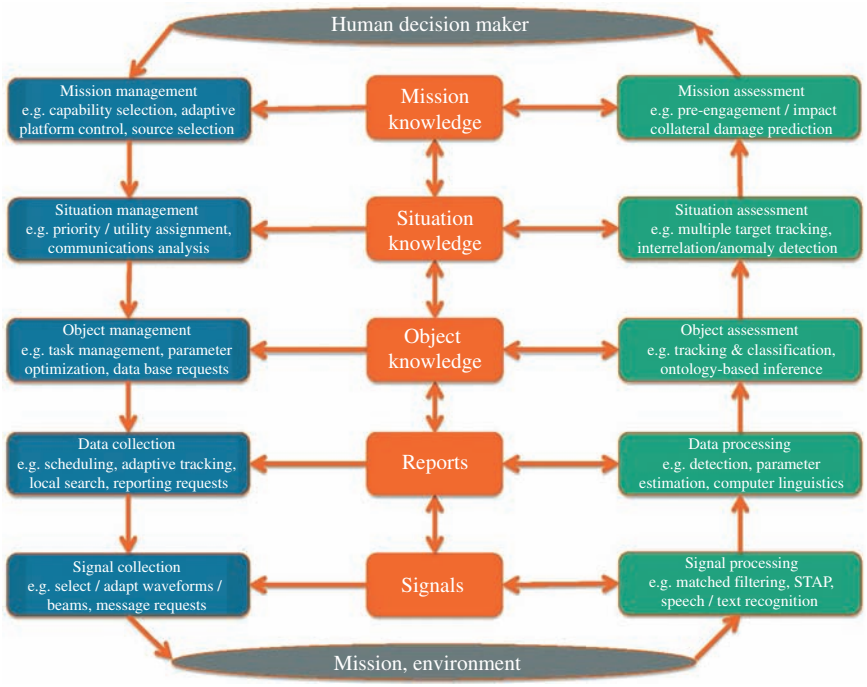

Figure 2 Schematic overview of selected assessment and management algorithms on various perception levels in the context of the overall flow of information

Figure 2 provides a schematic overview of selected assessment and management algorithms on various perception levels in the context of the overall flow of information. Among the data exploitation products of radar systems, object 'tracks' are of particular importance. 'Tracking' faces an omnipresent aspect in every real-world application insofar as it is dealing with fusion of data produced at different instants of time, i.e. tracking is important in all applications where particular emphasis is placed on the fact that the radar reports to be exploited have the character of a time series. Tracks thus represent currently available knowledge on relevant, time-varying quantities characterizing the instantaneous 'state' of individual objects or object groups of interest, such as aircraft, ships, vehicles, or moving persons.

Quantitative measures that reliably describe the quality of this knowledge are an integral part of a track. The information obtained by tracking algorithms also includes the history of the objects considered. If possible, a one-to-one association between the object trajectories in the radar sensors' field of view and the produced tracks is to be established and has to be preserved as long as possible (track continuity).

The achievable track quality does not only depend on the performance of the radar sensors used, but also on the individual objects properties and the operational conditions within the scenario to be observed. If tracks 'match' with the underlying real situation within the bounds defined by inherent quality measures being part of them, we speak of 'track consistency'. Quite generally, a tracking algorithm is designed by answering a series of basic questions:

1. Which object properties are of interest? Define appropriate object state quantities at varying time instants.
2. Which information is to be fused? Consider time series of radar measurements and related context information.
3. How to describe imprecise information? Design certain functions of the object state, such as probability density functions or more generalized versions of them.
4. What does 'learning' from a time series of sensor reports mean? Iteratively calculate these functions.
5. What is required for the learning process? Appropriate models of the radar sensor and object evolution models.
6. How to initiate/terminate the learning procedure? Use sequential decision-making procedures (implicitly, explicitly).

According to this admittedly very generic scheme, the tracking task has basically to deal with two problems: First, solve the data association task, i.e. find those radar reports belonging to the same object of interest. Second, apply state estimation techniques that typically leading to solving non-linear estimation and filtering problems. Many tracking algorithms make explicitly use of these distinctions, such as the popular Probabilistic Data Association Filters and the various versions of Multiple Hypothesis Tracking.[2] More innovative approaches develop a unified methodology (Probability Hypothesis Density and Multi-Bernoulli Filtering approaches).

Active phased-array radar [4] is an example of a multifunctional sensor system that requires sophisticated management algorithms for its efficient operation. Such systems call for efficient exploitation of their degrees of freedom, which are variable over a wide range and may be chosen individually for each track. This is especially true in multiple object tracking tasks. Of special interest are air situations with agile objects significantly differing in their radar cross sections. Unless properly handled, such situations can be highly allocation time and energy consuming.

In this context, advanced sensor and dynamics models for combined tracking and radar management are discussed, i.e. control of data innovation intervals, radar beam positioning and transmitted energy management. By efficiently exploiting its limited resources, the total surveillance performance of such sensor systems can be significantly improved. For track-while-scan radar systems or operating modes, data acquisition and tracking are completely decoupled.

[2]See, e.g.: [1]. Chapter 3.

For phased-array radar operated in an active tracking mode, however, the current signal-to-noise ratio of the object (i.e. the detection probability) strongly depends on the correct positioning of the pencil-beam, which is now taken into the responsibility of the tracking system. Sensor control and data processing are thus closely interrelated. This basically local character of the tracking process constitutes the principal difference between phased-array and track-while-scan applications from a tracking point of view. By using suitable sensor and object evolution models, however, this fact can be incorporated. The potential of this approach thus also applies to phased-array radar.

A last remark is related the role of context information. The exploitation of radar reports in decision-support systems critically depends on the quality of appropriate context information as well as on the underlying algorithms that take them into account. It seems reasonable to distinguish between physical context information, derived from facts from engineering, environmental context information, determined typically while operating the system, partially known context information, often described by statistical models and even language-encoded context information, such as certain limitations required by law or the underlying rules of engagement.

In many cases, these categories of context information do not appear isolated from each other. Radar models, for example combine physical and partially known context for describing imprecise radar measurements with environmental context, e.g. when a clutter background has to be estimated online. Another example for language-encoded context information is a plan to be followed by certain objects of interest in the course of time. A plan, i.e. a certain mode of expected motion, comprises the description of geographical way-point coordinates to be passed at a given instants of time via particular paths along with quantitative measures of tolerance.

Often, radar signals and reports are referred to as ‘hard’ data, while observer reports and context information are considered to be ‘soft’ pieces of information [5]. Besides speaking of ‘hard’ and ‘soft’ data, one could also characterize the data to be fused with respect to the time scale they are referring to. In this sense, we may distinguish between ‘close-to-object evolution data’, where the informational content of the data streaming in may change on a relatively short time scale, from data with a more stable or slowly changing informational content.

The technological evolution is driven by algorithms for extracting high-value information from sensor data streams of even poor quality. Due to the complexity of the real-world phenomena to be observed, however, and their inherently unpredictable nature, the role context information and its integration on various levels in systems engineering are particularly crucial. In a sense, also legal and moral constraints can be viewed as context information shaping the very design of informational decision support systems, especially for public safety and security [6].

In summary, modern and future radar and radio frequency sensors are and will be the backbone of multi-functional, multiple sources, multiple platform sensing

systems for supporting decision makers. Mission relevant radar-based sensing systems

- have to be embedded into overarching information systems,
- have to profit from advanced communications links,
- have to be cyber-safe and resistant to electronic warfare,
- have to be integrated seamlessly into unmanned platforms,
- have to have intuitive human machine interfaces.

References

[1] W. Koch (2014). *Tracking and Sensor Data Fusion. Methodological Framework and Selected Applications*. Springer Mathematical Engineering Series 2014.

[2] M.E. Liggins, D.L. Hall, J. Llinas (eds.), *Handbook of Multisensor Data Fusion—Theory and Practice*, 2nd edn. (CRC Press, Boca Raton, FL, 2008), Chap. 2, p. 24.

[3] S. Haykin (2006). 'Cognitive Radar: A Way of the Future'. *IEEE Journal of Signal Processing*, Vol. 23, No. 1, pp. 30–40.

[4] W.-D. Wirth, *Radar Techniques Using Array Antennas*, 2nd edn. (IEE Press, London, 2013).

[5] W. Koch, T. Pham (eds.), *Proceedings of the NATO STO Symposium on Information Fusion (Hard and Soft) for ISR*, SET-IST-126, Norfolk, VA, USA, May 4–5 2015.

[6] W. Koch (2014). 'Towards Cognitive Tools: Systems Engineering Aspects for Public Safety and Security'. *IEEE Aerospace and Electronic Systems Magazine*, Vol. 15, No. 9, pp. 14–26.

This page intentionally left blank

Chapter 9

Posterior Cramér–Rao bounds for target tracking

Marcel Hernandez, Alfonso Farina** and Branko Ristic****

Abstract

In this chapter, we present a review of recent developments in the calculation of estimation error performance bounds for target tracking. We concentrate on the posterior Cramér–Rao bound (PCRB), which is computationally the simplest of a general class of lower bounds. We present full details of an efficient recursive formula for the PCRB for the general non-linear filtering problem, and of PCRB methodologies in cluttered environments (i.e. in which there can be missed detections and spurious false measurements). In such environments, the measurement origin uncertainty is shown to manifest itself as an information reduction factor that degrades tracking performance according to the severity of the clutter. A tutorial of the key PCRB methodologies in cluttered environments is provided, and via simulations, PCRBs are calculated for a scenario in which a single target is tracked using measurements generated by a stationary radar. The PCRBs are compared to the performance of an extended Kalman filter, and the results demonstrate the efficacy of the PCRB as an efficient theoretical predictor of the capability of the tracker. We also present a discussion of applications that would benefit greatly from the development of a PCRB methodology. These applications include sensor scheduling in passive coherent location networks; and performance assessment of algorithms designed for image fusion, data assimilation for meteorology/oceanography, simultaneous localization and mapping and quantum estimation.

9.1 Introduction

In this chapter, a review of recent developments in the calculation of mean square error (MSE) tracker performance bounds is presented. In the context of target tracking, performance bounds are a powerful tool, enabling one to quantify the

*Hernandez Technical Solutions Ltd, UK
**Selex ES (retired), Italy
***RMIT University, School of Engineering, Australia

optimal achievable accuracy of target state estimation. This provides a mechanism for establishing the maximum degree by which sub-optimal filtering algorithms could potentially be improved (e.g. [1]). Furthermore, by establishing the physical performance limit, these bounds enable one to identify scenarios in which the required tracking accuracy cannot be achieved without enhancements to the sensor system (e.g. additional sensors, or upgrades to existing sensors). Tracker performance bounds give long-run average MSE. They are dependent on the uncertainty in the target motion, the accuracy of the available sensor measurements and the clutter density. Critically, such bounds are independent of any particular scenario realization (i.e. target trajectory and measurement sequence realization). As a result, performance bounds can be pre-calculated without the requirement for extensive simulation. Therefore, these bounds offer an invaluable tool both in system design and in sensor management applications (e.g. see [2]).

There are a number of MSE performance bounds (e.g. see [3,4]), including the Bhattacharya lower bound (BLB) [5], Weiss–Weinstein lower bound (WWLB) [6] and Bobrovsky–Zakai lower bound (BZLB) [7]. However, the posterior Cramér–Rao bound (PCRB) [8] is the most well-known MSE performance bound, primarily because of its low computational complexity compared to the other bounds. Indeed, there has been an explosion of interest in the PCRB in the last 15 years as a result of the establishment of an efficient recursive formula for the bound for non-linear filtering [9]. This chapter reviews recent developments in the calculation, and exploitation, of PCRBs, with the emphasis on formulations of the bound in cluttered environments (in which there can be both missed detections and false alarms). Details are provided of the different approaches in this case, all of which use an 'information reduction factor' (IRF) to scale the contribution of each measurement according to the magnitude of the measurement origin uncertainty.

As a result of these recent developments, the PCRB provides an efficient mechanism for predicting optimal system performance in many tracking applications. Indeed, the PCRB has been extensively used in the evaluation and comparison of different system architectures and sensor configurations during the design phase [10]. In time-critical applications, the PCRB has been used in automating the deployment of passive sonobuoys in anti-submarine warfare [2,11]; controlling a large network of bandwidth limited sensors in multi-target tracking (MTT) [12,13]; unmanned aerial vehicle trajectory planning in bearings-only tracking [2,14−16]; controlling a phased array radar in order to geo-locate anti-ship missiles [17]; selection of bistatic channels of multistatic radar systems [18], to name a few.

This chapter is organized as follows. Section 9.2 provides a review of key developments in the calculation of the PCRB, together with brief details of applications that have exploited the bound. In Section 9.3, the basic filtering problem is defined, and details are provided of a general class of lower bounds that includes as special cases the PCRB, BLB, WWLB and BZLB. In Section 9.4, details are provided of the excellent paper of [9] that introduced an efficient recursion for the PCRB, together with details of methodologies for calculating the constituent matrices, and other related work. In Section 9.5, details are provided of computationally efficient formulations of the PCRB in cluttered environments.

In Section 9.6, simulation results are presented comparing the various PCRBs with the performance of an extended Kalman filter (EKF) tracking methodology, for a scenario with a single target and a stationary radar. In Section 9.7, a discussion of potential avenues for further development of PCRBs is provided. Finally, a summary of the chapter appears in Section 9.8.

9.2 Literature review

Target tracking involves exploiting sensor (e.g. radar) measurements in order to form and maintain a track of each moving target in the surveillance volume. The target tracking problem is so complex that tracking algorithms typically consist of several layers of logic, including *non-linear filtering*, *manoeuvre handling* and *data association*. Hence, despite its long history, research into the PCRB (also referred to as the Bayesian Cramér–Rao bound) for target tracking has not resulted in a universally applicable bound. Instead, the PCRB has been formulated only for particular components of the target tracking problem, as discussed below.

Non-linear filtering is a problem of sequential state estimation of a *single* stochastic dynamic system. The assumptions are (a) the dynamic system (i.e. the target) is present throughout the observation interval; (b) the target (stochastic) motion model does not change; and (c) all sequentially received measurements originate from the target. The general formulation of the recursive PCRB for the non-linear filtering problem has been formulated in [9], in which a Riccati-like equation was determined. This was a seminal paper which resulted in application to various target tracking modalities, such as bearings-only tracking (see [19], pages 103–152) and range-only tracking (see [19], pages 153–178), ballistic object tracking [20], bistatic radar tracking [21] and Doppler-only target tracking [22]. Furthermore, the bound has been extended to distributed estimation [23], coloured noise [24], quantized measurements [25] and extended target tracking [26].

Motivated by [9], in [27], the Markov property of the state transition equation was again exploited to show that the BLB and BZLB are also given by Riccati-like recursions, but with more complex constituent matrices in these cases. Moreover, the authors of [27] also introduced a fully recursive form for the information sub-matrix for the WWLB for the estimation of the current target state (see also [28]).

For tracking manoeuvring targets, clearly the assumption that the target stochastic motion model does not change throughout the observation interval needs to be relaxed. This was done by adopting Markovian model switching dynamics, which results in a hybrid estimation problem where it is required to estimate sequentially both the *continuous*-valued target state and the *discrete*-valued target motion model. Direct application of the PCRB recursive formula for non-linear filtering [9] would lead to differentiation of terms involving the discrete-valued model variable. Since this cannot be done analytically, in one's quest for the lower bound, there are two options at one's disposal. The first is to explore alternatives to the Cramér–Rao bound, which are potentially applicable to hybrid system estimation problem (e.g. BLB, WWLB and BZLB [29]). The difficulty with these

bounds is that the derivations are extremely complex and their implementation is quite involved.

The second option is to consider *approximations* to the PCRB for Markovian switching systems. In [30], an approach was presented in which a conditional PCRB was calculated by conditioning on the manoeuvre sequence. The unconditional PCRB was then determined as a weighted sum of these conditional bounds. However, this formulation typically provides an overly optimistic lower bound, because at each stage, one implicitly *knows* the sequence of manoeuvres that the filtering algorithm is required to estimate.

In [31,32], the multi-modal prior target probability density function (PDF) of the manoeuvring target was approximated by a best-fitting uni-modal Gaussian (BFG) distribution. The key idea is to match the first two moments of the state evolving according to the jump Markov system, with the first two moments of the state evolving according to a linear/Gaussian uni-modal system. The Riccati-like recursive formula of [9] was then applied to calculate an MSE performance measure. This measure is not a lower bound, because of the approximation involved. Despite this, the performance measure is an accurate predictor of the steady-state performance of state-of-the-art tracking algorithms, such as the interacting multiple model filter [33]. Furthermore, the mean and covariance of the uni-modal BFG distribution are given by an elegant recursive formula, allowing the BFG measure to be calculated extremely efficiently.

This makes the approach of [31,32] invaluable in predicting system performance in manoeuvring target scenarios. The BFG approach was later modified [34] to match the transition mean and covariance matrix of the uni-modal system to those of the jump Markov system. The resulting BFG performance measure is computationally demanding but is generally lower than both the BFG measure of [31,32], and the achievable estimation MSE. More recently, Svensson [35] proposed estimating the PCRB for Markovian switching systems using a Monte Carlo method. Surprisingly, the resulting bound is found to be even more optimistic than the conditional PCRB [30] and therefore is not useful in practice.

Relaxation of the assumption that all sequentially received measurements for target tracking originate from the (same) target introduces additional uncertainty into the target tracking problem: the measurement origin uncertainty. This situation is prevalent in radar systems with a probability of detection less than unity (i.e. $P_d < 1$) and a probability of false alarm greater than zero (i.e. $P_{\text{fa}} > 0$). In such cases, measurements in a typical scan may include false detections (due to clutter), while the target originating detection may be missing. Efficient PCRB formulations now exist for this case, as discussed next.

For example, for the problem with deterministic (i.e. not randomly evolving) target dynamics, the measurement origin uncertainty was shown (in [36]) to manifested itself as a constant IRF. This IRF scales the measurement contribution such that the Cramér–Rao bound increases in magnitude (i.e. optimal performance is degraded) as the environment becomes more cluttered (i.e. as the number of false positives increases). The paper [37] (see also [38]) then derived a general expression for the PCRB for the linear filtering problem with randomly evolving target

dynamical equations. The paper [39] extended [37] to provide a PCRB for the nonlinear filtering problem. The methodology detailed in the papers [37−39] is referred to as the 'IRF approach'. It is also noted that an IRF was determined earlier in [40], to quantify the impact of measurement origin uncertainty on the performance of probabilistic data association filters.

However, it has recently been shown that the IRF approach provides an optimistic bound on tracker performance [41−43]. This is primarily because the IRF approach does not take into account the exact sequence of missed detections, which can have a considerable impact on performance, particularly during the early stages of tracking. In [41], an enumeration approach was introduced for the case with missed detections (i.e. $P_d \leq 1$) but no false alarms (i.e. $P_{\text{fa}} = 0$). This enumeration approach created a bound conditional on the sequence of detections and then created an unconditional bound as a weighted average. It was then shown in [40] that the enumeration bound was greater (i.e. tighter) than the IRF bound, and therefore less optimistic.

The paper [43] generalized the enumeration bound of [41] to the case where false alarms are possible (i.e. $P_d \leq 1$ and $P_{\text{fa}} \geq 0$) by introducing the 'measurement sequence conditioning' (MSC) approach. The MSC approach created a bound conditional on the number of measurements at each sampling time and then created an unconditional bound as a weighted average (weighted by the probability of each particular sequence occurring). It was then shown (again, see [43]) that the MSC bound was also tighter (less optimistic) than the corresponding IRF bound.[1] In simulations, it was then shown that differences between the two bounds are greatest initially, when the impact of the actual measurement sequence is most significant (again, see [43]).

In [44], the measurement existence sequence conditioning (MESC) approach was introduced. This is similar to the MSC approach, but rather than condition on the number of measurements, MESC conditions on at least one measurement existing at each sampling time. In simulations, the resulting MESC bound was shown to be almost identical to the MSC bound [44]. In the case with no false alarms, it has recently been shown in [45−47] that a modified Riccati (MR) equation provides an upper bound on the enumeration bound [39], but with a much lower computational overhead[2]. In simulations, the MR equation was shown to bound the enumeration PCRB reasonably tightly, making it an effective measure of system performance. However, the MR equation cannot be guaranteed to provide a bound on tracker performance and can only be applied in the case $P_{\text{fa}} = 0$.

Multi-target formulations of the PCRB in the presence of measurement origin uncertainty have also been studied, see for example [12,13]. This formulation added the complexity of associating measurements across multiple targets, leading to extremely complex expressions of the IRFs, which are then given by an information reduction matrix [13]. The work of [12,13] builds on the PCRB recursion

[1]Which generalized the finding of [40] to the case in which $P_{fa} \geq 0$.
[2]The MR approach has a computational complexity similar to that of the IRF approach [37].

for MTT first introduced in [48], which assumed a constant and known number of targets during the observation period.

Attempts to formulate a theoretical error bound for multiple appearing/disappearing targets in the presence of measurement origin uncertainty have been more recently considered in the framework of random finite set (RFS) theory [49]. These error bounds at present can only be derived for a single time instance (i.e. no recursive formulation exists). Also, since the targets can appear/disappear at any time, the RFS bounds replace the MSE with the optimal sub-pattern assignment error, which captures both the MSE and the error in the cardinality (i.e. the number of targets).

The PCRB for MTT is much simpler to derive in the context of track-before-detect (TBD) [50]. The main idea is to work with pre-detection (raw) sensor data (e.g. range-azimuth-Doppler map). Assuming that the number of targets is known and constant during the observation period, the PCRB for the MTT problem can be solved using the non-linear filtering formulation of [9]; for details see [51,52]. The motivation for TBD is its capacity to detect and track very low signal-to-noise ratio (SNR) targets. Unfortunately, the PCRB cannot predict the well-known SNR threshold effect in TBD; and the Barankin bound was studied for this purpose in [53].

9.3 Bayesian performance bounds

9.3.1 Discrete time estimation

Let $X_k \in R^{n_x}$ denote the target state at discrete sampling time t_k, $k = 0, 1, \ldots$. The target state evolves according to a Markov process given as follows: $X_{k+1} = f_k(X_k, \omega_k)$ where $f_k(.)$ is potentially a non-linear function of the target state and ω_k is an independent and identically distributed (IID) process noise sequence.

Measurements $Z_k \in R^{n_z}$ are available at the discrete sampling times t_k, $k = 1, 2, \ldots$. Each measurement is given as follows: $Z_k = h_k(X_k, \epsilon_k)$, where $h_k(.)$ is also potentially a non-linear function of the target state and ϵ_k is also an IID measurement noise sequence. The objective is to estimate the target state vector $X_{0:k} \triangleq \{X_0', \ldots, X_k'\}'$ at each sampling time k based on the sequence of measurements $Z_{1:k} \triangleq \{Z_1', \ldots, Z_k'\}'$. The superscript $'$ denotes the transpose operator.

9.3.2 General class of lower bounds

Let $\hat{X}_{0:k}$ denote any unbiased estimator of $X_{0:k}$, based on the sequence of measurements $Z_{1:k}$. Invoking the Cauchy–Schwarz inequality enables a general class of MSE performance bounds for the non-linear estimation problem to be determined. This class of lower bounds is given as follows [29]:

$$E\left[\left(X_{0:k} - \hat{X}_{0:k}\right)\left(X_{0:k} - \hat{X}_{0:k}\right)'\right] \geq V_{0:k} J_{0:k}^{-1} V_{0:k}' \tag{9.1}$$

The inequality in (9.1) means that the difference is a non-negative definite matrix; $J_{0:k}$ is referred to as the *Fisher information matrix* (FIM).

The $(k+1)n_x \times (k+1)n_x$ matrices $V_{0:k}$ and $J_{0:k}$ are given by:

$$V_{0:k} = E\left[X_{0:k} \times \Psi(X_{0:k}, Z_{1:k})'\right] \tag{9.2}$$

$$J_{0:k} = E\left[\Psi(X_{0:k}, Z_{1:k}) \times \Psi(X_{0:k}, Z_{1:k})'\right] \tag{9.3}$$

The expectations are with respect to $X_{0:k}$ and $Z_{1:k}$; and $\Psi(X_{0:k}, Z_{1:k})$ is a vector of dimensionality $(k+1)n_x$ of real-valued, measurable functions that satisfy:

$$\int_{X_{0:k}} \Psi(X_{0:k}, Z_{1:k}) p(X_{0:k}, Z_{1:k}) \mathrm{d}X_{0:k} = 0 \tag{9.4}$$

where $p(X_{0:k}, Z_{1:k})$ denotes the joint PDF of $X_{0:k}$ and $Z_{1:k}$

The vector function $\Psi(X_{0:k}, Z_{1:k})$ defines the bound. For example, the general BLB is obtained by setting $\Psi(X_{0:k}, Z_{1:k})$ as follows (e.g. [27]):

$$\Psi(X_{0:k}, Z_{1:k}) = \sum_{i=1}^{M} \frac{a_i}{p(X_{0:k}, Z_{1:k})} \nabla^i_{X_{0:k}} p(X_{0:k}, Z_{1:k}) \tag{9.5}$$

where $\nabla^i_v = \left[\partial^i / \partial v^i_1, \ldots, \partial^i / \partial v^i_n\right]'$ for a vector $v = [v_1, \ldots, v_n]'$, i.e. ∇^i_v, denotes the ith-order partial derivative operator with respect to v. The parameter M is an arbitrary natural number, $a_1 = 1$ and a_i $(i > 1)$ are arbitrary real numbers. It can easily be shown that for this choice of Ψ, (9.4) holds.

Of particular interest, the PCRB (e.g. [8]) is a special case of the BLB in which $M = 1$, i.e.:

$$\Psi(X_{0:k}, Z_{1:k}) = \frac{\nabla_{X_{0:k}} p(X_{0:k}, Z_{1:k})}{p(X_{0:k}, Z_{1:k})} \tag{9.6}$$

In this case, it can easily be shown that $V_{0:k} = -I_{(k+1)n_x}$, where I_m denotes the m-dimensional identity matrix. The PCRB is then given as follows:

$$E\left[\left(X_{0:k} - \hat{X}_{0:k}\right)\left(X_{0:k} - \hat{X}_{0:k}\right)'\right] \geq J^{-1}_{0:k} \tag{9.7}$$

where $J_{0:k}$ is given by:

$$J_{0:k} = E\left[\frac{\nabla_{X_{0:k}} p(X_{0:k}, Z_{1:k}) [\nabla_{X_{0:k}} p(X_{0:k}, Z_{1:k})]'}{[p(X_{0:k}, Z_{1:k})]^2}\right] \tag{9.8}$$

$$= E\left[-\Delta^{X_{0:k}}_{X_{0:k}} \log p(X_{0:k}, Z_{1:k})\right] \tag{9.9}$$

Δ is a second-order partial differential operator, defined as follows: $\Delta^{\Theta}_{\Psi} = \nabla_{\Psi} \nabla'_{\Theta}$.

In [29], a further class of vectors $\Psi(X_{0:k}, Z_{1:k})$ satisfying (9.4) is introduced, giving the multiple parameter WWLB. Furthermore, in [27], a general expression for the multiple parameter BZLB is provided.

In exemplar scenarios, the PCRB has been shown to be the least tight of the performance bounds [27], although the result has not been proven in general. However, the relative optimism of the PCRB is not surprising when one considers the fact that the PCRB is a special case of the BLB and is also a limiting case of the WWLB and BZLB. The BLB, WWLB and BZLB all contain free parameters that can be optimized in order to make the bound as tight (i.e. large) as possible.

However, of critical importance, the PCRB is computationally (by far) the simplest of the performance bounds. This makes it an appealing measure of system performance in time-critical sensor management applications, in which the ability to quickly evaluate and compare sensor configurations is invaluable.

9.4 Posterior Cramér–Rao bound for non-linear filtering

9.4.1 General recursion

The limitation with each of the bounds in Section 9.3.2 is that the dimensionality of the bound grows linearly as the sampling time k increases. As a result, the matrix manipulations required in calculating each bound become increasingly complex and must be re-calculated at every time step. However, in [9], the authors considered the general non-linear filtering problem and were interested only in the PCRB for the estimation of the target state at time k, i.e.:

$$E\left[\left(X_k - \hat{X}_k\right)\left(X_k - \hat{X}_k\right)'\right] \geq J_k^{-1} \tag{9.10}$$

where J_k^{-1} is the bottom right $n_x \times n_x$ block of the matrix $J_{0:k}^{-1}$, with $J_{0:k}$ given by (9.9).

In [9], the Markov property of the target state transition equation was exploited in order to provide the following fixed dimensionality, Riccati-like recursion for the sequence J_k:

$$J_k = D_{k-1}^{33} - \left(D_{k-1}^{12}\right)'\left(J_{k-1} + D_{k-1}^{11}\right)^{-1} D_{k-1}^{12} + J_Z(k) \tag{9.11}$$

where:

$$D_{k-1}^{11} = E_{X_{0:k},Z_{1:k}}\left[-\Delta_{X_{k-1}}^{X_{k-1}} \log p(X_k|X_{k-1})\right] \tag{9.12}$$

$$D_{k-1}^{12} = E_{X_{0:k},Z_{1:k}}\left[-\Delta_{X_{k-1}}^{X_k} \log p(X_k|X_{k-1})\right] \tag{9.13}$$

$$D_{k-1}^{33} = E_{X_{0:k},Z_{1:k}}\left[-\Delta_{X_k}^{X_k} \log p(X_k|X_{k-1})\right] \tag{9.14}$$

$$J_Z(k) = E_{X_{0:k},Z_{1:k}}\left[-\Delta_{X_k}^{X_k} \log p(Z_k|X_k)\right] \tag{9.15}$$

The Riccati-like recursion (9.11) generalizes the CRLB of [54] to non-deterministic systems.

The initial FIM is given by:

$$J_0 = E_{X_0}\left[-\Delta_{X_0}^{X_0} \log p(X_0)\right] \tag{9.16}$$

It is typical to assume that the prior target distribution X_0 is Gaussian with a large covariance C_0, reflecting limited (or no) knowledge of the initial target state. In such cases, $J_0 = C_0^{-1}$.

9.4.2 Calculating the constituent matrices

9.4.2.1 Case 1: Exploiting target ground-truth data

Monte Carlo methods can be used to approximate the involved expectations given in (9.12)–(9.15), with respect to the target states and measurements. However, these methods require an ensemble of true target states and measurement sequences. Sensor readings are often available from historical datasets, but true target states may not be available, except in simulations (such as those presented in Section 9.6), or in appropriately designed experiments (e.g. in which accurate GPS data are available).

Nevertheless, if the true target state evolutions and measurement sequences are available, (9.12)–(9.15) can be estimated as follows:

$$D_{k-1}^{11} \approx \frac{1}{N}\sum_{i=1}^{N}\left[-\Delta_{X_{k-1}}^{X_{k-1}} \log p\left(X_k^i \middle| X_{k-1}^i\right)\right] \tag{9.17}$$

$$D_{k-1}^{12} \approx \frac{1}{N}\sum_{i=1}^{N}\left[-\Delta_{X_{k-1}}^{X_k} \log p\left(X_k^i \middle| X_{k-1}^i\right)\right] \tag{9.18}$$

$$D_{k-1}^{33} \approx \frac{1}{N}\sum_{i=1}^{N}\left[-\Delta_{X_k}^{X_k} \log p\left(X_k^i \middle| X_{k-1}^i\right)\right] \tag{9.19}$$

$$J_Z(k) \approx \frac{1}{N}\sum_{i=1}^{N}\left[-\Delta_{X_k}^{X_k} \log p\left(Z_k^i \middle| X_k^i\right)\right] \tag{9.20}$$

where N denotes the number of true target state evolutions and corresponding measurement sequences available; X_k^i is the true target state at sampling time k in the ith state evolution and Z_k^i is the measurement generated at sampling time k for the ith state evolution. Hence, the expectations in (9.12)–(9.15) are replaced with values averaged over true target states evolutions and historical measurements.

9.4.2.2 Case 2: The case of hidden states – exploiting historical sensor data

In many practical applications, the true target state data will be unavailable or unmeasurable, and the approximations in (9.17)–(9.20) cannot be calculated. Such

applications include surveillance operations of unknown (e.g. red-force) targets, or when performing predictive sensor management.

However, historical sensor data are typically available. Recently, methodologies have been developed that exploit this historical sensor data in order to estimate the hidden target state and then use this estimate to approximate the expectations (9.12)–(9.15). In particular, in [55], the hidden target state was estimated using either an EKF (e.g. [56]) or unscented Kalman filter (UKF) [57] methodology, whereas in [58], a particle filter (PF) approach [59] was employed. In each case, an accurate PCRB approximation was determined. It is noted that the approach of [58] more readily applies itself to non-linear, non-Gaussian applications, for which the PF approach does not require the linearisation performed the EKF, or the assumption of Gaussianality inherent in both the EKF and UKF approaches.

When using the PCRB as a mechanism for estimating future tracking performance (e.g. when performing adaptive sensor management in order to optimize tracking accuracy), there is a requirement to *predict* the *future* PCRB conditioned on the measurements available up to the current time step. In [60], such a conditional PCRB is determined, with matrices analogous to (9.12)–(9.15) determined (in the absence of the true target states) via a sequential Monte Carlo (i.e. PF) approach. The conditional PCRB of [60] can be calculated in real time and was shown to be less optimistic (i.e. greater) than the unconditional PCRB of [9]. Following this, in [61], two alternative conditional bounds were proposed, which were shown to be in close agreement with the conditional PCRB of [60]. The approaches of [60,61] are similar in principle to the renewal strategy introduced in [11], which restarts the unconditional PCRB [9] each time sensor scheduling is performed, using the most recent target state estimate based on the measurements generated up to that time.

9.4.3 Simplifications – Linear models and Gaussian noise

If $f_k(.)$ is a linear function of X_k, with additive Gaussian distributed noise (i.e. $f_k(X_k, \omega_k) = A_k X_k + \omega_k$, where $\omega_k \sim \mathcal{N}(0, \Sigma_k)$), the calculation of the D_k matrices is straightforward. Indeed, it can easily be shown that (e.g. [62]):

$$D_k^{11} = A_k' \Sigma_k^{-1} A_k \tag{9.21}$$

$$D_k^{12} = -A_k' \Sigma_k^{-1} \tag{9.22}$$

$$D_k^{33} = \Sigma_k^{-1} \tag{9.23}$$

In this case, substituting relations (9.21)–(9.23) into (9.11) and applying the matrix inversion lemma gives:

$$J_k = \left(\Sigma_{k-1} + A_{k-1} J_{k-1}^{-1} A_{k-1}'\right)^{-1} + J_Z(k) \tag{9.24}$$

Furthermore, if the measurement model is a linear function of the target state, with additive Gaussian distributed measurement errors (i.e. $h_k(X_k, \epsilon_k) = H_k X_k + \epsilon_k$,

where $\epsilon_k \sim \mathcal{N}(0, R_k)$), it can easily be shown that:

$$J_Z(k) = H_k' R_k^{-1} H_k \tag{9.25}$$

which is independent of the true target state and measurement sequence realizations.

It is noted that if the system and measurement models are linear, with additive Gaussian noise, the Kalman filter is the minimum mean squared error estimator, achieving the PCRB. Furthermore, in this case, calculation of the PCRB is independent of the target state and measurement sequence realizations, making the complications noted in Section 9.4.2 redundant.

9.5 Posterior Cramér–Rao bounds for non-linear filtering in cluttered environments

9.5.1 Target generated measurements and false alarms

We consider the problem of tracking a single target in a cluttered environment, in which there can be both missed detections and false alarms. Purely for notational simplicity, analysis focuses on a single sensor scenario. The extension to multi-sensor systems is straightforward provided that the sensors have independent measurement processes (conditional on the target state). The key expressions in the multi-sensor case are included for completeness.

The measurement model specified in [37] is used throughout. In this model, there can be a maximum of one target generated measurement per sampling time, which occurs with constant probability P_d. Each target generated measurement, Z_k^{TG} is a non-linear function of the target state, corrupted by white Gaussian noise, i.e.:

$$Z_k^{\mathrm{TG}} = h_k(X_k) + \epsilon_k \tag{9.26}$$

where $\epsilon \sim \mathcal{N}(0, R_k)$.

At each sampling time, the number of false alarm measurements has a Poisson distribution with mean λV, where V denotes the volume of the surveillance region A and λ is the density of false alarms per unit volume. Each false alarm measurement Z_k^{FA} is uniformly distributed throughout the surveillance region, i.e.:

$$Z_k^{\mathrm{FA}} = u_k \tag{9.27}$$

where $p(u_k) = 1/V$ for $u_k \in A$.

In the PCRB recursion (9.11), only the $J_Z(.)$ matrix is dependent on the measurement model, with the D-matrices dependent solely on the target dynamical model. In the following sections, several different formulations of the PCRB are presented in cluttered environments. These formulations differ in the way in which they condition on the measurement sequence.

9.5.2 Information reduction factor bound

9.5.2.1 General approach

The IRF PCRB is given by J_k^{-1}, with the sequence of FIMs given by the recursion (9.11), or by the recursion (9.24) if the target dynamics are linear. The measurement contribution is calculated as follows [37–39]:

$$J_Z(k) = E_{m_k}[J_Z(k : m_k)] \tag{9.28}$$

$$= \sum_{m_k=1}^{\infty} p(m_k) J_Z(k : m_k) \tag{9.29}$$

where:

- m_k is the number of measurements (each of dimensionality n_z) generated within a *gated* observation region[3] at sampling time k; m_k is a count of both measurements generated by the target and false alarms.
- $p(m_k)$ is the probability that there are m_k measurements in the gated observation region at sampling time k.

$J_Z(k : m_k)$ is the measurement contribution at time k given that there are m_k measurements at that time. This is given as follows:

$$J_Z(k : m_k) = E_{X_k, Z_k}\left[\left[\nabla_{X_k} \ln p(Z_k|X_k, m_k)\right] \left[\nabla_{X_k} \ln p(Z_k|X_k, m_k)\right]'\right] \tag{9.30}$$

The measurement likelihood, $p(Z_k|X_k, m_k)$, is a mixture distribution, i.e. a mixture of the PDFs of target generated measurements (given by (9.26)) and false alarm measurements (given by (9.27)). This makes $J_Z(k : m_k)$ difficult to calculate. However, conditional on several unrestrictive assumptions (see the 'Assumptions' section overleaf), and after significant calculations [39,43], it can be shown that:

$$J_Z(k : m_k) = q_k(m_k) E_{X_k}\left[H_k' R_k^{-1} H_k\right], \quad \text{for } m_k > 0 \tag{9.31}$$

where $q_k(m_k) \in [0, 1]$ is an IRF conditional on there being m_k measurements at sampling time k [43]; and $H_k = \nabla_{X_k}\left[h_k(X_k)'\right]'$ is the Jacobian of the measurement vector (of target generated measurements). Clearly, $J_Z(k : 0) = 0$, i.e. there is no contribution, if there are no measurements.

It is then straightforward to show that:

$$J_Z(k) = q_k E_{X_k}\left[H_k' R_k^{-1} H_k\right] \tag{9.32}$$

[3]This region is an n_z-dimensional hyper-cube centred on the ground-truth (i.e. errorless) measurement, with edge lengths $2g\sigma_1, \ldots, 2g\sigma_{n_z}$; where σ_i is the measurement error standard deviation of the ith component of each measurement; n_z is the dimensionality of each measurement; and g is a constant (typically $g = 4$). The gated observation region is analogous to the gated region used in performing data association in filtering; and the hyper-cube design has appealing features when manipulating the resulting multi-dimensional expectation for $J_Z(k : m_k)$.

where:

$$q_k = \sum_{m_k=1}^{\infty} p(m_k) q_k(m_k) \tag{9.33}$$

The parameter $q_k \in [0, 1]$ is the overall IRF [39]. The IRFs q_k and $q_k(m_k)$ ($m_k > 0$) are independent of the target state and quantify the effect of missed detections and false alarms. If there is no clutter and there are no missed detections, then $m_k = 1$ and $q_k(m_k) = q_k = 1$. In all other cases, $q_k(m_k)$ and q_k are less than unity; and, the IRF reduces the measurement contribution (compared to the no clutter case) and therefore increases the PCRB.

For completeness, in the 'General expression' section overleaf, (9.35) provides a general expression for the IRF $q_k(m_k)$ (taken from [43]). In the 'Numerical approximation' section on page 277, (9.39) then provides a numerical approximation of (9.35). Of particular note, if the measurement, clutter and detection models are time invariant then so too is the IRF $q_k(m_k)$, which need then only be calculated once (for each sensor). This calculation can be performed offline, enabling the PCRB to be calculated efficiently, and implemented in real-time applications, e.g. [11].

An extension of the IRF approach also exists for the problem of tracking multiple targets in cluttered environments [13]. The sequence of manipulations is even more complex in that case, and the measurement origin uncertainty can be shown to manifest itself as an information reduction matrix.

9.5.2.2 Calculation of the information reduction factors

Assumptions

In calculating the IRFs, the following unrestrictive assumptions are made (e.g. see [2,43]).

1. There is a maximum of one target generated measurement per sampling time, which occurs with probability P_d. P_d does not have to be constant (e.g. in [11] the probability of detection was range dependent), but the IRF must be calculated for each potential value of P_d.
2. False alarm measurements are independent of the target state. It is also commonly assumed (e.g. see [37−39]) that the number of false alarms has a Poisson distribution with rate λ per unit volume of the observation region. However, it is not necessary to use a Poisson distribution to model the number of false alarms.
3. We only consider false alarms that fall in the gated observation region (given in footnote 3) of volume V_g around the target (e.g. see (9.39) in [43]). The gated observation region is analogous to the gated region used in performing data association in filtering. The average number of false alarms considered per sampling time is then given by λV_g.
4. The error covariance of target generated measurements is a diagonal matrix, i.e. is given by $R_k = diag(\sigma_1^2, \ldots, \sigma_{n_z}^2)$. If this assumption does not hold an information reduction matrix (rather than an IRF) quantifies the effect of the measurement origin uncertainty.

General expression

The IRFs, $q_k(m_k)$, are given as follows (e.g. see (9.54) in [43]):

$$q_k(0) = 0 \tag{9.34}$$

$$q_k(m) = \frac{\epsilon(m)^2 |R_k|^{(m-2)/2}}{m V_g^{2m-2} (2\pi)^{n_z}} \times \left\{ \int_{Z_{mn_z}=-g}^{g} \cdots \int_{Z_{m1}=-g}^{g} \cdots \int_{Z_{1n_z}=-g}^{g} \cdots \int_{Z_{11}=-g}^{g} \frac{Z_{11}^2 \exp\left\{ -\sum_{i=1}^{n_z} Z_{1i}^2 \right\}}{\left[\frac{(1-\epsilon(m))}{V_g^m} + \frac{\epsilon(m)}{m V_g^{m-1} \sqrt{(2\pi)^n |R_k|}} \sum_{r=1}^{m} \exp\left\{ -\frac{1}{2} \sum_{j=1}^{n_Z} Z_{rj}^2 \right\} \right]} \mathrm{d}Z_{11} \cdots \mathrm{d}Z_{mn_z} \right\} \tag{9.35}$$

for $m > 0$. The volume of the gated observation region is given by:

$$V_g = (2g)^{n_z} \prod_{i=1}^{n_z} \sigma_i \tag{9.36}$$

The parameter $\epsilon(m_k)$ is the probability that one of the m_k measurements is target generated. This is given as follows:

$$\epsilon(m_k) = \frac{P_d^g}{p(m_k)} \frac{(\lambda V_g)^{m_k - 1} \exp(-\lambda V_g)}{(m_k - 1)!} \tag{9.37}$$

To remind the reader, $p(m_k)$ is the probability that there are m_k observations in the gated observation region. This is given as follows:

$$p(m_k) = (1 - P_d^g) \frac{(\lambda V_g)^{m_k} \exp(-\lambda V_g)}{m_k!} + P_d^g \frac{(\lambda V_g)^{m_k - 1} \exp(-\lambda V_g)}{(m_k - 1)!} \tag{9.38}$$

P_d^g is the probability of obtaining a target generated measurement in the gated observation region. Clearly, provided g is not small (and typically $g \geq 4$), then $P_d^g \approx P_d$.

It is again noted that if the measurement, clutter and detection models are time invariant then so too are the IRFs, $q_k(m_k)$, $m_k > 0$, which then need only be calculated once.

Numerical approximation

A Monte Carlo approximation of (9.35) is given as follows (see (9.58) in [43]):

$$q_k(m_k) \approx \frac{(2g)^{n_z m_k}\epsilon(m_k)^2|R_k|^{(m_k-2)/2}}{m_k V_g^{2m_k-2}(2\pi)^{n_z}} \times \frac{1}{N_p}\sum_{l=1}^{N_p} \frac{U_{11}[l]^2 \exp\left\{-\sum_{i=1}^{n_z} U_{1i}[l]^2\right\}}{\left[\frac{(1-\epsilon(m_k))}{V_g^{m_k}} + \frac{\epsilon(m_k)}{m_k V_g^{m_k-1}\sqrt{(2\pi)^{n_z}|R_k|}}\sum_{r=1}^{m_k}\exp\left\{-\frac{1}{2}\sum_{j=1}^{n_z} U_{rj}[l]^2\right\}\right]} \tag{9.39}$$

where $U_{ij}[l]$, $i = 1, \ldots, m_k$; $j = 1, \ldots, n_z$; $l = 1, \ldots, N_p$ are N_p IID random variables drawn from a Uniform distribution on $[-g, g]$ (i.e. each $U_{ij}[l] \sim U[-g, g]$).

In applications for which this numerical approximation is too computationally expensive, analytical approximations, such as those presented in [40], may prove invaluable.

9.5.2.3 Extension to multi-sensor systems

In the case of an N_s sensor system, with independent measurement processes at each sensor, (9.32) generalizes to:

$$J_Z(k) = \sum_{i=1}^{N_s} q_k^i E_{X_k}\left[\left(H_k^i\right)'\left(R_k^i\right)^{-1}H_k^i\right] \tag{9.40}$$

where the superscript 'i' denotes the terms corresponding to sensor i.

9.5.3 Measurement sequence conditioning bound

9.5.3.1 General approach

Let $m_{1:k}$ denote the sequence comprising of the number of measurements available at sampling times $1, \ldots, k$, i.e. $m_{1:k} \triangleq \{m_1, \ldots, m_k\}$. The MSC approach [43] creates an MSE estimator performance bound as follows:

$$E\left[\left(\hat{X}_k - X_k\right)\left(\hat{X}_k - X_k\right)'\right] = E_{m_{1:k}}\left[E\left[\left(\hat{X}_k - X_k\right)\left(\hat{X}_k - X_k\right)'|m_{1:k}\right]\right] \tag{9.41}$$

$$\geq E_{m_{1:k}}\left[J_k^{-1}(m_{1:k})\right] \tag{9.42}$$

$$= \sum_{m_{1:k}}\left[Pr(m_{1:k}) \times J_k^{-1}(m_{1:k})\right] \tag{9.43}$$

$$\triangleq \text{MSC PCRB} \tag{9.44}$$

where $Pr(m_{1:k})$ is the probability of the sequence of measurements $m_{1:k}$ occurring, i.e.:

$$Pr(m_{1:k}) = \prod_{i=1}^{k} p(m_i) \tag{9.45}$$

with $p(m_i)$ given by, e.g. (9.38). $J_k(m_{1:k})$ is the FIM conditional on the measurement sequence $m_{1:k}$.

Conditioning on $m_{1:k}$, and repeating the derivation of [9], the recursive formula for the conditional FIM is given by:

$$J_k(m_{1:k}) = D_{k-1}^{33} - \left(D_{k-1}^{12}\right)' \left[J_{k-1}(m_{1:k-1}) + D_{k-1}^{11}\right]^{-1} D_{k-1}^{12} + J_Z(k : m_k) \tag{9.46}$$

$J_Z(k : m_k)$ is again the measurement contribution at sampling time k given that there are m_k measurements at that time (see (9.30) and (9.31)). The initial FIM is given by $J_0 = C_0^{-1}$ irrespective of the sequence $m_{1:k}$.

If the target dynamics are linear, then (9.46) can be simplified as follows (see (9.24)):

$$J_k(m_{1:k}) = \left(\Sigma_{k-1} + A_{k-1} J_{k-1}(m_{1:k-1})^{-1} A_{k-1}'\right)^{-1} + J_Z(k : m_k) \tag{9.47}$$

The MSC approach generalizes the enumeration approach of [41] to the case in which there are both false alarms and missed detections. To see this, if there are no false alarms (i.e. $\lambda = 0$), then $m_k = 0$ or 1 and it can easily be shown that $q_k(1) = 1$. Hence, the approach of conditioning on the measurement sequence reduces to conditioning on the detection sequence, as in [41].

9.5.3.2 Extension to multi-sensor systems

To extend the MSC formulation to an N_s sensor system, $m_{1:k}$ is replaced with $\mathcal{M}_{1:k} \triangleq \{M_1, \ldots, M_k\}$ in the recursions (9.46) and (9.47), where $M_k \triangleq \left\{m_k^1, \ldots, m_k^{N_S}\right\}$ and m_k^i denotes the number of measurements generated by sensor i at sampling time k. The measurement contribution given by (9.31) then generalizes to:

$$J_Z(k : M_k) = \sum_{i=1}^{N_s} q_k^i\left(m_k^i\right) E_{X_k}\left[\left(H_k^i\right)'\left(R_k^i\right)^{-1} H_k^i\right] \tag{9.48}$$

Again, the superscript 'i' denotes the terms corresponding to sensor i.

9.5.4 Measurement existence sequence conditioning bound

The MESC approach [44] is similar in principle to the MSC approach [43], but rather than condition on the number of measurements generated at each sampling time, the MESC approach conditions on the *existence* of at least one measurement. Therefore, instead of conditioning on $m_{1:k}$, the MESC approach conditions on

$e_{1:k} \triangleq \{e_1, \ldots, e_k\}$ where $e_k = 1$ if $m_k \geq 1$ and $e_k = 0$ otherwise. The performance bound is then given as follows:

$$\text{MESC PCRB} \triangleq \sum_{e_{1:k}} \left[Pr(e_{1:k}) \times J_k^{-1}(e_{1:k}) \right] \tag{9.49}$$

Repeating the derivation of the recursive formula (9.11), conditional this time on $e_{1:k}$, it can easily be shown that:

$$J_k(e_{1:k}) = D_{k-1}^{33} - \left(D_{k-1}^{12}\right)' \left[J_{k-1}(e_{1:k-1}) + D_{k-1}^{11} \right]^{-1} D_{k-1}^{12} + J_Z(k : e_k) \tag{9.50}$$

Again, the measurement contribution is zero if there are no measurements, i.e. $J_Z(k : e_k = 0) = 0$. In the case $e_k = 1$, it can then be shown that [44]:

$$J_Z(k : e_k = 1) = \frac{q_k}{Pr(e_k = 1)} E_{X_k}\left[H_k' R_k^{-1} H_k \right] \tag{9.51}$$

where $Pr(e_k = 1) = [1 - p(0)]$, with $p(0)$ again given by, e.g. (9.38). The IRF, q_k, is again as given in (9.33). Finally, if the target dynamics are linear, (9.50) can be simplified as follows (see (9.24)):

$$J_k(e_{1:k}) = \left(\Sigma_{k-1} + A_{k-1} J_{k-1}(e_{1:k-1})^{-1} A_{k-1}' \right)^{-1} + J_Z(k : e_k) \tag{9.52}$$

The extension to multi-sensor systems is again straightforward but is omitted for brevity.

9.5.5 *Relationships between the performance bounds*

The following relationships, proven in [44], hold between the three performance bounds:

$$\text{IRF PCRB} \leq \text{MESC PCRB} \leq \text{MSC PCRB}, \quad \text{for all sampling times, } k \tag{9.53}$$

It is noted that IRF PCRB $\leq$ MSC PCRB was first proven in [42] for the case with no false alarms and later proven in [43] in the general case. It is also noted that the inequalities (9.53) hold in general and are not reliant on the measurement model prescribed in Section (5.1). Indeed, the proofs of the inequalities (9.53) are reliant only on convexity of the matrix inversion operation and Jensen's inequality (e.g. see Appendix A in [42]).

There are three special cases that are worthy of consideration. These are as follows:

- *Case 1:* There are no false alarms (i.e. $\lambda = 0$). In this case, $m_k = e_k$ $(= 0 \text{ or } 1)$ for all k and the MSC and MESC approaches give identical bounds, equal to the enumeration bound of [41].
- *Case 2:* There are no missed detections (i.e. $P_d = 1$). In this case, $e_k = 1$ for all k, $Pr(e_k = 1) = 1$ and the IRF and MESC approaches give identical bounds.

- *Case 3:* There are no false alarms and no missed detections. In this case, $m_k = e_k = 1$ for all k; and $q_k = q_k(1) = 1$. Clearly, in this case, all three performance bounds are identical, with each giving the no-clutter PCRB.

The IRF PCRB is computationally the simplest of the three performance bounds but does not consider the impact of the actual sequence of measurements (it simply scales the measurement contribution by a constant factor at each sampling time). However, the actual sequence of measurements can have a critical impact on tracking performance, particularly after track formation, in which target state uncertainty can be high. At such times, the IRF PCRB can be optimistic compared to the MSC PCRB [42,43]. Differences between the two bounds are greatest when the measurements are accurate and the initial target state uncertainty is large.

The MESC approach has the advantage that it can be enumerated exactly, because there are precisely 2^k existence sequences $e_{1:k}$ at each sampling time k. By comparison, the MSC approach has an infinite number of potential measurement sequences. Many of these sequences have an extremely low probability of occurrence and can be instantly discounted. However, in implementing both the MSC and MESC approaches, the number of sequences that need to be considered is still prohibitively large, even for relatively small values of k. A more scalable method of estimating the MSC PCRB (or MESC PCRB) is to sample measurement (or existence) sequences and determine the average value of the sequence dependent bound (see Section VI in [43]). Although the MSC approach produces the tightest performance bound, simulations have yielded insignificant differences between the MESC and MSC bounds [44]. Furthermore, as the number of sampling times increases, all three bounds converge to the same steady-state value [43,44].

9.6 Simulations

9.6.1 Scenario specification

We consider the problem of tracking a single target in a three-dimensional Cartesian space. The target state is denoted by $X_k \triangleq [x_k \ \dot{x}_k \ y_k \ \dot{y}_k \ z_k \ \dot{z}_k]'$, where notation is standard. The target motion in the x- and y- coordinate directions is nearly constant velocity (NCV) (e.g. [56]), with the target having constant velocity in the z-coordinate direction. The target state evolution is therefore given by:

$$X_{k+1} = F_k X_k + \omega_k \tag{9.54}$$

where $\omega_k \sim \mathcal{N}(0, \Sigma_k)$. The matrices F_k and Σ_k are given as follows:

$$F_k = I_3 \otimes \begin{pmatrix} 1 & T \\ 0 & 1 \end{pmatrix} \qquad \Sigma_k = \ell \times \begin{pmatrix} T^3/3 & T^2/2 & 0 & 0 & 0 & 0 \\ T^2/2 & T & 0 & 0 & 0 & 0 \\ 0 & 0 & T^3/3 & T^2/2 & 0 & 0 \\ 0 & 0 & T^2/2 & T & 0 & 0 \\ 0 & 0 & 0 & 0 & 0 & 0 \\ 0 & 0 & 0 & 0 & 0 & 0 \end{pmatrix} \tag{9.55}$$

The symbol $\otimes$ denotes the Kronecker product; ℓ is the 'power spectral density' of the NCV motion and T is the time interval between successive measurements.

A single sensor, positioned at the origin, provides measurements of range (r_k), azimuth (θ_k) and elevation (ϕ_k). Each target generated measurement is therefore given by:

$$Z_k^{\mathrm{TG}} = (r_k \;\; \theta_k \;\; \phi_k)' + \epsilon_k \tag{9.56}$$

where:

$$r_k = \sqrt{x_k^2 + y_k^2 + z_k^2} \tag{9.57}$$

$$\theta_k = \tan^{-1}(y_k/x_k) \tag{9.58}$$

$$\phi_k = \tan^{-1}\left(z_k/\sqrt{x_k^2 + y_k^2}\right) \tag{9.59}$$

The measurement error $\epsilon_k \sim \mathcal{N}(0, R_k)$, with covariance $R_k = \mathrm{diag}(\sigma_r^2, \sigma_\theta^2, \sigma_\phi^2)$. The parameters σ_r, σ_θ and σ_ϕ are the range, azimuth and elevation measurement error standard deviations (SDs), respectively. The sensor has a field of view of $[-\pi, \pi]$ in azimuth, and $[-\pi/2, \pi/2]$ in elevation. The maximum detection range is 50 km. The parameter settings used in the simulations are summarized in Table 9.1.

9.6.2 *Tracking methodology*

The tracking methodology has the following features:

1. Nearest neighbour data association is used to associate measurements to tracks, using a gate of $g = 4$ SDs.
2. Tracks are initialized based on 'three-out-of-three' logic, whereby measurements on three successive scans that are not associated with an existing track must be consistent with the potential trajectory of a target, allowing for a maximum velocity of 2 km/s. [This velocity is significantly greater than the achievable velocity of the target, but extensive analysis demonstrated that this value results in timely initialization of the (true) target track, whilst creating very few false tracks.]

Table 9.1 Target and sensor parameter settings used in the simulations

Parameter	**Value**
Initial target state, X_0	(20 km, −200 m/s, 20 km, 0 m/s, 1 km, 0 m/s)
Power spectral density, ℓ (of NCV motion)	30 $\mathrm{m}^2/\mathrm{s}^3$
Sensor location (stationary)	(0 m, 0 m, 0 m)
Sampling interval, T	1 s (i.e. a sampling rate of 1 Hz)
Range measurement error SD, σ_r	50 m
Azimuth measurement error SD, σ_θ	0.01 rad ($\sim$0.6°)
Elevation measurement error SD, σ_ϕ	0.01 rad ($\sim$0.6°)
Target probability of detection, P_d	0.8, 0.9 or 1.0
False alarm rate (FAR), λ	0.1 or 0.01 $\mathrm{m}^{-1}\,\mathrm{rad}^{-2}$

3. For each track that is formed, the initial target state estimate is determined using 'two-point' initialization, based on the two most recent measurements.[4]
4. For each track, the prediction and update steps are performed using an EKF.
5. A track is deleted if no measurement is associated with it on any one of 10 successive scans or the estimated target velocity exceeds 4 km/s.

These are all standard tracker features, and the reader is referred to [56] for further details.

9.6.3 Quantifying the performance of the tracker

The performance of the tracking algorithm is evaluated using 1,000 simulations, each of duration 100 s. The initial target state, X_0 for each trajectory is given in Table 9.1, and each trajectory evolves according to the model (9.54). The 1,000 target trajectories are shown in Figure 9.1(a).

To reduce the influence of outliers, the $100\alpha\%$ worst runs (in terms of tracker location root mean square error [RMSE]) are removed from the analysis.[5] The tracker location RMSE and velocity RMSE, at each sampling time, are then given as follows:

$$\text{location RMSE at time } k = \sqrt{\frac{1}{1000(1-\alpha)}\sum_{i=1}^{1000(1-\alpha)}\left\{\left(x_k^i-\hat{x}_k^i\right)^2+\left(y_k^i-\hat{y}_k^i\right)^2+\left(z_k^i-\hat{z}_k^i\right)^2\right\}} \tag{9.60}$$

$$\text{velocity RMSE at time } k = \sqrt{\frac{1}{1000(1-\alpha)}\sum_{i=1}^{1000(1-\alpha)}\left\{\left(\dot{x}_k^i-\hat{\dot{x}}_k^i\right)^2+\left(\dot{y}_k^i-\hat{\dot{y}}_k^i\right)^2+\left(\dot{z}_k^i-\hat{\dot{z}}_k^i\right)^2\right\}} \tag{9.61}$$

where $(\hat{x}_k^i,\hat{\dot{x}}_k^i,\hat{y}_k^i,\hat{\dot{y}}_k^i,\hat{z}_k^i,\hat{\dot{z}}_k^i)$ is the EKF target state estimate at sampling time k on (the included) run number i; and the true target state at sampling time k for this run is given by $X_k^i \triangleq (x_k^i,\dot{x}_k^i,y_k^i,\dot{y}_k^i,z_k^i,\dot{z}_k^i)$.

In implementing the tracker, in order to keep the number of false alarm measurements manageable, false alarms (occurring with rate λ) are only considered in an extended region around the true target location (rather than throughout the sensor field of view).[6]

[4]That is, the location estimate is determined from the most recent measurement, with the velocity estimated using the difference between the locations specified by the two most recent measurements. It is straightforward to determine the error covariance of this initial estimate, using the measurement error covariances associated with each measurement.

[5]In the simulations that follow, the 0.5% worst runs (i.e. 5 runs) are excluded from the RMSE calculations.

[6]This extended region is [±250 m, ±0.05 rad, ±0.05 rad], in the [range, azimuth, elevation] measurement space. This gives an average of 0.5 (when $\lambda = 0.1$) or 0.05 (when $\lambda = 0.01$) false alarm measurements per sampling time.

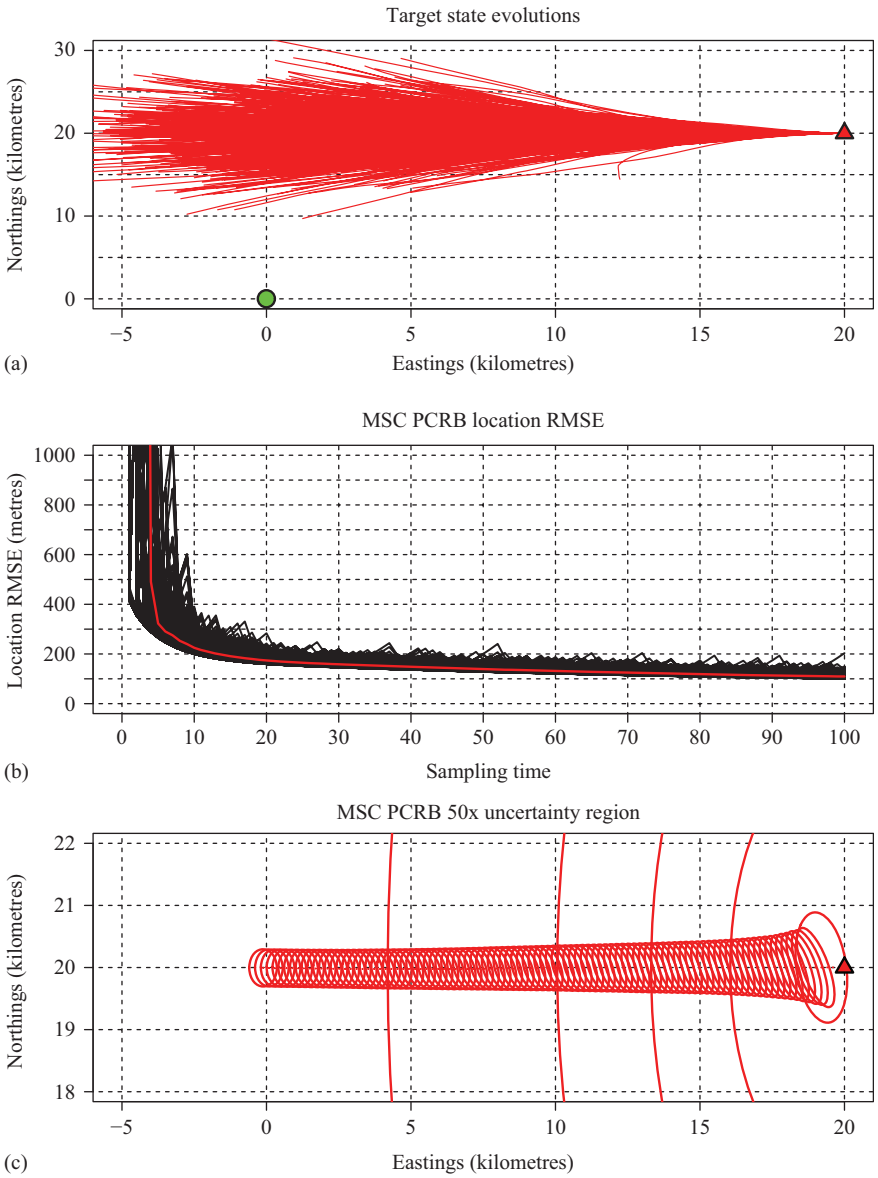

Figure 9.1 ***(a)*** *The 1,000 target trajectories used in the simulations (red lines, the starting location of each trajectory is shown by the triangle); also shown is the sensor location (circle).* ***(b)*** *The MSC PCRB location RMSE (red line), plotted against sampling time; also shown are the 1,000 conditional PCRBs used in calculating the bound (black lines).* ***(c)*** *The MSC PCRB location RMSEs shown in the flat-Earth plane; each ellipse gives a 50 standard deviation uncertainty region. In this exemplar,* $P_d = 0.8$ *and* $\lambda = 0.1$

At sampling times for which multiple tracks exist (as a result of tracks being formed from false alarm measurements), the track closest to the true target location (based on the Mahalanobis distance) is used in the analysis.

9.6.4 Calculating the posterior Cramér–Rao bounds

The IRF PCRB and the MSC PCRB are calculated. In the scenarios considered, the MESC PCRB is indistinguishable from the MSC PCRB and is not shown.

9.6.4.1 Information reduction factor bound

The IRF PCRB is given by J_k^{-1}, with the sequence of FIMs given by the recursion (24). The measurement contribution at time k (see (9.32)) is estimated as follows:

$$J_Z(k) \approx \frac{q_k}{1000} \sum_{i=1}^{1000} H_k(i)' R_k^{-1} H_k(i) \tag{9.62}$$

In Table 9.2, the value of the overall IRF, q_k, is shown for each parameter combination considered.

Each IRF is calculated using the numerical approximation (9.39) of the 'Numerical approximation' section, using 100,000 samples; and the overall IRF is given by (9.33).

It is noted that $\lambda = 0.01$ results in very few false alarms being generated (i.e. an average of 0.0256 false alarms in the gated observation region per sampling time). Hence, in this case, $q_k(1) \approx 1.0$ and $p(1) \approx 1.0$, which gives $q_k \approx P_d$.

$H_k(i)$ is the Jacobian of the measurement vector evaluated at sampling time k for the ith target trajectory (i.e. $H_k(i) = \nabla_{X_k}[h_k(X_k^i)']$). This Jacobian is given as follows:

$$H_k = \begin{pmatrix} x_k/r_k & 0 & y_k/r_k & 0 & z_k/r_k & 0 \\ -y_k/d_k^2 & 0 & x_k/d_k^2 & 0 & 0 & 0 \\ -x_k z_k/r_k^2 d_k & 0 & -y_k z_k/r_k^2 d_k & 0 & d_k/r_k^2 & 0 \end{pmatrix} \tag{9.63}$$

where d_k is the flat-Earth range, i.e. $d_k = \sqrt{x_k^2 + y_k^2}$.

Table 9.2 The overall IRF, q_k, for each of the parameter combinations considered

FAR, λ	Probability of detection, P_d	Overall IRF, q_k
0.1	0.8	0.74
”	0.9	0.85
”	1.0	0.97
0.01	0.8	0.80
”	0.9	0.90
”	1.0	1.00

The PCRB is initialized with $J_0 = C_0^{-1}$, with the initial target state covariance C_0 given in Table 9.3. The value of the initial target state covariance is motivated by the following:

1. The initial target location and velocity in the flat-Earth plane (i.e. x–y plane) are highly uncertain.
2. Target altitude is more constrained, and the target is likely to have a relatively low velocity in the vertical plane.

9.6.4.2 Measurement sequence conditioned bound

The MSC PCRB is estimated using 1,000 measurement sequences, $m_{1:k}^j$, $j = 1, \ldots, 1{,}000$, i.e.:

$$\text{MSC PCRB} \approx \frac{1}{1{,}000} \sum_{j=1}^{1{,}000} J_k^{-1}\left(m_{1:k}^j\right) \tag{9.64}$$

with $J_k(m_{1:k}^j)$ given by (9.47), and referred to as the 'conditional PCRB'. Each conditional PCRB is initialized with $J_0 = C_0^{-1}$.

The measurement contribution at time k given that there are m_k measurements at that time (see (9.31)) is estimated as follows:

$$J_Z(k : m_k) \approx \frac{q_k(m_k)}{1{,}000} \sum_{i=1}^{1{,}000} H_k(i)' R_k^{-1} H_k(i) \tag{9.65}$$

In Figure 9.1(b), an example is provided showing 1,000 conditional PCRBs and the resulting MSC PCRB for the scenario in which $P_d = 0.8$ and $\lambda = 0.1$. In Figure 9.1(c), a representation of the MSC PCRB in the flat-Earth plane is shown. Following this, in Figure 9.2, the IRFs $q_k(m_k)$, $m_k = 1, \ldots, 5$, are shown for the parameter combinations considered (i.e. $P_d = 0.8,\ 0.9,\ 1.0$; and $\lambda = 0.1,\ 0.01$). Table 9.3 summarizes all of the parameters used in the PCRB calculations.

Table 9.3 Parameter values used in the PCRB calculations

Parameter	Value
Initial target state covariance, C_0	$\text{diag}\left(10^{10}, 10^6, 10^{10}, 10^6, 10^6, 10^2\right)$
Number of target state evolutions, N (see Figure 9.1(a))	1,000
Number of measurement sequences, m_k (MSC approach)	1,000
Number of samples in IRF approximations, N_p	100,000
Gate standard deviations, g	4
Gate volume, V_g	2.56 m rad^2
Average false alarms in the gated observation region, λV_g	0.256 ($\lambda = 0.1$), 0.0256 ($\lambda = 0.01$)

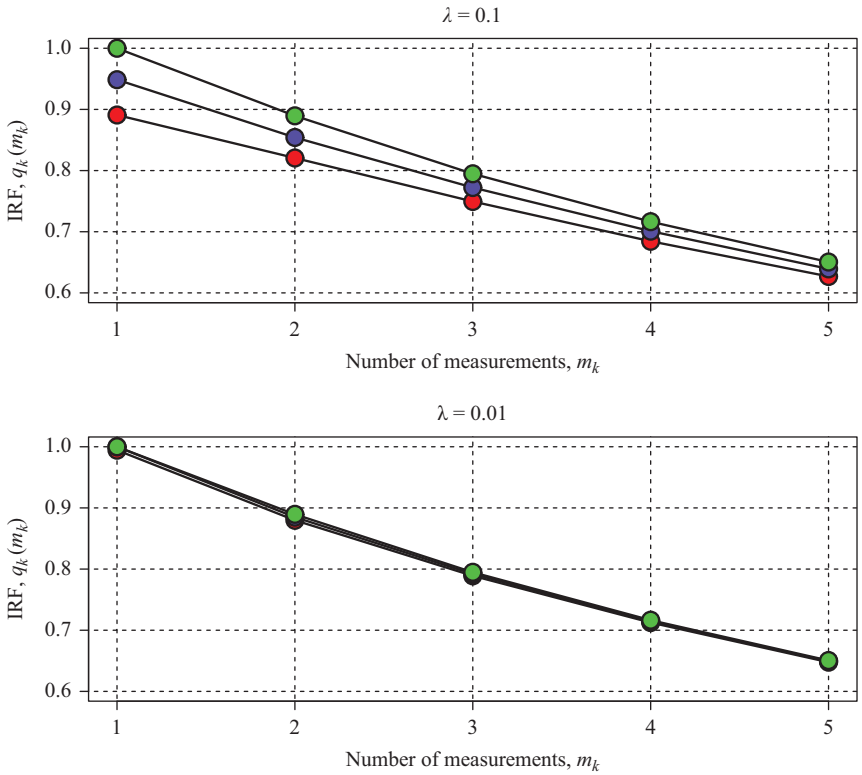

Figure 9.2 The IRF, $q_k(m_k)$, plotted against the number of measurements, m_k, for three P_d values and two λ values. Key: red circles: $P_d = 0.8$, blue circles: $P_d = 0.9$, green circles: $P_d = 1.0$. Each IRF is calculated using the numerical approximation (39) of the 'Numerical approximation' section, using 100,000 samples

9.6.5 Simulation results

Simulations results are shown in Figures 9.3–9.6 and Table 9.4. To elaborate, in Figure 9.3, the location and velocity RMSEs of the IRF PCRB, MSC PCRB and EKF are shown, for $\lambda = 0.1$. The corresponding RMSEs for $\lambda = 0.01$ are shown in Figure 9.5. Figures 9.4 and 9.6 then show the percentage increases in the values of the MSC PCRB and EKF RMSE over that of the IRF PCRB for $\lambda = 0.1$ and $\lambda = 0.01$, respectively. A comparison of the algorithm runtimes is given in Table 9.4. It is noted that $\lambda = 0.01$ results in very few false alarms (i.e. an average of 0.0256 false alarms in the gated observation region per sampling time). As a result, the IRF and MSC PCRBs are virtually unaffected by false alarms in this case.

The following observations are made:

1. Differences between the IRF PCRB and the MSC PCRB are greatest initially, when the actual sequence of measurements can have a critical impact on tracking performance.

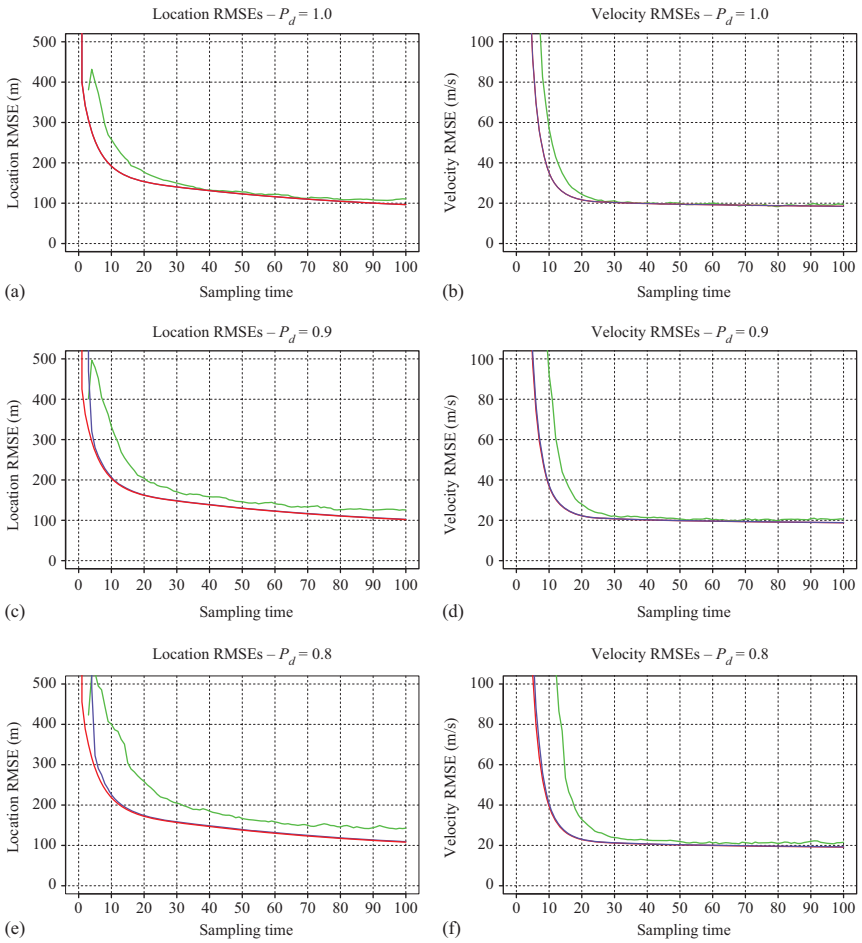

Figure 9.3 Comparison between the PCRB RMSEs and tracker RMSEs for $\lambda = 0.1$, and three different P_d values. Key: red lines: IRF PCRB RMSE, blue lines: MSC PCRB RMSE, green lines: EKF RMSE. In each case, the 0.5% worst performing runs are excluded from the tracker RMSE calculations

2. The IRF PCRB and MSC PCRB converge to the same steady-state values as the number of sampling times increases.
3. When the probability of detection is unity (i.e. $P_d = 1.0$), there is always at least one measurement per sampling time, and the IRF PCRB and MSC PCRB are virtually identical at all sampling times.[7]

[7]This is likely to be generally true as a result of the following facts: (i) when $P_d = 1.0$, the IRF and MESC bounds are identical; (ii) the MESC and MSC bounds have been shown to be virtually identical [44].

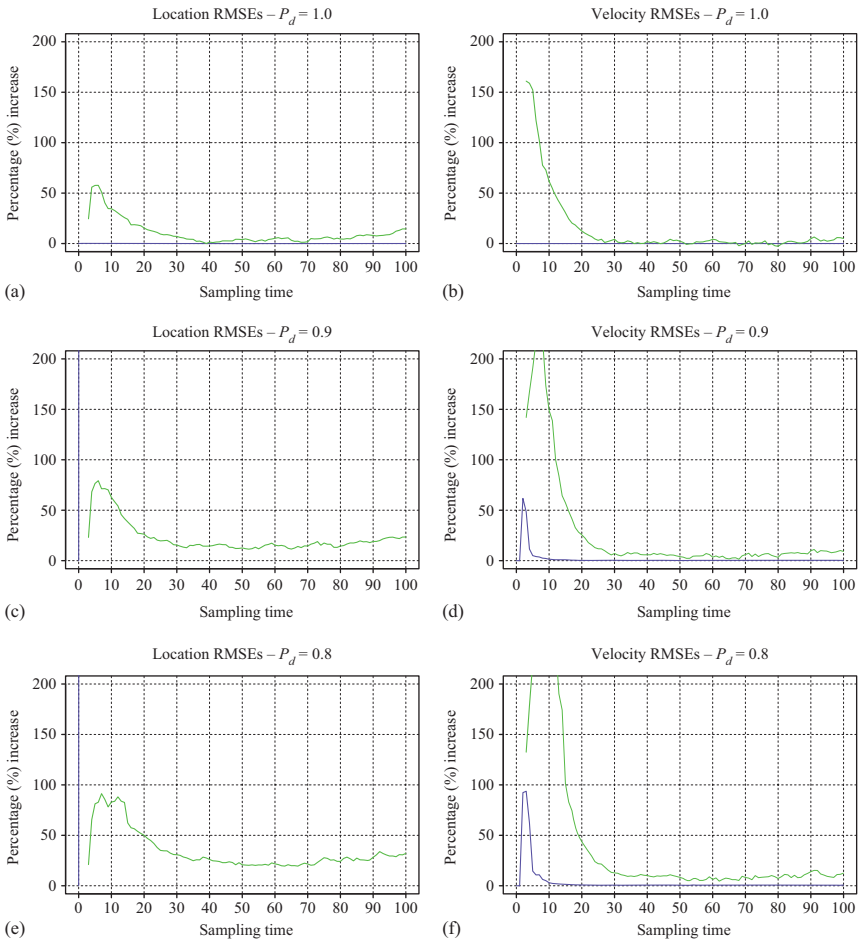

Figure 9.4 Percentage increase in the value of the MSC PCRB RMSE over that of the IRF PCRB RMSE (i.e. $100 \times \frac{(RMSE_{MSC} - RMSE_{IRF})}{RMSE_{IRF}}$; blue lines); and the percentage increase in the value of the EKF RMSE over that of the IRF PCRB RMSE (i.e. $100 \times \frac{(RMSE_{EKF} - RMSE_{IRF})}{RMSE_{IRF}}$; green lines). The corresponding RMSE values are shown in Figure 9.3

4. Differences between the PCRB RMSEs and EKF RMSEs are greatest immediately following track formation, because of the difficulty in accurately estimating the initial velocity of the target.
5. In the long-run, the EKF RMSE is consistently with 30% of the PCRB RMSEs, with differences often much smaller (albeit with the 5 worst runs [i.e. 0.5% of runs] excluded from the EKF RMSE calculations). Hence, as well as providing an estimation accuracy bound, the PCRB is an accurate predictor of the long-run performance of the tracking algorithm.

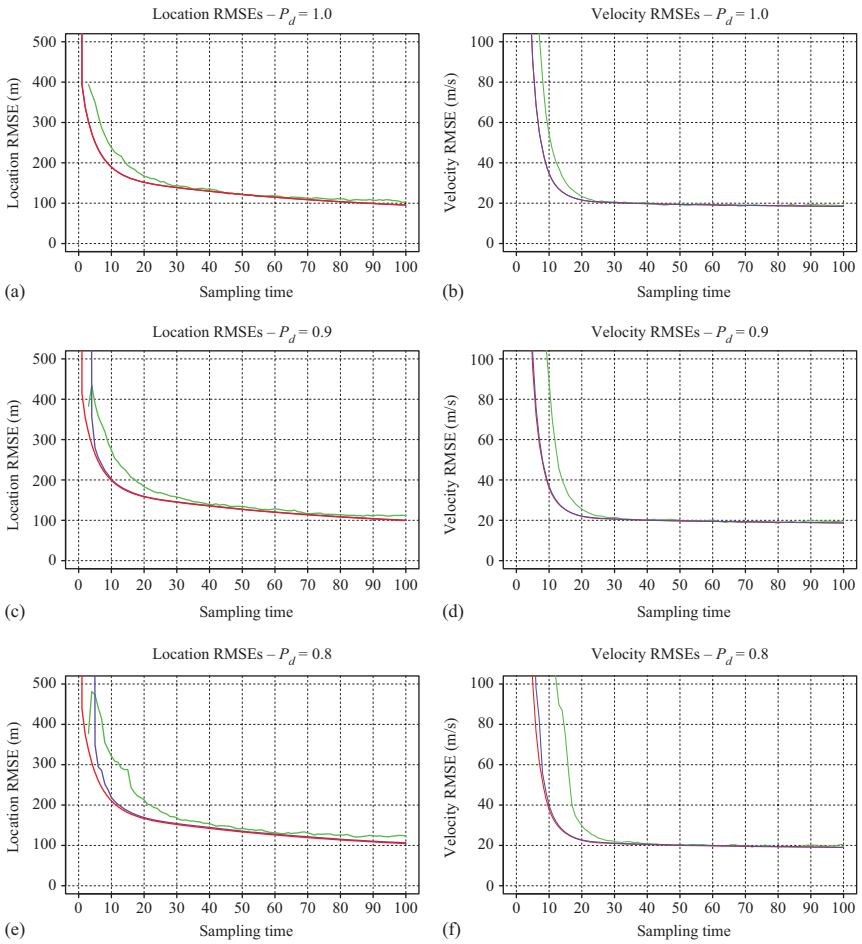

Figure 9.5 Comparison between the PCRB RMSEs and tracker RMSEs for $\lambda = 0.01$, and three different P_d values. Key: red lines: IRF PCRB RMSE, blue lines: MSC PCRB RMSE, green lines: EKF RMSE. In each case, the 0.5% worst performing runs are excluded from the tracker RMSE calculations

6. The PCRB and EKF RMSEs increase only very slightly as the FAR is increased from 0.01 to 0.1. This is because even at the higher rate, the prevalence of false alarms is still quite low.
7. The runtime of the MSC PCRB increases almost linearly with the number of measurement sequences and is over 300 times greater than the runtime of the IRF PCRB when 1,000 measurement sequence realizations are used.
8. The runtime of the tracker is highly dependent on the FAR, which has a critical impact on the track initialization logic. Furthermore, higher FARs result in a greater number of tracks being formed, which thereby increases the number of

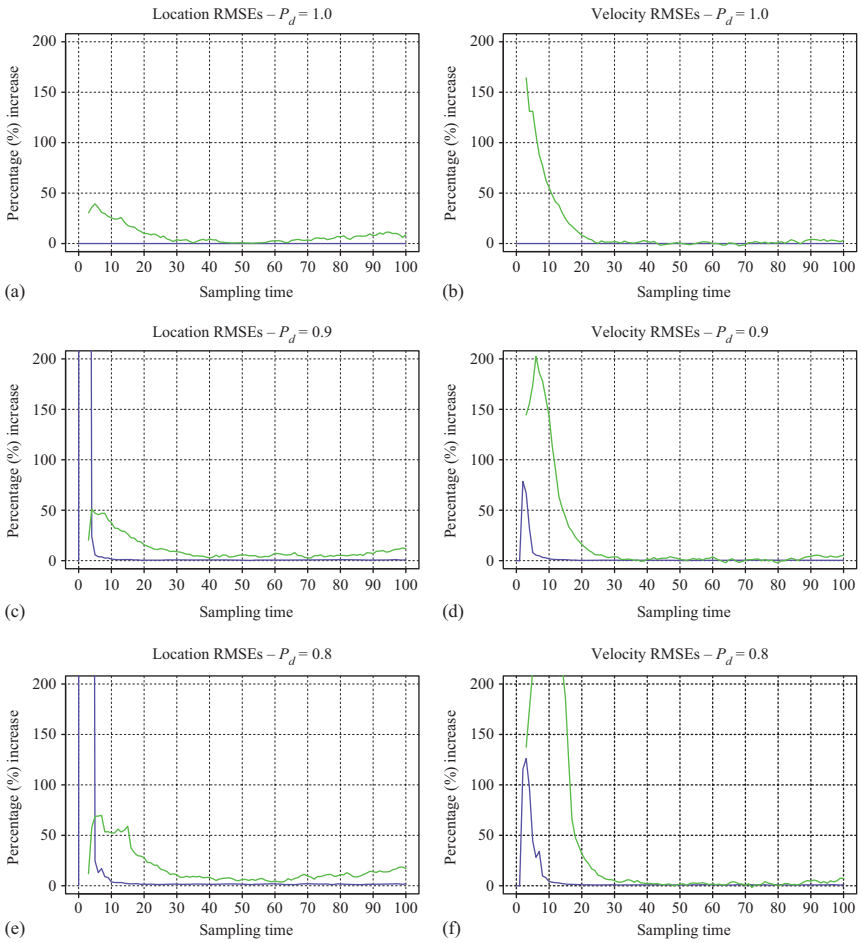

Figure 9.6 Percentage increase in the value of the MSC PCRB RMSE over that of the IRF PCRB RMSE (i.e. $100 \times \frac{(RMSE_{MSC} - RMSE_{IRF})}{RMSE_{IRF}}$; blue lines); and the percentage increase in the value of the EKF RMSE over that of the IRF PCRB RMSE (i.e. $100 \times \frac{(RMSE_{EKF} - RMSE_{IRF})}{RMSE_{IRF}}$; green lines). The corresponding RMSE values are shown in Figure 9.5

parallel EKFs that have to be utilized. Consequently, even when the FAR is low, the time required for the tracker to perform 1,000 simulations is over 20 times greater than that of the MSC PCRB approach; and over 7,000 times greater than the runtime of the IRF PCRB approach.

Observations #2 and #7 highlight the fact that only in the early stages following track initialization should the MSC PCRB be preferred to the IRF PCRB, because of the increased computational overhead of the MSC approach.

Table 9.4 Runtime of each algorithm (in seconds), for each of the parameter combinations considered

FAR, λ	P_d	EKF	MSC PCRB	IRF PCRB
0.1	0.8	158	2.3	0.007
”	0.9	184	”	”
”	1.0	188	”	”
0.01	0.8	50	”	”
”	0.9	51	”	”
”	1.0	52	”	”

Furthermore, observations #5 and #8 demonstrate the utility of using a PCRB as a predictor of the performance of a tracker, particularly in sensor management applications. The PCRB allows the (predicted) performance of different combinations of sensors to be quickly evaluated, without the need to resort to computationally expense tracker Monte Carlo simulations.

The EKF run time is based on 1,000 simulations, each with 101 sampling times. The MSC PCRB run-time is based on approximating the bound using 1,000 measurement sequences. All simulations were programmed in C and run on an Intel® Core™ i5-430M processor (2.26 GHz).

9.7 Further development of posterior Cramér–Rao bounds

9.7.1 Improvements in computational efficiency

Cluttered environment PCRB methodologies can be computationally expensive, as a result of the requirement to sample a large number of measurement or existence sequences [43,44]. However, there may be the potential to develop more computationally efficient bounds that have the bounding capability of the MSC [43] and MESC [44] approaches.

Furthermore, the conditional PCRB (CPCRB)[8] [60] would potentially be invaluable for sensor management (e.g. [11]) and cognitive radar [63] applications. However, additional work is required to express the CPCRB as a recursion without the need to ‘restart’ the computation on each iteration. This would improve computational efficiency and enable the CPCRB to be utilized in time-critical, multi-step sensor management applications. These include multi-step sensor selection problems for which the number of potential sensor combinations requiring evaluation is currently prohibitively large.

It is noted that the cluttered environment PCRB methodologies [43,44] and the CPCRB approach [60] have the common need to condition, invert and average. The order in which these computations are performed impacts on the ‘tightness’ of the bound. There is then a trade-off between computational efficiency and tightness.

[8]The CPCRB is conditional on the measurements that have already been generated up to the current sampling time.

9.7.2 Passive coherent location networks

9.7.2.1 General scenario

Consider the problem of optimizing the transmitter–receiver pairings in a passive coherent location (PCL) network [64] in order to accurately track an evasive target (e.g. see Figure 9.7).

For a bistatic system, there is a requirement to optimally select the transmitter–receiver pair. For a multistatic system, the requirement is to associate a set of transmitters to each receiver which will enable the target location to be estimated via multi-lateration (e.g. [65]).

The tracking accuracy achievable by a PCL network is dependent on a number of factors, including (but not limited to) the following:

1. The sampling rate ($1/T$ Hz), probability of detection (P_d) and FAR (λ).
2. The receiver (RX) and transmitter (TX) locations.
3. The bistatic ambiguity function of the received waveforms.
4. The accuracy of the range (i.e. σ_r), azimuth (i.e. σ_θ) and elevation (i.e. σ_ϕ) measurements.
5. The target trajectory and manoeuvrability.
6. The signal-to-noise power ratio.

It is noted that a PCL network can also potentially exploit a wide spectrum of 'waveforms of opportunity', e.g. FM, DAB, DVB-T, LTE, GSM, UMTS, WiFi and WiMax. This would enable the network to take advantage of the best properties of each waveform in order to provide extended coverage and potentially improve target detection/localization capability. For example, FM signals may provide early

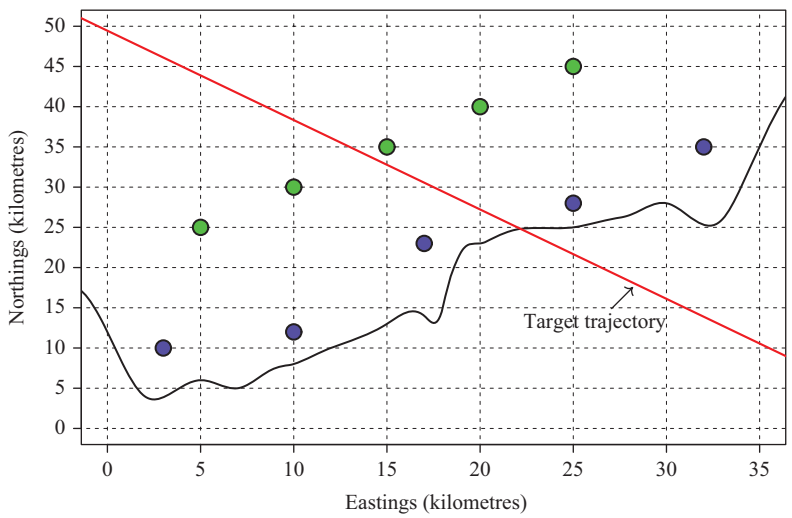

Figure 9.7 A PCL network. Transmitters of opportunity are shown by green circles, and receivers are shown by blue circles. A target trajectory (moving in a North-Westerly direction) is shown by the red line

warning due to their long range capability. FM detections could then be used to cue the DVB-T and DAB components of the passive receiver, which are able to provide improved range resolution and extended elevation coverage.

9.7.2.2 Complicating factor – state-dependent measurement errors

The PCRB is well established as an invaluable tool for predicting the performance of a network of sensors. The PCRB also depends on 1–6 and enables the accuracy of target state estimation to be predicted without the need to resort to computationally expensive Monte Carlo simulations. Exploiting the PCRB enables suitable selection of either an RX/TX pair (for the bistatic case) or an RX/TX cluster (for the multi-static case) to be performed in order to minimize estimation error. However, direct application of the PCRB is not straightforward in this application, because the measurement error SD can be a function of the transmitter–receiver-target geometry.

In Figure 9.8, this phenomenon is demonstrated for a bistatic system, with co-planar transmitters, receiver and target (see Figure 9.8(a); this exemplar is taken

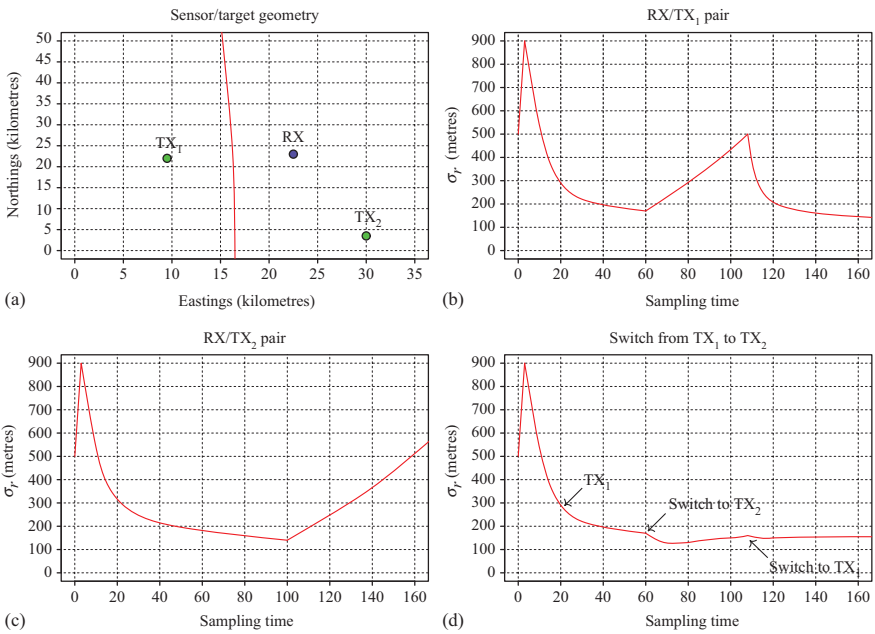

Figure 9.8 An exemplar demonstrating how the sensor/target geometry can affect sensor performance. ***(a)*** *The sensor/target geometry: the target trajectory is shown by the red line, with the target moving in a Northerly direction at around 300 m/s; the receiver (RX) and transmitter (TX_1, TX_2) locations are marked by circles.* ***(b)–(d)*** *The range measurement error SD as a function of time; in* ***(b),*** *the receiver is paired with receiver TX_1; in* ***(c),*** *the receiver is paired with receiver TX_2; in* ***(d),*** *the transmitter is switched from TX_1 to TX_2 and back again at the times indicated*

from slides 51–52 of [64]). When the target is close to the RX/TX_1 baseline, the range measurement error SD increases rapidly (i.e. between sampling times 60 and 108), as shown in Figure 9.8(b). The peak in the range measurement error SD is the result of both the deterministic null in the detection probability and the de-focus of the bistatic ambiguity function. The deterministic null in the receiver antenna pattern is set in the direction of the transmitter in order to avoid directly receiving the transmitter radiation, which would blind the receiver. However, the target trajectory is such that the RX/TX_2 pair is not prone to this effect (see Figure 9.8(c)). Therefore, the range measurement error SD can be kept consistently low by temporarily switching the transmitter from TX_1 to TX_2 as the target approaches the RX/TX_1 baseline (see Figure 9.8(d)).

Direct application of either the MSC or MESC PCRB approaches is problematic in this case. This is because the state-dependent range measurement error SD results in the volume of the gated observation region (see footnote 3), used in generating measurement sequences, also being dependent on the target state. Hence, the target state evolution cannot be decoupled from the generation of the measurement sequences, with the result that the conditional FIM given in (9.46) is dependent on the target state. A possible mechanism for resolving this problem is to use the 'path-dependent conditioning' methodology introduced in Section III of [66], which provides performance measures that are upper bounds on the PCRB. Despite not being lower bounds, these measures can be accurate predictors of the performance of the system. Application of the approach of [66] to PCL network performance prediction is left for future work.

9.7.3 Image fusion

Multi-sensor image fusion typically requires images (e.g. from satellites) to be combined that are generated at different frequencies, view angles and/or polarizations. Furthermore, there is the potential for missed detections of objects of interest (i.e. $P_d < 1$, particularly at low resolutions) and false alarms (i.e. $\lambda > 0$), which can occur at different rates in different imagery. The multi-scale Kalman filter (MKF) [67] provides a valuable tool to optimally fuse such imagery and has found successful applications in radar image fusion [68,69] and remote sensing [70].

There is an ongoing need to determine PCRBs to quantify the optimal performance of image fusion algorithms in estimating the states of objects of interest. Such bounds would need to take into account the changes in resolution, clutter density and probability of detection that can occur in different imagery and would be invaluable in assessing the performance of multi-scale estimation algorithms, such as the MKF.

9.7.4 Data assimilation for meteorology/oceanography

Data assimilation, via the incorporation of noisy measurements into a computer simulation of a real system (e.g. via an ensemble Kalman filter [71,72]), has wide application in the estimation of various spatial–temporal variables (e.g. temperature, pressure, humidity, water-height) for weather forecasting and oceanographic purposes. Forecasting typically utilizes partial differential equation (PDE)

models and exploits sensors that can be prone to missed detections and/or false alarms.

Therefore, there is the potential to exploit cluttered environment PCRB approaches in order to quantify the performance of meteorological/oceanographic forecasting algorithms, e.g. quantify spatial–temporal effects, and the impact of missed detections and false alarms. In developing a PCRB methodology, there is a need to account for the complex dynamic behaviour that can occur within meteorological/oceanographic system, that is characterised via the PDEs models.

9.7.5 Simultaneous localization and mapping

Simultaneous localization and mapping (SLAM) (e.g. see [73,74]) consists of jointly estimating the state of an autonomous agent and generating a map of the surrounding environment via measurements generated by on-board sensors. SLAM lies at the core of most remote sensing and GPS denied robotic navigation applications. In a sense, SLAM is a multi-object estimation problem analogous to MTT. Both SLAM and MTT aim to detect/localize objects of interest, i.e. environmental features/landmarks in the case of SLAM, non-cooperative targets in MTT.

To date, the PCRB has been developed for SLAM only in simplified scenarios (see [75] and references therein). For example, in [75], a SLAM PCRB was determined that assumed perfect data association and used an approximation that required the process noise to be small. In developing a general PCRB methodology for SLAM, it is necessary to take into account the usual sources of uncertainty (e.g. measurement error), as well as the complex data association uncertainty that results from the fact that it is not known whether each measurement is generated by an established map feature, a new feature, or is clutter. Given the similarity to MTT, there is therefore the potential to extend PCRB approaches developed for MTT (e.g. [13,48]) in order to determine a PCRB methodology for SLAM.

9.7.6 Quantum estimation

Quantum estimation theory [76,77] is a reformulation of classical estimation theory in quantum mechanical terms. In fact, classical statistical theory can be seen as a special case of the more general quantum theory. Quantum estimation theory has been exploited in a number of applications, including analogue communication via quantum channels [78]. Furthermore, recently, a quantum Kalman filter (QKF) methodology has been developed. Indeed, in [79], a QKF was developed in order to perform parameter estimation for an optical, probe-laser system. There remains the need to develop PCRBs for quantum applications in order to quantify the optimality of the estimation algorithms that have been developed.

9.8 Summary

This chapter has presented a review of recent developments in the calculation of mean squared error tracker performance bounds, with a strong emphasis on the PCRB. In the last 15 years, there has been an explosion of interest in the PCRB,

primarily as a result of the excellent paper [9], in which an efficient, fixed dimensional recursive formula was derived. As a result, the PCRB can be calculated relatively easily, making it an appealing metric both for assessing tracking algorithm optimality and in conducting predictive sensor resource management.

A review of recent developments provides details of PCRBs for non-linear filtering, manoeuvring target tracking, cluttered environments (i.e. in which there can be false alarms and missed detections) and MTT, as well as highlighting applications in which the bound has been exploited. Following this, details are provided of the recursive formula of [9] and of the PCRB approaches devised in cluttered environments. In such environments, there is a need to resolve the measurement origin uncertainty. This uncertainty is shown to manifest itself as an IRF that degrades tracking performance according to severity of the environment. A tutorial of the key PCRB approaches in cluttered environments [37,43,44] is provided, giving details of all of the key equations necessary to calculate the bounds.

Via simulations, the PCRBs are calculated for a cluttered environment scenario in which a single target is tracked using measurements generated by a stationary radar. The PCRBs are compared to the performance of an EKF tracker, and results demonstrate the utility of using the PCRB as a predictor of the estimation capability of the tracker. Moreover, it is shown that the PCRB allows the potential performance of the system to be efficiently evaluated, without the need to resort to computationally expense tracker Monte Carlo simulations. This confirms the efficacy of exploiting the PCRB in order to perform predictive sensor management.

This chapter also presents a discussion of applications that would benefit greatly from the development of a PCRB methodology. These applications include sensor scheduling in PCL networks, and performance assessment of algorithms designed for image fusion, data assimilation for meteorology/oceanography, SLAM and quantum estimation.

Acknowledgement

A. Farina acknowledges with thanks the exchange of opinions with K. Bell and L. Chisci concerning some parts of Section 9.7.

References

[1] Bergman N. ‘Posterior Cramér–Rao Bounds for Sequential Estimation’ in Doucet A., de Freitas N., Gordon N. (eds.). *Sequential Monte Carlo Methods in Practice*. New York: Springer-Verlag; 2001.

[2] Hernandez M. L. ‘Performance Bounds for Target Tracking: Computationally Efficient Formulations and Associated Applications’ in: Mallick M., Krishnamurthy V., Vo B.-N. (eds.). *Integrated Tracking, Classification, and Sensor Management: Theory and Applications*. John Wiley and Sons/IEEE Press; 2013. pp. 255–309.

[3] Van Trees H. L., Bell K. L. (eds.). *Bayesian Bounds for Parameter Estimation and Nonlinear Filtering/Tracking*. New York: John Wiley and Sons Ltd; 2007.
[4] Farina A., Ristic B. 'Book Review: Bayesian Bounds for Parameter Estimation and Nonlinear Filtering/Tracking'. *IET Radar, Sonar and Navigation*. 2009, vol. 3(3), pp. 285–286.
[5] Bhattacharyya A. 'On Some Analogues of the Amount of Information and their Use in Statistical Estimation'. *Sankhya: The Indian Journal of Statistics*. 1948, vol. 8, pp. 315–328.
[6] Weiss A. J., Weinstein E. 'A Lower Bound on the Mean Square Error in Random Parameter Estimation'. *IEEE Transactions on Information Theory*. 1985, vol. IT-31, no. 5, pp. 680–682.
[7] Bobrovsky B., Zakai M. 'A Lower Bound on the Estimation Error for Certain Diffusion Processes'. *IEEE Transactions on Information Theory*. 1976, vol. IT-22, no. 1, pp. 45–52.
[8] Van Trees H. L. *Detection, Estimation, and Modulation Theory, Part I*. New York: John Wiley and Sons; 1968.
[9] Tichavský P., Muravchik C. H., Nehorai A. 'Posterior Cramér–Rao Bounds for Discrete-Time Nonlinear Filtering'. *IEEE Transactions on Signal Processing*. 1998, vol. 46(5), pp. 1386–1396.
[10] Hernandez M. L., Horridge P. R. 'Advances in the Management of Multi-Sensor Systems with Associated Applications'. *Proceedings of the IEE Workshop on Target Tracking: Algorithms and Applications*; University of Sussex, UK, 2004.
[11] Hernandez M. L., Kirubarajan T., Bar-Shalom Y. 'Multisensor Resource Deployment Using Posterior Cramér–Rao Bounds'. *IEEE Transactions on Aerospace and Electronic Systems*. 2004, vol. 40(2), pp. 399–416.
[12] Tharmarasa R., Kirubarajan T., Hernandez M. L. 'Large-Scale Optimal Sensor Array Management for Multitarget Tracking'. *IEEE Transactions on Systems, Man, and Cybernetics: Part C*. 2007, vol. 37(5), pp. 803–814.
[13] Tharmarasa R., Kirubarajan T., Hernandez M. L., Sinha A. 'PCRLB Based Multisensor Array Management for Multitarget Tracking'. *IEEE Transactions on Aerospace and Electronic Systems*. 2007, vol. 43(2), pp. 539–555.
[14] Hernandez M. L. 'Optimal Sensor Trajectories in Bearings-Only Tracking'. *Proceedings of the 7th International Conference on Information Fusion*; Stockholm, Sweden, 2004, pp. 893–900.
[15] Smith M. I., Hernandez M. L., Cooper M. 'Simulating and Testing Autonomous Behaviour in Multiple Airborne Sensor Systems'. *Proceedings of the Society of Photo-Optical Instrument Engineers Conference on Unmanned Systems Technology IX*; Orlando, Florida, USA, 2007, vol. 6561.
[16] Hernandez M. L. 'Adaptive Horizon Sensor Resource Management: Validating the Core Concept'. *Proceedings of the Society of Photo-Optical Instrument Engineers Conference on Signal and Data Processing of Small Targets*; San Diego, California, USA, 2007, vol. 6699.

[17] Ristic B., Hernandez M. L., Farina A., Ong H.-T. 'Analysis of Radar Allocation Requirements for an IRST Aided Tracking of Anti-Ship Missiles'. *Proceedings of the Ninth International Conference on Information Fusion*; Florence, Italy, 2006

[18] Greco M., Gini F., Stinco P., Farina A. 'Cramér–Rao Bounds and Selection of Bistatic Channels for Multistatic Radar Systems'. *IEEE Transactions on Aerospace and Electronic Systems*. 2011, vol. 47(4), pp. 2934–2948.

[19] Ristic B., Arulampalam S., Gordon N. *Beyond the Kalman Filter: Particle Filters for Tracking Applications*. London: Artech House, 2004.

[20] Farina A., Ristic B., Benvenuti D. 'Tracking a Ballistic Target: Comparison of Several Nonlinear Filters'. *IEEE Transactions on Aerospace and Electronic Systems*. 2002, vol. 38(3), pp. 854–867.

[21] Stinco P., Greco M., Gini F., Farina A. 'Sequential Cramér–Rao Lower Bounds for Bistatic Radar Systems'. *Proceedings of the IEEE International Conference on Acoustics, Speech and Signal Processing (ICASSP)*; Prague, Czech Republic, 2011, pp. 2724–2727.

[22] Ristic B., Farina A. 'Recursive Bayesian State Estimation from Doppler-Shift Measurements'. *Proceedings of the IEEE International Conference on Intelligent Sensors, Sensor Networks and Information Processing (ISSNIP)*; Adelaide, Australia, 2011.

[23] Mohammadi A., Asif A. 'Full- and Reduced-Order Distributed Bayesian Estimation Analytical Performance Bounds'. *IEEE Transactions on Aerospace and Electronic Systems*. 2014, vol. 50(4), pp. 2468–2488.

[24] Lambert H. C. 'Cramér–Rao Bounds for Target Tracking Problems Involving Colored Measurement Noise'. *IEEE Transactions on Aerospace and Electronic Systems*. 2012, vol. 48(1), pp. 620–636.

[25] Zhou Y., Li J., Wang D. 'Posterior Cramér–Rao Lower Bounds for Target Tracking in Sensor Networks With Quantized Range-Only Measurements'. *IEEE Signal Processing Letters*. 2010, vol. 17(2), pp. 157–160.

[26] Zhong Z., Meng H., Wang X., 'A Comparison of Posterior Cramér–Rao Bounds for Point and Extended Target Tracking'. *IEEE Signal Processing Letters*. 2010, vol. 17(10), pp. 819–822.

[27] Reece S., Nicholson D., 'Tighter Alternatives to the Cramér–Rao Lower Bound for Discrete-Time Filtering'. *Proceedings of the 8th International Conference on Information Fusion*; Philadelphia, Pennsylvania, USA, 2005.

[28] Rapoport I., Oshman Y. 'Recursive Weiss-Weinstein Lower Bounds for Discrete-Time Nonlinear Filtering'. *Proceedings of the 43rd IEEE Conference on Decision and Control*; Bahamas, 2004, pp. 2662–2667.

[29] Weinstein E., Weiss A. J. 'A General Class of Lower Bounds in Parameter Estimation'. *IEEE Transactions on Information Theory*. 1988, vol. 34(2), pp. 338–342.

[30] Bessel A., Ristic B., Farina A., Wang X., Arulampalam M. S. 'Error Performance Bounds for Tracking a Manoeuvring Target'. *Proceedings of the 6th International Conference on Information Fusion*; Cairns, Queensland, Australia, 2003, pp. 903–910.

[31] Hernandez M. L., Ristic B., Farina A. 'A Performance Bound for Manoeuvring Target Tracking Using Best-Fitting Gaussian Distributions'. *Proceedings of the 8th International Conference on Information Fusion*, Philadelphia, Pennsylvania, USA, 2005.

[32] Hernandez M. L., Ristic B., Farina A., Sathyan T., Kirubarajan T. 'Performance Measure for Markovian Switching Systems Using Best-Fitting Gaussian Distributions'. *IEEE Transactions on Aerospace and Electronic Systems*. 2008, vol. 44(2), pp. 724–747.

[33] Blom H. A. P., Bar-Shalom Y. 'The Interacting Multiple Model Algorithm for Systems with Markovian Switching Coefficients'. *IEEE Transactions on Automatic Control*. 1988, vol. 33(8), pp. 780–783.

[34] Morelande M., Ristic B., Hernandez M. 'A New Best Fitting Gaussian Performance Measure for Jump Markov Systems'. *Proceedings of the 11th IEEE International Conference on Information Fusion*; Cologne, Germany, 2008.

[35] Svensson L. 'On the Bayesian Cramér–Rao Bound for Markovian Switching Dynamics'. *IEEE Transactions on Signal Processing*. 2010, vol. 58(9), pp. 4507–4516.

[36] Nui R., Willett P. K., Bar-Shalom Y. 'Matrix CRLB Scaling Due to Measurements of Uncertain Origin'. *IEEE Transactions on Signal Processing*. 2001, vol. 49(7), pp. 1325–1335.

[37] Zhang X., Willett P. K. 'Cramér–Rao Bounds for Discrete Time Linear Filtering with Measurement Origin Uncertainty'. *Proceedings of the Workshop on Estimation, Tracking and Fusion: A Tribute to Yaakov Bar-Shalom*; Monterey, California, USA, 2001.

[38] Zhang X., Willett P. K., Bar-Shalom Y. 'Dynamic Cramér–Rao Bound for Target Tracking in Clutter'. *IEEE Transactions on Aerospace and Electronic Systems*. 2005, vol. 41(4), pp. 1154–1167.

[39] Hernandez M. L., Marrs A. D., Gordon N. J., Maskell S., Reed C. M. 'Cramér–Rao Bounds for Non-Linear Filtering with Measurement Origin Uncertainty'. *Proceedings of the 5th International Conference on Information Fusion*; Annapolis, Maryland, USA, 2002, vol. 1, pp. 18–25.

[40] Kershaw D., Evans R. 'A Contribution to Performance Prediction for Probabilistic Data Association Tracking Filters'. *IEEE Transactions on Aerospace and Electronic Systems*. 1996, vol. 32(3), pp. 1143–1148.

[41] Farina A., Ristic B., Timmoneri L. 'Cramér–Rao Bound for Non-Linear Filtering with $P_d < 1$ and its Application to Target Tracking'. *IEEE Transactions on Signal Processing*. 2002, vol. 50(8), pp. 1916–1924.

[42] Hernandez M. L., Ristic B., Farina A., Timmoneri L. 'A Comparison of Two Cramér–Rao Bounds for Non-Linear Filtering with $P_d < 1$. *IEEE Transactions on Signal Processing*. 2004, vol. 52(9), pp. 2361–2370.

[43] Hernandez M. L., Farina A., Ristic B. 'PCRLB for Tracking in Cluttered Environments: Measurement Sequence Conditioning Approach'. *IEEE Transactions on Aerospace and Electronic Systems*. 2006, vol. 42(2), pp. 680–704.

[44] Meng H., Hernandez M. L., Liu Y., Wang X. 'Computationally Efficient PCRLB for Tracking in Cluttered Environments: Measurement Existence Conditioning Approach'. *IET Signal Processing*. 2009, vol. 3(2), pp. 133–149.
[45] Boers Y., Driessen J. N. 'Modified Riccati Equation and Its Application to Target Tracking'. *IEE Proceedings on Radar, Sonar and Navigation*. 2006, vol. 153(1), pp. 7–12.
[46] Boers Y., Driessen J. N. 'Results on the Modified Riccati Equation: Target Tracking Applications'. *IEEE Transactions on Aerospace and Electronic Systems*. 2006, vol. 42(1), pp. 379–384.
[47] Boers Y., Driessen J. N. 'A Note on Bounds for Target Tracking with Pd < 1'. *IEEE Transactions on Aerospace and Electronic Systems*. 2009, vol. 45(2), pp. 640–646.
[48] Hue C., Le Cadre J.-P., Pérez P. 'Posterior Cramér–Rao Bounds for Multi-Target Tracking'. *IEEE Transactions on Aerospace and Electronic Systems*. 2006, vol. 42(1), pp. 37–49.
[49] Lian F., Liu J., Han C. 'Error Bound for Joint Detection and Estimation of Multiple Targets with Random Finite Set State and Observation'. *Signal Processing.* 2015, vol. 40, pp. 247–257.
[50] Boers Y., Ehlers F., Koch W., Luginbuhl T., Stone L. D., Streit R. L. 'Track Before Detect Algorithms'. *EURASIP Journal on Advances in Signal Processing*. Editorial to the Special Issue, 2008.
[51] Ristic B., Farina A., Hernandez M. 'Cramér–Rao Lower Bound for Tracking Multiple Targets'. *IEE Proceedings on Radar, Sonar and Navigation*. 2004, vol. 151(3), pp. 129–134.
[52] Ristic B., Morelande M. 'Comments on Cramér–Rao Lower Bound for Tracking Multiple Targets'. *IET Proceedings on Radar, Sonar and Navigation*. 2007, vol. 1(1), pp. 74–76.
[53] Morelande M., Ristic B. 'Signal-to-Noise Ratio Threshold Effect in Track Before Detect'. *IET Radar, Sonar and Navigation*. 2009, vol. 3(6), pp. 601–608.
[54] Taylor J. 'The Cramér–Rao Estimation Error Lower Bound Computation for Deterministic Nonlinear Systems'. *IEEE Transactions on Automatic Control*. 1979, vol. 24(2), pp. 343–344.
[55] Ming L., van Wyk B. J., Yong Q. 'Online Estimation of the Approximate Posterior Cramér–Rao Lower Bound for Discrete-Time Nonlinear Filtering'. *IEEE Transactions on Aerospace and Electronic Systems*. 2011, vol. 47(1), pp. 37–57.
[56] Bar-Shalom Y., Li X., Kirubarajan T. *Estimation with Applications to Tracking and Navigation*. New York: John Wiley and Sons Inc.; 2001.
[57] Julier S. J., Uhlmann J. K. 'A New Extension of the Kalman Filter to Nonlinear Systems'. *Proceedings of AeroSense: The 11th International Symposium on Aerospace/Defence Sensing, Simulation and Controls*; Orlando, Florida, USA, 1997.
[58] Tulsyan A., Biao H., Gopaluni R. B., Forbes J. F. 'A Particle Filter Approach to Approximate Posterior Cramér–Rao Lower Bound: The Case of Hidden

States'. *IEEE Transactions on Aerospace and Electronic Systems*. 2013, vol. 49(4), pp. 2478–2495.

[59] Gordon N. J., Salmond D. J., Smith A. F. M. 'Novel Approach to Nonlinear/Non-Gaussian Bayesian State Estimation'. *IEE Proceedings-F*. 1993, vol. 140, pp. 107–113.

[60] Zuo L., Niu R., Varshney P. K. 'Conditional Posterior Cramér–Rao Lower Bounds for Nonlinear Sequential Bayesian Estimation'. *IEEE Transactions on Signal Processing*. 2011, vol. 59(1), pp. 1–14.

[61] Zheng Y., Ozdemir O., Niu R., Varshney P. K. 'New Conditional Posterior Cramér–Rao Lower Bounds for Nonlinear Sequential Bayesian Estimation'. *IEEE Transactions on Signal Processing*. 2012, vol. 60(10), pp. 5549–5556.

[62] Ristic B., Zollo S., Arulampalam S. 'Performance Bounds for Manoeuvring Target Tracking Using Asynchronous Multi-Platform Angle-Only Measurements'. *Proceedings of 4th International Conference on Information Fusion*; Montreal, Québec, Canada, 2001.

[63] Bell K. L., Baker C. J., Smith G. E., Johnson J. T., Rangaswamy M. 'Cognitive Radar Framework for Target Detection and Tracking'. *Journal of Selected Topics in Signal Processing*. 2015, vol. 9(8), pp. 1427–1439.

[64] Farina A. 'Green Radar State of Art: Theory, Practice and Way Ahead'. *International Conference on Acoustic, Speech and Signal Processing (ICASSP)*; Florence, Italy, 2014, plenary talk, video recorded for the IEEE Signal Processing Society, available at: http://www.icassp2014.org/final200614/er2/0005/index.html.

[65] Wikipedia page on multilateration, https://en.wikipedia.org/wiki/Multilateration.

[66] Hernandez M. L., Benavoli A., Graziano A., Farina A., Morelande M. 'Performance Measures and MHT for Tracking Move-Stop-Move Targets with MTI Sensors'. *IEEE Transactions on Aerospace and Electronic Systems*. 2011, vol. 47(2), pp. 996–1025.

[67] Chou K. C., Willsky A. S., Benveniste A. 'Multiscale Recursive Estimation, Data Fusion, and Regularization'. *IEEE Transactions on Automatic Control*. 1994, vol. 39(3), pp. 464–478.

[68] Costantini M., Farina A., Zirilli F. 'The Fusion of Different Resolution Radar Images: A New Formalism'. *Proceedings of IEEE, Special Issue on Data Fusion*. 1997, vol. 85(1), pp. 139–146.

[69] Signorini A. M., Farina A., Zappa G. 'Application of Multiscale Estimation Algorithm to SAR Image Fusion'. *International Symposium on Radar, IRS98*; Munich, Germany, 1998, pp. 1341–1135.

[70] Simone G., Farina A., Morabito F. C., Serpico S. B., Bruzzone L. 'Image Fusion Techniques for Remote Sensing Applications'. *Information Fusion.* 2002, vol. 3(1), pp. 3–15.

[71] Evensen G. 'Sequential Data Assimilation with Nonlinear Quasi-Geostrophic Model using Monte Carlo Methods to Forecast Error Statistics'. *Journal of Geophysical Research*. 1994, vol. 99, no. C5, pp. 143–162.

[72] Houtekamer P., Mitchell H. L. 'Data Assimilation using an Ensemble Kalman Filter Technique'. *Monthly Weather Review*. 1998, vol. 126, pp. 796–811.

[73] Smith R. C., Cheeseman P. 'On the Representation and Estimation of Spatial Uncertainty'. *The International Journal of Robotics Research*. 1986, vol. 5(4), pp 56–68.

[74] Smith R. C., Self M., Cheeseman P. 'Estimating Uncertain Spatial Relationships in Robotics'. *Proceedings of the Second Annual Conference on Uncertainty in Artificial Intelligence (UAI '86)*; Philadelphia, Pennsylvania, USA, 1986, pp. 435–461.

[75] Selvaratnam D., Shames I., Ristic, B., Manton, J. 'The Effect of Sensor Modality on Posterior Cramér–Rao Bounds for Simultaneous Localisation and Mapping'. *Proceedings of the 9th IFAC Symposium on Intelligent Autonomous Vehicles IAV 2016 (IFAC 2016)*; Leipzig, Germany, 2016, pp. 242–247.

[76] Helstrom C. W. 'Quantum Detection and Estimation Theory'. *Journal of Statistical Physics*. 1969, vol. 1(2), pp 231–252.

[77] Helstrom C. W. *Quantum Detection and Estimation Theory*. New York: Academic Press; 1976.

[78] Personick S. D. 'Application of Quantum Estimation Theory to Analog Communication over Quantum Channels'. *IEEE Transactions on Information Theory*. 1971, vol. 17(3), pp. 240–246.

[79] Iida S., Ohki F., Yamamoto N. 'Robust Quantum Kalman Filtering under the Phase Uncertainty of the Probe-laser'. *IEEE International Symposium on Computer-Aided Control System Design*; Yokohama, Japan, 2010, pp. 749–754.

Chapter 10

Tracking and fusion in log-spherical state space with application to collision avoidance and kinematic ranging

Dietrich Fränken[1]

Abstract

This chapter is devoted to a special state representation for target tracking. The considered coordinates possess, in comparison with classical Cartesian ones, distinct advantages in particular in applications where angles are the only measurements available like, e.g. for jammed radar. In those applications, measurements are not Cartesian-complete and the range of a moving object under track is not observable unless the sensor platform performs manoeuvres.

This chapter presents basic relations and properties of log-spherical coordinates. In particular, it is shown how those coordinates decouple the remaining coordinates from the unobservable range in angular-only tracking. The chapter discusses recursive filter algorithms and corresponding performance bounds. As an application example, it uses data fusion in a collision avoidance system based on a suite of sensors. The final topic is the so-called kinematic ranging, i.e. the extraction of range information from angular-only measurements by suitably chosen manoeuvres of the sensor platform. Presentation in this chapter covers both mathematical derivations as well as numerical simulation results.

10.1 Introduction

When processing radar measurements in tracking and fusion applications, the measurement space to be used depends on the underlying sensor technology. A modern radar delivers range and usually also Doppler plus two angular measurements. For mechanically steered antennas, those are azimuth and elevation (yielding in total polar measurements). But, the angular measurements of electronically steered phased array antennas are better modelled as sine angles. In any case, the state of the target to be estimated is usually taken as Cartesian, and measurement updates are either performed via pseudo-Cartesian converted measurements or using non-linear

[1]Hensoldt Sensors GmbH, Germany

filtering techniques as, e.g. the *extended Kalman filter* (EKF) or the *unscented Kalman filter* (UKF) and its relatives (just to name a few).

Radar may be jammed by means of electronic counter-measures (cf. [1,2] and the references cited therein). In such a case, it will fail to provide range information, and its measurements will not be Cartesian-complete. Especially, if in this case neither the platform carrying the radar nor the jammer perform any manoeuvres, tracking in *log-spherical coordinates* (LSCs) becomes highly advantageous. They effectively de-couple the observable (state) sub-space from the non-observable one, and robust estimates of the observable quantities can be obtained. Tracking in LSCs comes with further advantages if the complete state of the target is to be estimated by means of own-ship manoeuvres, an approach commonly called kinematic ranging.

From a measurement space point of view, passive optical sensors like electro-optics or infrared are, after plot extraction, somewhat comparable to jammed radar. Thus, kinematics estimation can be performed in the same fashion. Such a unified tracking approach is of particular interest for systems equipped with a suite of different sensors where each sensor might lack a different sub-space in its respective measurement set. A typical example is a collision avoidance system [3–6] where a system like TCAS [7] alone may fail to provide (reliable) azimuth information. Here, radar or optical sensors can provide valuable support.

10.2 Log-spherical coordinates

Throughout this chapter, the state to be tracked consists of the three-dimensional (3D) position of the target of interest plus its corresponding 3D velocity. Therein, positions as well as their spherical representations (ranges and angles) are considered in a Cartesian coordinate system with constant orientation. This is, e.g. an *east-north-up* system, centred within and moving with the sensor platform. Velocities and log-spherical rates are defined relative to that in a consistent manner.

Starting point on the way to LSCs is a spherical representation of the (relative) position $\boldsymbol{p}$ with range r, bearing angle β (measured in mathematically positive direction from the x-axis) and elevation angle ε as depicted in Figure 10.1. With unitary rotation matrices

$$\boldsymbol{B}(\beta) = \begin{bmatrix} \cos\beta & -\sin\beta & 0 \\ \sin\beta & \cos\beta & 0 \\ 0 & 0 & 1 \end{bmatrix} \quad \text{and} \quad \boldsymbol{E}(\varepsilon) = \begin{bmatrix} \cos\varepsilon & 0 & -\sin\varepsilon \\ 0 & 1 & 0 \\ \sin\varepsilon & 0 & \cos\varepsilon \end{bmatrix} \tag{10.1}$$

and the unit vector $\boldsymbol{u}_x = [1,0,0]^T$, this representation can be written as follows:

$$\begin{aligned} x &= r\cos\beta\cos\varepsilon \\ y &= r\sin\beta\cos\varepsilon \\ z &= r\sin\varepsilon \end{aligned} \quad \Rightarrow \quad \boldsymbol{p} = \begin{bmatrix} x \\ y \\ z \end{bmatrix} = r\boldsymbol{B}(\beta)\boldsymbol{E}(\varepsilon)\boldsymbol{u}_x \tag{10.2}$$

Differentiation with respect to time delivers, after some ordering of terms,

$$\boldsymbol{v} = \begin{bmatrix} v_x \\ v_y \\ v_z \end{bmatrix} = \begin{bmatrix} \dot{x} \\ \dot{y} \\ \dot{z} \end{bmatrix} = r\boldsymbol{B}(\beta)\boldsymbol{E}(\varepsilon) \begin{bmatrix} \dot{r}/r \\ \omega \\ \dot{\varepsilon} \end{bmatrix} \quad \text{with} \quad \omega = \dot{\beta}\cos\varepsilon \tag{10.3}$$

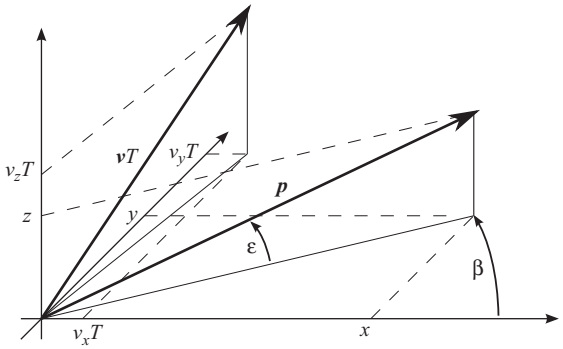

Figure 10.1 Position $\boldsymbol{p}$ *and velocity* $\boldsymbol{v}$ *in the reference coordinate system with Cartesian components and spherical angles. There holds* $\|\boldsymbol{p}\| = r$

where ω is the *projected bearing rate*. Tracking in log-spherical space is based on the use of the logarithmic range and its rate (the *normalized range rate*), i.e.

$$\rho = \log\left(\frac{r}{R}\right) \text{ with some normalizing range } R \Rightarrow \dot{\rho} = \left(\frac{\dot{r}}{r}\right) \tag{10.4}$$

as states. In addition, the angles β and ε plus the rates ω and $\dot{\varepsilon}$ are used. Herein, the three rate components ρ, ω and $\dot{\varepsilon}$ form an orthogonal basis for the coordinate system of the (normalized) velocity. Its $\dot{\rho}$-axis is co-aligned with the *line of sight* from sensor platform to tracked target. Compactly, the log-spherical state vector thus is composed of $\boldsymbol{q} = [\rho, \beta, \varepsilon]^T$ and $\dot{\boldsymbol{q}} = [\dot{\rho}, \omega, \dot{\varepsilon}]^T$. Here, brevity caused a slight abuse of notation as $\dot{\boldsymbol{q}}$ is not the time derivative of $\boldsymbol{q}$ when it comes to its second component.

Benefits of using this particular set of state variables become apparent when a *constant velocity* (CV) *motion model* is considered for both tracked target and sensor platform. Let subscript 0 denote all quantities at some given time t_0 and subscript 1 all at some time $t_1 = t_0 + T$. Furthermore, introduce the abbreviation $\beta_{10} = \beta_1 - \beta_0$. Then, there always holds $\boldsymbol{B}(\beta_1) = \boldsymbol{B}(\beta_0)\boldsymbol{B}(\beta_{10})$ while the CV motion implies both $\boldsymbol{v}_1 = \boldsymbol{v}_0$ and $\boldsymbol{p}_1 = \boldsymbol{p}_0 + T\boldsymbol{v}_0$ to hold. In combination with the equations above, one thus obtains as decisive propagation relation

$$r_1\boldsymbol{B}(\beta_{10})\boldsymbol{E}(\varepsilon_1)\boldsymbol{u}_x = r_0\boldsymbol{g}_{10} \quad \text{with} \quad \boldsymbol{g}_{10} = \boldsymbol{E}(\varepsilon_0)(\boldsymbol{u}_x + T\dot{\boldsymbol{q}}_0) \tag{10.5}$$

This implies

$$\begin{aligned} r_1 &= r_0\|\boldsymbol{g}_{10}\| \Rightarrow \rho_1 = \rho_0 + \log(\|\boldsymbol{g}_{10}\|) \\ \beta_{10} &= \arctan_2(\omega_0 T, [1 + \dot{\rho}_0 T]\cos\varepsilon_0 - \dot{\varepsilon}_0 T \sin\varepsilon_0) \\ \varepsilon_1 &= \arcsin\left(\{[1 + \dot{\rho}_0 T]\sin\varepsilon_0 + \dot{\varepsilon}_0 T\cos\varepsilon_0\}/\|\boldsymbol{g}_{10}\|\right) \end{aligned} \tag{10.6}$$

with

$$\|\boldsymbol{g}_{10}\| = \sqrt{(1 + \dot{\rho}_0 T)^2 + (\omega_0 T)^2 + (\dot{\varepsilon}_0 T)^2} \tag{10.7}$$

Once β_{10} and ε_1 have been determined, the rates can be computed via

$$\dot{\boldsymbol{q}}_1 = \frac{1}{\|\boldsymbol{g}_{10}\|}\boldsymbol{E}_1^T\boldsymbol{B}_{10}^T\boldsymbol{E}_0\dot{\boldsymbol{q}}_0 \Rightarrow T\dot{\rho}_1 = 1 - \frac{1 + \dot{\rho}_0 T}{\|\boldsymbol{g}_{10}\|^2} \tag{10.8}$$

where the latter implication is verified by some more detailed analysis.

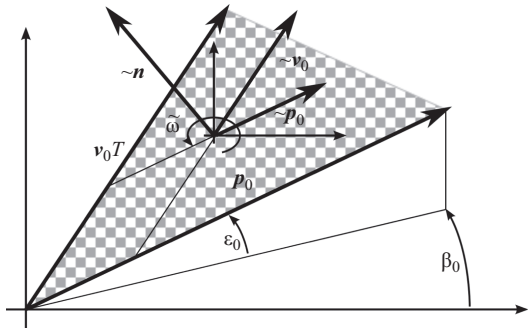

*Figure 10.2 Motion plane with normal vector **n** defined by position **p** and velocity **v***

The propagation equations in LSCs reveal a high level of de-coupling for the CV motion: The additive increments for logarithmic range and bearing as well as the propagation equations for elevation and for all three rate components depend neither on the range nor on the bearing of the tracked target. In addition to that, both the additive increment for logarithmic range and the propagation equation for the normalized range rate are independent of the elevation.

An additional level of de-coupling shows up for a modification of the reference coordinate system. As indicated in Figure 10.2, the CV movement of the tracked-target relative to the platform determines a plane. Unless the movement is zero or heading directly either towards or away from the platform, this plane is uniquely determined as going through the initial origin of the platform-oriented coordinate system and possessing a normal vector $\boldsymbol{n} = (\boldsymbol{p}_0 \times \boldsymbol{v}_0)/\|\boldsymbol{p}_0 \times \boldsymbol{v}_0\|$. Let $\tilde{\rho}$, $\tilde{\beta}$, $\tilde{\varepsilon}$, $\dot{\tilde{\rho}}$, $\tilde{\omega}$ and $\dot{\tilde{\varepsilon}}$ denote the quantities of the state vector with respect to a rotated coordinate system whose z-axis is co-aligned with $\boldsymbol{n}$. Then, elevation $\tilde{\varepsilon}$ and elevation rate $\dot{\tilde{\varepsilon}}$ will be zero throughout, while (logarithmic) range and normalized range rate are not affected by the rotation of the coordinate system. A formal replacement of each variable $*$ by $\tilde{*}$ in (10.5) to (10.8) honouring $\tilde{\varepsilon} = 0$ and $\dot{\tilde{\varepsilon}} = 0$ leads to the two-dimensional (2D) log-polar propagation equations in the variables $\tilde{\rho} = \rho$, $\tilde{\beta}$, $\dot{\tilde{\rho}} = \dot{\rho}$ and $\tilde{\omega}$. It turns out that the original rates ω and $\dot{\varepsilon}$ are related to the *effective bearing rate* $\tilde{\omega}$ via $\omega = \tilde{\omega} \cos \vartheta$ and $\dot{\varepsilon} = \tilde{\omega} \sin \vartheta$ with $|\tilde{\omega}| = \sqrt{\omega^2 + \dot{\varepsilon}^2}$ and some angle ϑ. A detailed analysis delivers, in accordance with the conservation law of the angular momentum,

$$\tilde{\omega}_1 = \frac{1}{\|\boldsymbol{g}_{10}\|^2}\,\tilde{\omega}_0 \quad \Leftrightarrow \quad r_1^2\tilde{\omega}_1 = r_0^2\tilde{\omega}_0 \tag{10.9}$$

as a final result. This shows that the propagation equation of the effective bearing rate does not depend on the (original) elevation, neither.

10.3 Tracking with angular-only measurements

Among the many existing proposed approaches to tracking targets by means of angular-only measurements, the application of LSCs often provides a very good

compromise between computational implementation effort and accomplishable estimation accuracy.

10.3.1 Filter principles

The field of state estimation and filtering in the context of tracking is vast and many are the possible methods treated in the existing literature. To get an introductive overview, the reader is referred to [8].

A large (although by far not the most general) class of state estimation problems can be described by dynamic state equations of the form $\boldsymbol{x}_{k+1} = \boldsymbol{f}(x_k) + \boldsymbol{v}_k$ and measurement equations of the form $\boldsymbol{y}_k = \boldsymbol{h}(\boldsymbol{x}_k) + \boldsymbol{w}_k$. Here, the additive so-called process noise $\boldsymbol{v}_k$ causes a stochastic deviation from the otherwise undisturbed transition of the target state $\boldsymbol{x}$ from one time t_k to another t_{k+1}. Similarly, the otherwise undisturbed mapping from a target state to the measurement $\boldsymbol{y}$ is subject to the additive stochastic measurement noise $\boldsymbol{w}_k$. The goal is to find for the state $\boldsymbol{x}_k$ the best possible estimate $\boldsymbol{x}_{k|\ell}$ as well as the corresponding estimation error covariance matrix $\boldsymbol{P}_{k|\ell}$ based on all received measurements up to and including $\boldsymbol{y}_\ell$. Here, the functions $\boldsymbol{f}$ and $\boldsymbol{h}$ as well as the distributions of $\boldsymbol{v}_k$ and $\boldsymbol{w}_k$ have an impact on the selection of a suitable estimation method. They are all assumed to be known with sufficient precision.

A very simple case is that of linear equations with additive noise described by $\boldsymbol{x}_{k+1} = \boldsymbol{F}\boldsymbol{x}_k + \boldsymbol{v}_k$ and $\boldsymbol{y}_k = \boldsymbol{H}\boldsymbol{x}_k + \boldsymbol{w}_k$ with $\boldsymbol{v}_k$ and $\boldsymbol{w}_k$ being zero-mean, (mutually) white, state-independent and normally distributed with covariances $\boldsymbol{Q}$ and $\boldsymbol{R}$, respectively. Here, the best possible estimate is provided recursively by the *Kalman filter* (KF) [9]. Its prediction equations read $\boldsymbol{x}_{k+1|k} = \boldsymbol{F}\boldsymbol{x}_{k|k}$ and $\boldsymbol{P}_{k+1|k} = \boldsymbol{F}\boldsymbol{P}_{k|k}\boldsymbol{F}^T + \boldsymbol{Q}$. The update equations are given by the equations $\boldsymbol{x}_{k+1|k+1} = \boldsymbol{x}_{k+1|k} + \boldsymbol{K}_k\boldsymbol{d}_k$ and $\boldsymbol{P}_{k+1|k+1} = \boldsymbol{P}_{k+1|k} - \boldsymbol{K}_k\boldsymbol{S}_k\boldsymbol{K}_k^T$ with *innovation* $\boldsymbol{d}_k = \boldsymbol{y}_k - \boldsymbol{H}\boldsymbol{x}_{k+1|k}$, corresponding error covariance $\boldsymbol{S}_k = \boldsymbol{H}\boldsymbol{P}_{k+1|k}\boldsymbol{H}^T + \boldsymbol{R}$ and *Kalman gain* $\boldsymbol{K}_k = \boldsymbol{P}_{k+1|k}\boldsymbol{H}^T\boldsymbol{S}_k^{-1}$.

If any of the two equations (state transition or measurement) is non-linear, the KF cannot be applied as is any more. However, various approximative variants of it have been developed for such cases, among which only the EKF is treated in the upcoming sections of this chapter. It uses $\boldsymbol{x}_{k+1|k} = \boldsymbol{f}(\boldsymbol{x}_{k|k})$ for state prediction and replaces in the covariance prediction $\boldsymbol{F}$ by the Jacobian of $\boldsymbol{f}$, evaluated at the state estimate $\boldsymbol{x}_{k|k}$ prior to prediction. Within the update step of the EKF, the innovation is computed as $\boldsymbol{d}_k = \boldsymbol{y}_k - \boldsymbol{h}(\boldsymbol{x}_{k+1|k})$. The Jacobian of $\boldsymbol{h}$, evaluated at the predicted state estimate $\boldsymbol{x}_{k+1|k}$, replaces $\boldsymbol{H}$ in the computation of the innovation error covariance and the Kalman gain. These replacements boil down to a linearisation with approximations of the form $\mathrm{E}[\boldsymbol{f}(\boldsymbol{x})] \approx \boldsymbol{f}(\mathrm{E}[\boldsymbol{x}])$ and $\mathrm{Var}[\boldsymbol{f}(\boldsymbol{x})] \approx \boldsymbol{F}\,\mathrm{Var}[\boldsymbol{x}]\boldsymbol{F}^T$. Herewith, it is in general not guaranteed that the computed state estimates are unbiased and that the estimation error covariances as computed by the EKF match their true counterparts. The mismatch may cause filter divergence, so a certain caution is advised.

If required, deterministic sampling may be used to replace linearisation at any place in the upcoming presentations. That method is applied in various filters like, e.g. the UKF [10] or the *Gauß filter* [11]. It uses a deterministically selected set of sample points $\boldsymbol{x}_i$ and weights w_i matching the mean $\mathrm{E}[\boldsymbol{x}] = \overline{\boldsymbol{x}} = \sum w_i\boldsymbol{x}_i$ and

the variance $\mathrm{Var}[\boldsymbol{x}] = \sum w_i(\boldsymbol{x}_i - \overline{\boldsymbol{x}})(\boldsymbol{x}_i - \overline{\boldsymbol{x}})^T$ (plus possibly higher-order moments) and approximates $\mathrm{E}[\boldsymbol{f}(\boldsymbol{x})] \approx \overline{\boldsymbol{f}} = \sum w_i \boldsymbol{f}(\boldsymbol{x}_i)$ as well as $\mathrm{Var}[\boldsymbol{f}(\boldsymbol{x})] \approx \sum w_i(\boldsymbol{f}(\boldsymbol{x}_i) - \overline{\boldsymbol{f}})(\boldsymbol{f}(\boldsymbol{x}_i) - \overline{\boldsymbol{f}})^T$. Deterministic sampling produces better estimation results than linearisation in most cases.

When tracking, based on angular-only measurements, targets performing (disturbed) CV (relative) movements, a Cartesian state representation would come with a linear state transition but a non-linear measurement equation. For a state representation in LSCs, the situation would be just reversed. Starting from this latter alternative, a sub-division of the log-spherical propagation step into three sub-steps leads to the following filter cycle:

1. Convert state and covariance from log-spherical to Cartesian space.
2. Perform KF propagation for state and covariance in Cartesian space.
3. Convert propagated state and covariance from Cartesian to log-spherical space.
4. Perform (E)KF update for state and covariance in log-spherical space.

This scheme combines in a straightforward manner the sub-division suggested by the derivation of a 2D filter in modified-polar coordinates [12], the extension to 3D modified-spherical coordinates [13] and the replacement of the inverse range of the modified coordinates by the logarithmic range for improved filter performance like in 2D [14]. No time-costly numerical integration of continuous-time stochastic differential equations as, e.g. in [15] is performed. The different steps of the scheme are detailed next.

10.3.2 Filter update

For a state representation in LSCs according to $\boldsymbol{x}^T = \left[\boldsymbol{q}^T, \dot{\boldsymbol{q}}^T\right]$ and measured bearing and elevation, the measured quantities β and ε are components of the state vector. The measurement matrix can thus be chosen as $\boldsymbol{H} = [\boldsymbol{h}_\beta, \boldsymbol{h}_\varepsilon]^T$ with $\boldsymbol{h}_\beta^T = [0,1,0,0,0,0]$ and $\boldsymbol{h}_\varepsilon^T = [0,0,1,0,0,0]$. Herewith, the linear KF update is trivial and can be performed by two sequential scalar updates if measurement errors are mutually independent. The only smaller pitfall to be avoided is related to the computation of the innovation. Care must be taken that the magnitude of the innovation for the bearing component does not exceed π. But, that can always be ensured by possible 2π-shifts.

A phased-array antenna, whose antenna plane coincides with the *yz*-plane as shown in Figure 10.3, is commonly modelled to deliver, in addition to the range r, the sine angles u and v as measurements ($w = \sqrt{1-u^2-v^2}$ is not measured). Measurement errors are assumed independent of each other and of the measured values (cf. [16]). A jammed radar with such an antenna would only provide u and v. This can be honoured in an EKF update as (omitting the subscript $k+1|k$ throughout for the sake of brevity)

$$\begin{aligned} \boldsymbol{h}(\boldsymbol{x}) &= \begin{bmatrix} u \\ v \end{bmatrix} = \begin{bmatrix} \sin\beta\cos\varepsilon \\ \sin\varepsilon \end{bmatrix} \quad \Rightarrow \\ \boldsymbol{H}(x) &= \frac{\partial \boldsymbol{h}}{\partial \boldsymbol{x}} = \begin{bmatrix} 0 & \cos\beta\cos\varepsilon & -\sin\beta\sin\varepsilon & 0 & 0 & 0 \\ 0 & 0 & \cos\varepsilon & 0 & 0 & 0 \end{bmatrix} \end{aligned} \tag{10.10}$$

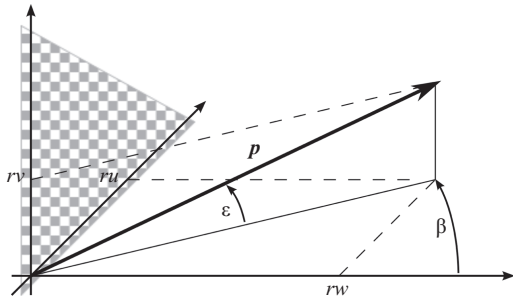

Figure 10.3 Sine angles u and v defined in relation to the antenna plane and its associated normal direction

10.3.3 Filter propagation/prediction

As derived in Section 10.2, the state transition function $\boldsymbol{f}(\boldsymbol{x})$ relating to a Cartesian CV movement becomes highly non-linear in log-spherical space. Although the corresponding Jacobians can be elaborated starting from (10.6) to (10.8), this elaboration is somewhat tedious and creates fairly lengthy results (cf. [17]). Moreover, an additive process noise in this case comes with no clear physical meaning and thus is not easy to quantify when tuning the filter. In Cartesian space, however, an additive process noise can be both modelled with physical meaning and intuitively quantified according to an assumed manoeuvrability of the targets to be tracked.

A conversion by linearisation in steps 1 and 3 of the filter cycle is straightforward. The corresponding mapping is directly applied to the estimated state, while the covariance matrix $\boldsymbol{P}$ is multiplied from left and right by the Jacobian $\boldsymbol{J}$ of the mapping, i.e. it becomes $\boldsymbol{JPJ}^T$. As $\boldsymbol{p}$ depends on $\boldsymbol{q}$ only while $\boldsymbol{v} = \dot{\boldsymbol{p}}$ depends on both $\boldsymbol{q}$ and $\dot{\boldsymbol{q}}$, the Jacobians of both mappings are lower block-triagonal matrices. With $\boldsymbol{T} = \boldsymbol{T}(\beta, \varepsilon) = \boldsymbol{B}(\beta)\boldsymbol{E}(\varepsilon)$, the Jacobian for getting to Cartesian from log-spherical is composed of

$$\begin{aligned}
\boldsymbol{J}_{pq} &= \frac{\partial \boldsymbol{p}}{\partial \boldsymbol{q}} = r\boldsymbol{T}\begin{bmatrix} 1 & 0 & 0 \\ 0 & \cos\varepsilon & 0 \\ 0 & 0 & 1 \end{bmatrix} & \boldsymbol{J}_{p\dot{q}} &= \frac{\partial \boldsymbol{p}}{\partial \dot{\boldsymbol{q}}} = \boldsymbol{0} \\
\boldsymbol{J}_{vq} &= \frac{\partial \boldsymbol{v}}{\partial \boldsymbol{q}} = r\boldsymbol{T}\begin{bmatrix} \dot{\rho} & -\omega\cos\varepsilon & -\dot{\varepsilon} \\ \omega & \dot{\rho}\cos\varepsilon - \dot{\varepsilon}\sin\varepsilon & 0 \\ \dot{\varepsilon} & \omega\sin\varepsilon & \dot{\rho} \end{bmatrix} & \boldsymbol{J}_{v\dot{q}} &= \frac{\partial \boldsymbol{v}}{\partial \dot{\boldsymbol{q}}} = r\boldsymbol{T}
\end{aligned} \tag{10.11}$$

while the Jacobian for the transformation to log-spherical from Cartesian contains

$$\begin{aligned}
\boldsymbol{J}_{qp} &= \frac{\partial \boldsymbol{q}}{\partial \boldsymbol{p}} = \frac{1}{r}\begin{bmatrix} 1 & 0 & 0 \\ 0 & 1/\cos\varepsilon & 0 \\ 0 & 0 & 1 \end{bmatrix}\boldsymbol{T}^T & \boldsymbol{J}_{qv} &= \frac{\partial \boldsymbol{q}}{\partial \boldsymbol{v}} = \boldsymbol{0} \\
\boldsymbol{J}_{\dot{q}p} &= \frac{\partial \dot{\boldsymbol{q}}}{\partial \boldsymbol{p}} = \frac{1}{r}\begin{bmatrix} -\dot{\rho} & \omega & \dot{\varepsilon} \\ -\omega & \dot{\varepsilon}\tan\varepsilon - \dot{\rho} & 0 \\ -\dot{\varepsilon} & -\omega\tan\varepsilon & -\dot{\rho} \end{bmatrix}\boldsymbol{T}^T & \boldsymbol{J}_{\dot{q}v} &= \frac{\partial \dot{\boldsymbol{q}}}{\partial \boldsymbol{v}} = \frac{1}{r}\boldsymbol{T}^T
\end{aligned} \tag{10.12}$$

State-transition matrix and process noise covariance in step 2 of the described filter cycle are given by

$$\boldsymbol{F} = \begin{bmatrix} \mathbf{1} & T\mathbf{1} \\ \mathbf{0} & \mathbf{1} \end{bmatrix} \quad \text{and} \quad \boldsymbol{Q} = q \begin{bmatrix} \frac{T^3}{3}\mathbf{1} & \frac{T^2}{2}\mathbf{1} \\ \frac{T^2}{2}\mathbf{1} & T\mathbf{1} \end{bmatrix} \tag{10.13}$$

where $\mathbf{1}$ is the identity matrix of dimension three and q the noise level for an assumed isotropic white acceleration superimposed on the CV movement.

Steps 1 to 3 of the filter cycle together define a nested function from log-spherical to log-spherical for the state, the function $\boldsymbol{f}(\boldsymbol{x})$ of Section 10.2. An application of the chain rule of differentiation produces the aforementioned corresponding Jacobian in the somewhat more compact form

$$\boldsymbol{J}_{10} = \begin{bmatrix} \boldsymbol{J}_{\boldsymbol{q}_1\boldsymbol{p}_1} & \mathbf{0} \\ \boldsymbol{J}_{\dot{\boldsymbol{q}}_1\boldsymbol{p}_1} & \boldsymbol{J}_{\dot{\boldsymbol{q}}_1\boldsymbol{v}_1} \end{bmatrix} \begin{bmatrix} \mathbf{1} & T\mathbf{1} \\ \mathbf{0} & \mathbf{1} \end{bmatrix} \begin{bmatrix} \boldsymbol{J}_{\boldsymbol{p}_0\boldsymbol{q}_0} & \mathbf{0} \\ \boldsymbol{J}_{\boldsymbol{v}_0\boldsymbol{q}_0} & \boldsymbol{J}_{\boldsymbol{v}_0\dot{\boldsymbol{q}}_0} \end{bmatrix} \tag{10.14}$$

This Jacobian does not depend on range, because range therein only shows up as an overall factor $r_0/r_1 = 1/\|\boldsymbol{g}_{10}\|$. Without any process noise, linearisation yields $\boldsymbol{P}_1 = \boldsymbol{J}_{10}\boldsymbol{P}_0\boldsymbol{J}_{10}^T$.

Angular-only measurements provide no range information at all for CV movements, the range is not observable (also cf. Section 10.3.5). Still, any arbitrarily chosen initial range produces the correct state transition for all log-spherical quantities except for the range itself where at least the range increment is still the correct one (i.e. the filter produces over time in itself consistent albeit usually not correct range estimates), and the same arbitrarily chosen initial range produces the correct covariance transition for zero process noise. In contrast to that, the chosen initial range does have an impact on filter output and performance in case the process noise is non-zero. $\boldsymbol{Q}$ is effectively scaled by $1/r_1^2$ in log-spherical space:

$$\boldsymbol{P}_1 = \boldsymbol{J}_{10}\boldsymbol{P}_0\boldsymbol{J}_{10}^T + \begin{bmatrix} \boldsymbol{J}_{\boldsymbol{q}_1\boldsymbol{p}_1} & \mathbf{0} \\ \boldsymbol{J}_{\dot{\boldsymbol{q}}_1\boldsymbol{p}_1} & \boldsymbol{J}_{\dot{\boldsymbol{q}}_1\boldsymbol{v}_1} \end{bmatrix} \boldsymbol{Q} \begin{bmatrix} \boldsymbol{J}_{\boldsymbol{q}_1\boldsymbol{p}_1}^T & \boldsymbol{J}_{\dot{\boldsymbol{q}}_1\boldsymbol{p}_1}^T \\ \mathbf{0} & \boldsymbol{J}_{\dot{\boldsymbol{q}}_1\boldsymbol{v}_1}^T \end{bmatrix} \tag{10.15}$$

Maximum (and possibly minimum) detection range of the sensor may help to obtain a rough estimate of the initial range (see the next section). However, if the thus determined initial filter range is still far larger than the true one, the process noise will effectively be under-estimated and the filter will become too stiff. This may finally lead to divergence. Vice versa, the smoothing effect of the filter is not as pronounced as it could be in case the initial range is chosen way too small. For improved estimation performance, a monitoring of innovation consistency may be used either to steer a multiple-model filter or to adaptively adjust the scaling of the process noise.

The key property of LSCs is given by the fact that they de-couple the propagation equations from the unobservable range. It is worth to note that this is mainly

caused by using the normalized range rate $\dot{\rho}$ as state variable. The use of the projected bearing rate ω instead of the bearing rate $\dot{\beta}$ induces a certain additional de-coupling from elevation. It is a nice feature that the normalized range rate is the time derivative of the logarithmic range (also cf. Section 10.3.5), but the choice of the latter does not contribute to de-coupling at all. The inverse range $1/r$, as has been proposed for the 2D *modified-polar filter* [12], or even the range r itself (in fact, any bijective function of r) would fulfil the same purpose. However, filters based on the logarithmic range have been shown to often provide superior performance when compared to the other ones. Unlike r and $1/r$, ρ is not restricted to be positive. No special measures must be taken due to possibly violated sign restrictions after filter update. Moreover, the values of ρ possess a similar order of magnitude as the other state variables for a large scope of ranges. This significantly reduces numerical problems when implementing the filter.

10.3.4 Filter initialization

For the initialization of a Cartesian KF with states position and velocity by means of position-only measurements, the following approaches are most popular:

1. Initialize position by first measurement and velocity as zero with chosen initial covariance (one-point initialization with prior).
2. Initialize position by second measurement, velocity by analytic solution of state transition equation based on first two position measurements, compute covariance accordingly (two-point differencing) [18].
3. Apply linear regression on multiple measurements to determine state and covariance (multiple-point-initialization). Variant 2 is a special case of this one.

For an initialization of log-spherical states with angular-only measurements, variants 1 and often 3 are applicable up to the fact that the unobservable range requires a prior in any case. With (at most) five observable states, no general analytic solution as in variant 2 can be provided, the system of (at least) three equations is over-determined.

10.3.4.1 One-point initialization with prior

Initially, measured bearing and elevation plus their measurement error variances can be used un-alteredly to initialize the respective angular states and covariances of the filter. For all remaining states, initial state estimates as well as covariances are computed based on assumptions with respect to prior distributions [19].

The prior distribution for the (Cartesian) position is assumed to be diffuse. Then, the detection of a target by a sensor with some minimum and maximum detection range $r_{\min}$ and $r_{\max}$ generates a homogeneous density $p(x, y, z)$ on a spherical shell yielding

$$p(r) = p_0 r^2 = \frac{r^2}{(1/3)(r_{\max}^3 - r_{\min}^3)} \quad \text{for } r_{\min} \leq r \leq r_{\max} \tag{10.16}$$

and $p(r) = 0$ elsewhere. Consequently, the initial estimate of the logarithmic range is taken as its expected value

$$\overline{\rho} = \mathrm{E}[\rho] = p_0 \int_{r_{\min}}^{r_{\max}} \log(r/R) r^2 \mathrm{d}r = \frac{r_{\max}^3 \rho_{\max} - r_{\min}^3 \rho_{\min}}{r_{\max}^3 - r_{\min}^3} - \frac{1}{3} \tag{10.17}$$

with $\rho_{\min} = \log(r_{\min}/R)$ and $\rho_{\max} = \log(r_{\max}/R)$. The corresponding estimation error variance can be computed to be

$$\mathrm{Var}[\rho] = \int_{r_{\min}}^{r_{\max}} \log^2\left(\frac{r}{R}\right) r^2 \mathrm{d}r - \overline{\rho}^2 = \frac{1}{9} - \frac{r_{\max}^3 r_{\min}^3 (\rho_{\max} - \rho_{\min})^2}{(r_{\max}^3 - r_{\min}^3)^2} \tag{10.18}$$

In the limit of zero minimum detection range, the results obtained simplify to

$$\mathrm{E}[\rho] = \rho_{\max} - \frac{1}{3} \quad \text{and} \quad \mathrm{Var}[\rho] = \frac{1}{9} \tag{10.19}$$

This in particular means that the filter is initialized with slightly more than half the maximum detection range according to $r_{\text{initial}} = \exp(-1/3) r_{\max} \approx 0.53 r_{\max}$.

In order to derive corresponding expressions for the log-spherical rates, the simplified case of a fixed platform is investigated first. Therein, an isotropic prior in the Cartesian velocity with zero-mean and independent of position is chosen. In particular, $\mathrm{E}[\boldsymbol{v}] = \boldsymbol{0}$ and $\mathrm{E}[\boldsymbol{v}\boldsymbol{p}^T] = \boldsymbol{0}$ as well as $\mathrm{E}[\boldsymbol{v}\boldsymbol{v}^T] = \sigma_{\text{vel}}^2 \boldsymbol{1}$ are assumed to hold. From $\dot{\boldsymbol{q}} = (1/r) \boldsymbol{T}^T(\beta, \varepsilon) \boldsymbol{v}$, there follows $\mathrm{E}[\dot{\boldsymbol{q}}] = \mathrm{E}\big[(1/r) \boldsymbol{T}^T(\beta, \varepsilon)\big] \mathrm{E}[\boldsymbol{v}] = \boldsymbol{0}$ as well as

$$\mathrm{E}\big[\dot{\boldsymbol{q}} \boldsymbol{q}^T\big] = \mathrm{E}\left[\frac{1}{r} \boldsymbol{T}^T(\beta, \varepsilon) \underbrace{\mathrm{E}[\boldsymbol{v}]}_{=\boldsymbol{0}} \boldsymbol{q}^T\right] = \boldsymbol{0} \tag{10.20}$$

and

$$\mathrm{E}\big[\dot{\boldsymbol{q}} \dot{\boldsymbol{q}}^T\big] = \mathrm{E}\left[\frac{1}{r^2} \boldsymbol{T}^T(\beta, \varepsilon) \underbrace{\mathrm{E}\big[\boldsymbol{v}\boldsymbol{v}^T\big]}_{=\sigma_{\text{vel}}^2 \boldsymbol{1}} \boldsymbol{T}(\beta, \varepsilon)\right] = \mathrm{E}\left[\frac{1}{r^2}\right] \sigma_{\text{vel}}^2 \boldsymbol{1} \tag{10.21}$$

As there holds

$$\mathrm{E}\left[\frac{1}{r^2}\right] = p_0 \int_{r_{\min}}^{r_{\max}} \frac{1}{r^2} r^2 \mathrm{d}r = 3 \frac{r_{\max} - r_{\min}}{r_{\max}^3 - r_{\min}^3} \tag{10.22}$$

the variances of the rate components read

$$\mathrm{Var}[\dot{\rho}] = \mathrm{Var}[\omega] = \mathrm{Var}[\dot{\varepsilon}] = 3\sigma_{\text{vel}}^2 \frac{r_{\max} - r_{\min}}{r_{\max}^3 - r_{\min}^3} \quad \overset{r_{\min} \to 0}{\to} \quad \frac{3\sigma_{\text{vel}}^2}{r_{\max}^2} \tag{10.23}$$

A non-zero own-ship velocity v_{own} of the sensor platform requires modifications of the derivations above. Just like the position, Cartesian velocity must be taken

relative to the one of the sensor platform in order to get the desired de-coupling of the remaining components from the range in LSCs. But, an assumption of a zero-mean initial value only makes sense for a Cartesian velocity defined in a stationary coordinate system that happens to have its origin in the platform position at initialization time. However, a detailed analysis of the resulting priors starting from a relative velocity v with expected value $-v_{\text{own}}$ and an isotropic variance matrix as above is tedious. In context with the filter cycle considered, it may even yield an unexpected outcome because the delivered velocity will be non-zero with respect to the stationary coordinate system. This unwanted behaviour favours a heuristic and much simpler approach to initialization:

1. Initialize $\boldsymbol{q}$ with prior logarithmic range $\overline{\rho}$ plus measured bearing $\beta_{\text{m},0}$ and elevation $\varepsilon_{\text{m},0}$ and the covariance matrix as $\text{Var}[\boldsymbol{q}] = \text{diag}\left\{\text{Var}[\rho], \sigma_\beta^2, \sigma_\varepsilon^2\right\}$.
2. Convert $\boldsymbol{q}$ and $\text{Var}[\boldsymbol{q}]$ from log-spherical to Cartesian space.
3. Append initial velocity $\boldsymbol{v} = -\boldsymbol{v}_{\text{own}}$ to state and $\text{Var}[\boldsymbol{v}] = \sigma_{\text{vel}}^2\mathbf{1}$ to covariance.
4. Continue with step 2 of the filter cycle.

For conversion via linearisation, this is the same as using initial rate components

$$\dot{\boldsymbol{q}}_0 = -\boldsymbol{E}^T(\varepsilon_{\text{m},0})\boldsymbol{B}^T(\beta_{\text{m},0})\frac{\boldsymbol{v}_{\text{own}}}{r_{\text{initial}}} \quad \text{with} \quad r_{\text{initial}} = R\exp(\overline{\rho}) \tag{10.24}$$

and a covariance that, with the Jacobians given earlier on, can be condensed to read

$$\boldsymbol{P} = \begin{bmatrix} \text{Var}[\boldsymbol{q}] & \text{Var}[\boldsymbol{q}]\boldsymbol{D}^T \\ \boldsymbol{D}\text{Var}[\boldsymbol{q}] & \boldsymbol{D}\text{Var}[\boldsymbol{q}]\boldsymbol{D}^T + \dfrac{\sigma_{\text{vel}}^2}{r_{\text{initial}}^2}\mathbf{1} \end{bmatrix} \quad \text{with} \quad \boldsymbol{D} = \boldsymbol{J}_{\dot{\boldsymbol{q}}\boldsymbol{p}}\boldsymbol{J}_{\boldsymbol{p}\boldsymbol{q}} \tag{10.25}$$

10.3.4.2 Multiple-point initialization with batch estimate

Based on measured values $\beta_{\text{m},i}$ and $\varepsilon_{\text{m},i}$ at times t_i, optimal values β_0, ε_0, $\dot{\rho}_0$, ω_0 and $\dot{\varepsilon}_0$ are sought assuming an undisturbed CV motion. But, the minimization of

$$\sum_i \left(\frac{(\beta_{\text{m},i} - \beta_i)^2}{\sigma_\beta^2} + \frac{(\varepsilon_{\text{m},i} - \varepsilon_i)^2}{\sigma_\varepsilon^2} \right) \text{with} \begin{matrix} \beta_i = \beta(\beta_0, \varepsilon_0, \dot{\rho}_0, \omega_0, \dot{\varepsilon}_0, t_i, t_0) \\ \varepsilon_i = \varepsilon(\beta_0, \varepsilon_0, \dot{\rho}_0, \omega_0, \dot{\varepsilon}_0, t_i, t_0) \end{matrix} \tag{10.26}$$

states a non-linear *least-squares* (LS) problem without closed form solution. Standard iterative methods for solving general non-linear LS problems can be applied but may be costly with respect to computational implementation effort. Moreover, it is not clear whether local optima exist for the concrete problem stated here which would make the solution process even more demanding.

A still iterative, yet fairly simple approximative approach makes use of the tilted plane shown in Figure 10.2 and consists of the following steps [19]:

1. Find an estimate of the normal vector $\boldsymbol{n}$ of the tilted plane.
2. Transform all values into the estimated tilted plane.
3. Set up non-linear equations based on a CV movement in that plane.

4. Iteratively determine the LS solution of the resulting equations.
5. Transform the solution back from the tilted plane into the original coordinates.

As all true position vectors $\boldsymbol{p}_i$ are orthogonal to $\boldsymbol{n}$, all true unit-length direction vectors $\boldsymbol{w}_i = [\cos(\beta_i)\cos(\varepsilon_i), \sin(\beta_i)\cos(\varepsilon_i), \sin(\varepsilon_i)]^T$ must fulfil $\boldsymbol{n}^T\boldsymbol{w}_i = 0$. An LS estimate of $\boldsymbol{n}$ can thus be obtained from the measured unit vectors $\boldsymbol{w}_{\mathrm{m},i}$ by selecting it to yield, under the constraint $\|\boldsymbol{n}\| = 1$,

$$\min_{\boldsymbol{n}} \left\{ \sum_i \left(\boldsymbol{n}^T \boldsymbol{w}_{\mathrm{m},i}\right)^2 \right\} = \min_{n} \left\{ \boldsymbol{n}^T \boldsymbol{W} \boldsymbol{n} \right\} \quad \text{with} \quad \boldsymbol{W} := \sum_i \boldsymbol{w}_{\mathrm{m},i} \boldsymbol{w}_{\mathrm{m},i}^T \tag{10.27}$$

Consequently, the estimate $\boldsymbol{n}$ in step 1 is chosen as a unit-length eigenvector referring to the smallest eigenvalue of $\boldsymbol{W}$.

With the true normal vector written as $\boldsymbol{n} = [\cos(\overline{\beta})\cos(\overline{\varepsilon}), \sin(\overline{\beta})\cos(\overline{\varepsilon}), \sin(\overline{\varepsilon})]^T$, the unitary transformation matrix

$$\boldsymbol{U} = \begin{bmatrix} -\cos(\overline{\beta})\sin(\overline{\varepsilon}) & -\sin(\overline{\beta}) & \cos(\overline{\beta})\cos(\overline{\varepsilon}) \\ -\sin(\overline{\beta})\sin(\overline{\varepsilon}) & \cos(\overline{\beta}) & \sin(\overline{\beta})\cos(\overline{\varepsilon}) \\ \cos(\overline{\varepsilon}) & 0 & \sin(\overline{\varepsilon}) \end{bmatrix} \tag{10.28}$$

produces according to $\tilde{\boldsymbol{w}}_i = \boldsymbol{U}^T\boldsymbol{w}_i = [\cos(\tilde{\beta}_i), \sin(\tilde{\beta}_i), 0]^T$ transformed unit vectors with zero z-components. In step 2 of the batch estimator, the estimated $\boldsymbol{n}$ is used to compute $\overline{\beta}$ and $\overline{\varepsilon}$ and herewith $\boldsymbol{U}$. The values $\tilde{\boldsymbol{w}}_{\mathrm{m},i} = \boldsymbol{U}^T\boldsymbol{w}_{\mathrm{m},i} = [\tilde{w}_{\mathrm{x},i}, \tilde{w}_{\mathrm{y},i}, \tilde{w}_{\mathrm{z},i}]^T$ then determine estimates for the tilted bearing angles via $\tilde{\beta}_i = \arctan_2(\tilde{w}_{\mathrm{y},i}, \tilde{w}_{\mathrm{x},i})$.

The transition equation for any true tilted bearing angle can be deduced from (10.6). It implies $\sin(\tilde{\beta}_i - \tilde{\beta}_0)(1 + \dot{\rho}_0 T_i) - \cos(\tilde{\beta}_i - \tilde{\beta}_0)\tilde{\omega}_0 T_i = 0$ with $T_i = t_i - t_0$. That can be written as $\boldsymbol{t}^T\boldsymbol{m}_i = 0$ with the vectors $\boldsymbol{t} = [c_0, s_0, c_0\dot{\rho}_0, s_0\dot{\rho}_0, c_0\tilde{\omega}_0, s_0\tilde{\omega}_0]^T$ and $\boldsymbol{m}_i = [s_i, -c_i, s_i T_i, -c_i T_i, -c_i T_i, -s_i T_i]^T$ using the abbreviations $c_i = \cos(\tilde{\beta}_i)$ as well as $s_i = \sin(\tilde{\beta}_i)$. Moreover, there must hold $\boldsymbol{t}^T\boldsymbol{m} = 1$ with $\boldsymbol{m} = [c_0, s_0, 0, 0, 0, 0]^T$. Step 3 of the batch estimator computes from the measured values vectors $\boldsymbol{m}_{\mathrm{m},i}$ and $\boldsymbol{m}_{\mathrm{m}}$. Herewith, $\boldsymbol{t}$ is defined as yielding the minimum of $\sum_i (\boldsymbol{t}^T\boldsymbol{m}_{\mathrm{m},i})^2 + (\boldsymbol{t}^T\boldsymbol{m}_{\mathrm{m}} - 1)^2$ under the constraint $c_0^2 + s_0^2 = 1$ and honouring the special structure of $\boldsymbol{t}$.

In step 4 of the batch estimator, the minimization task is re-written to an alternate form where $\boldsymbol{t}$ must, under the mentioned constraints, deliver

$$\min_{\boldsymbol{t}} \left\{ \boldsymbol{t}^T \boldsymbol{M} \boldsymbol{t} - 2\boldsymbol{t}^T \boldsymbol{m}_{\mathrm{m}} + 1 \right\} \quad \text{with} \quad \boldsymbol{M} := \boldsymbol{m}_{\mathrm{m}}\boldsymbol{m}_{\mathrm{m}}^T + \sum_i \boldsymbol{m}_{\mathrm{m},i}\boldsymbol{m}_{\mathrm{m},i}^T \tag{10.29}$$

For constrained minimization, $L(\lambda) := \boldsymbol{t}^T\boldsymbol{M}t - 2\boldsymbol{t}^T\boldsymbol{m}_{\mathrm{m}} + \lambda(1 - \{c_0^2 + s_0^2\})$ is used as Lagrange function with multiplier λ. It must be differentiated with respect to c_0, s_0, $\dot{\rho}_0$, $\tilde{\omega}_0$ and λ setting derivatives to zero (where the differentiation with respect to λ just yields the constraint). This results in a set of polynomial equations where a closed-form solution is unknown. However, the pair $(\dot{\rho}_0, \tilde{\omega}_0)$ can be determined as

a function of the pair (c_0, s_0) and vice versa. This way, an iterative scheme can be set up. Derivatives can compactly be written considering $\boldsymbol{M}$ decomposed into (2×2)-blocks $\boldsymbol{M}_{ij}$ with $\boldsymbol{M}_{ji} = \boldsymbol{M}_{ij}^T$ and abbreviating $\boldsymbol{a} = [c_0, s_0]^T$, $\boldsymbol{a}_\mathrm{m} = [c_{\mathrm{m},0}, s_{\mathrm{m},0}]^T$ and

$$\boldsymbol{A}^T = \begin{bmatrix} 1 & 0 & \dot{\rho}_0 & 0 & \tilde{\omega}_0 & 0 \\ 0 & 1 & 0 & \dot{\rho}_0 & 0 & \tilde{\omega}_0 \end{bmatrix} \tag{10.30}$$

Differentiation of $L(\lambda)$ with respect to $\dot{\rho}_0$ and $\tilde{\omega}_0$ yields

$$\begin{aligned} \boldsymbol{0} \stackrel{!}{=} \frac{1}{2}\frac{\partial L}{\partial[\dot{\rho}_0, \tilde{\omega}_0]} &= \begin{bmatrix} \boldsymbol{0}^T & \boldsymbol{a}^T & \boldsymbol{0}^T \\ \boldsymbol{0}^T & \boldsymbol{0}^T & \boldsymbol{a}^T \end{bmatrix} (\boldsymbol{M}\boldsymbol{t} - \boldsymbol{m}_\mathrm{m}) \\ &= \begin{bmatrix} \boldsymbol{a}^T\boldsymbol{M}_{12}^T\boldsymbol{a} & \boldsymbol{a}^T\boldsymbol{M}_{22}\boldsymbol{a} & \boldsymbol{a}^T\boldsymbol{M}_{23}\boldsymbol{a} \\ \boldsymbol{a}^T\boldsymbol{M}_{13}^T\boldsymbol{a} & \boldsymbol{a}^T\boldsymbol{M}_{23}^T\boldsymbol{a} & \boldsymbol{a}^T\boldsymbol{M}_{33}\boldsymbol{a} \end{bmatrix} \begin{bmatrix} 1 \\ \dot{\rho}_0 \\ \tilde{\omega}_0 \end{bmatrix} \end{aligned} \tag{10.31}$$

which delivers $\dot{\rho}_0$ and $\tilde{\omega}_0$ for a given a. On the other hand, differentiation with respect to c_0 and s_0 leads to

$$\boldsymbol{0} \stackrel{!}{=} \frac{1}{2}\frac{\partial L}{\partial \boldsymbol{a}^T} = \boldsymbol{A}^T\boldsymbol{M}\boldsymbol{t} - \lambda\boldsymbol{a} - \boldsymbol{a}_\mathrm{m} \quad \Leftrightarrow \quad \boldsymbol{a} = -(\lambda\boldsymbol{1} - \boldsymbol{A}^T\boldsymbol{M}\boldsymbol{A})^{-1}\boldsymbol{a}_\mathrm{m} \tag{10.32}$$

Computation of the inverse as quotient of adjoint and determinant plus successive insertion into the constraint $\boldsymbol{a}^T\boldsymbol{a} = 1$ yields a fourth-order polynomial in the multiplier λ. Once among the real roots of the polynomial that one minimizing $L(\lambda)$ has been determined (for given $\dot{\rho}_0$ and $\tilde{\omega}_0$), $\boldsymbol{a}$ is known, too. Starting from initial value $\boldsymbol{a}_\mathrm{m}$, $\boldsymbol{a}$ can be determined as fixed point of the mentioned iterative scheme. Convergence appears to be quite fast and can be accelerated by commonly known methods if necessary.

With estimates c_0 and s_0 as well as $\dot{\rho}_0$ and $\tilde{\omega}_0$ obtained, the final step of the estimator transforms the results back from the tilted plane into the original coordinate system. The estimated angles β_0 and ε_0 are obtained from the vector

$$\frac{\boldsymbol{p}_0}{r_0} = \begin{bmatrix} \cos(\beta_0)\cos(\varepsilon_0) \\ \sin(\beta_0)\cos(\varepsilon_0) \\ \sin(\varepsilon_0) \end{bmatrix} = \boldsymbol{U} \begin{bmatrix} c_0 \\ s_0 \\ 0 \end{bmatrix} \tag{10.33}$$

while the rates are computed via

$$\dot{\boldsymbol{q}}_0 = \boldsymbol{E}^T(\varepsilon_0)\boldsymbol{B}^T(\beta_0)\frac{\boldsymbol{v}_0}{r_0} = \boldsymbol{E}^T(\varepsilon_0)\boldsymbol{B}^T(\beta_0)\boldsymbol{U} \begin{bmatrix} c_0\dot{\rho}_0 - s_0\tilde{\omega}_0 \\ s_0\dot{\rho}_0 + c_0\tilde{\omega}_0 \\ 0 \end{bmatrix} \tag{10.34}$$

An explicit expression for the expected squared estimation error of the presented batch estimator is unknown. Only for certain geometries it seems to be justified to let the filter report as error covariance the *Cramér–Rao lower bound* (CLRB) of the upcoming section, evaluated at the estimates instead of the (unknown) true target state. The estimator sometimes tends towards degraded performance, especially in

cases of very large elevations and elevation rates. Here, the one-point initialization with prior and successive updates often proves much more robust. Better performance of one-point vs. multi-point initialization has also been reported for Cartesian-complete position measurements [20].

10.3.5 Performance bounds and observability

When trying to predict the achievable estimation accuracy based on a set of noisy measurements, the *Fisher information matrix* (FIM) plays a crucial role. It quantifies the joint contribution of all measurements to the available information about the originating state. The inverse of the FIM, if it exists, is the minimum estimation error covariance that no unbiased estimator can undercut. This absolute performance limit is called CLRB. For ease of presentation, zero-process noise is assumed next when computing FIM and CRLB for non-stochastic states to be estimated.

10.3.5.1 Fisher information and Cramér–Rao lower bound

For independent angular-only measurements and without prior knowledge, the FIM at time t_j based on some measurements received at times t_i with $i \leq j$ is given by

$$\boldsymbol{I}(t_j) = \sum_{i \leq j} \left(\frac{1}{\sigma_\beta^2} \boldsymbol{b}_{ij} \boldsymbol{b}_{ij}^T + \frac{1}{\sigma_\varepsilon^2} \boldsymbol{e}_{ij} \boldsymbol{e}_{ij}^T \right) \text{ with } \boldsymbol{b}_{ij}^T = \frac{\partial \beta_i}{\partial \boldsymbol{s}_j} \text{ and } \boldsymbol{e}_{ij}^T = \frac{\partial \varepsilon_i}{\partial \boldsymbol{s}_j} \tag{10.35}$$

Depending on the context within the following presentations, $\boldsymbol{s}_j$ will be either the full log-spherical state $\boldsymbol{x}$ or only the reduced one coming without range component, i.e. $\boldsymbol{s}_j = [(\rho_j), \beta_j, \varepsilon_j, \dot{\rho}_j, \omega_j, \dot{\varepsilon}_j]^T$. Furthermore, let $\boldsymbol{u}_\beta = [(0), 1, 0, 0, 0, 0]^T$ denote the unit vector related to the β-component and $\boldsymbol{u}_\varepsilon = [(0), 0, 1, 0, 0, 0]^T$ the one corresponding to the ε-component. Finally, define $\boldsymbol{u}_y = [0, 1, 0]^T$ and $\boldsymbol{u}_z = [0, 0, 1]^T$.

For now, the full log-spherical state $\boldsymbol{s} = \boldsymbol{x}$ is considered, and a CV movement is assumed. An application of the chain rule then yields the scaled information vectors

$$\frac{\partial \beta_i}{\partial \boldsymbol{s}_j} = \frac{\partial \beta_i}{\partial \boldsymbol{s}_i} \frac{\partial \boldsymbol{s}_i}{\partial \boldsymbol{s}_j} = \boldsymbol{u}_\beta^T \boldsymbol{J}_{ij} \quad \text{and} \quad \frac{\partial \varepsilon_i}{\partial \boldsymbol{s}_j} = \frac{\partial \varepsilon_i}{\partial \boldsymbol{s}_i} \frac{\partial \boldsymbol{s}_i}{\partial \boldsymbol{s}_j} = \boldsymbol{u}_\varepsilon^T \boldsymbol{J}_{ij} \tag{10.36}$$

with Jacobians $\boldsymbol{J}_{ij}$ in analogy to (10.14). In consequence, the scaled information vectors are given by the second and the third row of the $\boldsymbol{J}_{ij}$ or, equivalently, by

$$\begin{bmatrix} \boldsymbol{b}_{ij}^T \\ \boldsymbol{e}_{ij}^T \end{bmatrix} = \begin{bmatrix} \boldsymbol{u}_y^T \\ \boldsymbol{u}_z^T \end{bmatrix} \left[\boldsymbol{J}_{\boldsymbol{q}_i \boldsymbol{p}_i} \left(\boldsymbol{J}_{\boldsymbol{p}_j \boldsymbol{q}_j} + T_{ij} \boldsymbol{J}_{\boldsymbol{v}_j \boldsymbol{q}_j} \right), T_{ij} \tilde{\boldsymbol{J}}_{ij} \right], \quad \tilde{\boldsymbol{J}}_{ij} = \boldsymbol{J}_{\boldsymbol{q}_i \boldsymbol{p}_i} \boldsymbol{J}_{\boldsymbol{v}_j \dot{\boldsymbol{q}}_j} \tag{10.37}$$

with $T_{ij} = t_j - t_i$. Their ρ-components read $\boldsymbol{b}_{ij}^T \boldsymbol{u}_x = (\boldsymbol{T}_i \boldsymbol{u}_y)^T \boldsymbol{p}_i / (r_i \cos \varepsilon_i)$ as well as $\boldsymbol{e}_{ij}^T \boldsymbol{u}_x = (\boldsymbol{T}_i \boldsymbol{u}_z)^T \boldsymbol{p}_i / r_i$ due to (10.11) and (10.12). Both are always zero in accordance with the fact that there is no range-dependency in the transition equations. As a result, the (logarithmic) range is not observable, the FIM for the full six-dimensional state $\boldsymbol{x}$ is not invertible. But, if only the five-dimensional state

$\boldsymbol{s}$ without range-component is considered, the (5×5)-matrix $\boldsymbol{I}(t_j)$ can be inverted (for three or more measurement pairs obtained at distinct times) in most cases. If so, the CRLB can be computed for both angles and all three rate components.

The exception to that is the case when the target is performing a *strictly radial movement* (SRM), i.e. the target is moving with zero relative velocity or heading directly either towards or away from the platform and thus seen by the sensor under constant angles. Then, there holds $\omega = \dot{\beta} = \dot{\varepsilon} = 0$ as well as $\beta_i = \beta_j$ and $\varepsilon_i = \varepsilon_j$. Herewith, the matrix $\tilde{\boldsymbol{J}}_{ij}$ simplifies to a diagonal matrix and the $\dot{\rho}$-components of both information vectors $\boldsymbol{b}_{ij}^T = \boldsymbol{u}_y^T \boldsymbol{T}_{ij} \tilde{\boldsymbol{J}}_{ij} \boldsymbol{u}_x$ and $\boldsymbol{e}_{ij}^T = \boldsymbol{u}_z^T T_{ij} \tilde{\boldsymbol{J}}_{ij} \boldsymbol{u}_x$ become zero, too. Hence, the normalized range rate is not observable for an SRM. But, the CRLB for the remaining states can be computed. Prior to inversion, row and column referring to the non-observable $\dot{\rho}$-component in the FIM are to be omitted as well in order to get the sought CRLB.

10.3.5.2 Pseudo-measurements of normalized range rate

For jammed radar, there exists an at least conceptually possible way to gain probably missing information about the $\dot{\rho}$-component. It makes explicit use of the received signal power. If the jammer emits with constant radiation power, the received power will, under idealized conditions, be proportional to the inverse of the squared distance at time of emittance. So, for two measured received powers $S_0 = S(t_0)$ and $S_1 = S(t_1)$ emitted at corresponding distances r_0 and r_1, there holds $S_0/S_1 = (r_1/r_0)^2$. That can be used to compute $\log(S_0/S_1)/2 = \log(r_1/r_0) = \log(r_1/R) - \log(r_0/R)$. Now, the normalized range rate is the time derivative of the logarithmic range. Therefore, the approximation $\dot{r}/r = \dot{\rho} \approx \Delta\rho/\Delta t$ holds for sufficiently small Δt. In consequence,

$$\dot{\overline{\rho}} := \frac{1}{2} \frac{\log(S_0/S_1)}{t_1 - t_0} \approx \dot{\rho}(\overline{t}) \quad \text{with} \quad \overline{t} = \frac{1}{2}(t_0 + t_1) \tag{10.38}$$

provides a suitable pseudo-measurement of the normalized range rate. With some normalizing power S_n, linear regression in $\log(S/S_\mathrm{n})$ can be used to obtain improved pseudo-measurements of $\dot{\rho}$ based on batches of more than two power measurements. Then, (half of) the slope of the best fitting (in the LS sense) line determines $\dot{\overline{\rho}}$. Several of those pseudo-measurements have uncorrelated errors if the sets of power measurements used are disjoint. Like the angles bearing and elevation, the normalized range rate is a component of the log-spherical state vector. As before, a simple KF update is appropriate, and the additional information contained in one such measurement can be computed via the scaled information vector here being the fourth row of $\boldsymbol{J}_{ij}$.

In practice, the use of several shorter batches of a few power measurements each should yield better estimation performance than an increasingly long batch using all of them. Minor deviations of the tracked target from the CV movement are inevitable, so the use of at least some small process noise covariance matrix in the tracking filter is advised. Furthermore, a (at least almost) constant unknown factor between received power and squared inverse range cannot be safely assumed for too long-time intervals. Emitted power may fluctuate. And for targets not observed under constant angles, the aspect angle of the sensor-to-jammer-geometry changes

over time and herewith possibly the portion of emitted power being sent towards the sensor (via the antenna-pattern of the jammer). A receiving phased-array antenna with fixed orientation (electronically steered) will in addition vary in its effective cross-section. A compensation of this effect is in principle possible but, as it requires incorporating the angles, would introduce correlation. After all, the quality of the pseudo-measurements tends to decrease for larger angular rates while at the same time observability of the normalized range rate based on the angular measurements alone becomes increasingly better. Eventually, it will be better to refrain from incorporating the pseudo-measurements.

Deviations from the idealized free-space conditions will introduce further errors. Atmospheric attenuation is one of the effects to discuss here. Commonly, a constant attenuation per covered distance is assumed. When compared with the power S_k received under idealized conditions, the actually received one is written as $S_k^* = \exp(-r_k/r_\mathrm{d})S_k$ with some damping constant r_d. Therein, r_d is known to depend not only on radar frequency but also on air humidity and temperature. This attenuation introduces a (deterministic) bias error on the pseudo-measurement that becomes extremal for an SRM with constant radial velocity $\dot{r}$:

$$S_k^* = \exp(-r_k/r_\mathrm{d})S_k \quad \Rightarrow \quad \dot{\bar{\rho}}^* - \dot{\bar{\rho}} = \frac{1}{2r_\mathrm{d}}\frac{r_1 - r_0}{t_1 - t_0} \overset{\text{SRM}}{\rightarrow} \frac{\dot{r}}{2r_\mathrm{d}} \tag{10.39}$$

For example, an attenuation of 0.1 dB/km would yield $r_\mathrm{d} = 1\,\mathrm{km}/(0.01\log(10))$ and thus approximately $r_\mathrm{d} = 43.5$ km which in turn means about $2.3 \cdot 10^{-3}/\mathrm{s}$ systematic error on the pseudo-measurement for a jammer approaching with 200 m/s.

If at all, the pseudo-measurements described here may be useful for airborne radar. Surface-based radar can be expected to suffer much more from disturbing reflections and thus, in particular, from fluctuations in the received signal power.

10.3.5.3 Prior information

The prior derived in Section 10.3.4.1 comes with a certain information contribution, too. To honour it within the FIM as considered in this chapter, the prior values are treated like virtual measurements at initial time t_0 with according variances $\mathrm{Var}[\rho]$ and $\mathrm{Var}[\dot{\rho}]$ as in (10.18) and (10.23). With $\boldsymbol{u}_\rho$, $\boldsymbol{u}_{\dot{\rho}}$, $\boldsymbol{u}_\omega$ and $\boldsymbol{u}_{\dot{\varepsilon}}$ defined in an obvious way, the information matrix of (10.35) with dimension 6×6 is thus increased by

$$\boldsymbol{I}_\mathrm{p}(t_j) = \boldsymbol{J}_{0j}^T \left[\frac{1}{\mathrm{Var}[\rho]} \boldsymbol{u}_\rho \boldsymbol{u}_\rho^T + \frac{1}{\mathrm{Var}[\dot{\rho}]} \left(\boldsymbol{u}_{\dot{\rho}} \boldsymbol{u}_{\dot{\rho}}^T + \boldsymbol{u}_\omega \boldsymbol{u}_\omega^T + \boldsymbol{u}_{\dot{\varepsilon}} \boldsymbol{u}_{\dot{\varepsilon}}^T \right) \right] \boldsymbol{J}_{0j} \tag{10.40}$$

10.3.5.4 Sample scenario

Figure 10.4 compares tracking results with CRLBs for a scenario where a sensor provided angular measurements with accuracies $\sigma_\beta = \sigma_\varepsilon = 0.2$ deg at sample time $T = 1$ s. It was mounted on a platform starting from initial position zero and moving horizontally in pure x-direction with speed $v_\mathrm{own} = 200\ m/s$. Initial position and velocity of the tracked target were $\boldsymbol{p}_0^T = [27250, 9150, -300]$ m with

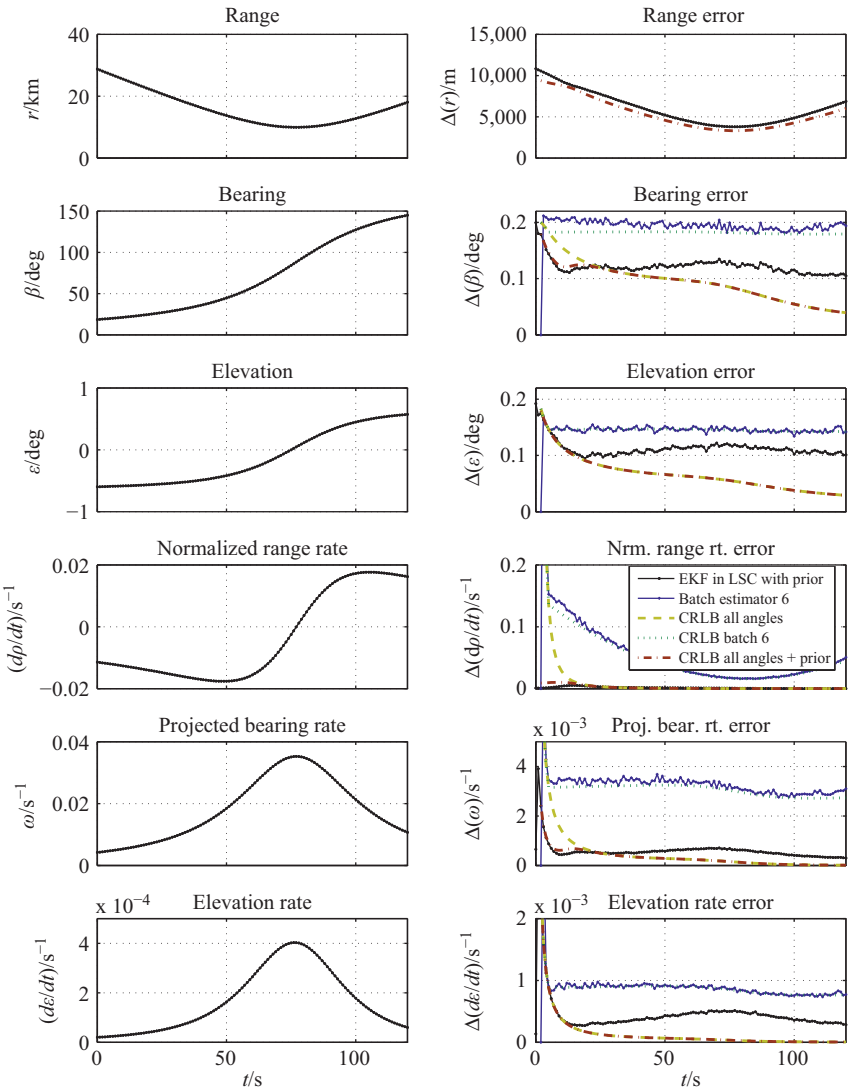

Figure 10.4 Target states in log-spherical coordinates (left) as well as Cramer–Rao lower bounds and filter root mean square errors (right) for a passing target, measured angles only

$\boldsymbol{\nu}_0^T = [-150, 10, 4]\,\mathrm{m/s}$. The described EKF in LSCs has been initialized with the derived prior (for $r_{\min} = 0\,\mathrm{m}$, $r_{\max} = 25\,\mathrm{km}$ and $v_{\max} = 250\,\mathrm{m/s}$). It has been run assuming some small process noise $q = 10\,\mathrm{m}^2/\mathrm{s}^3$ for it.

Filter results are displayed as *root mean square errors* (RMSEs) obtained in 1,000 Monte-Carlo runs. For a while, filter performance is close to the CLRB being computed with the prior contribution (10.40). Some initial deviation is caused by a

discrepancy between modelling assumption and simulation set-up for the prior. Later on, the CRLB is not matched well any more due to the process noise matrix applied when filtering. The non-observable range shows a consistent error induced by its prior because it is always initialized with a value being smaller than the true initial one.

Finally, the figure also shows the results obtained with the batch estimator of Section 10.3.4.2. Therein, up to the six (where available) most recently received measurement pairs were honoured. The corresponding CRLB clearly indicates that the level of observability of the normalized range rate decreases with increasing range. A low observability shows up with an even increased RMSE for the batch estimator.

10.4 Collision avoidance

In *collision avoidance* applications, a sensor-equipped platform is to detect whether an intruding target is going to collide with the platform. If so, the platform will have to perform avoiding manoeuvres. Not only collision avoidance itself is a must, it is commonly preceded with a phase in which much less abrupt separating manoeuvres are performed by the platform in order to keep a certain minimum distance between intruder and own-ship. In order to do so, a prediction is necessary on how close the intruder will ever get and at which time it will reach this crucial point.

In accordance with Figure 10.5, the position at the point of closest approach must be orthogonal to the velocity of the intruder. In consequence, an evaluation of the equation $0 = \boldsymbol{v}_1^T \boldsymbol{p}_1 = \boldsymbol{v}_0^T(\boldsymbol{p}_0 + T_c \boldsymbol{v}_0)$ delivers the *time to the closest approach* T_c, the corresponding *closest distance* r_c subsequently can be obtained from $r_c/r_0 = \|\boldsymbol{g}_c\|$. It turns out that both results do not require knowledge about the full set of quantities appearing in LSCs. With $\tilde{\omega}_0^2 = \omega_0^2 + \dot{\varepsilon}_0^2$, there holds

$$T_c = -\frac{\boldsymbol{v}_0^T \boldsymbol{p}_0}{\boldsymbol{v}_0^T \boldsymbol{v}_0} = -\frac{\dot{\rho}_0}{\dot{\rho}_0^2 + \tilde{\omega}_0^2} \quad \text{and} \quad \frac{r_c}{r_0} = \sqrt{\frac{\tilde{\omega}_0^2}{\dot{\rho}_0^2 + \tilde{\omega}_0^2}} \tag{10.41}$$

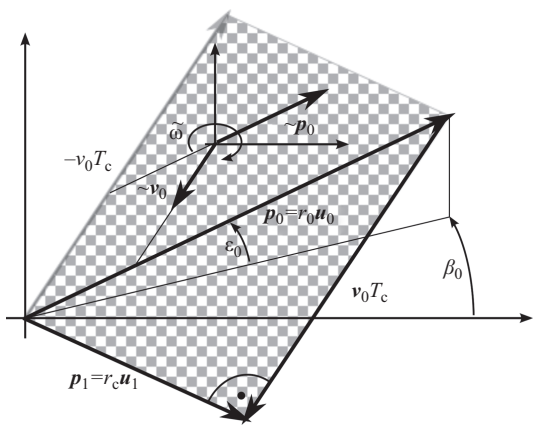

Figure 10.5 Orthogonality condition for the point $\boldsymbol{p}_1$ of closest approach

Table 10.1 Measured and observable states plus number of measurements required to obtain the states for some non-cooperative and cooperative sensors

Source	Measured	Observable	Requ.	Coop.
3D Doppler radar	$r, \beta, \varepsilon, \dot{r}$	$\rho, \beta, \varepsilon, \dot{\rho}, \omega, \dot{\varepsilon}$	2	No
Optical without size	β, ε	$\beta, \varepsilon, \dot{\rho}^*, \omega, \dot{\varepsilon}$	3	No
Optical with size	$\beta, \varepsilon, \dot{\rho}$	$\beta, \varepsilon, \dot{\rho}, \omega, \dot{\varepsilon}$	2	No
ACAS omni without altitude	r	$\rho, \dot{\rho}, \lvert\tilde{\omega}\rvert$	3	Yes
ACAS omni with altitude	r, z	$\rho, \varepsilon, \dot{\rho}, \lvert\omega\rvert, \dot{\varepsilon}$	3	Yes

*Observable only if $\omega^2 + \dot{\varepsilon}^2 > 0$.

So, both the time to closest approach and the ratio closest over initial range can be determined from the rates alone.

10.4.1 Sensor tracking

One key factor for a reliable and safe collision avoidance system is a suitably selected sensor suite. A variety of sensors exist, each class has its own pros and cons with respect to measurement accuracy, sensitivity to adverse weather conditions, energy consumption, required space, costs etc. Moreover, some sensors require cooperation and thus a certain equipment on the intruder's side. A survey on this matter can be found in [5], while Table 10.1 summarizes some facts detailed in the upcoming sections.

10.4.1.1 Radar

Among the sensors considered here for collision avoidance, a modern 3D Doppler radar probably is the most versatile one. It requires no cooperation of the intruder and at the same time is the only one delivering a completely observable state space.

The update with a pair of two independently measured angles has been discussed earlier on. A Doppler radar in addition measures range and range rate where, due to the internal processing, usually some correlation occurs between their measurement errors yielding a non-diagonal measurement error variance matrix $\boldsymbol{R}_{r\dot{r}}$. An EKF update with range and range rate in log-spherical state space can be performed using

$$\boldsymbol{h}(\boldsymbol{x}) = \begin{bmatrix} r \\ \dot{r} \end{bmatrix} \Rightarrow \boldsymbol{H}(\boldsymbol{x}) = \frac{\partial \boldsymbol{h}}{\partial \boldsymbol{x}} = r \begin{bmatrix} 1 & 0 \\ \dot{\rho} & 1 \end{bmatrix} \begin{bmatrix} \boldsymbol{u}_\rho^T \\ \boldsymbol{u}_{\dot{\rho}}^T \end{bmatrix} \tag{10.42}$$

Without any prior information, two measurement sets (with or without) Doppler are necessary and sufficient to obtain all six-state variables. The contribution of one measurement pair $(r_i, \dot{r}_i)$ at time t_i to the available information at time t_j reads, with the quantities above, $\boldsymbol{I}_{r_i,\dot{r}_i}(t_j) = \boldsymbol{J}_{ij}^T [\boldsymbol{H}(x_i)]^T \boldsymbol{R}_{r,\dot{r}}^{-1} \boldsymbol{H}(x_i) \boldsymbol{J}_{ij}$.

10.4.1.2 Passive optical sensor

After object extraction, a passive optical sensor delivers as measurements in particular the (pixel) position in a 2D image. With known sensor geometry, this image position can be transformed into two angles, e.g. bearing and elevation. Alternatively, the sine angles u and v can be considered an equivalent representation. Without any further information, the measured kinematic states are, although often coming with much smaller errors, analogous to those of jammed radar. As there, the (logarithmic) range is never observable for a CV movement while $\dot{\rho}$ is observable only if the intruder is neither on a collision course nor on an escape course (thus not performing an SRM). The estimation of the five observable states then requires three measurement pairs.

Again, missing information about the normalized range rate becomes available by generating pseudo-measurements thereof [17]. The results of Figure 10.6, generalized to two optical dimensions, show that the extent of the intruder translates into some area in the image plane that can be used instead of the received signal power. While neither fluctuation in physical size of the intruder nor an atmospheric attenuation play a role here, the influence of a changing aspect angle must be considered for an optical sensor as well. A significantly changed aspect angle may cause a complete change in the 2D projection of the rigid body. For intruders detected to perform an (almost) SRM however, the aspect angle should not change by any significant amount. Thus, the area in the image plane can be considered to be inverse proportional to the square of the range. Then, the rest works like before as long as pixel effects are small enough. Two measurement pairs of angles plus two size measurements (yielding one pseudo-measurement of $\dot{\rho}$) suffice to compute all five observable states.

10.4.1.3 ACAS or IFF with omnidirectional antenna

Consider a range-giving cooperative sensor with an antenna yielding only rough direction measurements or none at all. Typical representatives would be an

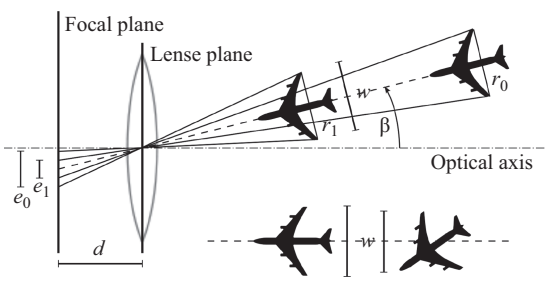

Figure 10.6 Schematic view of measured vs. physical size and influence of aspect angle in top view (not to scale). For distance d between lense and focal plane and an object of width w in distance r from the lense's centre seen under angle β, there holds $e/d = (w\cos\beta)/(r\cos\beta) = w/r$ for the extent e in the focal plane

air-collision avoidance system (ACAS) or an IFF (*interrogation friend or foe*) interrogator with an omnidirectional antenna. In case both the sensor platform and the intruder measure their respective barometric altitudes and the latter transmits (e.g. via Mode C) its measured value to the former, a measurement of the altitude difference between the two participants is available. This difference is the z-component in the sensor's local coordinate system as long as the distance is small enough such that the Earth's curvature can be ignored.

Both measurements of r and z possess mutually uncorrelated errors with respective variances σ_r^2 and σ_z^2, hence the error matrix is $\boldsymbol{R}_{r,z} = \mathrm{diag}\{\sigma_r^2, \sigma_z^2\}$. Herewith, an EKF filter update would be based on

$$\boldsymbol{h}(\boldsymbol{x}) = \begin{bmatrix} r \\ r\sin\varepsilon \end{bmatrix} \Rightarrow \boldsymbol{H}(\boldsymbol{x}) = \frac{\partial \boldsymbol{h}}{\partial \boldsymbol{x}} = r\begin{bmatrix} 1 & 0 \\ \sin\varepsilon & \cos\varepsilon \end{bmatrix}\begin{bmatrix} \boldsymbol{u}_\rho^T \\ \boldsymbol{u}_\varepsilon^T \end{bmatrix} \tag{10.43}$$

An inspection of (10.6) reveals that bearing cannot be estimated if it is not measured. Based on the first and third equations alone, it is also impossible to tell whether any increment in bearing is clockwise or counter clockwise. This is due to the fact that bearing rate occurs as ω^2 only. But, because it does occur at all, at least the magnitude of the bearing rate can be estimated. With the exception of bearing and sign of bearing rate, all states are observable by three measurement pairs. Each pair contributes $\boldsymbol{I}_{r_i,z_i}(t_j) = \boldsymbol{J}_{ij}^T[\boldsymbol{H}(\boldsymbol{x}_i)]^T\boldsymbol{R}_{r,z}^{-1}\boldsymbol{H}(\boldsymbol{x}_i)\boldsymbol{J}_{ij}$ to the information.

In case no altitude difference is available, the tilt angle of the motion plane with respect to the platform as shown in Figure 10.2 loses its observability and the tracking problem becomes range-only tracking. 2D log-polar tracking should then be used to estimate the remaining three observable states ρ, $\dot{\rho}$ and $|\tilde{\omega}|$ based on the scalar range measurements with $\boldsymbol{h}(\tilde{\boldsymbol{x}}) = r \Rightarrow \boldsymbol{H}(\tilde{\boldsymbol{x}}) = r\tilde{\boldsymbol{u}}_\rho^T$ and accordingly determined information contributions.

10.4.2 Track fusion

Like in all fusion systems, several general architecture approaches exist for systems used in airborne collision avoidance. A hierarchical structure as depicted in Figure 10.7 is often chosen. Herewith, data-association and kinematics estimation can run on sensor level, individually adapted to the different update rates of the sensors and making use of the underlying nature and specific features of the data.

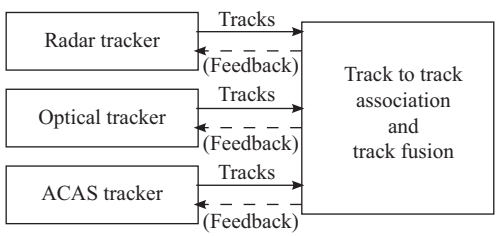

Figure 10.7 Simple hierarchical fusion scheme with sensor tracking, track-to-track association and fusion plus optional feedback

For example, electro-optical (EO) sensors can be expected to deliver individual measurements at high data rates. Feature-based data-association in high-rate images compensated for ego-motion in general is significantly easier than for radar usually coming with larger scan times and fewer features. In cooperative equipment, data association should be almost trivial as the intruder identifies itself. Feedback of existence information from the fusion centre to the sensor level tracking systems may be used to help track initiation or to avoid premature track drops in case of low detection probabilities.

In the fusion centre, the labelled sensor tracks undergo a track-to-track data association. Therein, the non-observability of certain states must and can be honoured in an appropriate fashion, e.g. for association of tracks based on passive optical measurements including size with ACAS/IFF based on range and altitude difference (without measured bearing), the quantities ε, $\dot{\rho}$, $|\omega|$ and $\dot{\varepsilon}$ can be evaluated. In case ACAS/IFF here has no elevation information, $\dot{\rho}$ and $|\tilde{\omega}|$ vs. $\sqrt{\omega^2 + \dot{\varepsilon}^2}$ remain as suitable variables to evaluate for matching.

Likewise, (non-)observability of sub-spaces influences the computation of joint estimates. This can be handled in an elegant manner by applying *convex combination* (CC) [21], an information-based fusion scheme. For two estimates $\boldsymbol{x}_1$ and $\boldsymbol{x}_2$ (the index here indicating the data source rather than the time) and corresponding error covariances $\boldsymbol{P}_1$ and $\boldsymbol{P}_2$, the information matrices $\boldsymbol{I}_1 = \boldsymbol{P}_1^{-1}$ and $\boldsymbol{I}_2 = \boldsymbol{P}_2^{-1}$ as well as information vectors $\boldsymbol{i}_1 = \boldsymbol{I}_1\boldsymbol{x}_1$ and $\boldsymbol{i}_2 = \boldsymbol{I}_2\boldsymbol{x}_2$ are computed. Subsequently, the information is added up according to $\boldsymbol{i} = \boldsymbol{i}_1 + \boldsymbol{i}_2$ and $\boldsymbol{I} = \boldsymbol{I}_1 + \boldsymbol{I}_2$ before computing for the joint estimate $\boldsymbol{x} = \boldsymbol{P}i$ with $\boldsymbol{P} = \boldsymbol{I}^{-1}$. Computation of information from state and covariance uses observable states only, missing information is then accounted for by using zero values to extend information vector and matrix to the dimension needed for addition. Despite its apparent simplicity, some care about details is necessary when applying information-based fusion in log-spherical state space. As in Section 10.3.2, one must avoid differences between bearings that exceed π in magnitude by according adjustments prior to conversion from state to information space. Values like, e.g. the elevation may be missing in one estimate (say in $\boldsymbol{x}_1$) yet would be needed for transformation. If provided by the other estimate (then $\boldsymbol{x}_2$), they safely can be taken from there for transforming the incomplete estimate as long as the information contribution is set to zero in the corresponding information matrix (here $\boldsymbol{I}_1$).

Information-based fusion by CC assumes uncorrelatedness between the estimation errors of the individual estimates that are fused. A common prior destroys this independence as well as common process noise does, but those effects usually are only marginal in collision avoidance applications. However, relevant correlation will occur if the feedback indicated in Figure 10.7 is not limited to existence indications, but rather encompasses kinematic information actually being used to update the estimates in the tracker. In this case, *covariance intersection* (CI) can be used to ensure conservative fused estimates [22]. These are always consistent in the sense that the actual mean squared estimation error never exceeds the covariance reported (as long as individual estimates have been consistent). Just like CC, CI is information-based, but rather uses $\boldsymbol{i} = w_1\boldsymbol{i}_1 + w_2\boldsymbol{i}_2$ and $\boldsymbol{I} = w_1\boldsymbol{I}_1 + w_2\boldsymbol{I}_2$ to

compute the fused information with some non-negative weights w_1 and w_2 summing up to one. The weights can be selected according to some optimization criterion or as $w_1 = (\det[\boldsymbol{I}_1 + \boldsymbol{I}_2] + \det[\boldsymbol{I}_1] - \det[\boldsymbol{I}_2])/(2\det[\boldsymbol{I}_1 + \boldsymbol{I}_2])$ and $w_2 = (\det[\boldsymbol{I}_1 + \boldsymbol{I}_2] + \det[\boldsymbol{I}_2] - \det[\boldsymbol{I}_1])/(2\det[\boldsymbol{I}_1 + \boldsymbol{I}_2])$. The latter choice requires no numerical optimization and yields good estimation results especially if correlation happens to be low [23], weights simplify to $1/2$ each in case that both individual estimates deliver incomplete information but the combined information is complete.

10.4.3 Performance bounds

Figure 10.8 depicts as performance bounds the CRLBs for different sensor suites based on a platform moving as in Section 10.3.5.4. At $\boldsymbol{p}_0^T = [31250, -850, -300]$ m, the intruder started with $\boldsymbol{v}_0^T = [-150, 10, 4]$ m/s and thus came as close to the platform as about 370 m. An update interval of $T = 1$ s was used for all sensors for simplicity, accuracies for EO were $\sigma_\beta = \sigma_\varepsilon = 0.2$ deg, radar had $\sigma_r = 20$ m and $\sigma_{\dot{r}} = 2$ m/s with correlation factor 0.3 as well as $\sigma_\beta = \sigma_\varepsilon = 0.5$ deg while $\sigma_r = 15$ m and $\sigma_z = 30$ m were used for ACAS.

All CRLBs have been computed without prior information. In accordance with the respective non-observability, no values are shown for the range of the EO and the bearing of the ACAS. The normalized range rate of the EO and the projected bearing rate of the ACAS are only weakly observable at larger distances and thus the corresponding bounds start from very high values. In the vicinity of the point of closest approach the ACAS shows, not surprisingly, weak elevation and hence also elevation rate performance. Due to the sudden change in platform-to-intruder geometry, also the remaining components are affected by this as are those for the other sensors.

As an example for the increased estimation accuracy achievable by fusion of data in a mixed sensor set-up, the combination radar/EO is considered in the figure. As indicated by the CRLBs, it is expected that this combination can yield better performance than each of the individual sensors alone.

10.5 Kinematic ranging

With the set-up of the four-step filter cycle of Section 10.3, the task of kinematic ranging with angular-only measurements can also be fulfilled. Herein, the platform performs suitable manoeuvres in order to gain the otherwise missing range information.

10.5.1 Propagation/prediction

Without a CV relative motion, (10.5) to (10.8) no longer hold. Rather than that, the propagation equation between the Cartesian states $\boldsymbol{x}_0$ and $\boldsymbol{x}_1$, both taken relative to the respective own-ship states $\boldsymbol{x}_0^{\text{own}}$ and $\boldsymbol{x}_1^{\text{own}}$, in general must be determined from $\boldsymbol{x}_1 + \boldsymbol{x}_1^{\text{own}} = \boldsymbol{F}(\boldsymbol{x}_0 + \boldsymbol{x}_0^{\text{own}}) + \boldsymbol{v}_k$ with the matrix $\boldsymbol{F}$ of (10.13). It consequently can be written as $\boldsymbol{x}_1 = \boldsymbol{F}\boldsymbol{x}_0 + \boldsymbol{v}_k + \left[\boldsymbol{F}\boldsymbol{x}_0^{\text{own}} - \boldsymbol{x}_1^{\text{own}}\right]$. The only formal change in

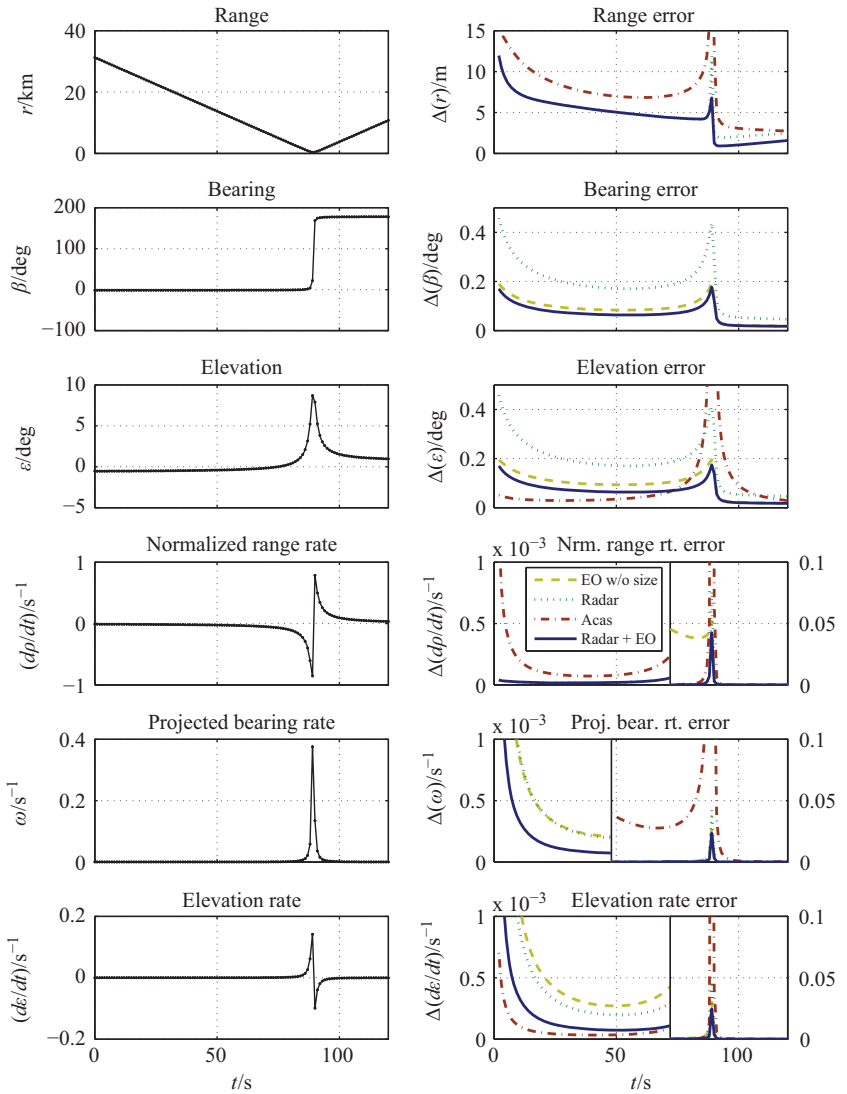

Figure 10.8 Target states in log-spherical coordinates (left) as well as Cramer–Rao lower bounds (right) for an almost colliding intruder, different sensors used

the nested approach of Section 10.3.3 thus is an additive term in the Cartesian state transition. As the values of this term are assumed to be provided with sufficient precision by the platform's inertial navigation system, they are considered as known control inputs. Thus, they do not change the manner to compute the overall propagation Jacobian (10.14), and the FIM can formally be computed as before. However, the term $\boldsymbol{F}\boldsymbol{x}_0^{\text{own}} - \boldsymbol{x}_1^{\text{own}}$ (vanishing for a non-manoeuvring platform) now

can be chosen to prevent the cancellation of certain terms in the FIM such that in particular the range becomes observable.

10.5.2 Sample scenario

The sample scenario shown in Figure 10.9 is based on a jammed platform where the on-board radar measured angles with precisions $\sigma_\beta = \sigma_\varepsilon = 0.2$ deg once a second. The platform started from position zero and initially moved horizontally in pure x-direction with speed $v_{\text{own}} = 200$ m/s before weaving along seven quarter-circles with cross-acceleration of about 3 g each in order to stay away from the jammer starting at $\boldsymbol{p}_0^T = [31250, -850, -300]$ m with $\boldsymbol{v}_0^T = [-150, 10, 4]$ m/s.

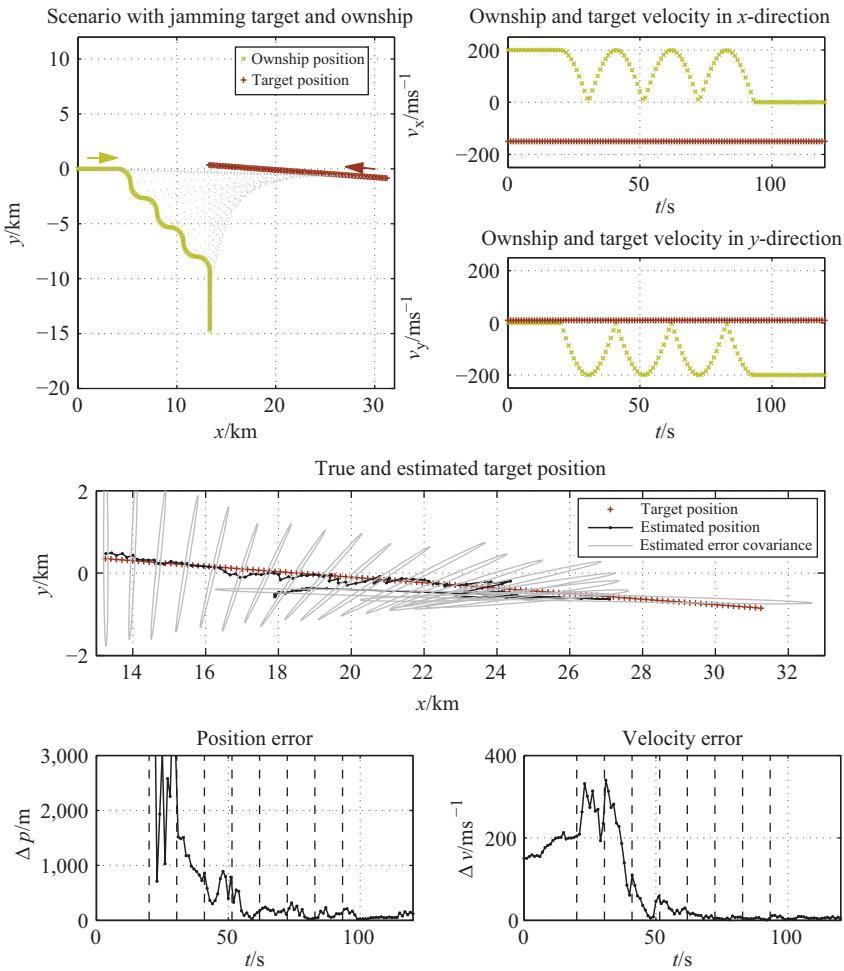

Figure 10.9 Scenario (top) as well as single-run filter output (middle) and errors (bottom) for a jamming target subject to kinematic ranging

The shown result of a single (very favourite) run with corresponding 90-per-cent error ellipses visualizes the changing geometry. In the beginning, the lack of range observability causes larger uncertainties in x-direction (based on the assumed prior). Observability builds up and improves significantly in manoeuvre phase before becoming weaker again (now with larger uncertainties in y-direction) as the platform escapes. The CRLBs as well as the outcomes of 1,000 Monte-Carlo runs in Figure 10.10 confirm these findings.

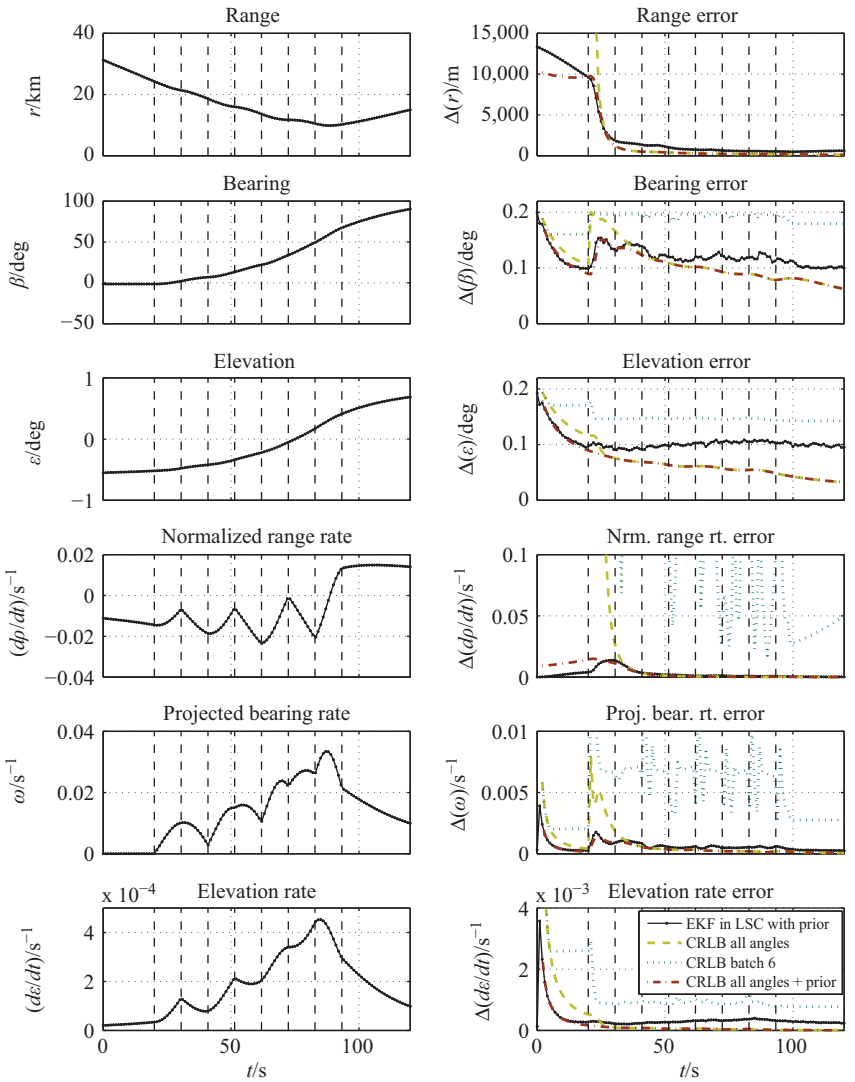

Figure 10.10 Target states in log-spherical coordinates (left) as well as Cramer–Rao lower bounds and filter root mean square errors (right) for a jamming target subject to kinematic ranging

10.5.3 Observer trajectory planning

With the possibility to enforce range observability by certain manoeuvres, the question arises on exactly how to choose the own-ship's flight path in order to gain maximum information about the jammer's dynamic state. The classical problem of *observer trajectory planning* has a long history and still is subject to on-going research.

In an early work [24], a thorough study has been performed on how to choose successive legs to obtain a maximum determinant of the FIM in the 2D bearings-only tracking problem known as *target motion analysis*. A solution has been given using a couple of simplifying assumptions and approximations.

Other authors [25] have claimed (without proof) that the maximization of the mutual information between observer trajectory and final target state is equivalent to minimizing the determinant of the error covariance matrix. Based on this, they proposed some sub-optimal strategies to determine suitable own-ship manoeuvres for bearings-only tracking [26]. In combination with the EKF in LSCs as described in this chapter, their simplest strategy would read as follows: Starting from estimates $\boldsymbol{x}_{k|k}$ and $\boldsymbol{P}_{k|k}$, specify a discrete set of possible manoeuvres for the next time interval. For each manoeuvre, perform the corresponding filter prediction step and compute the matrix $\boldsymbol{P}_{k+1|k+1}$ that would be the result of a measurement update. That result is independent of a (not yet received) measurement at time t_k in LSCs and corresponds in Cartesian coordinates to the outcome of an update with an assumed zero innovation. Among the candidate matrices, determine the one yielding the minimum determinant and herewith select the actual manoeuvre to perform. Instead of the determinant of $\boldsymbol{P}_{k+1|k+1}$, it has also been proposed to use its trace or its largest eigenvalue as value to minimize. Further on, the whole matrix $\boldsymbol{P}_{k+1|k+1}$ or only its position part can be considered on this behalf.

Figure 10.11 displays several outcomes of this simple 'one-step-ahead optimization' for different realizations of the measurement noise with an initial scenario set-up as in the previous section. Herein, coordinated turns with cross-accelerations ranging in magnitude from zero up to $40\,\mathrm{m/s^2}$ in steps of $5\,\mathrm{m/s^2}$ were selected after 20 s of straight flight. As a reference, the figure also shows a somewhat optimized trajectory (including corresponding single-run estimation results) that maximizes in each step the position part of the true FIM (which is not available to the trajectory planner). Typically, the own-ship trajectories tend to 'zoom in' on the target and certain manoeuvres must be excepted from the planning as to avoid collision here. To this end, $\boldsymbol{P}_{k+1|k}$ can be used to define a volume not to enter. The figure shows some bifurcation in the own-ship trajectories due to the fact that the scenario set-up is almost symmetric. Herewith, it emphasizes a general weakness of the simple strategy which only performs local optimization for a highly non-linear optimization problem.

More sophisticated trajectory planners honour the non-linearity by treating the planning task as a stochastic optimization problem. However, the solution of that problem turns out to be very demanding, and the resulting algorithms often require

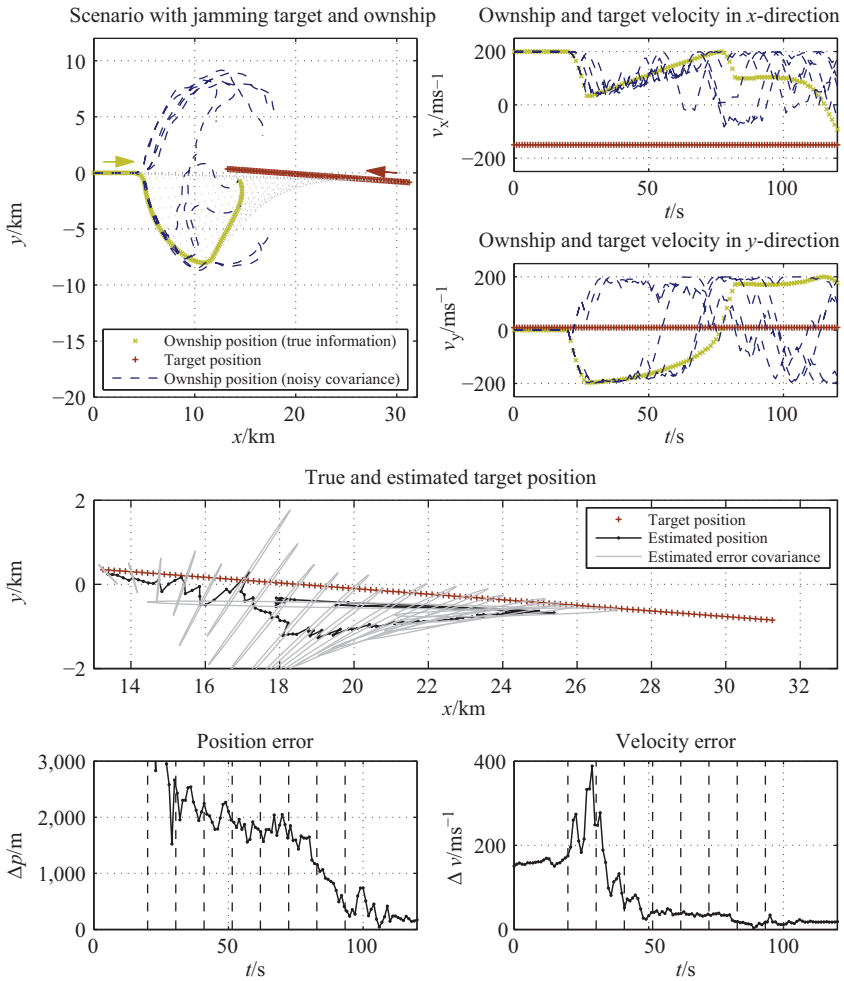

Figure 10.11 Own-ship trajectories resulting from observer trajectory planning

the application of stochastic integration methods (as they are also used, e.g. for so-called particle filters). Those methods are out of scope for this presentation, and the interested reader is referred to the corresponding literature like [27,28].

10.6 Summary

In certain tracking and data fusion applications, LSCs constitute an attractive alternative to Cartesian ones, especially when sensors provide measurements that are polar in nature but not Cartesian-complete. Those coordinates de-couple observable states from non-observable ones. This leads to robust estimators.

Glossary

Acronyms

2D/3D	two-/three-dimensional	IFF	interrogation friend or foe
ACAS	air-collision avoidance system	KF	Kalman filter
CC	convex combination		
CI	covariance intersection	LS	least-squares
CRLB	Cramer–Rao lower bound	LSC	log-spherical coordinate
CV	constant velocity		
EKF	extended Kalman filter	RMSE	root mean square error
ENU	east-north-up	SRM	strictly radial movement
FIM	Fisher information matrix	UKF	Unscented Kalman filter

References

[1] Blair W. D., Watson G. A., Kirubarajan T., Bar-Shalom Y. 'Benchmark for radar allocation and tracking in ECM'. *IEEE Transactions on Aerospace and Electronic Systems*. 1998;**34**(4):1097–1114.

[2] Blanding W., Koch W., Nickel U. 'Tracking through jamming using negative information'. *Proceedings of the 9th ISIF International Conference on Information Fusion*. 2006, pp. 1–8.

[3] *Airborne collision avoidance system II (ACAS II)* [online]. Available from http://www.eurocontrol.int/acas, [Accessed 27 Sep 2015].

[4] *Unmanned aircraft systems – ATM collision avoidance requirements* [online]. Available from http://www.eurocontrol.int/articles/acas-ii-studies, [Accessed 27 Sep 2015].

[5] Lacher A. R., Maroney D. R., Zeitlin A. D. *Unmanned aircraft collision avoidance – Technology assessment and evaluation methods*, 2007 [online]. Available from http://www.mitre.org/sites/default/files/pdf/07_0095.pdf, [Accessed 27 Sep 2015].

[6] *Mid air collision avoidance system (MIDCAS)* [online]. Available from http://www.midcas.org, [Accessed 27 Sep 2015].

[7] Kuchar J. K., Drumm A. C. 'The traffic alert and collision avoidance system (TCAS)'. *MIT Lincoln Laboratory Journal*. 2007;**16**(2):277–295.

[8] Bar-Shalom Y., Li X. R., Kirubarajan T. *Estimation with Applications to Tracking and Navigation: Theory, Algorithms and Software*. New York: *Wiley*; 2001.

[9] Kalman R. E. 'A new approach to linear filtering and prediction problems'. *Transactions of the ASME – Journal of Basic Engineering*. 1960;**82**(0): 35–45.

[10] Julier S. J., Uhlmann J. K. 'Unscented filtering and nonlinear estimation'. *Proceedings of the IEEE*. 2004;**92**(3):401–422.

[11] Huber M. F., Hanebeck U. D. 'Gaussian filter based on deterministic sampling for high quality nonlinear estimation'. *Proceedings of the 17th IFAC World Congress*. 2008, pp. 13527–13532.
[12] Aidala V., Hammel S. 'Utilization of modified polar coordinates for bearings-only tracking'. *IEEE Transactions on Automatic Control*. 1983;**28**(3):283–294.
[13] Stallard D. V. 'An angle-only tracking filter in modified spherical coordinates'. *Proceedings of the AIAA Guidance and Control Conference*. 1987, pp. 542–550.
[14] La Scala B., Morelande M. 'An analysis of the single sensor bearings-only tracking problem'. *Proceedings of the 11th ISIF International Conference on Information Fusion*. 2008, pp. 525–530.
[15] Mallick M., Arulampalam S., Mihaylova L., Yan Y. 'Angle-only filtering in 3D using modified spherical and log spherical coordinates'. *Proceedings of the 14th ISIF International Conference on Information Fusion*. 2011, pp. 1–8.
[16] Li X.-R., Jilkov V. P. 'Survey of maneuvering target tracking: III. Measurement models'. *Proceedings SPIE Signal and Data Processing of Small Targets*. 2001;4473:423–446.
[17] Fränken D., Hüpper A. 'Unified tracking and fusion for airborne collision avoidance using log-polar coordinates'. *Proceedings of the 15th ISIF International Conference on Information Fusion*. 2012, pp. 1246–1253.
[18] Bar-Shalom Y. 'Tracking methods in a multitarget environment'. *IEEE Transactions on Automatic Control*. 1978;**23**(4):618–626.
[19] Fränken D. 'Filter initialization and batch estimation for tracking with angular-only measurements'. *Proceedings of the 18th ISIF International Conference on Information Fusion*. 2015, pp. 1542–1549.
[20] Mallick M., La Scala B. 'Comparison of single-point and two-point difference track initiation algorithms using position measurements'. *Acta Automatica Sinica*. 2008;**34**(3):258–265.
[21] Kailath T., Sayed A. H., Hassibi B. *Linear Estimation*. Upper Saddle River: Prentice Hall; 2000.
[22] Julier S. J., Uhlmann J. K. 'A non-divergent estimation algorithm in the presence of unknown correlations'. *Proceedings of the American Control Conference*. 1997;4:2369–2373.
[23] Fränken D., Hüpper A. 'Improved fast covariance intersection for distributed data fusion'. *Proceedings of the 8th ISIF International Conference on Information Fusion*. 2005, pp. 154–160.
[24] Le Cadre J. P., Jauffret C. 'Discrete-time observability and estimability analysis for bearings-only target motion'. *IEEE Transactions on Aerospace and Electronic Systems*. 1997;**33**(1):178–201.
[25] Logothetis A., Isaksson A., Evans R. J. 'An information theoretic approach to observer path design for bearings only tracking'. *Proceedings of the 36th Conference on Decision and Control.* 1997, pp. 3132–3137.
[26] Logothetis A., Isaksson A., Evans R. J. 'Comparison of suboptimal strategies for optimal own-ship maneuvers in bearings-only tracking'. *Proceedings of the 1998 American Control Conference*. 1998, pp. 3334–3338.

[27] Singh S. S., Kantas N., Vo B.-N., Doucet A., Evans R. J. 'Simulation-based optimal sensor scheduling with application to observer trajectory planning'. *Automatica.* 2007;**43**:817–830.

[28] Skoglar P., Orguner U., Gustafsson F. 'On information measures based on particle mixture for optimal bearings-only tracking'. *Proceedings of the IEEE Aerospace Conference*. 2009, pp. 1–14.

This page intentionally left blank

Chapter 11

Multistatic tracking for passive radar applications

Martina Brötje[1] and Wolfgang Koch[1]

Abstract

Bistatic and passive radar systems enjoy various advantages, which have been discussed in detail in Part III of Volume 1 of this book. Multistatic configurations, where multiple transmitters (Txs) and/or multiple receivers (Rxs) are located separately, are of particular importance in this context. They provide detection of a target from different aspect angles. Furthermore, the fusion of the measurements from different Tx/Rx pairs can be used to overcome the low quality of a single measurement. Associating measurements of the same target from different Tx/Rx combinations (i.e. multi-sensor association), as well as improving the target state estimate over time belongs to the tasks of target tracking.

In this chapter, the tracking task is discussed for different passive radar systems. Solutions based on multiple hypothesis-tracking techniques are proposed and tested.

11.1 Introduction

The classical approach to sensor data processing follows the three-stage procedure of information extraction: extraction of receiver (Rx) data, extraction of target parameters (by signal processing) and extraction of target dynamics (by target tracking). Typically, a clear separation between the signal processing and the data fusion and target tracking task is assumed. This implies that there are different detection processes. The first decision is taken at the signal-processing level, where a threshold is applied e.g. to the matched filter output. Hereby, a reduction of the data amount is achieved. At the tracking and data fusion level, the measurements from different bistatic configurations are further evaluated in terms of the target origin. Further thresholding accounting for the target state model results in the extraction of target tracks that are, for example displayed to a human operator.

[1]Fraunhofer FKIE, Germany

The hard decisions by thresholding are well suited to reduce the data rate, but this holds the danger of suppressing weak targets. To overcome this difficulty track-before-detect strategies (e.g. [1]) have been suggested. The idea is to reduce information loss at the signal-processing stage and increase information gain in the tracking stage. However, the advantage is accompanied with an increased complexity, which increases the already high complexity of the target-tracking task in passive radar applications. We base our work on tracking after detection at signal-processing level. The results of the detection are termed measurements; they are a product of each bistatic sensor pair [transmitter (Tx) and Rx] as well as of the associated signal processing. To efficiently interpret the measurements by the tracking algorithm, the measurements need to be correctly understood and modelled depending on the application.

For example, in conventional signal processing for each measurement, a signal-to-noise ratio (SNR) is estimated. By decreasing the detection threshold applied to the measurements, the probability of detection (P_D) of the targets increases, while simultaneously the false alarm probability (P_{FA}) increases. In the tracking algorithm, we use estimates of these values in the model of the sensor performance. Thus, the estimated values of P_D and P_{FA} have significant influence on the tracking performance. Equivalently, the assumptions for the measurement noise influence the tracking result. Rating the information content of the measurements too pessimistically causes information loss, while a too optimistical rating may even result in track instability.

The design of the passive radar tracking filter needs to be adapted to the individual application. In the literature, a wide range of tracking filters exists and has been applied to passive radar data.

One of the first passive radar systems used analogue radio (frequency modulation, FM). This technology is commercially available with the 'Silent Sentry' of the Lockheed Martin Company and the 'Homeland Alerter' HA100 of the Thales Group. System development including tracking for a bistatic Tx/Rx pair is considered e.g. in [2,3]. The problem of multistatic FM passive radar target tracking is addressed in detail in [4].

The use of digital radio or video signals (DAB/DVB-T), see also Chapter 18, has the advantage of a large and content independent bandwidth. This results in good range resolution compared to the FM illumination. However, this advantage is accompanied by the problem of Tx-origin uncertainty. Several Txs are arranged in a single-frequency network (SFN), which means from a tracking perspective that the association of measurements and Txs is unknown. This is a key challenge with regard to the design of the target tracking algorithm. Besides our own work [5], the problem has e.g. been discussed by Tharmarasa *et al.* [6] and Choi *et al.* [7].

Signals of the second-generation (2G) mobile phone (GSM) base stations have digital coding and use frequency diversity. The challenge of GSM passive radar lies in dealing with the low transmit power and small effective bandwidth. However, this is accompanied by a multitude of available Txs [8]. To overcome the limitations from a single bistatic Tx–Rx pair, fusion of measurements from different geometries is the key component of a GSM passive radar system [9].

Oriented towards the specific requirements of passive radar, we will in the following describe the task of state estimation and data association. Implementation of the multiple hypothesis tracking (MHT) technique will be discussed and analysed by simulations. Real data results with GSM passive radar data finally confirm the expected gain from fusing measurements from multiple Tx/Rx pairs and underline the importance of incorporation of specific context knowledge.

11.2 Measurement model

A bistatic radar system consists of a pair of a single Tx and Rx placed at different locations. A signal is emitted by the Tx at $s = (s_x, s_y, s_z)$ and is reflected at the target at $q = (x, y, z)$ (see Figure 11.1) producing an echo of the original signal. By comparing at the Rx at $o = (o_x, o_y, o_z)$ the emitted signal with the target echo, the target state parameters can be estimated. Since the time of transmission is usually unknown, the time difference of arrival τ between the arrival of the direct signal and the delayed signal at the Rx is measured. From the known distance between the Tx and Rx $||o - s||$, the bistatic range is calculated by $r = \tau \cdot c + ||o - s||$.

The contours of constant bistatic range describe ellipses in 2D Cartesian and ellipsoids in 3D Cartesian coordinates. In dependency on the Cartesian position of the target, the bistatic range equation is given by

$$r = ||q - o|| + ||q - s|| \tag{11.1}$$

To describe the Doppler shift f_d as a function of the target state, we use the bistatic range-rate $\dot{r}$ equation given by

$$\dot{r} = -f_d \lambda = \left(\frac{q - o}{||q - o||} + \frac{q - s}{||q - s||} \right)^T \cdot v \tag{11.2}$$

where v is the velocity component of the target. Tx and Rx are assumed stationary.

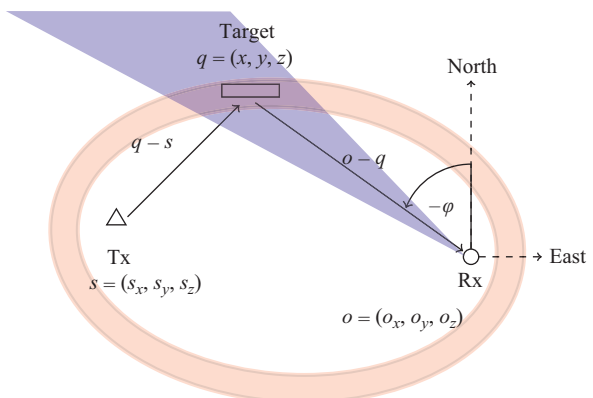

Figure 11.1 Bistatic set-up; signal from transmitter at s is reflected by the target at q and received at the observer o

The angle of the incoming echo can be determined by scanning the receiving antenna (mechanically or electronically) to find the angle of incidence by the maximum response. We consider here the angle of incidence in the $x - y$ plane (azimuth). It is related to the geometry by the four-quadrant inverse tangent

$$\varphi = \text{atan2}(x - o_x, y - o_y) \in (-\pi, \pi] \tag{11.3}$$

When defining the target state vector by $x = (q, v) = (x, y, z, \dot{x}, \dot{y}, \dot{z})$ the functional relationship between target state and measurements for the ith Tx and Rx pair can be expressed by the non-linear measurement equation $\mathbf{h}^{(i)}(x) = (r, \dot{r}, \varphi)$ with $\mathbf{h}^{(i)}$ defined by (11.1)–(11.3).

11.2.1 Modelling of the bistatic measurement accuracy

The technical equipment (consisting of the sensors with subsequent signal processing) delivers measurements of r, $\dot{r}$ and possibly φ with certain accuracies. We model the target state at time t_k by a random variable (r.v.) $\underline{\mathbf{X}}_k$ and the corresponding target measurement by $\underline{\mathbf{Z}}_k$. For simplification, we model the measurement noise as unbiased and Gaussian distributed. Strictly speaking, the Gaussian model is violated in real applications. For example, all measured values have only a limited range. However, it is a reasonable approximation in many tracking applications.

Following these assumptions, the measurement $\underline{\mathbf{Z}}_k$ of the ith Tx and Rx pair is modelled by

$$\underline{\mathbf{Z}}_k = \mathbf{h}^{(i)}(\underline{\mathbf{X}}_k) + \underline{\mathbf{W}}_k, \quad \text{with } \underline{\mathbf{W}}_k \sim N(\mathbf{0}, \mathbf{R}_k) \tag{11.4}$$

where $\mathbf{R}_k$ denotes the positive definite measurement covariance matrix. If the individual measurements are uncorrelated (as assumed here), $\mathbf{R}$ is a diagonal matrix, and the diagonal elements correspond to the variances of the individual measurements, $\mathbf{R} = \text{diag}(\sigma_r^2, \sigma_{\dot{r}}^2, \sigma_\varphi^2)$. The measurements are generated at the Rx at discrete times t_i with $i \in \mathbb{N}$. We also say that measurements belong to time scan i.

The magnitude of the error variances can vary considerably depending on the application and has to be chosen in accordance with the accuracy of the respective passive radar system. This work does not aim at a general comparison of different passive radar systems, since this is not only a question of the type of signal but also of the operational dedication. For example, a FM passive radar system is a good choice for wide area surveillance due to its high transmits power. In Section 11.6, we roughly typify the different systems according to their measurement errors and discuss on the basis of simulations which impact this has on the design of a proper tracking architecture.

Some characteristics of different passive radar systems are summarized in Table 11.1. The range accuracy is mainly dependent on the range-resolution of the system, which can be derived from the bandwidth of the signal. We use here the formula $\Delta r = \frac{c}{2B}$, see [10] p. 5. Typical values of the range accuracy are 10−100 m for DAB/DVB-T and 300−1,000 m for GSM/FM.

Table 11.1 Some characteristics of different passive radar systems, see [8,11,12]

	DAB	**DVB-T**	**FM**	**GSM**
Effective bandwidth [MHz]	1.5	7.6	∼0.055 Content-dependent	0.081
Frequency [MHz]	220–234	513–750	87.5–108	925–960 1,805–1,880
Transmit power [kW]	∼10	∼8	0.04–250	∼0.01
Range resolution [m]	100	20	∼2,725	1,851

The azimuth accuracy depends mainly on the frequency of the signal and on the size of the antenna aperture. The angle accuracy is assumed here to be in range of 3° and 7°. Of course, for low frequency signals (e.g. FM), this would assume a larger aperture size.

The Doppler accuracy depends mainly on the integration time. The choice of this parameter depends on how long a target stays in a resolution cell. For systems with low range resolution, a longer integration time can be used (see Chapter 18). The integration time depends also on the application, for slow targets, a longer integration time can be used. A typical value of Doppler accuracy is in the range of 1 Hz Doppler. The accuracy in range rate further depends on the signal frequency.

11.3 General methodology for target tracking

Mathematically, the aim of target tracking can be formulated as determining the conditional probability density of the target state given the measurement history of all data from the multistatic Tx/Rx pairs. This conditional probability density is derived from a probabilistic target dynamics model (state model) and sensor performance model (sensor model). The tracking and fusion problem can be described in the Bayesian framework. For practical considerations and for leading to real-time-capable algorithms, several approximation techniques are necessary [13].

The sensor data at time t_k contain measurements of the targets as well as false alarms, the set of measurements is denoted by $Z_k = (z_k^{(1)}, \ldots, z_k^{(m_k)})$, where m_k is the number of measurements. According to Bayes' rule, the conditional probability density of the targets state ξ_k at time t_k, given all sensor data $Z_{1:k} = \{Z_1, \ldots, Z_k\}$ up to and including time t_k can be sequentially calculated by

$$\begin{aligned} p(\xi_k|Z_{1:k}) &= \frac{p(Z_k, \xi_k|Z_{1:k-1})}{p(Z_k|Z_{1:k-1})} \\ &= \frac{p(Z_k|\xi_k) \cdot p(\xi_k|Z_{1:k-1})}{p(Z_k|Z_{1:k-1})}, \end{aligned} \tag{11.5}$$

$$= \frac{p(Z_k|\xi_k) \cdot \int p(\xi_k|\xi_{k-1}) \cdot p(\xi_{k-1}|Z_{1:k-1}) d\xi_{k-1}}{p(Z_k|Z_{1:k-1})} \tag{11.6}$$

Note that $p(Z_k|\xi_k, Z_{1:k-1}) = p(Z_k|\xi_k)$ due to conditioning on the true target state.

For a single target state, i.e. $\xi_k = x_k$, the Bayes formula is well understood, for discussion of the multi-target version, i.e. $\xi_k = (x_k^{(1)}, \ldots, x_k^{(n)})$, we refer to [14].

The transitional density $p(\xi_k|\xi_{k-1})$ describes the prediction of the targets state to the next time scan, this uses e.g. a model of the target motion.

The likelihood function $p(Z_k|\xi_k)$ can be understood as a weighting function, scoring possible target states by the new incoming data. The likelihood reflects the match between the measurements and target states and has to be adapted to the characteristics of the respective sensor system. It provides the description of the estimation problem and the association ambiguity as is discussed in the following.

11.3.1 Estimation task

If the association of measurements to targets is known, the conversion of multistatic measurements into target state estimates in Cartesian coordinates is a non-linear estimation problem. The sensor and target model define the *a posteriori* density as description of the estimation problem.

For known association, the maximum-*a posteriori* estimator can be obtained by evaluating the likelihood function together with *a priori* knowledge according to Bayes' rule.

Under the following assumptions,

- linear measurement equation: $p(z_k|x_k) = \mathcal{N}(z_k; \mathbf{H}x_k, \mathbf{R})$ (sensor model)
- linear target motion model: $p(x_k|x_{k-1}) = \mathcal{N}(x_k; \mathbf{F}x_{k-1}, \mathbf{Q})$ (target model)

the Bayes formalism leads to the well-known sequential Kalman Filter update formulas, see e.g. [13] pp. 64–65:

$$\begin{aligned} p(x_k|Z_{1:k}) &\propto p(z_k|x_k)p(x_k|Z_{1:k-1}) = p(z_k|x_k)\int p(x_k|x_{k-1})p(x_{k-1}|Z_{1:k-1})dx_{k-1} \\ &= \mathcal{N}(z_k; \mathbf{H}x_k, \mathbf{R}) \cdot \int \mathcal{N}(x_k; \mathbf{F}x_{k-1}, \mathbf{Q}) \cdot \mathcal{N}(x_{k-1}; \hat{\mathbf{x}}_{k-1|k-1}, \hat{\mathbf{P}}_{k-1|k-1})dx_{k-1} \\ &= \mathcal{N}(z_k; \mathbf{H}x_k, \mathbf{R}) \cdot \mathcal{N}(x_k; \hat{\mathbf{x}}_{k|k-1}, \hat{\mathbf{P}}_{k|k-1}) \\ &= \mathcal{N}(z_k; \mathbf{H}\hat{\mathbf{x}}_{k|k-1}, \mathbf{H}\hat{\mathbf{P}}_{k|k-1}\mathbf{H}^T + \mathbf{R}) \cdot \mathcal{N}(x_k; \hat{\mathbf{x}}_{k|k}, \hat{\mathbf{P}}_{k|k}) \end{aligned} \tag{11.7}$$

where $\hat{\mathbf{x}}_{k|\ell}$ and $\hat{\mathbf{P}}_{k|\ell}$ describe the estimated target state and covariance matrix of time t_k using measurements up to time t_ℓ.

The Kalman Filter equations follow the two steps of prediction and filter update:

Prediction: $\hat{\mathbf{x}}_{k|k-1} = \mathbf{F}_{k|k-1}\hat{\mathbf{x}}_{k-1|k-1}$ and $\hat{\mathbf{P}}_{k|k-1} = \mathbf{F}_{k|k-1}\hat{\mathbf{P}}_{k-1|k-1}\mathbf{F}_{k|k-1}^T + \mathbf{Q}$

Update: $\hat{\mathbf{x}}_{k|k} = \hat{\mathbf{x}}_{k|k-1} + W \cdot (z_k - \mathbf{H}\hat{\mathbf{x}}_{k|k-1})$ and $\hat{\mathbf{P}}_{k|k} = \hat{\mathbf{P}}_{k|k-1} - \mathbf{WSW}$

where

$$\mathbf{S} = \mathbf{H}\hat{\mathbf{P}}_{k|k-1}\mathbf{H}^T + \mathbf{R}, \quad \mathbf{W} = \hat{\mathbf{P}}_{k|k-1}\mathbf{H}^T\mathbf{S}^{-1}$$

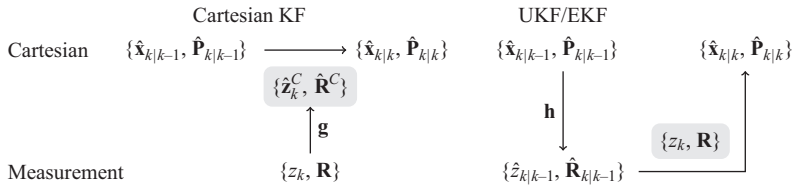

Figure 11.2 Track update schemes: Cartesian KF (left): Transformation of measurement $\mathbf{z}_k$ into Cartesian state; UKF/EKF (right): Transformation of predicted track state into measurement space

The Kalman Filter provides an optimal analytic solution in sense of minimizing the mean squared error. If the assumption of linearity is not fulfilled, approximations are needed. Two common approximation techniques are linearization [15] and unscented transform (UT) [16]. Both fit well in the framework of MHT as we discuss later. However, a good performance is not guaranteed and has to be discussed for a given application.

The Kalman Filter can be implemented in two ways (see also Figure 11.2):

- Transform the measurements into Cartesian coordinates (using UT or linearization) and process via Linear Kalman Filter.
- Transform the Cartesian estimate into measurement coordinates and perform the measurement update in mixed coordinates (the result is again in Cartesian coordinates). This is called the unscented Kalman filter (UKF) and extended Kalman filter (EKF).

The two variants have been discussed for multistatic tracking in more detail in [17]. The UKF version has shown to be appropriate to handle the non-linearity of the bistatic measurement equation, if the track is appropriately initialized.

The Doppler measurement of a bistatic measurement alone cannot be transferred to the higher dimensional Cartesian velocity component. UKF and EKF have the additional advantage that they allow processing of the Doppler measurement without transformation.

However, the UKF and EKF rely on an initial estimate in Cartesian coordinates, thus, the transformation of measurements into Cartesian coordinates has to be done at least once. To provide insight into the task of track initialization from bistatic measurements, the densities of bistatic measurements are displayed in Cartesian coordinates (position only) in Figure 11.3. Figure 11.3(a) shows an example with a relatively good range, but poor azimuth measurement (e.g. DAB, DVB-T). The density of the measurement transformed into the Cartesian coordinate system is non-Gaussian. Curves of equal density values in the Cartesian space have banana shape, UT (red) or linearization (green) provide only a poor approximation. Figure 11.3(b) shows the same scenario as Figure 11.3(a), but with larger range error (GSM, FM). Even through the estimation, error increases the approximations via UT or linearization show a better match. In case the approximation via UT or Linearization fails, the density of the target estimate that is used for track initialization can be

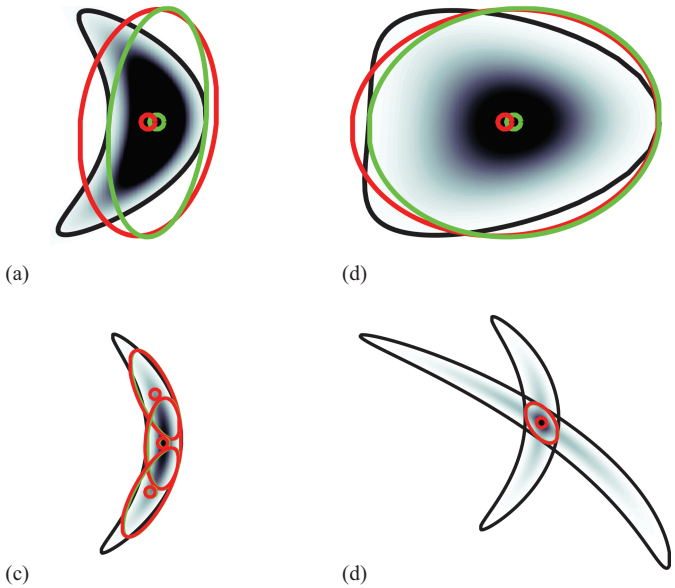

Figure 11.3 Position Estimation uncertainty described by the likelihood function. Approximations via UT (red) and Linearization (green) are shown by ellipses. (a) Good range, poor azimuth, (b) poor range and azimuth, (c) Gaussian mixture approximation and (d) target localization by ellipse intersection

approximated by a Gaussian sum (see Figure 11.3(c)). Alternatively, the combination of measurements from multiple bistatic pairs via ellipse intersection, as displayed in Figure 11.3(d), see e.g. [18], can be used to approximate the initial target density.

The velocity component is typically initialized with mean zero and appropriate variance. In case that the measurements from multiple bistatic pairs are available, the velocity can be initialized by combination of Doppler measurements.

The 2D approximation of the target state is appropriate for targets with low altitude (e.g. maritime traffic surveillance). Track initialization with unknown target height via Gaussian mixture initialization is discussed in [18].

11.3.1.1 Theoretical performance bounds

From the likelihood function, the Cramér–Rao Lower Bound (CRB) (Chapter 28) can be calculated to evaluate the expected performance of the estimation task. This theoretical performance bound can be used to analyse the influence of geometrical and sensorial features and to check the efficiency of an estimator [9]. The CRB of the *i*th Tx/Rx pair for a single time scan is calculated by the inverse of the Fisher Information Matrix (**FIM**)

$$\mathbf{FIM}^{(i)}(x_k) = \frac{\partial \mathbf{h}^{(i)}(x_k)}{\partial x_k}^T \mathbf{R}^{-1} \frac{\partial \mathbf{h}^{(i)}(x_k)}{\partial x_k} \tag{11.8}$$

see e.g. [19]. $\mathbf{h}^{(i)}$ is the measurement function defined in (11.4). The result for fusion of multiple bistatic geometries is obtained from the sum of the FIM, i.e.

$$\mathbf{FIM}(x_k) = \sum_{i=1}^{N} \mathbf{FIM}^{(i)}(x_k) \tag{11.9}$$

The additivity is a property of the information matrix, see [20], and does not depend on the fusion scheme, which is applied in tracking. In particular, this reflects the theoretical consideration that adding measurements of an additional Tx–Rx pair will result in an increase of information and consequently in a decrease of the estimation uncertainty (described by the CRB). This can be further extended to multiple time scans by incorporation of a target propagation model, see [21]. The probability of detection P_D is an input parameter for the calculation of the CRB. By use of the information reduction factor as introduced by [22], this results in a scaling of FIM according to

$$\mathbf{FIM}(x_k) = \sum_{i=1}^{N} P_D \mathbf{FIM}^{(i)}(x_k) \tag{11.10}$$

11.3.2 Association task

The association task comprises identifying if a measurement belongs to the target or is a false alarm. In case of multiple targets, we need to additionally associate target measurements with specific targets. The degree of difficulty further increases with multiple sensors. As the estimation task, the association task is described by the likelihood function.

11.3.2.1 Scenario with frequency diversity

In the case that the measurements of different Tx/Rx pairs are distinguishable (non-SFNs), the set of measurements of time t_k decomposes into individual sets i.e. $Z_k = \{Z_k^1, \ldots, Z_k^{\eta_S}\}$, where η_S is the number of Tx/Rx pairs and $Z_k^i = (z_{k,i}^{(1)}, \ldots, z_{k,i}^{(m_{k,i})})$, with $m_{k,i}$ the number of measurements of Tx/Rx pair i. Assuming that measurements from different bistatic pairs are independent, the likelihood function becomes

$$p(Z_k|\xi_k) = \prod_{i=1}^{\eta_S} p(Z_k^i|\xi_k) \tag{11.11}$$

For a single target state, i.e. $\xi_k = x_k$, the likelihood function is given by

$$p(Z_k^i|x_k) = \frac{P_D(x_k)}{m_{k,i}} \left(\sum_{\alpha} p\left(z_{k,i}^{(\alpha)}|x_k, \alpha\right) f_c\left(Z_k^i \backslash z_{k,i}^{(\alpha)}\right) \right) + (1 - P_D(x_k)) f_c(Z_k^i) \tag{11.12}$$

where the sum is overall possible association events α, with $\alpha = \ell$ describing the association of a measurement $z_{k,i}^{(\ell)}$ with the target. Each association of a measurement and a target is assumed *a priori* equally likely (factor $1/m_{k,i}$). $P_D(x_k)$ is the probability of target detection at x_k.

f_C describes the probability density function (pdf) with respect to the distribution of false alarms. Let $C_k \subseteq Z_k^i$ with m_F be the number of elements of C_k. The probability that the elements in C_k are false alarms is given by $f_C(C_k) = p_F(m_F) \cdot \prod_{\ell=1}^{m_F} p_C(z_{k,i}^{(\ell)})$; first, the probability that there are m_F false alarms and, second, the probability that the false alarm observations coincide with the elements in C_k. This is typically modelled by a Poisson Point Process (see e.g. [23]) to describe the rare event of false alarm occurrence for points in the field of view (FoV). Thus,

$$p_F(m_F) = e^{-\overline{m}} \frac{\overline{m}^{m_F}}{m_F!} \quad \text{and} \quad p_C(z_{k,i}^{(\ell)}) = \frac{\rho_F(z_{k,i}^{(\ell)})}{\overline{m}} \tag{11.13}$$

which is parametrized by the false alarm intensity ρ_F with $\overline{m} = \int_{\text{FoV}} \rho_F(z)dz$. The intensity is not equal to the pdf, in fact, the intensity and the pdf are proportional, and $\overline{m}$ is equal to the expected number of false alarms.

In composition we obtain

$$f_C(C_k) = e^{-\overline{m}} \frac{\overline{m}^{m_F}}{m_F!} \cdot \prod_{i=1}^{m_F} \frac{\rho_F(z_{k,i}^{(\ell)})}{\overline{m}} = e^{-\overline{m}} \frac{1}{m_F!} \cdot \prod_{\ell=1}^{m_F} \rho_F(z_{k,i}^{(\ell)}) \tag{11.14}$$

In particular

$$f_C(Z_k^i \backslash z_{k,i}^{(\alpha)}) \cdot \rho_F(z_{k,i}^{(\alpha)}) = m_{k,i} \cdot f_C(Z_k^i) \tag{11.15}$$

holds and the likelihood function can be written as

$$p(Z_k^i|x_k) = f_c(Z_k^i) \left(\sum_{\alpha} \frac{P_D(x_k)}{\rho_F(z_{k,i}^{(\alpha)})} p(z_{k,i}^{(\alpha)}|x_k, \alpha) + (1 - P_D(x_k)) \right) \tag{11.16}$$

A more detailed derivation can e.g. be found in [13] pp. 45–48.

Obviously, the choice of P_D and ρ_F will have a significant influence on the tracking process. To simplify the calculation, a fixed probability of detection and false alarm intensity ($P_D(x_k) = P_D$ and $\rho_F(z_{k,i}^{(\ell)}) = \rho_F$) is used in the following; however, this is not a general restriction as we will see in Section 11.7.4.

The multi-target likelihood function can be derived in a similar manner. Let ξ_k describes the multi-target state $(x_k^{(1)}, \ldots, x_k^{(n)})$. We define the association variable $\beta = (\beta(1), \ldots, \beta(n))$, with $\beta(s) = \ell$ meaning target $x_k^{(s)}$ associated with measurement $z_{k,i}^{(\ell)}$ and $\beta(s) = 0$ describing a missed detection. The sum of entries with $\beta(s) \neq 0$ in particular gives the number of detected targets n_β for association hypothesis β.

Assuming again that *a priori* each measurement is equally likely to be associated with each target; the multi-target likelihood is given by

$$\begin{aligned} p(Z_k^i|\xi_k) = \sum_{\beta} & \frac{(m_{k,i} - n_\beta)!}{m_{k,i}!} P_D^{n_\beta} (1 - P_D)^{n - n_\beta} f_c(Z_k^i \backslash \{z_{k,i}^{(\beta(\cdot))}\}) \\ & \cdot \prod_{j:\beta(j)\neq 0} p(z_{k,i}^{(\beta(j))}|x_k^{(j)}, \beta(j)) \end{aligned} \tag{11.17}$$

where the sum is in this case over all multi-target associations.

$f_c(Z_k^i \backslash \{z_{k,i}^{(\beta(\cdot))}\})$ is the probability that all measurements besides the measurements associated with the targets in β are false alarms. Using (11.15), it follows that

$$f_c(Z_k^i \backslash \{z_k^{\beta(\cdot)}\}) \cdot \rho_F^{n_\beta} = \frac{m_{k,i}!}{(m_{k,i} - n_\beta)!} \cdot f_C(Z_k^i) \tag{11.18}$$

and

$$p(Z_k^i|\xi_k) = f_c(Z_k^i) \sum_\beta \left(\prod_{j:\beta(j)\neq 0} \frac{P_D}{\rho_F} p\left(z_{k,i}^{(\beta(j))}|x_k^{(j)}, \beta(j)\right) \right) \cdot \left(\prod_{j:\beta(j)=0} (1 - P_D) \right) \tag{11.19}$$

For a detailed derivation of the multi-target likelihood, we refer to [24].

11.3.2.2 Example

An example is plotted in Figure 11.4 for a scenario with one Rx and two Txs. In the example, the measurements $z_1^{(1)}, z_1^{(2)}$ belong to the first and $z_2^{(1)}, z_2^{(2)}$ to the second Tx. Each measurement consisting of bistatic range and azimuth describes an uncertainty area (here banana shape). The maxima of the likelihood function form at the intersections of the ellipses as given by the range measurement. For example, the likelihood function is given by

$$p(Z_k|x_k) \propto \left(\frac{P_D}{\rho_F} \left(p(z_1^{(1)}|x_k) + p(z_1^{(2)}|x_k) \right) + (1 - P_D) \right) \cdot \left(\frac{P_D}{\rho_F} \left(p(z_2^{(1)}|x_k) + p(z_2^{(2)}|x_k) \right) + (1 - P_D) \right)$$

as displayed in Figure 11.4(a). For $P_D = 1$, this is

$$p(Z_k|x_k) \propto \left(p(z_1^{(1)}|x_k) + p(z_1^{(2)}|x_k) \right) \cdot \left(p(z_2^{(1)}|x_k) + p(z_2^{(2)}|x_k) \right) \tag{11.20}$$

$$\begin{aligned} &= \underbrace{p(z_1^{(1)}|x_k) p(z_2^{(1)}|x_k)}_{H_1: z_1^{(1)} \times z_2^{(1)}} + \underbrace{p(z_1^{(2)}|x_k) p(z_2^{(1)}|x_k)}_{H_2: z_1^{(2)} \times z_2^{(1)}} \\ &+ \underbrace{p(z_1^{(1)}|x_k) p(z_2^{(2)}|x_k)}_{H_3: z_1^{(1)} \times z_2^{(2)}} + \underbrace{p(z_1^{(2)}|x_k) p(z_2^{(2)}|x_k)}_{H_4: z_1^{(2)} \times z_2^{(2)}} \end{aligned} \tag{11.21}$$

displayed in Figure 11.4(b), showing four potential positions of the target coinciding with the four single-target hypotheses H_1, H_2, H_3 and H_4.

In the example, a two-target scenario was the basis of the simulation, thus, the single-target likelihood gives only a rough description of the estimation problem. The hypotheses H_2 and H_3 represent the true association, whilst H_1 and H_4 represent false associations. If the algorithm decides for one of these false associations, this would result in a so-called ghost track. A ghost track is based on a false association of true target measurements (e.g. measurements of different targets) and

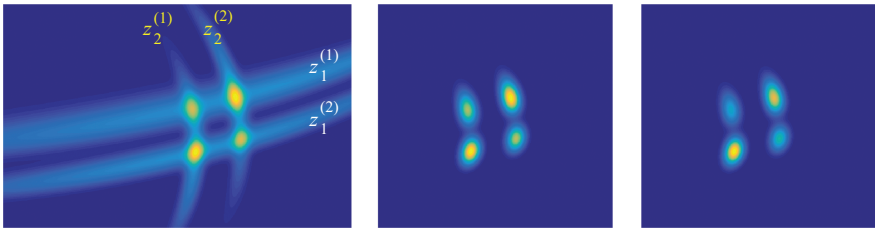

Figure 11.4 The likelihood function description of data ambiguity. (a) single-target likelihood ($P_D = 0.8$), (b) single-target likelihood ($P_D = 1$) and (c) marginalized two-target likelihood ($P_D = 1$)

can show similar kinematics than a true target. In contrast to the false tracks that are typically based on false detections at the signal processing level, ghost tracks arise at the data fusion level.

If, for the same scenario, we assume a two-target state $\xi_k = (x_k^{(1)}, x_k^{(2)})$, the likelihood for $P_D = 1$ is given by

$$
\begin{aligned}
p(Z|x_k^{(1)}, x_k^{(2)}) &= p(Z^2|x_k^{(1)}, x_k^{(2)}) \cdot p(Z^1|x_k^{(1)}, x_k^{(2)}) \\
&\propto (p(z_1^{(1)}|x_k^{(1)})p(z_1^{(2)}|x_k^{(2)}) + p(z_1^{(2)}|x_k^{(1)})p(z_1^{(1)}|x_k^{(2)})) \\
&\quad \cdot (p(z_2^{(1)}|x_k^{(1)})p(z_2^{(2)}|x_k^{(2)}) + p(z_2^{(2)}|x_k^{(1)})p(z_2^{(1)}|x_k^{(2)})) \\
&= p(z_1^{(1)}|x_k^{(1)})p(z_1^{(2)}|x_k^{(2)}) \cdot p(z_2^{(1)}|x_k^{(1)})p(z_2^{(2)}|x_k^{(2)}) \quad | \quad H_1 \times H_4 \\
&\quad + p(z_1^{(1)}|x_k^{(1)})p(z_1^{(2)}|x_k^{(2)}) \cdot p(z_2^{(2)}|x_k^{(1)})p(z_2^{(1)}|x_k^{(2)}) \quad | \quad H_3 \times H_2 \\
&\quad + p(z_1^{(2)}|x_k^{(1)})p(z_1^{(1)}|x_k^{(2)}) \cdot p(z_2^{(1)}|x_k^{(1)})p(z_2^{(2)}|x_k^{(2)}) \quad | \quad H_2 \times H_3 \\
&\quad + p(z_1^{(2)}|x_k^{(1)})p(z_1^{(1)}|x_k^{(2)}) \cdot p(z_2^{(2)}|x_k^{(1)})p(z_2^{(1)}|x_k^{(2)}) \quad | \quad H_4 \times H_1
\end{aligned}
$$

Obviously, $p(Z|x_k^{(1)}, x_k^{(2)}) \neq p(Z|x_k^{(1)}) \cdot p(Z, x_k^{(2)})$. However, multi-target associations can be constructed by combination of single-target associations under the constraint that a measurement is only associated with one target.

In the example only, the combination of the single-target hypotheses H_1 and H_4 as well as H_3 and H_2 gives feasible multi-target solutions (no measurement is used twice). The multi-target likelihood is displayed in Figure 11.4(c) by marginalization via $\int p(Z|x_k^{(1)}, x_k^{(2)})p(x_k^{(2)})dx_k^{(2)}$, where the *a priori* pdf $p(x_k^{(2)})$ is chosen from uniform distribution.

The calculation of the multi-target likelihood function is relevant in applications where multiple targets are closely spaced and can help to distinguish between true and ghosts hypotheses. As illustrated in Figure 11.4(a), association problems in multi-target scenarios are not only influenced by the geographical distance of targets,

but also on the size of the measurement error and the multistatic geometry (describing the extend of the bistatic measurement density in Cartesian coordinates).

11.3.2.3 Scenario with single-frequency property

For SFNs, the association between measurements and Txs within a network is *a priori* not known. In contrast to the case of frequency diversity (11.11), the decomposition of the likelihood function for different Txs is in general not true.

The association of measurements has to be done for targets and Txs. Therefore, the association variable γ becomes an array of dimension $\eta_S \times n$, where $\gamma(i,j) = \ell$ stands for associating measurement $z_k^{(\ell)}$ with target $x_k^{(j)}$ and Tx $\mathbf{s}^{(i)}$. Analogous to the derivation of the multi-target likelihood function (11.19), the multi-target likelihood function of a single-frequency network can be calculated by

$$p(Z_k|\xi_k) = f_c(Z_k)) \sum_{\gamma} \prod_{i} \left(\prod_{j:\gamma(i,j)\neq 0} \frac{P_D}{\rho_F} p\left(z_k^{(\gamma(i,j))}|x_k^{(j)}, \mathbf{s}^{(i)}, \gamma(i,j)\right) \cdot \prod_{j:\gamma(i,j)=0} (1-P_D) \right) \tag{11.22}$$

where the sum is over all multi-target/multi-Tx associations.

11.3.2.4 Example

For the previous example, we assume the single-frequency property. This means that the association between measurements $z_1^{(1)}, z_1^{(2)}, z_2^{(1)}$ and $z_2^{(2)}$ and the two Txs is assumed to be unknown. The single-target likelihood function, assuming that there are no false alarms, is displayed in Figure 11.5(a) and (b) for $P_D = 0.8$ and $P_D = 1$, respectively. The likelihood function for $P_D = 1$ can be explicitly written as

$$\begin{aligned}
p(Z_k|x_k) \propto\ & \underbrace{p(z_1^{(1)}|x_k,\mathbf{s}^{(1)})p(z_1^{(2)}|x_k,\mathbf{s}^{(2)})}_{H_1:z_1^{(1)}\times z_1^{(2)}} + \underbrace{p(z_1^{(1)}|x_k,\mathbf{s}^{(1)})p(z_2^{(1)}|x_k,\mathbf{s}^{(2)})}_{H_2:z_1^{(1)}\times z_2^{(1)}} \\
& + \underbrace{p(z_1^{(1)}|x_k,\mathbf{s}^{(1)})p(z_2^{(2)}|x_k,\mathbf{s}^{(2)})}_{H_3:z_1^{(1)}\times z_2^{(2)}} + \underbrace{p(z_1^{(2)}|x_k,\mathbf{s}^{(1)})p(z_1^{(1)}|x_k,\mathbf{s}^{(2)})}_{H_4:z_1^{(2)}\times z_1^{(1)}} \\
& + \underbrace{p(z_1^{(2)}|x_k,\mathbf{s}^{(1)})p(z_2^{(1)}|x_k,\mathbf{s}^{(2)})}_{H_5:z_1^{(2)}\times z_2^{(1)}} + \underbrace{p(z_1^{(2)}|x_k,\mathbf{s}^{(1)})p(z_2^{(2)}|x_k,\mathbf{s}^{(2)})}_{H_6:z_1^{(2)}\times z_2^{(2)}} \\
& + \underbrace{p(z_2^{(1)}|x_k,\mathbf{s}^{(1)})p(z_1^{(1)}|x_k,\mathbf{s}^{(2)})}_{H_7:z_2^{(1)}\times z_1^{(1)}} + \underbrace{p(z_2^{(1)}|x_k,\mathbf{s}^{(1)})p(z_1^{(2)}|x_k,\mathbf{s}^{(2)})}_{H_8:z_2^{(1)}\times z_1^{(2)}} \\
& + \underbrace{p(z_2^{(1)}|x_k,\mathbf{s}^{(1)})p(z_2^{(2)}|x_k,\mathbf{s}^{(2)})}_{H_9:z_2^{(1)}\times z_2^{(2)}} + \underbrace{p(z_2^{(2)}|x_k,\mathbf{s}^{(1)})p(z_1^{(1)}|x_k,\mathbf{s}^{(2)})}_{H_{10}:z_2^{(2)}\times z_1^{(1)}} \\
& + \underbrace{p(z_2^{(2)}|x_k,\mathbf{s}^{(1)})p(z_1^{(2)}|x_k,\mathbf{s}^{(2)})}_{H_{11}:z_2^{(2)}\times z_1^{(2)}} + \underbrace{p(z_2^{(2)}|x_k,\mathbf{s}^{(1)})p(z_2^{(1)}|x_k,\mathbf{s}^{(2)})}_{H_{12}:z_2^{(2)}\times z_2^{(1)}}
\end{aligned}$$

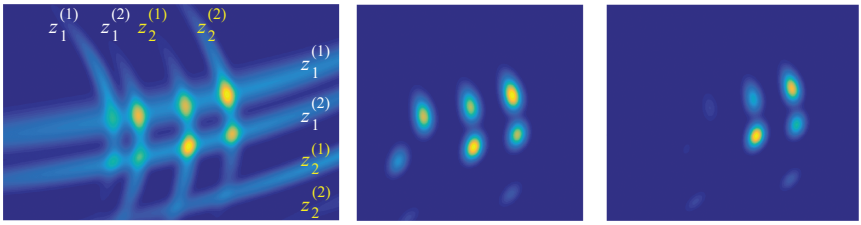

Figure 11.5 The likelihood function description of data ambiguity in single-frequency network. (a) Single-target likelihood ($P_D = 0.8$), (b) single-target likelihood ($P_D = 1$) and (c) marginalized two-target likelihood ($P_D = 1$)

The unknown association of measurements and Txs increases the association ambiguity and thereby the number of ghost hypotheses. Even measurements of the same target can result in a ghost hypothesis if the wrong association of Txs is considered. By combination of single-target hypotheses, we obtain 12 valid multi-target hypotheses:

$$H_1 \times H_9, \quad H_1 \times H_{12}, \quad H_2 \times H_6, \quad H_2 \times H_{11}$$
$$H_3 \times H_8, \quad H_3 \times H_5, \quad H_4 \times H_9, \quad H_4 \times H_{12}$$
$$H_5 \times H_{10}, \quad H_6 \times H_7, \quad H_7 \times H_{11}, \quad H_8 \times H_{10}$$

The marginalized multi-target likelihood is shown in Figure 11.5(c). The consideration of the multi-target likelihood in this case significantly helps unmasking the positions of the true targets.

Solving the association ambiguity is an important challenge in every passive radar application. However, the dimension of the association problem depends on multiple factors which are as follows:

- accuracy of the bistatic measurement
- distance between targets
- number of false alarms
- single-frequency property
- number of Txs
- bistatic geometry

The dimension of data ambiguity has an impact on the design of the tracking architecture. The basis of our algorithms is multiple hypothesis tracking (MHT), which is described in the following section.

11.4 Principle of multiple hypothesis tracking

The idea of MHT [24–26] is to evaluate the different association possibilities (Section 1.3.2) over time.

The literature differentiates between two different MHT approaches [27] pp. 365–367: *hypothesis-oriented* and *track-oriented* MHT. The hypotheses-oriented approach creates multi-target hypotheses by associating measurements with potential targets. The track-oriented approach (which we also follow here) generates single-target tracks, which are further evaluated by calculation of multi-target hypotheses.

11.4.1 Single-target tracks

In the MHT, a track is represented by a Gaussian mixture,

i.e. the prediction of the track from time t_{k-1} to t_k has the form

$$p(x_k|Z_{1:k-1}) \approx \sum_{j=1}^{\eta_{k-1}} p_{k-1}^{(j)} \mathcal{N}\left(x_k, \hat{\mathbf{x}}_{k|k-1}^{(j)}, \hat{\mathbf{P}}_{k|k-1}^{(j)}\right) \tag{11.23}$$

According to Bayes' rule, the measurement update is obtained by multiplication of the likelihood function (11.16), i.e. in the single sensor case under the assumptions of Section 11.3.1 this is

$$\begin{aligned} p(x_k|Z_{1:k}) &\propto p(Z_k|x_k)p(x_k|Z_{1:k-1}) \\ &= f_c(Z_k)\left(\frac{P_D}{\rho_F}\sum_{i=1}^{m_k}\mathcal{N}(z_k^{(i)};\mathbf{H}x_k,\mathbf{R}) + (1-P_D)\right)\cdot\sum_{j=1}^{\eta_{k-1}} p_{k-1}^{(j)}\mathcal{N}(x_k,\hat{\mathbf{x}}_{k|k-1}^{(j)},\hat{\mathbf{P}}_{k|k-1}^{(j)}) \end{aligned} \tag{11.24}$$

For each combination of an old hypothesis and a measurement this results in a Kalman Filter update step (11.7). The hypothesis of a missed detection is additionally considered. The updated hypotheses are weighted by

$$\begin{cases} f_C(Z_k)(1-P_D)\cdot p_{k-1}^{(j)} & \text{in case of a misdetection,} \\ f_C(Z_k)\dfrac{P_D}{\rho_F}\mathcal{N}\left(z_k^{(i)},\mathbf{H}\hat{\mathbf{x}}_{k|k-1}^{(j)},\mathbf{H}\hat{\mathbf{P}}_{k|k-1}^{(j)}\mathbf{H}^T+\mathbf{S}\right)\cdot p_{k-1}^{(j)} & \text{in case of detection with } z_k^{(i)} \end{cases} \tag{11.25}$$

The sum of hypotheses (according to their normalized weights) gives a description of the conditional probability density defined in (11.6).

Theoretically, the number of hypotheses increases in each time step by factor $(m_k + 1)$ (where m_k is the number of measurements). Thus, the MHT suffers from an exponential growth of the number of hypotheses. Appropriate hypotheses reduction techniques are needed to make it real-time capable, this includes

- hypotheses pruning: deleting hypotheses with low weights
- hypotheses merging: combining similar hypotheses
- gating: considering reliable measurement to track combinations only.

The MHT algorithm described above is designed to track a single target. However, it can be easily extended to handle multiple well-separated targets. This is realized

by a track management scheme overarching the MHT structure, see [26] for more details.

A *tentative track* is initiated from a single Gaussian (or Gaussian mixture see Section 11.3.1). This is the starting point for building a hypothesis tree by exploiting the measurement information of the following time scans. Gating methods ensure individual processing of well-separated targets.

The track will be tested for belonging to a true target by calculating the likelihood ratio (LR), see Section 11.4.2. Only tracks that pass this test will e.g. be displayed to a human operator (*extracted track*). The same procedure can be applied for track termination.

Further instances of track management imply merging of tracks and splitting of tracks.

11.4.2 Track extraction and track termination

The principle of LR testing is briefly summarized in this sub-section, see [26,28] for more details.

Given a sequence of measurements $Z_{1:k} = \{z_1, Z_2, \ldots, Z_k\}$ with an initial measurement z_1 and Z_ℓ denoting the incoming measurements at time t_ℓ, the LR is calculated according to the hypotheses

- h_1: the data $Z_{1:k}$ contain target measurements and false alarms
- h_0: the data $Z_{1:k}$ contain only false alarms

by

$$\mathrm{LR}(Z_{1:k}) = \frac{p^{h_1}(Z_{1:k})}{p^{h_0}(Z_{1:k})} \tag{11.26}$$

p^{h_n} describes the likelihood function given that there are n targets. Choosing thresholds A and B, we accept h_1 if $\mathrm{LR}(Z_{1:k}) > A$ (track extraction) and h_0 if $\mathrm{LR}(Z_{1:k}) < B$ (track termination). According to [28], the LR can be recursively calculated by:

$$\begin{aligned}\mathrm{LR}(Z_{1:k}) &= \frac{p^{h_1}(Z_k|Z_{1:k-1})}{p^{h_0}(Z_k|Z_{1:k-1})} \cdot \mathrm{LR}(Z_{1:k-1}) \\ &= \frac{\int p(Z_k|x_k)p(x_k|Z_{1:k-1})dx_k}{f_C(Z_k)} \cdot \mathrm{LR}(Z_{1:k-1})\end{aligned} \tag{11.27}$$

Note that MHT the LR of a single track can be calculated parallel to the MHT measurement update as the sum of the hypotheses weights from (11.25) where the weights are scaled by factor $1/f_C(Z_k)$.

11.4.3 Evaluation of multi-target/multi-sensor hypotheses

In case that multiple targets are not well separated, the evaluation of multi-target hypotheses becomes necessary as motivated in Section 11.3.2. In the tracking

context, well separation means that a track contains only measurements of a single target and false alarms. As discussed in Section 11.3.2, the level of association ambiguity does not only depend on the geographical distance between targets, but also on the Tx/Rx geometry and on the size of the measurement error.

The number of multi-target hypotheses increases even faster than exponentially with the number of targets. For this reason, the idea of track-oriented MHT has become popular.

In a first step, single-target tracks are built. Evaluation of multi-target associations is only necessary, if a measurement association conflict between multiple tracks exists. A solution to solve such a conflict is the application of the N-scan pruning technique. The idea is to enforce a non-conflicting history of tracks. The currently best multi-target hypothesis is found and track hypotheses N scans ago that are not ancestors of the currently chosen best global hypothesis are deleted (together with their descendants). For details, we refer e.g. to [27] pp. 367–369. The pre-requisite for using N-scan pruning is the solution of the multi-target association problem, which can be formulated as an N-scan assignment problem and has been shown to be non-deterministic polynomial time (NP) hard. The number of scans N depends on the number of time scans and the number of sensors. Convenient approximation methods are based on Lagrangian relaxation [29] or $0/1$ integer programming [30].

As shown in Section 11.3.2, if the measurements of different Tx/Rx pairs are uncorrelated, the likelihood function decomposes into the product of its individual terms. For the MHT, the multi-sensor fusion step can therefore be done by sequentially updating the mixture components according to the measurements of each Tx/Rx pair. However, this is not true for passive radar tracking in single-frequency networks. Here, the evaluation of multi-sensor hypotheses becomes necessary to ensure that a measurement is not associated with different Txs within a network. The concept of MHT is thereby not modified [31]. However, the consideration of additional hypotheses results in an increasing complexity, which might result in more restrictive hypotheses reduction schemes. This similarly holds for the s-dimensional (SD)-assignment approach ([6,32]). Approximations of the measurement update process based on the JPDA, the PMHT and the Particle Filter are discussed in [33,34].

11.5 Multi-sensor fusion strategies

For the fusion of measurements from different sensor pairs, the literature distinguishes between two different strategies, see e.g. [27] pp. 598–614: The theoretical optimal solution is the fusion of all available measurement information at a global fusion centre (*centralized tracking*). The alternative strategy is *distributed tracking*, where tracks are formed at local nodes. Only the pre-processed information is transferred to the fusion centre. In some applications due to communication constraints, the second strategy is the only option. The two strategies have been discussed in detail for multistatic tracking by Coraluppi *et al.* e.g. in [35]. They point out that there is no general best strategy even without communication constraints.

For high detection redundancy (measurements from multiple Tx/Rx pairs are available) and high false alarm environment centralized tracking outperforms the distributed strategy, which might be more robust in case of low detection redundancy. The analysis has been done for multistatic active sonar tracking.

For passive radar tracking, the pre-processing of the measurements by tracking in measurement coordinates has been discussed by several authors, see e.g. [5,32,36]. This corresponds to the distributed tracking scheme, but without transformation into Cartesian coordinates. Tracking in measurement coordinates has the advantage that the measurement function is linear, and thus approximation errors introduced by transformation into Cartesian coordinates (Section 11.3.1) can be avoided for the processing of a single bistatic sensor pair. A disadvantage of tracking in measurement coordinates is the definition of the motion model. The Doppler component is equivalent to the range rate except for a negative multiplicative factor. The bistatic range-rate describes the velocity component of the bistatic range. A constant target velocity in Cartesian coordinates typically defines parabolic curves in measurement coordinates, which can be described by a nearly constant acceleration model. However, the bistatic geometry has a significant impact on the exact motion in measurement coordinates. Tracking in measurement coordinates is in the following referred to as Range/Doppler (R/D) tracking, this goes back to the kinematic relationship between range and Doppler coordinates. If available, the azimuth is included as an additional state variable.

We define three fusion strategies, see also Figure 11.6:

- 1-stage MHT: uses a central node for tracking in Cartesian coordinates (centralized tracking). It uses a standard track-oriented MHT as motivated in the previous sub-sections. A new tentative track is initiated from measurements that are not used by existing tracks. For track initialization, the measurement of a single Tx/Rx pair is transformed into Cartesian coordinates using a Gaussian mixture approximation as shown in Figure 11.3(c). The measurement update from different Txs is performed sequentially according to the UKF equations.
- 2-stage MHT: uses R/D tracking followed by a correlation stage (equivalent to a distributed tracking strategy).
- 3-stage MHT: uses 2-stage MHT to initialize tracks that are further processed by a central node (compromise between centralized and distributed tracking).

The 2-stage and 3-stage MHT have been originally implemented to cope with the high complexity of tracking in SFN, see [5,31] for details. The idea is to perform the multi-sensor association and Cartesian estimation steps for a batch of measurements (measurements in R/D tracks) instead for individual measurements, thereby, the number of association possibilities can be drastically reduced.

The three tracking stages are summarized in the following. Details of the algorithm are described in [5].

- R/D tracking implies track-oriented MHT in measurement coordinates.

  A tentative track is started from measurements not used in existing tracks. For the propagation of the range/range-rate component, a nearly constant

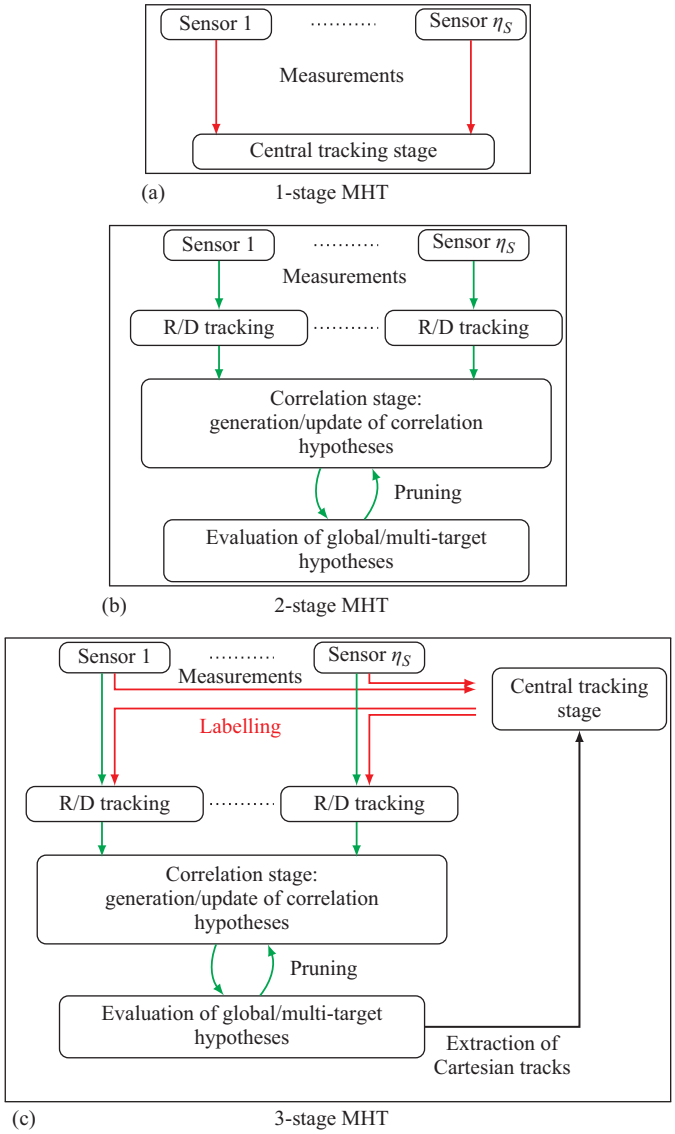

Figure 11.6 Overview of multi-stage tracking strategies

acceleration model is used. The association of measurements from multiple Txs is not considered. The first tracking stage provides estimates of the targets for each Tx/Rx pair but without Cartesian location.

- The correlation stage addresses the multi-sensor association problem.

  A correlation hypothesis is based on the association of R/D tracks from different (hypothesized) Txs to a single target (multi-sensor association),

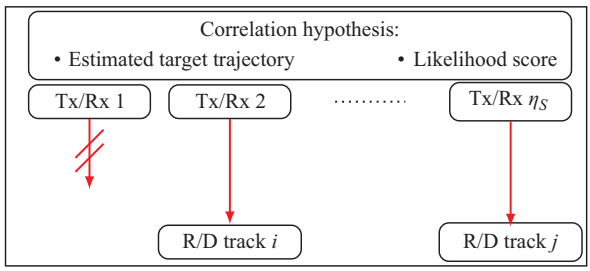

Figure 11.7 Schematic overview: correlation hypothesis

see Figure 11.7. The association over time is given by the history of the R/D tracks.

Thus, for a correlation hypothesis, the association of measurements can be assumed to be known and the target trajectory in Cartesian coordinates can be estimated as discussed in Section 11.3.1. As at least two R/D tracks are associated with a correlation hypothesis, we use ellipse intersection to initialize the Cartesian state. Measurements associated with additional R/D tracks are incorporated via the measurement update of the UKF. The correlation hypothesis in particular contains the information of a Cartesian track in terms of a target state estimate and the single-target LR score, which is calculated in parallel to the measurement update, compare Section 11.4.2.

The number of correlation hypotheses is typically much higher than the number of targets. To select correlation hypotheses that are likely to represent the true targets, multi-target hypotheses are built to resolve conflicting hypotheses. Correlation hypotheses that are contained in the best multi-target interpretation of the R/D tracks reach the status of Cartesian tracks. The number of Cartesian tracks that are displayed to a potential operator is further controlled by a threshold with respect to the single-target likelihood score.

Evaluation by multi-target association, deletion and re-organization of correlation hypotheses and R/D tracks is conducted in certain time intervals. In the meantime, existing correlation hypotheses are updated with new measurements of associated R/D tracks. A Cartesian track of the second tracking stage is treated in the same manner as a correlation hypothesis. Switching between correlation hypotheses that are displayed as Cartesian tracks is possible over time.

- Central tracking stage: The third tracking stage is reserved to Cartesian tracks for which the likelihood scores of the corresponding correlation hypotheses are high (as output of the second tracking stage). The association of measurements from different Tx/Rx pairs to Cartesian tracks is performed at a single node in an MHT framework. Cartesian tracks are updated with the associated measurements according to the UKF equations (compare 1-stage tracking).

Cartesian tracks at this level are not directly coupled to the R/D tracking stage. Thus, a measurement can be used twice by an R/D track and a Cartesian track. To avoid multiple tracks and to reduce complexity, R/D tracks that are based on

measurements also used by Cartesian tracks of the central tracking stage are labelled and removed from the correlation stage.

11.6 Simulation study

In this paragraph, the proposed algorithms are evaluated and discussed by Monte Carlo simulations.

We use a simulation with one Rx, 5 Txs and 10 targets. The geometry is displayed in Figure 11.8. The targets have been simulated to move at low constant altitude and with constant velocity over ground.

The values of probability of detection (P_D) of each Rx/Tx pair are obtained from the radar equation by assuming a constant radar cross section [37]. In Figure 11.8, the P_D is displayed by contour lines, representing the sum of P_D values from different bistatic pairs. The number of available measurements increases in a region near the Rx.

The scenario shows different target constellations:

- Constellation 1 (Targets 1 and 2): Two approaching targets are simulated entering into the FoV of the Rx.
- Constellation 2 (Targets 3, 4, 8 and 9): Multi-target scenario with approaching and parallel moving targets. Targets enter into the FoV.

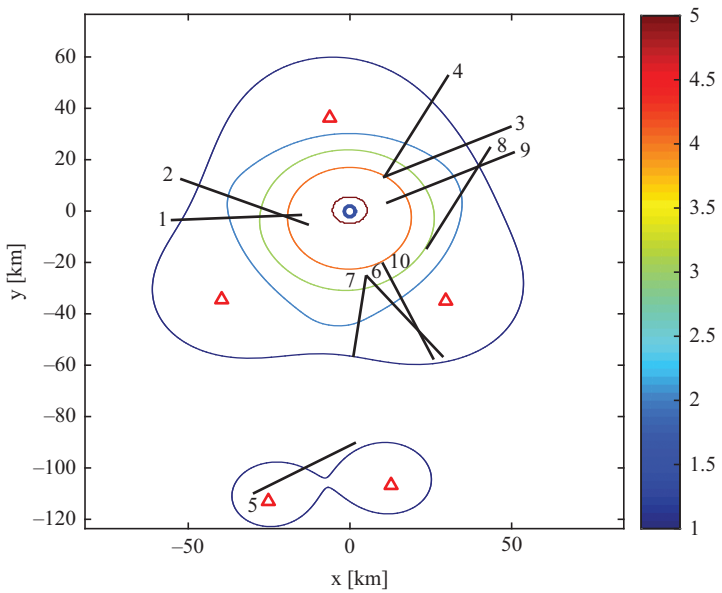

Figure 11.8 Scenario with 10 targets (black lines), 5 transmitters (triangles) and one receiver (blue circle at the origin). The contour lines mark the mean number of detections from different Tx/Rx pairs (summed probability of detection)

Table 11.2 Definition of tracking scenarios

	Scenario A	**Scenario B**	**Scenario C**
Bistatic range accuracy [m]	500	30	30
Azimuth accuracy [°]	3	3	5
Range-rate accuracy [m/s]	0.6	0.6	0.6

- Constellation 3 (Targets 6, 7, 10): Three targets in close distance moving from a region with high-sensor coverage into a region with low coverage.
- Constellation 4 (Target 5): Single target in region with low-sensor coverage.

The scenario is not based on the characteristics of a specific passive radar system. In fact, the constellation of targets and the model of P_D have been chosen to represent different multi-target scenarios in regions with low- and high-sensor coverage.

To test the influence of the single-frequency property, we use the same constellation of Txs and Rx in the scenario with and without frequency separation of the Txs. Furthermore, we vary the measurement errors to analyse the impact on the tracking architecture.

Three scenarios are defined, where the measurements are sampled according to a Gaussian distribution given in Table 11.2.

False alarms are sampled from a uniform distribution in measurement coordinates in the region of interest. When assuming that the Txs are arranged in an SFN, only one measurement set (containing entries of all Txs) is considered. The same assumption of false alarm intensity results for an SFN results therefore in effectively less false alarms than for frequency diversity. The mean number of false alarms in scenarios with frequency diversity is about 80 false alarms per Tx/Rx pair. For the SFN, the mean number of false alarms is about 160 for all Txs together.

Tracking results of 500 Monte Carlo runs are discussed in terms of the root-mean-squared-position error (RMSPOS) and the track probability of detection (track-P_D). A target is assumed to be detected at the track level when a Cartesian track is associated according to a distance criterion in Cartesian coordinates. The track-P_D is given by the mean number of detections at the track level for a given time scan averaged over the Monte Carlo runs. The results are averaged over targets within a constellation. The RMSPOS is compared to the root trace of the CRB (see Section 11.3.1.1).

11.6.1 Tracking results for scenario with frequency diversity

The results for the three fusion schemes (1-stage MHT, 2-stage MHT and 3-stage MHT) are shown in Figure 11.9 for scenario A and B and the four constellations of targets. The impact of the large range error (Scenario A) can be seen by the shift of CRB.

11.6.1.1 Comparison: track extraction time

For constellation 1, 2 and 4 (starting) in a region of low coverage, the 2-stage and 3-stage strategy results in faster extraction of tracks compared to 1-stage tracking.

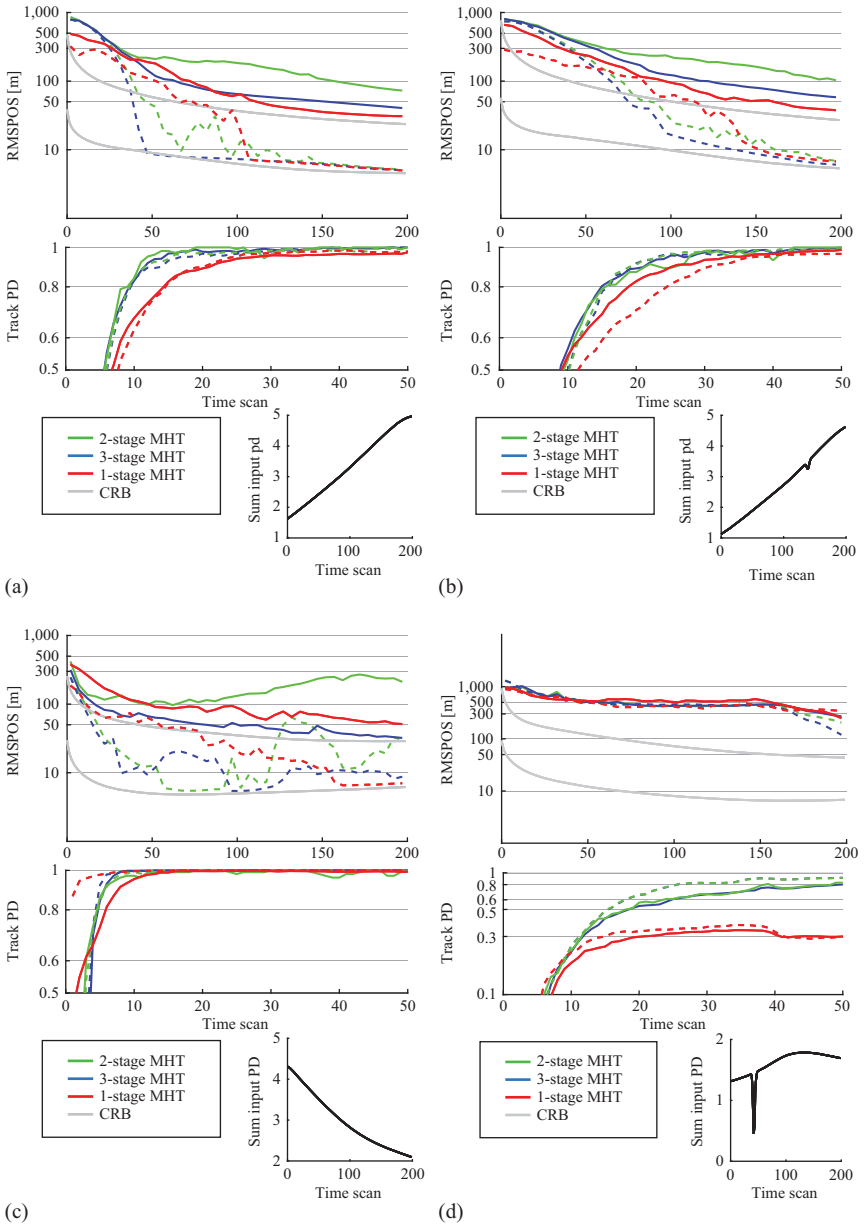

Figure 11.9 Comparison of tracking results for transmitters with frequency separation. Scenario A (solid lines) and Scenario B (dashed lines). (a) Constellation 1, (b) Constellation 2, (c) Constellation 3 and (d) Constellation 4

For Constellation 3, (starting in a region with high-sensor coverage) we observe the contrary.

All three tracking schemes use an LR test for track extraction. For the 2-stage/3-stage tracking approach, the LR test is applied on R/D tracks and therefore for each bistatic Tx/Rx separately. For 1-stage tracking, track extraction is applied on Cartesian tracks, which means that the LR test incorporates updates from different Tx/Rx pairs.

In the LR test, a miss-detection is penalized by decreasing the LR by the factor $1 - P_D$. As the exact P_D is typically unknown to the tracker, we use a fixed $P_D = 0.5$ as tracking parameter. This can be interpreted separately for R/D tracking and Cartesian tracking: for R/D tracking, a $P_D = 0.5$ means that for a given Tx/Rx pair the tracker expects a measurement update in each second time scan. For Cartesian tracking, it can be interpreted that in each time scan the tracker expects a measurement of half of the considered Tx/Rx pairs. Thus, in case that only 1 or 2 Txs provide detection of the target, the mismatch between assumed and simulated P_D leads to delayed track extraction in 1-stage tracking. In contrary, R/D track extraction is not influenced by missed detections from other Tx/Rx pairs but needs a frequent number of detections of the given Tx/Rx pair. In case that detections from multiple Tx/Rx pairs are available, the LR test in Cartesian coordinates can accelerate the track extraction process as seen in Figure 11.9(c).

Even though the described effect is mostly to be led back to the wrong P_D assumption, it shows that 2-stage/3-stage tracking is more robust in cases when the assumed tracking model is violated for some of the Tx/Rx pairs.

11.6.1.2 Comparison: estimation accuracy

For scenario A, the estimation performance (as stated by the RMSPOS) of the 1-stage tracking scheme is generally better than of the 2-stage tracking scheme. Also the estimation performance of 3-stage tracking is improved compared to 2-stage tracking. For scenario B, the estimation performance of the three approaches is comparable.

2-stage tracking can only use measurements for Cartesian localization that are contained in R/D tracks, this can lead to worse estimation performance compared to the 1-stage approach, which can choose from the set of all available measurements.

3-stage tracking uses a compromise between 2-stage and 1-stage tracking. It shows a similar trend than 2-stage tracking with respect to the track extraction and similar trend than 1-stage tracking with respect to the RMSPOS.

Constellation 4 considers a single target in a region of low-sensor coverage and bad estimation performance (near to the Tx/Rx line). Due to the association criterion of tracks and ground truth that we use in Monte Carlo evaluation, tracks with large estimation errors are not included in the statistic. A decrease of track-P_D and an increase of false track rate can therefore go back to increased estimation errors. However, we observe a significant improvement with respect to the track-P_D and/or track accuracy when using the 2-stage initialization scheme. None of our approaches reaches the CRB for this constellation. Tx/Rx pairs with very low P_D provide theoretically a gain to the estimation result (CRB). However, none of the fusion strategies is able to make use of these Tx/Rx pairs.

11.6.1.3 Comparison: false track rate

A comparison of the tracking schemes with respect to the false track rate is given in Figure 11.10(a). The false track rate generally decreases with decreasing measurement error. The worst performance is obtained for Scenario A and 2-stage tracking. 1-stage tracking shows the best performance in the initial phase of the scenario, the false track rate is on an equal level throughout the scenario.

The false track rate is mainly influenced by the size of the track gate (region where the track looks for new measurements). If the gate is very large, the probability that false alarms fall into this region increases. Centralized tracking is therefore typically more robust against the generation of false tracks, as the direct fusion of all available measurements results in small gates. The relatively high false track rate in this scenario goes back to tracks of Target 5 that have erroneously be declared as false tracks due to large estimation errors.

The false track rate of 2-stage tracking is mainly influenced by the false track rate of R/D tracking. Increasing the measurement error results in increased false

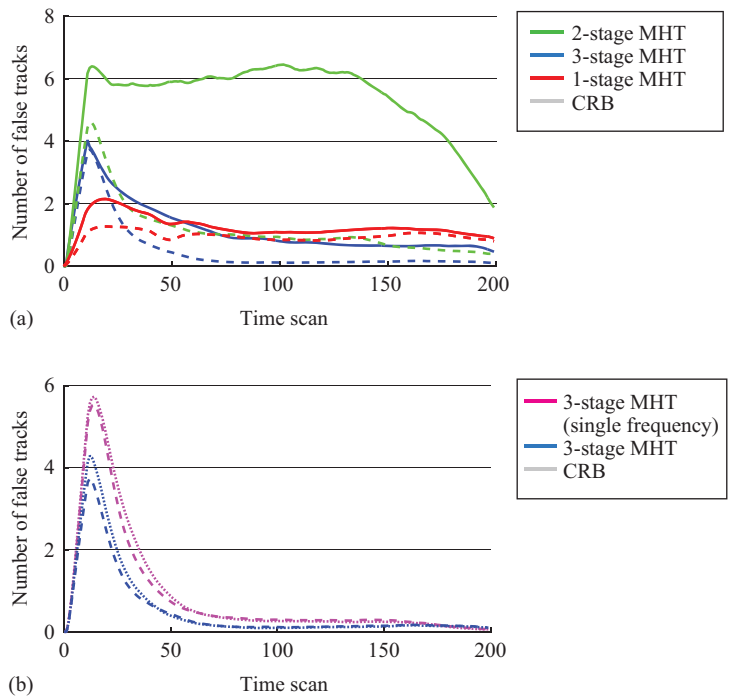

Figure 11.10 Comparison of false track rate. (a) Comparison of results for scenario A (solid lines) and scenario B (dashed lines) and (b) comparison of results for scenario B (dashed lines) and scenario C (dotted lines)

track rate for each individual subsystem. Here, the mean R/D false track rate of Scenario A is 2.3 times the mean R/D false track rate of Scenario B. Each R/D track may be able to generate a Cartesian output, reasoning that the Cartesian false track rate increases even more.

The tracking algorithms were implemented in FORTRAN 95 and executed at a HP Workstation with an Intel Corporation Xeon CPU W3565 processor with 3.20 GHz processor.

The runtime comparison of the three fusion schemes refers to 1 s of the scenario time:

- 1-stage MHT: 1.5 s
- 2-stage MHT: 1.32 s
- 3-stage MHT: 0.83 s.

The 3-stage tracking strategy gives the best results in terms of the runtime of the algorithm.

11.6.2 Tracking results for scenario with single-frequency property

In a second step, the Txs are assumed to be arranged in a single-frequency network. This only appears for DAB/DVB-T passive radar, thus, we consider Scenarios B and C only (assuming good bistatic range accuracy) and focus on evaluation of the 3-stage tracking scheme. In Figure 11.11, where we compare the tracking results with and without the assumption of an SFN. For constellation 3 (starting in the region of good sensor performance), the results are nearly identical. For the other constellations, we find that the track extraction is delayed due to the increased association ambiguity in SFNs. Figure 11.10(b) shows that also the false track-rate (especially in the initialization phase) increases.

A pure runtime comparison is not fair here, as the mean number of false alarms is different in SFNs. The runtime comparison (Table 11.3) is therefore split into the individual tracking stages.

The total runtime is dominated by the R/D tracking as a consequence of the simulated false alarms. The assumption of single frequency results in an increase with respect to the association effort in Stage 2 by a factor of 8.5 and in Stage 3 by a factor of 2.2.

11.7 Application to GSM passive radar

The use of GSM mobile phone signals for passive radar is attractive, because the base stations are worldwide spread even in out of area regions. The signals have digital coding and use frequency diversity. Compared to FM, DAB and DVB-T, the GSM base stations broadcast at relatively high frequencies, which allow a good discrimination in azimuth [8]. However, these advantages are accompanied by a modest range resolution (due to the low signal bandwidth) and low signal power. For appropriate target localization and to achieve a good target coverage, the fusion of multiple Txs/Rx pairs is a key requisite. Thus, data fusion and tracking is of particular importance in this application.

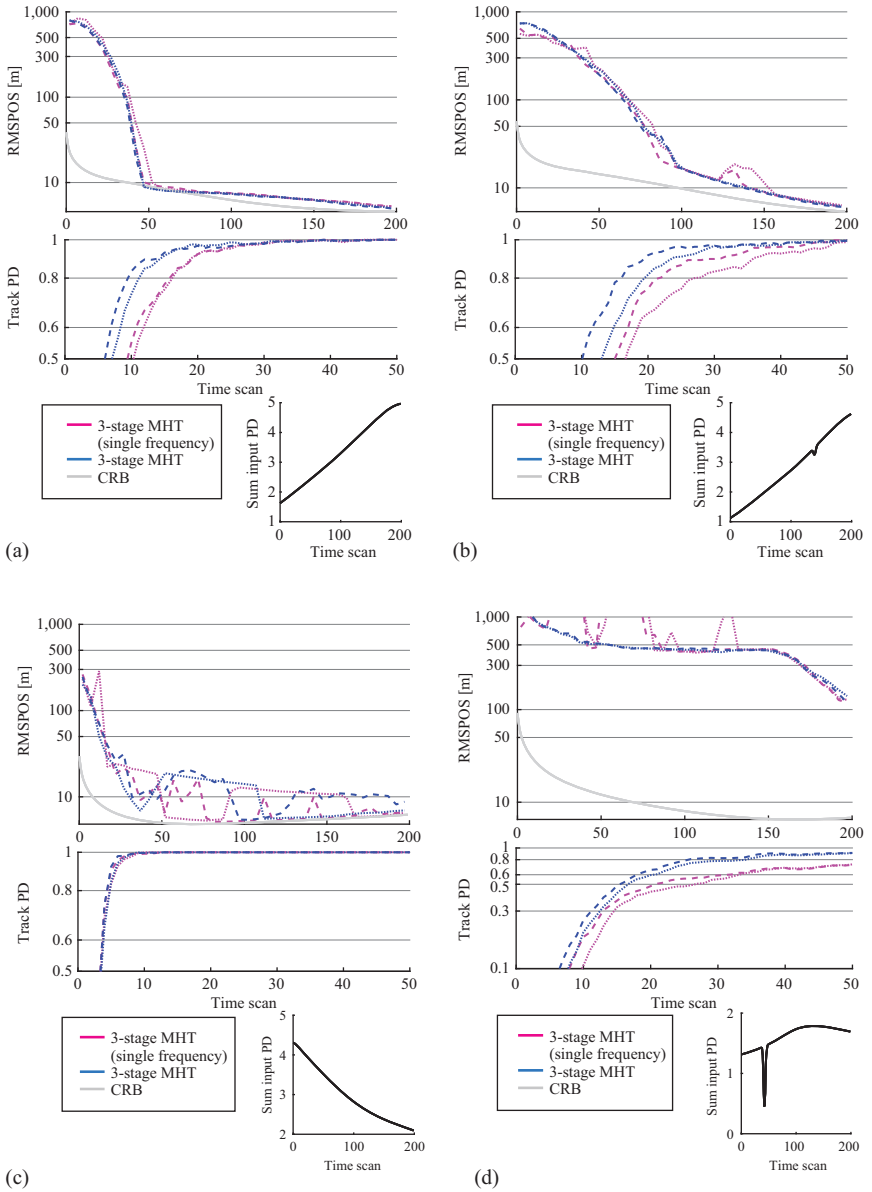

Figure 11.11 Comparison of tracking results with and without the assumption of a single-frequency network. Scenario B (dashed lines) and scenario C (dotted lines). (a) Constellation 1, (b) Constellation 2, (c) Constellation 3 and (d) Constellation 4

Table 11.3 Runtime comparison of 3-stage MHT

Tracking stage	Frequency diversity [s]	Single-frequency network [s]
R/D tracking	0.83	0.6
Correlation stage and evaluation	0.016	0.136
Central tracking stage	0.016	0.0346

In the previous section, we presented different adaptations of the MHT and discussed their strengths on the basis of simulated data. The 3-stage MHT seems to be a good compromise between good estimation accuracy and low false track rate [strength of the 1-stage tracking (centralized)] and short track extraction time [strength of the 2-stage tracking approach (distributed)]. It is especially suitable for application in single-frequency networks with high association ambiguity (see Chapter 18).

For the application to GSM passive radar, we choose the centralized approach (1-stage MHT), because we can directly benefit from the fusion gain from multiple Tx/Rx pairs. In the simulations, 1-stage MHT has shown best performance with respect to the number of false tracks and localization accuracy in the scenario with poor bistatic range accuracy. However, as we also discuss in Section 11.6, the disadvantage of 1-stage MHT is the sensitivity with respect to the match of the tracking model as shown for the example of P_D. Thus, besides the choice of the appropriate tracking strategy, in practice, the development of an appropriate sensor model and the incorporation of context knowledge are of particular importance. This will be discussed in this section by help of real data for the GAMMA-2 experimental system, which was deployed at Fraunhofer FKIE. Results are shown for the application of maritime surveillance. This was also published in [9].

11.7.1 Receiver and data processing

For completeness, we represent the features of the GAMMA-2 GSM system. The guideline for the system concept of GAMMA-2 was to realize a software-defined radar as much as possible [9]. This leads to the design of a uniform linear array (ULA) with 16 elements and 16 digital Rxs. The ULA guarantees maximum spatial target discrimination as well as deep and narrow nulling of interference for a given number of channels, hence minimizing the clutter in the Tx direction [38]. The output of this array can be used for all tasks: reference signal acquisition, surveillance signal extraction and base transceiver stations (BTS) monitoring.

In the trials, the FKIE-receiving system GAMMA-2 shown in Figure 11.12(d) has been used. Each element of the ULA is composed of columns of three Vivaldi antennas (frequency range: 1.5–2.15 GHz) which are summed in the analogue domain. Each column has a 3 dB elevation BW of 27° and a gain of 10 dB (at 1.8 GHz) resulting in an array gain equal to 22 dB. For reception of GSM1800 signals, the distance between the elements is chosen equal to 8 cm. This corresponds to a spacing of the half wavelength for a frequency of 1,874 MHz.

As a compromise between processing speed and flexibility, the digital Rx hardware has been designed to extract in parallel up to eight GSM frequency

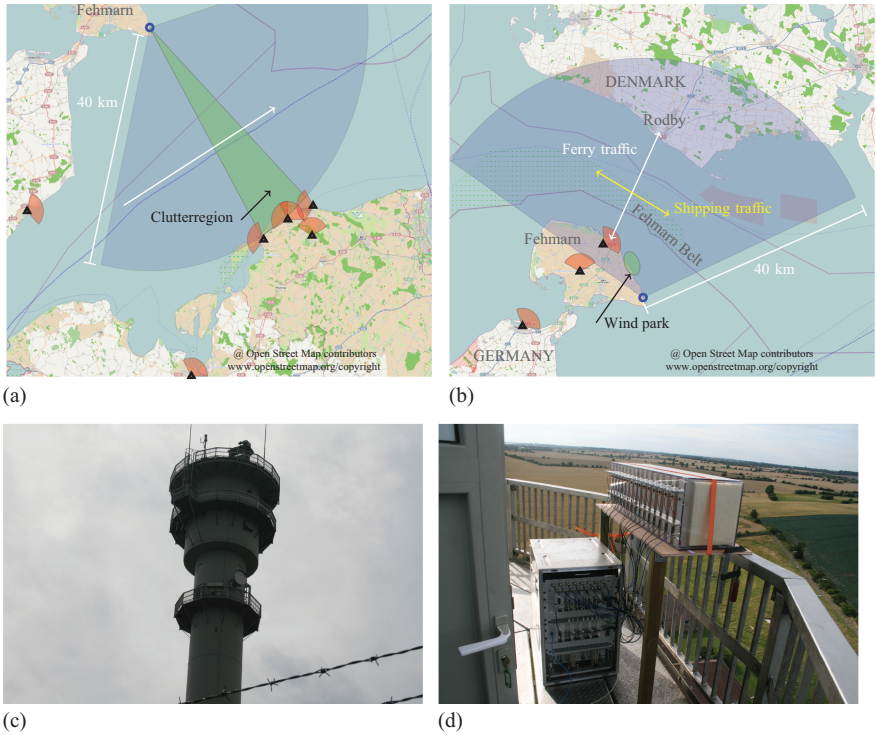

Figure 11.12 Scenario configurations, (a) Scenario 1, Bay of Mecklenburg, (b) Scenario 2, Fehmarn Belt, (c) GAMMA-2 mounted on the tower and (d) The GSM passive radar antenna and receiver GAMMA-2, after [9] ©2014 IET

channels (demodulated I&Q) of 200 kHz width within the system receiving bandwidth of 30 MHz. Each frequency channel is subsequently digitally down converted and stored for further signal processing steps. This special realization of the hardware limits the number of Txs that can be used in parallel. With hardware that is more expensive also full GSM bandwidth of 75 MHz could be realized.

For reasons of verification, we have considered standard signal processing: the reference signal is extracted by conventional beamforming [39] p. 506. The FoV for the surveillance signal (from -60° to 60°) is sampled by a set of fixed beams in azimuth. For each beam with given angle of arrival digital adaptive beamforming and clutter cancellation are performed to obtain the corresponding surveillance signal [38]. The clutter cancellation method in space and time used here is based on the projection of the received signal onto the sub-space orthogonal to the clutter sub-space [40]. The signal power is accumulated by coherent integration. The coherent integration time (CIT) is selected as the longest time in which the target with its dynamic remains in the resolution cell. According to [8] and the given

scenario, one obtains a CIT equal to 1.8 s producing theoretically a very fine Doppler resolution (0.56 Hz) corresponding to a radial velocity less than 0.05 m/s. The long CIT is suited for the detection of maritime targets. The Doppler is therefore an excellent criterion to distinguish closely located vessels in areas with high target density. Finally, the range-Doppler-bin for which the signal strength exceeds a pre-defined threshold is declared as detection and is forwarded to the tracker.

11.7.1.1 Parameter accuracies

To characterize the measurement accuracies for target tracking, a simple bin processing strategy is assumed. Of course, a detailed analysis of the achievable accuracies must include all effects, starting with the implemented estimation and calibration algorithms, the environmental effects like multipath and the target SNR. This will be a topic of future research.

We start by considering a simple grid search over the range domain. The grid cell dimension Δ_{cell} is selected according to the sampling frequency of the analogue-to-digital converter and is smaller than the resolution limit Δ_{range}. Thus, the range accuracy for high SNR values is determined by:

$$\sigma^2_{\text{range}} = \frac{\Delta^2_{\text{cell}}}{12} \tag{11.28}$$

This is based on the assumptions that (i) the unknown target position is uniformly distributed within the cell and (ii) no fine estimation technique is implemented (e.g. inter-polation or range mono-pulse).

In the experiment, the signals are sampled at a frequency equal to 240 kHz. Thus, the monostatic range accuracy is about 360 m. This is less than the range resolution but still not satisfying for a good position estimation of moving targets. It has to be stressed that, when operating in Cartesian coordinates, the achieved position estimation accuracy depends not only on the measurement errors but also on the bistatic geometry. Thus, the position estimate can be worse than 360 m.

For the angle estimation, we consider a simple search of the maximum response over the 16 look directions (beams) within the FoV. Thus, again the angular cell Δ_{angle} defines the angular accuracy. In the case of a uniformly distributed target over the angular cell and considering an angle bin of $\Delta_{\text{angle}} = 7.5^\circ$, the angular accuracy σ_{angle} is about 2.15°. Admittedly, such an angular accuracy can only be attained if targets are well separated without any clutter influence. In reality, clutter cancellation and especially direct signal cancellation is imperfect and this will influence the angular accuracy. To deal with this, we assume that the angle error is distributed over two adjacent beams. Thus, the angular accuracy is approximately 5°.

Following the same argumentation as above, the Doppler accuracy σ_{Doppler} for an integration time equal to 1.8 s results into 0.56 Hz. This high accuracy compensates the low accuracy in range and allows target discrimination and tracking as will be seen in the sequel.

11.7.2 Scenario description

Two trial scenarios were acquired in the Baltic sea. The first one considers the maritime traffic in the Bay of Mecklenburg. Figure 11.12(a) shows the scenario configuration with the Rx (indicated by circle). As Txs, seven BTS (black triangles) in six different locations with specific look directions were selected (two BTS were sharing one mast).

The Rx was mounted on a tower of 56 m height shown in Figure 11.12(c) located at the eastern cape of the Fehmarn island [41]. Its FoV is represented with the blue sector (120° FoV and 40 km range [41]). The illumination sectors of the individual BTS are indicated by small red sectors. Each BTS typically covers a 120° sector. Moreover, the white arrow within the Rx FOV shows a typical vessel trajectory following one of the sea lanes in this area. We will concentrate on vessels moving along this trajectory to analyse and discuss the obtained results in the following sections.

The second scenario features the frequent ferry traffic between the Fehmarn island and Rodby in Denmark. At the same time in orthogonal direction, dense shipping traffic through the Fehmarn Belt is crossing the ferry lane. For both scenarios, the Rx was mounted at the same position as in the first scenario (Figure 11.12(a)) but with a look direction changed to cover the area of interest. In fact, several potential BTS exist in this region, nevertheless they all could not be considered simultaneously. This is because of the limited Rx bandwidth (30 MHz) and the widespread carrier frequencies of the potential BTS. Here, we present results with a configuration restricted to the three Txs from Figure 11.12(b). This is clearly not an optimal configuration and shows constraints due to the hardware and the geometry, but it shows exemplary the good results that can be obtained.

11.7.3 Performance analysis on real data

For validation purposes, an Automatic Identification System (AIS) Rx has been used to obtain reference positions and velocities of the vessels in the observed area. The AIS information of existing vessels is transformed into the range-Doppler-azimuth domain and compared with the GSM measurements. Measurements associated with this ground truth are selected by the global nearest neighbour technique [27] pp. 8–11. The availability of the AIS ground truth can be used for theoretical evaluation and validation of experimental system performance. Specifically, we analyse two exemplary vessels. In Scenario 1, a ship moving through the Bay of Mecklenburg is considered. In Scenario 2, we consider a ferry which is approaching Fehmarn island from Rodby in Denmark.

The measurements that have been associated with the ground truth (see Section 11.7.3) are processed by the UKF to obtain estimates of the target position and velocity as well as the covariances (Section 11.3.1). Results are displayed in Figure 11.13. Please note that for data evaluation, we use a simplified association strategy based on the AIS data, tracking results for the full MHT (without AIS support) are discussed in Section 1.7.4. Specifically, Figure 11.13(a) and (b) show sequences of the estimation results. The AIS reference data of the vessel are

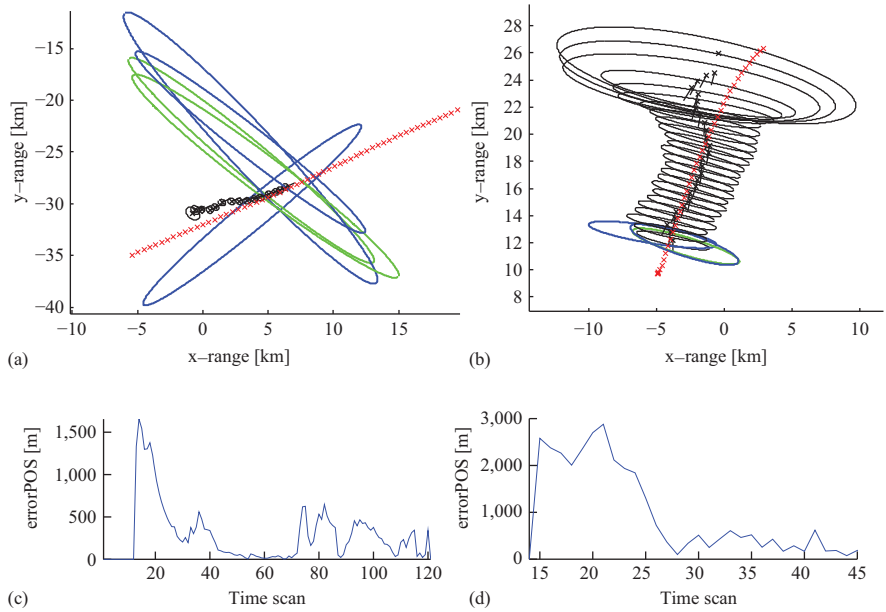

Figure 11.13 Accuracy improvement by multistatic fusion (real data), (a) Scenario Bay of Mecklenburg (screenshot, 15 time scans), (b) Scenario Fehmarn Belt (screenshot, 30 time scans), (c) Scenario Bay of Mecklenburg (position error over time) and (d) Scenario Fehmarn Belt (position error over time), after [9] ©2014 IET

depicted as red crosses. The GSM track (for several time scans) is represented by a black cross (mean value of estimated position) and an appended black line (mean velocity), while the black ellipses show the corresponding track position uncertainty (described by the track covariance). Finally, the blue and green bold ellipses illustrate the position uncertainty given by the plots (after transformation into Cartesian domain) of one time instant for each of the bistatic configurations that provide detection. Uncertainty ellipses are plotted according to the 3-sigma volume (3-times the standard deviation). In Figure 11.13(c) and (d), the RMSPOS is plotted over track time. The Bay of Mecklenburg scenario confirms the importance of the bistatic geometry. At the given time scan, six of seven BTS provide detection of the target (Figure 11.13(a)). Five of them are from closely spaced Txs, while one has a quasi-orthogonal geometry. The dramatic multi-sensor fusion gain can be seen clearly in this example (black ellipses). Fusion over time (assuming the nearly constant velocity motion model) finally improves the accuracy down to 200 m (Figure 11.13(c)). Specifically, the exploitation of the BTS with the error covariance orthogonal to the other configurations enhances the localization capability. At the end of the scenario, the error increases, which is consistent with

our expectation from CRB analysis [9]. At the beginning of the scenario, the error values are higher than expected, which can be traced back to missed detections from some Txs.

For the Fehmarn Belt scenario, the fusion of the three BTS delivers indeed a more accurate position estimation than with only one BTS, but it is not satisfying (Figure 11.13(b)). This performance can be referred to the inconvenient choice of the BTS which are in this example almost on the same line with the trajectory of the ferry. Thus, the corresponding position ellipses coincide. No significant accuracy improvement can be expected from the fusion of the BTS during the first half of the scenario. Only the fusion over time (according to the adopted motion model and exploiting the Doppler measurement) improves the performance. At the second half of the scenario, the target is moving into an area of better estimation performance, which is confirmed by the tracking result (Figure 11.13(d)).

These examples emphasize the importance of the Tx–Rx geometry. Orthogonal bistatic configurations deliver higher fusion gain. Hence, the optimization of a GSM passive radar system as considered in [8] is a key factor for the overall performance.

11.7.4 Tracking results

The number of false alarms limits the quality of target tracking. In particular, the increased occurrence of false alarms in a specific region will lead to unwanted false tracks. One should note that because of our conventional signal processing and hardware imperfections, we have many false alarms due to clutter residues in BTS direction for each bistatic pair. This applies in particular to the scenario of the Bay of Mecklenburg.

In the second scenario of Fehmarn Belt, a wind park at the coast of the Fehmarn island (see Figure 11.12(b)) caused major problems. Without any treatment, the tracking results are dominated by a large number of false tracks, as seen in Figure 11.14(a). Table 11.4 explains the visualization symbols of the tracking results.

To improve the tracker performance, procedures have been proposed to generate adaptively a clutter map based on all collected measurements of the same geographic region [42,43]. This uses the assumption that the clutter is stationary and targets average out. The clutter map identifies regions of high false alarm level. This means that for each BTS and for each range-Doppler cell, a probability value describing the appearance of a false alarm is assigned. The generated clutter map for one BTS is displayed in Figure 11.14(c). The target returns associated to AIS data have been removed from the adaptive statistic. The contribution of the wind park becomes apparent in the first two range cells. This context information is then exploited by the tracker in the plot to track association by the factor ρ_F (influencing the hypothesis weights as discussed in Section 11.4.1). In addition, we introduce a threshold on the false alarm probability to avoid track initiation in a region of high false alarm level. However, an existing track can be maintained in a clutter region.

In addition to the clutter map, the geographic information of the coastline can be inserted in order to discard detections on the land. A geographic map of admissible areas, Figure 11.14(d), is taken into account for the MHT. The use of

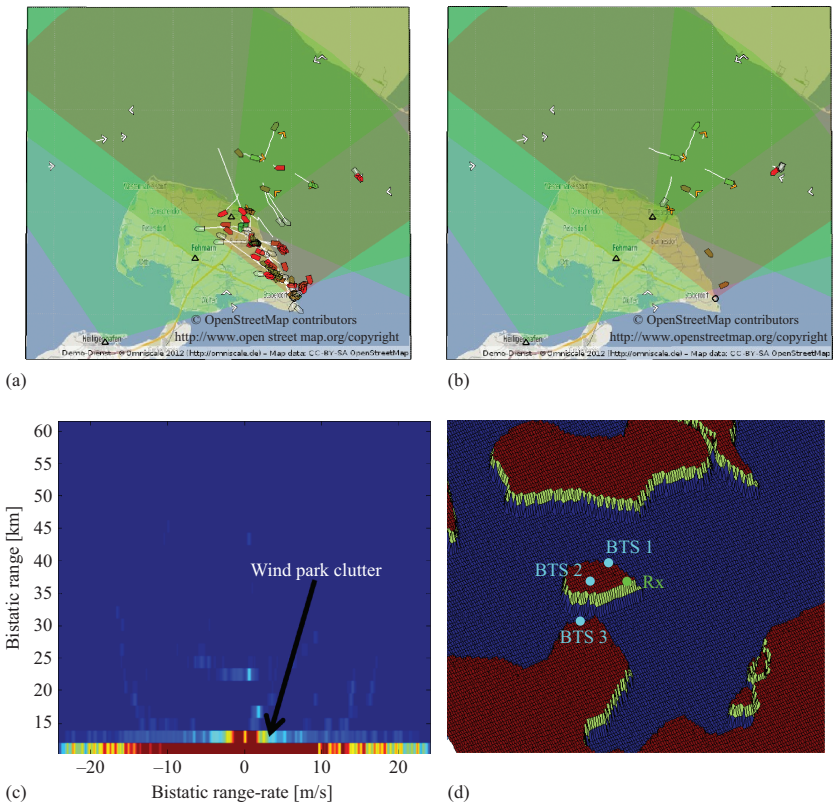

Figure 11.14 Clutter reduction (a) GSM Tracking results are mainly influenced by the high false alarm level, see also Table 11.4, (b) By use of Clutter and land maps a clean observation picture can be obtained, see also Table 11.4, (c) Clutter map for one BTS and (d) Geographic information map of coastline, after [9] ©2014 IET

Table 11.4 Visualization scheme: tracking results

Tracks	Small ship symbols	Green: high-probability track Red: low-probability track Grey: identify an inactive track
Ground truth (From AIS)	Triangles	Orange: AIS target detected by the GSM system White: no associated measurement
Look direction	Shaded area	Red: receiver Green: transmitter

context information has been already demonstrated as an effective mean for performance improvement in other maritime applications [44,45]. In our system, the geographic map is pre-loaded before the processing starts. The tracker listens to this context information in two different steps of the processing, which are as follows:

1. when new sensor measurements are received as input for the algorithm and
2. when already existing tracks are predicted.

In both cases, the unrealistic cases (e.g. measurements over land or tracks crossing land) are discarded in order to reduce the number of the hypotheses. Using both forms of context knowledge (clutter and land map), an impressively clean situation picture can be achieved only on the basis of GSM measurements (Figure 11.14(b)).

A more detailed discussion of the tracking results has been done in [9].

11.8 Summary

The fusion of measurements from multiple bistatic sensor pairs is a key feature of passive radar. It is the prerequisite for increasing the coverage of a sensor and to improve the estimation accuracy. The task of passive radar tracking is to realize this fusion gain by correctly associating measurements of the different bistatic sensor pairs and by appropriate estimation techniques.

For known associations of measurements to targets, target localization by combining information of different Txs is a non-linear estimation problem. Conventional approximation techniques like the unscented or EKF are appropriate to handle the non-linearity of the bistatic measurement equation, but rely on a good initial estimate.

The dimension of the association problem in passive radar applications depends strongly on the precision of the bistatic measurements. Multi-target conflicts can arise, even if the targets are geographically well separated. The association problem further increases when Txs are arranged in single-frequency networks. Ghost tracks result from misinterpretation of measurement data. Compared to false alarms that are contained in the sensor data, ghosts emerge at the fusion level and are to be traced back to multi-target and multi-sensor association conflicts.

A solution of the association task has been derived on the basis of the multiple hypothesis-tracking techniques. Different fusion schemes have been discussed with the help of simulated data.

The design of the tracking algorithms needs to be adapted to the specific characteristics of the passive radar system. For the example of GSM passive radar, we discussed real data results that demonstrate the gain from fusing measurements of different Tx/Rx pairs. Incorporation of prior information, if available, can further improve the tracking results. This has been demonstrated for a GSM passive radar application by incorporation of a clutter map and geographical information. This is of particular importance, when operating in dense clutter regions like wind parks and blind zones.

References

[1] Jishy K., Lehmann F. 'A Bayesian track-before-detect procedure for passive radars'. *EURASIP Journal on Advances in Signal Processing*, 2013. 2013(1):45.

[2] Howland P. 'Target tracking using television-based bistatic radar'. *IEE Proceedings – Radar, Sonar and Navigation*, 1999. 146(3):166–174.

[3] Howland P., Maksimiuk D., Reitsma G. 'FM radio based bistatic radar'. *IEE Proceedings – Radar, Sonar and Navigation*, 2005. 152(3):107–115.

[4] Tobias M. *Probability Hypothesis Densities for Multitarget, Multisensor Tracking with Application to Passive Radar Martin Tobias*. Ph.D. thesis, 2006.

[5] Daun M., Nickel U., Koch W. 'Tracking in multistatic passive radar systems using DAB/DVB-T illumination'. *Signal Processing*, 2011.

[6] Tharmarasa R., Nandakumaran N., McDonald M., Kirubarajan T. 'Resolving transmitter-of-opportunity origin uncertainty in passive coherent location systems'. *Proceedings of SPIE*, vol. 7445, 2009.

[7] Choi S., Berger C.R., Crouse D., Shengli Zhou P.W. 'Target tracking for multistatic radar with transmitter uncertainty'. *Proceedings of SPIE*, vol. 7445, 2009.

[8] Nickel U. 'System considerations for passive radar with GSM illuminators'. *2010 IEEE International Symposium on Phased Array Systems and Technology (ARRAY)*, 2010. pp. 189–195.

[9] Zemmari R., Broetje M., Battistello G., Nickel U. 'GSM passive coherent location system: performance prediction and measurement evaluation'. *Radar, Sonar Navigation, IET*, 2014. 8(2):94–105.

[10] Wehner D.R. *High-Resolution Radar*. Artech House Radar Library, 1994.

[11] Griffiths H.D., Baker C.J. 'Passive coherent location radar systems. Part 1: performance prediction'. *IEE Proceedings – Radar, Sonar and Navigation*, 2005. 152(3):153–159.

[12] Baker C.J., Griffiths H.D., Papoutsis I. 'Passive coherent location radar systems. Part 2: waveform properties'. *IEE Proceedings – Radar, Sonar and Navigation*, 2005. 152(3):160–168.

[13] Koch W. *Tracking and Sensor Data Fusion, Methodological Framework and Selected Applications*. Springer, 2014.

[14] Mahler R. Chap. 'Random set theory for target tracking and identification'. *Electrical Engineering & Applied Signal Processing Series*. CRC Press, 2001. doi:10.1201/9781420038545.ch14.0.

[15] Denham W., Pines S. 'Sequential estimation when measurement function nonlinearity is comparable to measurement error'. *AIAA Journal*, 1966. 4(4):1071–1076.

[16] Julier S.J., Uhlmann J.K. 'Unscented filtering and nonlinear estimation'. *Proceedings of the IEEE*, 2004. 92(3):401–422.

[17] Daun M., Ehlers F. 'Tracking algorithms for bistatic sonar systems'. *INFORMATIK'09 – Jahrestagung der Gesellschaft fuer Informatik e.V. (GI) 4th German Workshop Sensor Data Fusion (SDF'09)*. Lübeck, Germany, 2009. pp. 2283–2295.

[18] Daun M., Berger C.R. 'Track initiation in a multistatic DAB/DVB-T network'. *Proceedings of the 11th International Conference on Information Fusion*, 2008. pp. 1–8.

[19] Becker K. 'Target motion analysis aus Winkelmessungen: Parametrische Studie in drei Dimensionen'. FKIE Bericht 12, FGAN, Wachtberg-Werthoven, 2000.

[20] Trees H.L.V., Bell K.L. *Bayesian Bounds for Parameter Estimation and Nonlinear Filtering/Tracking*. New York: Wiley-Interscience, 2007.

[21] Tichavsky P., Muravchik C., Nehorai A. 'Posterior Cramér–Rao bounds for discrete-time nonlinear filtering'. *IEEE Transactions on Signal Processing*, 1998. 46(5):1386–1396.

[22] Zhang X., Willett P., Bar-Shalom Y. 'Dynamic Cramér–Rao bound for target tracking in clutter'. *IEEE Transactions on Aerospace and Electronic Systems*, 2005. 41(4):1154–1167.

[23] Mušicki D., Morlande M., La Scala B. 'Non parametric target tracking in nonuniform clutter'. *Proceedings of FUSION Conference*, 2005.

[24] Reid D. 'An algorithm for tracking multiple targets'. *IEEE Journal AC*, 1979. 24(6):843–854.

[25] Kurien T. 'Issues in the design of practical multitarget tracking algorithms'. In Y. Bar-Shalom (ed.), *Multitarget-Multisensor Tracking: Advanced Applications*. Artech House, 1990.

[26] Koch W., Koller J., Ulmke M. 'Ground target tracking and road map extraction'. *ISPRS Journal of Photogrammetry and Remote Sensing*, 2006. 61:197–208.

[27] Blackman S., Popoli R. *Design and Analysis of Modern Tracking Systems*. Artech House, 1999.

[28] van Keuk G. 'Sequential track extraction'. *IEEE Transaction on Aerospace and Electronic Systems*, 1998. 34:1135–1148.

[29] Pattipati K.R., Deb S., Bar-Shalom Y., Washburn R. B. J. 'A new relaxation algorithm and passive sensor data association'. *IEEE Journal AC*, 1992. 37(2):198–213.

[30] Morefield C. 'Application of 0-1 integer programming to multitarget tracking problems'. *IEEE Transactions on Automatic Control*, 1977. 22(3): 302–312.

[31] Broetje M. *Multistatic Multihypothesis Tracking Techniques for Underwater- and Air Surveillance Applications*. GCA, 2013. PhD. thesis.

[32] Tharmarasa R., Subramaniam M., Nadarajah N., Kirubarajan T., McDonald M. 'Multitarget passive coherent location with transmitter-origin and target-altitude uncertainties'. *IEEE Transactions on Aerospace and Electronic Systems*, 2012. 48(3):2530–2550.

[33] Choi S.M., Crouse D.F., Willett P., Zhou S. 'Approaches to Cartesian data association passive radar tracking in a DAB/DVB network'. *IEEE Transactions on Aerospace and Electronic Systems*, 2014. 50(1):649–663.

[34] Choi S., Willett P., Zhou S. 'The PMHT for passive radar in a DAB/DVB network'. *Journal of Advances in Information Fusion*, 2014. 9(1):27–37.

[35] Gerard O., Coraluppi S., Carthel C., Grimmett D. 'Benchmark analysis of NURC multistatic tracking capability'. *Proceedings of FUSION Conference*, 2006.
[36] Malanowski M., Kulpa K., Suchozebrski R. 'Two-stage tracking algorithm for passive radar'. *Proceedings of the 12th International Conference on Information Fusion*, 2009. pp. 1800–1806.
[37] Zemmari R., Nickel U. 'Range performance study of a GSM passive radar system'. *International Radar Symposium*, 2009. pp. 337–341.
[38] Zemmari R., Nickel U., Wirth W.D. 'GSM passive radar for medium range surveillance'. *European Radar Conference EuRAD*, 2009. pp. 49–52.
[39] Wirth W.D. *Radar Techniques Using Array Antennas*. IEE, 2001.
[40] Colone F., Cardinali R., Lombardo P. 'Cancellation of clutter and multipath in passive radar using a sequential approach'. *IEEE Radar Conference*, 2006. pp. 393–399.
[41] Zemmari R., Daun M., Nickel U. 'Maritime surveillance using GSM passive radar'. *13th International Radar Symposium*, Warsaw, 2012.
[42] Mušicki D., Suvorova S., Morelande M., Moran B. 'Clutter map and target tracking'. *Proceedings of the 8th International Conference on Information Fusion 2005*, 2005.
[43] Schlangen I., Daun M. 'Different tools for clutter mapping' . *INFORMATIK'10 – Jahrestagung der Gesellschaft fuer Informatik e.V. (GI) 5th German Workshop Sensor Data Fusion (SDF'10)*. Leipzig, Germany, 2010.
[44] Battistello G., Ulmke M. 'Exploitation of a priori information for tracking maritime intermittent data sources'. *2011 Proceedings of the 14th International Conference on Information Fusion (FUSION)*, 2011. pp. 1–8.
[45] Vespe M., Sciotti M., Burro F., Battistello G., Sorge S. 'Maritime multisensor data association based on geographic and navigational knowledge'. *IEE Radar Conference 2008*, 2008. pp. 1–6.

Chapter 12

Radar-based ground surveillance

Felix Opitz[1]

Abstract

Radar-based ground surveillance provided by airborne platforms or based on distributed land-based installations is an essential ingredient for modern activity-based intelligence. Therefore, ground moving target indication radar detects objects within wide areas on land and sea and reports them through extracted radar plots. Often these radar plots end up in a big data problem due to the high number of involved objects and the long duration of typical surveillance missions. Also, the object trajectories reported by radar plots may be interrupted due to terrain masking and radar blindness within the Doppler notch. Multi-object tracking techniques create continuous object trajectories by considering the radar plots collected by multiple platforms together with topography and infrastructure. Higher level aggregation methods, like convoy detection, group tracking and traffic flow estimation, are additional methods of data analytics. Applied on the radar-based ground picture they contribute to the overall situation assessment and are suitable for focussing the attention of the users. Besides these detection and tracking aspects, object classification and identification is necessary to complete the situational ground picture. Radar contributes e.g. with synthetic aperture radar or high-range resolution. Finally, data fusion is used to combine the radar picture with additional data coming from other sensors or transponder systems.

12.1 Introduction

Ground surveillance is of central interest in numerous domains like defence, border security, coastal surveillance, traffic supervision and emergency management to mention only a few. The surveyed objects can be individuals, vessels or critical facilities on sea or on land. The surveillance has to cover extended areas, complicated environments and dense scenarios with a high concentration of objects. Finally, the systems have to perform well in all weather conditions and provide permanent long-term availability.

[1]Airbus Space & Defence, Germany

Usually, radar meets these demands on surveillance systems very well. They are mounted on airborne platforms, on space-based satellites, on naval and ground vessels or they are part of fixed installations.

Radar is the preferred sensor for detection and tracking. This means the determination of all trajectories of moving ground objects based on subsequent sensor measurements. But ground surveillance is not limited to the pure determination of trajectories. Knowing the position and dynamics of the involved objects, the next question is their classification and identification. And even for this task, the radar contributes as synthetic aperture, via high-range resolution or via Doppler analysis.

Ground surveillance is related to numerous environmental models, e.g. road maps, digital elevation or geoid models. Their incorporation into the surveillance process is essential for the generation of a more comprehensive situational ground picture. And again, this set of environment data is often the result of radar measurement campaigns.

Further improvements for ground surveillance can be achieved by multiple-radar platforms instead of only a single one, which increases coverage and helps to improve the accuracy of the involved radar-based tracking.

In addition, the situational ground picture can be completed by the fusion with complementary sensors. Imaging sensors like infrared and daylight camera systems are often able to enrich the radar generated picture with additional information. Furthermore, the interrogation of transponders provided by various systems is very valuable for the tracking, classification and identification of co-operating objects.

Modern surveillance systems are integrated in a network-centric architecture and exchange information by several data links.

In the following sections, techniques for the situational ground picture compilation with the focus on radar sensors are described. First, an overview about radar characteristics and mounting platforms is presented. The individual tracking of ground objects based on radar detections taking into account co-ordinate systems, road map information and digital elevation models is considered in the second part. Another important aspect of ground surveillance is the tracking of object aggregation, or the usage of multiple-radar platforms. This is addressed in a separate section. Finally, an outlook is given to synergies offered by multi-sensor data fusion between radar sensors themselves, and with complementary sensors.

12.2 Radar systems in ground surveillance

A radar system used for ground surveillance has two essential factors: The radar itself and the platform, which carries the radar.

12.2.1 Radar platforms

One of the most critical issues for ground surveillance is masking caused by terrain, building development and vegetation.

Ground surveillance radar operates best mounted on airborne platforms, which offers an optimized line of sight between sensor and objects. Possible platforms include manned aircraft or unmanned aerial vehicles (UAVs), like high altitude long endurance or medium altitude long endurance UAVs [1]. These operate in heights starting from 5 km up to over 20 km and provide a coverage range up to several hundred kilometres. Also, blimps are used as static airborne sensor platforms, which ascent up to 5 km. Radar equipped satellites orbit in more than 500 km and possess a ground speed of several km/s. At present, these platforms are commonly equipped with SAR sensors, but it has also been proposed to add ground moving target indication (GMTI) functionality [2–4]. Further, high-altitude platform stations are sensor platforms, which address the gap between UAVs and satellites [5]. Ground-based GMTI sensors are mounted on stationary masts or vehicles. Normally, the resulting grazing angle is ten to hundred orders of magnitude smaller than the one achievable by airborne platforms. So, the surveillance range of these systems is highly terrain and object dependent, normally it can cover a few tens of kilometres. Often, ground surveillance radars are deployed within a whole sensor chain and are also effective in the detection of individuals.

12.2.2 Radar systems

12.2.2.1 Radar modes and types

Depending on the emitted waveform, pulsed and frequency modulated continuous wave radars are distinguished. Both variants are useful for ground surveillance. More details concerning wave form design and applications can be found in [6,7]. Here, only pulsed radars are considered.

Radar offers specialised modes for different surveillance tasks [8]. To detect and track moving objects, the GMTI is the preferred technology. GMTI radar exploits the Doppler to get a highly precise estimation of the object range rate, i.e. the speed of the object projected to the line of sight. Therefore, the Doppler information is used to distinguish between moving objects and the background clutter.

Synthetic aperture radar (SAR) allows the imaging of wide areas and static objects. While GMTI radar uses Doppler information to get the range rate of an object, SAR uses the Doppler information to improve the cross-range resolution of a radar image. To monitor an extended area, stripmap SAR is the most common mode. Here, the radar images the area perpendicular to the ground track (i.e. the projected trajectory) of its mounting platform. Conversely, spotlight mode SAR is suited for the imaging of limited areas but with increased resolution. If the aim is to classify objects, inverse SAR (ISAR) applies. This allows e.g. the classification of ships even under environmental conditions which are infeasible by optical or thermal systems. More advanced techniques for SAR processing can be found in [9].

Modern radars equipped with electronically scanning antennas are able to execute these modes quasi-simultaneously. A dedicated sensor management optimizes the switch between the available radar modes. Often a combination of GMTI and SAR is used where the former allows the detection and tracking of moving

ground objects and the latter is triggered by special events to establish a more detailed situation assessment based on imaging. Such events could be e.g. sinks, sources and aggregations of ground objects [10,11].

12.2.2.2 Characteristics of GMTI radar

The performance of ground surveillance depends strongly on radar specifications e.g. probability of false alarm and detection, update rate, accuracy and resolution, minimum and maximum detection range, transmission and pulse repetition frequency (PRF).

Depending on the used PRF the range or Doppler measurement becomes ambiguous. The low PRF mode is by definition Doppler ambiguous; high PRF is ambiguous in range. Medium PRF is ambiguous in both of them. Due to this ambiguity, the range rate is only known modulo the blind speed. There are methods to eliminate these ambiguities based on variations of the PRF and the Chinese reminder theorem, known as staggering [8]. However, the trade-off when using staggering must be considered, as it requires the emission of multiple bursts and complicates the radar-based classification processing. Often, it is preferred to eliminate ambiguities within the tracking (see [12] for an advanced discussion).

Today, GMTI radars offer an excellent range and Doppler resolution and accuracy, whereas the cross-range resolution and accuracy is a limiting factor especially in airborne systems and mobile ground systems, where the antenna size is limited. The expected cross-range resolution of a radar with wavelength λ and aperture size A is given by the 3-dB beam width and $k \approx 0.89$ (see [8], p. 12):

$$\Theta_3 = 2\arcsin\frac{1.4\lambda}{\pi A} \approx k\frac{\lambda}{A} \tag{12.1}$$

Therefore, the cross-range resolution depends on the antenna size and cannot be made arbitrarily small. It becomes very inaccurate whenever the object has a long distance to the radar. Methods to improve the cross-range accuracy include the utilization of road maps within compressive sensing [13] or tracking, which is discussed later on.

Another limiting factor is the platform motion-induced Doppler bandwidth – especially for GMTI radar carried by airborne platform. The Doppler bandwidth β_D of a side-looking radar moving with velocity v and having a squint angle ψ to the object and a projected antenna size A_ψ is given by [8], p. 125 and 390:

$$\beta_D \approx k\frac{2v}{A_\psi} \tag{12.2}$$

Hence, for radars on moving platform it is a problem to distinguish between ground clutter and slow moving objects based on the Doppler measurement [6,14].

This leads to another problem, the Doppler notch. To reject the ground clutter, usually a threshold is introduced, called minimum detectable velocity v_{MDV}. Radar plots with an absolute range rate less than this threshold are ignored. As a

consequence, also real objects moving perpendicular to the line of sight vector are eliminated. Further, the detection probability depends on the ratio between range rate $\dot{r}$ and MDV [12,15].

$$P_D = P_d\left(1 - e^{-(1/2)(\dot{r}/v_{\mathrm{MDV}})^2}\right) \tag{12.3}$$

P_d stands for the maximum probability of detection.

Pulse compression is a radar processing method to combine long detection range and fine resolution, especially if individuals are observed. But pulse compression has also a potential side effect, because it can cause an inner blind zone, which is absolutely unwanted in ground surveillance.

Further, advanced constant false alarm techniques helps to handle heterogeneous clutter that is also a characteristic phenomenon in ground surveillance [8,14].

Finally, to take full benefit out of modern array antennas space time adaptive processing (STAP) [16–18] is important. Ground object tracking with STAP radars is addressed in [19].

12.2.2.3 GMTI radar standard

There is a dedicated standard agreement for an optimal provision of GMTI related information to the surveillance system, see [20].

This takes care of modern radars which can execute multiple tasks – so-called jobs – quasi-simultaneously.

Radar plots are sorted into continuous revisits, and within a revisit they are arranged into so-called dwells (Figure 12.1). Hence, the tracking system is aware of the scanning behaviour of the radar and can also conclude when an object is not detected within a revisit.

Often the sensor only measures range, azimuth and Doppler and internally uses projections onto the earth surface to deliver a three-dimensional spatial plot. Therefore, the GMTI sensor also provides the reference of the used geoid and elevation model. This is necessary, because the GMTI standard delivers the position information in latitude, longitude and possible altitude and not the raw measurements. Also sensor performance data can be submitted, e.g. detection probability, false alarm probability, range rate ambiguity (blind speed) and the accuracies for the sensor measurements, i.e. range, cross-range and range rate. These are pre-requisites for the tracking capability. In addition, the GMTI standard supports HRR, such that plots can also get a reference to dedicated HRR measurements.

On the other side, the standard also provides means, to control the radar in its sensing.

However, much of these parameters are optional and it is a high effort to build surveillance systems that are able to handle all the possible combinations.

Also for the other radar aspects like the resulting tracks based on GMTI measurements [21] and for SAR [22] dedicated standardizations are available.

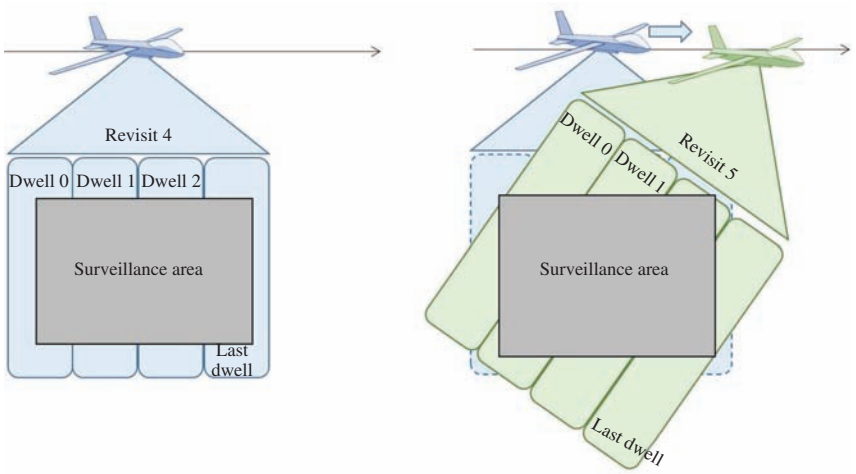

Figure 12.1 GMTI standard: The figure shows two revisits [l] and [r]. Revisits are composed out of dwells, which contains the plots. These dwells are enumerated within a revisit. The last dwell carries a marker (last dwell flag) that the revisit is finished. Also empty dwells are allowed to indicate missed plots (negative information)

12.3 Co-ordinate systems for ground surveillance

Different co-ordinate systems are used to represent the position and velocity of the monitored objects, radar platforms and radar measurements in ground surveillance.

12.3.1 WGS 84 ellipsoid

Concerning long range surveillance where the sensor has to keep a stand-off distance to the surveillance area, the curvature of the earth has to be taken into account. This is done by the approximation of the earth surface by an ellipsoid, which leads to the WGS 84 system [23]. The WGS 84 ellipsoid is defined by the semi-major and semi-minor axes:

$$\text{semi-major axis (equatorial axis):}\ \ a = 6378137\,\text{m}$$

$$\text{semi-minor axis (polar axis):}\ \ b = 6356752.3142\,\text{m}$$

$$\text{flattening:}\ f = \frac{1}{298.257223563}$$

$$\text{eccentricity:}\ \ \varepsilon = \sqrt{\frac{a^2 - b^2}{a^2}} = \sqrt{6.69437999014 \cdot 10^{-3}}$$

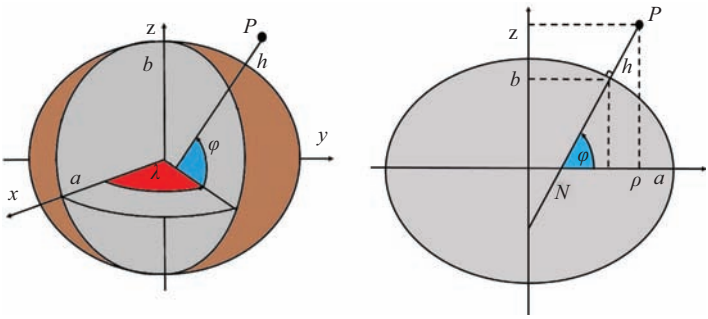

Figure 12.2 WGS 84 co-ordinate system. The figures show the definitions of WGS 84 co-ordinates: a, b are the semi-axes, X, Y, Z are the Cartesian earth centric earth fixed (ECEF) co-ordinates, ϕ, λ, h are latitude, longitude and altitude

12.3.2 Object co-ordinate systems – WGS 84 and ECEF

A spatial point is defined in WGS 84 by geodetic latitude ϕ, longitude λ and altitude h.

The ECEF co-ordinate system assigns three Cartesian positions to a point, written as X, Y, Z. Z is in the direction of the rotation axis of the earth and points to north, whereas X and Y spans the equatorial plane, such that X directs to the 0-longitude half circle. Given latitude, longitude and altitude, the computation of the transformation $T_{XYZ\leftarrow\phi\lambda h}$ and its derivative $DT_{XYZ\leftarrow\phi\lambda h}$ is straightforward:

$$\begin{pmatrix} X \\ Y \\ Z \end{pmatrix} = \begin{pmatrix} (N(\phi)+h)\cos\lambda\cos\phi \\ (N(\phi)+h)\sin\lambda\cos\phi \\ (N(\phi)(1.0-\varepsilon^2)+h)\sin\phi \end{pmatrix} \tag{12.4}$$

$$\begin{pmatrix} \dot{X} \\ \dot{Y} \\ \dot{Z} \end{pmatrix} = \begin{pmatrix} -N_1\cos\lambda\sin\phi & -N_2\cos\phi\sin\lambda & \cos\phi\cos\lambda \\ -N_1\sin\phi\sin\lambda & N_2\cos\phi\cos\lambda & \cos\phi\sin\lambda \\ N_1\cos\phi & 0 & \sin\phi \end{pmatrix} \begin{pmatrix} \dot{\phi} \\ \dot{\lambda} \\ \dot{h} \end{pmatrix} \tag{12.5}$$

with the following abbreviation:

$$N(\phi) = \frac{a}{\sqrt{1-\varepsilon^2\sin^2\phi}} \tag{12.6}$$

$$N_1(\phi) = \frac{1-\varepsilon^2}{a^2}N(\phi)^3 + h \tag{12.7}$$

$$N_2(\phi) = N(\phi) + h \tag{12.8}$$

The inverse transformation $T_{\phi\lambda h\leftarrow XYZ}$ from ECEF to WGS 84 is more difficult since no explicit formula exists. An iterative algorithm has to be used. Here, Fukushima's fast implementation of Bowring's formula is presented [24]. This

method delivers sufficiently accurate results after the first iteration for positions on the Earth surface:

First the iteration is initialized for $i = 0$ by:

$$\lambda = \arctan\frac{Y}{X} \tag{12.9}$$

$$c = a\varepsilon^2, \quad e' = \sqrt{1-\varepsilon^2}, \quad Z' = e'Z \tag{12.10}$$

$$T_0 = \frac{Z}{e'p} \tag{12.11}$$

The iterative step from $i \mapsto i+1$ is as follows:

$$C = \frac{1}{\sqrt{1+T_{i-1}^2}}, \quad S = CT_{i-1} \tag{12.12}$$

$$T_i = \frac{Z' + cS^3}{p - cC^3} \tag{12.13}$$

$$\phi = \arctan\frac{T_i}{e'} \tag{12.14}$$

$$h = \begin{cases} \dfrac{\sqrt{(1-\varepsilon^2)+T_i^2}}{e'}\left(p - \dfrac{a}{\sqrt{1+T_i^2}}\right) & \text{if } p > z \\ \sqrt{(1-\varepsilon^2)+T_i^2}\left(\dfrac{Z}{T_i} - \dfrac{b}{\sqrt{1+T_i^2}}\right) & \text{if } p \le z \end{cases} \tag{12.15}$$

For other methods see [25,26]. The derivative $DT_{\phi\lambda h \leftarrow XYZ}$ is best calculated by $DT_{XYZ \leftarrow \phi\lambda h}$ taking into account the chain rule.

12.3.3 Platform-centric system – ENU

The radar platform system is the east-north-up system (ENU), where the east and north direction generates the tangential plane to the WGS 84 ellipsoid and the third axis points skywards. The transformation $T_{XYZ \leftarrow \phi\lambda h}$ of ECEF to ENU co-ordinates relative to a position $(X_0 \quad Y_0 \quad Z_0)^T$ are given by:

$$\begin{pmatrix} x \\ y \\ z \end{pmatrix} = \begin{pmatrix} -\sin\lambda & \cos\lambda & 0 \\ -\sin\phi\cos\lambda & -\sin\phi\sin\lambda & \cos\phi \\ \cos\phi\cos\lambda & \cos\phi\sin\lambda & \sin\phi \end{pmatrix} \begin{pmatrix} X - X_0 \\ Y - Y_0 \\ Z - Z_0 \end{pmatrix} \tag{12.16}$$

The backward transformation from ENU to ECEF is given by:

$$\begin{pmatrix} X \\ Y \\ Z \end{pmatrix} = \begin{pmatrix} -\sin\lambda & -\sin\phi\cos\lambda & \cos\phi\cos\lambda \\ \cos\lambda & -\sin\phi\sin\lambda & \cos\phi\sin\lambda \\ 0 & \cos\phi & \sin\phi \end{pmatrix} \begin{pmatrix} x \\ y \\ z \end{pmatrix} + \begin{pmatrix} X_0 \\ Y_0 \\ Z_0 \end{pmatrix} \tag{12.17}$$

12.3.4 Sensor co-ordinate system – range, azimuth and Doppler

Finally, the co-ordinate system of the radar measurement is given by range r, azimuth ψ and range rate $\dot{r}$. For completeness, we also mention elevation ε. So $T_{r\psi\varepsilon\dot{r}\leftarrow xyz}$, respectively, $DT_{r\psi\varepsilon\leftarrow xyz}$ at a point (x, y, z) are given by:

$$\begin{pmatrix} r \\ \psi \\ \varepsilon \\ \dot{r} \end{pmatrix} = \begin{pmatrix} \sqrt{x^2+y^2+z^2} \\ \arctan\dfrac{y}{x} \\ \arcsin\dfrac{z}{\sqrt{x^2+y^2+z^2}} \\ \dfrac{xv_x+yv_y+zv_z}{\sqrt{x^2+y^2+z^2}} \end{pmatrix} \tag{12.18}$$

$$\begin{pmatrix} \dot{r} \\ \dot{\psi} \\ \dot{\varepsilon} \end{pmatrix} = \begin{pmatrix} \dfrac{x}{r} & \dfrac{y}{r} & \dfrac{z}{r} \\ \dfrac{y}{x^2+y^2} & -\dfrac{x}{x^2+y^2} & 0 \\ \dfrac{xz}{r^2\sqrt{x^2+y^2}} & \dfrac{yz}{r^2\sqrt{x^2+y^2}} & -\dfrac{\sqrt{x^2+y^2}}{r^2} \end{pmatrix} \begin{pmatrix} \dot{x} \\ \dot{y} \\ \dot{z} \end{pmatrix} \tag{12.19}$$

The backward direction $T_{xyz\leftarrow r\psi\varepsilon}$, respectively, $DT_{xyz\leftarrow r\psi\varepsilon}$ from ENU to the sensor measurement system is given by:

$$\begin{pmatrix} x \\ y \\ z \end{pmatrix} = \begin{pmatrix} r\sin\psi\cos\varepsilon \\ r\cos\psi\cos\varepsilon \\ r\sin\varepsilon \end{pmatrix} \tag{12.20}$$

$$\begin{pmatrix} \dot{x} \\ \dot{y} \\ \dot{z} \end{pmatrix} = \begin{pmatrix} \sin\psi\cos\varepsilon & r\cos\psi\cos\varepsilon & -r\sin\psi\sin\varepsilon \\ \cos\psi\cos\varepsilon & -r\sin\psi\cos\varepsilon & -r\cos\psi\sin\varepsilon \\ \sin\varepsilon & 0 & \cos\varepsilon \end{pmatrix} \begin{pmatrix} \dot{r} \\ \dot{\psi} \\ \dot{\varepsilon} \end{pmatrix} \tag{12.21}$$

12.4 Environment models

As mentioned before, environment data are of central interest for ground surveillance. In the following, road maps and digital elevation models are briefly considered.

12.4.1 Road maps

There exist a large variety of different file formats to store road maps as so-called vector data. Several open source libraries are available to handle all these file formats. Widely used in the C++ world is Open GIS Simple Features Reference Implementation which is part of the open source Geospatial Data Abstraction

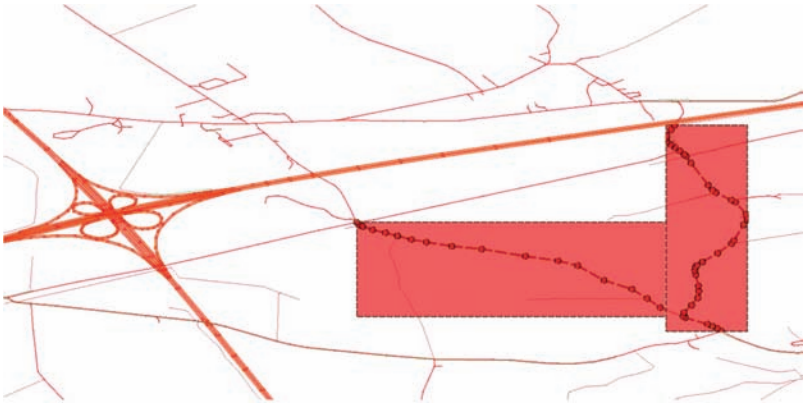

Figure 12.3 Road map information

Library [27–29]. Digital roads are typically represented by polygons. The nodes of these polygons are given by their latitude and longitude co-ordinates. Further, each road is modified by a unique key, a surrounding bounding box and possible additional tags, like speed limit, type of road, name of road, etc. Unfortunately, there is no common standard concerning these tags so that they are difficult to incorporate due to compatibility reasons. To use road map information, it is essential that these maps are highly efficient integrated in the surveillance system and a fast access is guaranteed [30].

The following nomenclature is used (see Figure 12.3):

$$\{p_j^i, j = 0, \ldots\} = \text{the nodes of the road } R^i \tag{12.22}$$

$$R_j^i = \text{the road segment spanned by } p_j^i \text{ and } p_{j+1}^i \tag{12.23}$$

$$n_j^i = \text{normal to } R_j^i \tag{12.24}$$

For the projection of a radar plot to a road segment its covariance Q has to be considered, see Figure 12.4. It defines the pullback metric given by the quadratic form (see [31] or [32]):

$$W = DT_{r\psi \leftarrow \phi\lambda}(\phi, \lambda) Q^{-1} DT_{r\psi \leftarrow \phi\lambda}(\phi, \lambda)^T \tag{12.25}$$

The plumb point to the road segment R_j^i with normal n_j^i and distance d_j^i is given by:

$$Pr_j^i p = p - W^{-1} n (n^T W^{-1} n)^{-1} (n^T p - d_j^i) \tag{12.26}$$

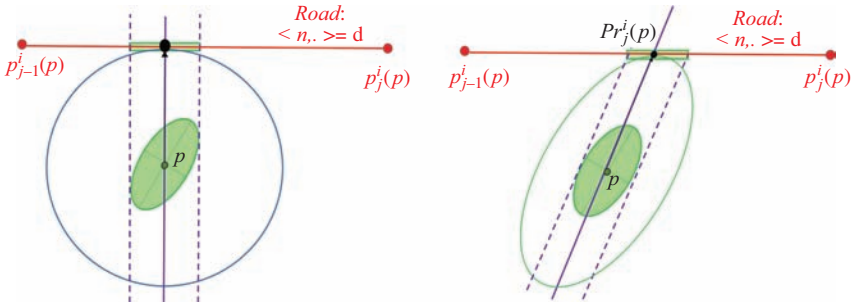

Figure 12.4 Orthogonal vs. probabilistic projection

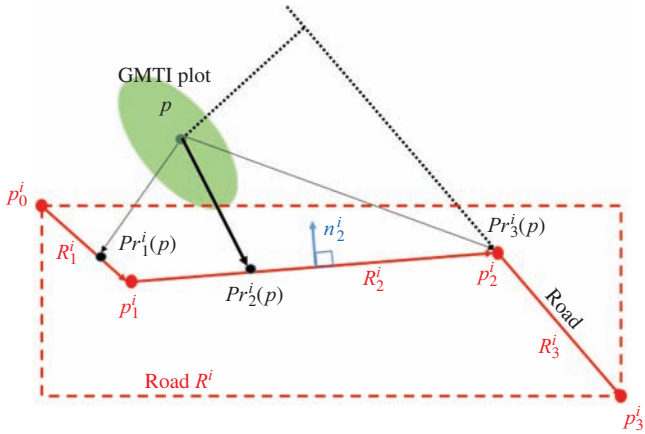

Figure 12.5 Projection of radar plots to road map

and its derivative by:

$$DPr^i_j(p) = \mathbb{I} - W^{-1}n(n^T W^{-1} n)^{-1} n^T \tag{12.27}$$

If the projection ends outside of the road segment, the nearest corner point has to be taken instead (see Figure 12.5). The final projection point is the one with the minimal distance over all available road segments, i.e.

$$Pr(p) = \text{argmin}_{Pr^i} \parallel p - Pr^i(p) \parallel \tag{12.28}$$

$$Pr^i(p) = \text{argmin}_{Pr^i_j} \parallel p - Pr^i_j(p) \parallel \tag{12.29}$$

12.4.2 Digital elevation models

Whenever no sufficient altitude is directly measured by the GMTI radar, the completion of two-dimensional localizations to spatial plots can be realized by the

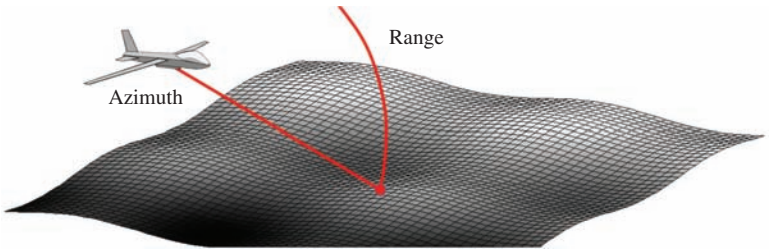

Figure 12.6 Projection onto DEM for radar plots

projection onto suited elevation models. Often coarse assumptions are taken like a fixed plane of constant altitude in the area of interest. More accurate are digital elevation models. The Digital Terrain Elevation Data (DTED) is represented by the elevation values of a rectangular grid. DTED level 2 has a latitude spacing of 1 arcs and a longitude spacing from 1 arcs at the equator to 6 arcs at the poles. This corresponds to approximately 30 m [33]. A whole amount of DEM data was captured during the Shuttle Radar Topography Mission in 2000 [34]. Today, WorldDEM^{TM} is an extremely accurate DEM model, which offers 2 m (relative), respectively, 4 m (absolute) vertical accuracy in a 12 × 12 m raster [35].

In the following, it is assumed that

$$\alpha(\varphi, \lambda) \tag{12.30}$$

is an elevation model which maps a latitude φ and longitude λ to their corresponding altitude value.

A GMTI plot – given by range r and azimuth ψ – can be projected to the earth surface by intersecting the circle defined by the measured range and directed along the measured azimuth with the chosen elevation model, as shown in Figure 12.6. The resulting planar position in latitude and longitude is denoted by

$$Pr_{\mathrm{DEM}}(r, \psi) = \text{Projected position in latitude and longitude} \tag{12.31}$$

12.5 Tracking in ground surveillance

In general, tracking has to perform two tasks:

- data association and
- filtering.

Data Association is responsible for establishing the correct plot track relation in multi-object scenarios.

There are several algorithms addressing the data association problem. An overview can be found in [36–41]. A classical approach is the multi-hypothesis tracking or the multi-dimensional data association. Special GMTI aspects can be found in [42–44]. Other approaches include two-dimensional data association like the

so-called Munkres [45], Auction [46], or Jonker-Volgenant-Castanon [47] algorithm. An opposite approach tries to avoid the data association at all and uses methods based on random sets. Very popular are the Gaussian mixture versions of the Probabilistic Hypothesis Density Filter and the Cardinalised Probabilistic Hypothesis Density Filter, see [41,44,48,49]. To support these advanced association methods, a complete implementation of the available GMTI standard [20] is essential, as discussed in Section 12.2.2.3.

Filtering realizes the state estimation of an existing track whenever a new plot arrives. It splits into a prediction and an assimilation (or update) step. Prediction extrapolates a track to the time of an actual radar plot, whereas the assimilation estimates the new track state based on the plot information and the previously predicted state. Multiple-filters exist. The most famous is the Kalman filter and its non-linear generalization, the extended Kalman filter. Other generalizations are the Unscented Kalman filter (UKF) and the whole class of particle filters [36–40,50].

In ground surveillance, the track states have to fulfil additional constraints. The tracks move on the surface of the earth and usually follow roads. These constraints are modelled by road maps and elevation models. The incorporation of these models leads to road-assisted or terrain-assisted tracking. Assisted tracking is an option to improve the track accuracy and continuity. Three alternatives to integrate state space constraints into filtering can be identified:

- Projection: The first one is the projection approach. This performs prediction with an adequate prediction model and afterwards the assimilation. The problem is that the state does not necessarily fulfil the environment constraints. A projection is necessary to get the track back into the constrained state space, i.e. this part of the state space which fulfils the constraints.
- Parameterization: The alternative approach is to choose a parameterization of the constrained state space and perform the tracking within the parameterization space. Once the plot is projected to the constrained state space to initialize the track, no further projection is necessary.
- Particle filter: A third alternative is the usage of particle filters. Therefore, the constraints are implemented into the particle prediction model.

Filters for ground surveillance which follows the first and second approach using Gaussian mixtures can be found in [51–54]. A UKF is proposed in [55,56]. Particle filters are suggested e.g. by [57,58]. Unfortunately, particle filters induce high computational load so that these filters may still not be feasible for real-time processing of extended multi-object scenarios.

A very important aspects in tracking with GMTI plots is the handling of blind zones [43,48,49,52–54]. In [19] also, the aspect of STAP is analysed, and in [12], the consequences of range and Doppler ambiguities.

Here, the second approach is used. The prediction of the object is given by a local parameterization $\gamma(s)$ of the road map, centred at the last known position, which assigns to each parameter s a path on the road map given by latitude and longitude. To add the altitude information, a digital elevation model is given, which assigns to each pair of latitude and longitude the corresponding altitude $\alpha(\phi, \lambda)$.

Afterwards, the resulting point can be mapped as predicted plot into the platform system and finally into the measurement space of the radar to perform the assimilation step. Figure 12.7 summarizes the concepts. In the following sub-sections, a filter algorithm for unassisted and road-assisted tracking is described.

12.5.1 Filtering with GMTI measurements

In the following, the filtering with GMTI plots is explained based on an Unscented Kalman filter [50,59–61]. The UKF uses the Unscented transformation (see Figure 12.8).

The Unscented transformation is a sampling method to approximate the image of a covariance under a non-linear function. Therefore, the shape of a covariance is

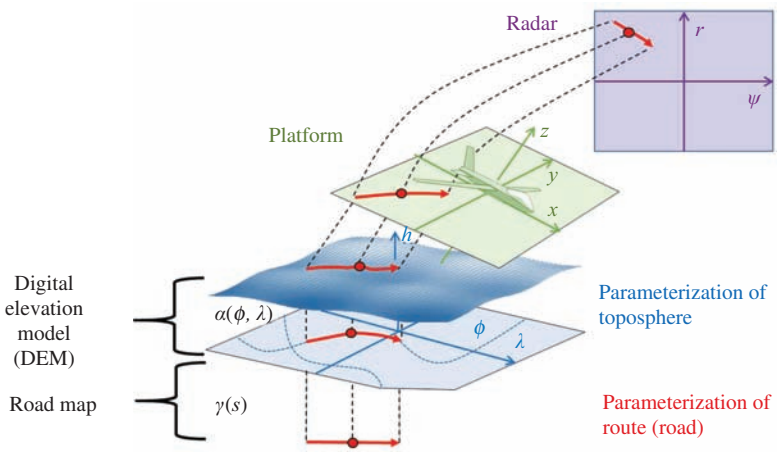

Figure 12.7 Radar tracking with digital elevation model and road maps. The figure shows all relevant models, spaces and transformations

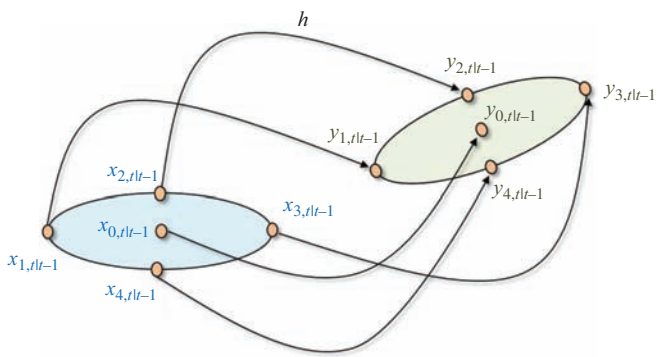

Figure 12.8 Unscented Transformation of covariance

described by so-called sigma points. These sigma points are transformed by the given function and afterwards determine the shape of the transformed covariance. For the generation of these sigma points, a Cholesky decomposition is applied.

The UKF allows a comfortable and flexible integration of roads and elevation models into the filter. Further, it is also suited, when we have to deal with the non-linearity caused by the Doppler (range rate) measurement.

12.5.1.1 State and measurement equation

Filtering is the solution of a problem defined by two equations. The first one is the prediction equation for an object state x_{t-1} at the time $t-1$.

$$x_t = Fx_{t-1} + r_t \tag{12.32}$$

F describes the prediction of the object. It is given by:

$$F = \begin{pmatrix} 1 & dt \\ 0 & 1 \end{pmatrix} \quad \text{respectively by} \quad F = \begin{pmatrix} 1 & 0 & dt & 0 \\ 0 & 1 & 0 & dt \\ 0 & 0 & 1 & 0 \\ 0 & 0 & 0 & 1 \end{pmatrix} \tag{12.33}$$

for a two-dimensional respectively four-dimensional track state. r_t is a Gaussian process noise with covariance R_t. A radar plot y_t relates with a track state through the measurement equation:

$$y_t = h(x_t) + q_t \tag{12.34}$$

h is the transformation from the track state to the measurement space. q_t is the measurement noise given by a Gaussian distribution with covariance Q_t:

$$Q_t = \begin{pmatrix} \sigma_r^2 & 0 & 0 \\ 0 & \sigma_\psi^2 & 0 \\ 0 & 0 & \sigma_{\dot{r}}^2 \end{pmatrix} \tag{12.35}$$

12.5.1.2 Parametrisation of the unscented transformation

To start the UKF filter the Unscented transformation has to be parametrized [59,60]. This means the spread of the sigma points and the weighting of the central sigma point compared to those on the boundary has to be defined, see Table 12.1.

Table 12.1 Unscented Transformation – Parametrisation

Parameter	Setting	Recommended range	Significance
α	1	$1 \leq \alpha \leq 10^{-4}$	Spread of sigma points
β	2		Prior knowledge of distribution $\beta = 2$ is optimal for Gaussian
κ	0	$\kappa \in \{0, 3 - L\}$	Secondary-scaling parameter

Further the following derived parameters are used:

$$\lambda = \alpha^2(L + \kappa) - L \tag{12.36}$$

$$\gamma = \sqrt{L + \lambda} \tag{12.37}$$

12.5.1.3 Initialization

The Unscented Kalman filter starts with an initial state and covariance:

$$x_0 = E[x] \tag{12.38}$$

$$P_0 = E[(x - x_0)(x - x_0)^T] \tag{12.39}$$

12.5.1.4 Prediction

Assuming that the state x_{t-1} and covariance P_{t-1} are known for iteration $t - 1$, the prediction steps calculate the sigma points and their weights through a Cholesky decomposition:

$$\mathcal{X}_{t-1,0} = x_{t-1} \tag{12.40}$$

$$\mathcal{X}_{t-1,i} = x_{t-1} + \gamma(\sqrt{P_{t-1}})_i, \quad i = 1, \ldots, L \tag{12.41}$$

$$\mathcal{X}_{t-1,i} = x_{t-1} - \gamma(\sqrt{P_{t-1}})_{i-L}, \quad i = L + 1, \ldots, 2L \tag{12.42}$$

The sigma points are transformed by an Unscented transformation and the predicted state and its covariance are calculated for iteration number t (based on iteration $t - 1$):

$$\mathcal{X}_{t|t-1,i} = f(\mathcal{X}_{t-1,i}), \quad i = 0, \ldots, 2L \tag{12.43}$$

$$x_{t|t-1} = \sum_{i=0}^{2L} \omega_i^{(m)} \mathcal{X}_{t|t-1,i} \tag{12.44}$$

$$P_{t|t-1} = \sum_{i=0}^{2L} \omega_i^{(c)} (\mathcal{X}_{t|t-1,i} - x_{t|t-1})(\mathcal{X}_{t|t-1,i} - x_{t|t-1})^T + R_t \tag{12.45}$$

The weights to build the predicted state and covariance are given by:

$$\omega_0^{(m)} = \frac{\lambda}{L + \lambda} \tag{12.46}$$

$$\omega_0^{(c)} = \frac{\lambda}{L + \lambda} + 1 - \alpha^2 + \beta \tag{12.47}$$

$$\omega_i^{(m)} = \omega_i^{(c)} = \frac{1}{2}\frac{1}{L + \lambda}, \quad i = 1, \ldots, 2L \tag{12.48}$$

12.5.1.5 Assimilation

For the assimilation step the predicted state is mapped into the measurement space. Therefore, the sigma point are generated first through:

$$\mathcal{X}'_{t|t-1,0} = x_{t|t-1} \tag{12.49}$$

$$\mathcal{X}'_{t|t-1,i} = x_{t|t-1} + \gamma(\sqrt{P_{t|t-1}})_i, \quad i = 1, \ldots, L \tag{12.50}$$

$$\mathcal{X}'_{t|t-1,i} = x_{t|t-1} - \gamma(\sqrt{P_{t|t-1}})_{i-L}, \quad i = L+1, \ldots, 2L \tag{12.51}$$

and afterwards are mapped into the measurement space:

$$\mathcal{Y}_{t|t-1,i} = h(\mathcal{X}'_{t|t-1,i}), \quad i = 0, \ldots, 2L \tag{12.52}$$

Then, the predicted measurement and the associated covariance are calculated:

$$y_{t|t-1} = \sum_{i=0}^{2L} \omega_i^{(m)} \mathcal{Y}_{t|t-1,i} \tag{12.53}$$

$$P_{yy,t|t-1} = \sum_{i=0}^{2L} \omega_i^{(c)} (\mathcal{Y}_{t|t-1,i} - y_{t|t-1})(\mathcal{Y}_{t|t-1,i} - y_{t|t-1})^T + Q_t \tag{12.54}$$

Finally, the Kalman gain and the state and covariance update is given by:

$$P_{xy,t|t-1} = \sum_{i=0}^{2L} \omega_i^{(c)} (\mathcal{X}_{i,t|t-1} - x_{t|t-1})(\mathcal{Y}_{i,t|t-1} - y_{t|t-1})^T \tag{12.55}$$

$$K = P_{xy} P_{yy}^{-1} \tag{12.56}$$

$$x_t = x_{t|t-1} + K(y_t - y_{t|t-1}) \tag{12.57}$$

$$P_t = P_{t|t-1} + K P_{yy} K^T \tag{12.58}$$

Next, the Unscented Kalman filter is applied to unassisted and assisted tracking.

12.5.1.6 Unassisted tracking

The state vector is given in planar WGS 84 co-ordinates and the corresponding angular velocities:

$$x_t = \begin{pmatrix} \phi_t & \lambda_t & \dot{\phi}_t & \dot{\lambda}_t \end{pmatrix}^T \tag{12.59}$$

The process noise is derived from a Gaussian distributed acceleration in λ and ϕ with covariance matrix $\begin{pmatrix} \sigma_{\phi\phi}^2 & \sigma_{\phi\lambda}^2 \\ \sigma_{\phi\lambda}^2 & \sigma_{\lambda}^2 \end{pmatrix}$, i.e.

$$R_t = G^T \begin{pmatrix} \sigma_{\phi\phi}^2 & \sigma_{\phi\lambda}^2 \\ \sigma_{\phi\lambda}^2 & \sigma_{\lambda}^2 \end{pmatrix} G \quad \text{and} \quad G = \begin{pmatrix} \frac{1}{2}dt^2 & 0 & dt & 0 \\ 0 & \frac{1}{2}dt^2 & 0 & dt \end{pmatrix} \tag{12.60}$$

To initialize the filter a GMTI plot is mapped onto a two-dimensional state vector, as explained before in (12.31). This delivers x_0 and P_0.

The projection h used in the filter is given through the co-ordinate transformation discussed in Section 12.3. It assigns to each state variable the co-ordinates in the measurement space given by range, azimuth and range rate:

$$h(\phi,\lambda,\dot{\phi},\dot{\lambda}) = (r(\phi,\lambda,\dot{\phi},\dot{\lambda}),\psi(\phi,\lambda,\dot{\phi},\dot{\lambda}),\dot{r}(\phi,\lambda,\dot{\phi},\dot{\lambda}))^T \tag{12.61}$$

12.5.1.7 Road-assisted tracking

The road-assisted tracking depends on a parametrisation of a possible route of the object, given by $\gamma(s)$. Hence, a two-dimensional state space is used given by the arc length s of the route:

$$x_t = (s_t \quad \dot{s}_t) \tag{12.62}$$

The process noise is directed along the road. It is derived from a Gaussian-distributed acceleration in s with covariance σ_s^2:

$$R_t = G^T(\sigma_s^2)G \quad \text{and} \quad G = \left(\frac{1}{2}dt^2 \quad dt\right) \tag{12.63}$$

To initialize the filter, a GMTI plot is mapped onto the elevation model of the earth and afterwards onto a road. A possible route $\gamma(s)$ is selected centred in this position.

Finally, the projection h used in the filter is given through the co-ordinate transformation, discussed in Section 12.3. It assigns to each position along the selected route $\gamma(s)$, the co-ordinates in the measurement space given by range, azimuth and range rate (see Figure 12.7)

$$h(s,\dot{s}) = (r(s,\dot{s}),\psi(s,\dot{s}),\dot{r}(s,\dot{s}))^T \tag{12.64}$$

So far, the filtering for a given route parameterization was described. What makes the situation more complex is that the object can turn at each junction to continue along another road, see Figure 12.9. These different routes are incorporated via a multiple model [62,63], i.e. the filter calculates several possible routes in parallel together with their likelihoods:

$$\Lambda^{\gamma_i} = \frac{1}{\sqrt{\det(2\pi P^{(\gamma_i)}_{yy,t|t-1})}} e^{-\frac{1}{2}(y^{(\gamma_i)}_{t|t-1}-y)^T (P^{(\gamma_i)}_{yy,t|t-1})^{-1}(y^{(\gamma_i)}_{t|t-1}-y)} \tag{12.65}$$

The upper index γ_i symbolizes the dependency of the chosen route γ_i. This is used to maintain a multiple model.

Further, it is possible to use the Doppler notch information, such that also missed detections are used to prefer routes which are in the notch as proposed in [12,57,64]. This can also be applied to other types of blind zones (e.g. terrain masking). Therefore, it is important, that a GMTI radar delivers not only plots but also hints about missed detections, as intended in the GMTI standard [20].

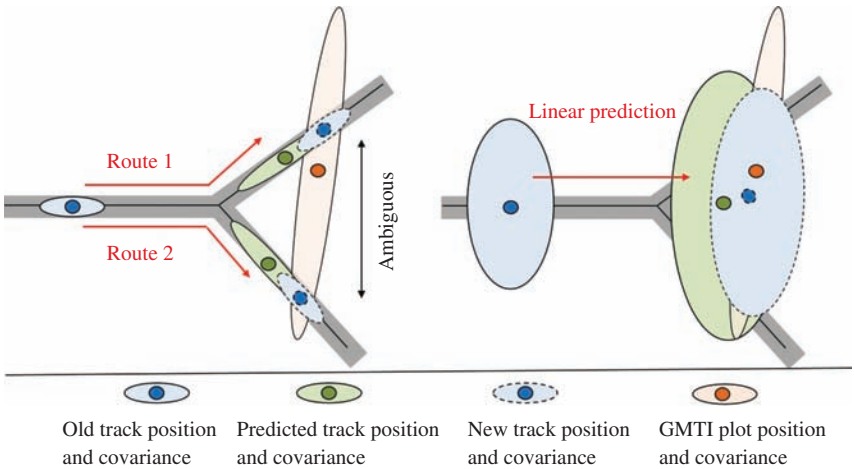

Figure 12.9 Road-assisted vs. non-assisted tracking: Road-assisted tracking keeps the error ellipses small by using the road constraint (in fact they are one dimensional). Therefore, the accuracy is improved and objects could also be better separated in the data association step. For the road-assisted tracking, all possible routes an object can take have to be considered

Figure 12.10 shows the result of assisted tracking. On the left side, GMTI plots are shown. It is easy to see how they deviate from the infrastructure. The right side shows the result of a road-assisted tracking together with the covariances of the assigned plots.

12.6 Further topics in radar tracking

12.6.1 On–off road tracking

The proposed concept can be extended to deal with on–off road tracking. Therefore, it is estimated whether an object leaves a road or enters a road. A multiple model is used to realize these model transfers.

Another realization using particle filters can be found in [57]. A different method using a VS-IMM is discussed in [64].

Figure 12.11 shows the result of automatic on-off road tracking based on simulation. Note the size of the covariance when the object is on or off road.

12.6.2 Tracking with multiple platforms

The use of multiple GMTI radar platforms is a significant measure to improve the accuracy and completeness of the tracking. In airborne ground surveillance, this can be realized by co-operating UAVs. In coastal or border surveillance, often a grid of dislocated radar towers or sensor vehicles is installed. The main goal is to

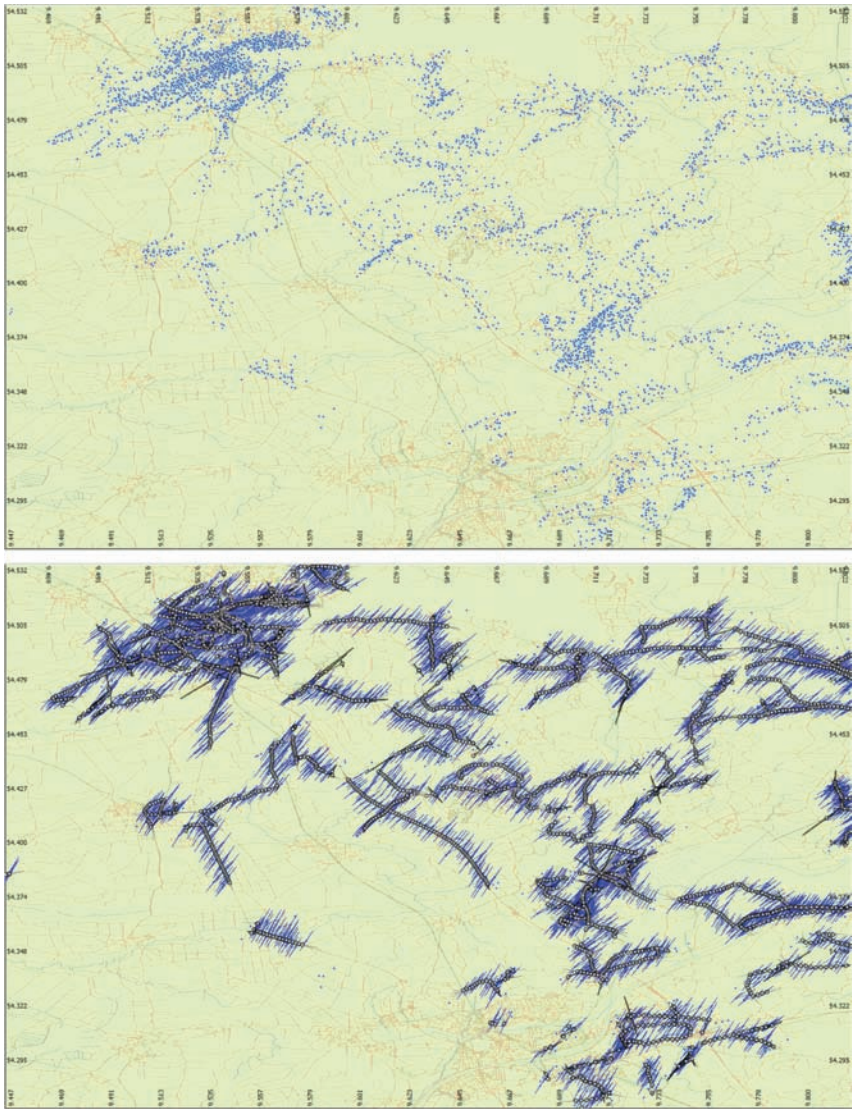

Figure 12.10 Road-assisted tracking: [l] raw data, [r] road-assisted tracking

improve the cross-range accuracy of the radar system by intersecting two more or less perpendicular ellipsoids. A further advantage is the avoidance of terrain masking and Doppler blind zones.

But using dislocated platforms increases the risk of out-of-sequence measurements (oosm). This may be caused by different delay times within the (radio) network or by delays in the radar processing itself. Therefore, techniques have to be applied to update also with oosm, especially to predict backwards in time for

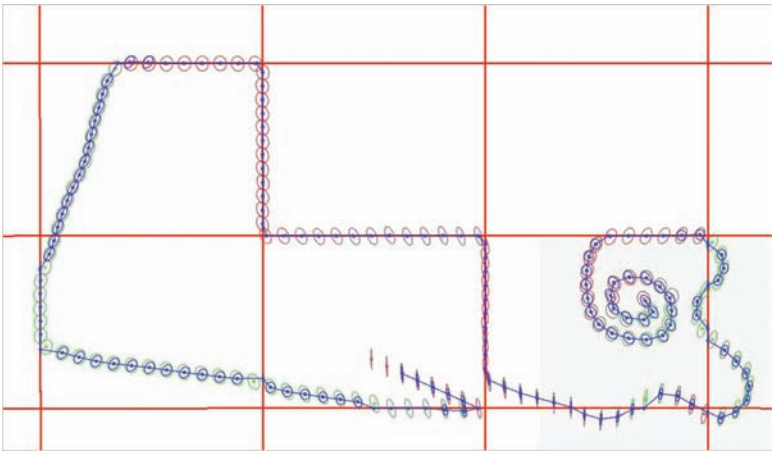

Figure 12.11 On–off road tracking: The red lines define the roads. The colour of the ellipses symbolize the different range rates

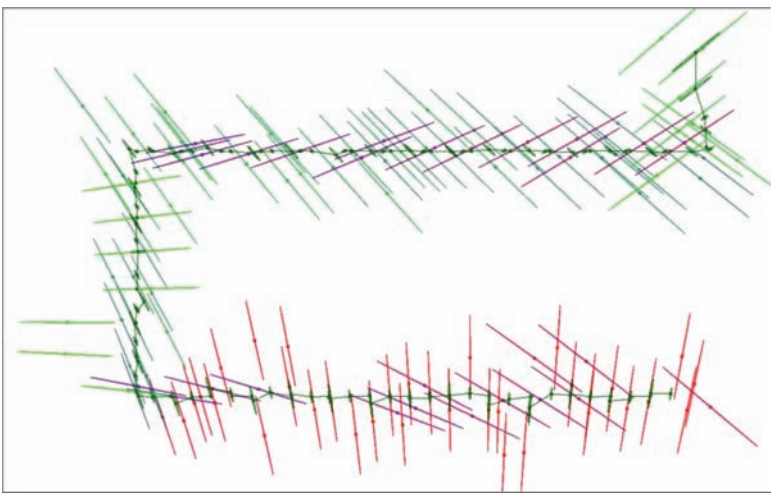

Figure 12.12 Multiple radar tracking with out of sequence measurement: The figure shows the plots and covariances of the radar plots of two sensors. The green line shows the resulting track. Unassisted tracking was applied

unassisted and assisted tracking [40,56,65]. If oosm occur while road-assisted tracking is used, also the road map has to be taken into account for back-propagation. In these situations, the benefit of road-assisted tracking is limited, because the geometry already realizes an improvement of the plot accuracy.

Figure 12.12 shows a situation where two sensors are involved.

12.6.3 Group tracking

In ground surveillance, often the situation arises where multiple objects are spaced closely together and move in a co-ordinated manner. A classical example is the so-called convoy, where the succeeding vehicles move with a nearly constant distance and with a common velocity [44]. These convoys typically follow the infrastructure, which creates a one-dimensional chain. For maritime situations, a convoy can often be arranged around a common centre, resulting in a more two-dimensional shape.

Often, it is the task of a cluster algorithm to find out, which objects belong to a convoy or more general to a group.

Next, a tracking method for the extracted groups has to be selected. Therefore, several options are possible:

- Individual tracking: Each object is tracked individually, so that only an attribution with cluster affiliation is required.
- Extended object tracking: This approach does not try to track the individual members of a cluster separately. Instead, the whole group is considered as an extended object, which has to be tracked. Therefore, the group may be abstracted as an ellipsoid and its centre. More details may be found in [40,66–68].
- Tracking of co-ordinated objects: This technique tries to use the co-ordinated behaviour of the group members to improve their individual tracking. This approach can be found in e.g. [69].

On top of these aspects also road-assisted tracking may apply. Also, the first and the second possibility can be combined.

In addition, there are situations where several groups are involved within a scenario which can merge, split and pass. Also, this has to be taken into account – especially in the clustering. So the resulting situations can be quite complicated.

12.7 Information fusion and sensor management

12.7.1 Multi-sensor data fusion and sensor management

The localization information carried by a GMTI plot can be combined with other sensors, which are advantageous in complementary dimensions: While GMTI measures range, azimuth and range rate some transponder systems deliver a GPS position given by latitude, longitude and altitude. So-called interrogation friend foe (IFF) transponders are also able to deliver the barometric height for example within mode 3C. Passive optical or infrared sensors do not provide a range measurement but have very accurate azimuth and elevation measurements. So, there is potential to improve or at least complete the localization based on GMTI radar plots with other localization sources.

Complementary sensors measure attributes which may be of interest for situation awareness. It is not only the task to localize the objects within a scenario, objects have to be classified and identified. This means that the type and the

intention of an object have to be estimated. Information fusion and automated sensor management are necessary to obtain synergies out of a diverse, dislocated and networked sensor grid [11].

12.7.2 Traffic flow, areas, corridors and routes

The result of a tracker can be evaluated, to derive additional information. Traffic flow analysis is used to determine how intensively the parts of an infrastructure are frequented. It is possible to determine sinks and sources, i.e. areas where objects regularly appear and disappear, which is of strategic interest to determine points of concentrations. Group tracking delivers also merger and split points of groups which are of interest for the monitoring of on-going deployments [10,11].

Areas, which are known to be friendly or suspect can be used to support identification. If it is possible to backtrack the trajectory of an object to such an area, the object has most probably the same disposition. Also, it is possible to give some way points, which have to be passed by objects belonging to the same coalition.

Finally, it is possible to generate infrastructure information out of GMTI tracking, as addressed in [70].

12.7.3 Radar-based classification

SAR contributes to ground surveillance systems, especially if extended terrain should be observed or non-moving objects have to be detected which remain undiscovered by GMTI radar. Especially, objects which are observed in GMTI mode are candidates for a SAR acquisition if they stop. Similar sink and sources areas found by traffic flow analysis may be investigated within the SAR radar mode.

Further, the Doppler spectrum can be used to differentiate between object classes like wheeled or tracked vehicles, helicopters, planes or humans respectively animals as far as the relevant features are visible [71,72]. This applies especially for ground-based MTI radars used in security applications. Radar classification is possible during day and night and under poor weather conditions. So, the radar detection is possible when electro-optical sensors have to struggle with challenging environmental conditions.

12.7.4 Transponder systems

To enrich the situational ground picture the interaction with transponder systems is useful.

The secondary surveillance radar or the non-civilian IFF interrogates transponders, which are mainly installed on air platforms but also on several naval vessels. It measures range and azimuth to a transponder directly. The transponder of the object gives additional information. For instance, the so-called mode 3A/C code provides a squawk code and pressure altitude in 100-ft increments. Further ADS-B is a co-operative surveillance technology in which an aircraft determines its position via satellite navigation and provides its position to nearby aircraft or air traffic control.

The Automatic Identification System (AIS) is an automatic tracking system used on ships and by vessel traffic services for identifying and locating vessels. It contains the GPS position and further attributes about the object like its route, identity, name, task, etc. Other Blue force tracking systems deliver the position of own land based units based on GPS position and specific tags.

This information can be correlated with radar tracks to complete the localization, to determine the object environment and to add relevant attributes to the tracks.

12.7.5 Electro-optical and IR sensors

Optical sensors are used to detect, recognize and identify objects at day and night time. There are long-range daylight camera systems, infrared systems, laser scanners, light intensifiers and newest range gating vision systems. The latter one is also able to look through windows and read labels at night.

Unfortunately, optical sensors like infrared are more weather and environment dependent than radar sensors. Even if the objects are in the field of view of such a system, a sufficient temperature difference or contrast is needed [73,74]. Motion or atmospheric blur may hamper the detection of objects either visual by an operator or also by automatic systems (e.g. change detection) etc. Disadvantageous weather condition like sandstorm can stop detection at all. However, within complex multi-object situations optical sensors are essential for identification and final situation assessment.

Also for optical sensors software which detects (ATD) and recognizes (ATR) objects automatically is available [75]. ATD software that uses change detection techniques works best when the objects move perpendicular to the line of sight, which is also complementary to the radar behaviour. However, it is in general more difficult to eliminate the background, especially for moving sensor platforms or turning camera systems. Newer concepts propose compressive sensing technology for this purpose [76,77].

Detected objects are normally marked within a video, i.e. their pixel co-ordinates are determined. Knowing the direction of the camera systems and DEM model, their real world position can be estimated by ray tracing. DEM may also be essential to realize the required absolute alignment of a camera system with a high-zoom capability [78,79].

Best usability is ensured if optical sensors are combined with radar systems, such that the radar is used for volume search and the camera is used slaved to the radar. Within this constellation, very high zoom has to be used which results in a small field of view. This requires a very accurate alignment between camera, radar and the environment and an excellent radar tracker performance to control the camera movement.

12.7.6 Network-centric sources

In the network-centric environment, radar and additional data is shared between participating units – called the sensor and information grid in newer terminology.

Track data is exchanged by tactical data links like Link 16 or Link 22 via radio. So, the system correlates the external tracks with its own and sends out its internal track, whenever it has a higher track quality than the reporting unit i.e. the unit with the highest track quality for an object has the reporting responsibility for this individual track. These data links are still driven by limited data rates.

Newer track exchange standards that share more information have recently become available for ground surveillance [21]. So, higher data rates will enable distributed radar tracking with higher performance track–track fusion. This is a step forward into the direction of optimal track–track fusion as described in [80].

There are further standards to share GMTI plots, primary or secondary radar data, IFF, AIS and ESM. It is possible to distribute image and video information within ground surveillance systems and persisting the information in data bases – often called coalition shared database.

12.8 Conclusion

Radar is the most important sensor for ground surveillance systems due to its all-weather availability at day and night. Mounted on airborne platforms, it benefits additionally from an excellent line of sight and enables a continuous surveillance.

Its performance can be significantly increased by *a priori* information like road maps or digital elevation models. These can be integrated by radar tracking techniques or perhaps in the future also with compressive sensing technologies.

Optimal tracking has to take into account all the radar specifics. Very important for ground object tracking is the incorporation of the Doppler notch information to support e.g. track-continuity. Similar, other blind zones caused by terrain masking have to be considered.

A significant increase of the radar based ground surveillance can be realized by dislocated and co-operating platforms. These may be ground, airborne or satellite based platforms. So radar will profit from trends related to platform development, like autonomous UAVs or swarms of sensor platforms. Radar-based surveillance will establish synergies out of these developments. It will also increase the performance of the surveillance systems when wide band data links are available, which enables distributed tracking and advanced track-track fusion.

The high amount of radar data collected in ground-based surveillance leads to a big data problem, which must also be solved to be able to profit from the sensor capabilities. Radar related topics are group tracking within the radar trackers, identification of suspicious behaviour by identifying and tracking on and off road objects, traffic flow analysis, or other means. Also the fusion and automated sensor management between the available radar modes like GMTI, SAR, ISAR, HRR are methods to obtain situation awareness and leads inevitably to what is called cognitive radar.

Radar is the best suitable sensor to support the integration of other sensor types like infrared, range gated vision systems, daylight cameras, actual and future transponder systems in a network-centric approach. The optimal performance of

ground surveillance is established if the sensors are linked together using the tools which are provided by information fusion.

Acknowledgements

The author thanks his colleagues at Airbus Defence and Space for all the valuable suggestion and their excellent support, especially Elke Schmid, Kaeye Dästner and Bastian von Hassler zu Roseneckh-Köhler.

Further, he thanks the members of Fraunhofer-FKIE for all the inspiring discussions and the close collaboration during the last decade.

Abbreviations

ADS-B	Automatic-Dependent Surveillance Broadcast
AIS	Automatic Identification System
ATD	Automatic Target Detection
ATR	Automatic Target Recognition
CFAR	Constant False Alarm Rate
CPHD	Cardinalised PHD
DEM	Digital Elevation Model
DTED	Digital Terrain Elevation Data
ECEF	Earth Centric Earth Fixed
EKF	Extended Kalman Filter
ENU	East North Up
ESM	Electronic Support Measurement
GDAL	Geospatial Data Abstraction Library
GMTI	Ground Moving Target Indication
HALE	High-Altitude Long Endurance
HAPS	High-Altitude Platform Station
HPRF	High PRF
HRR	High-Range Resolution
IFF	Identification Fried Foe
ISAR	Inverse SAR
KF	Kalman Filter
LPRF	Low PRF
MALE	Medium-Altitude Long Endurance
MIT	Moving Target Indication
MPRF	Medium PRF
PHD	Probabilistic Hypothesis Density Filter
PRF	Pulse repetition frequency

SAR	Synthetic aperture radar
SSR	Secondary Surveillance Radar
STAP	Space time adaptive processing
UAV	Unmanned Aerial Vehicle
UKF	Unscented Kalman Filter
WGS 84	World Geodetic System 1984

References

[1] Austin R. *Unmanned Aircraft Systems: UAVS Design, Development and Deployment*. West Sussex, UK: John Wiley & Sons; 2010.

[2] Gierull C . H., Cerutti-Maori D., Ender J. 'Ground moving target indication with tandem satellite constellations'. *IEEE Geoscience and Remote Sensing Letters*. 2008; **5**(4): 710–714.

[3] Baumgartner S. V., Krieger G. 'Large along-track baseline SAR-GMTI: First results with the TerraSAR-X/TanDEM-X satellite constellation'. *IEEE International Geoscience and Remote Sensing Symposium*; Vancouver, Canada; 24–29 July 2011.

[4] Schaefer C., Wagner A. 'Analysis of potential GMTI performance of TanDEM-X'. *7th European Conference on Synthetic Aperture Radar*; Friedrichshafen, Germany; 2–5 June 2008.

[5] Williams H. 'Farnborough 2016: Airbus releases Zephyr T details, outlines CONOPS for systems'. 14 July 2016. Available from http://www.janes.com/article/62274/farnborough-2016-airbus-releases-zephyr-t-details-outlines-conops-for-systems.

[6] Skolnik M. I. *Introduction to Radar Systems*. Singapore: McGraw-Hill; 1980.

[7] Levanon N., Mozeson E. *Radar Signals*. Hoboken, NJ, USA: Wiley-Interscience; 2004.

[8] Richards M. A. *Fundamentals of Radar Signal Processing*. New York: McGraw-Hill; 2005.

[9] Moreira A., Prats-Iraola P., Younis M., Krieger G., Hajnsek I., Papathanassiou K.P. 'A Tutorial on Synthetic Aperture Radar'. *IEEE Geoscience and Remote Sensing Magazine (GRSM)*, 2003; **1**(1), *Institute of Electrical and Electronics Engineers (IEEE)*. pp. 6–43.

[10] Entzminger J. N., Fowler C. A., Kenneally W. J. 'Joint STARS and GMTI: Past, Present and Future', *IEEE Transactions on Aerospace and Electronic Systems*. 1999; **35**(2): 748–761.

[11] Opitz F., Dästner K., von Hassler zu Roseneckh-Köhler B. 'Situation assessment in airborne ground surveillance'. *Proceedings of the 16th International Radar Symposium*; Dresden, Germany, June 2015. pp. 351–356.

[12] Mertens M., Nickel N. 'GMTI tracking in the presence of Doppler and range ambiguities'. *Proceedings of the 14th International Conference on Information Fusion*; Chicago, Illinois, USA; 5–8 July 2011. pp. 1–8.

[13] Ender J., Kohlleppel R. 'Knowledge based ground moving target detection and tracking using sparse representation techniques'. *Proceedings of the International Radar Symposium*; Dresden, Germany; 24–26 Jun 2015.
[14] Ludloff A. K. *Praxiswissen Radar und Radarsignalverarbeitung*. Wiesbaden: Vieweg; 1998.
[15] Koch W. 'On negative information in tracking and sensor data fusion: Discussion of selected examples'. *Proceedings of the Seventh International Conference on Information Fusion*; Stockholm, Sweden; June 2004. pp. 91–98.
[16] Klemm R. *Principles of Space-Time Adaptive Processing*. London: Institution of Electrical Engineers (IEE); 2002.
[17] Klemm R. *Applications of Space-Time Adaptive Processing*. London: Institution of Electrical Engineers (IEE); 2004.
[18] Guerci J. R. *Space-Time Adaptive Processing for Radar*. Boston: Artech House; 2014.
[19] Koch W., Klemm R. 'Ground target tracking with STAP radar'. *IEE Proceedings-Radar, Sonar and Navigation*; 2001; **148**(3): 173–185.
[20] NATO. *Ground Moving Target Indication (GMTI) Format STANAG 4607 Implementation Guide*. NATO Standardization Database; 2013-05-13. Available from http://nso.nato.int/nso/nsdd/listpromulg.html.
[21] NATO. *ISR Tracking Standard*. NATO Standardization Database; 2014-05-20. Available from http://nso.nato.int/nso/nsdd/listpromulg.html.
[22] NATO. *Secondary Imagery Format (NSIF) STANAG 4545 Implementation Guide*. NATO Standardization Database; 2013-05-13. Available from http://nso.nato.int/nso/nsdd/listpromulg.html.
[23] International Civil Aviation Organization. *World Geodetic System 1984 (WGS-84) Manual*. Second Edition; 2002.
[24] Fukushima T. 'Fast transform from geocentric to geodetic coordinates'. *Journal of Geodesy*. 1999; **73**(11): 603–610.
[25] Ligas M., Banasik P. 'Conversion between Cartesian and geodetic coordinates on a rotational ellipsoid by solving a system of nonlinear equations'. *Geodesy and Cartography*. 2011; **60**(2): 145–159.
[26] Burtch R. 'A comparison of methods used in rectangular to geodetic coordinate transformations'. *Proceedings of the American Congress on Surveying and Mapping (ACSM) Annual Conference and Technology Exhibition*; 2006.
[27] Obe R., Hsu L.S. *PostGIS in Action*. Cherry Hill, NJ, USA: Manning Publications Co.; 2011.
[28] Mitchell T., Emde A. *Web-Mapping mit Open-Source-GIS-Tools*. O'Reilly; 2008.
[29] Open Source Geospatial Foundation. *GDAL – Geospatial Abstraction Library*. October 2016; Available from http://www.gdal.org.
[30] Dästner K., von Hassler zu Roseneckh-Köhler B., Opitz F. 'Realtime multitarget tracking with airborne GMTI sensors'. *Proceedings of the 16th International Radar Symposium*; Dresden, Germany; June 2015. pp. 339–344.

[31] do Carmo Valero, MP *Riemannian Geometry*. 1992.
[32] Frankel T. *The Geometry of Physics: An Introduction*. Cambridge University Press; 2011.
[33] National Geospatial-Intelligence Agency. *MIL-PRF-89020B Performance Specification Digital Terrain Elevation Data (DTED)*; 23 May 2000; Available from http://earth-info.nga.mil/publications/specs/.
[34] NASA Jet Propulsion Laboratory. *U.S. Releases Enhanced Shuttle Land Elevation Data*. 2014; Available from http://www2.jpl.nasa.gov/srtm/.
[35] Airbus Defence and Space. *WorldDEM^{TM} – The New Standard of Global Elevation Models*, http://www.intelligence-airbusds.com/worlddem/.
[36] Blackman S. S. *Multiple-Target Tracking with Radar Applications*. Dedham, MA: Artech House Inc.; 1986.
[37] Blackman S., Popoli R. *Design and Analysis of Modern Tracking Systems*. Norwood, MA: Artech House; 1999.
[38] Bar-Shalom Y., Li X. R., Kirubarajan T. *Estimation with Applications to Tracking and Navigation: Theory Algorithms and Software*. Hoboken, New Jersey, USA: John Wiley & Sons; 2004.
[39] Bar-Shalom Y., Li X. R. *Multitarget-Multisensor Tracking: Principles and Techniques*. Storrs, Conn., USA: YBS; 1995.
[40] Koch W. *Tracking and Sensor Data Fusion: Methodological Framework and Selected Applications*. Heidelberg: Springer; 2013.
[41] Mahler R. *Statistical Multisource-Multitarget Information Fusion*. Norwood, MA: Artech House Inc.; 2007.
[42] Koller J., Ulmke M. 'Multi hypothesis track extraction and maintenance of GMTI sensor data'. *Proceedings of the 8th International Conference on Information Fusion*; Philadelphia, Pennsylvania, USA; July 2005.
[43] Mertens M., Ulmke M. 'Ground Moving Target Tracking with context information and a refined sensor model'. *Proceedings of the 11th International Conference on Information Fusion*; Cologne, Germany; June 2008.
[44] Pollard E., Pannetier B., Rombaut M. 'Convoy detection processing by using the hybrid algorithm (gmcphd/vs-immc-mht) and dynamic Bayesian networks'. *Proceedings of the 12th International Conference on Information Fusion*, Seattle, Washington, USA; 6–9 July 2009. pp. 907–914.
[45] Munkres. J. 'Algorithms for the assignment and transportation problems'. *Journal of the Society for Industrial and Applied Mathematics*; 1957; **5**(1): 32–38.
[46] Bertsekas D. P. *Network Optimization: Continuous and Discrete Models*. Belmont, Massachusetts, USA: Athena Scientific, 1998.
[47] Jonker R., Volgenant A. 'A shortest augmenting path algorithm for dense and sparse linear assignment problems'. *Computing*. 1987; **38**(4): 325–340.
[48] Ulmke M., Erdinc O. Willett P. 'Gaussian mixture cardinalized PHD filter for ground moving target tracking'. *Proceedings of the 10th International Conference on Information Fusion*; Quebec, Canada; 9–12 July 2007. pp. 1–8
[49] Ulmke M., Erdinc O., Willett P. 'GMTI tracking via the Gaussian mixture cardinalized probability hypothesis density filter'. *IEEE Transactions on Aerospace and Electronic Systems*. 2010; **46**(4): 1821–1833.

[50] Simon D. *Optimal State Estimation: Kalman, H_∞, and Nonlinear Approaches*. Hoboken, New Jersey, USA: John Wiley & Sons; 2006.
[51] Streller D., 'Road map assisted ground target tracking'. *Proceedings of the 11th International Conference on Information Fusion*; Cologne, Germany; June 2008. pp. 1–7.
[52] Clark J.M., Kountouriotis P. A., Vinter R. B. 'A new algorithm for GMTI tracking problems, subject to a Doppler blind zone constraint'. *IET Seminar on Target Tracking and Data Fusion: Algorithms and Applications*; Birmingham, UK; 2008. pp. 51–58.
[53] Clark J. M., Kountouriotis P. A., Vinter R. B. 'A new Gaussian mixture algorithm for GMTI tracking under a minimum detectable velocity constraint'. *IEEE Transactions on Automatic Control*. 2009; **54**(12): 2745–2756.
[54] Ulmke M., Koch W. 'Road-map assisted ground moving target tracking'. *IEEE Transactions on Aerospace and Electronic Systems*. 2006; **42**(October (4)): 1264–1274.
[55] Opitz F., Dästner K., Köhler B. 'Non linear techniques in GMTI tracking'. *Proceedings of the 12th International Radar Symposium*; Leipzig, Germany; September 2011. pp. 187–192.
[56] Plett G.L., Zarzhitsky D., Pack D.J. 'Out-of-order Sigma-Point Kalman filtering for target localization using cooperating unmanned aerial vehicles'. *Advances in Cooperative Control and Optimization*. 2007: pp. 21–43.
[57] Arulampalam M. S., Gordon N., Orton M., Ristic B. 'A variable structure multiple model particle filter for GMTI tracking'. *Proceedings of the Fifth International Conference on Information Fusion*; Annapolis, MD, USA; July 2002. pp. 927–934.
[58] Oliver P., Marrs A. 'An unscented particle filter for GMTI tracking'. *IEEE Aerospace Conference*; Big Sky, *Montana*, USA; March 2004.
[59] Van Der Merwe R, Wan EA. 'The square-root unscented Kalman filter for state and parameter-estimation'. *Proceedings of the IEEE International Conference on Acoustics, Speech, and Signal Processing*; 2001; pp. 3461–3464.
[60] Wan EA, Van Der Merwe R. 'The Unscented Kalman Filter', in *Kalman Filtering and Neural Networks* Edited by Simon Haykin, New York: Wiley; 2001 Sep.
[61] Hauberg S., Lauze F. Pedersen K. S. 'Unscented Kalman filtering on Riemannian manifolds'. *Journal of Mathematical Imaging and Vision*. 2013; **46**(1): 103–120.
[62] Bar-Shalom, Y. *Multitarget-Multisensor Tracking: Advanced Applications*. Norwood, MA: Artech House; 1990.
[63] Li X.R. 'Engineer's guide to variable-structure multiple-model estimation for tracking'. *Multitarget-Multisensor Tracking: Applications and Advances*; 2000 Dec;**3**:499–567.
[64] Kirubarajan T., Bar-Shalom Y., Pattipati K.R., Kadar I. 'Ground target tracking with variable structure IMM estimator'. *IEEE Transactions on Aerospace and Electronic Systems*. 2000; **36**(1):26–46.

[65] Bar-Shalom Y. 'Update with out-of-sequence measurements in tracking: exact solution'. *IEEE Transactions on Aerospace and Electronic Systems*. 2002;**38**(Jul (3)):769–777.
[66] Feldmann M., Koch W. 'Road-map assisted convoy track maintenance using random matrices'. *Proceedings of the 11th International Conference on Information Fusion*. Cologne, Germany; 30 June–3 July 2008. pp. 1–8.
[67] Koch W. 'Bayesian approach to extended object and cluster tracking using random matrices', *IEEE Transactions on Aerospace and Electronic Systems*, 2008; **44**(3):1042–1059.
[68] Koch W. 'Information fusion aspects related to GMTI convoy tracking'. *Proceedings of the 5th International Conference on Information Fusion*; Jul 2002. pp. 1038–1045.
[69] Huang H. A., Yang R., Foo P.H., Ng G. W., Mertens M., Ulmke M., Koch W. 'Convoy tracking in Doppler blind zone regions using GMTI radar'. *Proceedings of the 16th International Conference on Information Fusion*. Istanbul, Turkey; Jul 2013. pp. 1768–1775.
[70] Ulmke M., Koch W. 'Road map extraction using gmti tracking'. *Proceedings of the 9th International Conference on Information Fusion*. Florence, Italy; 2006 Jul 10. pp. 1–7.
[71] Kouemou G., Neumann C., Opitz, F. 'Sound and dynamics of targets – Fusion technologies in radar target classification'. *Proceedings of the 11th International Conference on Information Fusion*. Seattle, USA, 2008.
[72] Chen V. C., Ling H. *Time-Frequency Transforms for Radar Imaging and Signal Analysis*. Boston: Artech House; 2002.
[73] Young S. S., Driggers R. G., Jacobs E. L. *Signal Processing and Performance Analysis for Imaging Systems*. Artech House; 2008.
[74] Budzier H., Gerlach G. *Thermal Infrared Sensors: Theory, Optimisation and Practice*. John Wiley & Sons; 2011.
[75] Richard S. *Computer Vision*. Heidelberg, Germany: Springer; 2011.
[76] Foucart S., Rauhut H. *A Mathematical Introduction to Compressive Sensing*. Basel: Birkhäuser; 2013.
[77] Patel V. M., Chellappa R. *Sparse Representations and Compressive Sensing for Imaging and Vision*. Heidelberg: Springer; 2013.
[78] Dästner K., Köhler B., Opitz F. '3d object extraction and tracking for infrared and day light camera systems'. *Proceedings of the International Radar Symposium*. Leipzig, Germany; 7–9 Sept. 2011. pp. 737–742.
[79] Köhler B., Dästner K., Opitz F., Kouemou G. 'Sensor Integration in the Security Domain'. *Proceedings of the GI Jahrestagung*; 2009. pp. 2445–2453.
[80] Govaers, F., Koch W. 'An exact solution to track-to-track-fusion at arbitrary communication rates'. *IEEE Transactions on Aerospace and Electronic Systems*; 2012, **48**(3), pp. 2718–2729.

This page intentionally left blank

Chapter 13

Radar multi-platform system for air surveillance

Hervé Fargetton[1]

Abstract

The chapter is about air surveillance system composed of several platforms equipped with primary and secondary radars. Currently, air situational awareness is obtained by data fusion of platform tracks exchanged via normalized Tactical Data Links. The performances of air surveillance can be significantly improved, taking into account the game changing due to telecommunication progress: High Data Rate network is now available on almost all the multiplatform systems, even those composed of mobile platforms as ships and aircrafts. Via HDR network, platforms can share plots (raw detections) of all their radars and a common improved air picture can be elaborated by plot data fusion on each platform.

The first section presents the objectives of multiplatform air surveillance system in civil and military domains. The second section describes the theoretical multi radar performance gains under the hypothesis that the HDR network is perfect (no loss, no delay) and that the radar plots of all the platforms are exchanged. The third section describes the evolution of architectures for civil and military multiplatform systems over a 40 years period. For the upgraded multiplatform architecture, the fourth section presents its external interface and its main functions. The fifth section provides some examples of western multiplatform systems and gives some results of performance gains obtained by a multiplatform system in development. Finally, multiplatform systems' future challenges are discussed in the sixth section.

13.1 Introduction

A radar multi-platform system is composed of several platforms (equipped with primary radars and secondary radars) which shares sensor data via a high data rate network (HDR network). A platform may be a ground station or a mobile platform such as a ship or an aircraft.

[1]DGA Techniques Navales, France

13.2 Role and objective

The role of multi-platform systems is different in civil and military domains

13.2.1 Civil domain

Air traffic management (ATM) relies on many platform systems inter-connected by low bandwidth link but also on some multi-platform systems. We will consider here regional ATM systems controlling the planes along their flight.

Secondary surveillance radar (SSR) are the key components of regional ATM systems but primary radar detections are also needed to ensure airplane safety towards unexpected and non-cooperative aircrafts. Regional systems sometimes have their own primary radars but more often, they have a link with a military air defence system that allows them to benefit from its primary radar detections.

Preliminaries

ATM relies on a set of ground stations equipped with SSR and sometimes with primary radar: regional ATM centres, which exploit one or more ground stations, must track each flight from departure to arrival, control their trajectories, avoid collision, re-route flights in case of plane engine failure, meteorological event, ...

SSR requires aircraft to be equipped with transponders. When interrogated by SSR, the plane transponder sends answers. The SSR power budget is better than that of primary radar: it depends only on transponder features and losses due to a single path. SSR periodically scans the sky by emitting interrogations to locate and identify civil flights; the civil planes equipped with a transponder deliver answers depending on interrogations:

- On two pulses separated by 8 μs, answer is mode A, code of 4 octal digits (4,096 possibilities only) given by ground controllers to the plane.
- On two pulses separated by 24 μs, answer is mode C, barometric altitude.
- On three pulses, transponder with mode S extension answers Aircraft ID on 24bits (unambiguous ID delivered by ICAO), barometric altitude in 25 feet.

The ground station receiving answers locates the plane in azimuth-range by the measurement of direction-delay and in altitude by barometric altitude (mode C). Mode S station is an extension of basic SSR:

- Elementary Surveillance Mode S (ELS), compared to basic SSR, improves the precision of measurement in range (15 vs 30 m) and in altitude (25 vs 100 ft). The precision in azimuth is better than 1.1 milliradians.
- With Enriched Surveillance Mode S (EHS), the station can interrogate a plane by its ICAO ID to obtain cockpit information: altitude, roll angle, track angle rate, ground speed, magnetic heading, vertical rate, etc.

ADS-B (Automatic Dependent Surveillance-Broadcast) completes SSR in ground stations: aircraft equipped with *ADS-B out* periodically emit squitters; in other words, they periodically broadcast their aircraft-tracking data without solicitation. The 1090 MHz Extended Squitter contains the same information than the Enriched Surveillance Mode S (EHS). Therefore, without solicitation, the ground station can

receive cockpit information from aircraft equipped with *ADS-B out*. The plane position is not measured by the station but is provided by the Global Navigation Satellite System (GNSS) of the aircraft.

As a backup, the primary radar associated to a ground station or to a neighbouring military air defence system provides detections on the aircraft that are not equipped with transponder and ADS-B out: tourism aircraft micro-lights, drones, etc.

Objectives of civil multi-platform systems

At the moment, some regional ATM centres, at national level or on a larger scale (e.g., Eurocontrol), share ground stations that are distributed on the territory.

These regional ATM centres and their ground stations can be considered as a multi-platform system, because they exchange sensor data via a HDR network.

The objectives of the multi-platform system are as follows:

- Providing each regional ATM centre with the access to the sensor data (SSR, ADS-B out, primary radar) of any ground station, in order to achieve redundancy in case of ground station failure.
- Having, in each regional ATM centre, exactly the same tracks (kinematics and identification) to ensure continuity of control in the areas where the planes come under the control of a neighbouring regional ATM centre.
- Improving range detection and tracking of non-cooperative aircrafts to ensure the security of the civil air traffic.

13.2.2 Military domain

Because threats are not co-operative, primary radars are the key components of air defence system but secondary surveillance radar (SSR) is also necessary to identify friends.

Reminder

An air defence system must:

- detect and track all objects in its area of responsibility,
- establish the friend awareness (blue force tracking) and the neutral situational awareness (civil traffic),
- identify the threat as soon as possible,
- if necessary, engage the threat with its effectors (e.g., anti-missile system).

Primary radars, crucial components, are designed to detect and track non-cooperative targets, characterized by their radar cross-sections (RCS) and their altitude-speed-acceleration profiles. If the radar is associated to an effector, the radar track must also be able to give accurate designation of the target to the effector in its domain of engagement.

Electronic support measurement (ESM) gives complementary information on non-cooperative objects for their localization and their identification: electronic warfare (EW) bearings and their attributes on detected radio and radar emitters are also considered as crucial sources in air defence systems.

Military SSR is compatible with civil SSR (mode 3, mode A and sometimes mode S) to identify all the neutral planes, but it has other modes to establish a secured blue force tracking (position and identification of friends).

The possible answers of an allied transponder to military SSR are as follows:

- On two pulses separated by 3 μs, mode 1 gives the military mission on two octal digits.
- On two pulses separated by 5 μs, mode 2 gives military plane identification on four octal digits (4,096 possibilities only).
- On two pulses separated by 8 μs, mode 3 is equivalent to civil mode A, code of four octal digits (4,096 possibilities only) given by ground controllers to the plane.
- On two pulses separated by 24 μs, mode C gives barometric altitude.
- On specific interrogation, mode 4 is composed of three-pulse reply, delay being based on the encrypted challenge known only by friend allied planes.
- On specific interrogation, transponder with mode 5 extension provides a cryptographically secured version containing the equivalent of mode 4 and, in addition, information as GNSS position.

Modes 4 and 5 are the basis of identification friend or foe (IFF) on the battlefield: when an unidentified aircraft does not answer to this interrogation, it will be classified suspect or hostile.

ADS-B out is also used to establish neutral situational awareness. Military systems must assess the reliability and the consistency of ADS-B reports with radar and intelligence information before taking them into account. Care must be taken to detect the intruders emitting fake reports.

Objectives of military multi-platform system

The majority of allied air defence systems inter-operates by tactical data link (TDL), standardized NATO Links (L11, L16, L22, JREAP). TDL supports the exchange of tactical tracks and command-control messages between units to co-ordinate their actions but does not support the exchanges of sensor data.

However, some air defence systems are multi-platform systems exchanging sensor data via an HDR network. The objectives of these multi-platform systems vs those based on TDL are as follows:

- Providing each platform with access to sensor data (primary radars, SSR, ADS-B) of all the platforms, to reduce the visibility gaps (relief, infrastructure) and to improve the probability of detection in over-lapping radar coverages;
- Improving first detection range and tracking continuously and accurately the high-spectrum threats (low RCS, high manoeuvrability and high speed, e.g., missiles);
- Improving the number of automatically and correctly identified objects;
- Having, on all the platforms, exactly the same tracks (kinematics and identification) so as to have a more efficient co-ordination of their actions.

13.3 Theoretical gains of multi-platform approach

For this analysis, the hypothesis is to consider that the HDR network is perfect (no loss, no delay), and the sensor data of all radars are available without delay

everywhere in the multi-platform system. Two types of gains are identified: gain due to the diversity of frequencies and waveforms of the primary radars, gain due to the spatial repartition of primary radars and also of SSRs.

13.3.1 Gains due to frequency and waveform diversity

If the multi-platform system relies on several radars working in different frequency bands and using several waveforms, the theoretical improvements are as follows:

- *Range coverage and accuracy improvement due to frequency band diversity*
  Since the attenuation due to the propagation is important at high frequencies, a long-range radar exploits the low frequency band (<2 GHz) but its accuracy is limited. A weapon system radar exploits the high-frequency band (>6 GHz) and is accurate. The multi-functional radar exploits the middle frequency band (3–5 GHz) and is an interesting compromise, but it has some limitations in range coverage. A multi-platform system, with long-range radars, multi-functional radars and weapon radars, will have extended coverage for early detection, more robust tracking in middle range and more accurate tracking in short range for weapon engagement, due to the over-lapping coverages.
- *Detection of stealth targets by radars due to frequency band diversity*
  The following figure shows how RCS (radar cross-section) of missiles depends on frequency: the very low RCS values of new missiles are only achieved in the high-frequency bands. The low frequency band radars can give the first detections and the system will require that the other radar bands perform cueing on these first detections, in order to track the missile with accuracy (Figure 13.1).

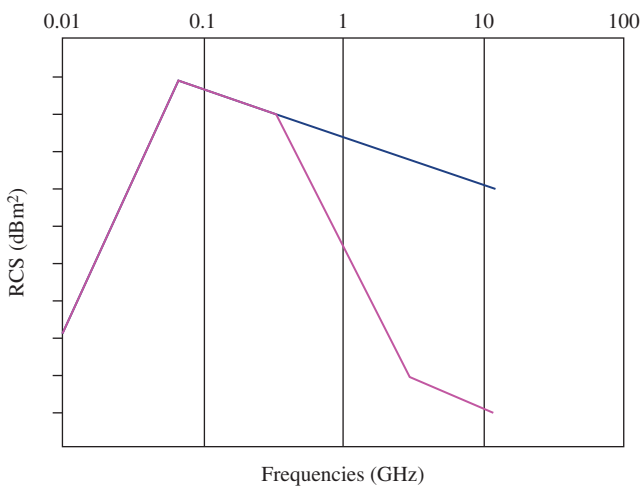

Figure 13.1 Missile RCS as function of frequency legend: blue line classical missile – pink line new missile; the scales of frequencies and RCS are logarithmic

For example, an AEW platform with UHF radar (e.g. Hawkeye) can give a decisive advantage against a low RCS missile to the multi-platform system on. After the first detections by UHF radar, the system will send, via HDR network, cueing information to middle- and high-band radars in order to track the missile with accuracy.

- *Robustness to electronic jamming due to frequency and waveform diversity*
  Jamming is a hostile activity to desensitize radar and blind it or to deceive it. Sweep jamming or barrage jamming have some limitations against multi-radar systems which exploit several frequency bands and different waveforms: it is difficult for jammers to simultaneously jam extreme bands, the sweep period is longer when the number of frequencies to jam increases, the full power of jammer is spread across all the frequencies.
- *Robustness in abnormal EM propagation* (e.g., vaporation ducts on the sea, surface and altitude ducts) because the effect of propagation is not the same in the different frequency bands.
- *Robustness to clutter* because cloud, land, coast, sea have not the same impact on the different radars depending on their frequency band and their waveform.

13.3.2 Multi-radar improvements due to the diversity of viewpoints

The spatial repartition of radars in the network provides several improvements:

- *Detection probability improvement on a stealthy threat* if the primary radars see the threat under different viewing angles, mainly because side RCS is greater than front RCS.
- *Discrimination probability improvement* when the objects are seen by radars (primary or SSR) under different look angles.

Numerical example: Based on a simplified model (see Figure 13.2), the two following tables provide the minimum gap between objects to be discriminated either by R1 or by R2 with a probability of one. Features of radars are: R1 range bin = 16 m, theta 3 db = 2,5°; R2 range bin = 10 m theta 3 db = 2°.

Distance to R1 (km)	30	60	90	120	150
Radial discrimination (m)	48	48	48	48	48
Transversal discrimination (m)	1,275	2,550	3,825	5,100	6,375

Distance to R2 (km)	30	60	90	120	150
Radial discrimination (m)	30	30	30	30	30
Transversal discrimination (m)	1,020	2,040	3,060	4,080	5,100

The resulting discrimination of R1 + R2 in case of Figure 13.3 is then:

	R1 (120 km)	R2 (30 km)	R1 + R2
X discrimination (m)	48	1,020	48
Y discrimination (m)	5,100	30	30

The discrimination of R1 on *Y* axis is improved by a factor 170 with R1 + R2; the four objects of Figure 13.3 will be easily discriminated with R1 + R2.

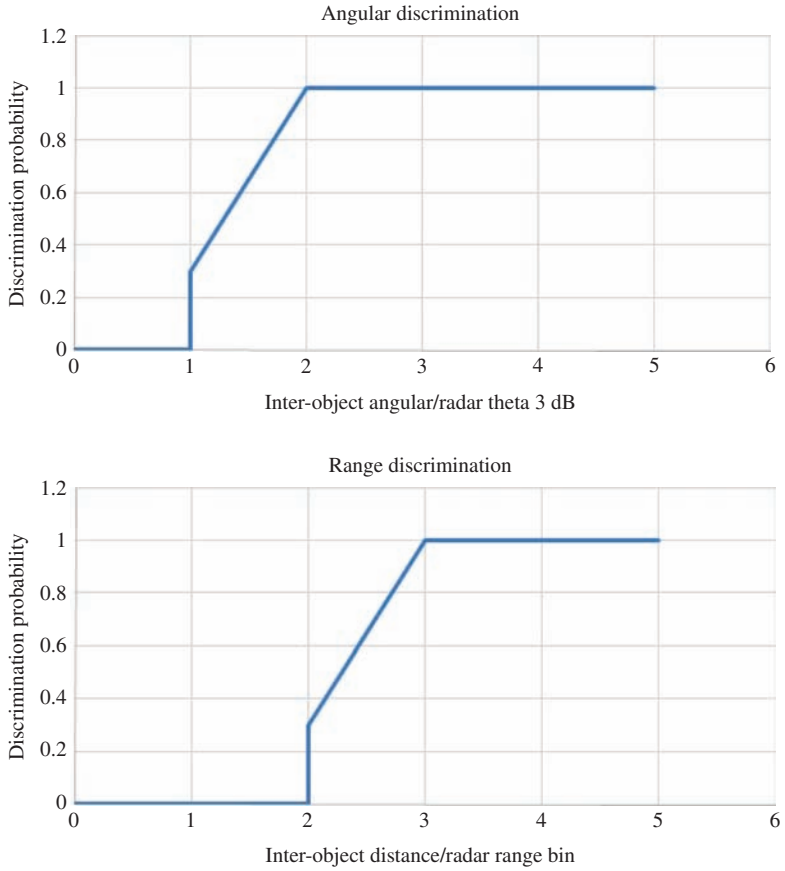

Figure 13.2 Simplified model of primary radar discrimination performances

Figure 13.3 Illustration of discrimination gain with two perpendicular radars. Radar R1 is unable to discriminate (a,b,c) objects and R2 to discriminate (c, d) objects due to their bad angular resolution; R1 + R2 discriminates the four individual objects, thanks to their range resolution

- *Location accuracy improvement* of an object when the object is seen by radars (primary radars and SSR) under different directions;

  The accuracy of modern radars is very good and nearly constant along radial axis (range bin quantification noise) while the accuracy on transversal axis grows with range.

Numerical example: The two tables give the Gaussian accuracy at 3*sigma for different ranges. Features of radars are: R1 range bin = 16 m, theta 3 db = 2,5°; R2 range bin = 10 m theta 3 db = 2°.

Radial accuracy is equal to range accuracy; if range accuracy is approximated by Gaussian quantification noise:

$$\text{range accuracy} = 3 * \text{range bin}/\sqrt{12}$$

Transversal accuracy is equal to azimuth accuracy multiplied by range; if azimuth sigma is approximated by 10% of theta 3 db:

$$\text{transversal accuracy} = 3 * (0,1 * \text{theta 3b}) * \text{range}$$

Distance to R1 (km)	30	60	90	120	150
Radial accuracy (m)	14	14	14	14	14
Transversal accuracy (m)	392	785	1,178	1,571	1,963

Distance to R2 (km)	30	60	90	120	150
Radial accuracy (m)	9	9	9	9	9
Transversal accuracy (m)	314	628	942	1,256	1,570

The resulting accuracy on the object of Figure 13.4 is then:

	R1 (120 km)	R2 (30 km)	R1 + R2
X accuracy (m)	14	314	14
Y accuracy (m)	1,571	9	9

The R1 accuracy on *Y* axis is improved by a factor 175 by R2. The R2 accuracy on *X* axis is improved by a factor 35 with R1.

Figure 13.4 Accuracy improvement with two perpendicular radars. Resulting accuracy benefits from the good range accuracy on the two axes (red area)

- *Localization of the objects by triangulations of EW bearings*
  Localization of non-cooperative objects can be obtained by triangulation of EW bearings: the operational advantage is to locate objects without indiscrete radar emissions. When several emitting objects are present, de-ghosting treatment is necessary to eliminate false inter-sections (red points of Figure 13.5): de-ghosting may be based on kinematic analysis of inter-section points and on coherency of EW attributes.
- *In complement of radar elevation measurement, improvement of the altitude estimation* by triangulations of (azimuth, range) measurements in multi-radar over-lapping area (Figure 13.6).

In this example, the altitude estimation accuracy by triangulation is good at 30 km from the platforms (<300 m). On low altitude objects, for which the noise on radar elevation measurements is important (multi-path effect), altitude estimation obtained by triangulation is more accurate than elevation measurement.

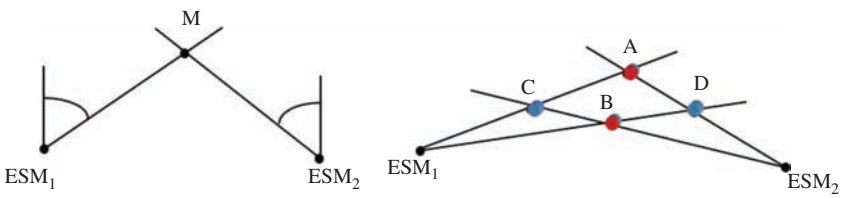

Figure 13.5 Localization of non-cooperative object by triangulation of EW bearings

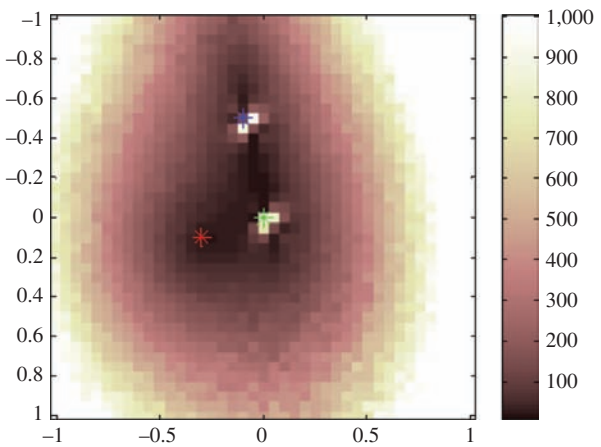

Figure 13.6 Altitude estimation by triangulation of (azimuth, range) measurements. The x–y unit is 100 km, altitude accuracy is represented by colours (scale on the right in metres)

- *Detection complementarity towards masks of relief*
  Air surveillance can benefit from complementary detections by coastal radars and ship-borne radars to detect low altitude threat which follows the coast exploiting the relief.

13.4 Multi-platform architecture

The multi-platform architecture relies on data exchanges and on data fusion.

- Data exchanges in a multi-platform system rely on high data rate (HDR) networks: a presentation of operational HDR networks is first done.
- Data fusion may take into account high level data or sensor raw detections. It may be centralized or distributed: advantages and drawbacks of these choices are discussed afterwards.

In Section 13.1.3.3, several multi-platform architectures are presented, two architectures corresponding to legacy systems and a new promising one based on sensor data exchanges.

13.4.1 Operational high data rate networks

Infrastructure networks have been deployed on western countries' territory since 40 years. These networks rely on Hertzian waves, steel wires and optical fibres. Former point-to-point protocols, such as X25, are now replaced with IP protocols. The availability of these redundant HDR networks explains that multi-platform civil and military systems with permanent installation have been operational since 1980. While the exchange of sensor data is effective since its beginning, the exchange of images/videos in real time is nowadays also possible.

The deployment of HDR networks between mobile platforms is more recent. A modern military HDR network is an IP network federating several media (SATCOM, UHF, HF, etc.) and managing different levels of confidentiality (public, restricted, confidential, secret). On each unit, a federated router selects media depending on distances to recipients.

In the above example (Figure 13.7), two ships are linked together via direct radio frequency and linked to a NATO air defence system and to another ship via SATCOM.

This type of network is less powerful than an infrastructure network. The latest HDR networks enable the exchange of sensor data as plots, under the condition that the platform number is limited.

13.4.2 Choices of data fusion

The first choice of data fusion is the nature of the inputs:

- Inputs may be plots (sensor raw detections) delivered by sensor extractor.
- Inputs may be tracks resulting from plot filtering, delivered by sensor tracker.

Because a tracker filters only chains of plots with spatio-temporal coherence, the volume of sensor tracks is less critical than the volume of plots.

Compared to plot data fusion, track data fusion requires less network and computer resources. Because a sensor track is multi-dimensional (position, kinematics,

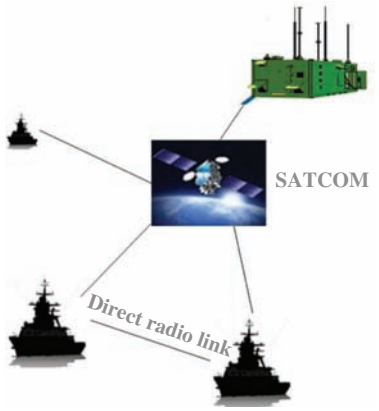

Figure 13.7 HDR network fitted with different media for the inter-connection of military platforms

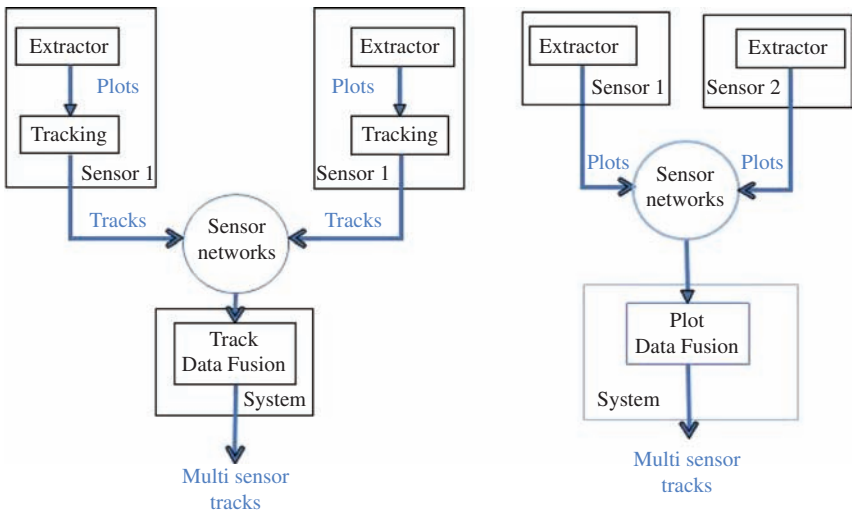

Figure 13.8 Sensor track data fusion vs plot data fusion

attributes), the correlation of sensor tracks from different sources is simpler to realize than plot correlation (Figure 13.8).

However, track data fusion has limited performance compared to plot data fusion:

- Track data fusion is unable to create system tracks on a low RCS target when the detection probability of individual sensor is not sufficient to create a sensor track and even if the cumulated detection probability of all the sensors is good.
- Furthermore, it is impossible to have rigorous data fusion because:
  - Sensor trackers designed by different providers are not homogeneous,
  - Sensor track errors are often characterized by a simple scalar (track quality) under the hypothesis that track uncertainties are spherical,

- Even if a tracker sends the covariance matrix of the track, this matrix may be inconsistent during manoeuvring phases,
- Track data fusion is sensitive to sensor track imperfections (lags, drops, recreations) and may provide multiple designations or track discontinuity, especially on manoeuvring objects in sensor overlapping areas.

Multi-sensor plot data fusion does not have these limitations and can optimally process detection complementarities of sensors:

- Plot data fusion can create system tracks on low RCS object by chaining multi-sensor plots.
- It is possible to have a rigorous plot data fusion because plot errors are well mastered under representative noise, often given by the sensor. Therefore, all the theoretical improvements seen in Section 13.3.2 are accessible with this rigorous plot data fusion.
- Plot data fusion can update system tracks at the rate of all sensor plot arrivals, improving the track update rates and their continuity.

The second choice for a multi-platform system is the architecture of data fusion: centralized or distributed data fusion.

With centralized data fusion, all the platforms send their plots to a central platform and the data fusion is performed on this platform (platform 1 on the example of Figure 13.9); the system tracks resulting from data fusion are then distributed to the other platforms. The advantage is that data fusion is done in one point, so that all the platforms will receive the same system tracks. The main drawback is that, if there is a problem on the central platform, the benefit of data fusion is lost for all the platforms. The architecture of data fusion is not robust and each platform has to switch to its local tracks obtained with its sensors.

With distributed data fusion, all platforms exchange their plots and the data fusion is realized simultaneously on each platform: given the same inputs, the same data fusion algorithm will give the same system tracks on each platform. The first advantage is that the track is available on each platform with a limited delay by the network latency; the second advantage is robustness of data fusion because the architecture is not dependant on a central platform. The drawback is complexity: a unified picture management based on exchange of system tracks between platforms is necessary to have the same labels (number and identification) of system tracks.

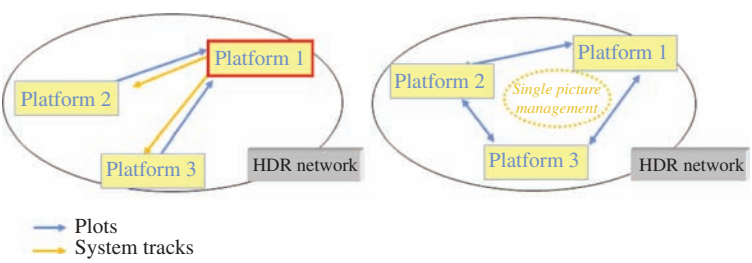

Figure 13.9 Centralized vs decentralized plot data fusion

To summarize: the distributed plot data fusion is more complex but is the best data fusion option for multi-platform systems because of its performance and robustness.

13.4.3 Evolution of multi-platform architectures

The architecture of multi-platform radar surveillance systems mainly depends on the communication network connecting the platforms. The capacity of the network (data rates, latency, surety of exchanges, etc.) determines the level of information exchange.

These multi-platform systems are based on plot data fusion but also have the capability to integrate radar tracks when the radar has a track interface, only.

In the example of Figure 13.10, all the radars have a plot interface except radar 4; each control system utilizes the radars covering its area of responsibility. The exchange of system tracks allows the two control systems to have a coherent track picture at the common border of their area of responsibility. Data fusion has in fact two levels: the first level is plot data fusion, and the second level is track data fusion to integrate system tracks and, potentially, radar tracks.

For this first generation of multi-platform systems, the sensor interface has been standardized very rapidly: this is the objective of the ASTERIX standard of Eurocontrol (reference: http://www.eurocontrol.int/services/asterix).

These multi-platform systems work well with fixed and rotating surveillance radars but are unable to take into account mobile platforms and more complex multi-function radars (MFR).

It was necessary to adopt other architectures for modern air defence systems based on ground stations, ships and aircrafts which are mobile and often have MFR.

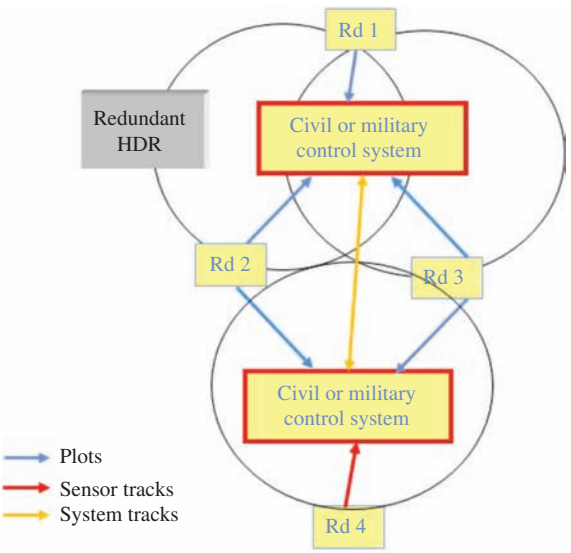

Figure 13.10 First architecture with fixed distant radars based on sensor data exchanges

Before the deployment of HDR-network-supporting mobile platforms, an intermediate architecture was adopted based on tactical data link (TDL). TDL denotes NATO standardized data links of low (L11 and L22) and intermediate data rates (L16, JREAP). The track exchanges obey to a protocol of reporting and responsibility (R2 protocol): simultaneous exchanges of tracks on the same object are forbidden, limiting the improvement due to the track data fusion. Only the platform detecting the objet with the best track quality (TQ) can report its tracks on the TDL network (Figure 13.11).

In this example, the exchanges between a platform and its radars are rich of plots and also tracks for MFR. The data fusion at platform level can be very efficient. However, across platforms, the improvement due to multi-platform data fusion is limited by the constraint of TDL protocol (track exchanges, low track update rate and the fact that only the tracks of the 'best' platforms are exchanged).

With the recent deployment of IP high data rate networks on mobile units, plot data fusion at multi-platform level can be considered for an optimal exploitation of sensor complementarity. An upgraded architecture based on sensor data exchanges is proposed (Figure 13.12).

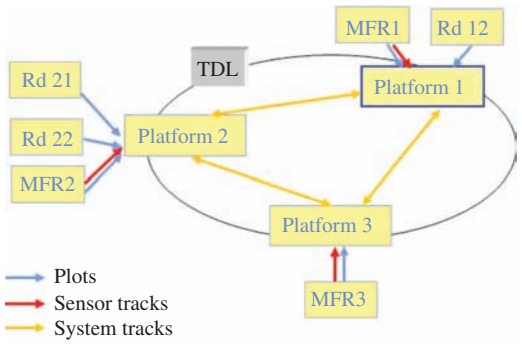

Figure 13.11 Intermediate multi-platform architecture based on TDL

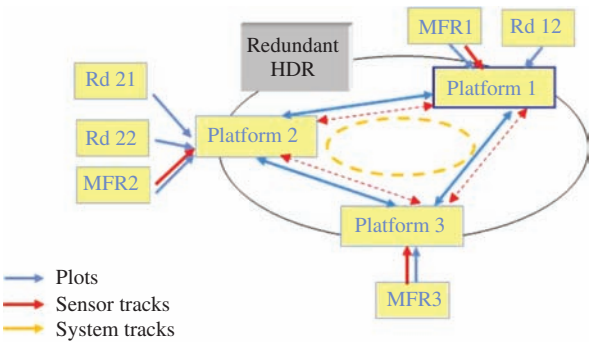

Figure 13.12 Upgraded multi-platform architecture based on sensor data exchanges

The key principles are to share the plots between platforms (and also tracks for MFR) and to have on each platform the same application of data fusion: same inputs and same application will give the same multi-platform tracks on each platform. Tracks will be exactly identical if a single picture management is added to give the same label to these tracks on each platform and to correct the likely divergence of tracks due to the network imperfections (latencies, loss, etc.).

13.5 Description of the upgraded multi-platform architecture

Each system platform hosts a multi-platform sub-system. This sub-system has interfaces with the platform sensors, with the navigation system of the platform and with the other platforms via HDR network. A multi-platform protocol standardizes these interfaces:

- Interface with sensors: generic sensor data message are defined (generic plot message, generic sensor track message, generic sensor command and control message). Sensor gateways on each platform convert local sensor data messages from their native formats to the generic formats. Following these conversions, all the sensor data exchanges in multi-platform system are done in generic formats.
- Interface with navigation system: generic navigation messages are defined for position, kinematics and attitude of the platform in a geographical referential. A navigation gateway on each platform converts local navigation data in a generic message and following this conversion, all navigation data are exchanged across platforms using the generic format.
- Interface with HDR network: each platform sub-system is connected to the HDR network via a router: sensor data and navigation data in a standardized format are exchanged between platforms but also system tracks for single picture management.

The multi-platform sub-system is based on the so-called composite tracking (see below) in charge of sensor data fusion, and it is composed of four other functions (Figure 13.13).

Composite tracking

Composite tracking realizes the data fusion of platform sensor data with remote sensor data received from the other platforms. Composite tracking produces multi-platform system tracks. It is important that the composite tracking satisfies the following requirements:

- Composite tracking shall be able to take into account latencies in remote sensor data received via the HDR network as the platform sensor data is received without latency via the platform network.

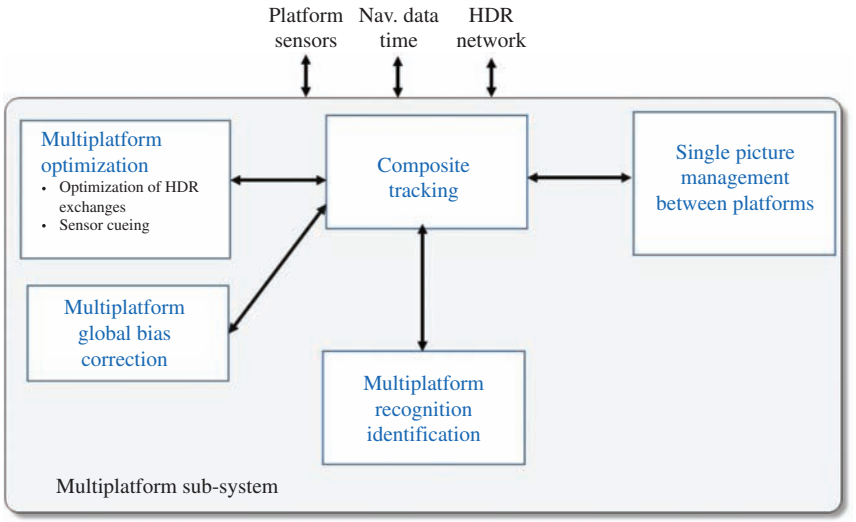

Figure 13.13 Main functions of evolved multi-platform system based on sensor data exchanges

- Composite tracking must establish identical tracks (position, kinematics) on all platforms whatever the chronological dates of plot arrival dates on each platform.
- Composite tracking must be robust to alignment errors between sensor data.

Single picture management between platforms

If composite tracking is able to produce identical tracks in position and kinematics on each platform, the single picture management will provide identical numbers of these tracks on all the platforms. Another objective of single picture management is to correct the divergence of the system track picture on the platforms that have not received all the sensor data because of HDR network losses.

Exchanges of system tracks between platforms are necessary to realize the synchronization of track numbers and the correction of divergences.

Multi-platform global bias correction

Even if composite tracking is robust to misalignment errors, global bias correction is necessary for sensor cueing or effector engagement by a platform that has not yet detected an object with its own sensors. Global bias correction is made in two steps:

- Bias estimation

  Biases are navigation errors of the platforms and offsets (azimuth and distance bias) of the sensors. Estimation of bias is based on the correlation between sensors plot pictures.
- Validation of estimated bias

  Validation of bias estimation may be made automatically or under operator control.

Multi-platform optimization

Multi-platform optimization has two main objectives:

- Exchange the most useful sensor data via HDR network, taking into account network bandwidth limitation.
- Decide on sensor cueing to improve the quality of system tracks (continuity, accuracy).

Exchange of the most useful sensor data may be obtained in different ways:

- By selection of the best sensors in each cell of multi-platform coverage, depending on their performances and their disturbance level,
- By selection of the plots, depending on their utility for each track [1] or for the satisfaction of operational needs [2].

The bandwidth constraints must be monitored in real time. The supervision of an HDR network must provide this information to multi-platform optimization.

The decision on sensor cueing is an important challenge with the modern radar as MFR because their cueing capability is determinant to continuously track high-spectrum threat (low RCS, high manoeuvring and speed). Multi-platform subsystem offers the possibility to make inter-platform sensor-to-sensor cueing by request on the system tracks.

For each track, multi-platform optimization analyses the quality of tracking and, if the quality has to be improved for a specific operational need (e.g., effector engagement, identification), it has to request sensor cueing to the more capable neighbouring MFR.

Multi-platform recognition and identification

The objective is to determine automatically the type of each aircraft (e.g., recognition as liner or fighter) and their intention (identification as friend, neutral, hostile), utilizing all sensors of the multi-platform system.

The co-operative sources such as SSR, mode S, mode 5 and ADS-B (see Sections 13.2.1 and 13.2.2) are key assets for the blue force tracking and the neutral situational awareness. Multiple platforms offer redundancy of these co-operative sources. Multi-platform global bias correction will place all their information in a common geographical referential (e.g. GPS referential) and will avoid ambiguity or dual tracks due to mis-correlation of the co-operative data.

The MFR high resolution cueing is an important means to recognize the non-cooperative objects. The multi-platform offers the possibility to action this type of cueing on system tracks. Because other sensors may take care of the surveillance tasks in a multi-platform system, high resolution capability of MFR may be activated more often.

13.6 Examples of western multi-platform systems

For 40 years, multi-platform radar surveillance has been a reality for the regional ATM centres and for the air defence system with rotating and fixed radars. These

systems are included in Eurocontrol (European civil ATM) or in NATO Air Command and Control System (ACCS). They rely on infrastructure networks with high bandwidth and redundancy.

The deployment of HDR networks between mobile platforms is more recent, and only some multi-platform systems have been developed in the military domain for the Navy: e.g., CEC (US Navy), VCN (French Navy).

US CEC

US Navy has acquired an operational capability called co-operative engagement capability (CEC), after 30 years of research and development. CEC gains are described in [3]. CEC relies on a proprietary HDR network. CEC was at first a sub-system beside the operational ship system. CEC is now integrated as a software module in the operational ship system.

French VCN

The French capacity was at first called 'Tenue de Situation Multi-Plates-formes' (TSMPF); its name is now 'Veille Co-operative Navale' (VCN). The French capacity is based on the upgraded architecture presented in Section 13.5.

After a preliminary study demonstrating performance gains for anti-missile defence (see Section 13.6.1), France has decided to initiate an important programme of research with industry. The choice of architecture and the design of data fusion algorithm were made during the research phase. In 2010, research ended with an at sea evaluation between a frigate and two shore sites [4,5].

Since then, VCN capacity is in development. In 2013–14, experiments have been realized with air force platforms to prepare inter-operability of VCN [6].

In 2015–16, France has carried out the first operational at sea evaluation of VCN with frigates and aircraft carrier vessels [7].

13.6.1 Preliminary study for French Navy

A preliminary study in 1999 has demonstrated significant gains for the anti-missile defence of a navy force before modernization of former generation radars.

This study compared the air defence capability of a three-ship force in missile scenarios under different hypotheses:

- No exchange: the ships do not communicate; each ship generates local system tracks by plot data fusion of its radars, engagement is made on local tracks of the ship.
- With exchange of system tracks: each ship generates tracks by plot data fusion of its radars and exchanges its tracks with other ships every X seconds ($X < 10$). Engagement is made on local tracks enriched by exchanged tracks.
- Sensor data exchanges: each ship generates tracks by multi-platform data fusion of all radar plots. Engagement is made on multi-platform tracks.

The selected scenario assumes three missiles with typical trajectories: low-altitude trajectory or diving trajectories. The scenario was played in four environments for which real plots were recorded: two offshore environments (standard propagation

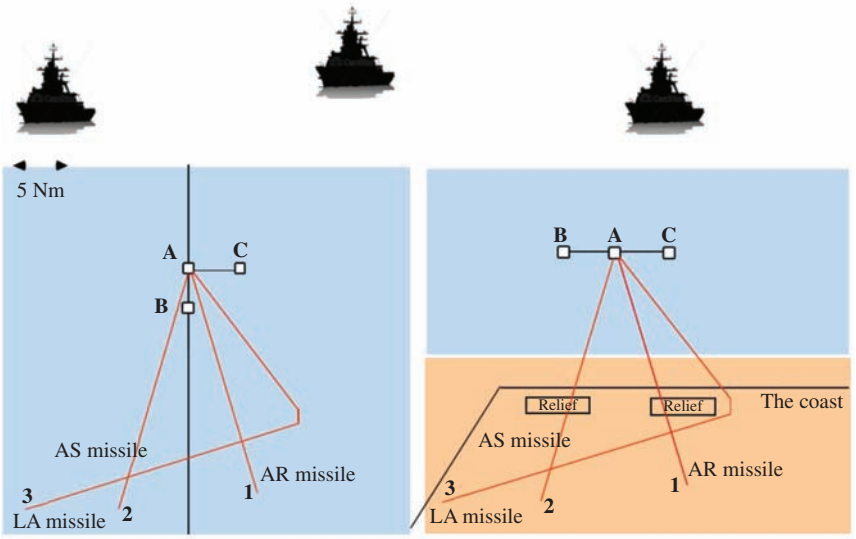

Figure 13.14 Operational navy scenario. Ship A protected by two ships (B, C) is attacked by three missiles (1 anti-surface missile, 2 anti-radar missile, 3 low-altitude missile)

and duct) and two coastal environments (standard propagation and duct). The coastal environments introduce topography masks, which affected the detection of low-altitude missile (Figure 13.14).

Figures 13.15 and 13.16 present the results of engagement success rates obtained by Monte-Carlo evaluation. The engagement is possible when the accuracy of the track is sufficient (track position accuracy in a 3D template depending on the effector). Figure 13.15 shows the possibilities of engagement in the most difficult environment (coastal and duct).

Left column figures are above top views of the scenarios. Central figures are 3D views; on these figures, the parts of missile trajectories for which the engagement is possible are highlighted in green colour. In the right figures, the histograms present the possibilities of engagement (x axis: 0%–100%) for the 90 instances of missile trajectories of Monte-Carlo evaluation (y axis).

The success of engagement is low (36%) in mono-platform and increases with the exchange of system tracks (41%) because continuity on AS missile is improved. With exchange of sensor data, the success of engagement grows up to 62%: gain is observed on the AS missile behind the relief and also in the final acceleration of 15 g.

Figure 13.16 presents the engagement success rates for four environments. In the two coastal environments, the improvement of engagement success grows up to 50%. Multi-platform data fusion is especially interesting in difficult environments where the complementarity of sensors can suppress the topography masks. It improves the probability of detection above the ground or in presence of surface duct over the sea.

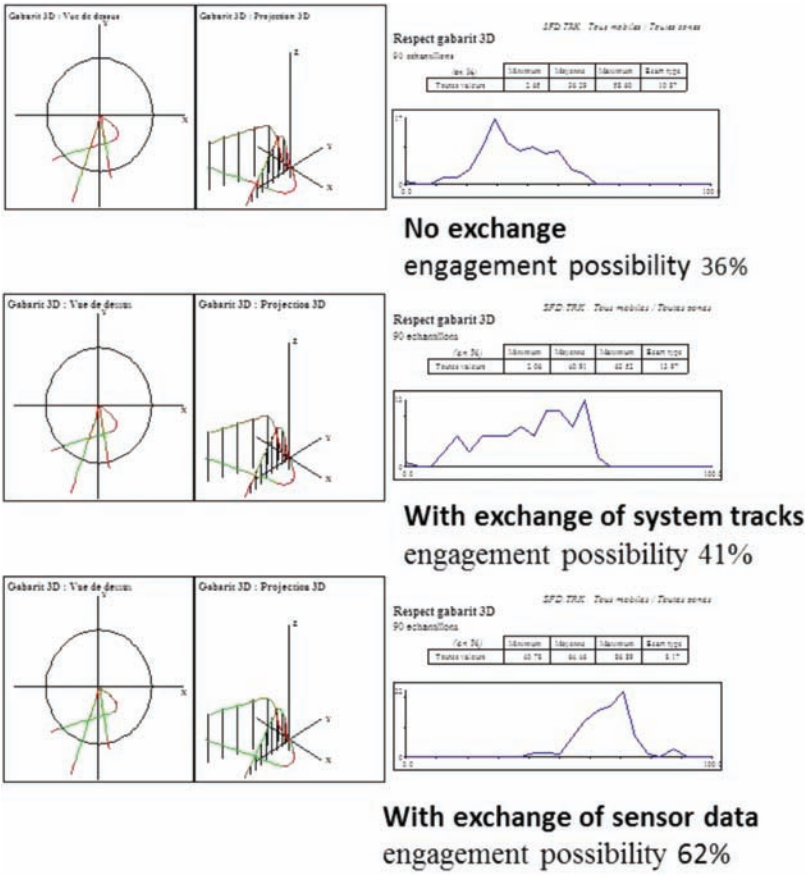

Figure 13.15 Engagement results for coastal environment with duct

Engagement possibility	Env 1 : offshore standard propa.	Env 2 : offshore surface duct	Env 3 : near the coasts standard propa.	Env 4 : near the coasts surface duct.
No exchange	51.2%	51.9%	40%	36%
Exchange of system tracks	52.5%	52%	43%	40.9%
Exchange of sensor data	63.6%	63.5%	60.5%	62%

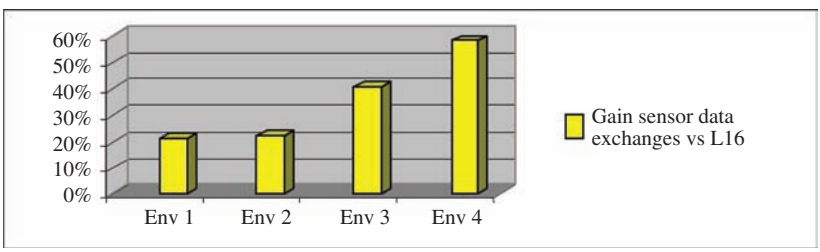

Figure 13.16 Synthesis of engagement results

13.7 Next challenges

The next two challenges for multi-platform systems are discussed: standardization of multi-platform inter-operability protocol and integration of a multi-platform sub-system in operational systems.

Standardization of multi-platform protocol

The inter-operability offered by a multi-platform protocol (see Section 13.4) is a first step to integrate platform in a multi-platform system. The former multi-platform systems with fixed radars have their protocol: ASTERIX and STANAG 5532. The modern multi-platform systems, such as CEC and VCN, have proprietary protocols. The inter-operability of platform begins with the definition of non-proprietary standards (civil standard, STANAG).

Integration of multi-platform sub-system in operational system

Inter-operability by multi-platform protocol is a first step but the performance of a multi-platform system will be optimal if the same application is deployed on all the host systems (key principle 'same inputs and same application will give the same multi-platform tracks').

There are at least two solutions to deploy the capability on a host operational system:

- The multi-platform sub-system is on specific hardware and is connected to the operational system to update its track table.
- The multiplatform sub-system is a software module integrated in the operational system software.

For an existing operational system, the first solution has the advantage of limited modifications to the operational system; the drawback is that it is not fully integrated in the operational system. In particular, the operators will have two interfaces, the main interface carrying the operational system and a specific one to support the multi-platform sub-system.

For a new operational system, the second software solution is recommended: the application will be fully integrated; operators will have coherent interfaces with all the operational functions. There is an integration issue if the technology of the multi-platform software is different to the technology of operational system. Open architecture is an important orientation to support the deployment of multi-platform software on host operational systems.

Acronyms

ACCS	air command and control system
ADS-B	automatic dependent surveillance-broadcast
AEW	aircraft early warning
ASTERIX	all-purpose structured EUROCONTROL surveillance information exchange
ATM	air traffic management

EHS	enriched surveillance mode S
ELS	elementary surveillance mode S
EM	electro magnetic
ESM	electronic support measurement
EUROCONTROL	European Organization for the Safety of Air Navigation
EW	electronic warfare
FAA	federal administration agency
GIS	geographical information system
GNSS	Global Navigation Satellite System
IFF	identification friend or foe
JREAP	Joint Range Extension Applications Protocol
LOS	line of sight
LRR	long range radar
MFR	multi-function radar
ICAO	International Civil Aviation Organization
RCS	radar cross-section
SoS	system of systems
SSR	secondary surveillance radar
STANAG	standardization agreement
TDL	tactical data link
TN	track number
TQ	track quality
UAV	unmanned air vehicle
UHF	ultra-high frequency
VCN	'Veille Co-opérative Navale' French Navy multi-platform capability

References

[1] F. Govaers, A. Charlish and W. Koch, 'Information fusion under network constraints', in: *Proceedings of IEEE Military Communications and Information Systems Conference* (MCC, October 2012, Gdansk, Poland), pp. 1–6 (2012).

[2] Leon Kester, Maarten Ditzel, TNO The Netherlands, 'Maximising effectiveness of distributed mobile observation systems in dynamic situations', presented at *FUSION 2014*, Spain.

[3] 'Mountain top: Beyond-the-horizon cruise missile defence', *Johns Hopkins APL Technical Digest*, vol. 18, no. 4 (1997).

[4] Félix Alvarez, DCNS, 'Multiplatform tactical picture (MPTP): First sea-trial results', presented at *MAST 2011*, France.

[5] Hervé Fargetton, Ministry of Defence (DGA Technique Navale), 'Evaluation of the DCNS multiplatform situational awareness capability', presented at *MAST 2011*, France.
[6] Hervé Fargetton, DGA, 'Joint experimentations between French air warfare multiplatform capabilities', presented at *MAST ASIA 2015*, Japan.
[7] Hervé Fargetton, DGA, 'First operational evaluation of the new French multiplatform capability', presented at *MAST 2016*, The Netherlands.

This page intentionally left blank

Chapter 14

People tracking and data fusion for UWB radar applications

Snezhana Jovanoska[1,2], Felix Govaers[2], and Reiner Thomä[1]

Abstract

Localization of people that do not carry active tags is needed in security as well as in rescue applications. Ultra-wideband (UWB) technology is promising due to its high ranging resolution capability, robustness against multipath interference and obstacle penetration among others. In this chapter, an approach for detection, localization and tracking of people using either a single UWB sensor or a distributed network of UWB sensor nodes is described. The background behind UWB sensing, a description of UWB sensor nodes and a concept for a distributed sensor network is presented. The basic principle of person detection based on the changes the person induces on the channel impulse response is explained. Two approaches for localization based on range-only observations that can be applied in single-sensor or multiple-sensor scenarios or in the presence of a single person or multiple people are presented. The concept and each step of the approach are illustrated using data obtained in a measurement campaign at TU Ilmenau from an office environment.

14.1 Introduction

Investigations into Ultra-wideband (UWB) started 60–70 years ago for needs in radar and communication technology. Since then, UWB technology has been found useful in many industrial, medical, surveillance, security, search and rescue applications among others. High-power medium and long-range radar systems are reserved for (typically) military use. High-resolution short-range devices deal with low power (< 1 mW) and are of interest for civil applications. Reference [1] gives a good overview on UWB technology, sensing, radar architecture and some applications.

[1]Technical University Ilmenau, Germany
[2]Fraunhofer FKIE, Germany

In many people localization applications, the people to be tracked carry a device or tag such as radio frequency identification chip that aids in their localization. However, for some applications, the person to be tracked cannot or does not want to cooperate with the localization system. This kind of non-cooperative or device-free target detection and localization is also sometimes referred to as passive localization. Indoor localization and tracking of people in passive manner has many applications such as intruder detection, emergency response, surveillance and security [2,3]. UWB signals have a very good time resolution due to the large bandwidth and allow for centimetre accuracy in ranging. UWB systems can operate regardless of the visibility conditions (dark or smoke-filled environments) and through non-metal obstacles (e.g. through-wall).

Dependent on the size of the object of interest, multiple echoes per object can be detected. Time-variant multipath components can be separated easily due to the high spatial resolution as a function of time delay. If the transmitting and receiving antennas are stationary throughout the measurement time, changes in the measured impulse responses indicate presence of moving objects which in our scenario corresponds to moving people. Different parameters for object characterization can be estimated from the channel impulse response; however, the most reliable and common ones are the time-based parameters.

By using any of the parameters corresponding to a person that can be estimated from the channel impulse response, we ultimately want to estimate the location of that person. If the available information regarding the location is insufficient or noisy, tracking can be used to improve the location estimate. In addition to the noisy observations, position estimates based on the previous states of the detected people are used to improve the current location estimates.

The Kalman filter is the optimal solution for single target Bayes filter in linear Gaussian systems. For multiple-target tracking, different methods have been developed over the years. Many require the number of targets to be known and use measurement-to-track association before estimating the target states [4–7]. A combinatorially and computationally less complex solution that does not require explicit data association is the probability hypothesis density (PHD) filter [8–10].

Target localization and tracking based on UWB radar technology has been previously investigated in [11–19] among others. References [11–13] only consider single target localization and tracking. Reference [14] uses single target detection per sensor and imaging-based data fusion. Reference [15] uses multiple hypothesis tracking for both person localization and characterization based on parameters estimated from the channel impulse response. Reference [16] considers people as extended targets and utilizes both range and Doppler information for target localization. Reference [17] describes an approach for detection and localization of multiple people using multiple-UWB sensors similar to the approach presented here in Section 14.4.4. A PHD filter is used for location fusion and tracking. Reference [19] considers multipath reflections to localize a person behind a corner and [18] considers the dynamic occlusions induced by people in the scenario within the localization and tracking approach. In this chapter, indoor localization and tracking of multiple people using a network of UWB sensors is considered. Target

classification, localization of targets behind a corner and dynamic occlusions are not considered.

An overview of the UWB-sensing principle is given in Section 14.2. Within the section, a UWB sensor node is defined as used within this work and a concept for distributed UWB sensor network is presented. In Section 14.3, the principle of person detection from a measured channel impulse response is explained. Methods for moving people detection and range estimation are explained in greater detail. The people localization principle based on range-only observations is explained in Section 14.4. A short explanation of Bayes-based target tracking is presented, followed by two methods for people localization and tracking by a distributed UWB sensor network, and finally verification and comparison of the two methods in an office scenario.

14.2 UWB sensing

In the time domain radar equation, all objects that do not move too fast and are in the radar channel may be considered as a linear time-invariant system. The information about the channel propagation (transmission, reception and scattering) can be formally described by impulse response functions. Bistatic radar can be considered as a two-port system. Let antenna 1 be the transmitting antenna denoted by *Tx* and antenna 2 be the receiving antenna denoted by *Rx*. Disregarding polarization, dispersion, angular and range dependencies, and assuming a limited target size in the far field and no antenna coupling, the transmission between the two antennas can be written in terms of M scatterers [1]:

$$\begin{aligned} & b_2(t) = S_{21}(t) * a_1(t) \Rightarrow b_2(t) \sim S_{21}(t) \;\text{ for }\; a_1(t) \approx \delta(t) \\ & \text{and }\; S_{21}(t) = T_1(t) * R_2(t) * \sum_{m=1}^{M} \frac{\Lambda_{21}^m\left(t - \left(r_{Tx}^m + r_{Rx}^m\right)/c\right)}{r_{Tx}^m r_{Rx}^m} \end{aligned} \tag{14.1}$$

where a_1 is the stimulus signal, b_2 is the received signal, $c = 3 \cdot 10^8$ m/s is the signal propagation velocity in air, r_{Tx}^m and r_{Rx}^m are the distances of the mth scatterer to the transmitter and receiver, T_1 and R_2 are the antenna impulse responses for the transmitting and receiving mode and Λ_{21}^m is the scatterer pulse response for incidence from antenna 1 and observation by antenna 2 and contains all information about the mth target accessible by the measurement. Λ_{21}^m responses can be interpreted either as a reaction of a single body onto an incident field or the reaction of distinct scattering centres of a composed target. The scattering response $\Lambda_{21}^m(t)$ of a complex structured target is typically composed of many peaks caused by specular reflections and damped oscillations that represent the eigenmodes of the target. To resolve these properties, the temporal width of the sounding wave must be shorter than the peak distances and the sounding bandwidth should cover the eigenfrequencies of the target [1]. Using a UWB sensor, we primarily determine the impulse response function $S_{21}(t)$ from the test scenario. The impulse response function contains information about possible targets and the environments based on

their reflections. Depending on the application-specific data, processing techniques can be used to extract the desired information from these responses. For people localization, the primary interest is to extract information from the impulse response regarding the position of a person. This information can be time of arrival (ToA), time difference of arrival (TDoA), Doppler, angle and amplitude among others.

UWB signals have large fractional and huge absolute bandwidth. They are composed of only few oscillations compared to the many in narrowband signals. A large fractional bandwidth is needed to achieve specular reflections separation and mix of natural frequencies. The absolute bandwidth depends on the smallest dimensions that need to be resolved. For detection of moving targets within a stationary clutter environment, the weak variations in the backscattered signal induced by the movement of the target can be used. Large fractional and absolute bandwidth is needed for penetration of objects, detection of weak movements and target separation.

The stimulus signal a_1 may have different waveforms, e.g. chirp signal, short-impulse signal, binary sequence. An appropriate stimulus signal should be used depending on the application where it is required. Chirp signals are not appropriate for real-time surveillance (slow measurement rate). Short-impulse signals also result in low measurement rate and these systems are susceptible to jitter and drift. Pseudo-random binary sequences allow for real-time operation are generated in stable manner and have low crest factor (allowing signal energy maximization at low peak voltages). The UWB-sensing system used in this chapter is an *m*-sequence UWB radar [20] which uses a maximum length binary signal (MLBS) as stimulus signal. The MLBS generator can be realised on integrated circuit technology, meeting the bandwidth, low jitter and high signal-to-noise requirements. In addition, its spectral shape follows the $(\mathrm{sinc})^2$ function with around 80% of its energy concentrated at frequencies below half of the clock rate [1].

14.2.1 UWB sensor

A UWB sensor node within this work is defined by an autonomous UWB module with one transmitter, two receivers and a local processing unit as shown in Figure 14.1. In [21], it is referred to as a bistatic bat-type UWB sensor node. The two receiving antennas are positioned on each side of the transmitting antenna forming a bat-type structure. The transmitter and receivers are synchronized and from each of the two impulse response functions the ToA of possible targets can be obtained.

Due to the proximity of both receivers, we often can detect people by both receivers. The data obtained by each receiver are locally processed to first separate the echoes of possible targets in the scenario and then estimate their range. As two receivers are present on the module, a target range can be estimated with respect to both receivers. Using these two range estimates, the two-dimensional (2D) target location can also be estimated. Each range estimate corresponds to an ellipse in the 2D Cartesian space where the location of the transmitter and receiver is the foci of that ellipse. The ellipses intersection ideally corresponds to the 2D location of the target. The number of intersections of two ellipses can be zero if the ellipses never

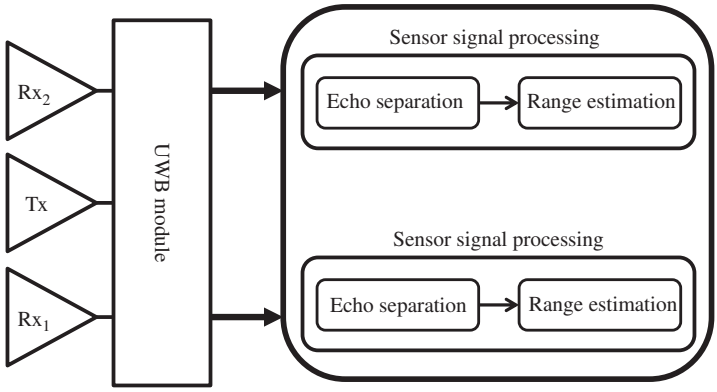

Figure 14.1 UWB sensor node structure

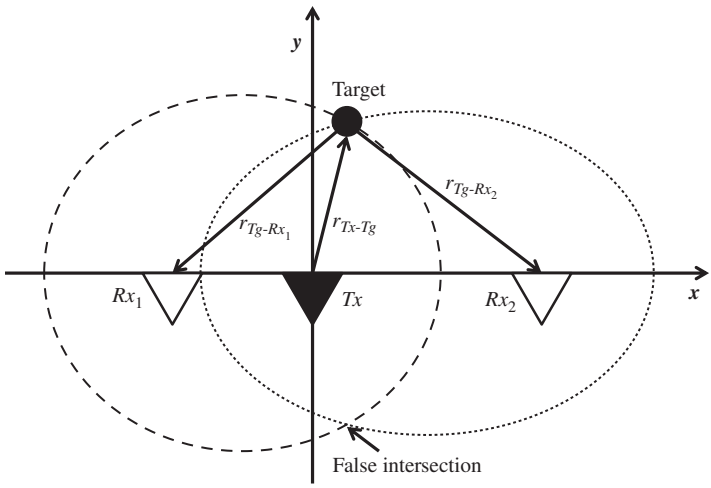

Figure 14.2 ToA-based localization

touch, infinity if the ellipses overlap and one, two, three or four if the ellipses touch or cross each other. As the transmitter and receivers lie on the same line at distinct points, there can be only zero, one or two intersections. In the presence of a target, there are two intersection points. Each should have the same likelihood of being the target location; however, the sensor node is typically positioned on one of the edges of the area of interest and thus one of the intersection points can be directly discarded as undesirable by being outside of the area of interest or behind the sensor antenna when directional antennas are used. The principle of ToA-based localization using a single sensor is illustrated in Figure 14.2.

A sensor defined in this manner is applicable in many scenarios where the sensor node needs to be used from one side of the scenario of interest such as

through-wall. A portable sensor that can operate in a 'plug-and-play' mode would be ideal. This means that the sensor should be quickly ready for use in an unknown scenario and can provide real-time or near-real-time information for the presence of people in that scenario.

14.2.2 Distributed UWB sensor network

UWB systems often suffer from interference with other systems that transmit at higher power level over the same spectrum [22]. A single sensor node is not well suited for multiple target detection. Targets close to the receiver or transmitter of a sensor node shadow other targets in the environment, making them invisible or barely detectable by the sensor. A network of multiple autonomous sensors covers a larger area and many shadowed regions and blind-spots in the area of interest of one sensor are covered by another sensor of the network. Targets in the area of interest may be detected by multiple sensors of the network, providing information regarding the target from different angles. This information has to be properly fused so that a target detected by two different sensors does not appear in the final results as two targets close to each other.

When developing a distributed sensor network, attention must be paid to the performance of the overall system in real time. Both the detection of the targets by the sensors and the fusion of this information must be provided in real or near real time. Different sensor-distribution schemes for UWB systems have been discussed in literature [21,23]. The distributed UWB sensor network scheme used here is based on multiple autonomous bistatic bat-type UWB sensor nodes as described in Section 14.2.1 and given in the example scenario in Figure 14.3. The connection between each sensor node and the fusion centre node is either wired or wireless.

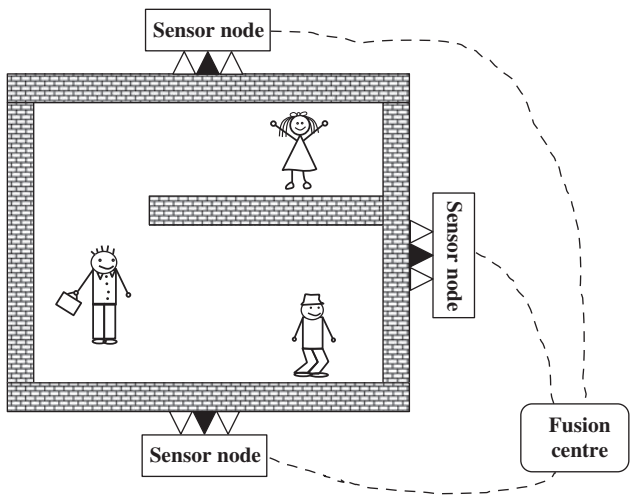

Figure 14.3 Example of possible scenario of interest surrounded by multiple-UWB sensor nodes

To synchronize the system, a common system clock should be shared among all sensor nodes either via coax, optical cables or wirelessly. The wired synchronisation offers more precise and stable measurements; however, it requires the use of long cables.

In this distributed sensor network, two operating principles can be defined: parallel and sequential. For a parallel operating principle, the synchronisation of the sensor nodes is not required. By relaxing the synchronisation requirement, each sensor node operates using a local system clock. Thus, the transmitters of all sensor nodes may operate in parallel, and the signals scattered by the environment can only be resolved by using those receivers that are synchronized with the transmitter. This means that for each transmitter of a sensor node, only the two receivers of the same sensor node can be used. Otherwise, the cross-correlation between the received and transmitted signal will produce a noisy signal. The advantage of the parallel mode is the reduced measurement time for acquisition of the 'reduced' multiple-input–multiple-output (MIMO) impulse response function and the lack of synchronisation between the sensor nodes. To measure the full MIMO impulse response function which should provide more target information, a sequential operating mode should be used. For the sequential mode, synchronisation or a shared system clock between all sensor nodes is required. In addition, only one transmitter can be active at a time, thus increasing the measurement time by the number of transmitters being used in the network.

In this chapter, it is assumed that there is no synchronisation between the different sensor nodes; however, there is cooperation of each sensor node with a central fusion centre node that also acts as control centre. The fusion centre node controls the sensor nodes that are distributed around the area of interest. It is responsible for sensor discovery and definition of the sensor network. The data received by each sensor are first aligned to account for delayed and missing data. Then it is passed to a processing unit where it is fused defining location estimates and tracks for each of the detected targets in the scenario. A common reference coordinate system is defined at the fusion centre with the knowledge of the locations of each of the operating sensor nodes. It is assumed that the sensor nodes are stationary and with known location, i.e. sensors are capable of self-localization.

14.3 Person-detection principle

In a typical scenario, the backscattered signal from the people is one of the weakest components in the received impulse response and the system is subject to many perturbations. The source of these perturbations can come from electronic noise, jamming, stationary and non-stationary clutter, etc. Knowing the motion profile of the targets (person walking speed), it is possible to separate the moving target echo from the stationary clutter (antenna crosstalk and stationary reflections) by a method known as background subtraction (see Section 14.3.1). Non-stationary clutter arises from reflections of objects with the same range profile as the desired target or from distant objects, in which case the clutter may be gated out if the unambiguous range of the radar is sufficiently large. The different motion profiles

may be used to distinguish between a person and non-stationary clutter. Non-stationary clutter is not considered at this stage; however, [1] suggests that non-stationary clutter often contains strong signal components at frequencies below the breathing rate that can be used to cut the clutter components out.

Once the echoes of the targets are separated from the stationary background reflections, parameters can be estimated that help localize the targets. Time-based parameters provide more reliable and accurate target localization compared to other parameters as shown in [22]. Time-based parameters can be estimated if there is some sort of cooperation and synchronisation between the transmitter and receivers of the system. ToA is defined as the absolute travel time from the transmitter to the person and back to the receiver. To acquire the ToA, synchronisation and no clock bias is needed between the transmitter and the receiver of the system. TDoA is defined as the difference between the arrival times of the signal to each of the synchronized receivers. Only synchronisation between the receivers is required for acquiring the TDoA. The ToA, or correspondingly the range between the target and the sensor, is one of the most useful parameters for target localization when using UWB.

14.3.1 Moving target echo separation

To detect the weak echoes of the moving people, the time-invariant strong background reflections should be removed. The first step is to estimate the time-invariant background. Different methods for background subtraction exist [24,25]. If a measurement of the static background is available, subtracting the background template is a reliable method for target echo separation. In many application scenarios, the background cannot be measured ahead of time and thus needs to be estimated. Most common background estimation methods are based on mean, median or mode [26], exponential averaging [11] and low-pass filters and predictors [25]. Methods based on mean, median or mode are applicable for offline processing as they require access to all measured impulse responses. Exponential averaging can be applied in scenarios that require near-real-time performance, as the background is iteratively computed from the previous background estimation. It is a well-suited method for background estimation as it is simple and it is controlled by only one parameter. Background subtraction algorithms that rely on prediction filters can provide more precise adaptation to the specifics of the environment; however, they are computationally expensive due to matrix inversion for finding the predictor coefficients.

Due to its simplicity, good performance, high robustness and low computational complexity, exponential averaging is one of the most popular methods for background subtraction. The background estimate as seen by receiver j of sensor s at time t, $u^b_{s,j}(t)$ is computed using the previous background estimate $u^b_{s,j}(t-1)$ and the newly received impulse response $u_{s,j}(t)$

$$u^b_{s,j}(t) = \alpha u^b_{s,j}(t-1) + (1-\alpha)u_{s,j}(t) \tag{14.2}$$

with α being a constant scalar weighting or forgetting factor between 0 and 1. This factor determines whether recent events ($\alpha \to 0$) or long-term trends ($\alpha \to 1$)

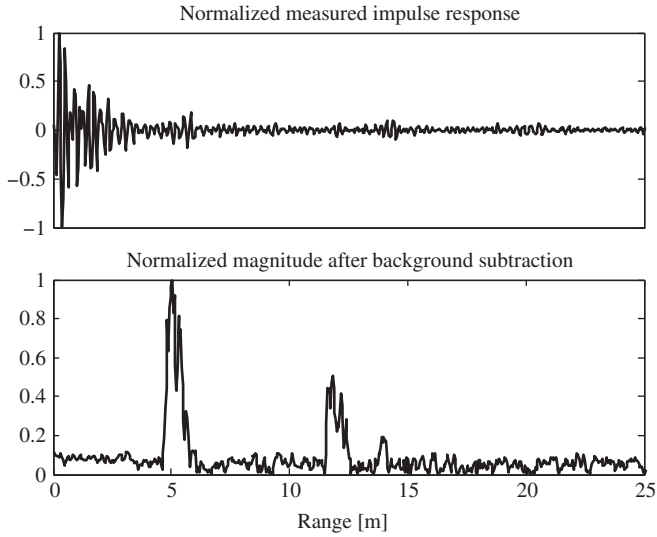

Figure 14.4 Target echo detection – normalized measured impulse response (above) and normalized signal magnitude after background subtraction (below)

in the background estimation are emphasized. For person motion $\alpha \rightarrow 1$ should be used as it allows for detection of slow motion in the received signal. The signal of interest containing the person echoes is then

$$u^p_{s,j}(t) = u_{s,j}(t) - u^b_{s,j}(t). \tag{14.3}$$

In Figure 14.4, the normalized measured channel impulse response, $u_{s,j}(t)$, and the resulting signal after background subtraction, $u^p_{s,j}(t)$, are shown. As can be noticed, the echoes from the moving people are so weak that they are undetectable in the directly measured signal. The radargrams of people walking in a room before and after background subtraction (over time) are given in Figure 14.5(a) and (b), respectively.

14.3.2 Range estimation

The signal $u^p_{s,j}(t)$ contains echoes from the people in the coverage area of the sensor as well as some low peaks corresponding to shadowed background that mimics time-variant reflections. In most cases, clutter arrives later in the fast time (range) compared to the first target. Thus, the estimation of the range of the closest target can be simplified as no clutter models are necessary. The simplest method is peak detection. However, since a person is an extended target, threshold-based approaches are more appropriate. They have low computational complexity and are suited for completely analogue implementation. These approaches are suited for scenarios with only one target or where only the closest target is of interest.

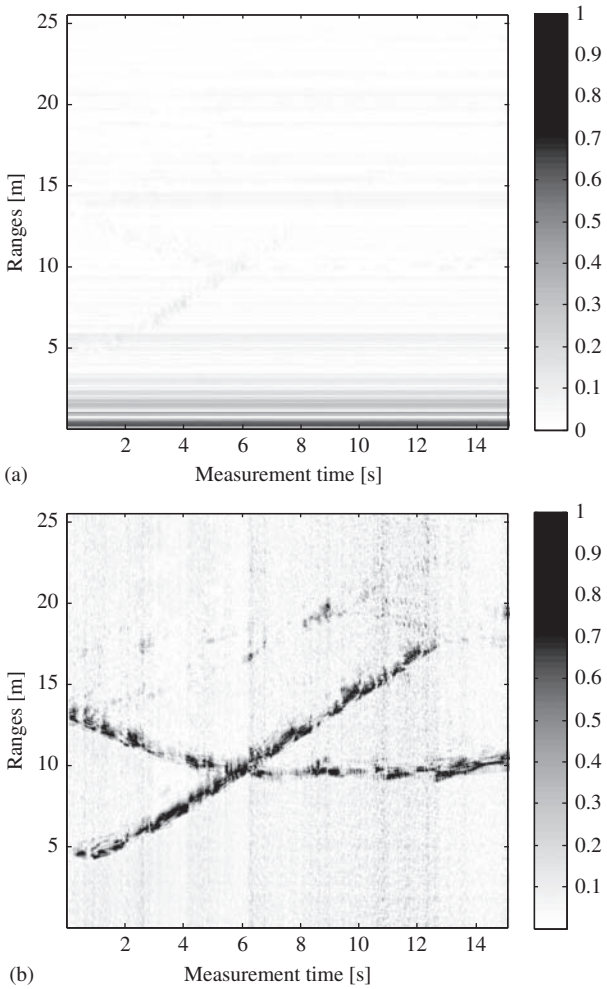

Figure 14.5 Radargram of (a) the raw radar signal and (b) the signal after background subtraction

For multiple target scenarios, more sophisticated methods are needed. For most multiple target-detection methods, the background subtraction data need to be analysed over a certain period of time to derive a test statistic and threshold values. According to these values, a decision between two hypotheses, H_0 – absence of a target and H_1 – presence of a target, should be taken. The output of the detector is then discrete corresponding to the two hypotheses. Optimum detectors often rely on Bayes or Neyman–Pearson criteria. The most common detectors in UWB systems for person detection are (N, k) detectors [27], inter-period correlation processing [28] and constant false alarm rate (CFAR) detectors [29].

CFAR detectors provide good and robust performance for through-wall moving target detection using UWB systems. Here, we give some more detail on the Gaussian-adaptive threshold CFAR detector as used in [30]. It provides the maximum probability of detection for a given false alarm rate based on the Neyman–Pearson optimum criterion. Although the detector is simple and assumes a Gaussian clutter model, it shows a good and robust performance for many through-wall scenarios. The adaptive threshold is determined using exponential weighted moving average (EWMA) filter. A test statistic X is defined using an EWMA over the unbiased, normalized signal magnitude of $u_{s,j}^{p}(t)$. The background Y is then estimated using a slower moving EWMA over the signal magnitude and the signal variance σ^2 is defined by using a slow-moving EWMA filter over the signal energy. The adaptive threshold is defined as

$$\theta = \eta\sigma + Y \tag{14.4}$$

where η satisfies

$$P_{\mathrm{FA}} = 1 - \int_{-\infty}^{\eta} \frac{1}{\sqrt{2\pi}} e^{-(1/2)\xi^2} d\xi \tag{14.5}$$

for a given false alarm rate P_{FA}. The output of the CFAR detector is then

$$H(X) = \begin{cases} 1 & \text{if } X > \theta \\ 0 & \text{if } X \leq \theta \end{cases} \tag{14.6}$$

The output is a binary sequence which is used to define the time indices of the signal when a target has been detected (the indexes of the 1's). Each index corresponds to the ToA information, $\tau_{s,j}(\mathbf{x}_t)$, of a detected person with unknown state $\mathbf{x}_t$ at time t with respect to the jth receiver of sensor s.

As a person is an extended target when UWB sensors are used for short-range localization, multiple detections per person are available. As the extent of a person with respect to the sensor resolution decreases with increasing distance, it can happen that people further from the sensors are represented by fewer observations. This has to be considered when modelling the likelihood function for statistically processing the detections.

The performance of the CFAR detector depends on the false alarm rate and the choice of parameters for the EWMA filters. Although these parameters can be adjusted, depending on the position, quality and direction of the sensors, some clutter points will still be classified as targets. These false positives hinder the target localization and should be removed.

To reduce the multiple detections per target to one, different clustering techniques can be used. Hierarchical clustering [31] with a predefined threshold corresponding to a typical spread of a person in range can be applied as the number of detected people in the scenario is unknown. However, clustering may hinder detection of multiple targets when they have similar range distance from the sensor. The range detections after CFAR and subsequent hierarchical clustering are shown in Figure 14.6.

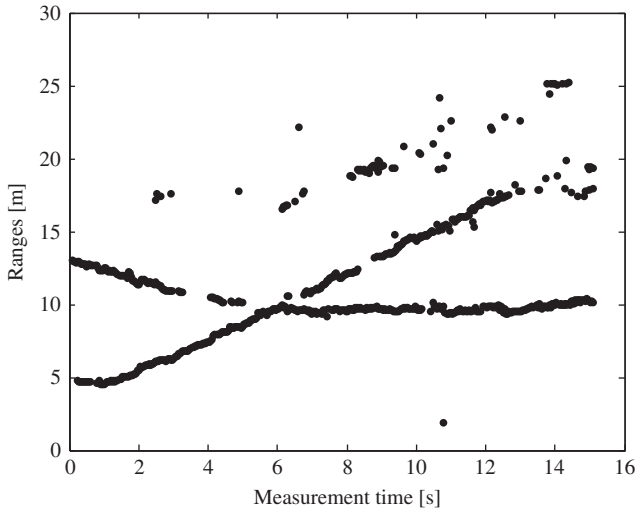

Figure 14.6 Output of CFAR based detector and range estimator

In cases where the leftover clutter and false detections after using the CFAR detector are significantly hindering the localization of the people, a range-tracking algorithm can be applied for removing the clutter and any false detections that do not follow a possible target trajectory. In through-wall scenarios, a wall effect compensation procedure as in [32] can be applied. If the walls are thin with small relative permittivity, the wall effect can be considered negligible.

14.4 Person localization principle

In single sensor localization, one UWB sensor node is used to localize and track possibly multiple people in the area of interest. Ranges are estimated for each detected person in the impulse response of each transmitter–receiver pair. The number of people detected by each sensor varies. It depends on the sensor position, antenna direction and polarization, as well as location of people in the scenario. A sensor does not always detect all people in its coverage area. Some are shadowed by other people in the area and cannot be detected. Others may move on the range ellipse of a sensor and appear as not moving to the sensor, resulting in subtraction of their echoes when the static background is subtracted. The range information of each detected person by each transmitter–receiver pair is sent to the fusion centre where this information is fused aiming to estimate the number and location of the people in the scenario at a given time. One has to be careful with fusing the range information of the detected targets. In the case of multiple targets, ghost target locations may arise. In Figure 14.7, an example of a scenario with two targets and their range estimates is presented. As can be noticed, four plausible target locations can be extracted in addition to the false intersections, out of which two are target

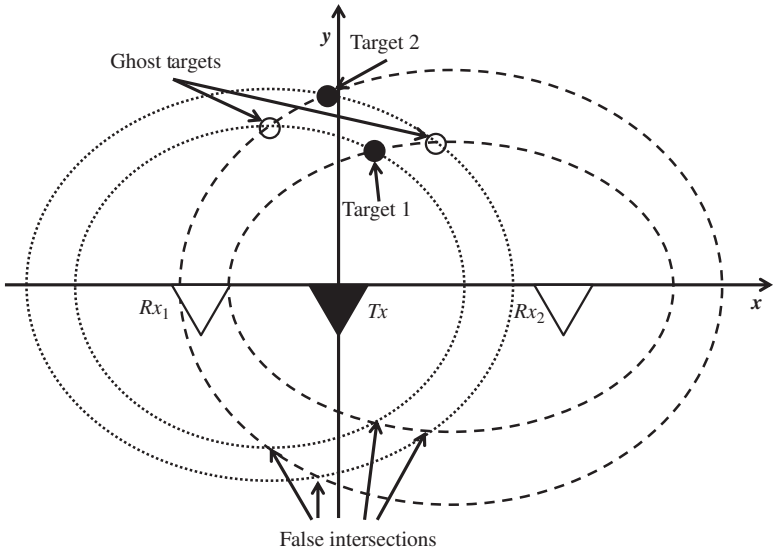

Figure 14.7 Simple scenario with two targets, their range and location estimates with the emergence of two ghost target locations

locations and two are ghost target locations. In the presence of more targets, clutter and when multiple distributed sensors are used, the problem becomes more complex. When using multiple distributed sensor nodes, one has to also consider and account for possible communication delays between the sensor nodes and the fusion centre.

Tracking methods can be applied to improve the localization of the detected people. The target location is estimated based on the current observations of the target and its previous position. In many tracking systems, simple or advanced modifications of the Kalman filter (extended, unscented, etc.) or particle filters are used.

14.4.1 Range-based localization of a single target

The true range of a target $\mathbf{x}_t$ with coordinates (x_t, y_t) at time t detected by sensor s using receiver j is defined as the distance from the transmitter to the target, $r_{Tx}(\mathbf{x}_t)$ plus the distance from the target to receiver, $r_{Rx_j}(\mathbf{x}_t)$, i.e.

$$\begin{aligned} r_{s,j}(\mathbf{x}_t) &= r_{Tx}(\mathbf{x}_t) + r_{Rx_j}(\mathbf{x}_t) \\ &= \sqrt{(x_t - x_s)^2 + (y_t - y_s)^2} + \sqrt{\left(x_t - x_{s,j}\right)^2 + \left(y_t - y_{s,j}\right)^2} \end{aligned} \tag{14.7}$$

where (x_s, y_s) are the transmitter coordinates of sensor s and $(x_{s,j}, y_{s,j})$ are the coordinates of the jth receiver of sensor s. The estimated target range is corrupted by additive noise, i.e. random distance estimation error, and can be represented as

$$d_{s,j}(\mathbf{x}_t) = r_{s,j}(\mathbf{x}_t) + e_{s,j,t} \tag{14.8}$$

where $e_{s,j,t}$ is the random distance estimation error at time t for the transmitter–receiver j channel of sensor s, i.e. additive noise of the ToA estimation.

The target range can also be expressed based on the estimated ToA, $\tau_{s,j}(\mathbf{x}_t)$, of the target using the algorithms presented in Section 14.3:

$$d_{s,j}(\mathbf{x}_t) = \tau_{s,j}(\mathbf{x}_t)\, c. \tag{14.9}$$

The target localization can then be redefined as estimation of the target coordinates (x_t, y_t) based on the set of non-linear equation (14.8) for all s and j. In the case when a single sensor is used ($s = 1$), the solution of two non-linear equations, each corresponding to one of the sensor receivers ($j = 1, 2$), should be found.

A popular method for solving the set of non-linear equations is based on Taylor series expansion [33]. The non-linear equations are linearized by expanding the Taylor series around a guess of the solution and only keeping the first-order terms. The linear equations are then solved by using the least-squares method and thus estimating the target coordinates. The solution is then used for the next iteration as a point around which the equations are linearized. The iterations continue until a predefined criterion such as minimum error is satisfied.

If a perfect ToA estimate is assumed, Equations (14.7) and (14.9) can be rewritten as

$$\tau_{s,j}(\mathbf{x}_t)\, c = \sqrt{(x_t - x_s)^2 + (y_t - y_s)^2} + \sqrt{\left(x_t - x_{s,j}\right)^2 + \left(y_t - y_{s,j}\right)^2} \tag{14.10}$$

which is the equation of an ellipse with foci (x_s, y_s) and $(x_{s,j}, y_{s,j})$ and semi-major axis $\tau_{s,j}(\mathbf{x}_t)\, c/2$ as previously explained in Section 14.2.1. The ellipse represents all possible 2D locations of a target at range $r_{s,j}(\mathbf{x}_t)$ from the sensor. As such an ellipse is defined for all transmitter–receiver pairs (s, j) where the target is detected, the target location can be estimated as the intersection point of those ellipses. A closed-form solution for the ellipse intersection problem can be derived by rewriting Equation (14.10) as a bivariate quadratic equation and solving the fourth-degree polynomial using standard linear elimination of variables (for the case of two ellipse intersections) by applying Bézout's Theorem. As the two ellipses share one focus (the transmitting node) and the major axis, there are at most two solutions as ellipse intersection points. Due to the specifics of our scenario, i.e. the sensors are on the borders of the area of interest, we can easily discard one of the intersections as it does not lie within the area of interest.

14.4.2 Multiple-sensor fusion

With the above approach, the locations of the targets detected by each sensor are estimated. A target would be typically detected by more than one sensor. In the ideal case with no ToA estimation error, the target locations estimated by each sensor coincide (Figure 14.8(a)). However, in practical applications, there is always a non-zero estimation error. The case when the range estimation error is small is shown in Figure 14.8(b). It can be observed that the target location estimates with respect to each sensor (grey point intersections) are close to the true target location

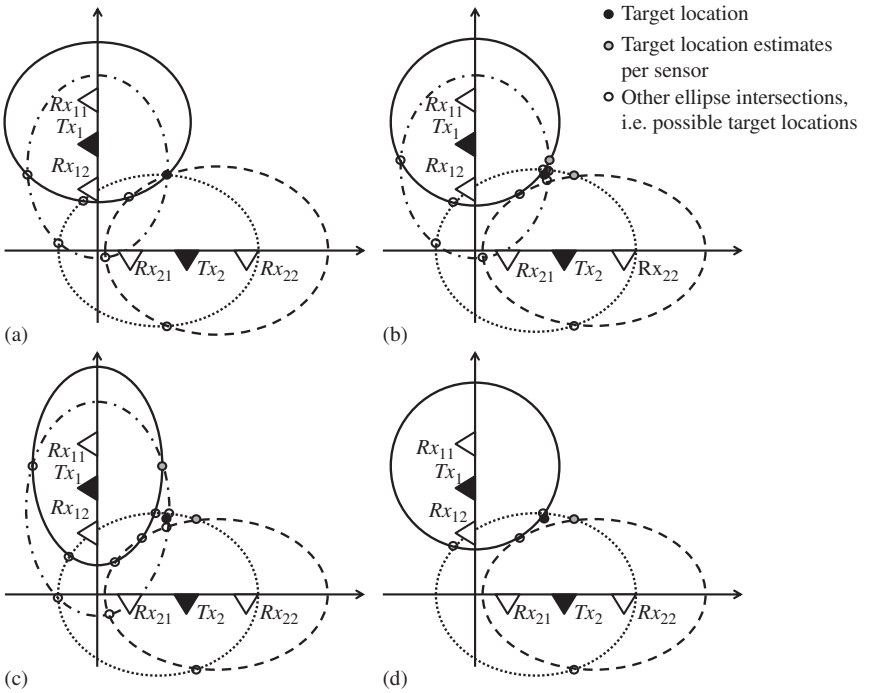

Figure 14.8 Multiple sensor localization scenarios: (a) ideal localization, no range estimation error, (b) small-range estimation error, (c) large-range estimation error by one sensor and (d) target miss-detection by one receiver of one sensor

(black point intersection). In some scenarios, such as through-wall, the range estimation error is large, leading to the situation depicted in Figure 14.8(c) where the target location estimate using sensor 1 is further from the true target location. Finally, it can also happen that a target is not detected in one of the impulse responses of a sensor as depicted in Figure 14.8(d).

The above cases have also been considered in [34] where single target localization by two UWB sensor nodes is considered. A method for joining the intersections of ellipses is proposed, where the additional ellipse intersections close to the true target position are utilized to form a cluster of intersections which is later used for target positioning. This approach is shown to be better than simple averaging of single sensor results and Taylor series methods. However, it is also computationally expensive as all possible ellipse intersections should be determined to form the cluster of intersections. In the presence of multiple targets and high clutter, this method would be impractical mainly due to the many ellipse intersections that need to be determined. In addition, in multiple target scenarios, it can happen that the cluster of intersections determines a false target location instead of two separate targets, as shown in Figure 14.9, where one target is

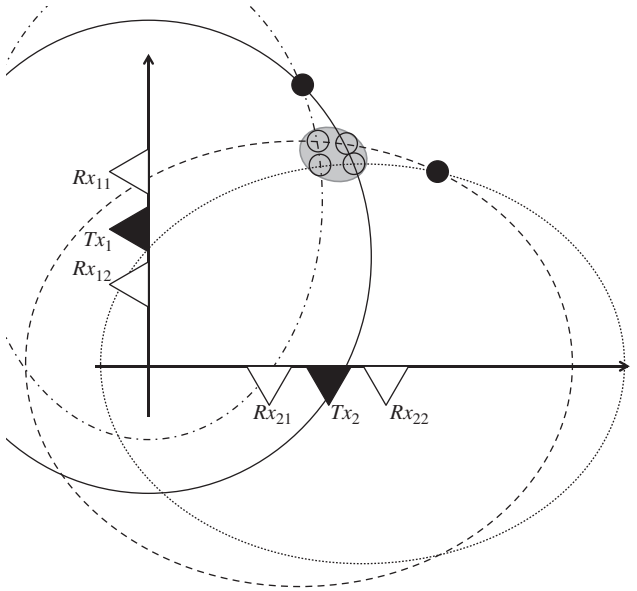

Figure 14.9 Possible false intersections chosen as single target location (grey) instead of the true locations of two targets (black)

detected by one sensor and the other target by the other sensor. If it is not known how many targets are present in the scenario, the cluster of intersections determines one target location (grey ellipse) instead of the actual two targets (black).

In this chapter, two methods for multiple target multiple sensor localization are presented. The first method is a two-step localization approach that localizes detected targets for each sensor and then fuses the estimated locations. This method has the advantage of low computational complexity as only corresponding ellipse intersections are calculated. In addition, only the estimated target locations by each sensor are sent to the fusion centre node where the target locations are fused. The second method is a direct localization approach where all range estimates by all sensors are used to determine the locations of the detected targets. Its advantage is that the range estimation errors are not directly propagated into location estimation errors and target detection of a receiver is not discarded if the other receiver of the sensor did not detect the target.

14.4.3 Tracking principle

The target-tracking problem can be summarized as an estimation of the number of targets and their states at each point in time using a set of noisy measurements and the information of the previous target states. A state contains all the relevant information to describe the target such as location, velocity and identity. Within this chapter, we consider target localization in 2D and thus a four-term target states containing the x and y coordinates of the target and the respective velocities are

estimated. Nevertheless, the methods explained here are expandable for differently defined target states.

The Bayes filter is a successful approach to the sequential estimation of the state of a dynamic system by using a sequence of noisy measurements. It requires a suitable dynamic model that describes the state evolution over time as accurate as possible and a measurement model that relates the noisy measurements to the state.

The main idea of the single-target Bayes filter is to construct a posterior probability density function (pdf) $p(\mathbf{x}_t|Z_{1:t})$ of a single-target state $\mathbf{x}_t$ based on all the available information, including the sequence of received measurements $Z_{1:t} = \{Z_1, Z_2, \ldots Z_t\}$. Recursive filtering provides an estimate sequentially every time a new measurement is available. It incorporates two stages: prediction and update. In the prediction stage of the single-target Bayes filter, the system model is used to predict the pdf of the state at a given time instant:

$$p(\mathbf{x}_t|Z_{1:t-1}) = \int p(\mathbf{x}_t|\mathbf{x}_{t-1})p(\mathbf{x}_{t-1}|Z_{1:t-1})dx_{t-1} \tag{14.11}$$

where $p(\mathbf{x}_t|\mathbf{x}_{t-1})$ is the state transition pdf defining the target motion. Equation (14.11) is also known as the Chapman–Kolmogorov equation.

In the update stage, the last received measurements are used to correct or modify the predicted pdf by using the Bayes formula

$$p(\mathbf{x}_t|Z_{1:t}) = p(\mathbf{x}_t|Z_t, Z_{1:t-1}) = \frac{p(Z_t|\mathbf{x}_t)p(\mathbf{x}_t|Z_{1:t-1})}{\int p(Z_t|\zeta)p(\zeta|Z_{1:t-1})d\zeta}. \tag{14.12}$$

$p(Z_t|\mathbf{x}_t)$ is the measurement likelihood function. From the posterior pdf, the optimal state estimates with respect to a given criterion can be computed. An analytic solution exists only in some situations such as the Kalman filter in linear-Gaussian cases. In other cases, suboptimal solutions such as Extended or Unscented Kalman filters or particle filters are used.

In case of multiple targets, the single-target Bayes filter is extended to jointly estimate the states of all targets. The multi-target Bayes filter propagates the multi-target posterior density to find an optimal solution in terms of the minimum covariance. The states of all $N_{x,t}$ targets at time t are represented by the set $X_t = \{\mathbf{x}_t^i\}_{i=1}^{N_{x,t}}$. The prediction and update equations are as follows:

$$p(X_t|Z_{1:t-1}) = \int p(X_t|X_{t-1})p(X_{t-1}|Z_{1:t-1})dX_{t-1} \tag{14.13}$$

$$p(X_t|Z_{1:t}) = \frac{p(Z_t|X_t)p(X_t|Z_{1:t-1})}{\int p(Z_t|X)p(X|Z_{1:t-1})dX} \tag{14.14}$$

where $p(X_t|Z_{1:t})$ is the multi-target posterior density that is conditional on the measurements $Z_{1:t}$ up to time t. $p(X_t|X_{t-1})$ is the transition density and $p(Z_t|X_t)$ is the measurement multi-target likelihood function. In the Finite Set Statistics terminology, the set X_t and the set $Z_t = \{\mathbf{z}_t^i\}_{i=1}^{N_{z,t}}$ are random finite sets (RFS) of

the states and observations, respectively, at time t [8]. $N_{z,t}$ is the number of observations at time t. Each $\mathbf{z}_t^i$ is either a noisy observation of one of the targets or clutter. Each target state is represented by $\mathbf{x}_t^i$. The set-based approach allows for varying number of targets to appear and disappear without any particular order while avoiding explicit data association. One thing that has to be noted here is that the integral used in Equations (14.13) and (14.14) is not an ordinary integral but a set integral as explained in [8].

As the multi-target Bayes filter is NP hard, i.e. numerically intractable, it is too complex to be applied in practical scenarios. One of its approximations based on point process theory leads to the PHD filter [8–10].

The PHD of a point process is the first-order moment of the multi-target posterior distribution. It is a multi-modal distribution over the target space and each mode, or peak, represents a high probability of target presence. As at a given time, the target population is described by a set-valued state, it operates on the single-target state space and avoids the complexities arising from data association. A drawback of this superposition target space is the loss of target identities. Thus, if the target identity is needed, target labels have to be obtained in a separate post processing step [35].

The PHD is not a pdf and its integration over any subset of the space gives an estimated number of the targets in this subset. The propagation of the posterior intensity function v_t uses the following recursion:

$$v_{t|t-1}(\mathbf{x}_t) = \int \phi_{t|t-1}(\mathbf{x}_t, \mathbf{x}_{t-1}) v_{t-1}(\mathbf{x}_{t-1}) d\mathbf{x}_{t-1} + \gamma_t(\mathbf{x}_t), \tag{14.15}$$

$$\begin{aligned} v_t(\mathbf{x}_t) &= [1 - p_D(\mathbf{x}_t)] v_{t|t-1}(\mathbf{x}_t) \\ &\quad + \sum_{\mathbf{z}_t \in Z_t} \frac{\psi_{z,t}(\mathbf{x}_t) v_{t|t-1}(\mathbf{x}_t)}{\kappa_t(\mathbf{z}_t) + \int \psi_{z,t}(\zeta) v_{t|t-1}(\zeta) d\zeta}. \end{aligned} \tag{14.16}$$

The transition density in (14.15) is defined as

$$\phi_{t|t-1}(\mathbf{x}_t, \mathbf{x}_{t-1}) = p_S(\mathbf{x}_{t-1}) p(\mathbf{x}_t|\mathbf{x}_{t-1}) + \beta_{t|t-1}(\mathbf{x}_t|\mathbf{x}_{t-1}) \tag{14.17}$$

where $p(\mathbf{x}_t|\mathbf{x}_{t-1})$ is the single target transition density, $p_S(\mathbf{x}_{t-1})$ is the probability of survival and $\beta_{t|t-1}(\mathbf{x}_t|\mathbf{x}_{t-1})$ is the PHD for spawned target birth. $\gamma_t(\mathbf{x}_t)$ is the PHD for spontaneous birth of new targets at time t. In the update Equation (14.16),

$$\psi_{z,t}(\mathbf{x}_t) = p_D(\mathbf{x}_t) p(\mathbf{z}_t|\mathbf{x}_t) \tag{14.18}$$

where $p(\mathbf{z}_t|\mathbf{x}_t)$ is the single-target likelihood function and $p_D(\mathbf{x}_t)$ is the probability of detection. The clutter intensity is defined as $\kappa_t(\mathbf{z}_t) = \lambda_t q_t(\mathbf{z}_t)$, where λ_t is the Poisson parameter defining the expected number of false alarms and $q_t(\mathbf{z}_t)$ is the clutter/false alarm probability distribution over the measurement space.

The main assumptions of the PHD filter are independence of the measurements generated by each target, the clutter is Poisson and independent from target-based

measurements and that the predicted multi-target RFS is Poisson. Two implementations of the PHD are common in literature, the Sequential Monte Carlo version [10] and the Gaussian Mixture (GM) version [9]. For the processing of the data presented in this chapter, the GM PHD was used.

For having a working multiple target tracking algorithm based on the PHD filter, defining an appropriate birth intensity is very important. The intensity of the spontaneous birth RFS is typically defined as

$$\gamma_t(\mathbf{x}_t) = \sum_{i=1}^{N_{\gamma,t}} w_{\gamma,t}^{i} \mathcal{N}\left(\mathbf{x}_t; m_{\gamma,t}^{i}, P_{\gamma,t}^{i}\right) \tag{14.19}$$

where $N_{\gamma,t}$ is the number of birth Gaussians at time t, $w_{\gamma,t}^{i}$ is the weight of the ith Gaussian with mean $m_{\gamma,t}^{i}$ and covariance $P_{\gamma,t}^{i}$. In this formulation, the intensity function of the newborn targets is independent of the measurements, and generally it covers the entire state space as new targets may appear anywhere. The mean of the newly born mixtures is chosen randomly from the state space, and the defining parameter is $N_{\gamma,t}$. Defining the birth intensity, this way is inefficient. An alternative birth intensity definition is to use only one big Gaussian with weight $N_{\gamma,t}$ at the centre of the field of view with large enough covariance to cover the whole field of view. This method is slightly more efficient; however, a measurement-based birth intensity as in [36] is the most efficient. The birth intensity also depends on whether a target is persistent or not. If a target is persistent, it cannot be considered as a newborn target. The subspaces where a target may appear are based on the previous observations and not randomly over the whole state space, i.e. newly born targets appear in regions with high likelihood. Within this work, we use the measurement-based birth intensity.

When using the GM PHD, after the update step, Gaussians with weight below a predefined threshold are pruned and Gaussians close to each other are merged. Gaussian terms with weight above a predefined confirmation threshold are considered for target state estimation [17].

14.4.4 Multiple-target–multiple-sensor two-step localization approach

In the presence of only one target, in theory, there is only one range estimate per receiver, leading to only one possible ellipse intersection for the target location. However, in the presence of multiple targets, multiple combinations of range estimates are possible giving rise to ghost target locations as shown in Figure 14.7. The calculation of the ellipse intersection points is computationally expensive and time consuming, thus it might be advantageous to first associate range estimates from both impulse responses corresponding to the same target.

In the scenarios considered in this chapter, the static sensor nodes have both receivers very close to the transmitter and thus a similar range estimate value is expected for a target by both receivers. An intersection threshold based on the range difference of a target detected by both receivers of the sensor node is defined. As the size of the area of interest A is known (or can be approximated based on the

sensor locations), the intersection threshold, T_s, for each sensor s can be calculated in advance for given transmitter and receiver positions as

$$T_s = \max_{\mathbf{x}\in A} |d_{s,1}(\mathbf{x}) - d_{s,2}(\mathbf{x})|. \tag{14.20}$$

Let ζ and χ denote two objects in the target space. If the range estimate of object ζ with respect to the first receiver, $d_{s,1}(\zeta)$, and the range estimate of object χ with respect to the second receiver, $d_{s,2}(\chi)$, satisfy

$$|d_{s,1}(\zeta) - d_{s,2}(\chi)| \leq T_s, \tag{14.21}$$

we conclude that the objects ζ and χ represent the same object. If multiple range estimates satisfy (14.21), the estimate resulting in the smallest absolute difference is chosen. The above association does not only reduce the computational load, but it also helps in reducing ghost location estimates which may result from the intersection of ellipses defined by ranges belonging to different targets, or by choosing multiple intersections of one ellipse with the other ellipses. The target location is estimated as the intersection point of the ellipses defined by the range estimates corresponding to the same target as explained in Section 14.4.1.

As a target is typically detected by more than one sensor, these location estimates are fused to result in a single target location per target. For location fusion of the estimates from the different sensors, a variation of the PHD filter explained in Section 14.4.3 is used. The observation set at time t is defined as $Z_t = \cup_{s=1}^{N_s} Z_{s,t}$, where $Z_{s,t}$ is the set of location estimates determined using the data from sensor s at time t. N_s is the number of sensors used. The observation equation is defined as $\mathbf{z}_{s,t} = H\mathbf{x}_t + \omega_{s,t}$, where $H = \begin{bmatrix} 1 & 0 & 0 & 0 \\ 0 & 1 & 0 & 0 \end{bmatrix}$ for a four-term target state, $\omega_{s,t} \sim \mathcal{N}(0, R_{s,t})$ is the observation process noise and $\mathbf{z}_{s,t}$ is the observation vector at time t with respect to sensor s. In this method, the observation $\mathbf{z}_{s,t}$ is not the directly measured parameter but the estimated location using the ellipse intersection method explained above. The observation process covariance is thus highly dependent on the range estimation error $e_{s,j}$ from (14.8) of the two transmitter–receiver pairs used for calculating the location estimate. The observation process covariance is thus defined as

$$R_{s,t} = \left(\frac{\partial r_{s,1}(\mathbf{x}_t)}{\partial \mathbf{x}_t} \sigma_{s,1,t}^{-1} \left(\frac{\partial r_{s,1}(\mathbf{x}_t)}{\partial \mathbf{x}_t} \right)^T + \frac{\partial r_{s,2}(\mathbf{x}_t)}{\partial \mathbf{x}_t} \sigma_{s,2,t}^{-1} \left(\frac{\partial r_{s,2}(\mathbf{x}_t)}{\partial \mathbf{x}_t} \right)^T \right)^{-1} \tag{14.22}$$

where $r_{s,j}(\mathbf{x}_t)$ is the range equation for a target with state $\mathbf{x}_t$ with respect to receiver j of sensor s given in (14.7), $\left(\partial r_{s,j}(\mathbf{x}_t)\right)/\partial \mathbf{x}_t$ is the Jacobian of the range equation and $\sigma_{sj,t}$ is the covariance of the range estimation error $e_{sj,t}$. The single target likelihood used within this work is

$$p(\mathbf{z}_{s,t}|\mathbf{x}_t) = \frac{1}{\sqrt{|R_{s,t}|(2\pi)^l}} \exp\left(-\frac{1}{2} (\mathbf{z}_{s,t} - H * \mathbf{x}_t)' R_{s,t}^{-1} (\mathbf{z}_{s,t} - H * \mathbf{x}_t) \right) \tag{14.23}$$

where l is the length of the measurement vector $\mathbf{z}_{s,t}$.

Linear Gaussian target dynamics are considered:

$$p(\mathbf{x}_t|\mathbf{x}_{t-1}) = \mathcal{N}(\mathbf{x}_t; F_t\mathbf{x}_{t-1}, Q_t) \tag{14.24}$$

with

$$F_t = \begin{bmatrix} I_2 & dtI_2 \\ O_2 & I_2 \end{bmatrix} \quad \text{and} \quad Q_t = \sigma_v^2 \begin{bmatrix} \frac{dt^4}{4}I_2 & \frac{dt^3}{2}I_2 \\ \frac{dt^3}{2}I_2 & dt^2 I_2 \end{bmatrix}$$

as the state transition matrix and the covariance. dt is the time interval between two observations, σ_v^2 is the variance of the process noise $v_t \sim \mathcal{N}(0, Q_t)$ and I_n and O_n denote $n \times n$ identity and zero matrices, respectively.

14.4.5 Multiple-target–multiple-sensor direct localization approach

The approach described above first associates the range estimates from the different transmitter–receiver pairs, then determines locations by ellipse intersection and finally fuses the location estimates from the different sensors and tracks the detected targets in the scenario. This method discards possible range estimates if only one of the transmitter–receiver pairs detects the target. Here, we describe a method that directly fuses all range estimates from all transmitter–receiver pairs in the scenario into location estimates and tracks the targets.

The range of the targets with respect to each transmitter–receiver pair defines the observations at time t as $Z_{sj,t} = \left\{z_{s,j,t}^i\right\}_{i=1}^{N_{z,t}^{sj}}$ where $N_{z,t}^{sj}$ is the number of targets detected by the jth receiver of sensor s. The observation set is defined as $Z_t = \cup_{s=1}^{N_s} \cup_{j=1}^{N_{s,j}} Z_{sj,t}$ where N_s is the number of sensors used and N_{sj} is the number of receivers of sensor s. The observations at time t can be defined as

$$\mathbf{z}_{sj,t} = h_{sj}(\mathbf{x}_t) + \omega_{sj,t} \tag{14.25}$$

where

$$h_{sj}(\mathbf{x}_t) = r_{s,j}(\mathbf{x}_t) = \sqrt{(x_t - x_s)^2 + (y_t - y_s)^2} + \sqrt{\left(x_t - x_{s,j}\right)^2 + \left(y_t - y_{s,j}\right)^2} \tag{14.26}$$

is the measurement equation, which is the same as the range equation (14.7), and $\omega_{sj,t} \sim \mathcal{N}\left(0, R_{sj,t}\right)$ is the observation process noise. The observation process noise is the same as the ToA estimation error $e_{sj,t}$ defined in (14.8).

The single target likelihood function for each transmitter–receiver pair is then defined as

$$p\left(\mathbf{z}_{sj,t}|\mathbf{x}_t\right) = \frac{1}{\sqrt{|R_{sj,t}|(2\pi)^l}} \exp\left(-\frac{1}{2}\left(\mathbf{z}_{sj,t} - J_h^{sj} * \mathbf{x}_t\right)' R_{sj,t}^{-1}\left(\mathbf{z}_{sj,t} - J_h^{sj} * \mathbf{x}_t\right)\right) \tag{14.27}$$

where $J_h^{sj} * \mathbf{x}_t$ is the Jacobian of $h_{sj}(\mathbf{x}_t)$ and $R_{sj,t} = \sigma_{sj,t}$ is the measurement covariance matrix for the s,j transmitter–receiver pair. The target dynamics are the same as for the two-step approach described in the above section.

14.4.6 Method comparison and experimental results

The two approaches for multiple target multiple sensor localization described above are verified on a scenario with two people moving perpendicular to each other with their paths crossing in the middle of the room. The person who has a shorter path turns and walks back. A sensor network consisting of four UWB sensor modules is used. One of the sensors (Sensor 3 in Figure 14.10) is placed behind one of the walls of the room, and the other three sensors are placed in three of the corners of the room. As mentioned earlier, each sensor consists of one transmitter and two receivers synchronized by an internal 7 GHz RF clock. About 25 impulse responses per second were measured. Directional horn antennas with different size and quality were used on all sensor nodes, resulting in varying sensor performance. No synchronisation between the different sensor nodes was considered, and all sensor nodes were running in parallel. The scenario is illustrated in Figure 14.10, where the start position of the people is shown by a circle and the end position by an arrow showing the direction of movement the person had at the end of their movement. The position of the transmitter and the two receivers of each sensor is shown in different colour for each sensor where the transmitter of each sensor is always placed between the two receivers of the sensor. The data used for target range estimation and consequently location estimation were obtained from a measurement campaign conducted at TU Ilmenau. The exact ground truth path of the motion is not available and thus for comparison a close approximation is used.

Figure 14.11(a) shows the estimated locations of the two targets by each sensor. The different colours of the location estimates correspond to the sensors whose

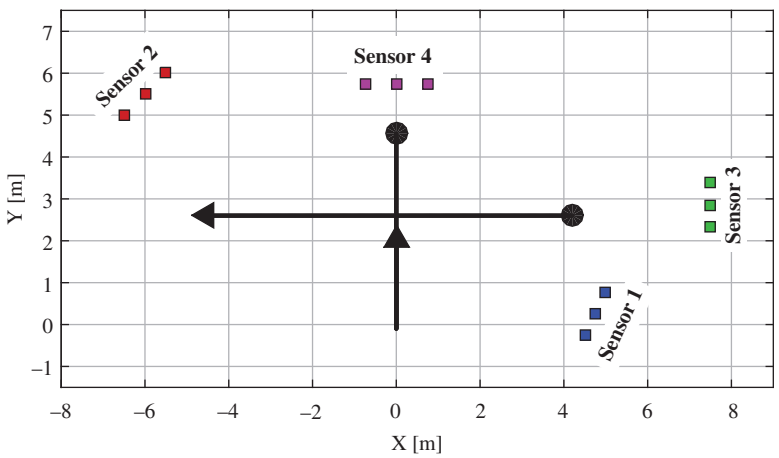

Figure 14.10 Measurement scenario used for method verification

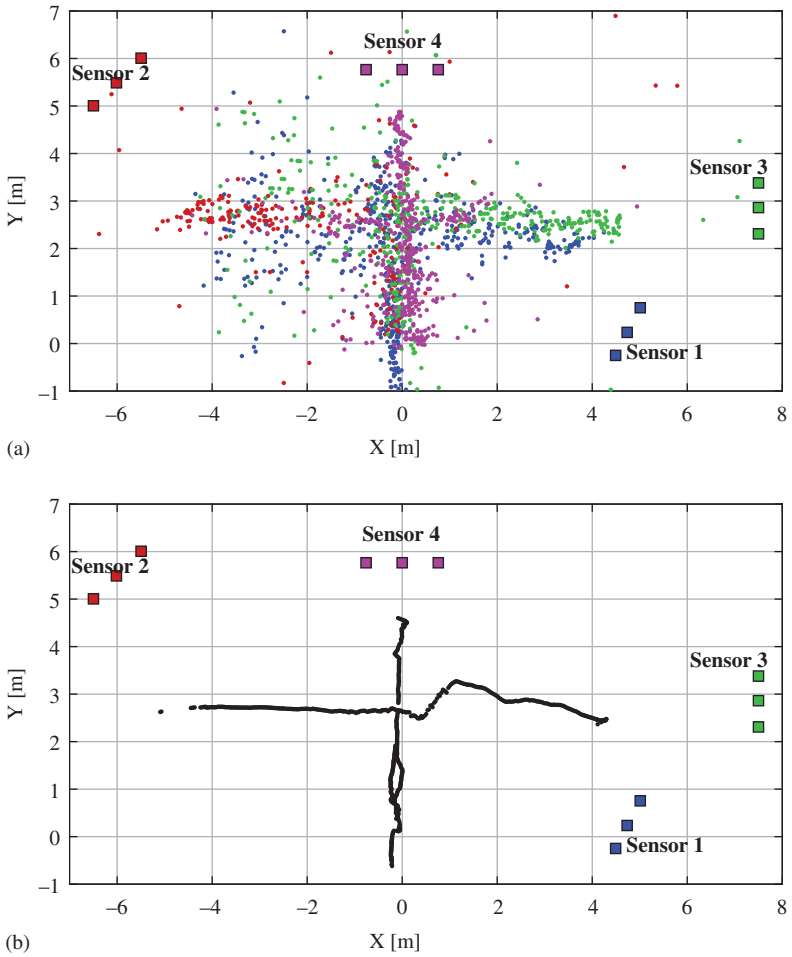

Figure 14.11 Location estimates (a) colour labelled according to the sensor that produced them and (b) fused by the fusion centre node

observations were used to determine the location. They correspond to the grey intersection points from Figure 14.8. It can be noticed that the location estimates of each sensor are less noisy when the target is closer to the respective sensor. In Figure 14.11(b), the fused location estimates are presented. As can be noticed, the fused location estimates are more accurate and less noisy than the direct location estimates per sensor and provide target tracks. The tracks of the direct localization approach are shown in Figure 14.12. As can be seen, both two-step and direct approach seem to properly track both targets and determine their locations. There are minor visible differences between the results from the two approaches, which are quantified in Figure 14.13. Here, the optimal sub-pattern assignment (OSPA) [37] metric with cut-off $c = 10$ and order $p = 1$ is shown. Although both methods

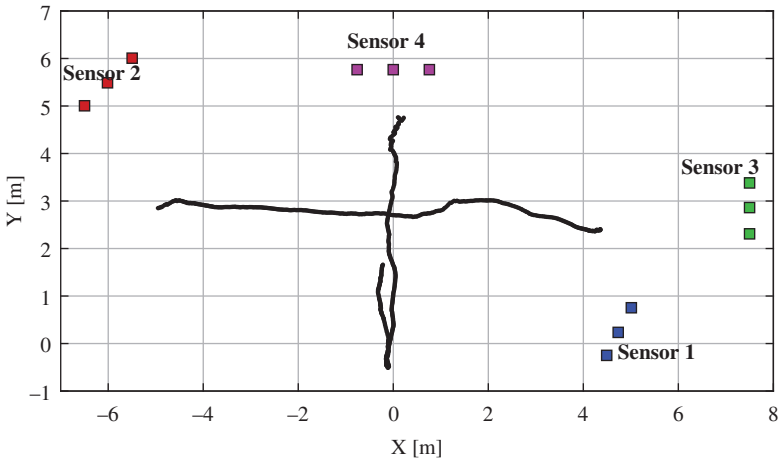

Figure 14.12 Target tracks using the direct range fusion approach

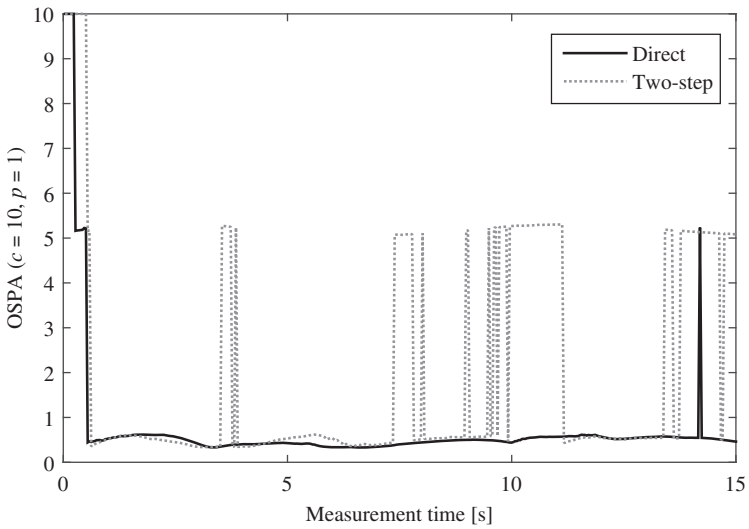

Figure 14.13 OSPA metric for the direct (dashed line) and two-step (dotted line) tracking approaches

have rather low location estimation errors, the direct approach has greater stability. For both approaches, a measurement-based birth intensity was used, and all other parameters required by the PHD filter were kept the same, except for the differences in the type of observations and likelihood function as explained in Sections 14.4.4 and 14.4.5.

14.5 Conclusion and future work

Indoor localization of people that do not cooperate with the system network, such as potential intruders, can be achieved and complemented by the use of UWB systems. Due to their high time resolution, various multipath components can be separated from the echoes of the people of interest. The large frequency spread makes UWB systems applicable for through-wall detection and localization by using the lower frequencies of the spectrum. In this chapter, the basis of UWB sensing, a structure and operating principle of a UWB sensor node and a distributed UWB sensor network is described. The main purpose of using a distributed sensor network is the extension of the coverage area and more accurate detection and localization of multiple people in the scenario. The processing of the measured impulse responses is also distributed in the network for reduction of the data transmission load between the network components.

This chapter also describes two approaches for localization of people using the measured target scatterings by the multiple sensor receivers in the sensor network. The described approaches are simplistic, computationally solid and implemented for real-time operation. The first approach relies on single-sensor localization being performed on the sensor node platform and fusion of the estimated locations at the fusion centre node using a PHD filter. The second approach does only range estimation on the sensor platform, and a direct localization and tracking PHD filter-based fusion is performed on the fusion centre platform. The approaches are evaluated in near-real-time operation in a measurement scenario using UWB baseband sounder modules as UWB sensors for the network, conducted in office scenarios that correspond closely to real application scenarios for security or smart-home applications.

The sensor network system and approach can be further improved by inclusion of other parameters corresponding to moving people, which can be extracted from the measured impulse responses. In addition, a higher cooperation level between the sensors can lead to additional information by using signals transmitted by one sensor node and received by another sensor node.

References

[1] Sachs J. *Handbook of Ultra-Wideband Short-Range Sensing: Theory, Sensors, Applications*. Wiley-VCH Verlag, Weinheim, 1st ed., 2012.

[2] Debono C., Sammut E. 'Location estimation of an intruder in wireless ad hoc networks'. *MELECON 2008 – The 14th IEEE Mediterranean Electrotechnical Conference*, 2008 pp. 158–162.

[3] Ko A., Lau H.Y.K., Lee N.M.Y. 'AIS based distributed wireless sensor network for mobile search and rescue robot tracking'. *Journal of Mathematical Modelling and Algorithms*, 2009. 8(2):227–242.

[4] Bar-Shalom Y., Fortmann T.E. *Tracking and Data Association*. Academic Press, New York, 1988.

[5] Blackman S., Popoli R. *Design and Analysis of Modern Tracking Systems*. Artech House, Norwood, MA, 1999.
[6] Pulford G.W. 'Taxonomy of multiple target tracking methods'. *IEE Proceedings – Radar, Sonar and Navigation*, 2005. 152(5):291–304.
[7] van Keuk G. 'Multihypothesis tracking with electronically scanned radar'. *IEEE Transactions on Aerospace and Electronic Systems*, 1995. 31(3):916–927.
[8] Mahler R. 'Multitarget Bayes filtering via first-order multitarget moments'. *IEEE Transactions on Aerospace and Electronic Systems*, 2003. 39(4): 1152–1178.
[9] Vo B.N., Ma W.K. 'The Gaussian mixture probability hypothesis density Filter'. *IEEE Transactions on Signal Processing*, 2006. 54(11):4091–4104.
[10] Vo B.N., Singh S., Doucet A. 'Sequential Monte Carlo methods for multitarget filtering with random finite sets'. *IEEE Transactions on Aerospace and Electronic Systems*, 2005. 41(4):1224–1245.
[11] Zetik R., Crabbe S., Krajnak J., Peyerl P., Sachs J., Thomä R. 'Detection and localization of persons behind obstacles using m-sequence through-the-wall radar'. *Proc. SPIE*, 6201, Sensors, and Command, Control, Communications, and Intelligence (C3I) Technologies for Homeland Security and Homeland Defense V, 62010I. May 2006.
[12] Zhou Y., Law C.L., Guan Y.L., Chin F. 'Localization of passive target based on UWB backscattering range measurement'. *2009 IEEE International Conference on Ultra-Wideband*, 2009 pp. 145–149.
[13] Zhao X., Gaugue A., Lièbe C., Khamlichi J., Ménard M. 'Through the wall detection and localization of a moving target with a bistatic UWB radar system'. *2010 European Radar Conference*, 2010 pp. 204–207.
[14] Zetik R., Jovanoska S., Thomä R. 'Simple method for localisation of multiple tag-free targets using UWB sensor network'. *2011 IEEE International Conference on Ultra-Wideband*, 2011 pp. 268–272.
[15] Chang S., Wolf M.T., Burdick J.W. 'Human detection and tracking via ultra-wideband (UWB) radar'. *2010 IEEE International Conference on Robotics and Automation*, 2010 pp. 452–457.
[16] He Y., Savelyev T., Yarovoy A. 'Two-stage algorithm for extended target tracking by multistatic UWB radar'. *2011 IEEE CIE International Conference on Radar*, 2011. 1:795–799.
[17] Jovanoska S., Thoma R. 'Multiple target tracking by a distributed UWB sensor network based on the PHD filter'. *2012 15th International Conference on Information Fusion*, 2012 pp. 1095–1102.
[18] Jovanoska S., Govaers F., Thoma R., Koch W. 'Dynamic-occlusion likelihood incorporation in a PHD filter based range-only tracking system'. *2015 18th International Conference on Information Fusion*, 2015 pp. 1078–1084.
[19] Zetik R., Eschrich M., Jovanoska S., Thoma R. 'Looking behind a corner using multipath-exploiting UWB radar'. *IEEE Transactions on Aerospace and Electronic Systems*, 2015. 51(3):1916–1926.
[20] Zetik R., Kmec M., Sachs J., Thomä R.S. 'Real-time MIMO channel sounder for emulation of distributed ultrawideband systems'. *International Journal of Antennas and Propagation*, 2014. 2014:16.

[21] Thomä R., Hirsch O., Sachs J., Zetik R. 'UWB sensor networks for position location and imaging of objects and environments'. *The 2nd European Conference on Antennas and Propagation*, 2007 pp. 1–9.

[22] Gezici S., Tian Z., Giannakis G., *et al.* 'Localization via ultra-wideband radios: a look at positioning aspects for future sensor networks'. *IEEE Signal Processing Magazine*, 2005. 22(4):70–84.

[23] Bartoletti S., Conti A., Giorgetti A., Win M. 'Sensor radar networks for indoor tracking'. *IEEE Wireless Communications Letters*, 2014. 3(2):157–160.

[24] Cheung S.C.S., Kamath C. 'Robust techniques for background subtraction in urban traffic video'. *SPIE Visual Communications and Image Processing*, 2004. 5308:881–892.

[25] Daniels D.J. (ed.). *Ground Penetrating Radar, Vol. 15 of IET Radar, Sonar, Navigation and Avionics*. Institution of Engineering and Technology, London, UK, 2nd ed., 2004.

[26] Piccardi M. 'Background subtraction techniques: a review'. *2004 IEEE International Conference on Systems, Man and Cybernetics*, 2004. 4:3099–3104.

[27] Spek G.A.V.D. 'Detection of a distributed target'. *IEEE Transactions on Aerospace and Electronic Systems*, 1971. AES-7(5):922–931.

[28] Taylor J.D. *Ultra-Wideband Radar Technology*. Baton Rouge, USA: CRC Press, 2002.

[29] Minkler G., Minkler J. *CFAR: The Principles of Automatic Radar Detection in Clutter*. Magellan Book Company, Baltimore, MD, 1990.

[30] Dutta P., Arora A., Bibyk S. 'Towards radar-enabled sensor networks'. *2006 5th International Conference on Information Processing in Sensor Networks*, 2006 pp. 467–474.

[31] Johnson S.C. 'Hierarchical clustering schemes'. *Psychometrika*, 1967. 32(3): 241–254.

[32] Rovnakova J., Kocur D. 'Compensation of wall effect for through wall tracking of moving targets'. *Radioengineering*, 2009. 18(2):189–195.

[33] Yu K., Montillet J.P., Rabbachin A., Cheong P., Oppermann I. 'UWB location and tracking for wireless embedded networks'. *Signal Processing*, 2006. 86(9):2153–2171. Special Section: Signal Processing in UWB Communications.

[34] Kocur D., Svecova M., Rovnakova J. 'Through-the-wall localization of a moving target by two independent ultra wideband (UWB) radar systems'. *Sensors*, 2013. 13(9):11969–11997.

[35] Panta K., Clark D.E., Vo B.N. 'Data association and track management for the Gaussian mixture probability hypothesis density filter'. *IEEE Transactions on Aerospace and Electronic Systems*, 2009. 45(3):1003–1016.

[36] Ristic B., Clark D., Vo B.N., Vo B.T. 'Adaptive target birth intensity for PHD and CPHD filters'. *IEEE Transactions on Aerospace and Electronic Systems*, 2012. 48(2):1656–1668.

[37] Schuhmacher D., Vo B.T., Vo B.N. 'A consistent metric for performance evaluation of multi-object filters'. *IEEE Transactions on Signal Processing*, 2008. 56(8):3447–3457.

This page intentionally left blank

Chapter 15

Sensor management for radar networks

Alexander Charlish[1] *and Roaldje Nadjiasngar*[1]

Abstract

Advancements in communication and information-processing technologies are driving an interest in networked radar systems, which are capable of compensating for the weaker attributes of the individual radars in the network. The role of a network of radar systems is to perform joint assessment of a surveillance region by fusing data generated at the individual radar nodes. To achieve best possible performance for the network, it is necessary to optimally configure the network and allocate its finite resources, such as radar time/energy budget, bandwidth, communication capacity and processing capacity. This chapter describes sensor and resources management techniques that can be applied to radar networks, focussing on radar network measurement scheduling and networked radar quality of service-based resources management.

15.1 Radar networks

A radar network can be envisaged in a large number of configurations, which can be characterized by a number of key features [1,2]. First, a radar network can be configured with varying degrees of coherency, which is the time period over which a local radar node knows the phase shifts at other nodes in the network. A radar network can also be characterized by the possible modes of operation, such as monostatic, bistatic or multistatic modes, as well as whether the nodes are situated on static or dynamic platforms. A monostatic radar uses common or co-located antennas, a bistatic radar uses transmit and receive antennas that are spatially separated, and a multistatic radar uses two or more spatially separated transmit and receive antennas. As a radar network has a wide scope for reconfiguration, especially if electronically steered array antennas are used, management of the configuration of the network is a key performance factor.

A network of radars performs joint assessment of a surveillance region, to generate situational awareness for the human operator. Joint assessment involves local

[1]Fraunhofer FKIE, Germany

processing of radar signals at each radar node to higher levels of information abstraction, as well as fusing data produced by the radar nodes at a desired information abstraction level. Data fusion in a radar network can be performed at the signal, detection, measurement/plot or track level, and many techniques for data fusion have been presented in the previous chapters. The way in which data in the radar network is fused can also be managed, for example, the choice of track-to-track or measurement-to-track fusion may depend on the time varying capacity of the communication links.

As with joint assessment, a radar network can perform joint management, such that the radar network resources are managed to optimize the network performance. Resources in the network are the communication capacity between radar nodes, bandwidth, the computation available at each node as well as the finite time/energy budget at each radar node. To enhance the performance of the radar network, the finite resources should be efficiently allocated and configuration control parameters for the resources optimally selected. As with data fusion, it is necessary to decide the information abstraction layer at which joint management is performed in the radar network. Joint management at a lower layer, such as the signal layer, is more complex than at higher levels as management decisions must be rapidly and reliably communicated.

15.2 Information fusion and management architectures

An architecture for a single cognitive radar was discussed in Chapter 5, which is an adapted version of the architectures by Smits *et al.* [3] and Kester [4]. The architecture is comprised of branches that represent the two key processes for a radar, which are assessment and management. At each level, knowledge is acquired and exploited to perform the assessment and management. In addition to the branches, the information abstraction levels of signal, measurement, object, situation and mission were proposed. A key characteristic of this architecture is that the data volume at the lowest level is the largest and decreases as the data is processed to higher levels of abstraction. In addition, the control time horizon and feedback cycle duration is smallest at the lowest level and longest at the highest level.

To extend the single radar architecture to a radar network architecture, it is necessary to consider which assessment and management modules are joined over the network, and which modules operate independently at each radar node. Only pure radar networks are considered; however, supplementing the radar with a network of complementary sensors has clear benefits [5,6].

15.2.1 Data fusion with monostatic radars

A radar network can apply data fusion at a specified level of information abstraction. This involves joining the assessment branches at and above the specified level, while the levels below and the management branch remain local to each radar node. The joint assessment branch can be located at a central fusion centre, such that each radar node has only local data, whereas the fusion centre has the global data. Alternatively, radar nodes can exchange data, so that the radar nodes have either all global data or data from a number of neighbouring nodes. This choice is a decision as to whether the joint assessment and hence the complete surveillance picture is

centralized or decentralized. The configuration is likely to be heavily application dependent, and many alternatives can be envisaged [7,8].

A key decision for monostatic radars applying data fusion is at which information abstraction level is data fused and the assessment branch joined. Track-to-track fusion requires the least amount of data to be communicated over the network; however, a lot of local pre-processing is applied which reduces the information available in the data fusion process. For example, a track must be extracted at each node alone, which may not be possible for difficult to detect targets. Transmission of radar measurements or plots requires a higher communication data rate but increases the information available in the data fusion process. Transmission of raw data would maximize the information in the fusion process; however, this is generally infeasible for practical applications due to the high data volume that needs to be communicated.

The following architectures can be adopted for tracking in a monostatic radar network:

Centralized Centralized tracking involves all radar nodes transmitting their measurements to a central fusion centre, which fuses the measurements into tracks. The fusion centre therefore possesses the global data, whereas each radar node only possesses local data. Although this configuration is optimal in terms of minimizing tracking mean squared error at the fusion centre, transmission of all measurements may not be possible due to limitations on the communication channel.

Distributed Like centralized tracking, distributed tracking also aggregates the global data at a centralized fusion centre. In a distributed radar network architecture, a number of radar nodes (at least one) contribute measurements to a local fusion centre which generates tracks. Then, all local fusion centres transmit local tracks to the central fusion centre, where track-to-track fusion is performed. This reduces the amount of data that needs to be communicated over the network; however, the track-to-track fusion process is suboptimal due to the cross-correlations between local tracks.

Decentralized In a decentralized tracking architecture, no central fusion centre with complete knowledge exists. Instead a large number of localized fusion centres are present, which can fuse measurements from its sensors and neighbouring fusion centres. This configuration is typical of sensor networks with a large number of small cheap sensors.

15.2.2 Coordinated monostatic radars

In addition to improving the global situational awareness by fusing data in a monostatic radar network, networked radar resource management can be applied, such that the radar management for a node is coordinated with other nodes in the network. This coordination enables the radar network resources to be management, so that the finite network resources are allocated, and the radar network is optimally configured. In addition, the deployment of the radars themselves can be managed, such as the number of nodes and locations or trajectories [9–12].

Similar to data fusion, coordinated management involves joining the management branches, such that a specified level and above are joined, and the

management levels below are performed independently at the radar nodes. Again, the joined management modules can be centralized, or distributed in the network. Centralized management has the benefit that management is based on global knowledge, however, centralized management is not scalable for large increases in the number of radar nodes and can be susceptible to communication link failures. Distributed management is based on local knowledge at the radar node and hence potentially suboptimal with respect to centralized management, but it is scalable and robust to communication link failures.

15.2.3 Multistatic radars

In a multistatic radar network, each radar node receives signals that have been transmitted by a remote radar node. This can include a single transmitter–receiver path, which is known as bistatic, or multiple transmitter–receiver paths, which is full multistatic operation. A multistatic radar network configuration ultimately increases the information generated in the network. For example, for a two-radar case, both a bistatic and a monostatic measurement can be simultaneously generated. In addition, a bistatic or multistatic configuration enables measurements of different aspects of a target, which can be beneficial for hard to detect, stealthy targets. Also, bistatic or multistatic geometries can enhance target detection in clutter, in comparison to a monostatic geometry.

A multistatic configuration places specific requirements on the assessment and management branches. Specifically, the signal management level must be jointly managed so that the transmission and reception of signals is synchronized, which is challenging due to timing constraints. For coherent operation, the radar nodes need a common phase reference, which can be achieved through a wired clock signal or alternatively through a common reference, such as the Global Positioning System. In addition, coordinated scheduling needs to be applied in the network, so that the transmit and receive beams from different radar nodes are directed towards the correct region at the correct time. For a radar network that is capable of multiple modes, the use of the multistatic mode itself may be managed. For example, the radar network may operate primarily monostatically, but schedule multistatic modes for specific targets or surveillance regions.

15.3 Radar measurement scheduling

If joint management is performed at the measurement level, then measurements from radar nodes can be scheduled based on a common set of radar tasks for the network. The tasks can be searching for new targets, or active tracking of previously detected targets. The majority of existing approaches focus on the tracking problem, which is also the topic of this section.

15.3.1 Problem formulation

The radar measurement scheduling problem considered in this section is the selection of a subset of radars in the network to generate measurements at each time instant on targets under track. The objective is to select this subset given that a constraint on the number of sensors that are active at each time step is not exceeded

and that the performance is optimized, according to a relevant criterion. As the radar network resources may be limited, a trade-off between tracking performance and resource usage can occur. In this section, it is assumed the radars are monostatic and transmit the generated measurements to a central fusion centre where measurement-to-track fusion is performed.

Let $\mathbf{x}_k$ denote the target state vector at sampling time k, which is comprised of Cartesian kinematic components, for example $\mathbf{x}_k = [x, x', y, y']^T$ where x and y are position components, and x' and y' are velocity components. As the target state is Cartesian, the target motion can be modelled by a linear state transition function $\mathbf{x}_{k+1} = \mathbf{F}_k\mathbf{x}_k + \mathbf{v}_k$ where $\mathbf{F}_k$ is a linear state transition matrix, and $\mathbf{v}_k$ is a process noise sequence with covariance matrix $\mathbf{Q}_k$. At each sampling step, measurements can be generated from a subset of radars in the network. The measurement $\mathbf{z}_k^l$ generated by node l is described by the non-linear measurement function $\mathbf{z}_k^l = h_k^l(\mathbf{x}_k) + \mathbf{w}_k^l$, where $h_k^l(\mathbf{x}_k)$ is the non-linear measurement function, and $\mathbf{w}_k^l$ is a measurement noise sequence with covariance matrix $\mathbf{R}_k^l$. The measurement function is non-linear as the radar generates polar or spherical measurements, and the target state is Cartesian.

The scheduling objective is to select an action vector $\mathbf{a}_k$ for time step k:

$$\mathbf{a}_k = \left[a_k^1, \ldots, a_k^L\right] \tag{15.1}$$

where $a_k^l \in \{0,1\}$ indicates whether radar node l is active or inactive at time step k and L is the total number of radar nodes.

15.3.2 Scheduling time horizon

In order to select the best subset of radar nodes for a time step, it is necessary to construct an objective function. Optimization criteria for radar network scheduling are discussed further in Section 15.3.3. The optimization criteria can evaluate a single action $\mathbf{a}_{k+1}$ for the next time step, or the criteria can evaluate a sequence of actions $\mathbf{a}_{k+1:k+m} = \{\mathbf{a}_{k+1}, \ldots, \mathbf{a}_{k+m}\}$ extending from time step $k+1$ over m time steps into the future.

In the following, the radar network scheduling is applied with receding horizon control, which executes the following process:

1. Track is updated to the current time k
2. All possible action sequences are evaluated over m future time steps based on the track at time k.
3. The first action from the highest evaluated action sequence is scheduled for time step $k+1$.
4. Measurements are generated based on the scheduled action for time step $k+1$.
5. Time is incremented and the process repeats.

Consequently, actions are selected at each time step based on a time horizon extending potentially over multiple steps in the future. Scheduling based only on a single step is termed myopic as it maximizes only the instantaneous reward. However, scheduling based on multiple time steps in the future is termed non-myopic, as it also considers future rewards.

For a single time step, an exhaustive evaluation of all possible actions may be possible. However, if non-myopic scheduling is performed, then the number of action sequence combinations rapidly prohibits an exhaustive search. Various methods can be used to tackle the complexity, such as tree search methods [13], or approximate dynamic programming techniques [14].

15.3.3 Optimization criteria

To select the radar node or nodes to activate for target tracking at a time step, it is necessary to formulate a selection criterion, which is the objective function used in the optimization problem. This section describes suitable optimization criteria that are valid for target tracking with single or multiple step ahead scheduling.

15.3.3.1 Posterior Cramér-Rao lower bound

The posterior Cramér-Rao lower bound (PCRLB) [15] is a filter independent lower bound on the error covariance in the target state estimate. Therefore, it is a suitable objective function when it is desired to minimize the error in the target state estimate. A detailed treatment of the PCRLB can be found in many texts, such as [15, 16, Chap. 2]. As an optimization criterion for scheduling a radar network, the PCRLB can be predicted over multiple future time steps based on the target motion model and the expected error covariances of future measurements.

Let $\hat{\mathbf{x}}_k(Z^k)$ denote an unbiased estimate of the target state $\mathbf{x}_k$ based on the set of all measurements Z^k received up to time step k. Then, the PCRLB $\mathbf{C}_{k|k}$ is defined as the inverse of the Fisher information matrix (FIM) $\mathbf{J}_k$:

$$\mathbf{C}_{k|k} \triangleq \mathbf{E}\left[(\hat{\mathbf{x}}_k(Z^k) - \mathbf{x}_k)(\hat{\mathbf{x}}_k(Z^k) - \mathbf{x}_k)^T\right] \geq \mathbf{J}_k^{-1} \tag{15.2}$$

where $\mathbf{E}$ denotes the expectation over $(\mathbf{x}_k, Z^k)$ and T denotes the transpose operator. The PCRLB can be found from the posterior FIM $\mathbf{J}_k$, which can be calculated recursively [17] according to:

$$\mathbf{J}_{k+1} = \mathbf{D}_k^{22} - (\mathbf{D}_k^{21})^T(\mathbf{J}_k + \mathbf{D}_k^{11})^{-1}\mathbf{D}_k^{12} + \mathbf{J}_{z,k+1} \tag{15.3}$$

where $\mathbf{J}_{z,k+1}$ represents the Fisher information contribution of the expected measurements generated at time step $k+1$. The terms involving the $\mathbf{D}_k$ matrices represent the contribution of the prior information on the target state from the previous time step. The $\mathbf{D}_k$ matrices are:

$$\mathbf{D}_k^{11} = \mathbf{E}\left\{-\Delta_{\mathbf{x}_k}^{\mathbf{x}_k} \ln p(\mathbf{x}_{k+1}|\mathbf{x}_k)\right\} \tag{15.4}$$

$$\mathbf{D}_k^{12} = \mathbf{E}\left\{-\Delta_{\mathbf{x}_k}^{\mathbf{x}_{k+1}} \ln p(\mathbf{x}_{k+1}|\mathbf{x}_k)\right\} \tag{15.5}$$

$$\mathbf{D}_k^{21} = (\mathbf{D}_k^{12})^T \tag{15.6}$$

$$\mathbf{D}_k^{22} = \mathbf{E}\left\{-\Delta_{\mathbf{x}_{k+1}}^{\mathbf{x}_{k+1}} \ln p(\mathbf{x}_{k+1}|\mathbf{x}_k)\right\} \tag{15.7}$$

where $p(\mathbf{x}_{k+1}|\mathbf{x}_k)$ is the state transition probability, which is modelled by a Gaussian transition density $p(\mathbf{x}_{k+1}|\mathbf{x}_k) = \mathcal{N}(\mathbf{x}_{k+1}; \mathbf{F}_k\mathbf{x}_k, \mathbf{Q}_k)$. Based on this assumption, the $\mathbf{D}_k$ matrices can be derived [17]:

$$\mathbf{D}_k^{11} = \mathbf{F}_k^T\mathbf{Q}_k^{-1}\mathbf{F}_k, \tag{15.8}$$

$$\mathbf{D}_k^{12} = -\mathbf{F}_k^T\mathbf{Q}_k^{-1}, \tag{15.9}$$

$$\mathbf{D}_k^{22} = \mathbf{Q}_k^{-1}. \tag{15.10}$$

To calculate the Fisher information contribution from the set of expected measurements associated with action $\mathbf{a}_{k+1}$ at time $k+1$, it can be assumed that the radars in the network have independent measurement processes and therefore:

$$\mathbf{J}_{z,k+1} = \sum_{l=1}^{L} a_{k+1}^l \cdot \mathbf{J}_{z,k+1}^l \tag{15.11}$$

where $\mathbf{J}_{z,k+1}^l$ is the Fisher information due to the expected measurement generated from just radar node l. The Fisher information for node l is by definition:

$$\mathbf{J}_{z,k+1}^l = \mathbf{E}\left\{-\nabla_{\mathbf{x}_{k+1}}^{\mathbf{x}_{k+1}} \ln p(\mathbf{z}_{k+1}^l|\mathbf{x}_{k+1})\right\} \tag{15.12}$$

which assuming perfect detection and no false measurements is:

$$\mathbf{J}_{z,k+1}^l = \mathbf{E}\left\{\left(\tilde{\mathbf{H}}_{k+1}^l(\mathbf{x}_{k+1})\right)^T\left(\mathbf{R}_{k+1}^l\right)^{-1}\tilde{\mathbf{H}}_{k+1}^l(\mathbf{x}_{k+1})\right\} \tag{15.13}$$

where $\tilde{\mathbf{H}}_k^l(\mathbf{x}_k)$ is the Jacobian of the non-linear measurement function for radar node l. In practice, the true target state is not known and, therefore, the Jacobian is evaluated at the predicted target state estimate. Therefore, in the following, we denote $\tilde{\mathbf{H}}_k^l$ as:

$$\tilde{\mathbf{H}}_k^l \triangleq \tilde{\mathbf{H}}_k^l(\mathbf{x}_k)|_{\mathbf{x}_k=\hat{\mathbf{x}}_k(Z^k)} = \left[\nabla_{\mathbf{x}_k} h_k^l(\mathbf{x}_k)|_{\mathbf{x}_k=\hat{\mathbf{x}}_k(Z^k)}\right]^T. \tag{15.14}$$

As no measurements are actually received when predicting the FIM m steps in the future, the Jacobian would be evaluated at the target state estimated for time step $k+m$ but based only on the history of measurements received up to time k. Imperfect detection and false measurements can be incorporated using the information reduction factor [18], modified Riccati equation [19] or enumeration method [20].

Substituting Equations (15.8)–(15.10) and Equation (15.11) into Equation (15.3) and applying the matrix inversion lemma gives a recursive form for the FIM:

$$\mathbf{J}_{k+1} = \left[\mathbf{Q}_k + \mathbf{F}_k\mathbf{J}_k^{-1}\mathbf{F}_k^T\right]^{-1} + \sum_{l=1}^{L} a_{k+1}^l \cdot \left(\tilde{\mathbf{H}}_{k+1}^l\right)^T\left(\mathbf{R}_{k+1}^l\right)^{-1}\tilde{\mathbf{H}}_{k+1}^l \tag{15.15}$$

Then, the PCRLB can be found by the matrix inversion of the FIM $\mathbf{J}_{k+1}$. This recursion can be initialized by taking the filter covariance as the initial PCRLB at time k.

Using Equation (15.15), the FIM can be predictively calculated over a single or multiple steps in the future, based on the target motion model and expected measurement covariances that result from the action sequence $\mathbf{a}_{k+1:k+m}$. The PCRLB can then be found by inverting the FIM at each of the future steps. Let $\mathbf{C}_{i|k} = \mathbf{J}_{i|k}^{-1}$ be the PCRLB at time i using the measurements received up to time k. Then, optimization criteria can be derived [13,21] from the sequence of PCRLBs, such as:

$$c_{k+1:k+m}(\mathbf{a}_{k+1:k+m}) = \sum_{i=k+1}^{k+m} \mathrm{tr}\left(\mathbf{C}_{i|k}\right) \tag{15.16}$$

where tr denotes the trace. This can be used as the basis for the following optimization problem:

$$\begin{aligned} &\underset{\mathbf{a}_{k+1:k+m}}{\textbf{minimize:}} \quad \sum_{i=k+1}^{k+m} \mathrm{tr}\left(\mathbf{C}_{i|k}\right) \\ &\textbf{subject to:} \quad \sum_{l=1}^{L} a_{k+j}^{l} \leq n \quad \forall \quad j = 1, 2, \ldots, m \end{aligned}$$

where n is the maximum number of radar nodes that can generate a measurement on a target at a single step.

Once the action sequence which minimizes the PCRLB over the m time steps is found, only the first action is scheduled, and then the process is repeated at the next time step. The PCRLB has also been used as an objective function in other sensor management problems, such as managing the deployment of sensors [9–11].

15.3.3.2 Information theoretic criteria

Information theoretic criteria can be used for radar measurement scheduling [22–24], motivated by the assumption that it is desirable to minimize the uncertainty in the surveillance picture or by the assumption that the radar network should maximize the production of information.

Entropy is a measure of the uncertainty in a random variable. Employing a measure of uncertainty is logical, as it is the role of the radar to reduce uncertainty about the environment. A radar network can be scheduled to update a target track or perform search based on the task with maximum entropy [25,26]. For search, a detection cell can be treated as a binary random variable, and hence the entropy is a function of the probability of target presence in the cell. For tracking, the prior entropy in the target state for the next time step $k+1$ but conditioned on all measurements received up to the current time k is [27, Chap. 2]:

$$H(\mathbf{x}_{k+1}|Z^k) = \int_{-\infty}^{\infty} p(\mathbf{x}_{k+1}|Z^k) \log p(\mathbf{x}_{k+1}|Z^k) d\mathbf{x}_{k+1}. \tag{15.17}$$

The posterior entropy at the current time can be written similarly by substituting $\mathbf{x}_{k+1}$ with $\mathbf{x}_k$.

Instead of scheduling based on entropy, the mutual information between two variables can be taken as a scheduling objective function. Mutual information can quantify the reduction in uncertainty in a random variable as a result of another random variable. For example, it can quantify the reduction in uncertainty in the target state $\mathbf{x}_k$ due to a new measurement $\mathbf{z}_k^l$. The mutual information can also be calculated predictively over a time horizon, based on expected future measurements. The mutual information between an expected measurement and the track state at the next time step is:

$$I(\mathbf{x}_{k+1}; \mathbf{z}_{k+1}^l | Z^k) = H(\mathbf{x}_{k+1}|Z^k) - H(\mathbf{x}_{k+1}|Z^k, \mathbf{z}_{k+1}^l) \tag{15.18}$$

which implies that the mutual information is the reduction in entropy in the target state due to the expected measurement. Let $\mathbf{z}_k^{a_k}$ denote the set of expected measurements generated from the active nodes that results from action vector $\mathbf{a}_k$. Then, the mutual information between the set of expected measurements and the target state is similarly:

$$I(\mathbf{x}_{k+1}; \mathbf{z}_{k+1}^{a_{k+1}} | Z^k) = H(\mathbf{x}_{k+1}|Z^k) - H(\mathbf{x}_{k+1}|\mathbf{z}_{k+1}^{a_{k+1}}, Z^k) \tag{15.19}$$

which is again the reduction in the entropy in the target state due to the set of expected measurements. It has been shown that entropy, mutual information and Kullback–Leibler divergence result in equivalent criteria for sensor management [28].

For multiple step ahead scheduling, it is necessary to find the mutual information between the set of states and the set of expected measurements over the time horizon. Let $\mathbf{x}_{k+1:k+m}$ denote the set of states from time $k+1$ to time $k+m$ and let $\mathbf{z}_{k+1:k+m}^{a_{k+1:k+m}}$ denote the set of expected measurements resulting from action sequence $\mathbf{a}_{k+1:k+m}$. Then, the mutual information between all states and all measurements in the time horizon can be broken down into the summation of the mutual information between each state and the measurements by applying the mutual information chain rule:

$$I(\mathbf{x}_{k+1:k+m}; \mathbf{z}_{k+1:k+m}^{a_{k+1:k+m}} | Z^k) = \sum_{i=k+1}^{k+m} I(\mathbf{x}_i; \mathbf{z}_{k+1:i}^{a_{k+1:i}} | Z^k, \mathbf{x}_{k+1:i-1}) \tag{15.20}$$

which from the definition of mutual information gives:

$$I(\mathbf{x}_{k+1:k+m}; \mathbf{z}_{k+1:k+m}^{a_{k+1:k+m}} | Z^k) = \sum_{i=k+1}^{k+m} \left(H(\mathbf{x}_i|Z^k, \mathbf{x}_{k+1:i-1}) - H(\mathbf{x}_i|Z^k, \mathbf{z}_{k+1:i}^{a_{k+1:i}}, \mathbf{x}_{k+1:i-1}) \right) \tag{15.21}$$

which is the difference in entropy between the state without the set of expected measurements and the state with the expected measurements, summed over all states in the time horizon.

In the following, it is assumed that a central extended Kalman filter is used, and consequently the state estimate is represented by a Gaussian. Therefore, the

prior is $p(\mathbf{x}_{k+1}|Z^k) = \mathcal{N}(\mathbf{x}_{k+1}; \mathbf{x}_{k+1|k}, \mathbf{P}_{k+1|k})$ where $\mathbf{x}_{k+1|k}$ and $\mathbf{P}_{k+1|k}$ denote the state and the covariance at time step $k+1$ given the measurements up to time step k. The prior entropy at the next time step but before the expected measurement is:

$$H(\mathbf{x}_{k+1}|Z^k) = \frac{1}{2} \ln\Big(\big(2\pi e\big)^{N_d} \cdot |\mathbf{P}_{k+1|k}|\Big) \tag{15.22}$$

where ln is the natural logarithm, e is its base and N_d is the number of dimensions in $\mathbf{x}_{k+1}$. It is intuitively obvious that the lower the covariance in the state estimate the lower the uncertainty and hence the lower the entropy.

The mutual information between an expected radar *measurement* and the track state (Equation (15.18)) is:

$$I(\mathbf{x}_{k+1}; \mathbf{z}^l_{k+1}|Z^k) = \frac{1}{2} \ln\Big(|\mathrm{I} + \mathbf{P}_{k+1|k} \cdot \mathbf{J}^l_{z,k+1}|\Big). \tag{15.23}$$

The mutual information between an expected *measurement set* and the track state (Equation (15.19)) has a similar form:

$$I(\mathbf{x}_{k+1}; \mathbf{z}^{a_{k+1}}_{k+1}|Z^k) = \frac{1}{2} \ln\big(|\mathrm{I} + \mathbf{P}_{k+1|k} \cdot \mathbf{J}_{z,k+1}|\big). \tag{15.24}$$

To calculate the mutual information for multiple steps ahead, it is again the case that the state estimate is represented by a Gaussian pdf and so $p(\mathbf{x}_i|Z_k, \mathbf{z}^{k+1:i}_{k+1:i}, \mathbf{x}_{k+1:i-1}) = \mathcal{N}(\mathbf{x}_i; \mathbf{x}_{i|k,i}, \mathbf{P}_{i|k,i})$ where $\mathbf{P}_{i|k,i}$ denotes the covariance at time i given the actual measurements up to time k as well as the expected measurements up to time i. Similarly, the state without the set of expected measurement has a pdf $p(\mathbf{x}_i|Z^k, \mathbf{x}_{k+1:i-1}) = \mathcal{N}(\mathbf{x}_i; \mathbf{x}_{i|k}, \mathbf{P}_{i|k})$ where $\mathbf{P}_{i|k}$ denotes the covariance at time i given only the actual measurements up to time step k. Then, the mutual information between all measurements and track states over the time horizon is:

$$I(\mathbf{x}_{k+1:k+m}; \mathbf{z}^{a_{k+1:k+m}}_{k+1:k+m}|Z^k) = \sum_{i=k+1}^{k+m} \frac{1}{2} \ln\left(\frac{|\mathbf{P}_{i|k}|}{|\mathbf{P}_{i|k,i}|}\right). \tag{15.25}$$

As the covariance matrix $\mathbf{P}_{i|k,i}$ can be written in the recursive information filter form:

$$\mathbf{P}^{-1}_{i|k,i} = [\mathbf{Q}_{i-1} + \mathbf{F}_{i-1}\mathbf{P}_{i-1|k,i-1}\mathbf{F}^T_{i-1}]^{-1} + \mathbf{J}_{z,i} \tag{15.26}$$

it is clear that calculating the mutual information and the PCRLB involve exactly the same recursion. Consequently, for the radar network scheduling scenario considered here, the PCRLB and the mutual information are similar optimization criteria. The PCRLB evaluates the covariance in the target state estimate, and the mutual information evaluates the change in entropy due to the measurements, which can be completely described by the filter predicted covariances with and without the expected measurements.

Based on the mutual information over multiple steps, the following optimization problem can be formulated:

$$\underset{\mathbf{a}_{k+1:k+m}}{\textbf{maximize:}} \quad \sum_{i=k+1}^{k+m} \frac{1}{2} \ln\left(\frac{|\mathbf{P}_{i|k}|}{|\mathbf{P}_{i|k,i}|}\right)$$

$$\textbf{subject to:} \quad \sum_{l=1}^{L} a_{k+j}^{l} \leq n \quad \forall \quad j = 1, 2, \ldots, m$$

where n is the maximum number of radar nodes that can generate a measurement on a target at a single step.

The mutual information is the change in entropy due to the measurements. Therefore, as an optimization criterion, it gives preference to accurate measurements of uncertain targets. Alternative information theoretic measures include the family of Renyi divergence (also known as alpha-divergence) measures, to which the Kullback–Leibler divergence belongs [23].

The PCRLB and information theoretic measures are bottom-up optimization criteria, as the radar network scheduling is optimized based on task-level performance without respect to the network's goal or objective, which can have disadvantages. For example, if the radar network is scheduled based on the mutual information, the generated information may not be operationally significant.

15.3.3.3 Covariance control

Covariance control [29–31] differentiates itself from the bottom-up optimization criteria as it enables the specification of a desirable goal as a covariance matrix that can be based on higher level objectives. This goal takes the form of a desired track covariance matrix $\hat{\mathbf{P}}$.

Based on the desired covariance matrix, a variety of optimization criteria can be constructed [30] for one step ahead scheduling. These criteria are based on the difference between the desired covariance matrix $\hat{\mathbf{P}}$ and the expected posterior covariance matrix $\mathbf{P}_{k+1|k+1}$ that would be achieved when radar nodes are activated from the action $\mathbf{a}_{k+1}$. If the difference $\hat{\mathbf{P}} - \mathbf{P}_{k+1|k+1}$ is positive and semi-definite, then the expected covariance is enclosed within the desired covariance, and hence the covariance requirement has been met. Therefore, a constraint can be applied:

$$\hat{\mathbf{P}} - \mathbf{P}_{k+1|k+1} > 0 \tag{15.27}$$

while the objective is to minimize the number of radar nodes that are active at each time step.

Another approach is the matrix norm algorithm where the objective is to select a sensor combination $\mathbf{a}_k$ that minimizes the norm of the difference $\| \hat{\mathbf{P}} - \mathbf{P}_{k+1|k+1} \|_2$. In this approach, the eigenvalues of the covariance difference can either be positive or negative. Positive eigenvalues imply that excess resource is allocated to the target, while negative eigenvalues imply that too little resource is allocated. By not taking into account the sign of the eigenvalues, the matrix norm algorithm does not

guarantee that the produced covariance will be within the desired covariance. The matrix norm approach can be relaxed by applying the constraint that the norm may vary within a boundary δ:

$$\| \hat{\mathbf{P}} - \mathbf{P}_{k+1|k+1} \|_2 < \delta \tag{15.28}$$

while selecting the fewest radar nodes to be active.

The norm matrix algorithm uses a single-step-ahead objective function to select the optimum sensor subset. It can be extended to multiple step ahead optimization by summing the norm over multiple steps to give the optimization problem:

$$\begin{aligned} \underset{\mathbf{a}_m}{\textbf{minimize:}} \quad & \sum_{i=k+1}^{k+m} \| \hat{\mathbf{P}} - \mathbf{P}_{i|k,i} \|_2 \\ & \sum_{l=1}^{L} a_{k+j}^{l} \leq n \quad \forall \quad j = 1, 2, \ldots, m \end{aligned}$$

The elements of the desired covariance matrix have different units, which can make the interpretation of the metrics difficult. For example, for a nearly constant velocity target dynamic, the covariance matrices have components with units m^2 and m^2/s^2, requiring a transformation which results in a common unit for each component of the matrix. In [29–31], the following transformation on $\hat{\mathbf{P}} - \mathbf{P}_{i|k,i}$ was suggested:

$$\mathbf{T}(\hat{\mathbf{P}} - \mathbf{P}_{i|k,i})\mathbf{T} \tag{15.29}$$

where $\mathbf{T}$ is a diagonal matrix based on $\hat{\mathbf{P}}$, as an example of a two-dimensional second order state vector this would be:

$$\mathbf{T} = \text{diag}\left(\left[\frac{1}{\sigma_x}, \frac{1}{\sigma_{\dot{x}}}, \frac{1}{\sigma_y}, \frac{1}{\sigma_{\dot{y}}} \right] \right) \tag{15.30}$$

where σ_x, $\sigma_{x'}$, σ_y and $\sigma_{y'}$ are the square roots of the diagonal elements of $\hat{\mathbf{P}}$.

Specifying goals, as with covariance control, have the benefit that resources are expended to achieve a mission-specific performance, instead of optimizing task-level criteria which may not be significant to the radar network objectives.

15.3.3.4 Energy and communication costs

The performance that can be achieved, determined by the selected criterion, has an associated resource cost. This resource cost can be taken as the usage of the radar at the time stage, as well as the communication cost required to transmit the radar measurement to a fusion centre. Generally, it is desired to achieve best or acceptable performance, while minimizing the resource cost. For example, when tracking is performed in the radar network, it is desirable to minimize the number of radar measurements on a target so that more resource is available for the radar network to maintain other tasks, such as searching. Minimizing the number of radar measurements while maintaining a desired performance is equivalent to the

covariance control method. In addition to minimizing the number of measurements or the number of active radars, the communication cost in the network can be optimized [21,32]. It is desirable to reduce the communication overhead required in the network, or alternatively, the radar network can be scheduled considering a constrained communication channel.

15.3.4 Simulations

In this section, simulation results for a radar network are presented, which highlight the difference between the scheduling time horizon length and the optimization criteria described in the previous section. In the simulated scenario, a target described by the two-dimensional state vector of position and velocity components $\mathbf{x}_k = [x, x', y, y']^T$ moves with a nearly constant velocity and is tracked by a network of six radars. The target initial state is $[85{,}000,\ 200,\ 85{,}000,\ 200]^T$m, and it travels for 80 s. Measurements are obtained with a sampling interval of $T = 1$ s.

As the state is Cartesian, the transition function is described by the linear transition matrix:

$$\mathbf{F}_k = \begin{bmatrix} 1 & T & 0 & 0 \\ 0 & 1 & 0 & 0 \\ 0 & 0 & 1 & T \\ 0 & 0 & 0 & 1 \end{bmatrix}, \tag{15.31}$$

and the process noise covariance is:

$$\mathbf{Q}_k = \sigma_q^2 \begin{bmatrix} \frac{T^3}{3} & \frac{T^2}{2} & 0 & 0 \\ \frac{T^2}{2} & T & 0 & 0 \\ 0 & 0 & \frac{T^3}{3} & \frac{T^2}{2} \\ 0 & 0 & \frac{T^2}{2} & T \end{bmatrix}, \tag{15.32}$$

where the target's random acceleration has standard deviation $\sigma_q = 5$ m/s ^{2}.

Figure 15.1 shows the complete target trajectory and the radar locations, which are [40, 20]km, [90, 0]km, [140, 20]km, [40, 180]km, [90, 200]km, [140, 180]km. Each radar can observe the range and bearing of the target. Therefore, the measurement function is:

$$h_k^l(\mathbf{x}_k) = \left[\sqrt{(x_l - x)^2 + (y_l - y)^2}, \operatorname{atan2}\left(\frac{y_l - y}{x_l - x}\right) \right]^T \tag{15.33}$$

where x_l and y_l are the x and y positions of radar node l, respectively. The measurement error covariance is:

$$\mathbf{R} = \operatorname{diag}\left(\sigma_r^2, \sigma_\theta^2\right) \tag{15.34}$$

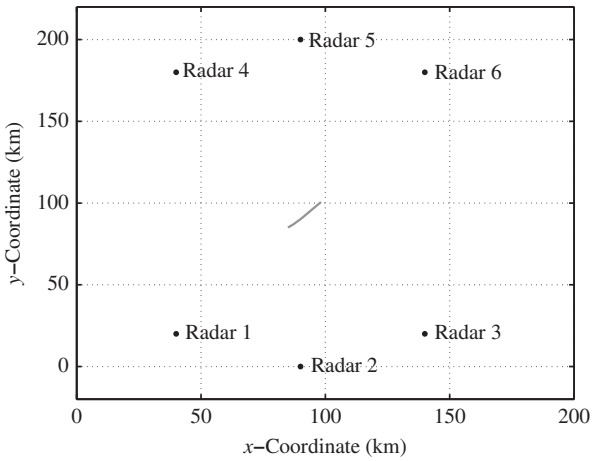

Figure 15.1 Radar network measurement scheduling scenario

The standard deviations of the measurements are given by:

$$\sigma_r = \frac{\Delta r}{k_n\sqrt{2\text{SNR}}}$$
$$\sigma_\theta = \frac{2\theta_B}{k_m\sqrt{2\text{SNR}}} \tag{15.35}$$

where Δr and θ_B are the range resolution and the antenna half beamwidth, respectively, $k_m \approx \sqrt{2}$ [33] and $k_n \approx 1.81$ [15, Chap. 2]. The SNR can be defined as:

$$\text{SNR} = \left(\frac{r_0}{r_t}\right)^4 \left(\frac{\rho}{\rho^n}\right)\left(\frac{\tau_c}{\tau_c^n}\right) \tag{15.36}$$

where r_0, ρ^n and τ_c^n are nominal values of the range, radar cross section and dwell length at which the signal-to-noise ratio is unity; τ_c, r_t and ρ are the coherent dwell length, the target range and target cross section, respectively. The parameters $r_0 = 140$ km, $\rho^n = 1$ m^2 $\tau_c^n = 60$ ms, $\tau_c = 5$ ms and $\rho = 20$ m^2 are unchanged throughout the simulations.

15.3.4.1 Single radar selection

In the first scenario, a limit is imposed such that at most one radar can generate a measurement at each time step. As the PCRLB and information theoretic criteria aim to minimize the PCRLB or maximize information production, respectively, a radar will always be active at each time step. In contrast, the covariance control approach selects either one or no radars at each step, depending on the desired covariance $\hat{\mathbf{P}}$, which is taken as $\hat{\mathbf{P}} = \text{diag}\left(\left[50^2, 15^2, 50^2, 15^2\right]\right)$.

Single-step-ahead scheduling

In the first simulation, the radar network is scheduled with a time horizon of one sampling step. The root mean squared error (RMSE) after 200 Monte Carlo runs is shown in Figure 15.2(a). It can be seen that the PCRLB and mutual information have an equivalent performance. The covariance control approach maintains a greater error in the target state estimate; however, this error is close to the specified desired error. As the optimization criterion attempts to minimize the difference

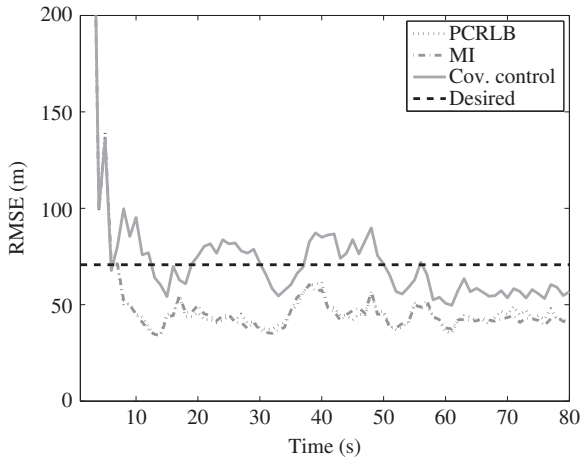

(a) RMSE

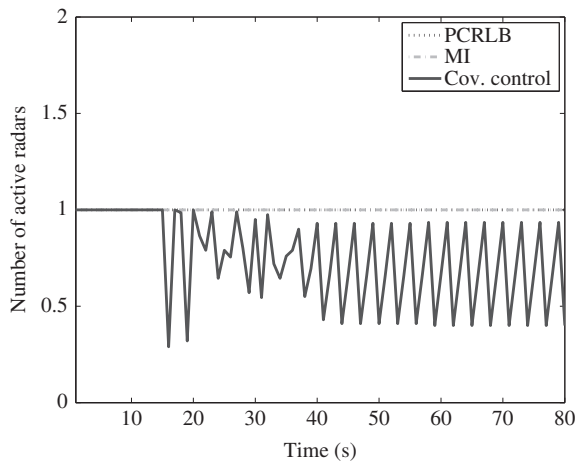

(b) Number of active radar nodes

Figure 15.2 Root mean squared error (RMSE) and number of active radar nodes for varying optimization criteria when performing one step ahead scheduling with a maximum of one active node per time step, averaged over 200 Monte Carlo runs

between the actual error and the specified desired error, the actual error may be above or below the specified desired error. It can be seen in Figure 15.2(b) that as a consequence of a greater RMSE, the covariance control approach does not schedule all nodes to be active at each time step. Hence, the covariance control approach uses only the required resource in order to achieve the desired RMSE that is specified by the desired covariance $\hat{\mathbf{P}}$.

The PCRLB aims to minimize the covariance in the target state estimate, and mutual information aims to schedule measurements to give the maximum reduction in uncertainty in the target state estimate. As a Gaussian representation was assumed, whose uncertainty is completely described by its covariance, it is clear that these criteria are equivalent for this case.

Multiple steps ahead scheduling

In the second set of simulations, the radar network is scheduled based on a multiple step future time horizon. Figure 15.3 shows the RMSE for varying step ahead scheduling for the optimization criteria. It can be seen that for all optimization criteria, the RMSE is unaffected by the number of step ahead scheduling that is

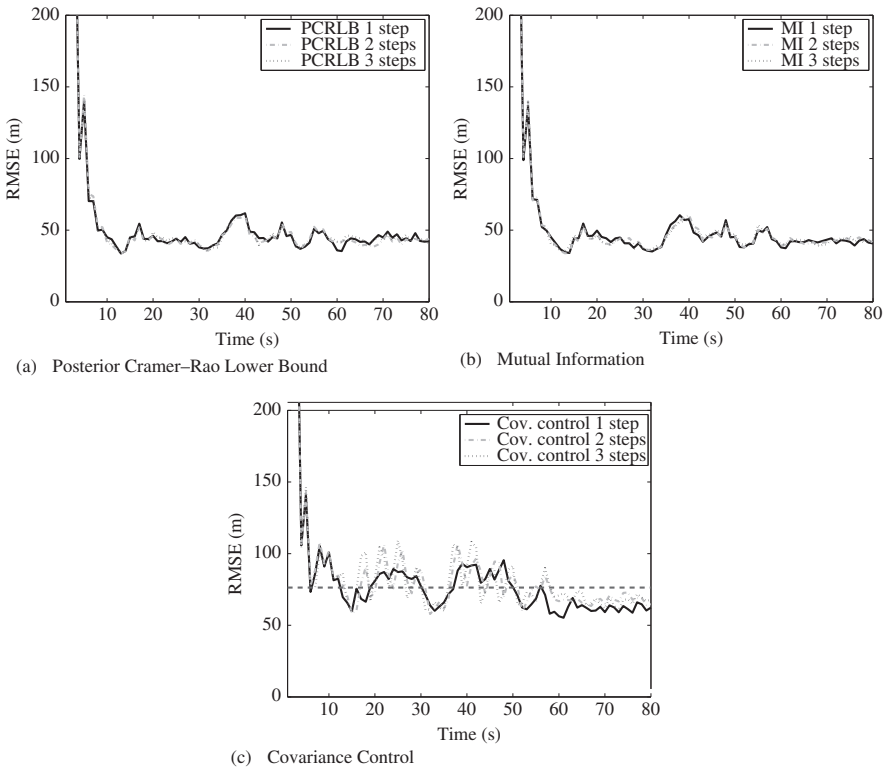

(a) Posterior Cramer–Rao Lower Bound

(b) Mutual Information

(c) Covariance Control

Figure 15.3 Root mean squared error (RMSE) for varying optimization criteria when performing multiple step ahead scheduling with a maximum of one active node per time step, averaged over 200 Monte Carlo runs

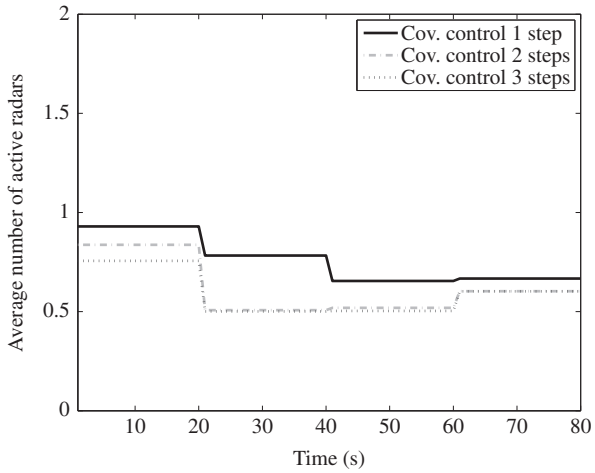

Figure 15.4 Average number of active radars per time step for multiple step ahead scheduling with covariance control criterion. The number of active radars is averaged over 20 *s intervals*

applied. This suggests that considering a future sequence of radar node activations gives no benefit in terms of the RMSE in comparison to the greedy strategy of selecting the best node for the next time step. This result echoes the recent surprising result that greedy strategies perform well for optimizing the estimation error [35].

Figure 15.4 shows the average number of active radars at each time step for the covariance control approach when scheduling with multiple time steps ahead. In the figure, the number of active radars has been averaged over 20 s intervals. The PCRLB and mutual information criteria have not been plotted, as they always select one sensor at each time step. It can be seen that multiple step ahead scheduling can reduce the number of active radars and hence the resource usage.

For this example, scheduling the network multiple steps in the future does not necessarily improve the RMSE; however, it does enable a reduction in the number of active radar nodes when covariance control is applied. Multiple step ahead scheduling would also be beneficial in complex scenarios, such as occlusions to the radar line of sight [36] or when there are many more targets than radar nodes.

15.3.4.2 Multiple radar selection

In the next set of simulations, the maximum number of active nodes at each time step was increased from one to four. The RMSE for one step ahead scheduling using the varying optimization criteria is illustrated in Figure 15.5(a). Similar to the previous results, it can be seen that the PCRLB and information theoretic criteria maintain an identical low RMSE. The covariance control maintains a greater RMSE, however, this is close to the specified desired error.

The number of active radars per time step is plotted in Figure 15.5(b). It can be seen that the PCRLB and the mutual information criteria always schedule four

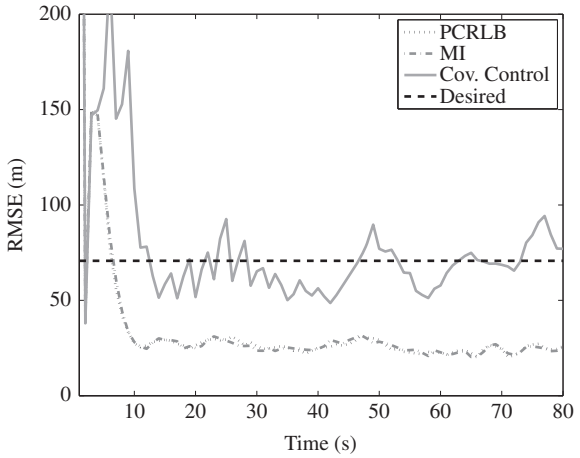

(a) Root mean squared error (RMSE)

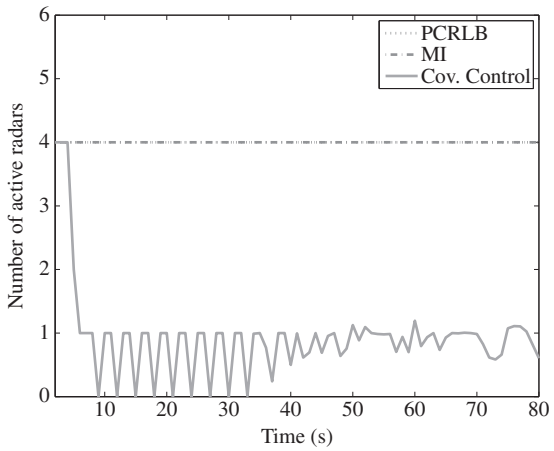

(b) Number of active radar nodes

Figure 15.5 Root mean squared error and number of active radar nodes for varying optimization criteria when performing one step ahead scheduling to select a subset of radar nodes, averaged over 200 Monte Carlo runs

active nodes, as this minimizes the PCRLB and maximizes the mutual information production, respectively. The covariance control approach aims to meet the specified covariance with the minimum number of active nodes and, therefore, significantly fewer radar nodes are active at each time step.

15.3.4.3 Discussion

Scheduling based on the PCRLB or mutual information has the disadvantage that it does not consider operational requirements. It is quite unlikely that the minimum

estimation error covariance or maximum information production is the ultimate objective of the radar system. It is more likely that estimation error bounds could be specified or a certain amount of information is required only on specific targets. The benefit of the covariance control approach is that it provides a mechanism to enable scheduling based on a track quality requirement. Despite this, for surveillance applications the track estimation error may be of less importance in comparison to track continuity or purity. In which case, alternative optimization criteria are required.

In these simulations, it was assumed that a perfect communication channel exists between the fusion centre and the radar nodes, which is not a realistic assumption. Measurement scheduling for the radar network would require a very reliable low latency communication. However, the result that multiple step ahead scheduling does not strongly influence the RMSE indicates that the sequence of measurements executed by the network is less important than the selection of the nodes to make the measurements. Therefore, a less communication intensive configuration can be to apply radar network management at the object level, while each radar node performs independent scheduling of measurements. This configuration is the topic of the next section.

15.4 Networked quality of service management

The radar network scheduling methods in the previous section optimize the scheduling of measurements from the available radars in the network. Alternatively, the radar network resources can be managed, while the scheduling of measurements is performed independently at each node. A quality of service (QoS) framework [37,38] can be used for the management of the multiple radar resources in the network [39,40]. This can combine both the assignment of tasks to radars as well as task control parameter optimization. In this section, it is assumed that the network comprises monostatic radars performing measurement-to-track fusion.

15.4.1 Management algorithms and network configurations

In this section, four different radar network configurations and management algorithms are considered. These algorithms differ in terms of whether QoS management or rule-based management is applied, whether the management is performed locally for each node or centrally for the whole network, and whether the fusion centre feeds fused track information back to each of the radar nodes. The radar network configurations are illustrated in Figure 15.6 and described in detail in the following sections.

15.4.1.1 Local rule-based management (RBM) without feedback

The local rule-based management without feedback approach (Figure 15.6(a)) selects task control parameters locally at each node based on rules that use only the local information available at the node. The rules can exploit varying degrees of

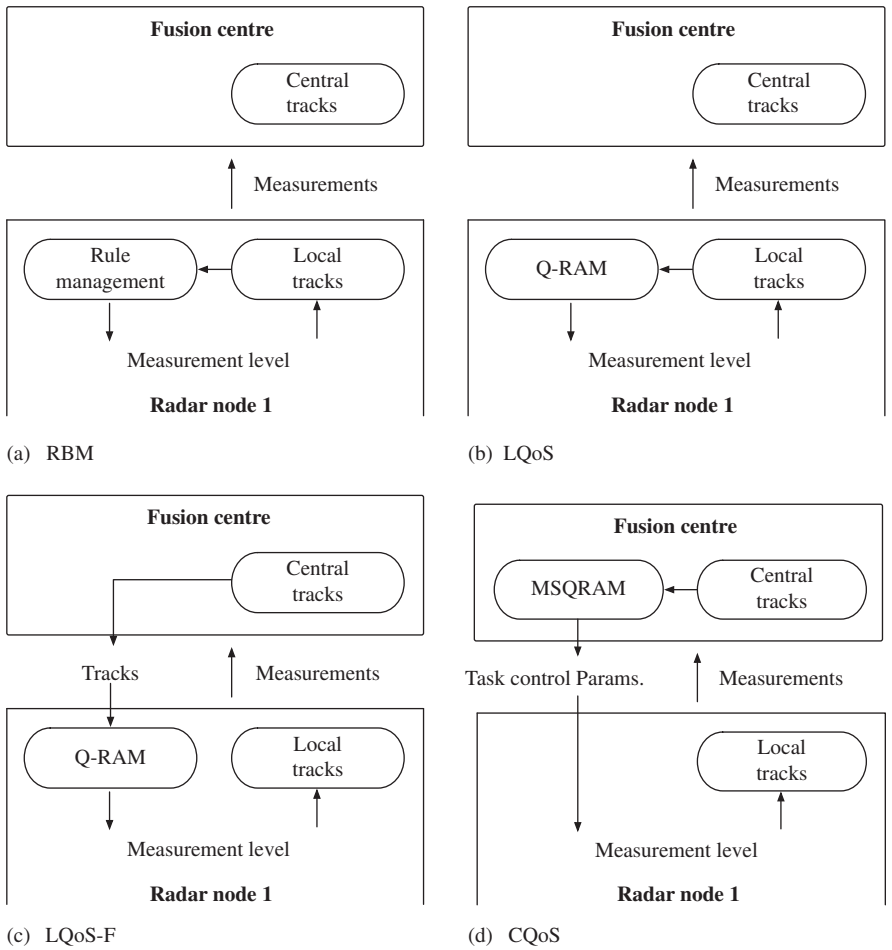

Figure 15.6 Considered network configurations and management algorithms

track information. As an example, the following rules can be applied for selecting tracking task control parameters:

- The dwell length for a target track update is varied to achieve a specified expected received SNR based on an estimate of the target radar cross section. Consequently, shorter dwells are used for closer targets and longer dwells for farther targets.
- The revisit interval between target track updates is fixed (e.g. 2 s).
- The finite radar time budget is allocated to targets in order of priority. For equal priority targets, the time budget can be allocated to targets that use the least temporal loading first.

These rules are applied in the following simulations.

Each radar node performs independent tracking and management; however, the radar nodes also transmit the measurements that are generated to a fusion centre where measurement-to-track fusion is performed. Only simplex communication is required, and failure in the communication links would not affect the radar nodes but would degrade the quality of the tracks at the fusion centre.

15.4.1.2 Local QoS management (LQoS) without feedback

The local QoS management without feedback configuration is illustrated in Figure 15.6(b). This approach is identical to the rule-based approach; however, QoS management is applied locally at each radar node instead of applying rules. The reader is referred to Chapter 5 for a detailed treatment of QoS management for a single radar. Applying local QoS management to all nodes in a network results in a set of locally optimized resource allocations based only on local information.

As with the rule-based approach, each radar node performs independent tracking and management but also transmits measurements to a central fusion centre where measurement-to-track fusion is performed. Only simplex communication is required, and failure in the communication links would not affect the radar nodes but would degrade the quality of the tracks at the fusion centre.

15.4.1.3 Local QoS management with feedback (LQoS-F)

The local QoS management with feedback configuration is illustrated in Figure 15.6(c). This approach also applies local QoS management; however, the management is based on the fused track information that is fed back from the fusion centre to the radar nodes. Therefore, the local management of the radar node can be based on all the information in the network. This approach leads to a set of locally optimized resource allocations based on the global network information.

This approach requires more communication as it is necessary for the fusion centre to distribute the global track information back to the radar nodes. If a communication link failure would occur between the fusion centre and a node, then the node can fall back to using only local track information. In addition, more communication (duplex) is required when compared to the management without feedback.

15.4.1.4 Centralized QoS management (CQoS) and fusion

In the centralized QoS management and fusion approach, the fusion centre receives measurements from all radar nodes and performs measurement-to-track fusion like for the previous methods. However, in this case, QoS management is applied centrally at the fusion centre for the entire network, based on the complete fused information. This network QoS management approach is described in detail in Section 15.4.2. The selected task control parameters for a radar node are coordinated with the control parameters selected at all the other nodes in the network. This approach leads to a set of globally optimized resource allocations based on the global network information. However, as the fusion centre controls the radar nodes, this approach is susceptible to communication link failures.

15.4.2 Multi-resource QoS problem

This subsection describes the centralized QoS management problem, which extends the single radar QoS problem formulation given in Chapter 5.

For the radar network case, there exists a set of K independent radar tasks $T = \{T_1, \ldots, T_K\}$, which must share the radar resources available at the L radar nodes $r = \{r_1, \ldots, r_L\}$. Let v_{kl} denote the control parameter selection for task k at radar l and let $v_k = \{v_{kl} | l = 1, \ldots, L\}$ be the set of parameter selections for task T_k for all radar nodes. Then, it is desired to select the set of complete control parameters $v = \{v_k | k = 1, \ldots, L\}$ for all tasks and all radar nodes. The parameter selection v_{kl} is itself a set of parameters with a number of dimensions which depends on the task, i.e. $v_{kl} = \left\{v_{kl}^1, v_{kl}^2, \ldots, v_{kl}^{M_{kl}}\right\}$ where M_{kl} is the number of control parameter dimensions for task T_k at radar l. The uncontrollable environmental parameters for task k are denoted e_k, which impact on the resource loading and quality achieved by the radar network.

The calculation of the resource loading is denoted by a resource function that maps the operational and environmental parameters into resource space:

$$r_{kl} = g_{kl}(v_{kl}, e_k) \tag{15.37}$$

The resource available at each radar node is constrained and so the resource function:

$$g_l(v) = \left(\sum_{k=1}^{K} g_{kl}(v_{kl}, e_k)\right) - r_l \tag{15.38}$$

must satisfy the set of resource constraints:

$$g_l(v) \leq 0 \quad \forall l \in \{1, \ldots, L\} \tag{15.39}$$

The control parameters selected at each radar node affect the performance that a radar task can achieve over a time horizon in the future, which is calculated through a quality function:

$$q_k = q_k(v_k, e_k) \tag{15.40}$$

Note that the quality achieved for the task depends on the control parameters for the task selected by all radar nodes.

The mission-specific requirement for task k is represented by a utility function, which describes the satisfaction associated with a task quality, and a task weighting, which describes the mission relevance of the task. The utility function is denoted as:

$$u_k = u_k(q_k(v_k, e_k)) \tag{15.41}$$

The task weight of task k is denoted ω_k and:

$$\sum_{k=1}^{K} \omega_k = 1 \tag{15.42}$$

The mission effectiveness can then be found as a weighted sum of task utilities:

$$u(v) = \sum_{k=1}^{K} \omega_k \cdot u_k(q_k(v_k, e_k)) \tag{15.43}$$

This mission effectiveness represents the ability of the radar system to meet the mission-specific task quality requirements.

The effective radar network resource management problem can be formulated as a constrained optimization problem:

$$\begin{aligned}
&\textbf{maximize:} \quad u(v) = \sum_{k=1}^{K} \omega_k \cdot u_k(q_k(v_k, e_k)) \\
&\textbf{subject to:} \quad g_l(v) \leq 0 \quad \forall l \in \{1, \ldots, L\} \\
&\textbf{where:} \quad g_l(v) = \left(\sum_{k=1}^{K} g_{kl}(v_{kl}, e_k) \right) - r_l
\end{aligned}$$

15.4.2.1 Optimality conditions

As shown in [39], the optimality conditions for the radar network QoS management problem can be derived in a similar way to the single radar case described in Chapter 5. The solution must be primal and dual feasible and either use all available resource or alternatively have no possible utility increase for further resource allocation. In addition, the stationarity condition must be satisfied, which can be re-arranged to give [39]:

$$\begin{aligned}
\mu_l = \frac{\partial_m \omega_k \cdot u_k(q_k(\{v_{k1}^*, \ldots, v_{kl}^*, \ldots, v_{kL}^*\}, e_k))}{\partial_m g_{kl}(v_{kl}^*, e_k)} \quad & \forall k \in \{1, 2, \ldots, K\} \\
& \forall l \in \{1, 2, \ldots, L\} \\
& \forall m \in \{1, 2, \ldots, M_{lk}\}
\end{aligned} \tag{15.44}$$

where ∂_m denotes the partial derivative with respect to v_{kl}^{m*}, as v_{kl} is itself a vector $v_{kl} = \{v_{kl}^1, v_{kl}^2, \ldots, v_{kl}^{M_{kl}}\}$. The stationarity condition implies that the gradients in resource utility space for all tasks at a specific radar node must be equal. However, the gradients can be different for each of the numerous radar nodes.

15.4.2.2 MSQRAM algorithm

The original Q-RAM algorithm can be extended to solve the network radar resource management problem formulation. To solve the problem, as described in the previous section, the marginal utilities and hence Karush–Kuhn–Tucker (KKT) multiplier for all tasks at a radar node must be equal. However, the marginal utilities and hence KKT multiplier need not be equal for all radar nodes. Consequently, the algorithm allocates resource while maintaining the gradients as close to

equal as possible at each radar node, while ensuring that all nodes run out of available resource at the same time. This is done by allocating resource to the radar with the most available resource and then to the task at that radar with the largest marginal utility. By switching between radars in this manner, the algorithm ensures all radars run out of resources at the same time, and the marginal utilities decrease at each radar similarly to the original Q-RAM method.

The proposed algorithm for solving the multiple resources QoS problem applies the following procedure:

1. The resource and utility values for every possible parameter selections are evaluated for every task for all radar nodes.
2. The concave majorant [41] for each task is extracted from the complete set of all possible parameter selections.
3. Each task is initialized with the feasible parameter selection that uses the least amount of resource.
4. The radar node with the greatest resource availability is selected.
5. Resource is allocated to the task whose next parameter selection on the concave majorant has the largest utility per resource increase, for the radar selected in step 4.
6. Step 4 is repeated until it is no longer possible to allocate anymore resource.

Both methods require the concave majorant to be evaluated. The convex hull operation becomes particularly computationally intensive as the number of radar nodes increases.

15.4.3 Performance model

As described in the previous section, a resource function (Equation (15.37)) and quality function (Equation (15.40)) are sought. As the problem considered here is target tracking, the standard deviation of the estimation error is taken as the quality measure. This section describes a method for numeric evaluation based on covariance analysis.

The covariance analysis procedure predictively evaluates the track estimation error standard deviation over a time horizon starting from the current time. This is based upon a possible operational parameter selection set for each radar, which is taken here as the coherent dwell time and the revisit interval time between measurement updates. An estimate of the target kinematic parameters and radar cross section at the current time is available, along with the associated estimation error covariance matrix. These estimates are used to give the environmental parameters, which are the target range, angle and radar cross section.

The covariance analysis procedure calculates the measurement times for each radar during the time horizon, based on the revisit interval times. At each measurement time, an expected measurement update is performed and between measurement times the track is predicted. This process gives a prediction of the estimation covariance matrix over the time horizon, which is used to calculate the quality.

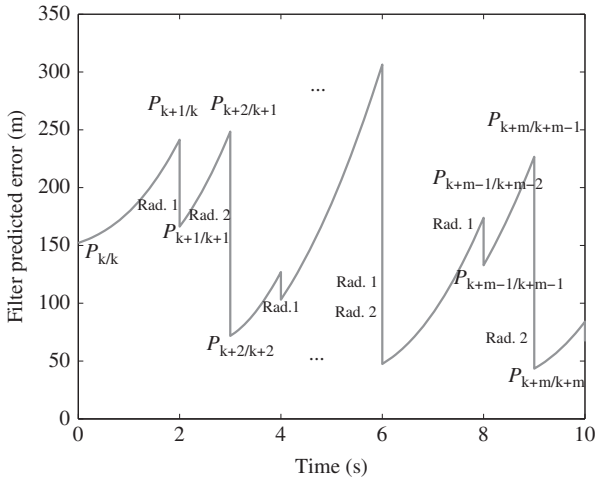

Figure 15.7 Covariance analysis procedure for two radars with operational parameters $\nu_{11} = \{5\ ms, 2\ s\}$ and $\nu_{21} = \{5\ ms, 3\ s\}$. Rad. 1 represents the time when an update for radar one is performed, and Rad. 2 represents the time when an update for radar two is performed. ©2015 IEEE. Reprinted, with permission, from Reference [42]

This covariance analysis procedure is illustrated in Figure 15.7 for two radars with operational parameters $\nu_{11} = \{5\ \text{ms}, 2\ \text{s}\}$ and $\nu_{21} = \{5\ \text{ms}, 3\ \text{s}\}$. It can be seen that the radars generate measurements at different times. It can also be seen that the measurement quality of radar 2 is better than that of radar 1, resulting in a larger drop in the estimation error. The greatest drop in the estimation error occurs at time $t = 6$ s, when both radars perform a measurement.

15.4.4 Simulations

In this section, all four resource management and network configuration approaches are analysed for a radar network comprising of two radar nodes. Each radar has a field of view of $[-60, 60]^\circ$ in bearing. The radars can achieve a unity signal-to-noise ratio at a range $r_0 = 300$ km with a nominal dwell length of 60 ms for a target on the antenna boresight with radar cross section of $\rho^n = 1\ \text{m}^2$. A radar range resolution of $r = 200$ m, beamwidth $\theta_{B0} = 1.5^\circ$ and false alarm probability $P_{\text{FA}} = 10^{-5}$ are chosen. These parameters are considered for the generation of radar measurements as well as for calculating the quality and utility values for the resource allocation.

A scenario of 20 targets (Figure 15.8) distributed uniformly over the radars' field of view is considered. All the targets have identical radar cross sections of $\rho = 20\text{m}^2$ and move with a nearly constant velocity with initial velocity selected randomly from the set $[10, 20, \ldots, 200]\ \text{m/s}^2$. The targets' motion is disturbed by random acceleration with standard deviation $\sigma_q = 5\ \text{m/s}^2$.

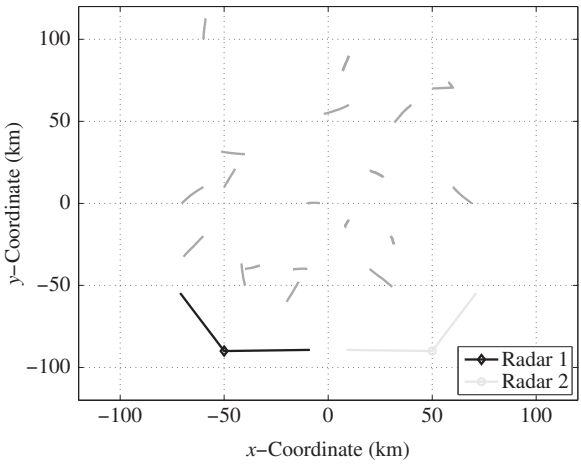

Figure 15.8 Scenario consists of 20 targets moving at nearly constant velocities

For management approaches that apply QoS management, a dwell from $[1, 2, \ldots, 10]$ ms and a revisit interval from $[1, 2, \ldots, 8]$ s can be selected by each radar node for each task. The rule-based method assumes fixed SNR of 22 dB and a fixed revisit interval of 1 s. Twenty Monte Carlo runs for each of the four management methods are performed.

Network tracking performance

Figure 15.9(a) and (b) shows the number of active tracks and the average trace of the covariance matrices over the number of active tracks. It can be seen that CQoS maintains the greatest number of tracks and also achieves the lowest error in the active tracks. This is to be expected as it performs joint optimization of all the radar node control parameters based on the complete network information. It can also be seen that LQoS-F maintains the same number of active tracks as CQoS but with a slightly greater average error. As the performance of LQoS-F comes close to centralized management, it can be applied as a compromise between achieving good estimation error and relaxing the constraint on the required communication. LQoS is noticeably worse, and RBM is worst overall.

Network resource allocation

The total amount of network resource allocated to each active track is illustrated proportionally to the size of a circle in Figure 15.10(a)–(d). The network resource is the summation of the resources allocated to a target by all radar nodes. The redundancy in the resource allocation for RBM and LQoS is clear, as a lot of resource is allocated to targets that are close in range. In comparison, LQoS-F, which is based on the global information, allocates less resource to nearer targets and more to farther targets. This behaviour is even more noticeable for CQoS.

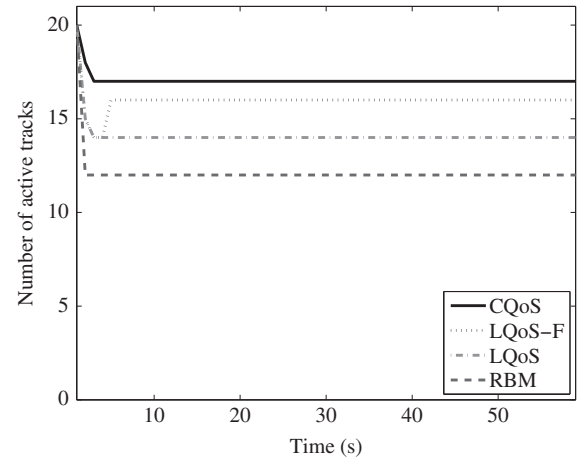

(a) Number of active tracks

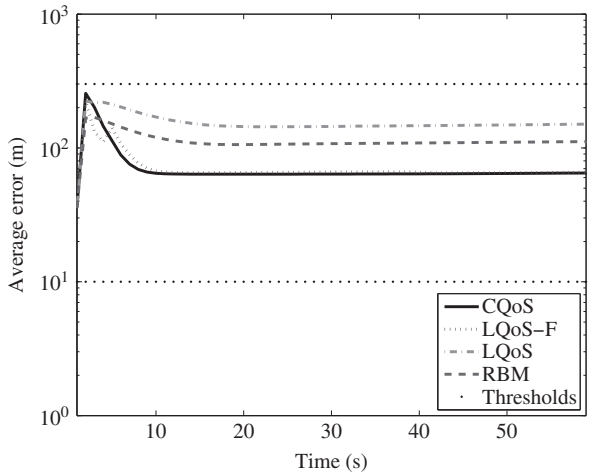

(b) Average RMSE

Figure 15.9 Comparison of number of active tracks and average RMSE for the different resource management methods and network configurations

Task quality

The average RMSE in the active tracks is illustrated in Figure 15.11(a)–(d) by the size of the circles. It can be seen that for the local rule-based approach, a good quality is achieved for near targets but far targets or targets at the edge of the field of view are not maintained or have a poor quality. This is due to the redundant allocation of resources to near targets. The local QoS management approach demonstrates a similar effect. LQoS-F, which performs local optimization based on global information, allocates less resource to nearer targets and uses this resource to

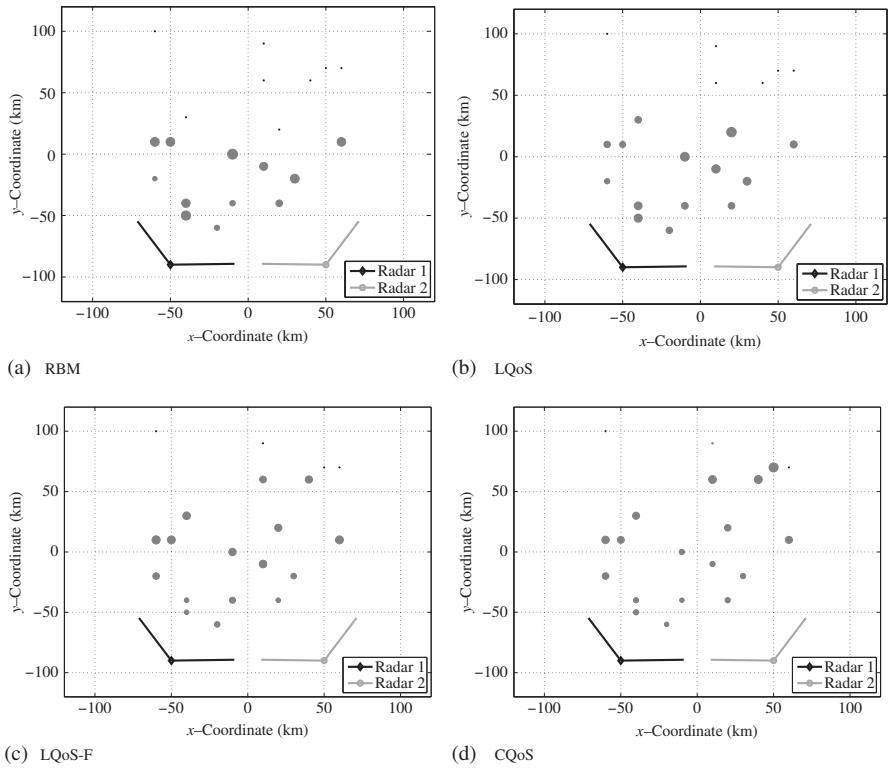

Figure 15.10 Total network resource allocation to each target is illustrated by the size of the circle for the different resource management methods and network configurations

improve the quality of far targets. CQoS achieves a good quality for all targets, as it eliminates the resource allocation redundancy.

15.5 Summary

A network of radars has substantial scope for configuration and, therefore, sensor management in the radar network can play a key role in ensuring best possible performance for the encountered scenario. By performing joint measurement management across the network, a subset of radars can be scheduled to generate measurements of a target under track. In this chapter, it was shown that scheduling based on the PCRLB or mutual information minimizes the track error but does so without consideration of the mission requirements. In contrast, covariance control methods schedule radar nodes such that a desired mission-specific track quality is achieved. An alternative approach is to perform joint management at the object level, in the form of QoS-based resource management, while each node performs independent scheduling. This chapter demonstrated that centralized QoS

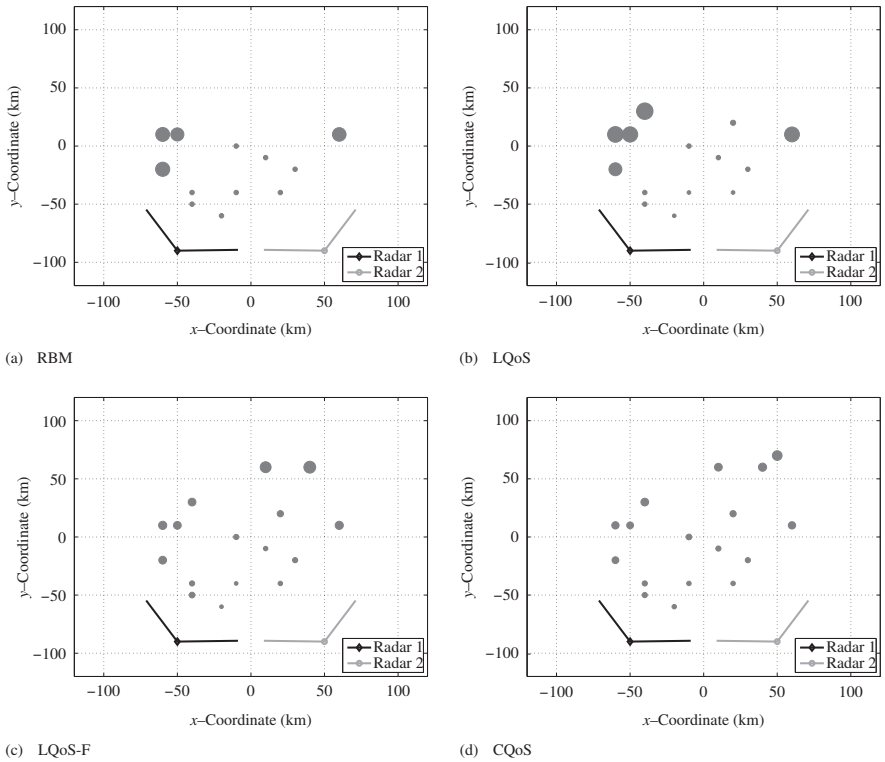

Figure 15.11 Track quality, which is taken as the estimation error, is illustrated by the size of the circle for the different resource management methods and network configurations

management can eliminate redundancy in the radar network's resource allocation, resulting in an increase in the number of tracked targets and a reduction in the track error. It was also shown that performing independent QoS management at each node while fusing the data in the network is performant with lesser requirements on communication and coordination.

Abbreviations

CQoS	centralized quality of service
FIM	Fisher information matrix
KKT	Karush–Kuhn–Tucker
LQoS	local quality of service
LQoS-F	local quality of service with feedback
MSQRAM	multiple resources quality of service resource allocation method

PCRLB	posterior Cramer–Rao lower bound
QoS	quality of service
Q-RAM	quality of service resource allocation method
RBM	rule-based method
RMSE	root mean square error
SNR	signal-to-noise ratio

References

[1] Baker C.J. 'An introduction to multistatic radar'. Tech. rep., RTO-EN-SET-133, 2009.

[2] Griffiths H.D. 'Multistatic, MIMO and networked radar: The future of radar sensors?'. *European Radar Conference*, 2010, pp. 81–84.

[3] Smits F., Huizing A., van Rossum W., Hiemstra P. 'A cognitive radar network: Architecture and application to multiplatform radar management'. *European Radar Conference*, 2008, pp. 312–315.

[4] Kester L. 'Method for designing networking adaptive interactive hybrid systems'. *Interactive Collaborative Information Systems*, 2010. 281:401–421.

[5] Watson G.A. 'Multisensor ESA resource management'. *IEEE Aerospace Conference*, vol. 5. IEEE, 1998 pp. 13–27.

[6] Blackman S.S., Dempster R.J., Roszkowski S.H., Sasaki D.M., Singer P.F. 'Improved tracking capability and efficient radar allocation through the fusion of radar and infrared search-and-track observations'. *Optical Engineering*, 2000. 39(5):1391.

[7] Liggins M.E., Chong C. 'Distributed multi-platform fusion for enhanced radar management'. *IEEE National Radar Conference*, 1997, pp. 115–119.

[8] Strömberg D., Andersson M., Lantz F. 'On platform-based sensor management'. *5th International Conference on Information Fusion*, 2002, pp. 600–607.

[9] Punithakumar K., Kirubarajan T., Hernandez M.L. 'Adaptive sensor placement for target tracking in the presence of uncertainties'. *SPIE Signal and Data Processing of Small Targets*, vol. 5204, 2003, pp. 608–619.

[10] Punithakumar K., Kirubarajan T., Hernandez M. 'Multisensor deployment using PCRLBS, incorporating sensor deployment and motion uncertainties'. *IEEE Transactions on Aerospace and Electronic Systems*, 2006. 42(4): 1474–1485.

[11] Akselrod D., Lang T., McDonald M., Kirubarajan T. 'Markov decision process-based resource and information management for sensor networks'. In *Sensor Networks*, pp. 167–216. Berlin: Springer, 2009.

[12] Ragi S., Chong E. 'UAV path planning in a dynamic environment via partially observable Markov decision process'. *IEEE Transactions on Aerospace and Electronic Systems*, 2013. 49(4):2397–2412.

[13] Chhetri A.S., Morrell D., Papandreou-Suppappola A. 'Energy efficient target tracking in a sensor network using non-myopic sensor scheduling'. *7th International Conference on Information Fusion*, 2005 pp. 558–565.
[14] Powell W.B. *Approximate Dynamic Programming*. Wiley-Blackwell, 2011.
[15] Hernandez M. 'Performance bounds for target tracking: Computationally efficient formulations and associated applications'. In M. Mallick, V. Krishnamurthy, B.N. Vo (eds.), *Ingegrated Tracking, Classification, and Sensor Management*, chap. 7, pp. 255–310. Wiley, 2013.
[16] van Trees H., Bell K. (eds.). *Bayesian Bounds for Parameter Estimation and Nonlinear Filtering/Tracking*. Wiley-Blackwell, 2007.
[17] Tichavsky P., Muravchik C.H., Nehorai A. 'Posterior Cramér–Rao bounds for discrete-time nonlinear filtering'. *IEEE Transactions on Signal Processing*, 1998. 46(5):1386–1396.
[18] Zhang X., Willett P., Bar-Shalom Y. 'Dynamic Cramer–Rao bound for target tracking in clutter'. *IEEE Transactions on Aerospace and Electronic Systems*, 2005. 41(4):1154–1167.
[19] Boers Y., Driessen H. 'Results on the modified Riccati equation: Target tracking applications'. *IEEE Transactions on Aerospace and Electronic Systems*, 2006. 42(1):379–384.
[20] Farina A., Ristic B., Timmoneri L. 'Cramer–Rao bound for nonlinear filtering with Pd < 1 and its application to target tracking'. *IEEE Transactions on Signal Processing*, 2002. 50(8):1916–1924.
[21] Chavali P., Nehorai A. 'Scheduling and power allocation in a cognitive radar network for multiple-target tracking'. *IEEE Transactions on Signal Processing*, 2012. 60(2):715–729.
[22] McIntyre G.A., Hintz K.J. 'Information theoretic approach to sensor scheduling'. *SPIE Signal Processing, Sensor Fusion, and Target Recognition V*, vol. 2755. SPIE, Orlando, FL, USA, 1996 pp. 304–312.
[23] Hero A.O., Castanon D.A., Cochran D., Kastella K.D. 'Information theoretic approaches to sensor management'. In *Foundations and Applications of Sensor Management*, pp. 33–57. Springer US, 2008.
[24] Zhao F., Shin J., Reich J. 'Information-driven dynamic sensor collaboration'. *IEEE Signal Processing Magazine*, 2002. 19(2):61–72.
[25] Romero R.A., Goodman N.A. 'Adaptive beamsteering for search-and-track application with cognitive radar network'. *IEEE Radar Conference*, 2011 pp. 1091–1095.
[26] Romero R.A., Goodman N.A. 'Cognitive radar network: Cooperative adaptive beamsteering for integrated search-and-track application'. *IEEE Transactions on Aerospace and Electronic Systems*, 2013. 49(2):915–931.
[27] Cover T.M., Thomas J.A. *Elements of Information Theory*. Wiley, 2nd ed., 2006.
[28] Aoki E.H., Bagchi A., Mandal P., Boers Y. 'A theoretical look at information-driven sensor management criteria'. *14th International Conference on Information Fusion*, 2011, pp. 1–8.

[29] Kalandros M., Pao L.Y. 'Randomization and super-heuristics in choosing sensor sets for target tracking applications'. *38th IEEE Conference on Decision and Control*, 1999, pp. 1803–1808.
[30] Kalandros M. 'Covariance control for multisensor systems'. *IEEE Transactions on Aerospace and Electronic Systems*, 2002. 38(4):1138–1157.
[31] Kalandros M., Pao L.Y. 'Multisensor covariance control strategies for reducing bias effects in interacting target scenarios'. *IEEE Transactions on Aerospace and Electronic Systems*, 2005. 41(1):153–173.
[32] Ranasingha M.C., Murthi M.N., Premaratne K., Fan X. 'Transmission rate allocation in multisensor target tracking over a shared network.' *IEEE Transactions on Systems, Man, and Cybernetics*, 2009. 39(2):348–62.
[33] Barton D.K. *Radar Systems Analysis and Modelling*. Artech House, rev. 1st. ed., 2004.
[34] Blackman S., Popoli R. *Design and Analysis of Modern Tracking Systems*. Artech House, 1999.
[35] Williams J.L., Fisher J.W., Willsky A.S. 'Performance guarantees for information theoretic active inference'. *Proceedings of the International Conference on Artificial Intelligence and Statistics*, 2007 pp. 616–623.
[36] Charlish A.B., Hoffmann F. 'Anticipation in cognitive radar using stochastic control'. *IEEE International Radar Conference*. Washington, DC, 2015, pp. 1692–1697.
[37] Rajkumar R., Lee C., Lehoczky J., Siewiorek D. 'A resource allocation model for QoS management'. *18th Real-Time Systems Symposium*. San Francisco, CA, 1997 pp. 298–307.
[38] Lee C., Lehoczky J., Siewiorek D., Rajkumar R., Hansen J. 'A scalable solution to the multi-resource QoS problem'. *20th IEEE Real-Time Systems Symposium*, 1999 pp. 315–326.
[39] Nadjiasngar R., Charlish A.B. 'Quality of service resource management for a radar network'. *IEEE Radar Conference.* Johannesburg, 2015, pp. 1–6.
[40] Charlish A.B., Nadjiasngar R. 'Quality of service management for a multi-mission radar network'. *Computational Advances in Multi-Sensor Adaptive Processing (CAMSAP)*. Cancun, 2015, pp. 1–4.
[41] Rajkumar R., Lee C., Lehoczky J., Siewiorek D. 'Practical solutions for QoS-based resource allocation problems'. *19th IEEE Real-Time Systems Symposium*. Madrid, Spain, 1998 pp. 296–306.
[42] Nadjiasngar R., Charlish A.B. 'A performance model for target tracking with a radar network'. *IEEE Radar Conference*. Johannesburg, 2015, pp. 1–6.

Index

Note: Page numbers preceded by "***V1***:" and "***V2***:" refer to Volume 1 and Volume 2, respectively.

Novel Radar Techniques and Applications

Volume 2: Waveform Diversity and Cognitive Radar, and Target Tracking and Data Fusion

Novel Radar Techniques and Applications presents the state-of-the-art in advanced radar, with emphasis on ongoing novel research and development and contributions from an international team of leading radar experts. Each section gives an overview of the latest research and perspectives of the future, and includes a number of chapters dedicated to specific techniques in conjunction with existing operational, experimental or conceptual applications.

This volume covers:

- **Waveform diversity and cognitive radar**, including holistic design of physical radar emissions; waveform design for spectral coexistence; adaptive OFDM waveform design for spatio-temporal-sparsity exploited STAP radar; applications of noise radar; bio-inspired radar techniques; concept of the intelligent radar network; clutter diversity; and cognitive radar management.
- **Target tracking and data fusion**, including posterior Cramér-Rao bounds for target tracking; tracking and fusion in log-spherical state space with application to collision avoidance and kinematic ranging; multistatic tracking for passive radar applications; radar-based ground surveillance; multiplatform radar surveillance for aerial and maritime surveillance; person tracking and data fusion for UWB radar applications; and sensor management for radar networks.

The companion volume 1 covers real aperture array radar, imaging radar (SAR, ISAR), and passive and multistatic radar.

About the Editors

Richard Klemm has recently retired after a distinguished career at FGAN FHR (now Fraunhofer FHR), a research institute working in the areas defence and security, and decades of service to the radar community. In his spare time Richard Klemm is a passionate classical pianist.

Hugh Griffiths holds the THALES/Royal Academy Chair of RF Sensors in the Department of Electronic and Electrical Engineering at University College London, England.

Wolfgang Koch is head of the Sensor Data and Information Fusion (SDF) department at Fraunhofer FKIE, an institute of the Fraunhofer Society, the largest institution for applied research in Europe.

ISBN 978-1-61353-226-3

9 781613 532263

Radar, Sonar & Navigation

SciTech Publishing an imprint of the IET/The Institution of Engineering and Technology • www.theiet.org

978-1-61353-226-3